STRUCTURAL AND GEOCHEMICAL EVOLUTION OF THE ROSARIO COPPER-MOLYBDENUM PORPHYRY DEPOSIT AND RELATED COPPER-SILVER VEINS, COLLAHUASI DISTRICT, NORTHERN CHILE

by

Glenton John

Glenton J. Masterman B.Sc. (Hons)

UNIVERSITY OF TASMANIA

Submitted in fulfilment of the requirements for the degree of Doctor of Philosophy

University of Tasmania

Australia

June, 2003

CODES SRC

Centre for Ore Deposit Research

Declaration and Statement on Authority of Access

This thesis contains no material which has been accepted for a degree or diploma by the University or any other institution and, to the best of my knowledge and belief, contains no material published or written by another person except where due acknowledgement is made in the text of this thesis.

Glenton Masterman

Date: 19/6/03

This thesis is not to be made available for loan and copying until January 1, 2004. Following that time, this thesis may be made available for loan and limited copying in accordance with the Copyright Act 1968.

Abstract

The Rosario Cu-Mo-Ag deposit is located in the Collahuasi district of northern Chile. It comprises high-grade Cu-Ag-(Au) epithermal veins, superimposed onto the core of a porphyry Cu-Mo orebody. Rosario has mining reserves of 1,094 Mt at 1.03% Cu. An additional 1,022 Mt at 0.93% Cu occurs in the district at the Ujina and Quebrada Blanca porphyry deposits. The Collahuasi district constitutes the northernmost known occurrence of late Eocene-early Oligocene porphyry deposits in Chile.

The Rosario deposit is hosted within Early Permian basement comprising a sequence of northeast dipping volcanic and sedimentary rocks. This package is characterised by basal submarine andesitic and upper subaerial dacitic to rhyodacitic (U/Pb age = 293 ± 14 Ma) facies. Graded feldspathic sandstones are interbedded with the andesites and dacites. Limestone lenses, interfingered with the dacite, are consistent with emergence of the submarine sequence, and a shallow subaqueous to subaerial volcanic arc depositional setting is inferred for the Permian host rocks. The volcanic sequence was intruded by Early Triassic granodiorite (U/Pb age = 245 ± 12 Ma) and late Eocene porphyritic quartz-monzonite ($^{40}Ar/^{30}Ar$ cooling age of primary biotite = 34.4 ± 0.4 Ma).

High-grade copper ore is hosted by the Rosario fault system, a series of northwest-trending faults that dip 50° southwest. Detailed structural mapping indicates that the main mineralising events at Rosario coincided with normal movement on this fault system. The main faults were reactivated as dextral wrench faults after the period of copper deposition. At Cerro La Grande, similar high-grade copper veins are hosted in north-northeast-trending, sinistral wrench faults. Normal movement on the Rosario fault system is inferred to have been synchronous with sinistral strike-slip deformation at La Grande. Stress modelling indicates that this brittle deformation event occurred under southeast-directed compression.

The Permian basement has been uplifted, relative to Mesozoic rocks west of Collahuasi, along the north-striking Domeyko Fault System. This 2000 km long, arc-parallel fault system consists of a series of fault segments, which are interpreted to be inverted basin-margin normal and strike-slip faults with highly varied movement senses. The orientation of the principal compressive stress axes in post-Eocene strike-

slip deformation at Rosario is consistent with that inferred for sinistral movement, during the same period, on the Domeyko fault system. However, this local paloestress regime is inconsistent with the regional stress expected for north-northeast-directed convergence during the late Eocene-early Oligocene, and implies that upper and lower crustal stresses were decoupled.

The calc-alkaline Rosario Porphyry is characterised by concave upwards REE profiles, and high La/Yb (>20) and Sr/Y (>20) values. Lead isotope data define a limited range bracketed by values of the Paleozoic host rocks. Initial $^{87}Sr/^{86}Sr$ and $^{143}Nd/^{144}Nd$ values range from 0.7050 to 0.7053 and 0.5124 to 0.5126, respectively. Although high Sr/Y values are a characteristic of adakites, the radiogenic isotopic signatures and high La/Yb values, indicate the ore-related magmas were derived from garnet-fractionated MASH zones at the mantle-crust interface, rather than from partial melting of subducted oceanic crust.

Hydrothermal alteration at Rosario is characterised by a K-feldspar altered core, focused on the Rosario Porphyry, that grades out to a secondary biotite-albite-magnetite assemblage. Paragenetic relations indicate that magnetite was the earliest-formed alteration product, but has been replaced by biotite-albite. Vein cross-cutting relationships indicate that K-feldspar formed during and after biotite-albite alteration. Chalcopyrite and bornite were deposited in quartz veins associated with both K-feldspar and biotite-albite assemblages. The hydrothermal fluid responsible for early alteration and mineralisation was a hypersaline brine (40 to 45 wt. % NaCl) that coexisted with vapour between 400° and >600°C. Weakly mineralised illite-chlorite (intermediate argillic) alteration of the early K- and Na-silicate assemblages was caused by moderate temperature (250° to 350°C), moderate salinity brines (10 to 15 wt.% NaCl). Molybdenite was precipitated in quartz veins during the transition between potassic and intermediate argillic alteration. These fluids were 350° to 400°C with salinities between 10 and 15 wt. % NaCl.

Porphyry-style ore and alteration minerals were overprinted by structurally-controlled quartz-alunite-pyrite, pyrophyllite-dickite and muscovite-quartz (phyllic) alteration assemblages. The quartz-alunite-pyrite alteration formed at 32.6 ± 0.3 Ma ($^{40}Ar/^{39}Ar$ age of alunite) from 300° to 400°C and 10 wt.% NaCl fluids. The pyrophyllite-dickite assemblage formed between 250° and 320°C from dilute (5 wt. % NaCl) fluids. An upward flared phyllic alteration zone surrounds the fault-controlled

domain of advanced argillic alteration. Muscovite from the phyllic assemblage has an $^{40}Ar/^{39}Ar$ age of 32.9 ± 0.6 Ma, indistinguishable from the age of earlier-formed alunite. Thick veins (0.5 to 2 m wide) of fault-hosted massive pyrite, chalcopyrite and bornite precipitated from 30 wt. % NaCl brines at temperatures of 250° to 300°C. Based on the vein and alteration paragenesis, sulfide deposition occurred after alteration of the rock by quartz-alunite-pyrite, but before pyrophyllite-dickite alteration.

The early, high temperature mineralising solutions were oxidised ($H_2S/SO_4 \approx 1$) and had a bulk sulfur composition ($\Sigma^{34}S$) of 3 per mil. The $\delta^{18}O$ composition of the fluids in equilibrium with hydrothermal biotite was 8.0 to 8.3 per mil, typical of hypersaline liquid exsolved from felsic magma. Cooling below 400°C, in the presence of H_2S, potentially deposited sulfides in the early veins, thus accounting for about half of the copper at Rosario. The acidic water that deposited alunite formed when magmatic vapour (+5.8 ‰ $\delta^{18}O$ and –30 ‰ δD) condensed into liquid, together with minor mixing with meteoric water. The bulk sulfur composition of the fluid was 3 per mil and the fluid was reducing ($H_2S/SO_4 \approx 5$), even though alunite is abundant.

The late, massive pyrite, chalcopyrite, bornite veins appear to have been associated with half of the total copper deposition. Textures indicative of hydraulic brecciation in massive sulfide veins, implies fluid overpressuring. Sulfide deposition potentially responded to flashing of slightly reduced brine ($H_2S/SO_4 \approx 2$), induced by hydraulic rupturing in the veins. The latest fluids, isotopically stable with pyrophyllite, consisted of mixed magmatic-meteoric water (-3 to –1.6 ‰ $\delta^{18}O$). Mixing of the magmatic fluids with meteoric water possibly caused deposition of tennantite and enargite.

Pressure-depth estimates indicate that at least 1 km of rock was eroded at Rosario between formation of the K-Na silicate and advanced argillic assemblages. This erosion was rapid, as $^{40}Ar/^{39}Ar$ geochronology indicates that a 1.8 m.y. period separates the early and late alteration events. The observed brittle structures did not control intrusion of the Rosario Porphyry, but may have indirectly influenced its emplacement. The Rosario Porphyry intruded immediately after the Incaic tectonic phase, implying that it was emplaced as the Domeyko Cordillera underwent gravitational collapse, consistent with the hypothesis that upper and lower crustal stresses were different. Gravitational slides potentially accelerated exhumation and

helped to promote telescoping of the high-sulfidation environment onto the Rosario Porphyry. Localisation of high-grade copper in the Rosario Fault System indicates that normal faults had developed in the Rosario deposit by at least 32.6 Ma.

The porphyry ore forming hydrothermal system at Rosario was partially exhumed prior to the formation, 1.8 m.y later, of high-sulfidation ore and alteration assemblages. Cooling and collapse of the Rosario porphyry hydrothermal system implies emplacement of a second blind intrusion, somewhere beneath the Rosario and Cerro La Grande high-sulfidation vein systems. Precious metal and sulfosalt zoning at the district scale, together with the overall fault geometries, suggest that rejuvenated magmatic-hydrothermal activity was focused beneath Cerro La Grande. Exploration for additional copper resources in the Rosario area should thus be guided by the distribution of phyllic assemblage beneath Cerro La Grande, as this alteration represents the root zone of the epithermal system, and potentially occurs at the top of an as-yet undrilled porphyry-style ore deposit.

Acknowledgements

First and foremost, I thank my wife Emma. This thesis would never have been possible without her love, support, encouragement and sacrifice. The home fire was always burning, and done in addition to raising our wonderful twin boys and being the sole provider for our family during the last six months of my postgraduate tenure. To Alex and Lachlan, thank you for coping with a graduate father these past two years.

I owe a great debt of gratitude to my supervisor Dr. David Cooke. Dave rescued me after my initial project crashed two months into my PhD. Ultimately he secured what I think was my ideal project. I thank him for his patience, understanding and perseverance. Dave, it was a fun journey and thanks also for those special travel moments. I doubt that I'll ever again see a suitcase compressed to the size and shape of a fútbol. I also thank Dave's wife Helen, who took our children off our hands on the occasions when Emma and I needed a break from it all.

I am grateful to my co-supervisors Drs. Ron Berry and John Walshe. Ron set me straight on the finer points of brittle structure, and completed numerous audits of my geological model. John I thank for the inspiring and insightful discussions over pizza and that something red. Thank you also for guiding me to the dark side of "sulfide replacement textures."

I thank all the geological staff from Compañia Minera Doña Inés de Collahuasi for obliging my visits, indulging my ideas and looking after me in the field. In particular I thank Manuel Durán, Héctor Lagunas, Claudio Bisso and Luciano Malhue. Ryan and Carmen Crosbie provided enormous support during my time in Chile. Their efforts to teach me Spanish were commendable, although my "rough" Castellano is by no means a reflection of their tuition. Ryan and Carmen also provided accommodation in Iquique on the weekends that I descended from the Andes for sea level "R and R." Thank you both for your friendship and generosity, and for saving me from the Hotel Barros Arana!

This project was sponsored by AMIRA International, and I thank Joe Cacuzza (AMIRA) and also Gem Midgley (formerly CSIRO) for their administration efforts. I would like to thank Francisco Camus and Jorge Skarmeta from Codelco. They arranged our visits to some spectacular Chilean copper deposits and guided several of our traverses through the Andes. I am also grateful to John-Mark Staude (BHP

Billiton) who supported my Re/Os work, and to Ryan Mathur (University of Arizona) for completing the analyses. I thank the Society of Economic Geologists for provision of a McKinstry student research grant in support of the geochronologic work.

To Alan Clark, Doug Archibald, Tom Ulrich, Kurt Kyser, Kerry Glassen and Joan Charboneau at Queens University, Kingston, Ontario. Thankyou for the help with the geochronologic and stable isotope analyses, as well as the logistics of travel in Ontario and accommodation in Kingston. In particular I thank Alan Clark for offering to collaborate and the thorough reviews of my "geochron chapter."

Thank you also to the other CODES academic staff including Tony Crawford and Pete Hollings who explained some of the inexplicable of igneous geochemistry. I also thank Sebastian Meffre for dating my zircons, Andrew Rae for teaching me the art of bubble bursting, and Fernando Della-Pasqua for handling my mineral separation requirements. I thank Noel White, Ross Large and Garry Davidson for organising a project that lured me to CODES in 1999 (before the birth of Collahuasi). Unfortunately we never got to Kamchatka, but at least we avoided the brown bears and black flies! Noel also reviewed several chapters in this thesis, for which I am very grateful.

To my current and former postgraduate colleagues who include Andy Stewart, Andrew Wurst, Neil Martin, Darryl Clark, Vanessa Lickfold, Steve Bodon, Alan Wilson, Peter Frikken, Andrew Davies, Kirstie Simpson, James Cannell, Karin Orth, Owen Hatton, Mike Agnew and Ben Jones. Thankyou for the friendship, support and encouragement. Sarah Jones and Mike Piper are especially thanked for their friendship and for opening their home to me at various times during the past few years.

I am also grateful to the CODES and Earth Sciences administrative staff L. Lazcano-Frikken, J. Pongratz, N. Hlaing, D. Steffans, C. Higgins and L. Star and the technical staff P. Cornish, S. Stevens, P. Robinson, and K. McGoldrick.

Finally I thank my extended families, the Mastermans and the Harrisons, for their love, support and encouragement, and for attending in times when we needed them!

Table of Contents

List of Figures

List of Tables

Chapter 1. Introduction

Preamble

Porphyry deposits in the central Andes constitute one of the largest concentrations of copper on Earth. In Chile, a total resource (including production) of 430 million tonnes of fine Cu has been identified in 55 porphyry Cu deposits (Camus, 2002), the most significant of which are shown in Figure 1.1 and listed in Table 1.1. Clark (1993) defined "giant" porphyry Cu deposits as those that contained >10 Mt of fine Cu. Chile is endowed with nine of the 17 giants located around the Circum-Pacific region. The three largest porphyry Cu deposits known, El Teniente, Rio Blanco-Los Bronces and Chuquicamata, all occur in Chile. The Collahuasi district is a porphyry province that potentially rivals those of El Teniente, Rio Blanco-Los Bronces and Chuquicamata, all of which contain in excess of 50 Mt of fine Cu (Camus, 2002).

Why are the terranes in northern and central Chile so well endowed, yet others are apparently not? Moreover, how and why do high-grade hypogene porphyry Cu deposits form? In a review of porphyry ore deposits worldwide, Clark (1993) concluded that the characteristics of the giants are no different to their smaller counterparts. Because the anatomy and environment of ore formation are not unique to either small or large porphyry deposits, understanding the processes of formation is required in order to approach the questions of what makes a quality deposit and in which terrane. The architectural and geodynamic setting, the nature of fluid reservoirs, mechanisms of fluid flow and the chemistry of metal transport and deposition are all important considerations towards understanding the basic and common elements of hydrothermal systems associated with porphyry ore deposits. Integration of information across various scales is critical, as regional-scale geophysical and isotopic data, combined with that generated at the deposit-scale, are fundamentally modifying perceptions of the physical dimensions of hydrothermal systems. Thus a holistic view is required to understand the formation of giant deposits, as they are the result of interactions on the scale of the whole system, rather than only at the site of deposit formation.

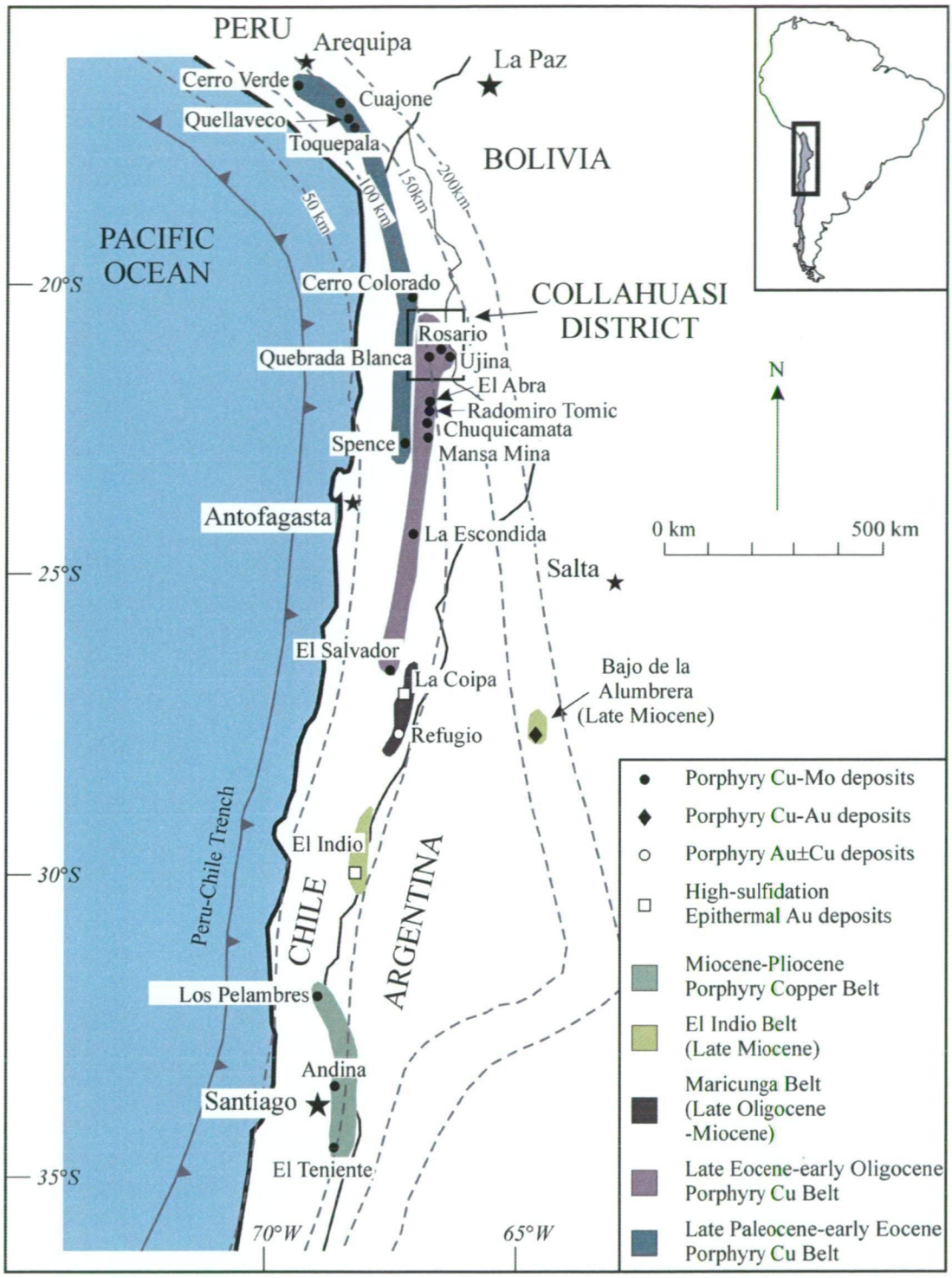

Figure 1.1. Map showing the major copper and gold deposits in Chile and western Argentina. Metallogenic belts of the five major copper provinces are also shown. Dashed contour lines are the depths to the Wadiff-Beniof zone. Modified from Muntean and Einaudi (2000).

Table 1.1. Summary of the key porphyry Cu-Mo deposits in Chile. Data for resources and contained metals from Camus (2002). Note that the contained metal data includes resource plus production figures.

Name	Age (Ma)	Resource (Mt)	Grades	Contained metal (metric tonnes)	Host rocks	References
El Teniente	7.1 to 4.6	12, 482	Cu: 0.63% Mo: 0.02% Au:0.04 g/t	Cu: 94.4 Mt Mo: 2.5 Mt Au: 437 t	andesite, diorite, dacite, tonalite, diatreme	(Camus, 1975; Clark et al., 1983; Skewes and Stern, 1995; Camus, 2002)
Chuquicamata	34 to 31	7,521	Cu: 0.55% Mo: 0.024% Au: 0.04	Cu: 66.4 Mt Mo: 1.8 Mt Au: 301 t	monzodiorite, granodiorite	(Lindsay et al., 1995; Camus, 2002)
Rio Blanco-Los Bronces	7.2 to 4.9	6,991	Cu: 0.75% Mo: 0.024% Au: 0.04 g/t	Cu: 56.7 Mt Mo: 1.3 Mt Au: 245 t	Granodiorite, biotite & tourmaline breccias, monzonite, andesite	(Warnaars et al., 1985; Skewes and Stern, 1995; Serrano et al., 1996; Vargas et al., 1999; Camus, 2002)
La Escondida	38, 35 to 31	2,262	Cu: 1.15% Mo: 0.021% Au: 0.1 g/t	Cu: 32.5 Mt Mo: 0.5 Mt Au: 226 t	Dacite, rhyolite, monzonite	(Zentilli and Maksaev, 1996; Richards et al., 1999)
Los Pelambres-El Pachon	10 to 8.9	4,193	Cu: 0.63% Mo: 0.02% Au: 0.02 g/t	Cu: 26.9 Mt Mo: 0.7 Mt Au: 84 t	Qtz-diorite, andesite, biotite breccia	(Sillitoe, 1988; Skewes and Stern, 1995; Atkinson et al., 1996; Camus, 2002)
Rosario	34 to 32	3,108 Mt	Cu: 0.82% Mo: 0.024% Au: 0.01 g/t	Cu: 25.5 Mt Mo: 0.7 Mt Au: 31 t	Monzonite, rhyolite, andesite	(DeBeer and Dick, 1994; Camus, 2002; Moore and Masterman, 2002)
Radomiro Tomic	33 to 32	4,970 Mt	Cu: 0.39% Mo: 0.15% Au: 0.0 g/t	Cu: 19.9 Mt Mo: 0.7 Mt Au: 0 t	Granodiorite, monzogranite	(Cuadra and Camus, 1998)

Project Aims and Objectives

This work constitutes part of AMIRA Project P511 (Giant Ore Deposit Systems), an industry-funded project involving collaborative research between the CSIRO Division of Exploration and Mining, the Centre for Ore Deposit Research (CODES – University of Tasmania) and the Centre for Global Metallogeny (CGM – University of Western Australia). The project consisted of three modules, which have focused on Archaean lode Au, Papua New Guinea Au-Cu and Chilean porphyry Cu-molybdenum deposits. Research for this PhD thesis was carried out in the porphyry Cu module, managed by CODES and CSIRO, and was conducted in the Collahuasi district, located at the northern end of the Eocene-Oligocene metallogenic belt in northern Chile. Most of the work was undertaken at the Rosario Co-Mo porphyry deposit and on the related

massive sulfide Cu-Ag-Au veins, although limited work was also carried out at the Ujina Cu-Mo porphyry deposit.

The main aims of this PhD project were to determine how the following factors are related to formation of the giant Rosario Cu-Mo porphyry deposit and related massive sulfide Cu-Ag-Au veins at both Rosario and elsewhere in the Collahuasi district:

(1) Basement architecture and tectonic setting

The impact of basement architectures, inherited during Paleozoic accretion and Mesozoic rifting, on Cenozoic evolution of the continental margin in northern Chile is reviewed in Chapter 2. Detailed structural maps and sections of the Rosario deposit, presented in Chapter 3, have been compiled to establish a robust model of the structural evolution in the Rosario area. This model, integrated up-scale to encompass the Collahuasi district, evaluates whether the regional structural architecture was important in focusing porphyry-related magmatism at Rosario, and in the district as a whole. Furthermore, the significance of Cenozoic subduction-related compression, basin inversion and fold and thrust belt development, as it relates to porphyry ore formation, is compared and contrasted with the models of strike-slip movement on the Domeyko Fault System. Changes in the rate and direction of plate convergence, and the relationship to the angle of subduction of the oceanic lithosphere are also examined, with respect to the timing of magmas associated with the Collahuasi porphyry ore deposits. Chapter 4 provides results of the igneous geochemistry from the Paleozoic host rocks and ore-related intrusions. Petrogenetic models are discussed in terms of evolution of the Andean crust in northern Chile.

(2) Magma suites and source regimes

Geochemistry of the various mineralised and barren intrusions at Rosario, as well as the country rocks, are documented in Chapter 4. This chapter provides insights into the petrogenetic evolution of magmatism in the Collahuasi district in response to changes in the tectonic regime between the Paleozoic and Cenozoic. Radiogenic isotope tracing and trace element geochemistry are used to assess crustal thickness and magma source regimes during the critical period of porphyry ore formation. In particular, the generation of anhydrous mineral assemblages and their potential as a source of fluids is discussed.

(3) Uplift rates

Determining the rate of exhumation in the Collahuasi district, relative to the timing of magma emplacement and ore formation at Rosario, has been a major objective of this research project. One of the ways to evaluate the rate and magnitude of uplift is to estimate the formation depth of temporally constrained ore and alteration mineral assemblages. The distribution and paragenesis of these assemblages in the Rosario and La Grande deposits were therefore mapped and sections compiled. The Rosario hydrothermal system is described in Chapter 5, and provides a framework for the isotopic geochronology ($^{40}Ar/^{39}Ar$ and Re/Os) and fluid inclusion studies presented in Chapters 6 and 7, respectively. Pressure-depth estimates obtained in the fluid inclusion study, combined with results of the radiogenic age dating, are used to estimate the magnitude and rate of exhumation that occurred at Rosario as the hydrothermal system evolved (Chapter 7). Whether or not exhumation favoured the formation of high-grade hypogene resources by the superposition (telescoping) of epithermal mineralisation into the porphyry environment is discussed in Chapter 8.

(4) Relative contributions of magmatic and external waters

Stable and radiogenic isotope tracing was completed on ore and alteration minerals to establish the origin of hydrothermal fluids, metals and sulfur in the various stages of ore formation at Rosario and La Grande (Chapter 7). The role of external waters that potentially entered or were present near the mineralised system is investigated. Oxygen and hydrogen compositions of the hydrothermal fluids were calculated to evaluate whether fluid mixing, and/or water-rock interaction modified fluid compositions and whether the addition of Cu in the late massive sulfide veins was introduced by evolved magmatic or external waters. Moreover, the origin of the large amounts of reduced sulfur added during each of the mineralisation stages at Rosario is evaluated, along with the potential for Au to have been transported by these fluids (Chapter 7).

(5) Holistic model of ore formation at Rosario

Ultimately this research aims to produce a holistic model of porphyry and epithermal ore formation at the Rosario deposit, incorporating all of the factors detailed above. Chapter 8 presents a genetic model that explains how structure and tectonics, igneous petrogenesis and uplift rates influenced hydrothermal evolution, and culminated in large tonnage and high-grade ore at Rosario. Chapter 8 also states the main conclusions of this research project and highlights some implications for porphyry and epithermal exploration at Collahuasi.

Area of Study

Location, discovery and reserves

The Collahuasi district (20°58' S and 68°43' W) is located in northeastern Chile, about 250 km southeast of the port of Iquique (Fig. 1.2). It defines a 1200 km^2 area near the Western Cordillera and hosts a cluster of three porphyry copper-molybdenum deposits, associated high level epithermal copper-silver vein deposits, and paleogravel-hosted exotic Cu deposits (Fig. 1.3). The Quebrada Blanca, Rosario (Fig. 1.4a) and Ujina (Fig. 1.4b) porphyry copper-molybdenum deposits are currently in production, as well as the Huinquintipa exotic copper deposit.

Mining in the Collahuasi district commenced with the Incas around 1400 A.D., and continues to the present day. Historically, mining activity focused on the Cerro La Grande, Poderosa and Monctezuma areas where high-sulfidation Cu-Ag-Au and low-sulfidation Ag mineralisation crops out in high-grade veins (Fig. 1.3). Up to 300,000 T, grading 25% Cu, 180 g/t Ag, and 2 g/t Au, were mined from these veins until 1930.

Modern exploration was first conducted at Quebrada Blanca by the Chilean arm of Anaconda, where they recognized the geology and alteration zones to be consistent with the Lowell and Guilbert (1970) model for porphyry-style Cu ore. In 1973, a joint venture, controlled by Superior Oil, was formed with Falconbridge, and in 1977 the Quebrada Blanca deposit was chosen for detailed investigation, based on the results of previous work by Anaconda. Although Codelco drilled the first hole into Quebrada Blanca, the deposit was not delineated until the Superior Oil/Falconbridge Group optioned the property from the Chilean authorities. The Rosario and Ujina areas were optioned from private interests and exploration subsequently led to the discovery of the Rosario porphyry system in 1979. The project was recast as a joint venture between

Falconbridge, Shell Chile and Chevron, in response to corporate restructuring and difficult economic times. This joint venture was operated by a management company controlled by Chevron and Shell Chile, and it conducted exploration that eventually led to the discovery of the economically important Ujina porphyry deposit in 1991. The main exploration tools used were induced polarization, surface mapping, and reverse circulation drilling (Moore and Masterman, 2002).

Figure 1.2. Locality map of the Collahuasi district.

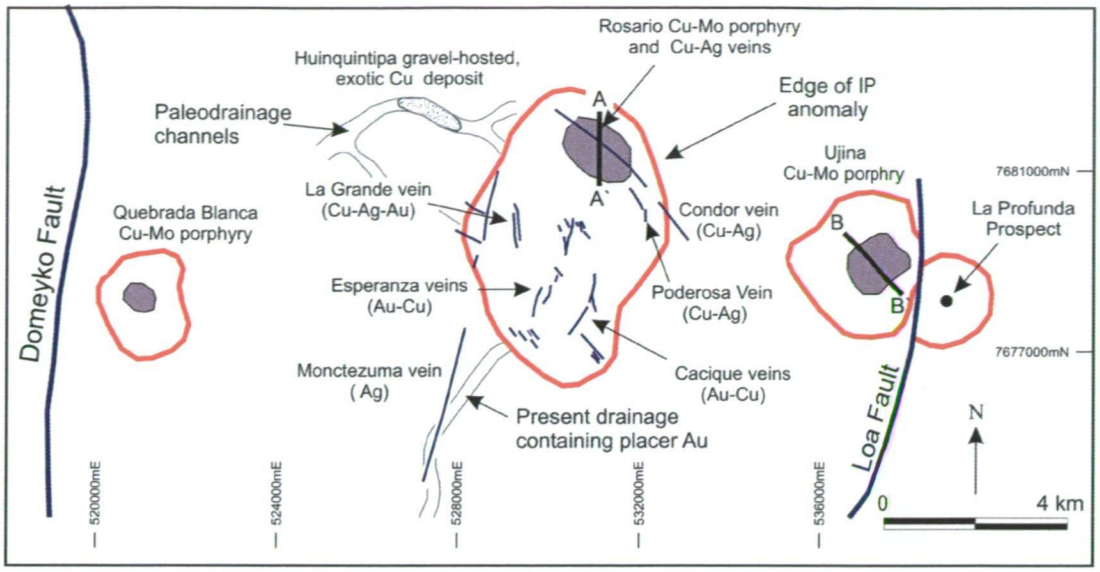

Figure 1.3. Schematic map showing the distribution of porphyry deposits and epithermal veins in the Collahuasi district. The IP anomalies surrounding each porphyry centre is interpreted to delimit the extent of hydrothermal alteration. The purple shaded areas are the outlines of mineralised zones. The gravel-hosted Huinquintipa exotic copper deposit occurs in a paleodrainage system that originated at Rosario. Present drainage systems south of Cerro La Grande contain placer gold. Section lines A-A' and B-B' represent cross-sections through the Rosario and Ujina deposits respectively. Modified from Dick et al. (1994).

With predominantly hypogene sulfide reserves of 1,094 Mt at 1.03% Cu (Moore and Masterman, 2002), Rosario constitutes an excellent example of an environment in which well-mineralised high-sulfidation style Cu-Ag veins have developed within a porphyry system. These veins have been estimated to account for approximately 10% of the hypogene Cu ore at Rosario (Dick et al., 1994). Mineral reserves, including hypogene and supergene (plus production), from the Ujina deposit, 7 km east of Rosario, are 741 Mt at 0.81% Cu (Moore and Masterman, 2002). La Profunda, a hydrothermally-altered intrusion intersected by drilling less than 2 km from Ujina has been tentatively identified as a further centre of mineralisation (Fig. 1.3). The Quebrada Blanca deposit, situated 8 km southwest of Rosario, contains reserves of 281 Mt at 1.23 % Cu. The Rosario and Ujina deposits are jointly owned by the consortium Falconbridge (44%), Anglo American (44%) and Mitsui (12%). Quebrada Blanca is owned 76.5% by Aur Resources, 13.5% by Sociedad Minera Pudahuel LTDA and 10% by Enami. Together, the deposits of the Collahuasi district comprise total reserves (plus production) of 2.2 Gt at 0.90% Cu.

Figure 1.4. **A)** Photograph looking northeast from Cerro La Grande across the Rosario deposit towards stratovolcanoes that define the border between Chile and Bolivia. This photograph was taken in April 1999, prior to the commencement of mining operations at Rosario in September 2002. **B)** Photograph of the Ujina open pit mine, looking east towards Volcan Olca (March, 2000). The bottom of the pit is about 400 m below the original land surface.

Access and working conditions

The Collahuasi district is situated in the Andes on a high, arid and dissected plateau between elevations of 3,800 and 6,200 m. Access is by sealed road that joins the Pan American Highway 150 km to the northwest of Collahuasi (Fig. 1.2). Unsealed roads via Quebrada Blanca to Pozo Almonte or to Calama, provide access by four-wheel-drive.

The high Andean region, in which Collahuasi is located, is known as the Altiplano. It consists of low hills, weakly incised within the plateau, but deeply incised along its western edge, from where it passes steeply down to the Longitudinal Valley 2,000 m below (Fig. 1.5). The eastern side of the Collahuasi district corresponds with the border between Chile and Bolivia, defined by a north-trending belt of stratovolcanoes that reach 5,000 to 6,200 m elevation (Fig. 1.6a). Collahuasi occurs near the Atacama Desert, and is subjected to a predominantly arid climate, typified by low annual rainfall (avg. 150 mm yr^{-1}) and rare snow (a few centimetres per year). Clear skies prevail 300 to 350 days a year and the prevailing winds are strong to light from the northwest. Seasons include normal summer and winter variations in temperature and precipitation, plus a summer monsoon season known as the "Bolivian winter."

During the normal "Chilean winter" (June to September) day time temperatures are +5° to –5°C and night time temperatures are –5° to -20°C. During summer months, (November to February) daytime temperatures range from 10° to 15°C with highs of 20°C. The bulk of precipitation occurs during the "Bolivian winter" (January to March) as afternoon showers, and rarely as hail or snow flurries, accompanied by spectacular lightning storms.

Altitude sickness is a common problem for workers in the Collahuasi district, and is most severe during the first weeks of a visit to the district. Working conditions are extreme, as exterior workers are commonly exposed to intense ultra-violet radiation and low humidity. The mine camp, located at Coposa, is situated at about 3,800 m elevation (Fig. 1.6b). The Ujina mine occurs at a surface elevation of 4,200 m, whereas Rosario and La Grande occur at 4,600 m and 4,800 m, respectively.

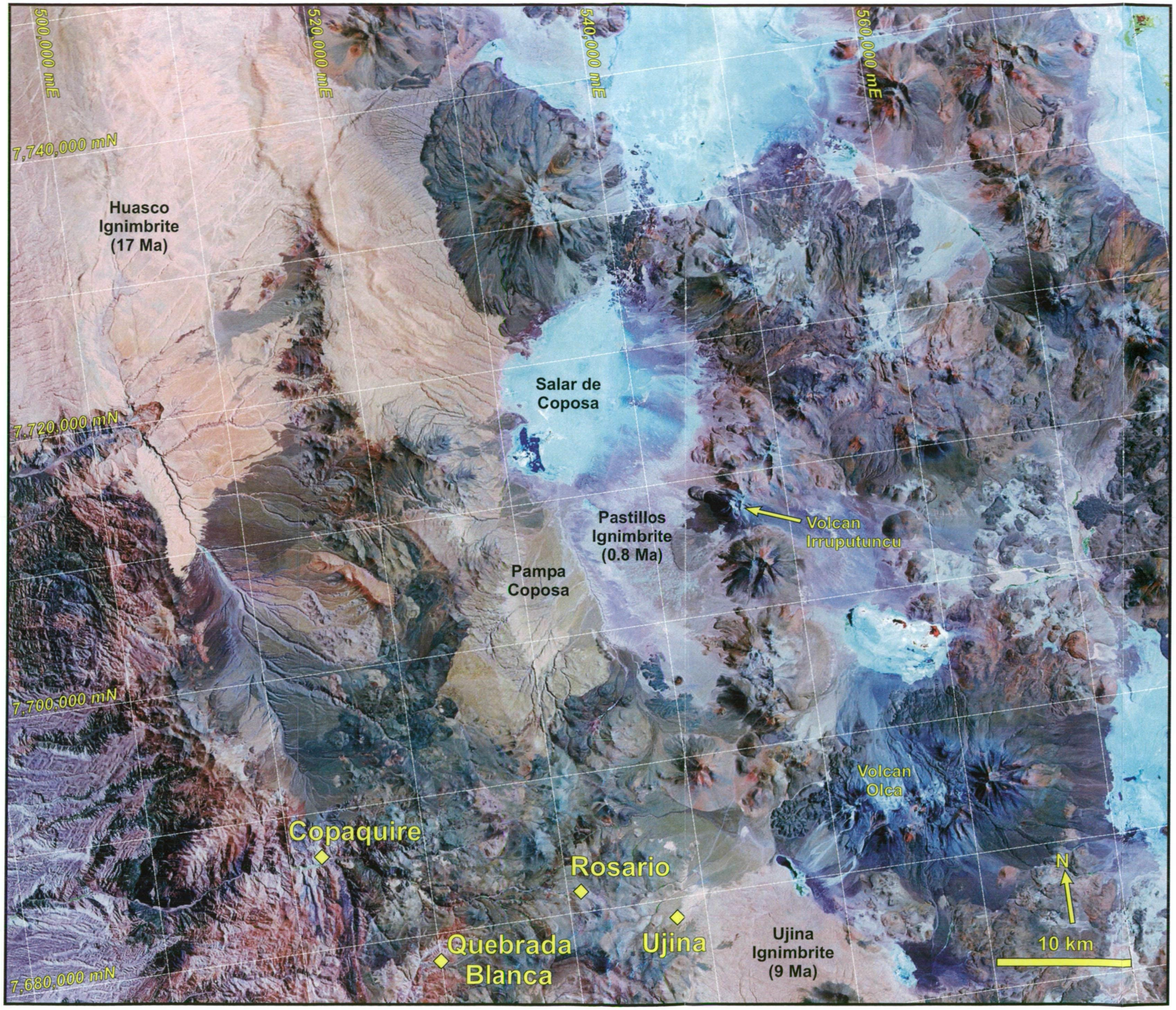

Figure 1.5. Landsat 741-SPOT merge image of the Collahuasi district. The image combines the colour information from a Landsat 741 image with the spatial detail from the SPOT black and white image. The image has been registered in the coordinate system UTM Zone 19, Southern Hemisphere (WGS 84). Locations of the Quebrada Blanca, Rosario and Ujina mines are shown for reference. Also shown is the Copaquire prospect, a molybdenite-rich, sub-economic porphyry system that crops out to the west of the Collahuasi district.

Previous work

Most of the previous work on the geologic setting of porphyry and epithermal ore at Rosario was completed by exploration geologists employed by Compañia Minera Doña Inés de Collahuasi. This work has been compiled as a series of internal company reports, the most notable of which was a detailed description of the geological setting of the Rosario deposit by Munchmeyer et al. (1984). A map of the regional geology of the 1:250,000 Collacagua map sheet, which encompasses the Collahuasi district, was provided by Vergara and Thomas (1984). Detailed work on sulfide paragenesis in the Rosario veins was published by Dick et al. (1994), and was followed shortly thereafter by a detailed study of the ore and alteration paragenesis in all hydrothermal stages at Rosario by Lee (1994). Two exploration shafts were sunk between 1985 and 1990 to explore the high-grade Rosario Vein System. Ultimately the program was unsuccessful as the high-grade Cu veins lacked continuity. Underground access along the main exploration drive and cross-cut was maintained until 1995. Between 1992 and 1993, Andy Lee mapped the underground workings, which included structural mapping of the Rosario Fault System.

All of the previous work at Rosario has been done at the scale of the deposit, and only limited attempts have been made to integrate the deposit models with tectonic events that occurred at the regional or continental margin scales. This research project builds on the previous work and seeks to integrate an understanding of the evolution of the Rosario ore forming system with the geodynamic and tectonic history of the Collahuasi district.

Field work

Mapping and sampling were completed during eight months fieldwork carried out over three field seasons between 1999 and 2001. Surface exposures in the Rosario area were mapped at scales of 1:10,000 regionally and 1:2,000 locally, using topographic map sheets provided by Compañia Minera Doña Inés de Collahuasi (CMDIC). This study has built on and modified previous high quality maps and geological interpretations by CMDIC exploration and mine geologists. Much of the area is covered by extensive alluvial gravel and scree, inhibiting continuous exposure of key rock unit and structural contacts. The best rock exposures occur on hill tops and along the numerous river valleys (quebradas). At Rosario, outcrop is restricted to slopes of valleys that have dissected the deposit. A system of northwest trenches and

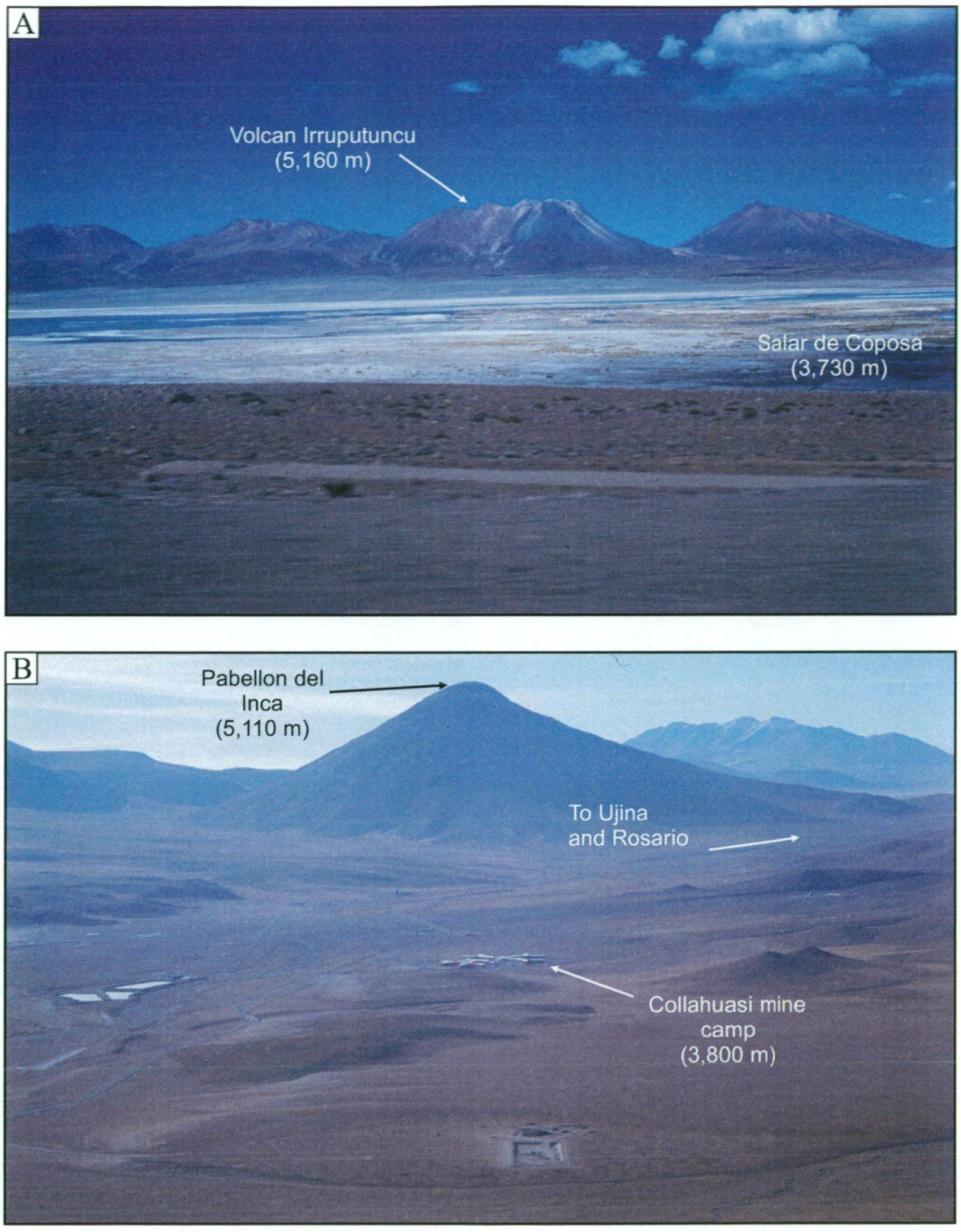

Figure 1.6. **A)** Photograph looking east to the stratovolcanoes that define the border between Chile and Bolivia. In the foreground is Salar de Coposa, one of the abundant salt lakes formed high in the Andean Altiplano. **B)** Photograph from the air looking southeast across the Collahuasi mine camp located in the Pampa Coposa (November, 2002). In the background is the extinct stratovolcano Pabellon del Inca.

orthogonal cross-cuts have been excavated (Fig. 1.4a) and provide additional rock exposures.

Geologic units, contacts and faults have been extrapolated between costeans, with degrees of confidence varying from moderate to high. Key contacts and structures were projected from surface to where they have been intersected by diamond drill holes. Nineteen Rosario holes (7,470 m) and two La Grande holes (1,100 m) were logged graphically to record rock type, structure, vein types and paragenesis, relative ages of intrusions, alteration and ore mineral associations and approximate volume percent of the main mineral constituents.

Chapter 2. Literature Review: Regional and Local Geological Setting

Introduction

This chapter provides an overview of the tectonic history of the South American continental margin from the Paleozoic to the present-day. The geodynamic evolution of northern Chile is also reviewed, including a synthesis of crustal and fault architectures, and major magmatic and deformation events since the Jurassic. The chapter concludes with a review of previous literature that has documented the geology and mineralisation of the Collahuasi district.

Tectonic Framework of the Andes Cordillera

The Andes Cordillera is the product of long-term subduction of the Nazca oceanic plate beneath the South American continent. It comprises the largest known cordilleran-type orogen, running the length of the western margin of South America, and reaching widths of 800 km. Orogenesis in the Andes has been occurring since the Jurassic. Progressive eastward migration of the magmatic arc has occurred in the central Andes from the Jurassic, exposed in the coastal region, to its present-day position, approximately 300 km inboard of the coast, along the border of Chile with Argentina and Bolivia.

Mineral deposits of the central Andes have been grouped into a series of longitudinal metallogenic belts (Fig. 1.1) corresponding to discrete periods of magmatic-hydrothermal activity (Sillitoe, 1988; Camus, 2002). Of these, there are three main porphyry Cu-Mo ore-forming episodes responsible for the spectacular copper endowment in the Andes Cordillera. The first of these occurred between 66 and 52 Ma in southern Peru and northern Chile, between latitudes of 16° to 20°S and 27° to 32°S. The second occurred between 42 and 32 Ma in northern Chile, between latitudes of 18°S and 31°S. The most recent Cu-Mo metallogenic event took place between 10 and 4 Ma in central Chile (32° to 34°S). Large epithermal gold deposits that formed in northern Peru (6° to 14°S), northern Chile (Maricunga Belt; 26° to 27°S) and central Chile (El Indio Belt; 28° to 30°S) during the mid to late Miocene, constitute additional major metallogenic provinces on the Andean margin.

Geodynamic Evolution of Northern Chile

The continental margin of northern Chile formed in three main stages. Subduction and development of an accretionary terrane occurred during the mid- to late-Paleozoic (Ramos et al., 1986). This was followed by Mariana-type subduction during the Mesozoic and Chilean-type subduction in the late Cretaceous. The change from steep, Mariana to shallow, Chilean-type subduction was caused by initial opening of the Atlantic ocean in the mid Cretaceous (Coira et al., 1982). Atlantic ridge push and subduction along the South American continental margin resulted in faster subduction and shallowing of the subducting slab. Chilean-type subduction has continued through to the present-day (Coira et al., 1982; Pardo-Casa and Molnar, 1987).

Six tectonostratigraphic provinces (illustrated in Figure 2.1, listed in Table 2.1) define the geomorphologic architecture and landscape of the northern Chilean Andes (Scheuber et al., 1994; Reutter et al., 1996; James and Sacks, 1999; Kuhn and Reuther, 1999). These provinces reflect multiple orogenic and magmatic events along the continental margin of South America, particularly since the Mesozoic.

Paleozoic History

The South American continent was part of the Gondwana supercontinent before its break-up at about 115 Ma (Fig. 2.2). Prior to the break up of Gondwana, the Chilean margin of South America faced the Paleo-Pacific Ocean, along which numerous terranes are interpreted to have accreted (Ramos, 1994). The Arequipa and Chilenia terranes, accreted to northern and central Chile, respectively, were the two main terranes that docked along the Chilean margin (Fig. 2.2). The Arequipa terrane

Table 2.1 Tectonic province of the north Chilean Andes (Reutter et al., 1996; Kuhn and Reuther, 1999).

Tectonic Province	Characteristics
Coastal Cordillera	Jurassic magmatic arc
Longitudinal valley	Cretaceous magmatic arc superimposed on Jurassic backarc sedimentary basins
Domeyko Cordillera or Chilean Precordillera	Paleozoic basement uncomformably overlain by Mesozoic and Cenozoic sequences
Western Cordillera	Main volcanic arc (present day volcanic centres)
Andean altiplano	Intermontane sedimentary basin
Eastern Cordillera	Oligocene-Miocene fold and thrust belt, inner volcanic arc
Sub-Andean ranges	Present-day fold and thrust belt

docked in the Late Proterozoic and existed as a passive margin during the Cambrian to Early Ordovician (Ramos et al., 1986). During the Late Ordovician to Silurian, eastward-directed subduction formed an accretionary prism on the continental margin, and was followed by docking of the Chilenia terrane in the Middle to Late Devonian (Fig. 2.2).

In the early Permian, subduction renewed beneath the Arequipa terranes in northern Chile, and formed the Late Permian-Early Triassic magmatic arc and back-arc basin. These rocks constitute the crystalline basement rocks in the Domeyko Cordillera and are host to the northern Chile porphyry copper province (Bahlburg and Breitkreuz, 1991). The distribution of Paleozoic volcanic and sedimentary rocks, related to this arc, is shown in Figure. 2.3.

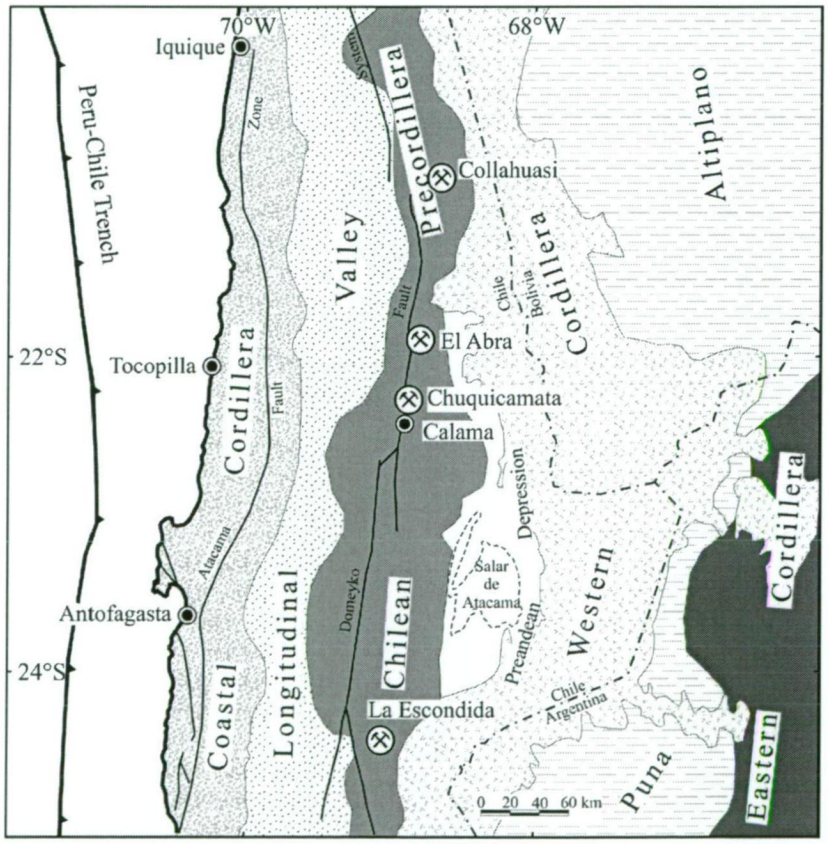

Figure 2.1. Tectonostraigraphic domains from Collahuasi to La Escondida (modified from Scheuber et al. (1994); Kuhn and Reuther (1999). The two main arc-parallel fault systems, Atacama Fault Zone and Domeyko Fault System, occur in the Coastal Cordillera and the Chilean Precordillera, respectively. Late Eocene-early Oligocene porphyry copper deposits are spatially associated with the Domeyko Fault System. Active stratovolcanoes along the Chilean border with Argentina and Bolivia define the Western Cordillera.

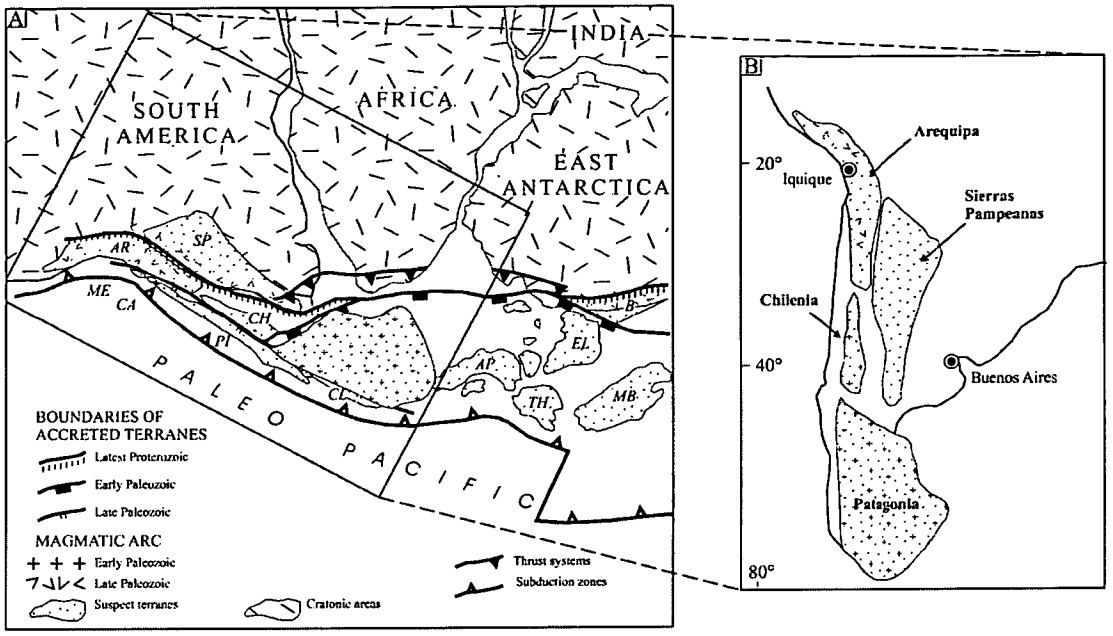

Figure 2.2. Southern Gondwanaland before the break up of the supercontinent at ~115 Ma (modified from Ramos, 1994). **A)** Outlines of accreted terranes. The Sierras Pampeanas (*SP*), Arequipa (*AR*) and Beardmore (*B*) terranes are interpreted to have accreted in the late Proterozoic. The Chilenia (*CH*), Patagonia, Antarctic Peninsula (*AP*), Ellsworth (*EL*), Thurston (*TH*) and Marie Bird (*MB*) terranes docked in the late Devonian-early Carboniferous. Accretion of the Mejillonia (*ME*) and Chañaral (*CA*) terranes occurred in the late Paleozoic to Triassic. **B)** Map of South America with outlines of the main accreted terranes rotated into the present frame of reference.

Mesozoic History

Extension in Triassic time (245 to 208 Ma) resulted in rifting along the margins of the accreted terranes (Fig. 2.2; Ramos, 1994). In the Jurassic, continental arc magmatism was established in the Coastal Cordillera (Fig. 2.3), with extensive back-arc sedimentation into rifted basins along the Longitudinal Valley (Prinz et al., 1994). The magmatic arc then migrated eastwards, so that by Cretaceous time, arc magmatism was localised within the Longitudinal Valley where voluminous intrusions were emplaced into the Jurassic backarc sedimentary rocks (Fig. 2.3). The transition from marine sedimentation in the Jurassic to subaerial sedimentation and volcanism during the Cretaceous is marked by late Jurassic evaporite deposits (Prinz et al., 1994).

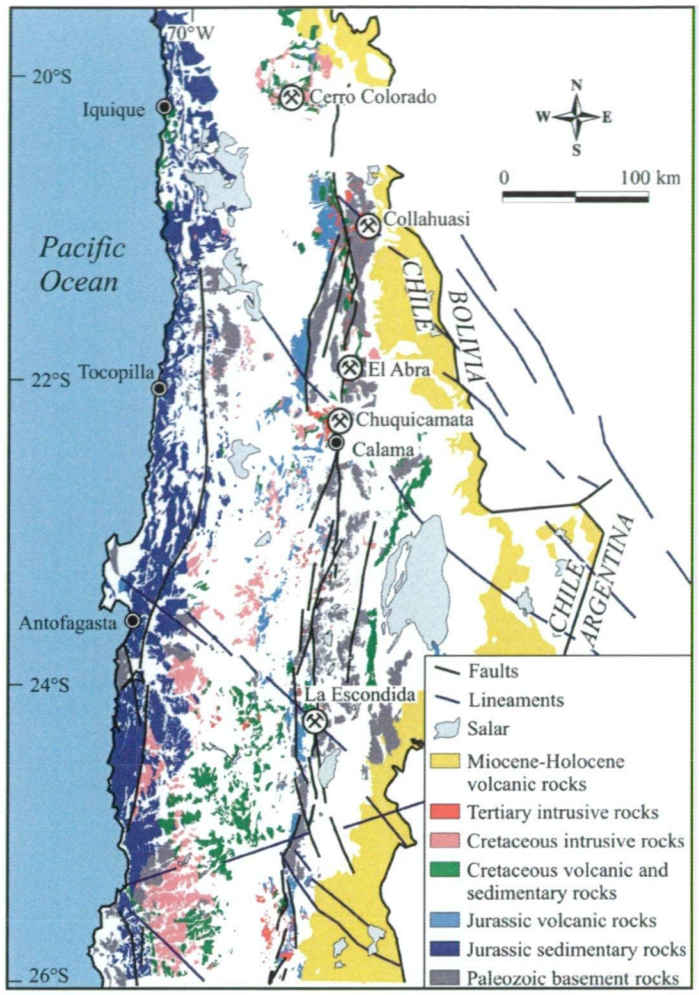

Figure 2.3. Geological map of northern Chile, showing distributions of the main geological provinces, the traces of the Domeyko and Atacama fault systems, and the location of major late Eocene-early Oligocene porphyry copper deposits. The Domeyko Fault System separates Mesozoic volcanic and sedimentary rocks from the Paleozoic basement rocks of the Chilean Precordillera. The largest porphyry Cu deposits are spatially associated with the intersections between the Domeyko Fault System and continental scale northwest-trending cross-orogen lineaments. Modified from Salfity, (1985); Richards (2000); Cooke et al. (2002).

Cenozoic History

Continental sedimentation and minor volcanism associated with the Cretaceous arc continued in northern Chile until the early Eocene. Volcanism ceased towards the end of the Eocene, with a volcanic hiatus continuing until the eruption of Miocene ignimbrites (Mpodozis et al., 1994). The intrusion of felsic to intermediate magmas associated with late Eocene-early Oligocene porphyry copper mineralisation occurred during the volcanic hiatus. The locus of magmatism shifted eastwards from the Cretaceous arc to beneath the Domeyko Cordillera. Compared to the Jurassic and Cretaceous arcs, the volume of magmatic and volcanic rocks during the Eocene-Oligocene period had decreased substantially (Coira et al., 1982).

The eastern edge of the main Jurassic back-arc basins in northern Chile was defined by the Domeyko Fault System (Gunther et al., 1997; Padilla Garza et al., 2001). During the Cenozoic, the Domeyko Fault System re-activated as a transcurrent structure, and localized at least six of the world's largest porphyry copper deposits, including Chuquicamata and La Escondida (Camus, 2002). Tectonic uplift coincided with magmatism associated with porphyry Cu mineralisation. Based on apatite fission track data, Maksaev and Zentilli (2000) estimated that between 4 and 5 km of rock was exhumed in the Domeyko Cordillera between the middle Eocene and early Oligocene.

The lull in central Andean volcanism between ~50 Ma and 27 Ma was attributed to subduction of a flat slab section beneath southern Peru and northern Chile (Clark et al., 1990; Sandeman et al., 1995; James and Sacks, 1999). In northern Chile, there appears to have been no significant volcanism from ~38 Ma until the resumption of felsic volcanic activity in the Eastern Cordillera at ~27 Ma (James and Sacks, 1999). The Miocene volcanic front broadened westward across the Bolivian Alitiplano (Jordan and Gardeweg, 1989; Sebrier and Soler, 1991; Gardeweg, 1993) into the main volcanic arc of the Western Cordillera.

Deformation Events

Since the Jurassic, deformation in the Domeyko Cordillera has occurred in two main tectonic cycles (Scheuber et al., 1994). Southeast-directed subduction of the Nazca plate produced sinistral plate convergence with high obliqueness (>45°), and resulted in an extensional to transtensional deformation regime between 200 and 90 Ma (Reutter et al., 1996). Subsequent deformation in the Domeyko Cordillera has been characterized by crustal extension or quiescence over prolonged periods, interrupted by short periods (~3 m.y.) of intense shortening and transpression. This phase was instituted during dextral plate convergence with obliqueness <45° (Reutter et al., 1996). Deformation events associated with each of the two tectonic cycles are outlined in Table 2.2.

Table 2.2. Tectonic framework of the north Chilean Andes (modified from Richards et al., 2001)

Period	Tectonic Event	Arc Magmatism	Character of deformation	Porphyry Cu deposits	References
Late Miocene-early Pliocene	Diaguita tectonic phase	Andesitic-dacitic stratovolanoes in the Western Cordillera, eruption of ignimbrite.	Small sinistral on arc-parallel faults in the Domeyko Cordillera, continued shortening in the arc (Western Cordillera) and backarc (Eastern Cordillera).		Kay et al. (1987) Maksaev and Zentilli (1988) Scheuber et al. (1994)
Miocene (~15 Ma to present)	Desertification		Small sinistral movements on arc-parallel faults in the Domeyko Cordillera, intense foreshortening in the backarc (Eastern Cordillera fold and thrust belt), continued shortening in the main arc (Western Cordillera).		Maksaev and Zentilli (1988)
Late Oligocene-middle Miocene	Quechua tectonic phase Renewed rapid convergence	Westward drift and resumption of calc-alkaline magmatism in the Western Cordillera.	Folding and reverse faulting in the Precordillera; uplift, erosion and supergene enrichment of porphyry Cu deposits; sinistral movement on the Domeyko Fault.	Supergene Cu enrichment Maricunga Belt Au-rich porphyry deposits	Pardo-Casas and Molnar (1987) Alpers and Brimhall (1989) Sillitoe and McKee (1996) Tomlinson and Blanco (1997b)
Late Eocene-early Oligocene (38-31 Ma)	End of Incaic tectonic phase	Magmatism in the Precordillera restricted to emplacement of porphyry centres associated with giant Cu deposits.	Relaxation of transpressive stress in the Precordillera, partial orogenic collapse and transtension.	El Salvador, Escondida, Chuquicamata, Radomiro Tomic, El Abra, Rosario	Scheuber et al. (1994) Reutter et al. (1996) Richards et al. (2001)
Middle-late Eocene (39-38 Ma)	Incaic tectonic phase Continued rapid convergence	Eastward migration of arc to the Precordillera,, calc-alkalic plutonism, no coeval volcanism.	Arc-normal shortening backarc basin closure and inversion on margin faults. Folding and thrusting, + dextral transpressive faulting and uplift in the Precordillera.		Coira et al. (1982) Mpodozis and Ramos (1989) Scheuber and Reutter (1992) Lindsay et al. (1995) Reutter et al. (1996) Tomlinson and Blanco (1997a)
Paleocene-early Eocene (59-52 Ma)	Rapid convergence	Magmatic arc shift eastward to the Longitudinal Valley, emplacement of porphyry Cu deposits (e.g. Cerro Colorado, Spence, etc.).	Shallow marine-continental foreland basin.	Cerro Colorado, Spence, Mocha, Toquepala, Cuajone, Cerro Verde	Sillitoe (1992) Scheuber et al. (1994)
Mid to late Cretaceous (~90-80 Ma)	Peruvian tectonic phase Atlantic opening, rapid sea-floor spreading	Cretaceous arc formed east of the Coastal Cordillera in the Jurassic foreland region. Continental arc volcanism and sedimentation.	Intense folding and thrusting caused by ridge push in the Atlantic ocean. Westward movement of the South American continent forced closure of Jurassic backarc basins and uplift of the Paleozoic crystalline basement.		Coira et al. (1982) Dalziel (1986) Padilla (1988)
Late Triassic to late Jurassic	Start of Andean cycle Araucanian tectonic phase (153-143 Ma)	La Negra magmatic arc and Tarapacá basin related to break-up of Gondwana Jurassic arc located in the Coastal Cordillera, calc-alkaline magmatic activity.	Volcanism in subsiding region, arc-normal extension (dykes, layered gabbros), back-arc sedimentation and basalt eruption. Strong arc-parallel sinistral displacement on the Atacama Fault and contemporaneous arc-normal extension.		Coira et al. (1982) Scheuber et al. (1994) Mpodozis and Cornejo (1997)

Crustal Architecture

Balanced cross-section models through the Andes of southern Peru and northern Chile have shown that the bulk of crustal shortening was accommodated in the eastern Altiplano, Eastern Cordillera and Sub-Andean regions (Schmitz, 1994; James and Sacks, 1999). The total amount of shortening is estimated to have been ~320 km since the late Cretaceous (assuming an initial crustal thickness of 35 km during the Cretaceous; Schmitz, 1994). However, this amount of crustal shortening cannot account for the total crustal volume without significant magmatic addition to the continental crust (up to 20%; Schmitz, 1994). James and Sacks (1999) proposed that the crustal structure of the Western Cordillera (and by implication the Domeyko Cordillera) has formed by magma addition to a previously thickened Andean continental crust. The thick crust of the Andean Altiplano was produced by a combination of sedimentation from the adjacent cordillera, foreland shortening along its eastern margin, and some magmatic addition. Conversely, the amount of foreshortening in the Eastern Cordillera and adjacent sub-Andes required no addition to crustal volumes by arc magmas (James and Sacks, 1999).

Flat Slab Subduction

James and Sacks (1999) interpreted that Cenozoic subduction in northern Chile changed from normal to flat subduction and then back to normal subduction again. The transition from normal to flat subduction took place in the early to late Eocene, beginning in southern Peru and migrating with time to northern Chile and central Bolivia. Similarly, the transition from flat to normal subduction began first in southern Peru and migrated south along the arc between the early Oligocene and middle Miocene. Clark et al. (1990) proposed that the distribution and nature of Tertiary volcanic rocks in southern Peru and northern Chile were the result of subduction of a flat oceanic slab. Two mechanisms have been proposed to explain flat slab subduction. Flattening of the down-going slab can occur by subduction of aseismic ridges or sea mounts, where thick segments of oceanic crust are buoyed by young and thin oceanic crust (James and Sacks, 1999; Gutscher, 2002). Alternatively, or at the same time, a dramatic increase in convergence rates (as a result of rapid mid-ocean ridge spreading in the Pacific and Atlantic oceans) would result in the South American continent over-riding young and buoyant oceanic crust that had not yet passed the basalt-eclogite transition (Clark et al., 1990).

According to James and Sacks (1999), the transition from normal to flat subduction in Northern Chile occurred between 38 and 35 Ma, coinciding with the Incaic tectonic phase (Reutter et al., 1996). The return to normal subduction occurred between 27 and 15 Ma (Quechua Orogeny) when hot asthenospheric mantle re-entered the expanded mantle wedge and caused widespread lithospheric melting beneath the Eastern Andes (James and Sacks, 1999). Weakening and thinning of the mechanical lithosphere along the Eastern Cordillera (inner arc) resulted in ductile deformation, uplift and lateral collapse of the Bolivian Orocline. Initial lithospheric melting beneath the Eastern Cordillera produced minor amounts of mafic (alkalic) magmas resulting in shoshonitic volcanic activity, and abundant felsic magmatism which caused the eruption of large volumes of ignimbrite.

Fault Architecture

Major faults in northern Chile comprise several arc-parallel fault systems as well as a series of northwest-striking regional lineaments that have been traced through western Argentina and northern Chile (Fig. 2.3; Salfity, 1985; Richards, 2000; Richards et al., 2001). The arc-parallel Atacama Fault, situated in the Coastal Cordillera, developed as a left-lateral wrench fault in response to southeast-directed (oblique) subduction of the Nazca plate in the Jurassic (Scheuber and Andrissen, 1990). Late Eocene-early Oligocene porphyry Cu deposits in the Precordillera are spatially associated with the Domeyko Fault System. This structure spans the 2,000 km length of the Precordillera, and has been the subject of numerous detailed investigations (e.g., Scheuber and Reutter, 1992; Lindsay et al., 1995; Reutter et al., 1996; Dilles et al., 1997; Tomlinson and Blanco, 1997a; Tomlinson and Blanco, 1997b).

Evolution of the Domeyko Fault System

The Domeyko fault system was active as a series of back-arc basin faults during the Jurassic (Padilla Garza et al., 2001) and has been reactivated as high-angle reverse and wrench faults during subsequent tectonic events. Tomlinson and Blanco (1997a) proposed that the Domeyko Fault System was probably established as a through-going transpressional fault by 37 to 34 Ma. Before this, faulting in the Domeyko Cordillera consisted of a series of N- to NNE-trending dextral fault segments that developed during Incaic compression between 45 and 37 Ma. This faulting was accompanied by N-trending folds and arc-parallel reverse faults inverted along Jurassic basin margin

structures. K-Ar biotite ages of biotite (34.8 ± 1.6 Ma; Maksaev, 1990) from dextrally sheared mylonites in the Fortuna Intrusive Complex indicate that dextral strike-slip movement was occurring on strands of the Domeyko Fault System at ~35 Ma.

At Chuquicamata, Lindsay et al. (1995) concluded that the intrusive complex was emplaced into a north-south dextral shear zone at the junction of the West Fissure (a branch of the Domeyko Fault System) and Mesabi faults. Early quartz-sulfide veins and associated biotite alteration were formed in orientations consistent with dextral strike-slip. Biotite ages from these vein arrays indicated that the Domeyko Fault was undergoing dextral movement in the late Eocene-early Oligocene (34 Ma; Zentilli and Maksaev, 1996). Lindsay et al. (1995) proposed that a reversal from dextral to sinistral movement occurred on the West Fissure after the formation of sericite alteration associated with intermediate-stage quartz-sulfide veins at Chuquicamata (~31 Ma). However, Reutter et al. (1996) argue that the strike-slip reversal occurred at ~33 Ma and was instrumental in the development of the quartz-sulfide veins associated with sericite alteration.

Post-mineralisation sinistral strike-slip along the West Fissure has displaced a large portion of the Chuquicamata orebody. Tomlinson and Blanco (1997a) and Dilles et al. (1997) suggested that wrench movement along the West Fissure resulted in the juxtaposition of the Chuquicamata orebody with the barren Fortuna intrusive complex. They argued that correlation of stratigraphy across the Domeyko Fault indicates that up to 37 km of sinistral strike-slip displacement occurred between 25 and 17 Ma. According to Tomlinson and Blanco (1997b), the maximum age of sinistral movement is constrained by syn-tectonic deposition into pull-apart basins of the Papajoy Formation. Volcaniclastic sequences near the top of the Papajoy Formation were deposited between 25 and 24 Ma (K-Ar ages of biotite and sanidine). The minimum age of sinistral displacement is delimited by the 17 Ma (mean age of K-Ar biotite dates) Huasco Ignimbrite, which overlies the northern continuation of the Domeyko Fault in the Collahuasi district.

Based on (U-Th)/He thermochronometry, McInnes et al. (1999) estimated that approximately 600m vertical displacement was accommodated by the West Fissure at Chuquicamata. The western crustal block containing the Fortuna Granodiorite was uplifted to an altitude of 3,600m relative to the eastern crustal block occupied by the Chuquicamata orebody. Topography on either side of the West Fissure does not reach

this altitude, suggesting that the western portion of the orebody was either eroded, or displaced by considerable post-mineral strike-slip displacement. Assuming that all of the displacement was accommodated on a single strand of the West Fissure, then the other half of the Chuquicamata intrusive complex would have been placed south of Calama in a sinistral wrench system.

Geology of the Collahuasi District

The Collahuasi district comprises three principal stratigraphic domains (Figs. 2.4 and 2.5; Bisso et al., 1998). The north-trending Domeyko fault system separates Cretaceous (Cerro Empexa Formation) and Jurassic sequences (Quehuita Formation) in the west from the Permo-Triassic Collahuasi Formation in the central part of the district. Extensive Cenozoic ignimbrite covers the basement stratigraphy in the north. Modern andesite stratovolcanoes cover the eastern edge of the Collahuasi Formation along the north-south trending Loa Fault. Late Eocene porphyry intrusive centres (Quebrada Blanca, Rosario and Ujina) occur in the central, uplifted Collahuasi Formation (Bisso et al., 1998).

Collahuasi Formation

Permian to Triassic andesite, dacite and rhyolite and small porphyry intrusions characterize the geology of the Collahuasi Formation (Vergara and Thomas, 1984). Volcanic units are intercalated with arenites (andesitic origin) and rare limestone lenses. The Domeyko fault system defines the the western edge of the Collahuasi Formation (Bisso et al., 1998). The eastern edge of the Collahuasi Formation is not exposed, but is probably the Loa Fault. The northern termination of the Collahuasi Formation is poorly defined as the sequence is buried beneath the Huasco Ignimbrite (Vergara and Thomas, 1984). The Collahuasi Formation extends south to Chuquicamata, but is absent beyond Calama (Figs. 2.3 and 2.4).

The Collahuasi Formation was emplaced onto Proterozoic to early Paleozoic basement of the Arequipa Terrane during the late Paleozoic (Shatwell, 1995). Deposition occurred in a continental setting, characterized by dacitic and minor andesitic volcanism. The topography of the Permo-Triassic landmass facilitated deposition of volcano-sedimentary rocks in fluvial basins and lakes (Vergara and Thomas, 1984).

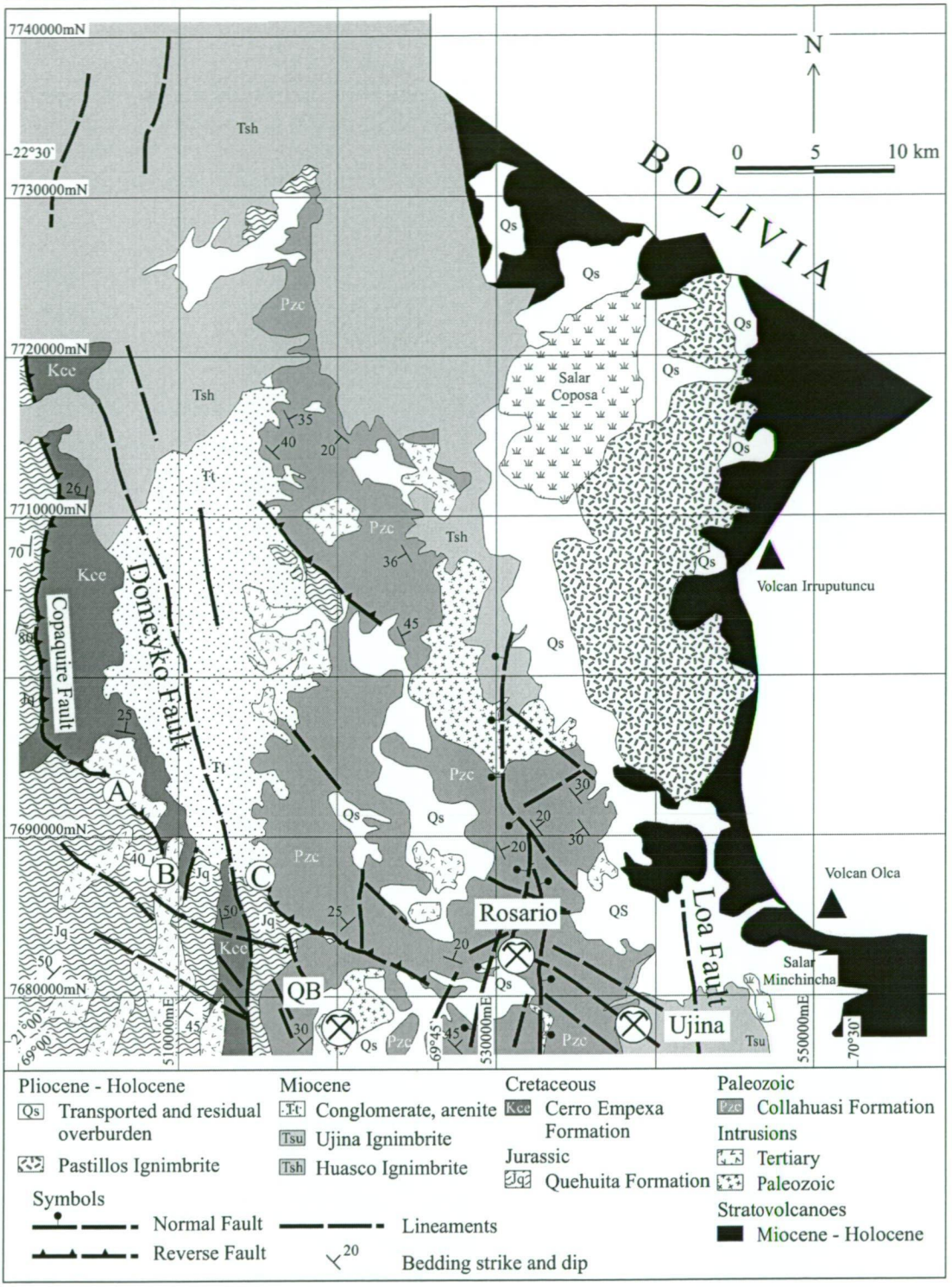

Figure 2.4. Simplified geologic map of the Collahuasi district. The Rosario, Ujina and Quebrada Blanca deposits occur in the Collahuasi Formation, which is bound in the east and west by the Loa and Domeyko faults respectively. Note that the Rosario and Ujina deposits occur on a northwest-striking photogeologic lineament interpreted from merged LandSat and SPOT imagery. Geology from Vergara and Thomas (1984).

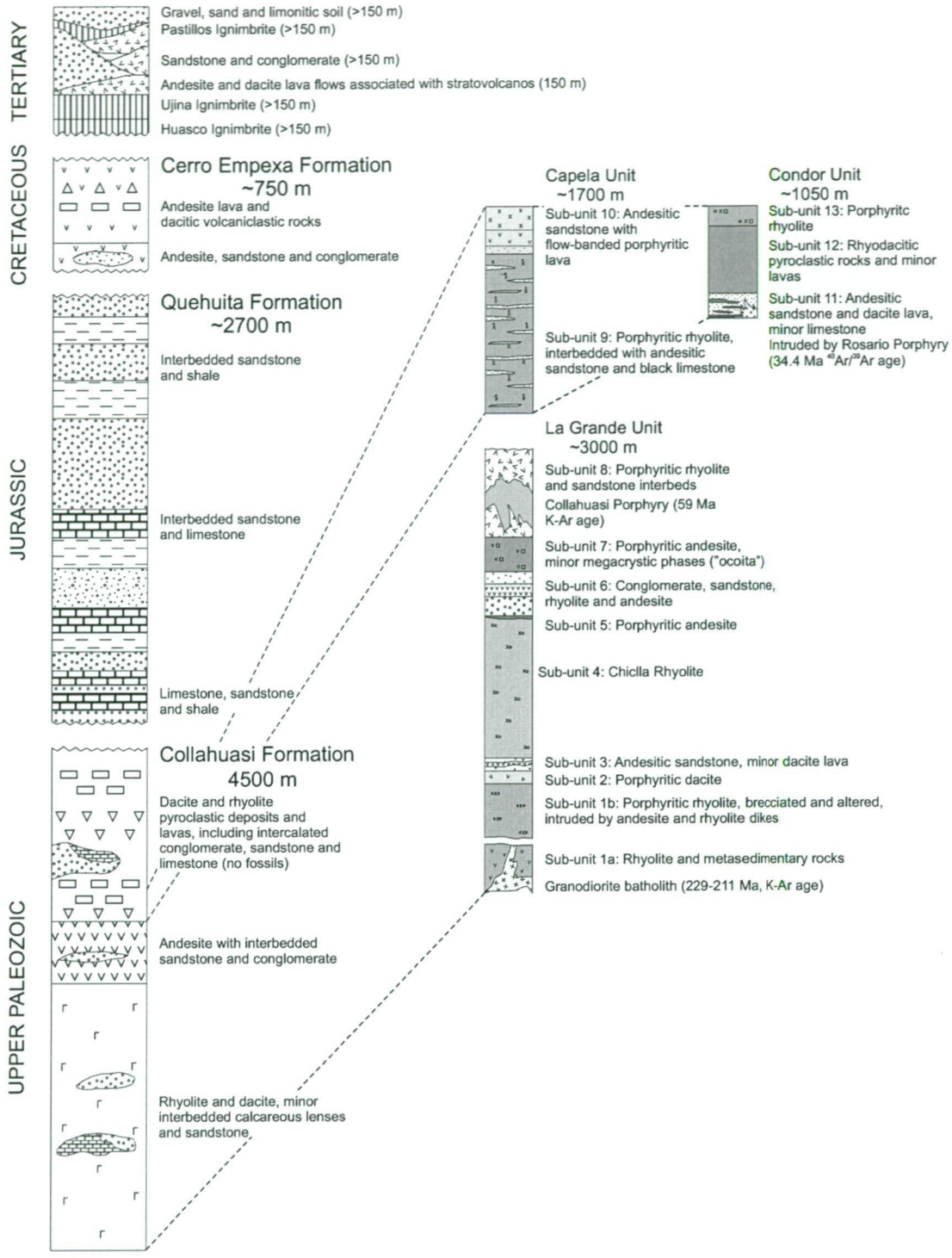

Figure 2.5. Collahuasi regional (left) and Rosario district (right) stratigraphic columns (after Muchmeyer et al., 1984; Vergara and Thomas, 1984). Munchmeyer et al. (1984) informally subdivided the Collahuasi Formation into thirteen sub-units based on their volcanic and sedimentary facies characteristics. The age of the Collahuasi Formation has been constrained by a late Triassic granodiorite pluton (229-211 Ma) that intruded the base of the volcanic and sedimentary sequence. Ore grade copper at Rosario is localised in the Rosario Porphyry, a monzonite stock, which has been emplaced at the base the Condor Unit.

Quehuita Formation

Sedimentary rocks of the Quehuita Formation, unconformably overlie the Collahuasi Formation (Fig. 2.6a), and are extensively exposed west of the Domeyko Fault. They consist of a lower member of deep marine mudstone and siltstone, and an upper member of shallow marine to subaerial continental limestones, calcareous sandstones, arenites and conglomerates (Vergara, 1978; Vergara and Thomas, 1984). Limestones and deep marine units in the lower marine member contain fossil associations that indicate a Jurassic age (Vergara and Thomas, 1984; Munchmeyer et al., 1984). Growth faults in both members indicate deposition occurred in an extensional setting that was initially deep water but gradually shallowed upward during seawater regression. Quehuita Formation sedimentation is associated with back-arc extensional basins that formed during development of the Jurassic arc in northern Chile.

Cerro Empexa Formation

The Cerro Empexa Formation is a north-trending, elongate sequence of andesite and dacite lavas, volcanic breccias, and interbedded red-bed arenites and conglomerates (Fig. 2.6b; Vergara and Thomas, 1984). The Domeyko fault system defines the eastern contact of the Cerro Empexa Formation. To the west, the Cerro Empexa Formation unconformably overlies the Quehuita Formation (Fig. 2.6c). Granite stocks, dated at 95 Ma, have intruded the Cerro Empexa Formation and led Vergara and Thomas (1984) to assign a Cretaceous age for these units. Continental deposition of the Cerro Empexa Formation consisted of andesitic-dacitic volcanic rocks and simultaneous emplacement of red bed deposits in an environment similar to the modern arc of the Eastern Cordillera.

Cenozoic Rocks

Three discrete ignimbrite bodies, the Huasco, Ujina and Pastillos Ingimbrites, occur in the northern and eastern parts of the Collahuasi district (Figs. 1.5 and 2.4). They have been dated by Vergara and Thomas (1984) at 17.1, 9.3 and 0.75 Ma, respectively (Table 2.3). Recent andesite flows erupted between 7.4 and 3.4 Ma (Vergara and Thomas, 1984), and originated from stratovolcanoes that mark the position of the modern arc.

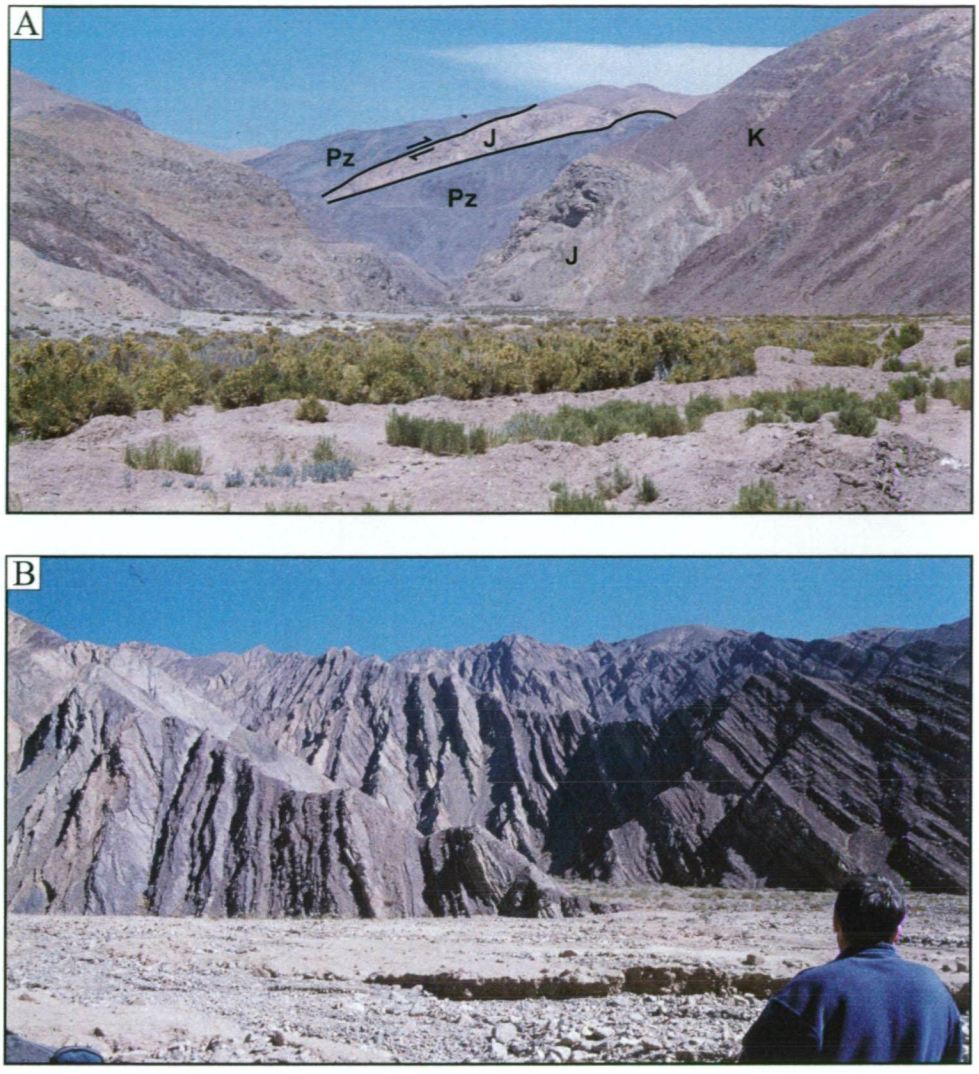

Figure 2.6. **A)** Photograph looking southeast along Quebrada Guatacondo towards the Domeyko Cordillera (location C on Fig. 2.4) . In the background, Quehuita Formation (J) unconformably overlies the Collahuasi Formation (Pz). A slice of Collahuasi Formation has been thrust over the Quehuita Formation. In the foreground is a contact, which has been folded, between the Cerro Empexa (K) and Quehuita Formations. The Collahuasi Formation has been uplifted, relative to the Cerro Empexa and underlying Quehuita Formations, exposed in the foreground. The bulk of uplift was accommodated on the Domeyko Fault System, which has been incised by the valley. **B)** Photograph looking south at red bed sedimentary rocks of the Cerro Empexa Formation (location B on Fig. 2.4). **C)** Photograph of an unconformity separating the Quehuita Formation (J) on the bottom from the Cerro Empexa Formation (K) on the top.

Table 2.3. Cenozoic ignimbrites in the Collahuasi District (Vergara and Thomas, 1984).

Unit	Age
Pastillos Ignimbrite	0.75 ± 0.2 Ma., K-Ar (Bi)
Ujina Ignimbrite	9.3 ± 0.4 Ma., K-Ar (Bi)
Huasco Ignimbrite	17.1 ± 0.8 Ma – 14.5 ± 0.5 Ma., K-Ar (Bi)

Intrusive rocks

Intrusive bodies ranging in composition from diorite to monzonite, granodiorite and granite occur throughout the Collahuasi district (Munchmeyer et al., 1984; Vergara and Thomas, 1984). Pre-continental arc Paleozoic granite and granodiorite are restricted to the Collahuasi Formation. Late Cretaceous – early Tertiary quartz diorite and granodiorite occur throughout the Cerro Empexa, Quehuita and Collahuasi Formations. Late Eocene quartz-monzonite intrusions, related to porphyry copper mineralisation, were emplaced exclusively within the Collahuasi Formation (Munchmeyer et al., 1984; Vergara and Thomas, 1984).

Structure of the Collahuasi District

Two major faults have segmented the Collahuasi district into three principal tectonic units (Fig. 2.4). The central, uplifted block of Collahuasi Formation corresponds with the northward continuation of the Domeyko Cordillera that is bound to the west by the Domeyko Fault. At Collahuasi, the eastern edge of the Domeyko Cordillera is defined by the active volcanic front of the Western Cordillera. West of the Domeyko fault system, sedimentary and volcanic units of the Cerro Empexa and Quehuita Formations are folded isoclinally and dip steeply into the Longitudinal Valley.

The Loa Fault is defined by a series of concave to the west arcuate faults (inverted basin structures). These structures, although not well exposed, extend north along the trace of the Loa River. At Collahuasi, the Loa Fault passes to the east of Ujina beneath the Ujina Ignimbrite. Several Collahuasi drill holes have intersected the Loa Fault, where it cuts the La Profunda Granite. Dick et al. (1994) and Clark et al. (1998) proposed that the Loa Fault splayed from the Domeyko Fault System north of El Abra.

Folding

Open, upright NW-trending folds have developed in the Collahuasi Formation. Vergara and Thomas (1984) interpreted the long wavelength north-trending fold at Quebrada Blanca to be related to doming by the Quebrada Blanca plutonic complex. The age of the oldest intrusive rocks at Quebrada Blanca is late Triassic-middle Jurassic, indicating that at least one of the folding events recorded in the Collahuasi Formation occurred during the Mesozoic. Tight north-trending anticlines and synclines, partitioned into the Quehuita and Cerro Empexa Formations, are characterised by subvertical and locally overturned fold limbs, some of which are related to reverse faults. The sub-horizontal strata of the Cenozoic volcanic and sedimentary rocks have not been folded.

Regional-Scale Faults

Paleozoic basement rocks of the Collahuasi Formation have been thrust over Mesozoic rocks west of the Collahuasi District along several northwest- trending reverse faults. (Fig. 2.4). In addition, Quehuita Formation has been overthrust by Cerro Empexa Formation along the high-angle Copaquire Fault west of Quebrada Blanca. The Copaquire Fault cuts the Malta Granite (Point A, Fig. 2.4) which has been dated at 45 ± 5.2 Ma (Vergara and Thomas, 1984). However, further south, the Copaquire Fault is intruded by Malta Granite (point B, Fig. 2.4), suggesting syn-tectonic magmatism along this structure (Vergara and Thomas, 1984).

Sinistral offset of the Copaquire Fault north of Quebrada Blanca (point C, Fig. 2.4), indicates that strike-slip movement along the Domeyko Fault occurred after the middle Eocene. The northern extension of the Domeyko Fault beyond the Collahuasi district is buried beneath Miocene-Pliocene ignimbrite and unconsolidated sedimentary rocks (Fig. 2.4), indicating that this strand of the Domeyko Fault System has not been reactivated since the Neogene.

District-Scale Faults

A system of north-south to north-northeast-trending, subvertical faults has cut the volcanic stratigraphy south of Rosario (Fig. 2.7). Some of these faults have localised high-grade Cu-Ag-Au veins. Munchmeyer et al. (1984) suggested that development of the La Grande and Monctezuma fault systems was related to strike-slip movement on the Domeyko Fault. A second group of faults striking northwest

(dipping 45°-60° SW) have also localised high-grade Cu-Ag-Au mineralisation at the Rosario Cu-Mo-Ag deposit (Dick et al., 1994; Lee, 1994; Masterman, 2000; Masterman, 2001).

At Quebrada Blanca, a series of shallow southwest-dipping faults has imposed structural control on late hydrothermal veins (Hunt et al., 1983; Rowland and Wilkinson, 1998). This orientation corresponds with the SW-dipping fault system at Rosario. The NE-trending Quebrada Blanca Fault cuts porphyry-style mineralisation (Fig. 2.7), but may have developed before intrusion of the complex and influenced its emplacement (Johny Bonilla, Chief Geologist Compañia Minera Quebrada Blanca S.A., pers. com. 2000).

Porphyry Copper-Molybdenum and Associated Epithermal Cu-Ag-Au Mineralisation in the Collahuasi District

The Quebrada Blanca, Rosario, and Ujina porphyry centres define a broad east-trending corridor between the Domeyko fault system and Loa faults (Fig. 1.3). At Rosario, high-grade, massive sulfide (Cu-Ag-Au) veins overprint porphyry-style Cu-Mo mineralisation (Dick et al., 1994). These veins, characterised by massive sulfide infill (e.g. pyrite, enargite, chalcopyrite, bornite, and tennantite) and narrow envelopes of quartz-alunite-pyrophyllite alteration, exhibit features that are typical of high-sulfidation epithermal deposits (Arribas, 1995), and are therefore classified as high-sulfidation veins using the nomenclature of Hedenquist (1987) and White and Hedenquist (1990; 1995). Similar high sulfidation veins occur in the La Grande and Poderosa areas south and southeast of Rosario respectively. East of Cerro La Grande, a 3 to 5 km long, semi-continuous vein, characterised by banded and colloform quartz, low-sulfidation state sulfides (Barton and Skinner, 1967) and calcite-rhodochrosite gangue, is hosted by the Monctezuma Fault. This vein has many characteristics of low-sulfidation epithermal veins (Hedenquist, 1987; White and Hedenquist, 1990; 1995).

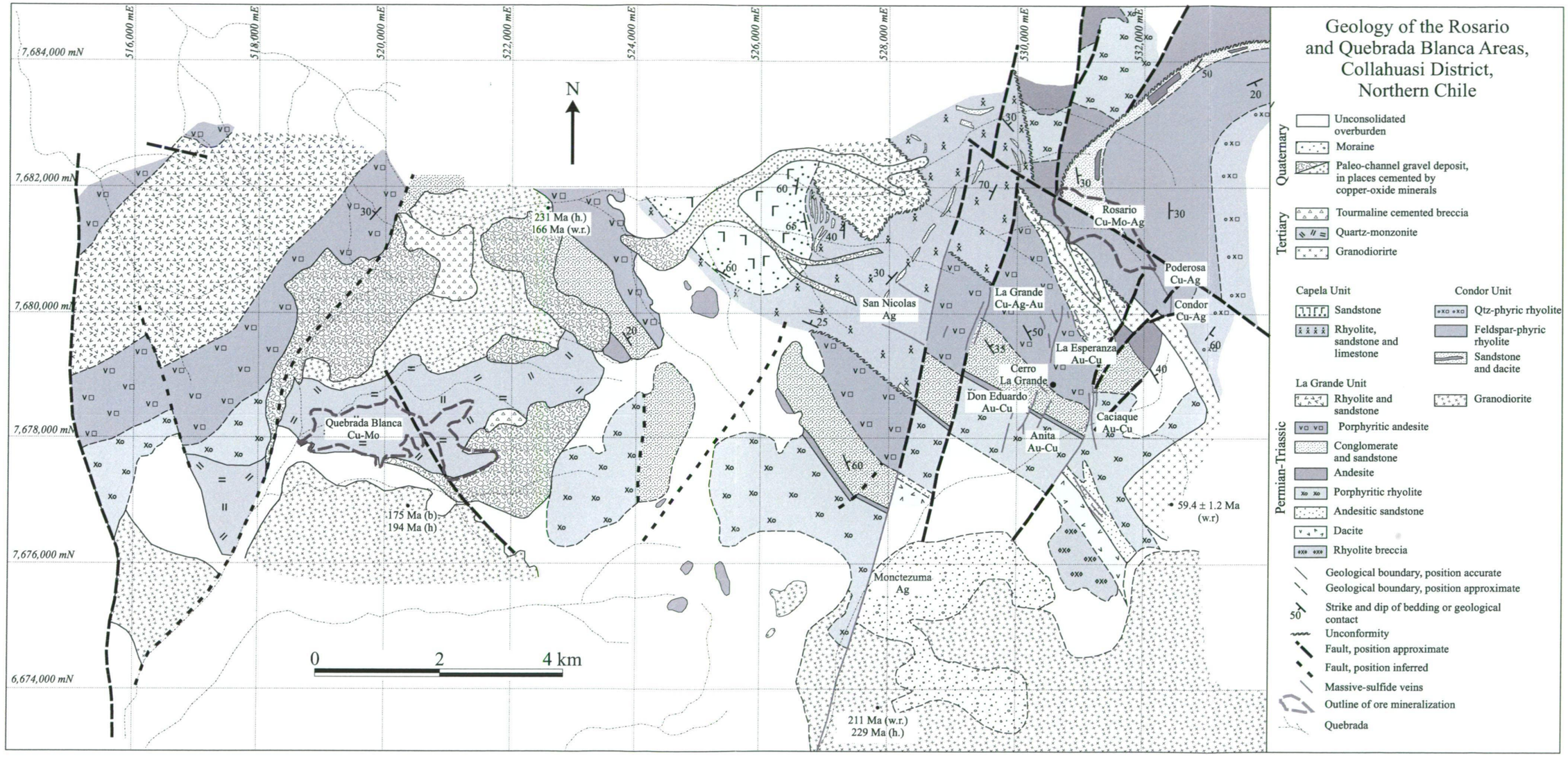

Figure 2.7. Generalised geology of the Rosario and Quebrada Blanca areas. The outline of copper mineralisation associated with the Rosario and Quebrada Blanca porphyry centres is shown, as well as vein-hosted Cu-Ag-(Au) massive sulfide occurrences in the Poderosa and La Grande areas, and the laminated quartz vein associated with high grade silver at Monctezuma. From Munchmeyer et al. (1984).

Quebrada Blanca

The Quebrada Blanca intrusive complex is hosted by a Permian granite batholith that intruded a N-trending anticline, formed in volcanic units from the Collahuasi Formation (Fig. 2.7; Munchmeyer et al., 1984; Rowland and Wilkinson, 1998) . The volcanic stratigraphy consists of several andesite flows intercalated with epivolcaniclastic sandstone of andesitic origin. Rhyolitic and dacitic pyroclastic rocks overlie the andesite and sandstone units (Hunt et al., 1983). The mineralised intrusions define an ENE-trend that cuts the axis of the anticline. Copper mineralisation is associated with several generations of igneous activity. The various intrusions are described in Table 2.4.

Copper ore at Quebrada Blanca is mined predominantly from the supergene zone. Hypogene mineralisation styles have been described by Rowland (1998). Early chalcopyrite-bornite mineralisation at Quebrada Blanca is associated with the quartz monzonite stock and a porphyry dyke suite, whereas late chalcopyrite-molybdenite-pyrite mineralisation is associated with the cross-cutting igneous and hydrothermal breccia bodies (Rowland, 1998; Rowland and Wilkinson, 1998; Hunt et al., 1983). Quebrada Blanca vein and alteration paragenesis is detailed in Table 2.5.

The Quebrada Blanca stock is intensely biotite-altered along its northern contact. Hunt et al. (1983) defined this facies as a discrete mafic (diorite) intrusion. Disseminated bornite-chalcopyrite mineralisation is spatially associated with potassic alteration in the granodiorite core of the quartz monzonite intrusion. The highest

Table 2.4. Pre-, syn- and post-mineralisation intrusions at Quebrada Blanca (Hunt et al., 1983; Maksaev et al., 1988; Maksaev, 1990; Rowland and Wilkinson, 1998).

Intrusion	Composition	Relationship to mineralisation
Andesite dykes	Plagioclase-hematite-magnetite	Post-mineralisation (?)
Igneous and hydrothermal breccias	Igneous: monzonite and porphyry clasts in quartz-biotite-K feldspar-sulfide matrix	Syn-mineralisation
	Hydrothermal: porphyritic clasts in quartz-sericite-sulfide matrix	
Mafic dykes	Plagioclase-biotite-amphibole, trace quartz	Syn-mineralisation
Porphyritic dykes	Quartz-feldspar with accessory biotite-amphibole	Syn-mineralisation
Quartz-monzonite stock (35 Ma)	Quartz monzonite grades to granodiorite in the centre of the intrusion	Pre- to syn– mineralisation

Table 2.5. Summary of vein and alteration paragenesis at Quebrada Blanca (Hunt et al., 1983; Rowland and Wilkinson, 1998).

Stage	Vein mineralogy	Alteration zone
Pre-ore	Biotite-magnetite	± potassic halo
Early	Quartz-K feldspar-anhydrite-magnetite-sulfides	± potassic or sericitic halo
	Quartz	± potassic/sericitic halo
Hydrothermal breccias	Quartz-molybdenite-chalcopyrite ± anhydrite	± sericitic halo
Tourmaline breccias	Tourmaline-chalcopyrite-bornite-molybdenite-pyrite	Tourmaline
Late	Pyrite > quartz	Strong phyllic to argillic halo

molybdenite grades occur along the Quebrada Blanca Fault. Potassic alteration grades out to chlorite-epidote in the southern sector of the deposit (Hunt et al., 1983). A funnel-shaped zone of pervasive sericite alteration surrounds the vuggy hydrothermal breccia unit (Rowland, 1998). Secondary copper-arsenic oxide minerals occur at the top of the hydrothermal breccia body in the supergene zone (Johny Bonilla: chief geologist CM Quebrada Blanca, pers. com. 2000) suggesting they were derived by oxidation of primary copper-sulfosalt minerals. The vuggy breccia zone and associated copper-sulfosalts may have originated from hydrothermal fluids of high sulfidation character (e.g., Hedenquist, 1987; White and Hedenquist, 1990; 1995).

At least two tourmaline breccia bodies containing chalcopyrite occur on the northern and eastern margins of the intrusive complex (Rowland and Wilkinson, 1999). Their relationship to breccia bodies in the central mineralised zone at Quebrada Blanca is unclear, however Hunt et al. (1983) speculated that tourmaline breccias postdate igneous breccias in the core of the Quebrada Blanca complex.

Rosario

The porphyry stock at Rosario intruded the base of the Condor Unit in the Collahuasi Formation (Figs. 2.5 and 2.7). The southwest-dipping Rosario Fault System cuts the intrusive and volcanic host-rocks of the La Grande and Condor units (Fig. 2.8a; Dick et al. 1994; Lee, 1994). The La Grande Unit is distinguished by andesitic and rhyolitic volcanic rocks facies, whereas the Condor Unit consists of interbedded sandstone, dacite and skarn, overlain by a thick rhyolitic volcanic sequence (≥400 m). Intrusive activity at Rosario is summarized in Table 2.6.

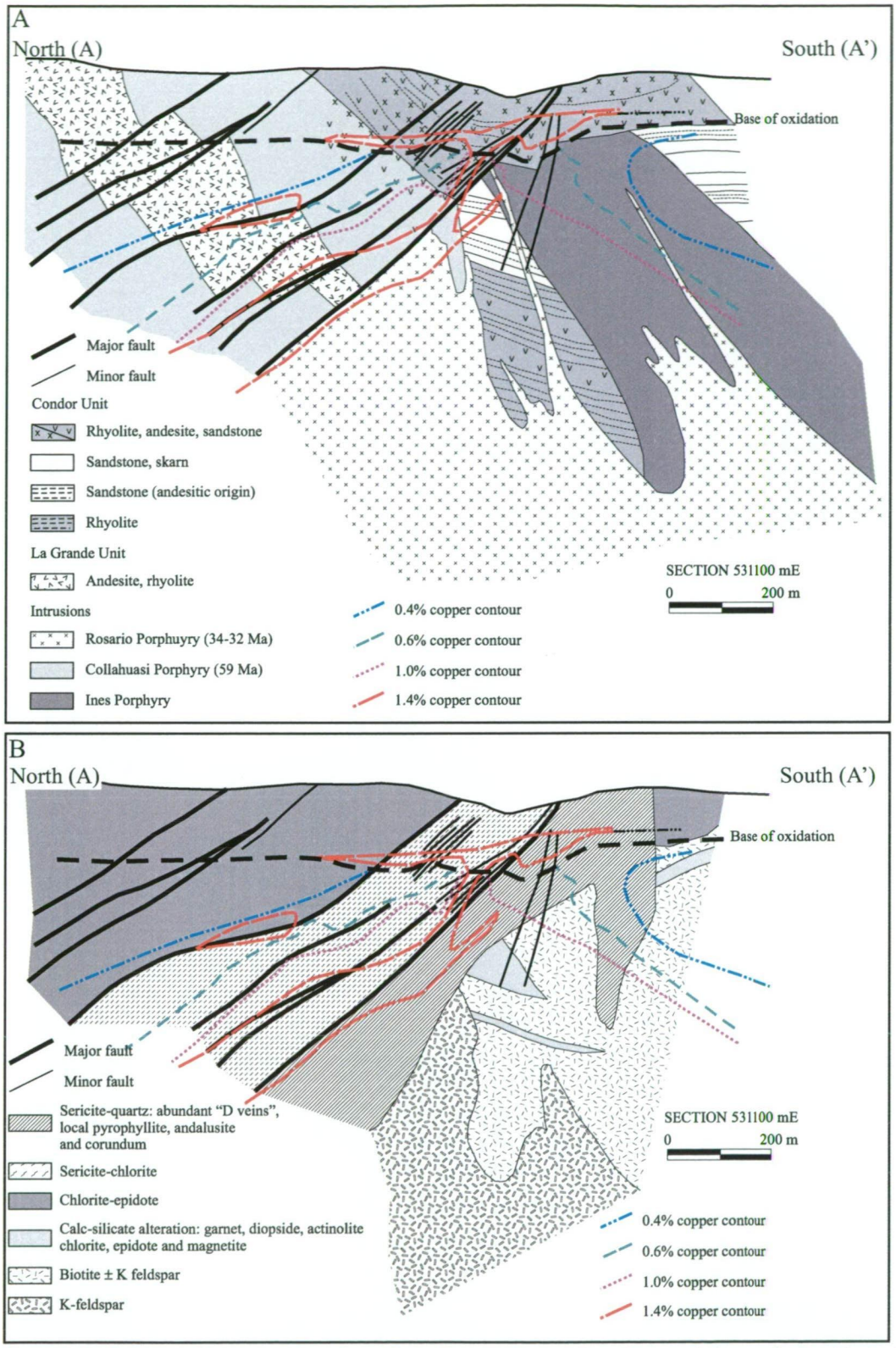

Figure 2.8. North-south cross-section through the Rosario deposit based on work done prior to this study (from Munchmeyer et al. (1984). Section line locality is shown in Figure 1.3. **A)** Geology. Permian-Triassic host rock units have been intruded by the Inés, Collahuasi and Rosario porphyries. Copper mineralisation at Rosario is spatially and temporally associated with the Rosario Porphyry. The highest copper grades (> 1.5% Cu) occur in the late-stage veins associated with the southwest dipping Rosario Fault System. **B)** Alteration. The Rosario Fault System has imposed strong structural control on intermediate argillic (sericite-chlorite) and phyllic (sericite-quartz) alteration assemblages. These assemblages overprint potassic alteration (biotite and K feldspar), which has been preserved deep in the footwall of the Rosario Fault System.

Table 2.6. Pre-, syn- and post-mineralisation intrusions at Rosario (Vergara, 1978; Munchmeyer et al., 1984; Clark et al., 1998).

Intrusion	Age	Composition	Relationship to mineralisation
Rosario Porphyry (RPO)	34.2 to 32.9 Ma	Quartz-monzonite	Syn-mineralisation
Collahuasi Porphyry (PCO)	59 Ma	Quartz-monzonite	Pre-mineralisation
Inés Porphyry (PIN)	Permo-Triassic (?)	Dacite	Pre-mineralisation

Multiple generations of mineralisation and alteration occurred at Rosario (Dick et al, 1994; Lee, 1994). These are grouped into three main paragenetic stages described in Table 2.7. The distribution of alteration facies is shown in Figure 2.8b. Early-stage alteration (secondary biotite-albite, albite-chlorite and K feldspar) and mineralisation associated with group1 veins occur in all rock units, overprinting widespread disseminated and vein magnetite-albite. Ore minerals consist of a central chalcopyrite-bornite zone grading out to chalcopyrite-only (Lee, 1994). Intermediate-stage group 2 and 3 veins extensively overprint early stage mineralisation and alteration assemblages (Lee, 1994). Based on underground mapping, Lee (1994) recognised that intermediate-stage veins occurred in steep and shallow SW-dipping orientations. He interpreted them to be a conjugate vein set that developed during a phase of extension on the Rosario Fault (Lee, 1994). Late-stage group 4 veins are localised by the Rosario Fault System (Dick et al., 1994). These veins define a SW-dipping high-grade zone where copper grades increase locally to above 10% (Fig. 2.8b). Vein sulfide associations consist of pyrite-bornite-chalcopyrite-tennantite and accessory chalcocite-covellite-mawsonite ($Cu_6Fe_2SnS_8$)-colusite $\{Cu_3(As,Sn,V,Fe)S_4\}$.

$^{40}Ar/^{39}Ar$ geochronology yielded ages of 32.9 ± 0.5 Ma. and 32.9 ± 0.6 Ma for hydrothermal biotite and muscovite, respectively (Clark et al., 1998). The absence of a clear hiatus between the early and late mineralisation events at Rosario implies that this extremely large hydrothermal centre was emplaced over a short time interval, or that the early ages were reset by later magmatic and/or hydrothermal activity.

Table 2.7. Vein and alteration paragenesis at Rosario (Lee, 1994)

Hydrothermal event	Vein type	Wall-rock alteration facies
Early-stage	Group 1: quartz-bornite-chalcopyrite-pyrite	(1) magnetite ± albite (2) biotite ± albite ± K-feldspar (3) albite ± chlorite (4) K-feldsapr
Intermediate stage	Group 2: quartz-chalcopyrite-pyrite-bornite Group 3: quartz-molybdenite ± pyrite ± chalopyrite	Sericite-quartz
Late stage	Group 4: quartz-pyrite-chalcopyritebornite-tennantite-enargite	Sericite-quartz

Ujina

The host rocks at Ujina are laterally equivalent to the volcanic facies at Rosario. The Ujina stratigraphy consists of a thick basal andesite (possibly several flows), overlain by rhyolite and sedimentary breccia (Fig. 2.9a; Bisso et al., 1998). Two main feldspar-quartz-biotite porphyry intrusions are recognized at Ujina. The host intrusion comprises a cylindrical granodiorite stock (1200m in diameter), intruded by a series of north- and northwest-trending granodiorite dikes assigned to the Inca Porphyry unit (Bisso et al., 1998). The relationship between the two intrusions is shown in cross-section in Figure 2.9a. The highest hypogene grades are associated with the Ujina Porphyry which displays varying degrees of K feldspar + biotite (potassic) and sericite-quartz-chlorite-pyrite alteration. The weakly mineralised Inca Porphyry is interpreted to have intruded the Ujina Porphyry before the cessation of hydrothermal activity. The history of intrusive activity at Ujina is summarized in Table 2.8.

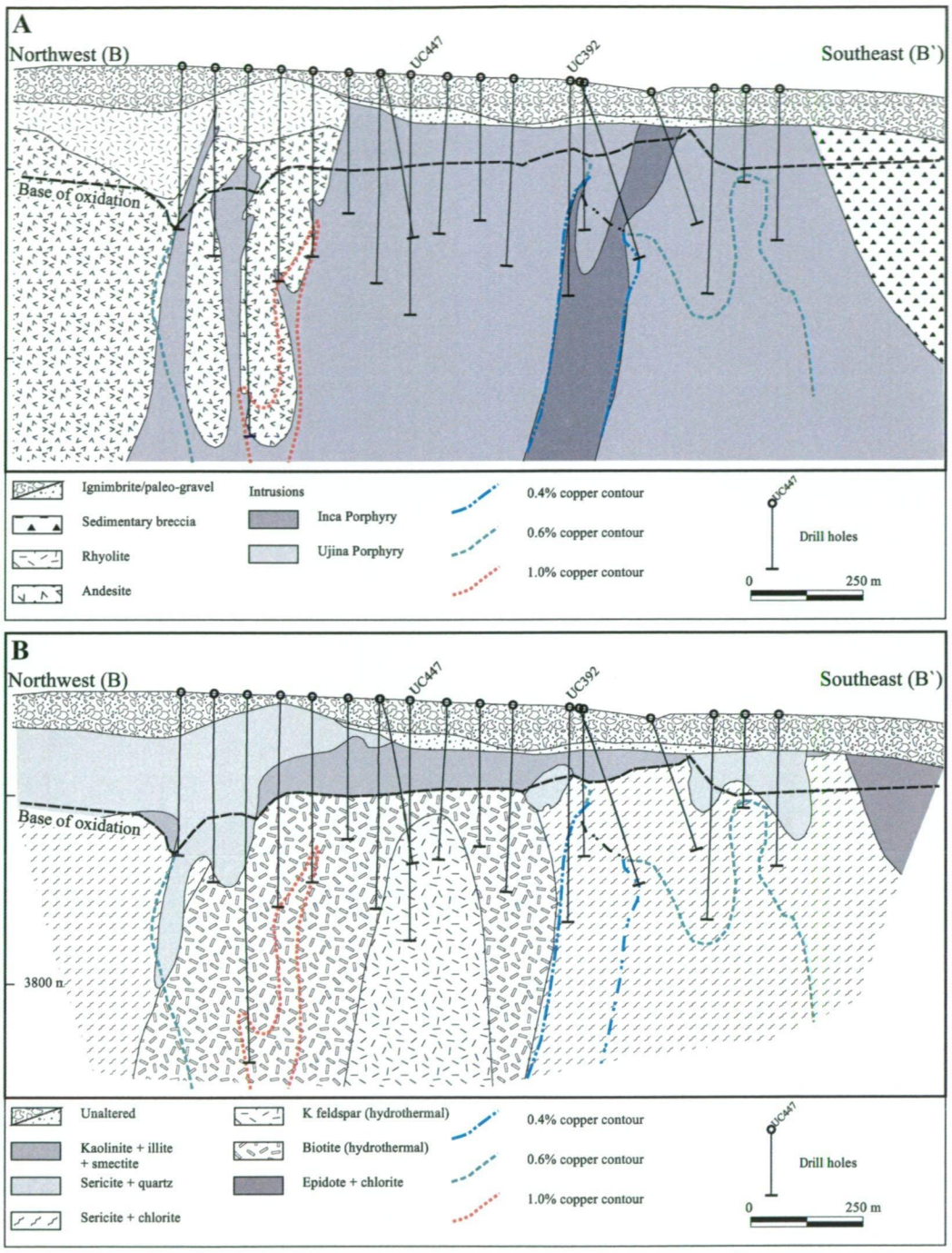

Figure 2.9. Northwest-southeast section through the Ujina deposit. Section locality shown in Figure 1.3. **A)** Geology (modified from Bisso et al. (1998). Highest hypogene copper grades occur in the Ujina Porphyry, whereas lowest grades (< 0.4% Cu) are spatially associated with the post-mineralisation Inca Porphyry. This has resulted in the highest grades occurring around the edges of the Ujina Porphyry. **B)** Alteration (modified from the Collahuasi Prefeasibility Study, 1993). Early potassic alteration is preserved on the northwest edge of the Ujina Porphyry and coincides with the highest grades. Intermediate argillic (sericite-chlorite) alteration has overprinted potassic assemblages and is closely associated with the Inca Porphyry. Propylitic alteration has enveloped the intermediate argillic zone.

Table 2.8. Syn- and post-mineralisation intrusions at Ujina (Bisso et al., 1998).

Intrusion	Age	Composition	Relationship to mineralisation
Inca Porphyry (PCA)	?	Quartz latite	Syn- to post-mineralisation
Ujina Porphyry (PUJ)	34 Ma	Quartz monzonite	Syn-mineralisation

In contrast to Rosario, there are two main hypogene mineralisation and alteration stages at Ujina. The early-stage potassic alteration, centred on the Ujina Porphyry, is characterised by a K feldspar-altered core that grades out to biotite alteration (Fig. 2.9b). Accessory calcite has been recognized in association with hydrothermal biotite and K feldspar. Ore minerals associated with the potassic alteration include disseminated and veinlet-style chalcopyrite-bornite. Quartz-molybdenite veins lacking recognizable alteration haloes cut the early-stage veins, but are themselves cut by the main-stage veins. The main-stage alteration facies consists of the assemblage sericite-chlorite (clay and mica phase not identified sprectrographically) and is associated with pyrite-chalcopyrite-quartz veins overprinting the early-stage potassic alteration. An argillic facies consisting of kaolinite and smectite occurs in patches across the top of the Ujina alteration system, and is possibly supergene. The distribution of alteration facies is illustrated in cross-section in Figure 2.9b.

Hypogene sulfide mineralisation at Ujina is concentrically zoned about the Ujina Porphyry (Bisso et al., 1998). DeBeer and Dick (1994) described a low sulfide core of chalcopyrite-bornite grading outwards through chalcopyrite-pyrite to an outer pyrite shell. Hypogene copper distribution is also concentrically zoned, with the highest Cu grades forming an annulus about the low sulfide potassic core (Fig. 2.9b; Bisso et al., 1998). This high-grade zone coincides with the cylindrical contact of the Ujina Porphyry with the Collahuasi Formation host rocks (Fig. 2.9b).

La Grande, Capela and Poderosa Vein Systems

The mineralisation and alteration styles at La Grande, Capela and Poderosa (Fig. 2.7) are similar to the late-stage hydrothermal veins at Rosario (Dick et al., 1994; Bisso et al., 1998). The distribution of these vein systems is shown in Figure 2.7. At La Grande, massive sulfide veins consist of pyrite-bornite-chalcocite-enargite with accessory mawsonite and colusite (Dick et al., 1994). Alteration facies consist of proximal advanced argillic associations (pyrophyllite-alunite-dickite) that grade

outward through sericite-quartz to epidote-chlorite alteration. The Capela vein group occurs southeast of Rosario and is characterized by a series of massive pyrite veins, locally enriched in copper. The copper-silver veins at Poderosa lie along a NNW-trending structure parallel to the Rosario Fault. The vein sulfide association consist of bornite-tennantite-chalcopyrite-enargite-pyrite (Munchmeyer et al., 1984).

Monctezuma Vein

The Monctezuma vein (Fig. 2.7) dips subvertically to the west and has been traced along surface and intersected in drill holes over a total strike length of 7 km. The vein varies in width from 1 to 5 m, and crops out as banded, cockade quartz that has been impregnated by manganese oxides and limonite. Below the base of surface oxidation, sphalerite, pyrite, galena and chalcopyrite occur with accessory polybasite, argentopyrite, argentite, stephanite, tetrahedrite, and native silver and gold in a quartz-rhodochrosite gangue. In a 1 km segment of the vein, several Collahuasi drill holes have intersected a narrow (20-30m) vertical enrichment zone that occurs at the base of oxidation. This interval grades between 500 and 1000 g/t Ag, and passes down dip into hypogene mineralisation grading 200 - 500 g/t Ag (Munchmeyer et al., 1984).

Huinquintipa

Gravels deposited in the east-striking Huinquintipa paleodrainage system (Fig. 1.3) have been cemented and impregnated by copper oxide minerals. Copper was originally sourced from eroded massive sulfide veins at the Rosario deposit (Munchmeyer, 1996). Modern valleys have dissected the Huinquintipa paleochannel into several isolated ore bodies (Munchmeyer et al., 1984). Economic copper mineralisation occurs over an area of 1 km by 150 m, averaging 10 m thick. Zonation of exotic copper species and hydrothermal alteration minerals is evident along the 6 km length of the paleochannel (Munchmeyer, 1996). Near Rosario, the gravels are unaltered and cemented by abundant limonite. Two kilometres from Rosario, pervasively kaolinised gravel fragments are cemented by copper wad and kaolinite. At Huinquintipa, weakly altered to unaltered gravel fragments are cemented by chrysocolla and accessory copper wad. The mineralised area abruptly terminates where the paleochannel enters a small paleobasin (1.5 km wide, 100 m deep). Munchmeyer (1996) interpreted that increasing pH (due to rock fragment reaction and possibly fluid mixing) triggered deposition of exotic copper at Huinquintipa. Copper concentrations are inferred to have been significantly depleted by the time the fluids reached the

paleobasin, thus preventing further precipitation of copper oxide species.

Discussion

In the Collahuasi District, basement architecture controlled the emplacement of late Eocene intrusive complexes. The Rosario and Ujina deposits were emplaced along a northwest-striking lineament (visible in Landsat/SPOT imagery; Figs. 1.5 and 2.3) that intersected the West Fissure north of Quebrada Blanca (Lee, 1994; Fig. 2.4). Brittle deformation at Quebrada Blanca, Rosario and La Grande localized late-stage metalliferous hydrothermal fluids in strike-slip faults. Multiple reactivation of the Rosario and La Grande fault systems was crucial in generating high grades at Rosario and La Grande as they gave hydrothermal fluids repeated access to the mineralised system (Dick et al., 1994; Lee, 1994).

Clark et al. (1998) used the geochronologic data from Quebrada Blanca, Rosario and Ujina to suggest that hydrothermal activity migrated eastward in the Collahuasi district, over a period of ca. 3 to 4 m.y. and became more potent with time. They speculated that Chuquicamata, La Escondida and Rosario, the three largest West Fissure-associated Cu-Mo porphyry systems, were emplaced simultaneously towards the final stages of the late Eocene-early Oligocene orogenic event. The absence of late Eocene-early Oligocene volcanic rocks in the Collahuasi district appears to indicates that the large porphyry magmas did not vent and disperse magmatic volatiles (Camus, 2002).

Chapter 3. Geology and Structure of the Rosario deposit

Introduction

This chapter describes the geology of the Rosario deposit, including new geochronological data for the country rocks and an analysis of the structural setting of the mineralised system. Surprisingly, only a few studies (e.g., Sierrita, Heidrick and Titley, 1982; Chuquicamata, Lindsay et al., 1995) have addressed the influence of regional- and local-scale structural controls on intrusions and fracture networks in porphyry systems. A major problem relates to the complex hierarchy of structures. Some structures influence magma emplacement, some are produced by magma intrusion, and others may be produced by mineralising processes. Basement structures that potentially influenced magma emplacement, may be poorly understood because they have been intruded by the mineralising stock, or are not well exposed at the present-day erosional level (Richards, 2000; Tosdal and Richards, 2001). The syn-, and in some cases, post-intrusion structural history can be masked by intense hydrothermal alteration (Lindsay et al., 1995).

Previous studies of the structural evolution of vein and mineralised fracture arrays in porphyry copper deposits have found that fracture orientations depend on whether the stress conditions were controlled by magmatic or tectonic forces (Heidrick and Titley, 1982; Tosdal and Richards, 2001). Magmatic stress, resulting from the physical process of intrusion, generates concentric and radial fractures above and around the intruding stock (Langerfield, 1964; Baumer and Fraser, 1975; Dunn, 1982; Heidrick and Titley, 1982). Following solidification, fracture geometries are influenced by tectonic activity. The fractures formed under conditions of tectonic stress alone are more ordered and linear in form (Lindsay et al., 1995; Tosdal and Richards, 2001).

Localisation and clustering of numerous porphyry copper deposits, including major centres such as Collahuasi, Chuquicamata, La Escondida and El Salvador, along major strands of the Domeyko fault system, have endowed Northern Chile with the largest known concentration of copper in the Andean Cordillera (Fig. 1.1; Camus, 2002). The Domeyko fault system defines a narrow structural corridor, 30-50 km wide and at least 1400 km long, between 19°S and 28°S (Lindsay et al., 1995; Richards et al., 2001). The Collahuasi porphyry deposits, situated near the northern end of this

porphyry belt are spatially associated with the Domeyko Fault (Fig. 1.3), but their emplacement was not directly controlled by this structure.

In the Rosario deposit, post-intrusion mineralised veins consistently strike northwest, parallel to a southwest dipping system of post-intrusion brittle faults of the Rosario fault system (Fig 2.7). Elongation of the Rosario stock, parallel to the Rosario fault system, suggests that this fault zone either formed contemporaneously with magmatism or may have been an older structure reactivated during magmatism. The timing of fault activity relative to magmatism and subsequent vein-style economic copper mineralisation is not well constrained, nor is the relationship between deformation at the scale of the Rosario deposit and that at the regional scale.

This chapter is divided into three parts. The first characterises the geological setting of the Rosario deposit, based on my surface mapping and drill core logging. A reconnaissance U/Pb geochronologic study was undertaken to further constrain the age of the rocks that host porphyry Cu-Mo mineralisation. In the second part of the chapter, the structural evolution of the Rosario deposit is discussed and a model for the structural controls to mineralisation is presented. Finally, the Rosario structural model is compared to those proposed for other porphyry Cu deposits in northern Chile. The discussion also focuses on the impact of tectonic events on the structural evolution of northern Chile and the implications for localisation of magma emplacement associated with porphyry ore deposits in the Domeyko Cordillera.

Geology of the Rosario Deposit

Copper mineralisation at Rosario is associated with a series of northwest-trending quartz-sulfide and massive sulfide veins occupying an area ≥1,500 m long and 1,200 m wide. Ore-grade mineralisation has been intersected to the current level of diamond drilling at depths of 900 m and is localised within and around a late-Eocene porphyritic quartz-monzonite, known as the Rosario Porphyry (Munchmeyer et al., 1984; Dick et al., 1994; Lee, 1994). This stock has intruded a porphyritic granodiorite, the Collahuasi Porphyry (59.4 ± 1.2 Ma; Vergara, 1978). The Rosario and Collahuasi Porphyries have intruded the Collahuasi Formation (Figs. 3.1 and 3.2), which Munchmeyer et al. (1984) informally divided into the La Grande and Condor Members (Chapter 2). The Condor Member appears to dominate the stratigraphy at Rosario. In this chapter, Munchmeyer et al.'s (1984) stratigraphy for the Collahuasi Formation is re-evaluated in terms of the main lithofacies that constitute the mine sequence.

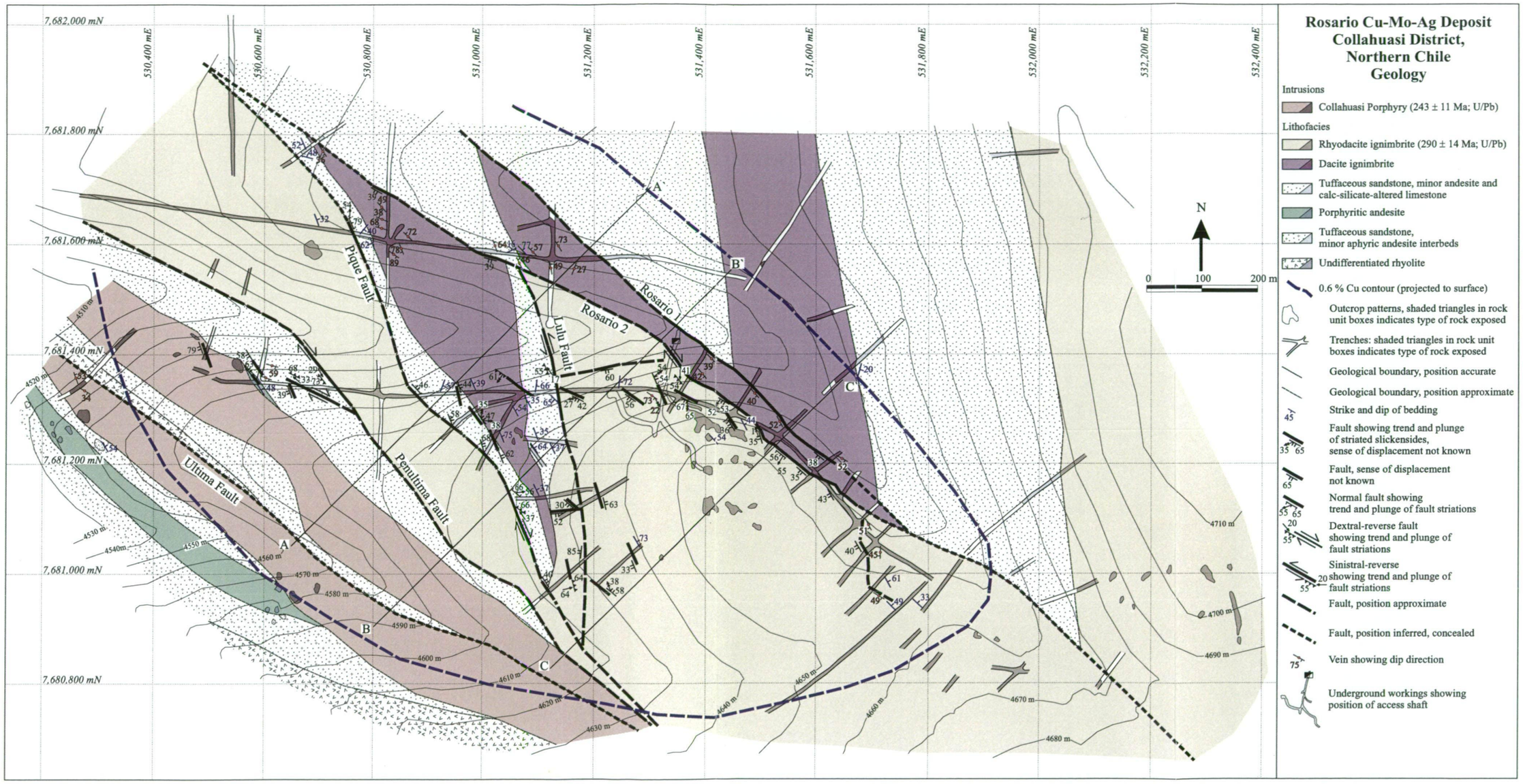

Figure 3.1. Interpreted basement geology of the Rosario deposit based on 1:2000 surface mapping and 1:200 graphic logging of diamond drill core. Surface exposure of the host-rock stratigraphy was generally restricted to outcrop in trenches as well as rare outcrop on hill slopes. The trajectories and dips of geologic contacts and major faults were projected along strike between trench cross-cuts. Fault kinematic indicators, where measured, are shown with apparent stratigraphic displacements reflecting the most recent movement history.

Lithofacies

Stratigraphic units at Rosario dip 30° to 50° northeast. Contacts between lithofacies are exposed at only a few localities (Fig. 3.1) and in drill core. The sequence dominantly comprises coherent and pyroclastic lithofacies, non-stratified or stratified volcaniclastic lithofacies and carbonate lithofacies. Descriptions and interpretations of the seven main facies are summarised in Table 3.1, and their distributions are shown in Figures 3.1 and 3.2. The phenocryst assemblage (feldspar, quartz and ferromagnesian phases) indicates that coherent lithofacies are andesitic in composition, whereas pyroclastic facies are dacitic and rhyodacitic. All lithofacies, except the carbonate facies, are volcanogenic. The lithofacies can be assigned to four main lithofacies associations: the primary volcanic facies association, the volcanogenic facies association, the carbonate facies association, and the pyroclastic facies association.

Primary volcanic facies association

Lithofacies of the primary volcanic facies association dominantly comprise coherent andesite and associated non-stratified monomict breccia (autoclastic breccia). Individual andesite units are distinguished by the distribution and abundance (or absence) of phenocrysts and amygdales (Figs. 3.3a to 3.3c). Andesite flows are normally separated by tuffaceous, crystal-lithic sandstone units (Fig. 3.3d).

Volcanogenic sedimentary facies association

The volcanogenic sedimentary facies association is characterised by volcanic lithic clasts (e.g., porphyritic andesite), and individual beds are generally ≤1 m thick. Typically, these units are characterised by massive to graded crystal- and/or lithic-rich tuffaceous sandstone. The sandstones are grain-supported, and the crystal population is dominated by plagioclase (up to 70 vol. %) in a chloritic matrix (Fig. 3.3d). Remnant biotite flakes, incipiently replaced by chlorite, are preserved in the matrix. Graded units are interbedded with thin siltstone beds (<0.5 m). This facies association is interpreted to have been deposited from low concentration turbidity currents, with siltstone predominantly deposited from suspension.

Figure 3.2. Stacked northeast-southwest geologic sections through the Rosario deposit. Surface traces of each section are shown in Figure 3.1. Hypogene copper grade contours are shown at the 0.6%, 1.0% and 1.5% levels. The highest copper grades (> 1.5% Cu) occur in the late-stage veins associated with the southwest dipping Rosario Fault System. The 1% Cu contour closely follows the outline of the Rosario porphyry. Geologic interpretations are based on drill hole logging completed in this study.

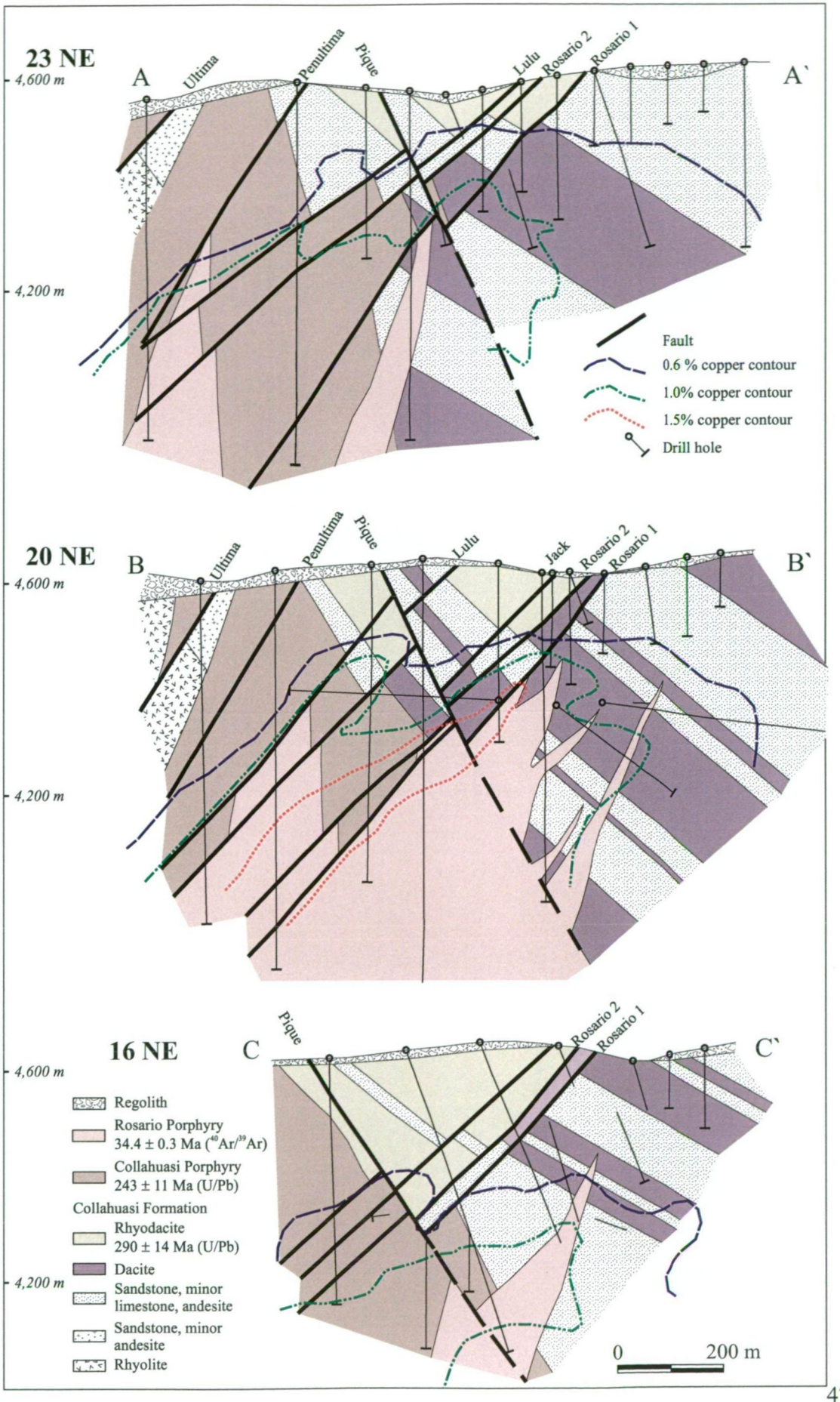
23 NE
4,600 m
4,200 m
A
A`
Ultima
Penultima
Pique
Lulu
Rosario 2
Rosario 1
Fault
0.6 % copper contour
1.0% copper contour
1.5% copper contour
Drill hole
20 NE
4,600 m
4,200 m
B
B`
Ultima
Penultima
Pique
Lulu
Jack
Rosario 2
Rosario 1
16 NE
4,600 m
4,200 m
C
C`
Pique
Rosario 2
Rosario 1
Regolith
Rosario Porphyry
34.4 ± 0.3 Ma (40Ar/39Ar)
Collahuasi Porphyry
243 ± 11 Ma (U/Pb)
Collahuasi Formation
Rhyodacite
290 ± 14 Ma (U/Pb)
Dacite
Sandstone, minor limestone, andesite
Sandstone, minor andesite
Rhyolite
0
200 m

Table 3.1. Summary of the main lithofacies at Rosario.

Lithofacies	Characteristics	Crystal/grain/lithic populations	Groundmass/matrix	Interpretation
Primary volcanic facies association				
Amygdaloidal andesite	Amygdaloidal, feldspar-phyric; 10-50 m thick	Plagioclase: 5 vol. %, 0.1-0.4 μm; elongate, euhedral Amygdales: 50 vol. %, 0.5-4.0 mm Amygdale infill = quartz, epidote, chlorite, illite	45 vol. %, 30-50 μm; plagioclase, skeletal magnetite, chlorite	Coherent facies of andesite lavas
Porphyritic andesite	Feldspar-phyric; 15-35 m thick	Plagioclase (An_{30} to An_{40}): 30-70 vol. %, 0.2-2.4 mm; euhedral, seriate, incipiently altered to sericite	30 vol. %, 10-20 μm; subhedral plagioclase, biotite	Coherent facies of sub-volcanic sills or lavas
Aphyric andesite	Massive, in parts feldspar-phyric; 10-30 m thick	Plagioclase: 30-50 vol. %, 1-4 cm; euhedral, seriate, incipiently altered to epidote	30 vol. %, 10-20 μm; subhedral plagioclase, hornblende	Coherent facies of andesite lavas
Volcanogenic sedimentary facies association				
Tuffaceous-crystal-lithic sandstone	Planar, laterally continuous beds, thin (10 to 70 cm) massive to normally graded, interbedded with siltstone; 5-70 m thick; some beds contain non-volcanic detritus	Plagioclase: 70 vol. %; coarse bands 0.4-1.5 mm, medium bands 0.2-0.5 mm, silty bands < 0.2 mm	30 vol. %, <0.2 mm; biotite, chlorite, feldspar; coarse bands grain supported, all others matrix supported	Sandstone beds deposited from low density turbidity currents; siltstone as background deposition
Carbonate facies association				
Massive to laminated silty limestone	Thin lenses, internally massive or laminated; 2-30 m thick		Calcite: 40-50 vol. %, 100-500 μm; garnet: 20-30 vol. %, 100-500 μm; quartz: 20-30 vol. %, 50-100 μm; accessory diopside, epidote and smectite	Carbonates deposited concomitantly with turbidite facies
Pyroclastic facies association				
Massive crystal-rich tuffaceous dacite	Feldspar-phyric (pseudo-porphyritic), locally pumiceous, with feldspars preferentially aligned with the weak to moderate compaction fabric; 30-200 m thick	Pumice: 20-30 vol. %, 2-5 cm long, ≤ 1.5 cm wide; contain axiolitic feldspar, flattened and crenulated Plagioclase: 10-15%, 0.6-1.8 mm K-feldspar: 3-5%, 0.6-1.5 mm; some simple twins (sanidine), minor micro-perthite; accessory apatite	55-85%, ≤60 μm, mostly 5-20 μm; micro-aplitic to granophyric quartz, K-feldspar, plagioclase, steely grey in hand specimen; deformed shards of devitrified glass define a eutaxitic texture; minor biotite, magnetite; accessory, zircon	Subaerial pyroclastic flow re-deposited into shallow subaqueous setting
Massive crystal-rich, fiamme-bearing rhyodacite	Feldspar-phyric (pseudo-porphyritic); repetition of internally banded, pumiceous and cohesive layers throughout; 50-200 m thick	Plagioclase: 5-20%, 0.3-3.0 mm; broken euhedral crystals K-feldspar: 5-15%, 0.2-2.0 mm; broken subhedral-euhedral crystals Pumice: 7-25%, 0.2-3.0 cm; flattened; comprise plagioclase-K-feldspar phenocrysts, fine radiating and axiolitic feldspar laths Lithics: 5-10%, 1.8-3.0 mm; mostly plagioclase-phyric andesite, minor feldspar-phyric granite and reworked pumice Quartz: 1-10%, 0.3-1.5 mm; rounded, some embayed crystals	45-75%, 2-50 μm; aphanitic to granophyric; plagioclase, K-feldspar; shards of deformed devitrified glass shards defining a eutaxitic texture; accessory apatite, magnetite, zircon	Subaerial pyroclastic flow deposit

Carbonate facies association

The carbonate facies association consists of limestone units that, in the mine area, have been altered to a calc-silicate association of garnet, diopside, actinolite, epidote, chlorite, and magnetite (Fig. 3.3e). Outside the mine area, limestone occurs as dark grey to black lenses that are devoid of fossils except for minor occurrences of stromatolite (Munchmeyer et al., 1984). Limestone is typically massive, with minor laminated domains, and contains up to 30% fine grained quartz and accessory clay. It is interpreted that limestone was deposited with turbiditic sandstone in a below wave-base sub-aqueous environment.

Pyroclastic facies association

The pyroclastic facies association comprises feldspar-phyric dacite (Fig. 3.3f) and rhyodacite (Fig. 3.3g). The dacite units, defined by Munchmeyer et al. (1984), Dick et al. (1994), and Lee (1994) as the Inés Porphyry, were interpreted as branched, porphyritic dykes and sills that had intruded the Condor Unit. This interpretation was based on the limited drilling available in the northeast sector of the deposit, where the Inés Porphyry is most abundant, and assumed that the medium-grained (0.8-2.0 mm), feldspar-phyric texture was diagnostic of an intrusion. However, at two prominent surface exposures, the same porphyritic dacite contains up to 30% flattened, wavy pumice (fiamme), and a groundmass of devitrified glass shards that define a eutaxitic texture. Ragged biotite, chlorite and sericite have replaced primary ferromagnesian minerals at depths >100 m, although a fine grained granophyric quartz-feldspar groundmass is generally preserved. No age dates are available, but in several drill holes the porphyritic dacite is cut by the Rosario Porphyry (Lee, 1994). The presence of fiamme, deformed glass shards and granophyric groundmass is interpreted as evidence that the porphyritic dacite is a welded ignimbrite (e.g., McPhie et al., 1993).

Figure 3.3. Examples of rock types from the Collahuasi Formation:

A) *Sample R990277.* Photograph of feldspar-phyric andesite (ocoita). Feldspar megacrysts (plag), incipiently altered to epidote, are enclosed in a dark, fine-grained groundmass (scale bar = 1 cm).

B) *Sample R990314.* Photomicrograph in cross-polarised light of a feldspar-phyric, amygdaloidal andesite. Phenocrysts of plagioclase (plag) and epidote-quartz-chlorite-filled amygdales (amyg) occur in a dark groundmass of aphanitic feldspar and ferromagnesian phases (scale bar = 1 mm).

C) *Sample R990092.* Photomicrograph in cross-polarized light of feldspar-pyroxene phyric andesite. Phenocrysts of plagioclase (plag) and pyroxene (px) are enclosed in dark groundmass of magnetite (opaque crystals) and shreddy biotite that has been incipiently replaced by chlorite. Edges of pyroxene phenocrysts have also been partly overprinted by biotite and chlorite (scale bar = 1 mm).

D) *Sample ROS038.* Photomicrograph in cross-polarized light of graded andesitic sandstone. Sedimentary grains are predominantly plagioclase with minor quartz and fine lithic fragments. The matrix consists dominantly of chlorite. Facing direction of this specimen is towards the left, with the bedding interface at the base of the coarse-grained plagioclase band (scale bar = 1 mm).

E) *Samples R990046, R990062 and R990063.* Selected drill core samples of skarn alteration in the Condor Unit. The sample on the left is characterized by kernels of red garnet enveloped by domains of light brown garnet. The centre sample consists of red garnet kernels enclosed in pervasive fine-grained pyroxene. The sample on the right comprises brown garnet bands separated by calcite domains. The centre and right samples have been cut by calcite-pyrite-chalcopyrite veins with magnetite-epidote selvages and chlorite alteration envelopes (scale bar = 2 cm).

F) *Sample R200171.* Photograph of feldspar-phyric dacite (formerly Inés Porphyry). White phenocrysts of plagioclase and minor K-feldspar are enclosed in a steel-grey, fine-grained groundmass. This sample is cut by a quartz-albite-chalcopyrite ± biotite veins with albite-biotite alteration envelopes (scale bar = 1cm).

G) *Sample R990254.* Photograph of feldspar-phyric rhyodacite. White feldspar phenocrysts, consisting of plagioclase, minor sanidine and K-feldspar, occur with lithic fragments and trace quartz eyes enclosed in a fine-grained devitrified glass groundmass. The faint layering (sub-horizontal to the right) reflects eutaxitic texture defined by fiamme. The rock is interpreted to be a welded ignimbrite (scale bar = 1 cm).

H) *Sample R990254.* Photomicrograph of feldspar-phyric rhyodacite in plane-polarized light. The flattened, horizontal pumice clast (fm) comprises coarse feldspar crystals enclosed in a fine-grained axiolitic feldspar groundmass. Feldspar phenocrysts (across the top) are surrounded by a compacted groundmass of devitrified glass shards that wrap around crystals and fiamme. This sample is interpreted to be a welded ignimbrite (scale bar = 1 mm).

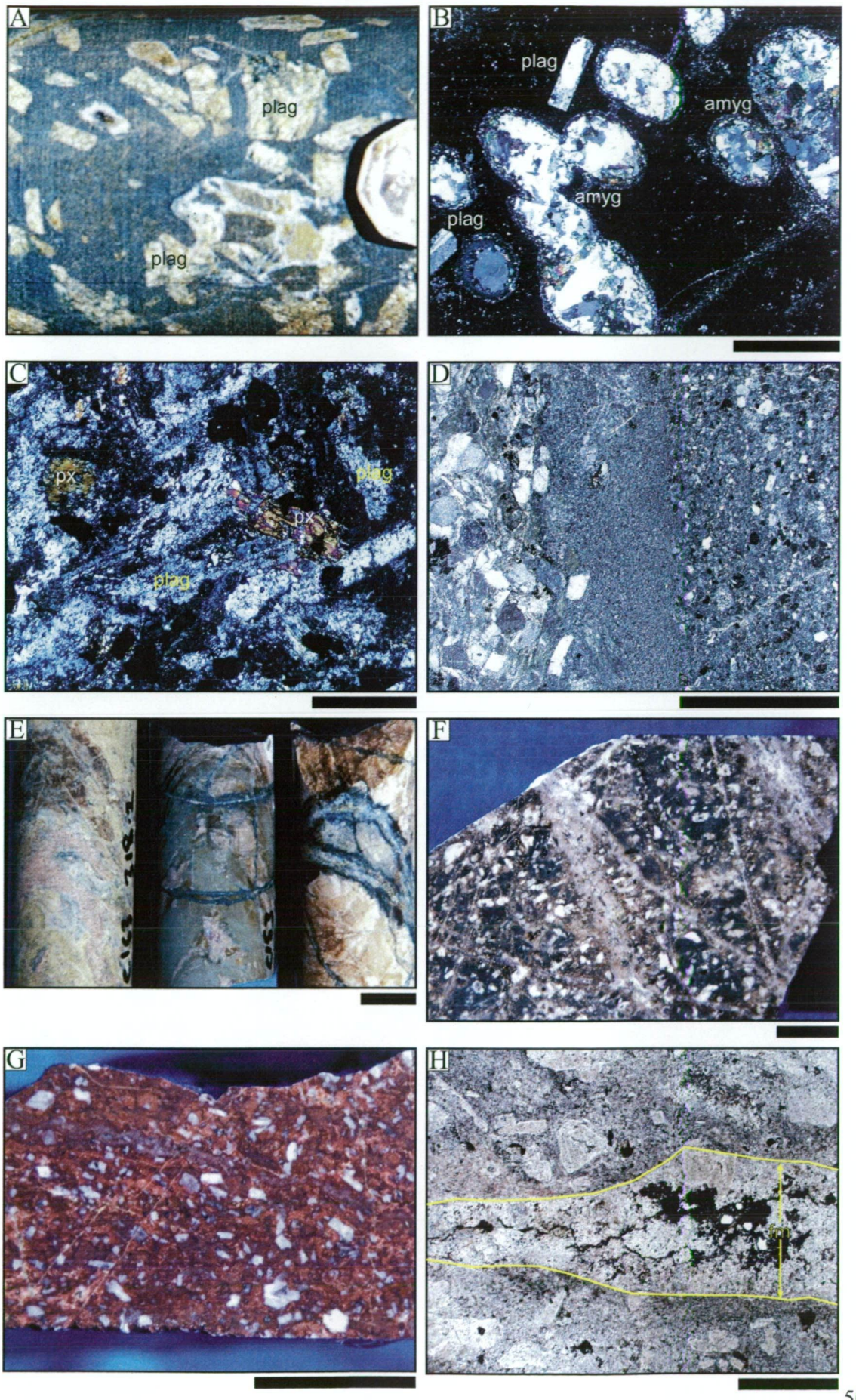
A
plag
plag
B
plag
amyg
amyg
plag
C
px
plag
px
plag
D
E
F
G
H

Rhyodacite units crop out as coarse-grained (0.3-3.0 mm) feldspar ± quartz-phyric and pumiceous (0.2-3.0 cm) rocks with well defined eutaxitic texture and a deep purple (at surface) to grey (>50 m deep) aphanitic groundmass containing disseminated magnetite. Primary ferromagnesian minerals are few, consisting mainly of hornblende. Where preserved, hornblende has been selectively replaced by epidote, chlorite and rare ragged biotite. Eutaxitic texture defines a planar fabric assumed to be parallel to bedding. Flow units are multiply zoned, distinguished by different proportions of plagioclase, K-feldspar, and quartz, and the presence or absence of strongly compressed fiamme, pumice lapilli or a primary compaction fabric. Where present, pumice lapilli and fiamme consist of fine axiolitic feldspar, granophyric quartz-feldspar mosaics and variable quantities of phenocrystic plagioclase and K-feldspar (locally composing 15-20 vol.% of the rock, but may be totally absent, Fig. 3.3h). Internal pumice-tube structures are uncommon. The groundmass typically comprises devitrified glass shards, visible under plane-polarised, but present as granophyric feldspar quartz mosaics when viewed in cross-polarized light (Fig. 3.3h). Deformed glass shards, compacted against feldspar phenocrysts, are common and define a preferred orientation parallel to the fiamme. These textures are typical of ignimbrites (McPhie et al., 1993).

Intrusions

Collahuasi Porphyry

The northwest-trending Collahuasi Porphyry, varies from 50m thick in surface exposures to >300 m thick at depth, and is exposed over a strike-length of 8 km (Munchmeyer et al., 1984). The southern end of exposed Collahuasi Porphyry occurs 3-4 km beyond the limit of the Rosario hydrothermal system. It is not exposed north of Rosario. Sub-rounded diorite, and rare granite and andesite ("ocoita") xenoliths, ranging in size from 1-15 cm, are common throughout the Collahuasi Porphyry. In the Rosario alteration zone (Figs. 3.1 and 3.2) primary ferromagnesian minerals have been replaced by hydrothermal biotite, chlorite and sericite (Fig. 3.4a). In thin section, feldspar phenocrysts display pristine, clear cores, surrounded by turbid margins (Fig. 3.4b). Core compositions are dominated by albitic (An_0-An_5) plagioclase and K-feldspar. Trace disseminated magnetite, displaying ilmenite exsolution lamellae, typically occurs together with ragged, groundmass biotite (see Table 3.2). Primary groundmass hornblende and biotite are preserved in the Collahuasi Porphyry, 2 km

Figure 3.4. Intrusive rocks from the Rosario porphyry centre.

A) *Sample R200143.* Photograph of the feldspar-quartz phyric Collahuasi Porphyry (granodiorite). White tabular plagioclase and K-feldspar phenocrysts occur with coarse-grained quartz eyes and chloritised ferromagnesian crystals in a fine-grained groundmass of feldspar and quartz. The specimen is cut by several chloritic veins (scale bar = 1 cm).

B) *Sample R200143.* Photomicrograph under cross-polarized light of the Collahuasi Porphyry. Tabular and sub-rounded plagioclase and K-feldspar, and rounded quartz phenocrysts are enclosed in an aplitic feldspar-quartz groundmass. Turbid feldspar phenocrysts have been partly replaced by illite. Aggregates of fine radiating chlorite are interpreted to have completely replaced primary ferromagnesian minerals (scale bar = 1 mm).

C) *Sample R200124.* Photograph of the feldspar-quartz-biotite-phyric Rosario Porphyry (granodiorite). White feldspar phenocrysts consist of albite and oligoclase enclosed in a fine-feldspar-quartz groundmass (scale bar = 1 cm).

D) *Sample R200130.* Photomicrograph under cross-polarized light of the Rosario Porphyry. Turbid plagioclase phenocrysts have been incipiently overprinted by illite. Biotite rims and some cleavage surfaces have been replaced by chlorite. Aplitic groundmass consists of feldspar and quartz (scale bar = 1mm).


A

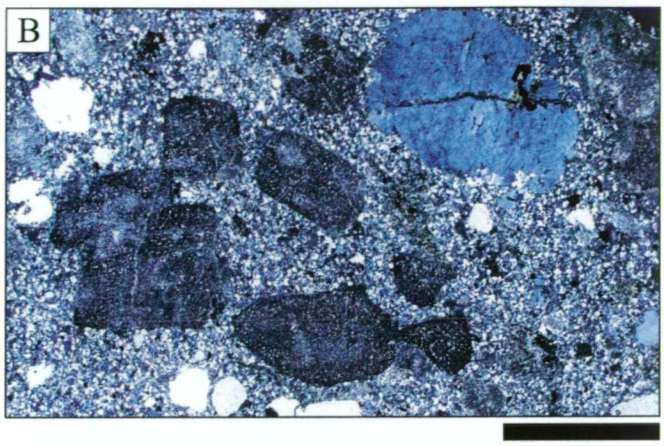
B

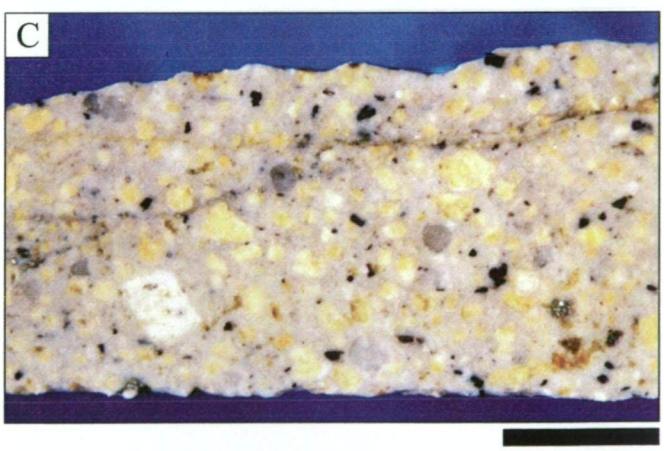
C

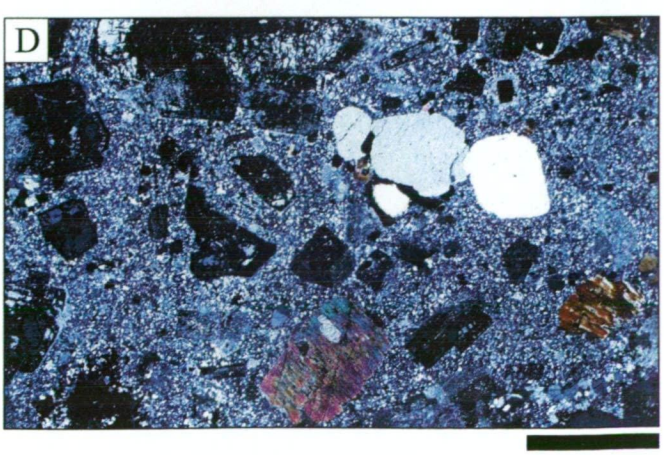
D

south of Rosario, beyond the limit of hydrothermal alteration (Vergara, 1978; Munchmeyer et al., 1984).

Rosario Porphyry

Shallow level apophyses of the Rosario Porphyry join together at depths of 400 to 600 m below surface into an elongate, northwest-trending stock 300 to 500 m wide and up to 1500 m long (Fig. 3.2). The intrusion, delineated to a depth of 1000 m, is mineralogically classified as a quartz monzonite using the scheme of Streickeisen (1979). The Rosario Porphyry is the only rock-type in the Rosario alteration system that contains relict primary ferromagnesian minerals, namely biotite (Fig. 3.4c). Most Ca-Na-feldspar phenocrysts are turbid due to partial alteration by illite (Fig. 3.4d), however where primary cores are preserved they have oligoclase-andesine compositions (An_{20}-An_{36}). K-feldspar does not occur as a primary phenocryst phase. In thin section, the groundmass is typically more aplitic than that of the Collahuasi Porphyry.

Table 3.2. Porphyritic Intrusive Rocks of the Rosario Deposit

Intrusive Unit	Characteristics	Phenocrysts[1]	Groundmass
Collahuasi Porphyry	Massive, porphyritic, minor xenoliths	Albite (An_0-An_5): 30%, ≤8 mm, mostly 0.6-5.0 mm; minor oscillatory zoning, euhedral, incipiently sericite-altered An_2-An_5 Quartz: 15-20%, ≤7 mm, mostly 0.5-3.0 mm, commonly rounded and resorbed K-feldspar: 10-15%, ≤5 mm, mostly 0.5-2.0 mm, incipiently to pervasively sericite-altered Accessory magnetite Xenoliths: ≤2%, feldspar-phyric diorite, rare rhyolite and mega-porphyritic andesite	40%, 20-400 μm; aphanitic to aplitic; subhedral to anhedral quartz, K-feldspar, plagioclase; accessory zircon, apatite
Rosario Porphyry	Massive, porphyritic	Calcic plagioclase: 20%, ≤3.5 mm, mostly 0.5-2.3 mm; subhedral to euhedral, seriate; An_{20} to An_{36} Albite: 5-10%, ≤3.5 mm, mostly 0.5-2.3 mm; An_2 to An_8 Quartz: 7-10%, ≤4 mm, mostly 0.2-3.2 mm; commonly rounded and resorbed Biotite: 3-5%, ≤2 mm, mostly 0.1-0.8 mm Accessory zircon, trace apatite	55-65%, 40-100 μm; aplitic, subhedral to anhedral quartz, albite, calcic plagioclase, K-feldspar (?), biotite

[1] feldspar phenocryst compositions listed in Appendix 2.

Facies Architecture

Coherent andesite units at the bottom of the northeast-dipping volcano-sedimentary sequence occur as semi-continuous lenses, interfingered with tuffaceous sandstone (Figs. 3.1 and 3.2). These are conformably overlain, in the middle of the sequence, by dacite ignimbrite, interbedded with thick beds of tuffaceous sandstone, minor limestone (2-10 m thick) and rare units of coherent andesite (<5 m thick). Massive rhyodacite ignimbrite at the top of the sequence is concordant with the underlying stratigraphy (Fig. 3.1). The sequence was intruded initially by the Collahuasi Porphyry, and afterwards by the Rosario Porphyry.

The occurrence of dacitic ignimbrite, interbedded with feldspathic sandstone and limestone suggests deposition in a shallow subaqueous to emergent environment. It is possible for ignimbrite units to weld in sub-aqueous environments providing that offshore topographic gradients are low and water depths are shallower than the thickness of the pyroclastic flow unit (McPhie et al., 1993). Thus the top of the flow, when deposited, was subaerial. The lensoidal shape of the dacitic ignimbrite flow unit suggests that it was channel-confined and possibly originated from a subaerial caldera eruption near the shoreline. Massive rhyodacitic ignimbrite at the top of the sequence lacks interflow sedimentary rocks, implying that by the time it was deposited, the environment had become entirely subaerial.

Geological re-interpretation

The sequence of volcanic and sedimentary rocks at Rosario is entirely concordant. The observations made in the current study are not consistent with the existence of an unconformity between the La Grande and Condor Members, as suggested by Munchmeyer et al. (1984). Moreover, the composition of volcanic rocks at the bottom of the sequence is andesitic, whereas that in the middle and at the top are dacitic and rhyodacitic, respectively. This evolution up sequence from intermediate to felsic rocks is consistent with co-genetic fractional crystallisation. It is thus interpreted that the host volcanic rocks at Rosario were sourced from a magma chamber that became more fractionated with time, with no major hiatus in deposition of the sequence.

The country rocks at Rosario are interpreted here to be a concordant volcano-sedimentary sequence deposited in an environment that evolved from shallow subaqueous to subaerial. The dacite facies, interpreted by Munchmeyer et al. (1984), Dick et al. (1994), and Lee (1994) as an intrusive facies, has been reinterpreted as a welded ignimbrite, based on textural evidence.

U/Pb Geochronology

One aim of the current geologic investigation has been to resolve ambiguous K-Ar age dates for the host Collahuasi Formation at Rosario. Vergara and Thomas (1984) and Munchmeyer et al. (1984) reported some unusually young ages for the host rocks based on whole-rock analyses of altered samples collected proximal to the Rosario Porphyry. These dates varied from Mid-Jurassic and Late Cretaceous to early Paleogene, and did not correlate with the generally accepted Permo-Triassic age for the Collahuasi Formation. Both workers doubted the validity of these ages and inferred that the K-Ar systematics had been reset by later events (e.g., emplacement of the Rosario Porphyry). Thus a reconnaissance U/Pb geochronologic study has been undertaken, using samples of the dacite ignimbrite and Collahuasi Porphyry. Zircons from these rocks have been dated by U/Pb laser ablation – inductively coupled plasma mass spectrometry (LA-ICPMS) in order to improve the temporal constraints on the age of volcanic and intrusive host rocks at Rosario.

Zircon separation and preparation

Samples were crushed in a tungsten-carbide jaw crusher to gravel size (2-4 mm) prior to milling in a chrome-steel mill to 0.05-0.5mm. Samples were then sieved, the <200μm fraction was collected and less dense fractions panned off. The zircons were separated from the <200μm fraction via conventional heavy-liquids techniques. The heavy mineral fractions were then washed, dried and magnetically separated using a Franz magnetic separator. Zircons 40μm long or greater were randomly selected. The selected zircons were mounted in epoxy blocks and polished.

Laser ablation ICPMS method

The use of LA-ICPMS for U-Pb dating of zircons has been applied to several geochronological studies worldwide (e.g., Machado and Gauthier, 1996; Machado et al., 1996; Belousova et al., 2001; Berry et al., 2001). Laser microprobes operate with spot diameters comparable to ion microprobes (30-50 μm) but the laser drills into the

grain at a considerably greater rate, degrading spatial resolution with depth into the grain during analysis. This is partially compensated by collecting the LA-ICPMS data in time-resolved mode so that zones with different U-Pb ratios can be identified and the data reduced accordingly (Belousova et al., 2001).

Instrument operating parameters

U-Th-Pb isotopic compositions of zircons were measured using an Agilent HP4500 ICPMS coupled with a Merchantek 266nm Nd:YAG laser at the Centre for Ore Deposit Research, University of Tasmania. Isotopic masses collected were ^{238}U, ^{235}U, ^{232}Th, ^{208}Pb, ^{207}Pb, ^{206}Pb, ^{204}Pb and ^{202}Hg. Zircons were analysed with a 30μm diameter beam, a laser repetition rate of 5 Hz, and a power setting of 0.37 mJ. The ICPMS was operated in time-resolved mode, collecting one point per mass per sweep of the mass range with a dwell time of 10 msec/mass. Each analysis consisted of measurement of gas background count rates on each mass for 60 sec prior to ablation, followed by 60 sec of ablation. Each analysis was followed by a 2 minute washout period during which the signal intensity returned to background level.

Data collection and reduction

Sample runs consisted of 6 unknowns bracketed by two sets of 4 standards. A total of 12 analyses of unknown zircons were made from the two samples. Four analyses of an in-house zircon standard from the 417 Ma Temora Gabbroic Diorite, NSW (Black et al., 2000) were completed before analysis of the 12 unknowns. After the unknowns were analysed, another four analyses of Temora Gabbroic Dolerite were made using the same analytical conditions. The measured $^{206}Pb/^{238}U$, $^{207}Pb/^{235}U$, and $^{207}Pb/^{206}Pb$ ratios of the 12 unknowns were corrected to the bracketing standard analyses using accepted values of the Temora Gabbroic Diorite zircons obtained by SHRIMP (Black et al., 2000).

Data were reduced and ages calculated using the LAMTRACE program (van Achterbergh, et al., 2001). Each time-resolved spectra was examined and net count rates for each mass were obtained by subtracting average background intensities (counts per second) from average signal intensities taken ~15 sec after beginning of ablation when the signal had stabilized. Under the operating conditions used for this study, homogeneous grains with low common Pb such as those from the Blind Gabbro produced near-steady signals with no resolvable change in $^{206}Pb/^{238}U$ or $^{207}Pb/^{235}U$ signal intensities during the analysis.

Corrections for common Pb were applied to the unknowns using the single step ^{208}Pb method of Cumming and Richards (1975). This method was used instead of a direct correction using ^{204}Pb (cf. Machado and Gauthier, 1996) to avoid uncertainties associated with potential interferences from ^{204}Hg, and the large errors associated with the low count rates for ^{204}Pb in most of these samples. Standard analyses indicating significant amounts of common Pb were excluded from the calibration.

Analytical precision of LA-ICPMS zircon analyses is primarily a function of count rate, which is controlled by spot diameter, abundance of U and Th, and age of the grain (M. Norman, written comm., 2002). An indication of analytical precision obtained by this study is gained from the distributions of apparent ages of secondary standards analysed on the same day as the unknowns and primary standard. Five zircons from Tasmanian Jurassic dolerite (182 ± 2 Ma; Williams and Hergt, 2000), nine zircons from Blind Gabbro, NSW (411 ± 4 Ma; W. Collins unpub. data) and 20 zircons from the Mud Tank Carbonatite, Northern Territory (732 ± 5 Ma, Black and Gulson, 1978) produced compiled ages of 189 ± 7 Ma, 419 ± 8 Ma and 727 ± 23 Ma, respectively.

U/Pb age data

Analytical results are shown in Figure 3.5 and listed in Table 3.3. Isoplot (Ludwig, 2001) was used to calculate Tukey's biweight robust mean ages (Hoaglin et al., 1983) and 2σ errors of each of the zircon fractions. Zircons from the dacite ignimbrite plot close to the concordia for the Early Permian period, and have a mean $^{206}Pb/^{238}U$ age of 293 ± 14 Ma. Zircons from the Collahuasi Porphyry also plot near the concordia. They yielded a robust mean $^{206}Pb/^{238}U$ age of 245 ± 12 Ma. Tukey's biweight robust mean $^{206}Pb/^{238}U$ ages were used because the Isoplot weighted mean $^{206}Pb/^{238}U$ ages incorporated only the assigned errors, so yielded high MSWD values of 3.8 and 7.3 for the dacite and Collahuasi Porphyry samples, respectively.

Although both dates are imprecise, the Tukey's biweight robust mean $^{206}Pb/^{238}U$ ages provide useful reconnaissance ages of the Rosario host rocks. Importantly, the ages are distinguishable from each other, and indicate that the Collahuasi Porphyry intruded the Collahuasi Formation in the Early Triassic. These ages are also distinguishable from the early Oligocene $^{40}Ar/^{39}Ar$ age of biotite alteration (32.9 ± 0.5 Ma), determined by Clark et al. (1998) to be associated with emplacement of the Rosario Porphyry.

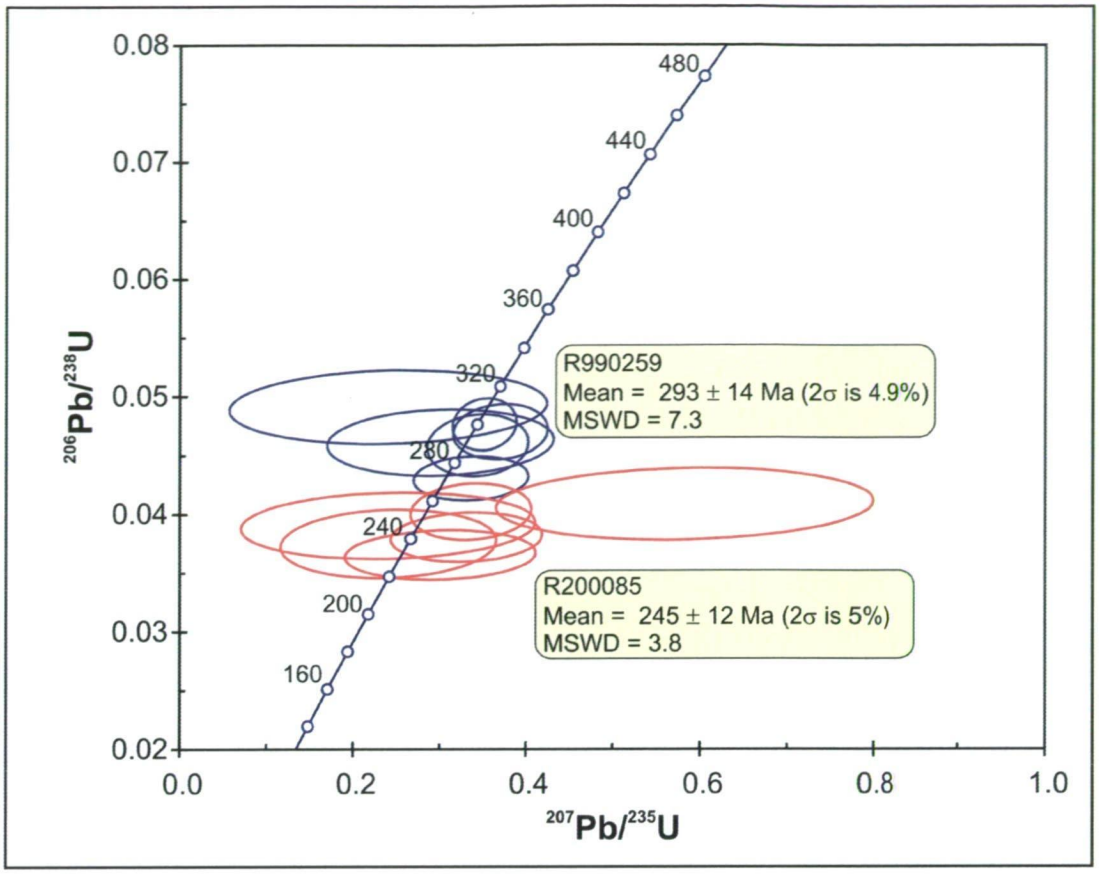

Figure 3.5. U-Pb data for samples of igneous rocks from the Collahuasi Formation. The weighted mean $^{206}Pb/^{238}U$ age of the rhyodacite sample (R990259) for the six concordant analyses is 290 ± 14 Ma. The mean concordia $^{206}Pb/^{238}U$ age of the Collahuasi Porphyry sample (R990085) is 243 ± 11 Ma. See text for discussion and Table 3.3 for analytical results.

Age of the host rocks at Rosario

Results of the U/Pb dating experiments on the host rocks at Rosario are consistent with the Permo-Triassic age assigned to the rocks by previous workers in the Collahuasi district (Munchmeyer et al., 1984; Vergara and Thomas, 1984). However, in their subdivision of the Collahuasi Formation, Munchmeyer et al. (1984) inferred that the Condor Unit was deposited in Jurassic times, based on the presence of limestone units that they correlated with Jurassic carbonate sequences in the Quehuita Formation. The new U/Pb age of the dacite ignimbrite, which occurs in their Condor Unit subdivision, indicates that these rocks were deposited in the Early Permian. This supports the hypothesis that no unconformity separates Permo-Triassic and Jurassic rocks in the Collahuasi Formation at Rosario. Instead, the package is interpreted to be entirely of Early Permian age. Large granodiorite plutons of Triassic age have intruded the Collahuasi Formation, 5 to 10 km south of Rosario (Fig. 2.7; Munchmeyer et al., 1984; Vergara and Thomas, 1984). These granodiorite intrusions (including the

Table 3.3. U/Pb data for zircons from the host rocks at Rosario .

Sample	U (ppm)	Pb (ppm)	$^{208}Pb/^{232}Th$	$^{207}Pb/^{206}Pb$	$^{207}Pb/^{235}U$	$^{206}Pb/^{238}U$	$^{206}Pb/^{238}U$ age (Ma)
Collahuasi Porphyry							
R200085	149	6	0.0117 ± 0.0011	0.045 ± 1.1335	0.241 ± 0.0825	0.0375 ± 0.0019	237 ± 12
R200085	165	7	0.0118 ± 0.0012	0.038 ± 0.0598	0.241 ± 0.1127	0.0390 ± 0.0019	247 ± 12
R200085	386	17	0.0123 ± 0.0007	0.051 ± 0.0587	0.337 ± 0.0463	0.0402 ± 0.0016	254 ± 10
R200085	242	10	0.0145 ± 0.0012	0.064 ± 0.0329	0.301 ± 0.073	0.0365 ± 0.0014	231 ± 9
R200085	317	20	0.0159 ± 0.0019	0.101 ± 0.0202	0.583 ± 0.1433	0.0409 ± 0.0020	258 ± 13
R200085	537	27	0.0127 ± 0.0006	0.060 ± 0.0258	0.332 ± 0.0579	0.0381 ± 0.0014	241 ± 9
Dacite Ignimbrite							
R990259	157	8	0.0158 ± 0.0016	0.053 ± 0.0696	0.301 ± 0.0867	0.0461 ± 0.0019	291 ± 12
R990259	980	51	0.0148 ± 0.0006	0.055 ± 0.0184	0.352 ± 0.0245	0.0477 ± 0.0015	300 ± 9
R990259	127	6	0.0134 ± 0.0016	0.048 ± 0.3060	0.241 ± 0.1214	0.0491 ± 0.0021	309 ± 13
R990259	551	30	0.0121 ± 0.0005	0.051 ± 0.0599	0.337 ± 0.0440	0.0431 ± 0.0012	272 ± 8
R990259	518	32	0.0151 ± 0.0005	0.054 ± 0.0298	0.371 ± 0.0364	0.0470 ± 0.0015	296 ± 10
R990259	431	27	0.0152 ± 0.0009	0.050 ± 0.0057	0.344 ± 0.0387	0.0459 ± 0.0017	289 ± 11

213 nm laser @ 5 Hz, 60% power, 0.37mJ, 30 μm spot size, HP4500 quadrupole ICPMS
Absolute element concentration assumed stoichiometric zirconium in the zircons and used NIST 612 to calculate mass bias.

Collahuasi Porphyry) are inferred to have intruded the Collahuasi Formation late in the evolution of a Permo-Triassic continental arc (Coira et al., 1982).

The new U/Pb age of the Collahuasi Porphyry (243 Ma) is considerably older than the whole-rock K/Ar age of 59.4 ± 1.2 Ma as determined by Vergara (1978). Furthermore, this new age proves that the Collahuasi porphyry is not a separate Paleocene mineralised porphyry, as suggested by Clark et al. (1998), so did not contribute to the metal budget at Rosario. Instead, the Collahuasi Porphyry is part of the host sequence that was intruded by the Rosario Porphyry in the late Eocene-early Oligocene.

Structural Geology

Several deformation phases have been recognised in the Collahuasi District, with contrasting deformation styles evident on either side of the Domeyko fault system. Most of the shortening has been accommodated by the Mesozoic rocks, west of the Domeyko fault system, which have been deformed by tight, upright and locally overturned folds, and by reverse faults (Fig. 3.6a). Shortening in the rheologically competent Paleozoic basement rocks of the Collahuasi Formation, east of the Domeyko Fault (Fig. 3.6b), has produced low amplitude, long wavelength folds cut by a complex array of brittle faults.

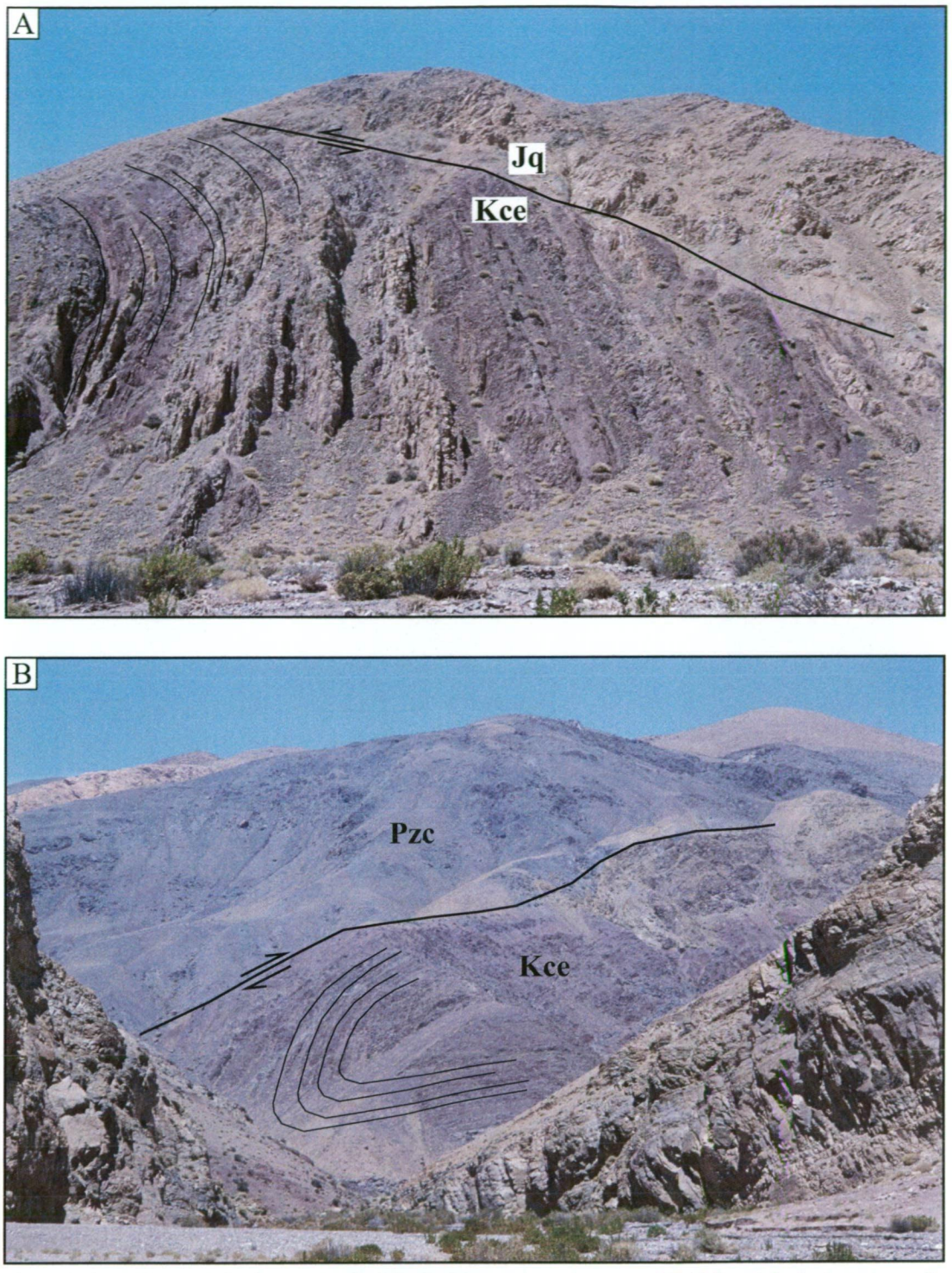

Figure 3.6. **A)** Photograph of a reverse fault in the Mesozoic rocks west of Collahuasi. In the hangingwall, marine sedimentary rocks of the Quehuita Formation (Jq) have been thrust over continental red beds in the Cerro Empexa Formation (Kce). Drag folds, indicative of reverse movement, have been highlighted in the footwall. **B)** Photograph of Permian basement (Pzc) in the hangingwall of a reverse fault, 12 km west of Rosario. Cretaceous red beds of the Cerro Empexa Formation (Kce) occur in the footwall. Note again the drag folds formed in the Cerro Empexa Formation.

In the Rosario-La Grande areas, brittle fault development succeeded folding of rocks in the Collahuasi Formation. Upright north to northwest trending folds are developed throughout the Collahuasi Formation (Figs. 2.4 and 2.7). Vergara and Thomas (1984) interpreted the broad north-trending anticline at Quebrada Blanca to be related to doming by the mineralised plutonic complex. South of Rosario, the volcano-sedimentary strata dip northeast at 30° to 50°, whereas west of Rosario the inward dipping strata define a broad northwest-plunging synform. No folds have formed in the Miocene to Pliocene ignimbrite flows that occupy the northern part of Collahuasi District, although some north-striking faults have cut this unit (e.g., Fig. 2.4).

The Rosario fault system comprises a series of moderate to steep (45° to 65°), southwest- and northeast-dipping faults that have cut the Rosario ore body (Figs. 3.1 and 3.2). These faults show considerable dextral (up to 1,100 m strike separation) and minor sinistral (≤300 m strike separation) offsets (Figs. 3.1). Some of these faults have localised the high-grade Cu-Ag-(Au) veins at Rosario. A second group of faults, striking north-northeast, occur in the La Grande area 1.5 to 2 km south of Rosario (Fig. 5.7). These faults have also localised high-grade Cu-Ag-(Au) veins (Dick et al., 1994; Lee, 1994).

Ductile Deformation

The Rosario deposit is situated on the western limb of a southeast-plunging syncline (Fig. 2.7). The upright and subvertical nature of both the Collahuasi and Rosario porphyries suggests that emplacement of both plutons succeeded the folding event. Evaluation of bedding data for the syncline formed in the Condor Unit reveals that a component of rotation has been accommodated on the main segments of the Rosario fault system. Figure 3.7 shows poles to bedding separated into hangingwall and footwall populations. A fold axis plunging 35° ESE, determined for the small footwall dataset, is interpreted to approximate the true plunge of the syncline, as the footwall rocks north of the Rosario fault system do not appear to have been rotated by fault movements. The fold axis in the hangingwall plunges 50° ENE, indicating approximately 15° of predominantly dip-slip rotational steepening of the hangingwall stratigraphy relative to the footwall volcanic units. This suggests either reverse fault drag associated with normal movement, or normal drag associated with reverse movement on the Rosario Fault.

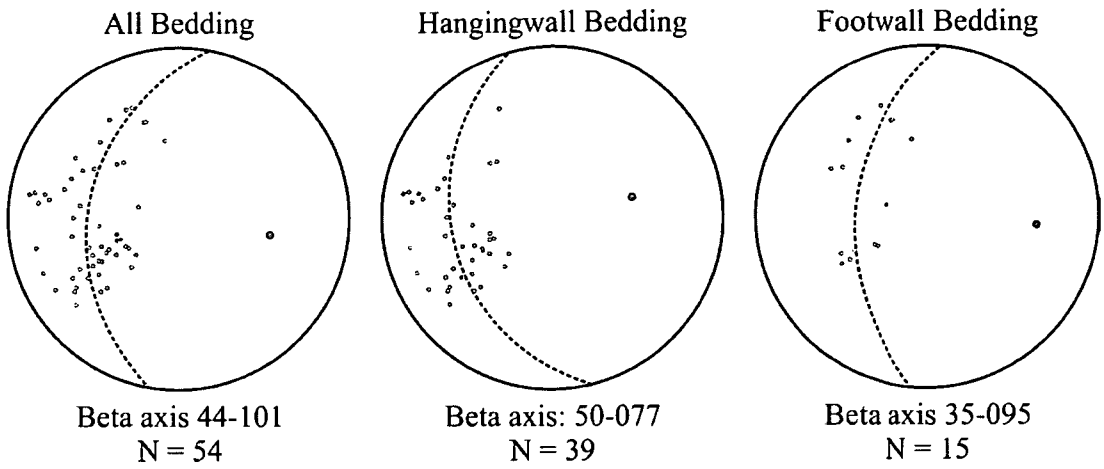

Figure 3.7. Compilation on equal area projections (lower hemisphere) of bedding orientation measurements (S_0) from the Rosario deposit. The data have been split into populations corresponding to the footwall and hangingwall sides of the Rosario Fault. Beta axes for each population are shown. The statistical fold axis calculation for the footwall population should be most representative of the regional folding pattern in the Collahuasi district. The statistical fold axis of the hangingwall population plunges more steeply than that of the footwall, suggesting rotation of the hangingwall stratigraphy relative to the footwall. This rotation is interpreted to have occurred during normal movement on the Rosario Fault.

Brittle Deformation

Overprinting kinematic indicators on the northwest-trending Rosario fault system signify episodic brittle reactivation on this structure. These faults cut the Collahuasi and Rosario porphyries (Fig. 3.2). The elongate shape of the Rosario Porphyry is consistent with having been structurally localised (e.g., Tosdal and Richards, 2001). The presently observed structures did not control emplacement of the stock, as they post-date its emplacement. Six fault segments, consisting of the Rosario 1, Rosario 2, Jack, Lulú, Penúltima and Pique faults, constitute the main branches of the Rosario fault system (Table 3.4). They are defined by continuous gouge zones and associated splays, either exposed in surface costeans or intersected at depth in diamond drill core (Figs. 3.1 and 3.2).

The principal structure of the Rosario fault system is defined by the Rosario 1 and Rosario 2 branches (Fig. 3.8a). Each consists of a separate argillaceous gouge zone dipping southwest at 40° to 45°. For most of their strike length, the Rosario 1 and Rosario 2 faults mark the contact between hangingwall ignimbrite, and footwall feldspathic sandstone. Dextral strike separation on each fault is between 500 and 600 m (Fig. 3.1), whereas sinistral strike separation on the Lulú Fault is ~300 m. Apparent dextral displacement on the steep, northeast-dipping Pique Fault (Fig. 3.8b) possibly exceeds 1 km, and resulted in a major right-lateral dislocation of the rhyodacitic ignimbrite (Fig. 3.1). Determination of net fault displacements along the northwest-

trending Medio and Penúltima faults was not possible, as reliable markers units were not disrupted by those faults (Fig. 3.1). The northwest-striking Ultima Fault is not exposed at surface, but is inferred from the dextral strike repetition of the Collahuasi Porphyry along a northwest-trending structure slightly oblique to the intrusion. Major mineralised veins, prevalent in the La Grande area 2 km south of Rosario (e.g. Monctezuma La Grande, La Esperanza and Don Eduardo veins), commonly occur in NNE-trending faults of variable strike offsets. Apparent stratigraphic displacements on these structures are consistently sinistral, with approximately 40 m on the La Esperanza and Don Eduardo veins, and up to 1 km on the Monctezuma and La Grande veins (Fig. 2.7).

Table 3.4. The Rosario fault system: segment characteristics

Fault Name	Attitude (average strike/dip)	Kinematic sense	Apparent displacement	Width and morphology
Rosario Fault 1 *(Falla Rosario)*	319°/45° SW	Normal and dextral indicators	~610 m dextral strike separation	0.5-5.0 m wide, argillic fault gouge with goethite-limonite-silica bands
Rosario Fault 2	321°/40° SW	Normal indicators	~520 m dextral strike separation	0.5-2.0 m wide
Jack Fault *(Falla Jack)*	260°/60° S	No indicators observed	Unknown	1-2 m wide, argillic fault gouge/ cleavage + minor foliated clay domains
Penúltima Fault *(Falla Penúltima)*	325°/71° SW	Dextral indicators	?	1-5 m wide, argillic fault gouge
Ultima Fault *(Falla Ultima)*			≥750 dextral strike separation	
Pique Fault *(Falla del Pique)*	331°/63° NE	Normal and dextral indicators	≥1000 dextral strike separation	0.5-2.0 m wide, fault cleavage + minor argillic gouge zones
Lulú Fault *(Falla Lulú)*	337°/43° SW	Sinistral indicators	≥330 m sinistral strike separation	1-5 m wide, argillic fault gouge/ rock flour + fault cleavage

Figure 3.8. Brittle fault reactivation at Rosario.

A) Outcrop photograph of the Rosario 2 Fault. At this locality, the Rosario Fault is about 1 m wide, dips 45° to the right hand side (southwest), and consists of a hematite-clay-rich gouge. The last movement on this fault was dextral (indicated by the movement vectors in the circle).

B) Outcrop photograph of the Pique Fault dipping 80° to the left hand side (northeast). Here the Pique Fault, characterized by a closely-spaced fault cleavage 50 cm wide, separates hangingwall andesitic sandstone from footwall ignimbrite. Alteration along the fault is restricted to weak development of kaolinite. The last movement on this fault was dextral (indicated by the movement vectors in the circle).

C) Outcrop photograph of fault striations exposed along the Don Eduardo vein at Cerro La Grande. The striations are pitching to the left (south) at ~25°. Small Riedel shear fractures indicating a sinistral sense of displacement (direction of arrow) can be seen below the index finger.

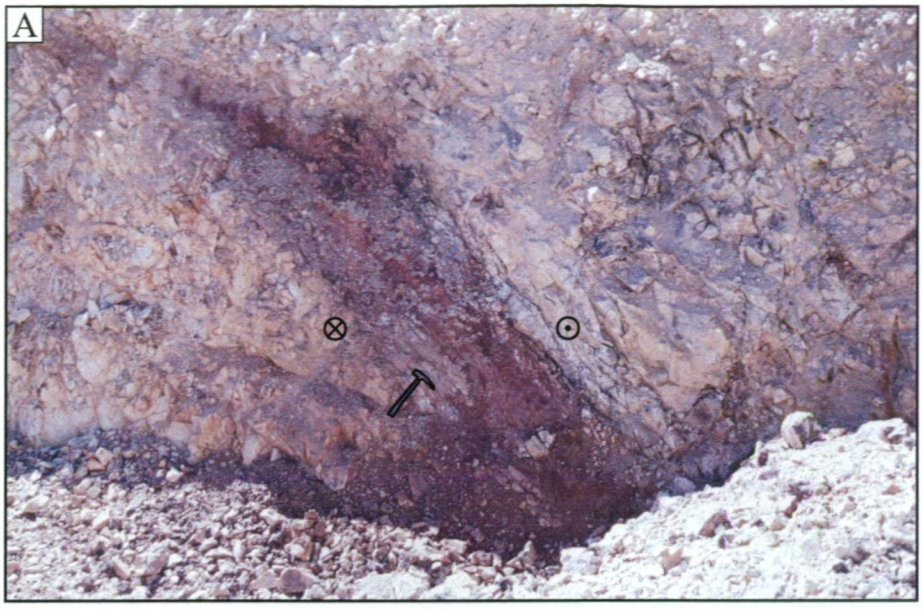
A


B


C

Cross-cutting and timing relationships between various fault generations at Rosario and on Cerro La Grande are difficult to determine as fault intersections are not exposed. Relationships have been established for some faults by mapping their continuation beyond projected fault intersections (Fig. 3.1). For example, if a fault did not continue beyond a projected intersection position, then it was considered to have been truncated by the other fault, or vice versa. On this basis, the Rosario Fault is interpreted to have cut the Lulú Fault, which in turn cut the Jack Fault (Fig. 3.1). Brittle structures hosting the Monctezuma and La Grande veins appear to have been truncated by the Rosario Fault.

Analysis of Fault Striations

Fault surface kinematic indicators are poorly developed in the volcanic host-rocks cut by brittle structures in the district. Sense of displacement has only been determined for 106 (30%) of the 371 measurements taken at Rosario and in other areas of the district. Internal gouge foliations and external drag indicators were observed on some faults. Fault surface striations proved to be the most reliable indicators of displacement sense (Fig. 3.8c), but they were commonly difficult to recognise. The most consistent kinematic indicator was the presence of striations on the upstream face of an irregularly corrugated fault surface (Fig. 3.9). Indicators defined by Petit (1987) and Doblas (1998) that were also used included quartz or mica fibres precipitated on the lee side of a ledge, deepening grooves associated with quartz grains, as well as striated Riedel fractures and tension surfaces (Fig. 3.9). In many cases, these criteria gave contradictory kinematic indicators. Much of the kinematic data was measured from micro-faults, because the projected positions of adjacent major faults were in most cases obscured by overburden. Consequently, two datasets were compiled, one for major faults and the other for minor faults. The relative age of striations was determined using overprinting criteria. For example, striations from a young reactivation event were, in several places, observed to truncate grooves of a different generation and orientation. On this basis of these timing relationships, two principal generations of striations, characterised by slickenlines, polished surfaces, and rarely fibre precipitates have been recognised. The first generation is steeply pitching to subvertical, whereas the second generation is sub-horizontal. Unambiguous overprinting relationships were observed at three localities where sub-horizontal striations consistently cut a steep-pitching striations. That subhorizontal striations cut the steep striations indicates strike-slip movement post-dated dip-slip.

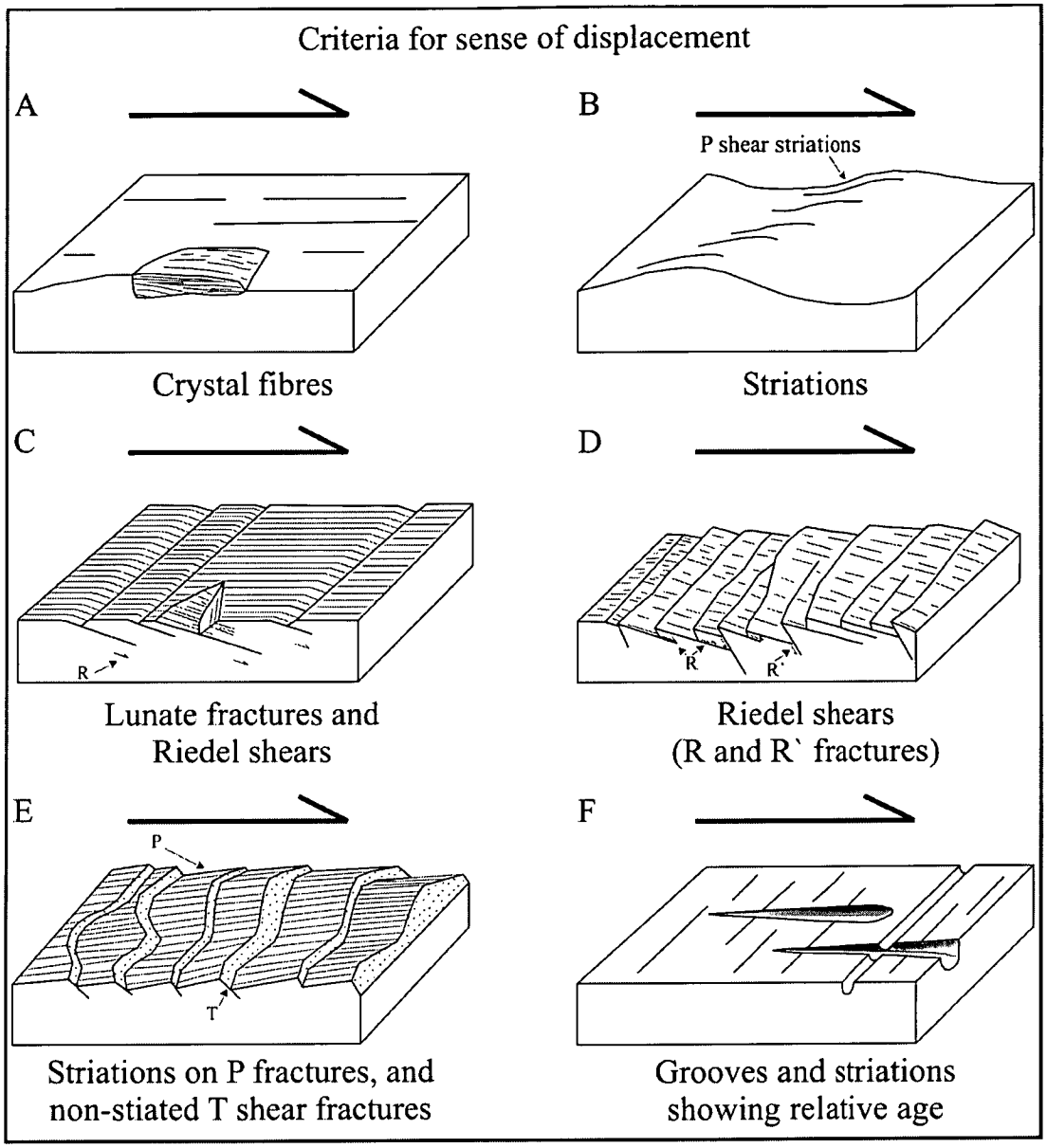

Figure 3.9. Criteria used to determine sense of displacement and relative age from fault striations. In all diagrams the missing fault block has moved in a right lateral sense relative to the remaining block. **A)** Mineral fibre crystallisation on the lee side of a ledge on the fault plane. **B)** Striations on the upstream face of an irregular fault surface. **C)** Striated Riedel shears and lunate fractures. **D)** Striated Riedel shears and conjugate anti-Riedel fractures. **E)** Secondary striated shear fractures of orientation P and non-striated secondary fractures of orientation T. **F)** Grooves and striations truncated by a later set of grooves indicating relative age. Modified from Petit (1987), Berry (1989) and Kitto (1994).

Major Faults

Stereoplots for the major faults are shown in Figure 3.10. Normal kinematic indicators were observed at various localities along the Rosario 2 and Pique faults (Fig. 3.10a). Sinistral kinematic indicators were measured on the Lulú Fault, as well as the fault-hosted La Esperanza and Don Eduardo high-sulfidation veins south of Rosario (Fig. 3.10b). Although no measurements were made on the Monctezuma, La Grande

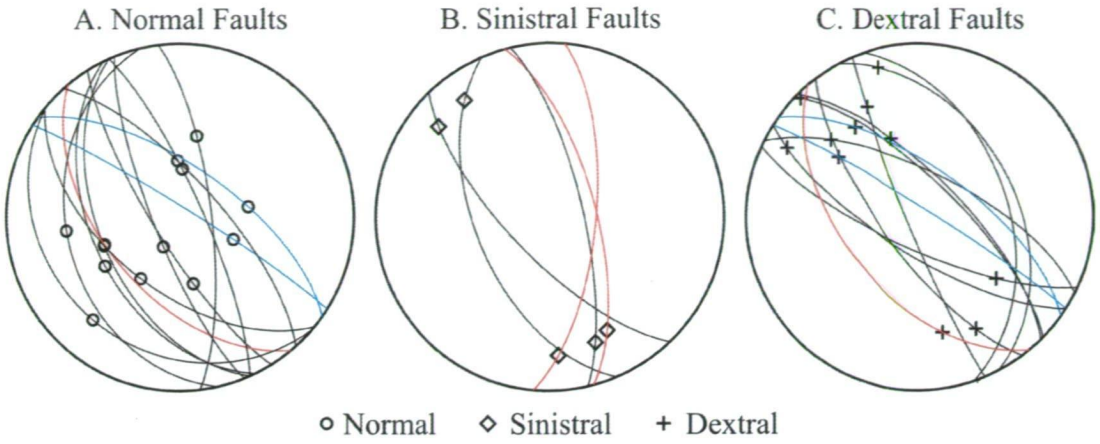

Figure 3.10. Lower hemisphere equal area projections of major faults at Rosario. **A)** Normal faults. **B)** Sinistral faults. **C)** Dextral faults. Red great circles are faults containing massive sulfide veins, blue great circles are reactivated faults.

and Cacique faults, their orientations and stratigraphic offset patterns are consistent with those along the La Esperanza and Don Eduardo faults. These relationships have been interpreted as evidence that sinistral strike-slip movement was accommodated on many faults that have north-northwest or north-northeast strikes. Dextral strike-slip indicators were observed on the same plane as normal indicators at three localities at Rosario. They were also measured, without normal indicators, at several stations along the Penúltima Fault (Fig. 3.10c). None of the major faults displayed evidence for reverse reactivation, although small individual reverse faults were observed at some localities.

Stress tensors for all major fault populations were modelled using the technique of Etchecopar et al. (1981). Results of the modelling are presented in Table 3.5. One hundred percent of the data from the normal fault population produced an exact solution for a near vertical maximum compressive stress (σ_1). The minimum compressive stress (σ_3) is subhorizontal, trending 219°, suggesting southwest-directed extension. The stress ratio ($R = [\sigma_2-\sigma_3/\sigma_1-\sigma_3]$) of 0.2 is low, implying that intermediate (σ_2) and minimum (σ_3) compressive stresses were similar in magnitude and are therefore not well constrained. Modelled stress tensors predict a subhorizontal, NW-trending (314°) σ_1 for 100% of the data associated with sinistral strike-slip faulting. The stress ratio is again low (0.2), suggesting that σ_3, plunging 73° SW, may have been interchangeable with σ_2 (17°/045°). Dextral faulting is associated with a maximum compressive stress (σ_1) that is subhorizontal to the southeast (160°). The stress ratio of 0.7 confirms the orientations of σ_2 and σ_3, with the minimum compressive stress (σ_3) plunging 52° SW. The stress model for dextral faulting satisfies 75% of the data, with

Table 3.5. Principal stress directions calculated from fault striations on major faults using (Etchecopar et al., 1981).

	σ_1		σ_2		σ_3					
Major fault populations	Trend	Plunge	Trend	Plunge	Trend	Plunge	R	Error	Data	
									Fitted	Total
Normal	009 ± 277	87 ± 9	129 ± 22	1 ± 13	219 ± 22	2 ± 10	0.2 ± 0.2	13	13	13
Sinistral	314 ± 21	2 ± 7	045 ± 23	17 ± 29	218 ± 29	73 ± 29	0.2 ± 0.2	14	5	5
Dextral	160 ± 22	9 ± 9	063 ± 27	37 ± 5	261 ± 13	52 ± 3	0.7 ± 0.2	7	8	12

the results suggesting a component of reverse movement associated with the dextral strike-slip reactivation.

Minor Faults

Minor faults have been grouped into three populations, two of which correspond with the orientations of the principal compressive stresses established in the stress tensor models for the major faults. Stereoplots for each population are shown in Figure 3.11. A population of normal faults displays orientations consistent with the synthetic (SW-dipping) and antithetic (NE-dipping) attitudes of the major faults. The prominent set of 045° to 100° striking faults in Figure 3.11a are interpreted to be transfer structures developed during extension on the Rosario fault system. Fault orientations in Figure 3.11b are consistent with northwest-directed compression, associated with dextral and sinistral brittle faulting. By contrast, stress inversion models of the measured fault orientations in Figure 3.11c are ambiguous, but produced the best fit when southwest-directed compression was used in the modelling (e.g., σ_1 subhorizontal, striking 243°, σ_3 subhorizontal, striking 340°). Southwest-directed compression is consistent with the regional data sets of Vergara and Thomas (1984), and with the orientation of the far field stress regime, predominant since early Eocene time, produced by the northeast-directed subduction of the Nazca Plate beneath the South American continental margin (Pardo-Casas and Molnar, 1987). A small fault subset, irreconcilable with any of the modelled stress tensors, is interpreted to reflect either inherited or superimposed brittle fault anisotropies. In all three examples, the modelled stress ratio (R) is very low, suggesting that the orientations of σ_2 and σ_3 are poorly constrained, and may have been interchangeable.

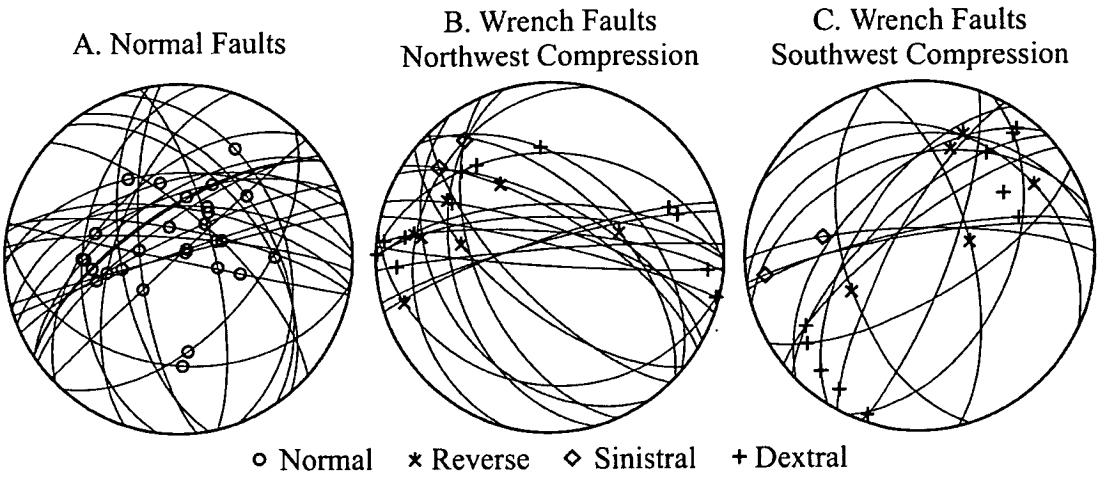

Figure 3.11. Lower hemisphere equal area projections of minor faults at Rosario. The data have been divided into populations corresponding with the principal compressive stress directions determined in stress modelling (Table 3.6).

Table 3.6. Principal stress directions calculated from fault striations on minor faults using (Etchecopar et al., 1981).

	σ_1		σ_2		σ_3					
Major fault populations	Trend	Plunge	Trend	Plunge	Trend	Plunge	R	Error	Data	
									Fitted	Total
Extensional	107 ± 159	84 ± 13	344 ± 47	3 ± 15	254 ± 47	5 ± 15	0.2 ± 0.2	13	21	28
(Rosario local stress tensor)										
Northwest - directed compression	126 ± 8	6 ± 8	035 ± 7	6 ± 21	262 ± 105	82 ± 16	0.3 ± 0.2	13	18	24
(Rosario local stress tensor)										
Southwest-directed compression	243 ± 12	16 ± 14	120 ± 44	62 ± 39	340 ± 16	22 ± 41	0.1 ± 0.3	16	9	13
(far field stress)										

Structural Controls on Mineralisation

Structural analysis of vein orientations, based on detailed underground mapping of the various vein generations by Lee (1994), revealed that most veins have a preferred orientation parallel to the Rosario fault system. Early-formed chalcopyrite-bornite veins in the Rosario Porphyry adjacent to the Rosario Fault, have no apparent preferred orientation (Fig. 3.12a). Later quartz-molybdenite veins have a preferred orientation of 320°/77° SW, occurring in high densities near the Rosario 1 and 2 faults (Fig. 3.12b). Late-stage polymetallic (Cu-Ag-Au) veins define southwest- and northeast-dipping conjugate populations of 339°/65 SW and 321°/50 NE, respectively

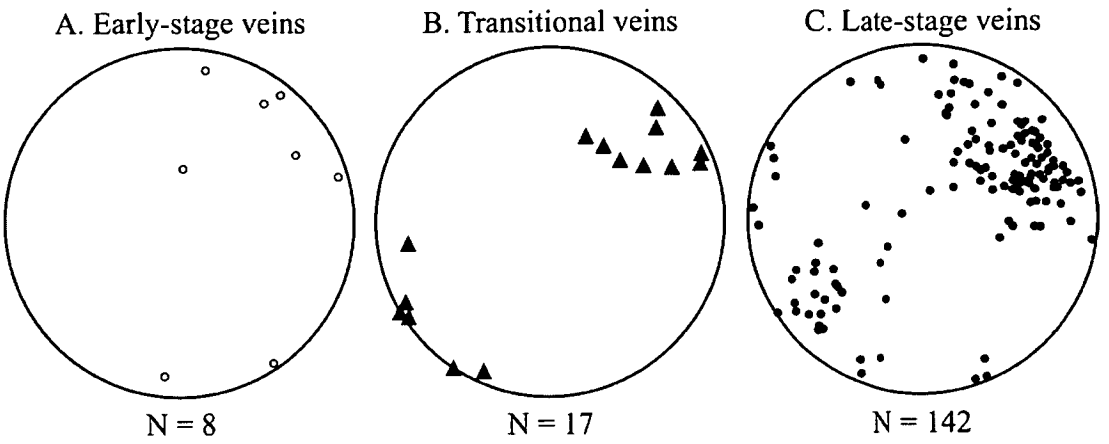

Figure 3.12. Lower hemisphere equal area projections of mineralized veins. Data are separated into the main paragenetic stages, as defined in Table 3.7. **A)** Early-stage chalcopyrite-bornite veins. **B)** Molybdenite-bearing veins. **C)** Late-stage polymetallic veins. Data from Lee (1994).

(Fig. 3.12c). The bisecting angle between the two averaged populations of the late-stage veins is ~65°. This pattern is interpreted as indicating the maximum compressive stress (σ_1) during vein formation was sub-vertical (Fig. 3.13a), with the minimum compressive stress (σ_3) subhorizontal southwest.

The stress tensor modelled for the late-stage veins is consistent with those modelled for the major and minor normal fault populations. Transitional-, intermediate-, and late-stage veins are interpreted to have formed during normal movement on the Rosario fault system. Correlation of late-stage veins exposed at surface with those intersected at depth has been complicated by the high magnitude of post-mineralisation dextral strike-separation along the Pique Fault (Fig. 3.1). This offset, as well as fault tears and brecciation of vein sulfides (Figs. 3.13b and 3.13c) in both dextral- and sinistral-strike-slip faults, suggests strike-slip fault reactivation overlapped and post-dated high-sulfidation mineralisation.

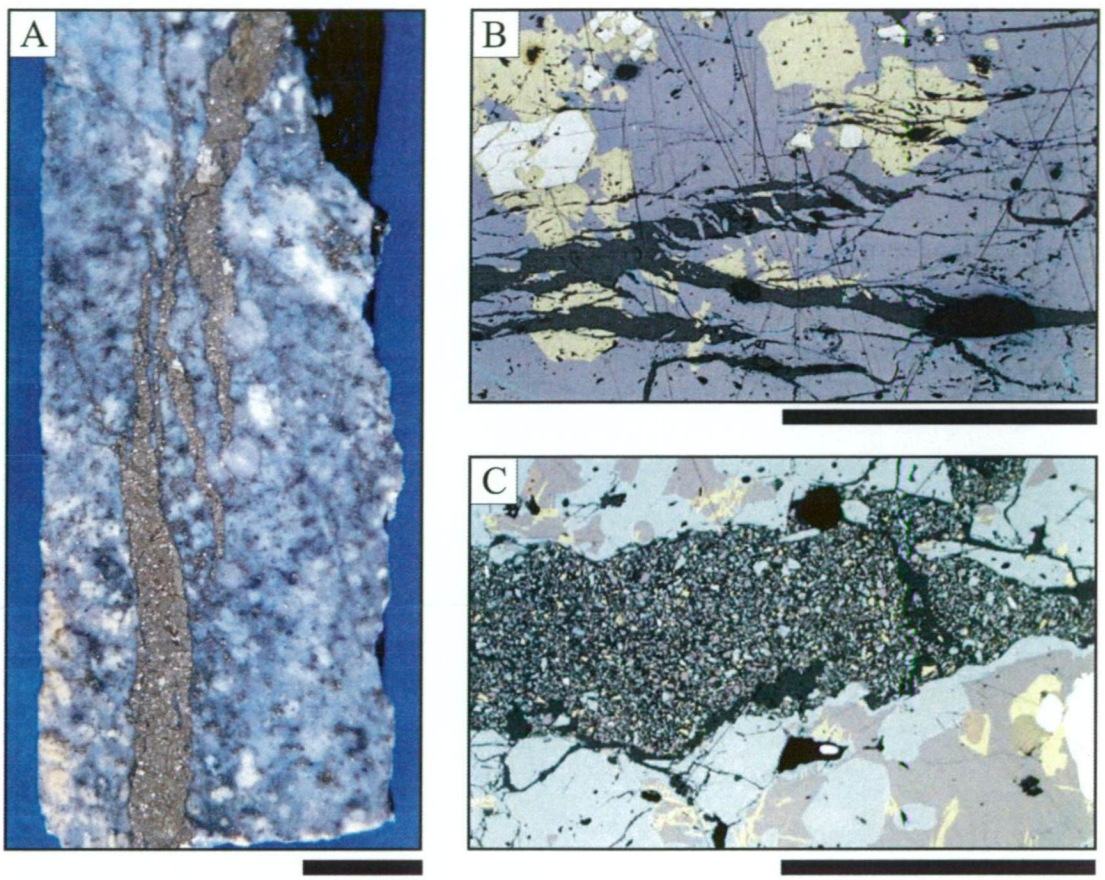

Figure 3.13. Vein sulfide textures. **A)** *Sample R200117.* Drill core sample showing en echelon pyrite veinlets in the Collahuasi Porphyry. Veinlets are sub-parallel to the vertical axis of the core. The drill hole was drilled vertically, indicating that the veins are sub-vertical, and that the direction of maximum compressive stress was also sub-vertical. The sigmoidal character of the pyrite veinlets suggests a small amount of post-vein rotation (scale bar = 1 cm). **B)** *Sample R200002.* Reflected light photomicrograph of post mineralization sigmoidal tension gashes in a bornite-chalcopyrite vein (scale bar = 2 mm). **C)** *Sample R990237.* Reflected light photomicrograph of a fault micro-breccia in a bornite-chalcopyrite-chalcocite vein (scale bar = 0.5 mm).

Fault Evolution

The orientation of the effective stress field at Rosario changed during the various brittle deformation phases associated with development and reactivation of the Rosario fault system. Two discrete events have been identified from detailed analysis of kinematic indicators on the major faults. First generation striations, characterised by steep-pitching grooves on polished surfaces, are associated with normal faulting formed under near vertical maximum compressive stress (σ_1), and subhorizontal minimum compressive stress (σ_3), trending SW. This marks the first phase of brittle deformation, during which the Rosario fault system developed as a series of synthetic and antithetic extensional faults. The principal fault structure is interpreted to have originated along the position of the Rosario 1 fault, with the Rosario 2 fault being a splay. This implies that the northeast-dipping Pique and Medio faults developed as antithetic structures in the hangingwall of the Rosario 1 fault. It is plausible that the Penúltima and Ultima faults also developed as hangingwall synthetic structures, but no kinematic evidence was observed on either fault to support this hypothesis.

A subsequent generation of sub-horizontal striations is associated with dextral strike-slip reactivation, directly documented on the Rosario 2 and Pique faults. This is particularly evident in the pronounced dextral strike separation of volcanic facies on either side of both faults. Dextral strike-slip displacement has also been directly observed on the Penúltima Fault, and is implied by the apparent dextral dislocation of the Collahuasi Porphyry along the Ultima Fault. The maximum compressive stress (σ_1) during brittle dextral strike-slip deformation was near horizontal, trending 160° during dextral strike-slip deformation.

At Rosario, the only major fault with sinistral strike-slip movement is the Lulú Fault. This fault has been truncated by dextral displacement on the Rosario 2 and Pique faults. The sinistral Monctezuma and La Grande faults have also been dextrally offset by the Rosario fault system (Fig.2.7). Munchmeyer et al. (1984) projected the Monctezuma and La Grande Faults northward beyond the Rosario Fault, and along corridors in which the volcanic rocks either side of these faults have been sinistrally offset. Temporal constraints, relative to the phase of extension on the Rosario fault system, are poorly defined for sinistral strike-slip deformation. Left lateral deformation on the Lulu, Monctezuma, La Grande and Cacique faults may have occurred either before, during or after normal movement on the Rosario fault system.

Paleostress fields

Evolution of the local paleostress field at Rosario is shown in Figure 3.14. Stress tensors modelled for the sinistral faults are consistent with those derived from kinematic data on the normal faults (Fig. 3.14a; Table 3.5). Moreover both fault systems host high-grade polymetallic Cu-Ag-(Au) veins and pre-date strong dextral movement. This evidence suggests that left lateral deformation on the north-northeast trending faults may have been synchronous with normal movement on the Rosario fault system. Based on the paleostress modelling, the minimum compressive stress (σ_3) during formation of these faults was southwest directed. This facilitated southwest escape on the Rosario fault system and caused left lateral displacement along the north-northeast trending faults at Cerro La Grande (Fig. 3.14a).

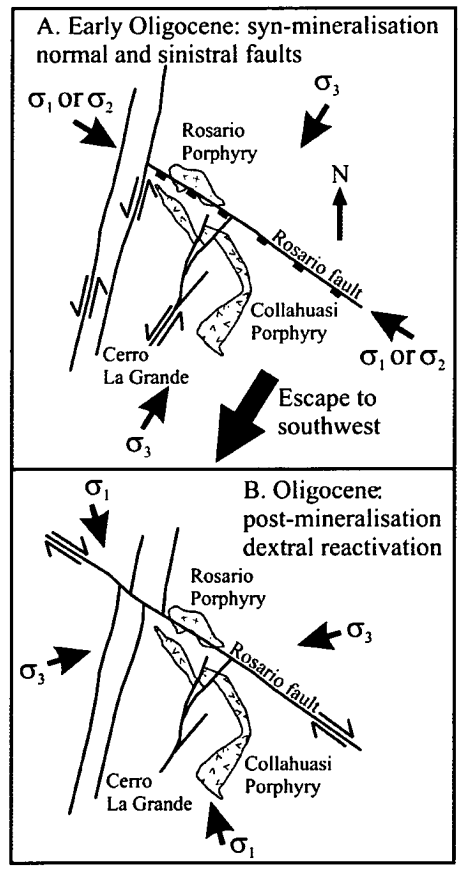

Figure 3.14. Schematic model for the local paleostress field and brittle deformation-reactivation in the Rosario and La Grande areas. Faults coloured blue are the active fault. **A)** Formation of high-grade Cu-Ag-(Au) veins in normal faults at Rosario and sinistral faults at Cerro La Grande in the early Oligocene. Paleostress modelling of kinematic data indicates that compression was directed locally to the southeast, with escape to the southwest parallel to the direction of σ_3. **B)** Post-mineralisation dextral reactivation of the Rosario fault system. Clockwise rotation of σ_1 to north-northwest directed resulted in dextral movement on the northwest-rending faults at Rosario. There may have also been some sinistral reactivation of the north-northeast trending faults.

The local stress field during post-mineralisation dextral reactivation of the Rosario fault system is shown in Figure 3.14b. The model shows that the principal compressive stress directions were rotated clockwise, relative to the stress field responsible for normal and sinistral movement. However the calculations of Etchecopar et al. (1981) used in the paleostress modelling assumed that these fractures were propagated in cohesive rock. The amount of rotation of the local stress field required to reactivate the Rosario Fault System as dextral faults was probably less than that indicated in Figure 3.14a.

Structural Model and Implications for Porphyry Copper Mineralisation at Rosario

Two main tectonic models have been advanced to attempt to explain the spatial and temporal emplacement of the cluster of world class porphyry copper deposits along the Domeyko fault system in northern Chile. The first model proposes that transtensional deformation on this arc-parallel fault system has favoured the emplacement of epizonal intrusions associated with copper mineralisation. The second model advocates the trapping of magmas related to porphyry Cu mineralisation at structural sites along inverted paleo-back-arc basin faults.

Strike-slip deformation (e.g., Lindsay et al., 1995; Reutter et al., 1996; Dilles et al., 1997; Tomlinson and Blanco, 1997a; 1997b) is interpreted to be an important element of Eocene-Oligocene tectonism associated with NE-directed oblique convergence. Richards (2000) and Richards et al. (2001) proposed that dilation at transtensional sites, initiated by a strike-slip reversal on the Domeyko fault system, provided a mechanism for arc magmas to ascend from the base of the crust. Conversely, McClay et al. (2002) concluded that subduction was never sufficiently oblique to induce propagation of a continuous arc-parallel structure, like the Domeyko fault system, along the entire length of the Domeyko Cordillera. Instead, they interpreted the Domeyko fault system to have formed by tectonic inversion of Jurassic basin-margin faults (such as those defined by Günther et al., 1997). They further argued that there is no evidence of significant strike-slip movement (tens of kilometres) along the Domeyko fault system, which contrasts with the amount of offset described in the models of strike-slip and transtension (e.g., Reutter et al., 1996; Dilles et al., 1997; Tomlinson and Blanco, 1997a; 1997b).

Strike-slip faulting has been recognised at numerous porphyry copper deposits in northern Chile. The temporal and spatial characteristics of strike-slip events at Chuquicamata have led to contradicting interpretations of their timing, relative to the mineralisation events (e.g., Lindsay et al., 1995; Reutter et al., 1996). At La Escondida (Fig. 1.1), a dextral to sinistral strike-slip reversal on a strand of the nearby Domeyko fault system was interpreted by Richards et al. (2001) to have promoted dilation and focused emplacement of porphyry magmas. At Rosario, it is interpreted that sinistral strike-slip faulting was contemporaneous with normal movement and the late-stage mineralisation event.

Conceivably, the ore-related intrusion at Rosario may have exploited transtensional basins that potentially opened in the Collahuasi district to accommodate strike-slip movement between the Domeyko and Loa Faults (e.g., as argued for La Escondida; Richards et al., 2001). However, sedimentary basins that may have formed in late Eocene-early Oligocene are not preserved at Collahuasi. The compressional model of structural traps in reverse faults that may localise ore-related intrusions (e.g., McClay et al., 2002) is not supported at Rosario, as deformation is characterised by extensional and strike-slip faulting. An alternative to these two models is that normal faults may have propagated by gravitational collapse in the uplifted basement block that hosts the Collahuasi deposits.

Gravitational Collapse Model

Reconstruction of convergence vectors along the South American continental margin has shown that at the time of porphyry ore formation in late Eocene-early Oligocene, subduction was east-northeast-directed (Fig. 3.15; Pardo-Casas and Molnar, 1987). The overall pattern of shortening in the Collahuasi district is consistent with that predicted for this convergence direction. However, syn- and post-mineralisation normal and strike-slip movement on the northwest- and north-northeast-trending faults at Rosario is associated with a local stress field not readily reconciled with that expected for the far field stress. If the regional stress field remained constant during this period, then normal fault development at Rosario may have reflected decoupling of upper and low crustal stresses (e.g., gravitational collapse at the end of an orogenic event). Alternatively, there may have been a fundamental change in lithospheric stress, possibly related to a transient change in the convergence direction, rate of subduction, or trench blockages (Richards, 1999).

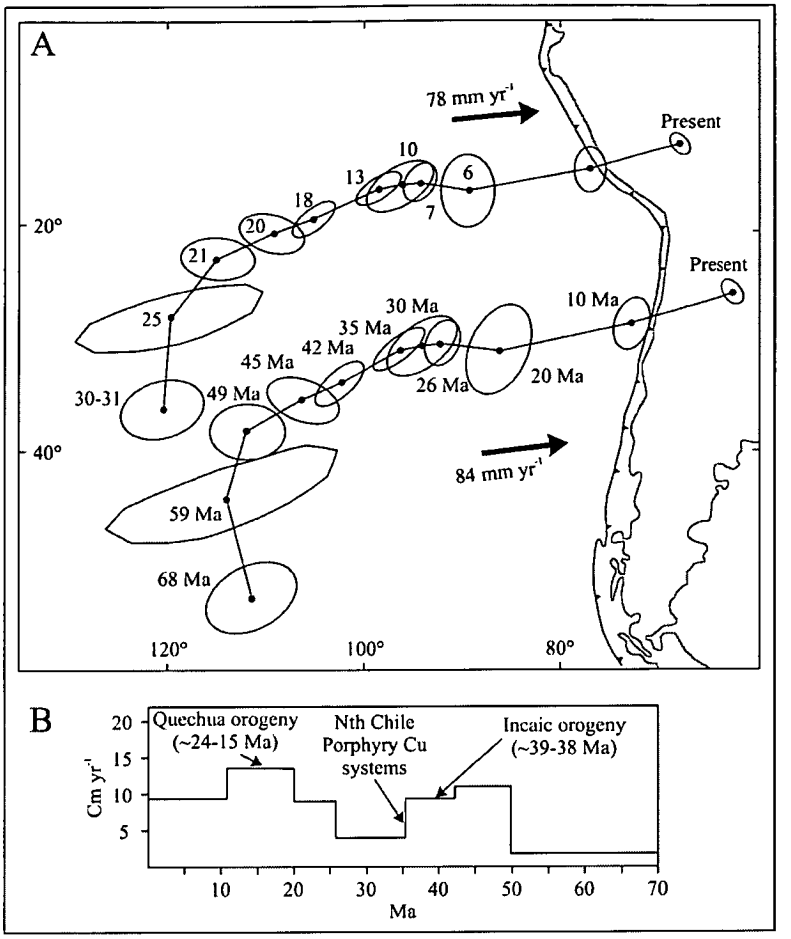

Figure 3.15. Directions and rates of convergence between the Nazca Plate and South America since the Cretaceous (Pardo-Casas and Molnar, 1987). **A)** Positions of two points on the Nazca Plate, which formed at the time of sea-floor magnetic anomaly 30-31, plotted with respect to South America at the time of various magnetic anomalies. The northeast direction of convergence has not changed significantly since 49.5 Ma (anomaly 21), implying that the far field principal compressive stress affecting deformation in the Andes should also have remained constant since this time. **B)** Average rate of convergence as a function of time for the corresponding time period in Figure 14a. The rate of convergence has not been constant, as highlighted by rapid convergence rates between 49 and 42 Ma (anomalies 21 to 18), and since 26 Ma (anomaly 7). The periods of rapid convergence coincide with the late Eocene Incaic and Miocene-Pliocene Quechua orogenies in the northern Chilean and Peruvian Andes. The timing of formation of giant porphyry copper deposits in northern Chile post-dates the Incaic Orogeny and overlaps with a period of tectonic quiescence.

The propagation of normal faults under regionally compressive tectonic conditions can be explained in several ways. Plausibly, the presence of a large batholith underlying the porphyry intrusions at Rosario could have produced normal faults associated with magma ascent and emplacement. However, the moderate dip angles (45-60°) of the Rosario fault system, as well as the apparent lack of associated radial and concentric structures suggest magmatism alone was an unlikely mechanism for the extension observed at Rosario. Furthermore, the consistent northwest trending attitudes of the mineralised fault system at Rosario imply that tectonic forces, not magmatic forces, prevailed during the period of hydrothermal activity.

Muscovite alteration associated with the fault-hosted massive sulfide veins has an $^{40}Ar/^{39}Ar$ age of 32.9 ± 0.6 Ma (Clark et al., 1998). This age indicates that normal movement on the Rosario fault system occurred in the early Oligocene and post-dated the Incaic orogeny (45-38 Ma; Scheuber and Reutter, 1992). Richards et al. (2001) hypothesised that a period of tectonic relaxation may have succeeded subduction-coupled compression in the Incaic orogeny. The model presented here therefore incorporates the conditions of fixed boundary gravitational collapse (e.g., Rey et al., 2001), whereby tectonic relaxation and magma intrusion at the end of a major orogeny are accompanied by normal fault propagation (Fig. 3.16; Vanderhaeghe and Teyssier, 2001). Under these conditions, gravitational sliding occurs in the brittle crust on divergent normal faults which transport the upper crustal units away from the uplifted lithosphere. These normal faults can be high angle in the upper crust and merge into low-angle detachment zones near the brittle-ductile transition (Vanderhaeghe and Teyssier, 2001), or connect to thrusts in the foreland and hinterland (Fig. 3.15; Rey et al., 2001).

Exhumation of the Collahuasi Formation

Normal movement on the Rosario fault system is interpreted to have controlled formation of the late high-grade veins at Rosario. Moreover, early-stage veins in the Rosario Porphyry are also inferred to have formed during extension. These relationships imply that extensional tectonics may have influenced, but not directly controlled emplacement of the Rosario Porphyry. It is inferred that a crustal block, comprising predominantly Permian basement, was raised between the Domeyko and Loa fault systems during the Incaic Orogeny (Fig. 3.16a). Most of the orogenic shortening was accommodated in the Mesozoic rocks west of Collahuasi (e.g., as reverse faults and inverted basin-margin faults; Fig. 3.16). In the period following rapid convergence, gravitational collapse along normal faults in the Collahuasi Formation assisted exhumation of the block containing the magmas (Fig. 3.16a). Detritus produced by erosion was either transported away, or may have accumulated in basins above the detachments. Examples of debris flows in the region may include the Sichal Formation (Marinovic and Lahsen, 1984), which was deposited in intermontane basins during the late Eocene to Oligocene. Continued exhumation reduced confining pressure on the shallow-crustal magmas facilitating processes of porphyry and high-sulfidation ore formation (Fig. 3.16b). Specific details concerning ore formation are discussed further in Chapters 5 and 7.

Error Name:
/undefined
Offending Command:
--file--
Operand Stack:
-null-

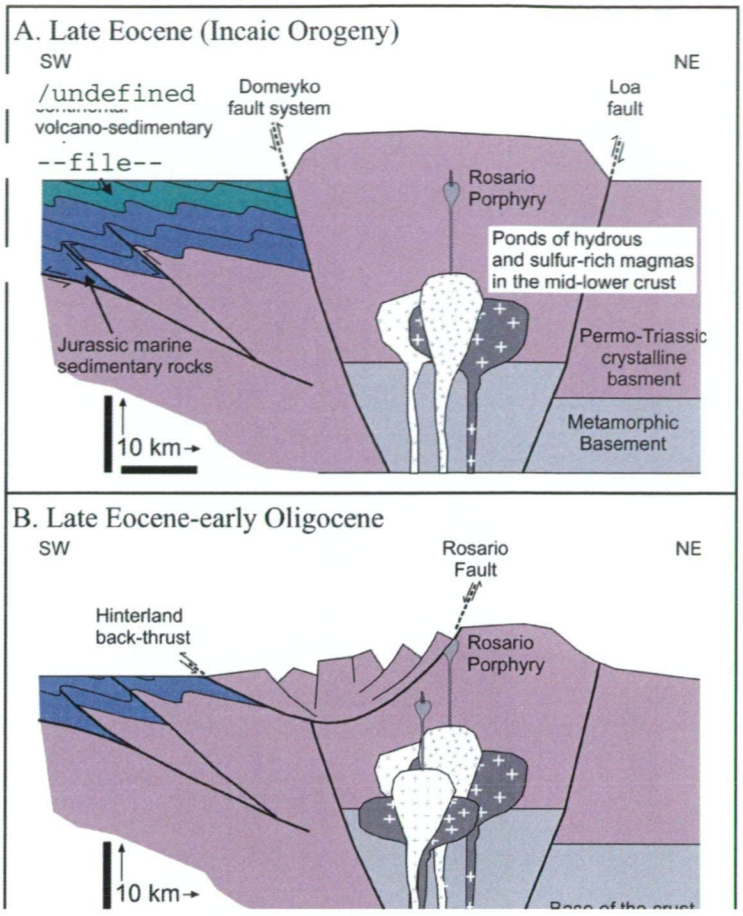

Figure 3.16. Northeast-southwest schematic section of divergent gravitational collapse inferred to have affected the Collahuasi district. **A)** Most of the late Eocene shortening was accommodated by isoclinal folds in the Mesozoic sedimentary and volcanic rocks. Note that the Permian basement was uplifted, relative to the Mesozoic sequences, along deep structures like the Domeyko Fault System. Thin-skinned deformation (e.g., reverse faults) was accommodated along low-angle thrusts and inverted basin-margin faults. Magmas ascended from a mixing, assimilation, storage and homogenization (MASH) zone at the base of the crust to levels of neutral buoyancy in the mid to upper crust. They did not erupt, but crystallized and produced high level intrusion-centred brittle-ductile veins (e.g., the early-stage veins at Rosario. **B)** Partial collapse of the orogenic belt is inferred to have occurred at the end the Incaic Orogeny. Crustal units were detached along gravity slides that were potentially connected to thrusts in the foreland. Detritus from erosion was either collected in basins above the detachments, or transported out of the system. Exhumation changed the environment from lithostatic to hydrostatic pressure at the site of ore formation, and coincided with formation of intermediate and late-stage veins at Rosario. That porphyry and superimposed high-sulfidation style mineralisation occur at the same crustal level implies protracted intrusive activity at Rosario and the existence of a well developed and replenished MASH zone at the base of the crust. Modified for the Collahuasi district from a diagram in Rey et al. (2001).

High-sulfidation deposits typically form at depths of 200 to 1000 m (Arribas, 1995; Cooke and Simmons, 2000), whereas porphyry ore deposits form between 1 and 3 km depth (Burnham, 1997). It is inferred, based on the depth of formation of the high-sulfidation environment, relative to that of the porphyry environment, that telescoping of high-sulfidation mineralisation onto early porphyry-style mineralisation at Rosario required exhumation of at least 1 km. Gravitational collapse is one possible mechanism that may have caused rapid tectonic erosion at Rosario. The presence of shallow normal faults is consistent with the hypothesis that gravitational sliding

propagated on the northwest-trending Rosario fault system.

Comparison with other models

Southwest escape on the Rosario fault system and concomitant sinistral movement on the north-northeast-trending faults may have been topographically driven. For example, the northern and southern margins of the Altiplano-Puna (Central Andes) are currently under horizontal extension, which is oriented at an oblique angle (55° to 60°) to the orogenic belt (Allmendinger et al., 1997). The margins of the plateau are not collapsing, but instead are being deformed by strike-slip faulting. It is possible that any continental escape in the late Eocene-early Oligocene was also oblique to the orogenic belt. Normal faulting potentially exploited pre-existing structural weaknesses that favoured escape to the southwest, such as the northwest-trending lineaments identified by Salfity (1985). The local paleostress field inferred for this scenario may not have required any significant change in the regional stress field (i.e., the stresses imposed by plate convergence), if lower and upper crustal stresses were decoupled.

Alternatively, gravitational collapse may have coincided with a transient rotation of the regional stress field from northeast- to southeast-directed (e.g., Richards et al., 2001). The rotated stress regime possibly caused a reversal from dextral to sinistral strike-slip movement on the Domeyko fault system and imposed a local southeast-directed compressive stress in the Collahuasi district. One possible mechanism driving rotation of the regional stress field and strike-slip reversal on margin-scale arc-parallel faults would be the subduction of a flat slab segment, as suggested by James and Sacks (1999). In their model, a southward propagating flat slab segment caused the cessation of volcanism and corresponded with the late Eocene Incaic orogeny in northern Chile (Fig.3.17). Although the direction of convergence was predominantly east-northeast during this period, southward propagation of a flat slab segment may have caused strike-slip movement on the Domeyko Fault System to reverse from dextral to sinistral. The timing of this reversal is consistent with that of brittle fault deformation at Rosario. A similar time period for a strike-slip reversal has been observed on the West Fissure where it cuts the Chuquicamata ore body (Lindsay et al., 1995; Reutter et al., 1996).

Stress field orientations imposed by each of these models appear to be consistent with the local orientations modelled for normal and strike-slip faulting. The gravitational collapse model is preferred because extensional and strike-slip

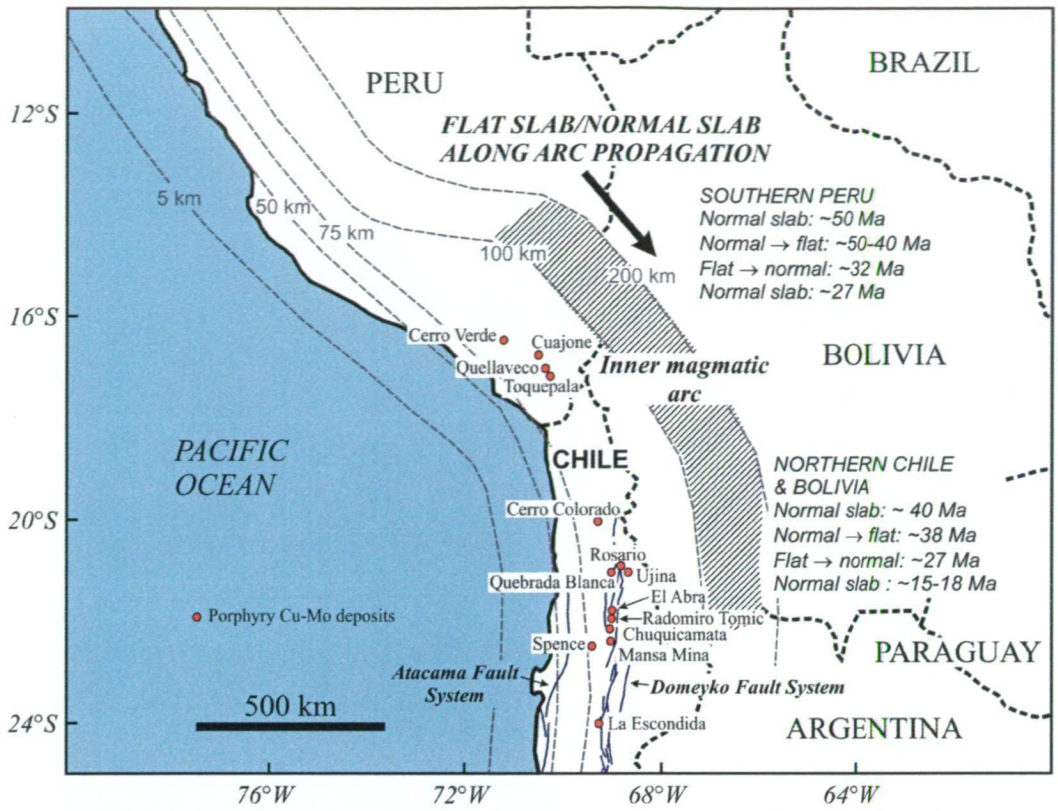

Figure 3.17. Map of northern Chile and southern Perú showing the hypothetical Wadati-Benioff contours, constructed for the late Eocene-Oligocene (James and Sacks, 1999). The contours are based on geologic and geochronological evidence, and by analogy with the present-day flexure from normal to flat subduction of the Nazca plate beneath southern Perú. The transition from normal to flat subduction began in the early to mid Eocene beneath southern Perú. The flexure, marking the transition from normal to flat subduction, propagated south with time and was beneath northern Chile and Bolivia in the late Eocene. Normal subduction was re-established first in southern Perú, and migrated south along the arc. The approximate timing of events is shown for southern Perú and northern Chile-central Bolivia.

deformation at Rosario appear to have occurred during a period of decreased convergence rates following the Incaic orogeny. These conditions are consistent with models of extensional deformation during isostatic rebound and exhumation of the crust following major orogenic events (Vanderhaeghe and Teyssier, 2001).

Conclusions

Porphyry Cu mineralisation at Rosario is hosted by a quartz-monzonite stock (Rosario Porphyry) that intruded Permo-Triassic volcanic, plutonic and sedimentary rocks of the Collahuasi Formation. The volcanic pile is characterised by submarine andesitic facies at the base, and subaerial dacitic to rhyodacitic (U/Pb age = 293 ± 14 Ma) facies in the middle and at the top, respectively. Graded feldspathic sandstones are interbedded with andesite and dacite units. Limestone lenses are interfingered with dacite in the middle of the sequence. A shallow subaqueous to subaerial volcanic arc setting is interpreted as the environment of deposition. The volcanic sequence was

intruded by an Early Triassic granodiorite (U/Pb age = 245 ± 12 Ma).

High-grade copper ore is hosted by the Rosario fault system, a series of northwest-trending faults that dip 50° southwest. Detailed structural mapping indicates that the main mineralising events coincided with normal movement on this fault system and sinistral strike-slip movement on north-northeast-trending structures at Cerro La Grande. The main northwest-trending faults at Rosario were re-activated as dextral wrench faults after the episode of ore formation.

Shortening and uplift in the Collahuasi district was localised on the Domeyko and Loa Faults. Normal faults are interpreted to have formed during partial collapse of the orogenic belt at the end of the Incaic orogeny. Propagation of normal faults was synchronous with exhumation and resulted in high-grade Cu-Ag veins being telescoped onto porphyry-style mineralisation at Rosario. This model is consistent with the strike-slip transtensional model proposed by Richards et al. (2001) for La Escondida, in that the mineralising event at Rosario was contemporaneous with local southwest-directed compression. The model proposed here differs from the compressional model (e.g., McClay et al., 2002), as there is no evidence at the current level of exposure that magma emplacement or mineralisation exploited reverse faults. At Rosario, the ore-related intrusions ascended during exhumation of the Permian basement block that hosts the deposit. Normal fault movement potentially influenced, but did not control, emplacement of the ore-related intrusion, as removal of the overburden by gravitational sliding destabilised the deeper magma chambers.

The Domeyko fault system is characterised by numerous fault segments, many of which show evidence of reverse movement. However, Cenozoic tectonic shortening appears to have been periodic, restricted to the middle Eocene Incaic orogeny and the Miocene Quechua orogeny (Vergara and Thomas, 1984). Brittle strike-slip deformation has been localised and preserved at the scale of many porphyry copper deposits (e.g. Rosario, Chuquicamata, Escondida, etc.), as these are potentially the only places where sufficient three dimensional exposure allows it to be recognised. Strike-slip deformation has possibly reflected transient tectonic events, e.g., changes in either the rate and directions of convergence, the dip angle of the down-going slab, or the subduction of ocean islands or ridges. These effects resulted in variable strike-slip movement on different segments of the Domeyko fault system. Their exact significance for porphyry copper mineralisation remains an area of ongoing research.

Chapter 4. Igneous Geochemistry

Introduction

Geochemical sampling was undertaken at Rosario and Ujina to characterise the geochemical and isotopic signatures of igneous rocks spatially and temporally associated with the porphyry-style vein deposits. Samples of the basement volcanic rocks were also analysed for comparative purposes. These data were used to compare compositions of the ore-related intrusions at Rosario and Ujina with the other late Eocene-early Oligocene porphyry Cu deposits of northern Chile.

Analytical Methods

Twenty-four drill core samples of igneous rocks were collected for X-ray fluorescence (XRF) analyses of major and trace element compositions. Twelve of these were also analysed by inductively-coupled plasma mass spectrometry (ICP-MS) for REE compositions. Good agreement was obtained between the ICP-MS and XRF analytical methods. Where available, ICP-MS data have been reported for the trace elements, with XRF (fused bead) data for the major elements (Table 4.1). Eight of the samples were also analysed for their Sr, Nd, and Pb isotopic compositions.

Samples were prepared at the University of Tasmania by crushing in a hydraulic steel-plate crusher, followed by pulverisation in a tungsten-carbide ring mill. Because contamination from the mill has been shown to introduce significant amounts of W, Co and Ta, values for these elements are not reported in Table 4.1. The mill was cleaned by 1-2 passes of high-purity quartz-sand between each sample, which may have produced minor SiO_2 contamination. Sample sizes varied according to grain size of the rock, with 30-40 g of sample milled for fine-grained rocks, compared to 60-80 g of sample for coarse-grained rocks.

Fusion discs and pressed powder pills were prepared and analysed for major and trace elements, respectively, using a Philips PW1480 X-ray spectrometer at the University of Tasmania. Reproducibility was better than 5%, and generally better than 1%, for major elements and around 5% for trace elements. Accuracy of measurements, as determined by analyses of international standards, is better than 5% for all elements, except Ba, Ni, Zn, Cu, and Cr for which accuracy is better than 10%. ICP-MS analyses were carried out at the University of Tasmania, by high-pressure dissolution of sample aliquots in hydrofluoric and sulfuric acid, and dilution to a standard volume in ultra-

pure water (e.g., Yu et al., 2001). Trace element compositions were measured using an Agilent HP4500 quadrapole ICP-MS, following the methods and instrument settings of Yu et al. (2000) and Robinson et al. (1999).

Sr, Nd, and Pb isotope ratios were measured on a Finnigan MAT 261 mass spectrometer at the University of Adelaide using the analytical techniques outlined in Foden et al. (1995) and Elburg and Foden (1998). The NBS SRM 987 and La Jolla standards, measured throughout the experiment, returned values of 0.7103 and 0.5118, respectively. Sr was fractionation corrected to $^{86}Sr/^{88}Sr = 0.1194$ and Nd to $^{146}Nd/^{144}Nd = 0.7129$. Pb ratios were corrected for ~1.2‰ per atomic mass unit fractionation using values recommended for standard SRM 981 (Todt et al., 1993). Total procedural blanks for Sr, Nd and Pb were typically ~1 ng, 200 pg and 300 pg, respectively.

Geochemistry of Magmatic Rocks in the Collahuasi District

Samples

Care was taken to analyse only the least hydrothermally altered rock specimens. Despite the selective sampling program, specimens analysed from the Rosario and Ujina intrusive complexes have been affected by incipient biotite, chlorite and sericite alteration. The Rosario samples selected for geochemical analysis include dacitic and rhyodacitic ignimbrite from the Collahuasi Formation, as well as the Collahuasi and Rosario Porphyries. Petrographic descriptions of the Rosario rocks are given in Chapter 3. The two Ujina samples are from the Ujina and Inca porphyries, and granodiorite was sampled from the La Profunda Pluton. The Ujina Porphyry is a feldspar-quartz-biotite-phyric monzonite that pre-dates alteration and mineralisation at Ujina. The Inca Porphyry is also a feldspar-quartz-biotite-phyric monzonite, but it has intruded the Ujina Porphyry, and post-dates hydrothermal alteration at Ujina. The Profunda Pluton is an equigranular feldspar-quartz-biotite phyric granodiorite that occurs 1 km east of the Ujina mine (Fig. 1.3). The geology of the Ujina deposit and La Profunda prospect is summarised in Chapter 2.

Table 4.1. Major (wt. %) and trace (ppm) element compositions of igneous rocks from the Collahuasi district.

Sample Number	R200064	R200145	R200146	R200171	R990004	R990008	R990214	R990252
Age (Ma)	290	290	290	290	290	290	290	290
Stratigraphic Unit	Collahuasi Fm	Collahuasi Fm	Collahuasi Fm	Collahuasi Fm	Collahuasi Fm	Collahuasi Fm	Collahuasi Fm	Collahuasi Fm
Rock Type	Dacite	Dacite	Dacite	Dacite	Dacite	Dacite	Rhyodacite	Rhyodacite
SiO_2	68.12	68.15	70.53	67.54	68.48	67.97	71.09	70.70
TiO_2	0.73	0.71	0.75	0.75	0.73	0.74	0.39	0.49
Al_2O_3	14.94	14.68	15.02	15.05	14.62	14.99	14.40	14.99
Fe_2O_3	3.00	2.81	5.02	2.70	2.68	2.72	2.85	2.41
MnO	0.03	0.02	0.00	0.01	0.01	0.01	0.06	0.05
MgO	1.42	1.60	0.60	1.12	1.07	1.08	0.61	0.76
CaO	0.51	0.46	0.08	0.47	0.16	0.41	0.91	0.96
K_2O	4.74	5.18	4.46	5.84	6.04	5.79	2.44	3.21
Na_2O	3.58	3.54	0.01	3.96	2.56	3.21	6.29	5.56
P_2O_5	0.18	0.14	0.15	0.19	0.06	0.20	0.09	0.10
LOI	2.10	1.97	2.61	1.03	2.03	1.71	0.49	1.01
Sum	100.16	99.66	100.07	99.62	99.82	100.09	99.65	100.24
Ti	3057.45	2757.70	479.60	2817.65	929.23	2457.95	5455.45	5755.20
P	785.52	610.96	654.60	829.16	261.84	872.80	392.76	436.40
Cr	4.80	4.60	5.60	4.60	5.30	3.90	2.10	1.70
Ni	4.16	4.78	2.50	4.78	4.68	4.16	0.83	1.46
Rb	133.00	147.80	130.30	145.90	175.40	161.30	80.30	135.10
Sr	76.50	99.20	114.80	84.80	51.20	59.00	125.10	273.90
Ba	888.30	844.00	722.20	704.60	779.80	828.20	681.40	978.50
Sc	13.70	12.60	13.40	14.60	13.80	12.20	8.60	10.50
V	58.02	53.49	53.88	55.55	65.40	57.43	17.34	42.95
Nb	12.30	12.30	12.70	13.10	11.60	11.90	7.80	14.50
Zr	317.80	325.90	313.10	309.90	297.40	305.00	206.30	377.50
Hf		8.85			8.41			
Th	16.80	16.60	16.80	16.20	16.20	15.30	12.10	15.80
U		4.07			4.10			
Y	38.00	39.30	40.10	36.90	37.30	37.40	28.80	47.60
La	27.30	31.30	33.00	31.20	32.50	31.30	29.80	33.10
Ce	62.33	73.40	79.04	66.54	71.66	70.43	58.64	86.53
Pr		9.39			8.93			
Nd	31.59	34.57	38.33	31.88	31.78	33.99	27.83	39.10
Sm		7.93			7.27			
Eu		1.50			1.42			
Gd		7.15			6.58			
Tb		1.24			1.15			
Dy		7.18			6.71			
Ho		1.54			1.44			
Er		4.47			4.22			
Yb		4.45			4.26			
Lu		0.69			0.66			
Cu	6500.00	3200.00	6700.00	7700.00	11300.00	10100.00	221.14	12.78
Zn	329.35	314.88	114.50	179.24	866.97	349.05	259.48	148.77
Mo	4.90	64.50	8.90	16.40	14.00	6.10	<1	<1
Tl		0.85			1.01			
Pb	7.88	7.32	47.26	8.53	8.33	6.41	5.73	9.87
Sn		2.63			5.68			
Sb		0.39			0.42			
La_{cn}/Yb_{cn}		5.04			5.47			
La_{cn}/Sm_{cn}		2.55			2.89			
Sm_{cn}/Yb_{cn}		1.98			1.89			
La_{cn}/Y_{cn}	4.76	5.28	5.45	5.60	5.77	5.54	6.85	4.61
Eu_{cn}/Eu^*_{cn}		0.61			0.63			
La_{cn}/Sr_{cn}	10.93	9.67	8.81	11.27	19.44	16.25	7.30	3.70
$^{143}Nd/^{144}Nd_{measured}$		0.5128			0.5125			
$^{143}Nd/^{144}Nd_{initial}$		0.5125			0.5123			
εNd_T		5.48			0.23			
$^{87}Sr/^{86}Sr_{measured}$		0.7062			0.7044			
$^{87}Sr/^{86}Sr_{initial}$		0.6883			0.6634			
$^{206}Pb/^{204}Pb$		18.6046			18.6699			
$^{206}Pb/^{204}Pb_{initial}$		16.9960			17.2446			
$^{207}Pb/^{204}Pb$		15.5647			15.5731			
$^{207}Pb/^{204}Pb_{initial}$		15.4827			15.5005			
$^{208}Pb/^{204}Pb$		38.4269			38.5460			
$^{208}Pb/^{204}Pb_{initial}$		36.3074			36.7254			

Table 4.1 continued.

Sample Number	R990260	R200065	R200079	R200085	R200113	R200116	R200142	R200041
Age (Ma)	290	243	243	243	243	243	243	80.4
Stratigraphic Unit	Collahuasi Fm	Collahuasi Porphyry	Collahuasi Porphyry	Collahuasi Porphyry	Collahuasi Porphyry	Collahuasi Porphyry	Collahuasi Porphyry	La Profunda Pluton
Rock Type	Rhyodacite	Granodiorite	Granodiorite	Granodiorite	Granodiorite	Granodiorite	Granodiorite	Granodiorite
SiO_2	72.85	65.39	70.40	69.42	74.36	72.36	70.87	62.53
TiO_2	0.39	0.48	0.35	0.35	0.29	0.28	0.33	0.68
Al_2O_3	13.99	16.13	14.90	15.45	12.30	13.04	15.20	14.64
Fe_2O_3	2.28	4.15	1.53	3.44	1.12	1.18	2.49	5.37
MnO	0.05	0.10	0.02	0.04	0.00	0.01	0.01	0.09
MgO	0.25	1.42	1.38	1.18	0.53	1.02	1.00	3.14
CaO	0.80	1.80	0.27	0.80	0.11	0.19	0.45	2.11
K_2O	2.63	2.32	4.49	2.48	4.47	7.92	2.56	3.48
Na_2O	6.24	5.30	3.90	4.90	2.45	0.43	5.78	3.89
P_2O_5	0.06	0.17	0.11	0.12	0.05	0.11	0.11	0.14
LOI	0.66	2.59	1.91	1.73	1.52	1.78	1.19	4.00
Sum	100.20	99.85	99.95	99.93	99.49	99.32	100.16	100.08
Ti	4796.00	10791.00	2098.25	2098.25	629.48	1139.05	2697.75	12649.45
P	261.84	741.88	480.04	523.68	218.20	480.04	480.04	610.96
Cr	0.80	4.70	2.80	3.00	2.30	3.00	2.20	32.90
Ni	1.00	1.66	2.70	3.54	1.98	4.68	2.18	12.38
Rb	71.00	68.00	129.10	74.50	104.80	215.00	72.20	111.40
Sr	80.90	244.50	80.70	180.20	58.70	66.50	133.80	100.20
Ba	655.00	605.30	613.40	597.80	527.70	660.10	815.30	731.00
Sc	9.60	11.30	7.60	7.60	6.60	5.90	6.60	21.70
V	13.69	78.31	56.15	45.21	49.84	56.34	42.75	149.92
Nb	13.10	5.80	6.56	6.50	4.50	5.10	6.30	8.22
Zr	328.70	131.70	110.00	124.60	79.70	96.50	121.90	234.90
Hf	8.76		2.78	2.92			3.63	6.28
Th	15.10	6.00	7.95	7.83	4.56	5.57	8.90	15.44
U	3.42		1.93	2.18			2.17	2.27
Y	40.80	14.90	15.38	10.45	13.70	10.80	14.10	21.60
La	39.00	18.20	18.93	18.66	12.50	12.30	19.30	25.14
Ce	78.63	35.37	36.91	36.04	25.42	31.88	37.93	50.81
Pr	8.99		4.09	3.87			4.20	6.14
Nd	36.40	13.48	14.27	13.25	10.69	12.33	13.77	21.67
Sm	7.40		2.88	2.54			2.87	4.14
Eu	1.41		0.84	0.56			0.70	0.78
Gd	6.81		2.51	2.12			2.40	3.57
Tb	1.21		0.42	0.33			0.42	0.63
Dy	7.21		2.54	1.88			2.47	3.84
Ho	1.57		0.55	0.39			0.54	0.80
Er	4.65		1.69	1.16			1.66	2.40
Yb	4.88		1.78	1.30			1.84	2.32
Lu	0.76		0.28	0.22			0.30	0.33
Cu	10.74	30.07	5500.00	144.35	18400.00	8000.00	1391.15	83.45
Zn	17.44	434.92	317.34	269.94	364.23	89.47	185.50	150.72
Mo	1.00	0.90	11.40	0.96	70.80	21.80	21.30	1.10
Tl	0.75		0.66	0.50			0.55	0.37
Pb	5.20	6.13	17.60	12.85	6.82	7.58	11.44	12.33
Sn	0.72		4.84	1.13			1.58	2.01
Sb	0.51		0.13	0.32			0.26	0.83
La_{cn}/Yb_{cn}	5.73		7.62	10.27			7.50	7.78
La_{cn}/Sm_{cn}	3.41		4.25	4.74			4.35	3.92
Sm_{cn}/Yb_{cn}	1.69		1.80	2.17			1.73	1.98
La_{cn}/Y_{cn}	6.33	8.09	8.15	11.83	6.04	7.54	9.07	7.71
Eu_{cn}/Eu^*_{cn}	0.61		0.95	0.73			0.82	0.62
La_{cn}/Sr_{cn}	14.77	2.28	7.18	3.17	6.52	5.67	4.42	7.69
$^{143}Nd/^{144}Nd_{measured}$	0.5125						0.5125	0.5125
$^{143}Nd/^{144}Nd_{initial}$	0.5123						0.5123	0.5124
εNd_T	0.40						0.08	-1.98
$^{87}Sr/^{86}Sr_{measured}$	0.7130						0.7090	0.7143
$^{87}Sr/^{86}Sr_{initial}$	0.7024						0.7036	0.7106
$^{206}Pb/^{204}Pb$	19.6989						18.7163	18.7229
$^{206}Pb/^{204}Pb_{initial}$	17.7675						18.2574	18.5774
$^{207}Pb/^{204}Pb$	15.6684						15.6352	15.6224
$^{207}Pb/^{204}Pb_{initial}$	15.5712						15.6123	15.6156
$^{208}Pb/^{204}Pb$	39.3653						38.7069	38.6872
$^{208}Pb/^{204}Pb_{initial}$	36.6161						38.0960	38.3632

Table 4.1 continued.

Sample Number	R200032	R200031	R200092	R200129	R990143	R990145	R990173	R990206
Age (Ma)	35.2	34.8	34.4	34.4	34.4	34.4	34.4	34.4
Stratigraphic Unit	Ujina Porphyry	Inca Porphyry	Rosario Porphyry	Rosario Porphyry	Rosario Porphyry	Rosario Porphyry	Rosario Porphyry	Rosario Porphyry
Rock Type	Monzonite	Monzonite	Monzonite	Monzonite	Monzonite	Monzonite	Monzonite	Monzonite
SiO_2	67.17	68.64	70.63	72.31	72.09	73.20	65.22	77.67
TiO_2	0.39	0.31	0.27	0.23	0.25	0.22	0.39	0.06
Al_2O_3	16.94	16.24	15.73	15.08	14.11	13.96	18.28	10.68
Fe_2O_3	2.48	1.96	1.24	0.73	0.85	0.74	2.89	0.41
MnO	0.07	0.02	0.00	0.00	0.03	0.04	0.04	0.00
MgO	1.14	0.93	0.70	0.64	0.73	0.74	1.34	0.14
CaO	2.13	2.34	0.08	0.73	0.33	0.48	0.49	0.00
K_2O	2.79	2.68	6.63	3.53	6.42	5.32	2.67	8.15
Na_2O	4.25	4.62	1.92	4.12	2.16	2.80	3.72	0.08
P_2O_5	0.16	0.12	0.06	0.08	0.09	0.09	0.11	0.04
LOI	1.80	1.84	1.80	2.02	2.29	1.97	4.42	1.54
Sum	99.56	99.82	99.92	99.86	100.23	100.04	99.71	100.03
Ti	12769.35	14028.30	1618.65	4376.35	1498.75	1318.90	2937.55	6.00
P	698.24	523.68	261.84	349.12	392.76	392.76	480.04	174.56
Cr	6.00	3.90	3.60	2.70	3.10	2.60	4.40	1.70
Ni	2.81	1.56	2.29	1.35	3.74	2.29	5.10	0.83
Rb	84.70	64.30	166.50	77.80	154.40	134.40	84.90	179.30
Sr	610.80	595.00	83.80	472.40	172.70	210.70	182.60	38.90
Ba	791.10	816.40	594.20	983.00	831.20	815.30	898.30	579.20
Sc	5.80	3.58	4.70	3.90	3.80	4.00	5.50	2.90
V	55.65	36.15	46.00	27.68	26.69	27.78	44.92	13.69
Nb	5.80	6.00	7.02	6.10	6.98	6.15	6.90	9.90
Zr	103.40	116.60	105.10	98.90	87.80	92.20	136.90	38.40
Hf	3.22	2.99	2.97		2.69	2.77		
Th	3.10	4.71	4.98	4.70	2.89	3.68	4.50	2.54
U	1.05	2.09	1.04		0.68	0.85		
Y	5.90	5.60	7.51	37.60	5.22	4.92	5.80	9.00
La	17.00	19.91	18.83	15.90	15.26	15.67	20.50	2.70
Ce	37.32	37.62	37.67	32.70	30.11	30.19	41.52	11.89
Pr	4.32	13.30	4.26		3.38	3.35		
Nd	17.72	15.38	15.12	13.10	11.94	11.75	17.72	7.22
Sm	2.74	2.47	2.70		2.05	1.99		
Eu	0.75	0.67	0.58		0.53	0.51		
Gd	1.79	1.59	2.06		1.37	1.29		
Tb	0.25	0.22	0.30		0.18	0.17		
Dy	1.26	1.09	1.56		0.98	0.91		
Ho	0.24	0.20	0.28		0.18	0.17		
Er	0.65	0.55	0.72		0.53	0.50		
Yb	0.61	0.52	0.64		0.49	0.51		
Lu	0.10	0.08	0.10		0.08	0.08		
Cu	1881.97	983.78	6900.00	3100.00	7000.00	3800.00	1107.19	10100.00
Zn	92.34	72.13	357.15	109.78	112.45	65.66	396.34	32.63
Mo	8.00	4.10	81.46	110.30	267.03	141.94	2.80	795.00
Tl	0.58	0.37	0.65		0.37	0.34		
Pb	9.53	15.70	3.97	5.82	3.17	4.15	16.90	5.20
Sn	1.02	1.19	7.20		2.26	2.31		
Sb	0.73	0.20	0.07		0.18	0.11		
La_n/Yb_n	20.05	27.49	21.18		22.28	22.18		
La_n/Sm_n	4.02	5.20	4.51		4.82	5.10		
Sm_n/Yb_n	5.00	5.29	4.71		4.63	4.36		
La_n/Y_n	19.09	23.55	16.61	2.80	19.36	21.07	23.41	1.99
Eu_n/Eu^*_n	1.04	1.04	0.75		0.97	0.98		
La_n/Sr_n	0.85	1.03	6.88	1.03	2.71	2.28	3.44	2.13
$^{143}Nd/^{144}Nd_{measured}$	0.5126	0.5125				0.5125		
$^{143}Nd/^{144}Nd_{initial}$	0.5126	0.5125				0.5124		
εNd_T	-0.29	-1.59				-3.21		
$^{87}Sr/^{86}Sr_{measured}$	0.7052	0.7052				0.7062		
$^{87}Sr/^{86}Sr_{initial}$	0.7050	0.7051				0.7053		
$^{206}Pb/^{204}Pb$	18.5932	18.6306				18.6507		
$^{206}Pb/^{204}Pb_{initial}$	18.5553	18.5854				18.5817		
$^{207}Pb/^{204}Pb$	15.5890	15.6123				15.6162		
$^{207}Pb/^{204}Pb_{initial}$	15.5872	15.6102				15.6130		
$^{208}Pb/^{204}Pb$	38.4646	38.5616				38.6258		
$^{208}Pb/^{204}Pb_{initial}$	38.4280	38.5282				38.5279		

Major Elements

Igneous rocks from the Rosario and Ujina deposits have SiO_2 concentrations from 63 to 78 wt. %. On a K_2O vs. SiO_2 discrimination diagram for volcanic and plutonic rocks (Fig. 4.1), all samples fall in the medium-K to high-K calc-alkaline fields (e.g., Le Maitre et al., 1989), with several samples from the Rosario Porphyry and dacite country rock plotting in the shoshonite field of Rickwood (1989). The samples with high K values contain hydrothermal K-feldspar and biotite, implying that K was added to the rocks during hydrothermal alteration. Thus, it is interpreted that the high K trend is a result of alkali metasomatism and does not reflect primary igneous compositions (e.g., shoshonite). Least altered examples of the Rosario Porphyry cluster with those of the Ujina and Inca porphyries on the boundary between medium and high K calc-alkaline rocks. These compositions are interpreted to be close to the primary igneous compositions of the rocks. Geochemical analyses of Miocene to Pliocene

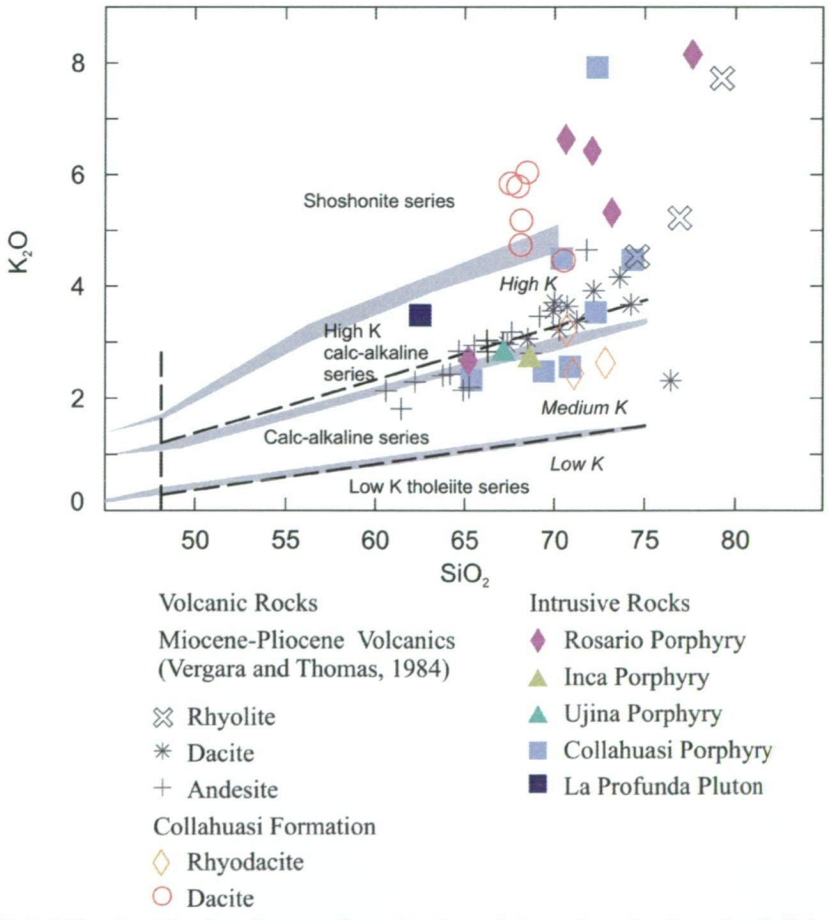

Figure 4.1. K_2O-SiO_2 classification diagram for volcanic and plutonic rocks from the Collahuasi district (boundaries are from Pericillo and Taylor, 1976, Le Maitre et al. (1989), and Rickwood, 1989). The data from Neogene volcanic rocks of various stratovolcanic centres in the Western Cordillera (Vergara and Thomas, 1984), near Collahuasi are shown for comparison. The trend towards high K values, relative to silica (e.g., the Rosario Porphyry samples), probably reflects potassium metasomatism rather than primary igneous (e.g., shoshonitic) compositions.

igneous rocks associated with Neogene to Recent volcanism in the Western Cordillera (Vergara and Thomas, 1984) are shown in Figure 4.1 for comparison. The Western Cordillera samples generally occupy the medium- to high-K fields and show increasing K_2O with increasing SiO_2 abundances. In contrast to volcanic and plutonic rocks at Rosario and Ujina, most igneous rocks of the Western Cordillera plot as a smooth linear trend, consistent with co-genetic fractional crystallisation.

Bivariate variation diagrams of major elements vs. SiO_2 are shown in Figure 4.2. All volcanic rocks from the Western Cordillera display linear trends of increasing SiO_2 with decreasing TiO_2, Al_2O_3, Fe_2O_3, MgO and CaO. K_2O increases with higher SiO_2 abundances (Fig. 4.1), although Na_2O is relatively constant for all values of SiO_2 (Table 4.1). Similar trends of major elements TiO_2, Al_2O_3, Fe_2O_3 and MgO are apparent for volcanic and intrusive rocks at Rosario. Although the Collahuasi volcanic and intrusive rocks exhibit apparent major element fractionation trends (except for Na_2O), they are not co-magmatic. This is because the country rocks are late Paleozoic to early Mesozoic in age, whereas intrusive rocks, temporally and spatially associated with hydrothermal alteration and mineralisation, are late Eocene-early Oligocene age (Chapter 6).

A subset of the least altered rocks, including samples of the Profunda Pluton (*R200041*), and Collahuasi (*R200065*), Ujina (*R200032*), Inca (*R200031*), and Rosario (*R990173*) porphyries have SiO_2 concentrations <69 wt. %, suggesting the data for these samples are most representative of their protolith major element abundances. High SiO_2 abundances (>70 wt. %) in other samples of Collahuasi (*R200079, R200085, R200113, and R200142*) and Rosario (*R200092, R200116, R200129, R990143, and R990145*) porphyry may reflect the addition of silica by minor quartz micro-veinlets, which were observed in some samples. Decreasing TiO_2, Al_2O_3, Fe_2O_3 and MgO with increasing SiO_2 in those rocks that are hydrothermally altered rocks possibly reflects dilution by addition of quartz, or minor leaching of major elements by acidic fluids during hydrothermal alteration (as indicated by the presence of illite in some samples).

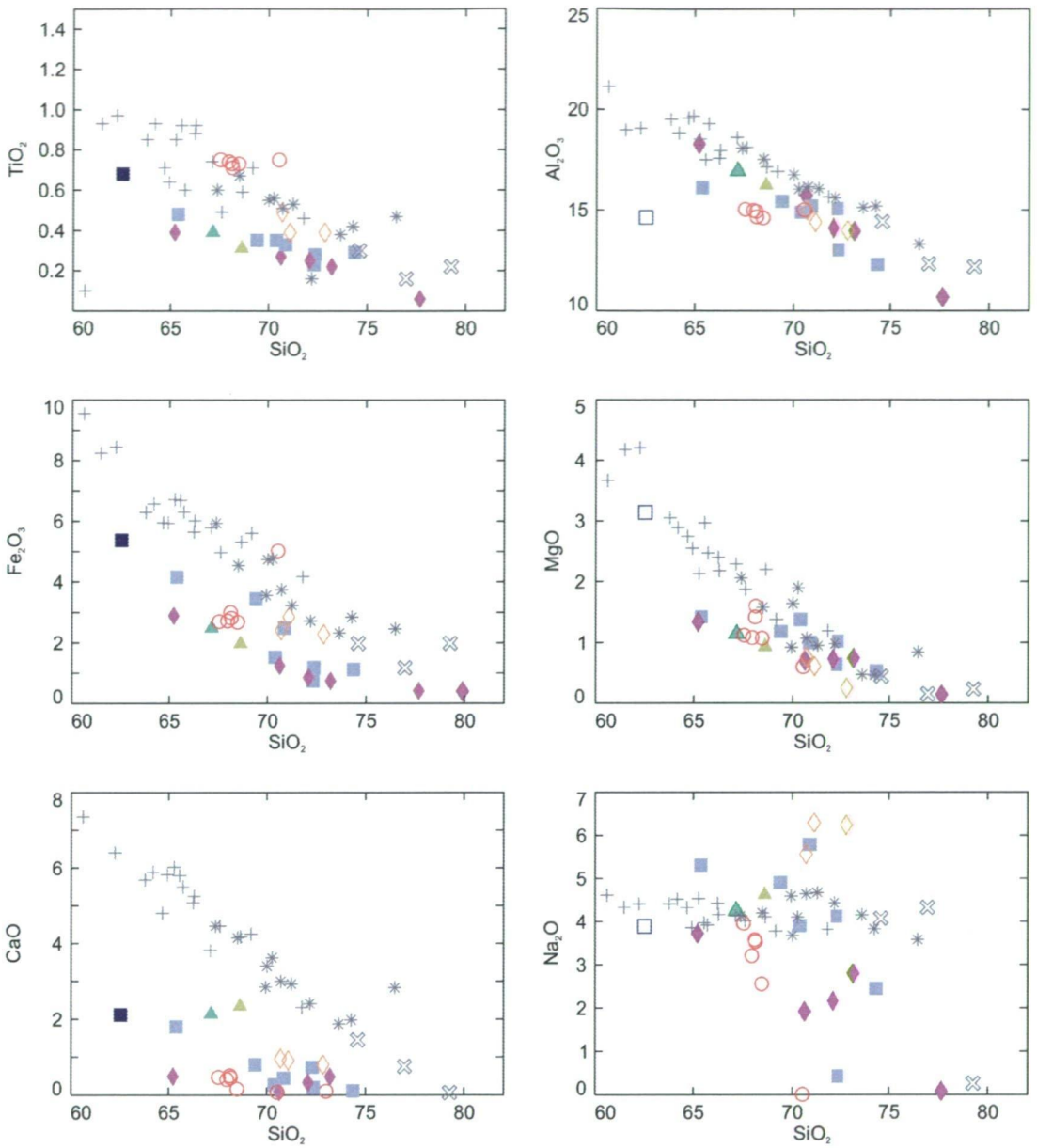

Figure 4.2. Major element bivariate diagrams plotted as a function of SiO_2 for igneous rocks of the Collahuasi district, including analyses from Vergara and Thomas (1984). Symbols used are the same as those used in Figure 4.1.

Trace Elements

Discrimination of igneous rocks at Rosario and Ujina using immobile trace elements is considered more reliable than discrimination by major elements, because the latter have been affected by the processes of hydrothermal alteration. The high field strength element (HFSE) bivariate plot of Zr/TiO_2-Nb/Y (Winchester and Floyd, 1976, 1977) is used here to distinguish geochemically the various rocks types from the Collahuasi district (Fig. 4.3). Ignimbrite country-rocks at Rosario (Fig 4.3a.) plot in the rhyolite and rhyodacite/dacite fields, the late Cretaceous Profunda Pluton plots in the granodiorite field, as does the mid-Triassic Collahuasi Porphyry (Fig. 4.3b). Intrusions

that are spatially and temporally associated with mineralisation and alteration at Rosario and Ujina (i.e., the ore-related Rosario, Ujina and Inca porphyries), cluster in the monzonite field (Fig. 4.3b).

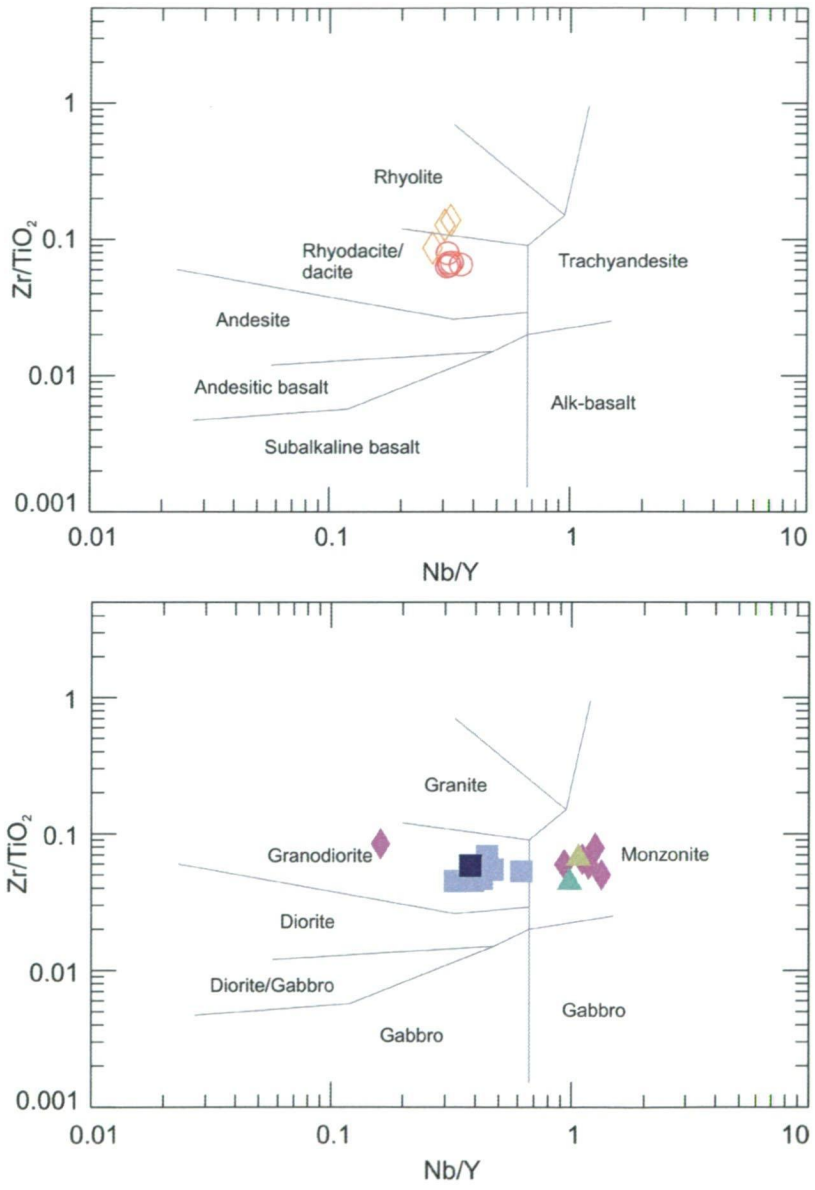

Figure 4.3. Trace element igneous rock discrimination diagrams of Winchester and Floyd (1976, 1977). A) Zr/TiO_2-Nb/Y diagram derived for volcanic rocks of the Collahuasi district. B) Zr/TiO_2-Nb/Y diagram derived for Collahuasi plutonic rocks. Symbols used are the same as those used in Figure 4.1.

Trace element concentrations are illustrated as a function of SiO_2 abundance in Figure 4.4. Concentrations of large ion lithophile elements (LILE) generally show a high degree of scatter, possibly reflecting their tendency to be mobilised during hydrothermal alteration. The HFSE show varying degrees of correlation with increasing SiO_2. For example, the subset of intrusive rocks from Rosario and Ujina, with SiO_2 concentrations <69 wt. %, show decreasing HFSE concentrations with respect to increasing SiO_2. Similarly, HFSE concentrations define a negative slope for altered rocks with SiO_2 >70 wt. %. Rhyodacite and dacite from Rosario are distinguished from plutonic rocks in the Collahuasi district by their high Sc, Nb, Zr, Y and La, consistent with their high abundances of apatite, rutile, magnetite and zircon.

REE Chemistry

REE profiles for igneous rocks in the Collahuasi district (Fig. 4.5) show that absolute REE abundances decrease systematically with decreasing age. The oldest volcanic rocks from the Collahuasi Formation have the highest overall REE abundances (Fig. 4.5a) and pronounced negative Eu anomalies (Eu/Eu* values of 0.59-0.62; Table 4.1). Triassic and Cretaceous intrusions have lower total REE concentrations, but still show a negative Eu anomaly (Eu/Eu* values of 0.60-0.93; Fig. 4.5b). The youngest rocks of the sample suite belong to the ore-related intrusions at Rosario and Ujina (Fig. 4.5c). Their REE profiles are steeper than the older volcanic and intrusive country rocks, show slight upwardly concave HREE concentrations with distinct HREE depletion, and lack a distinctive Eu anomaly (Eu/Eu* values of 0.91-0.98).

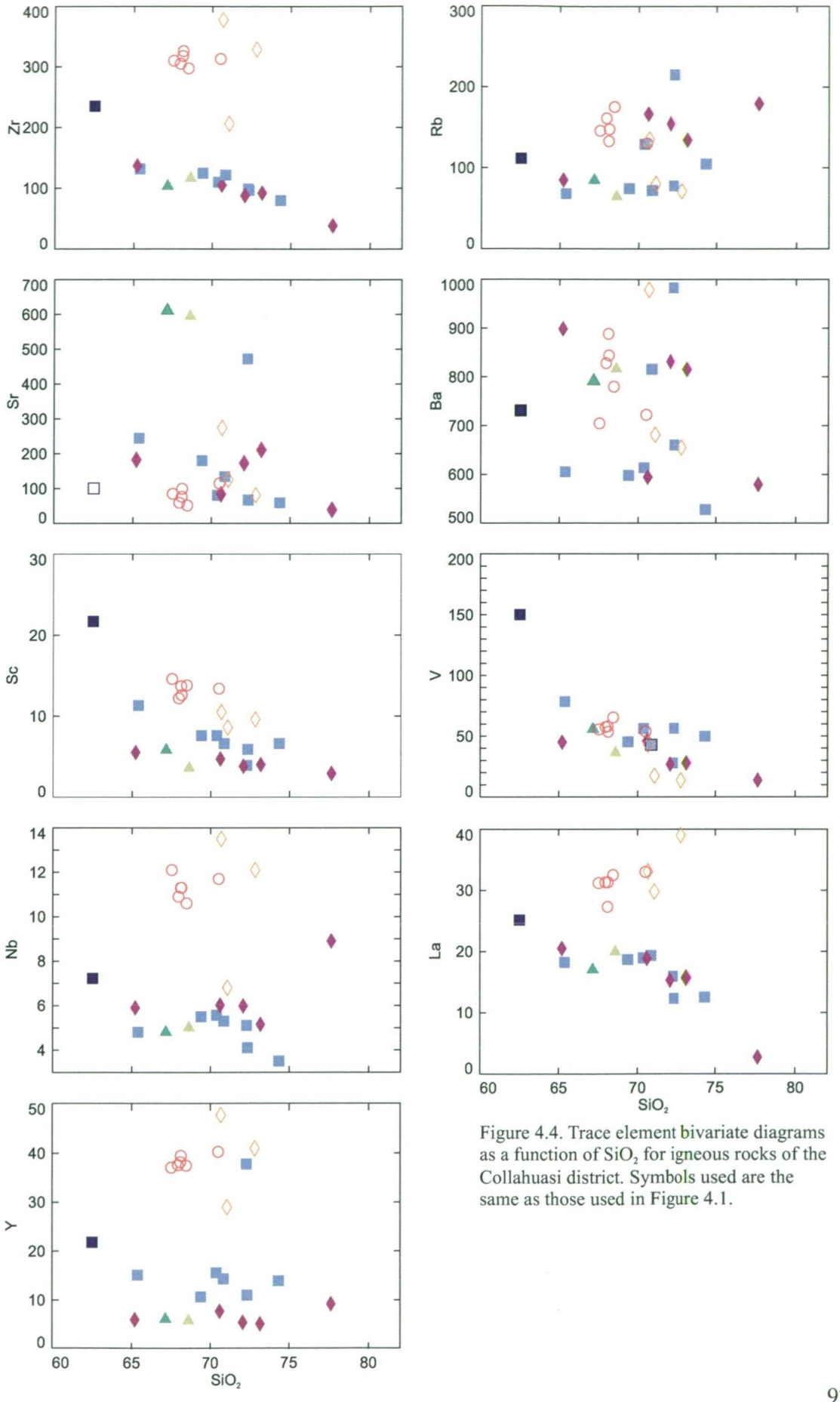

Figure 4.4. Trace element bivariate diagrams as a function of SiO_2 for igneous rocks of the Collahuasi district. Symbols used are the same as those used in Figure 4.1.

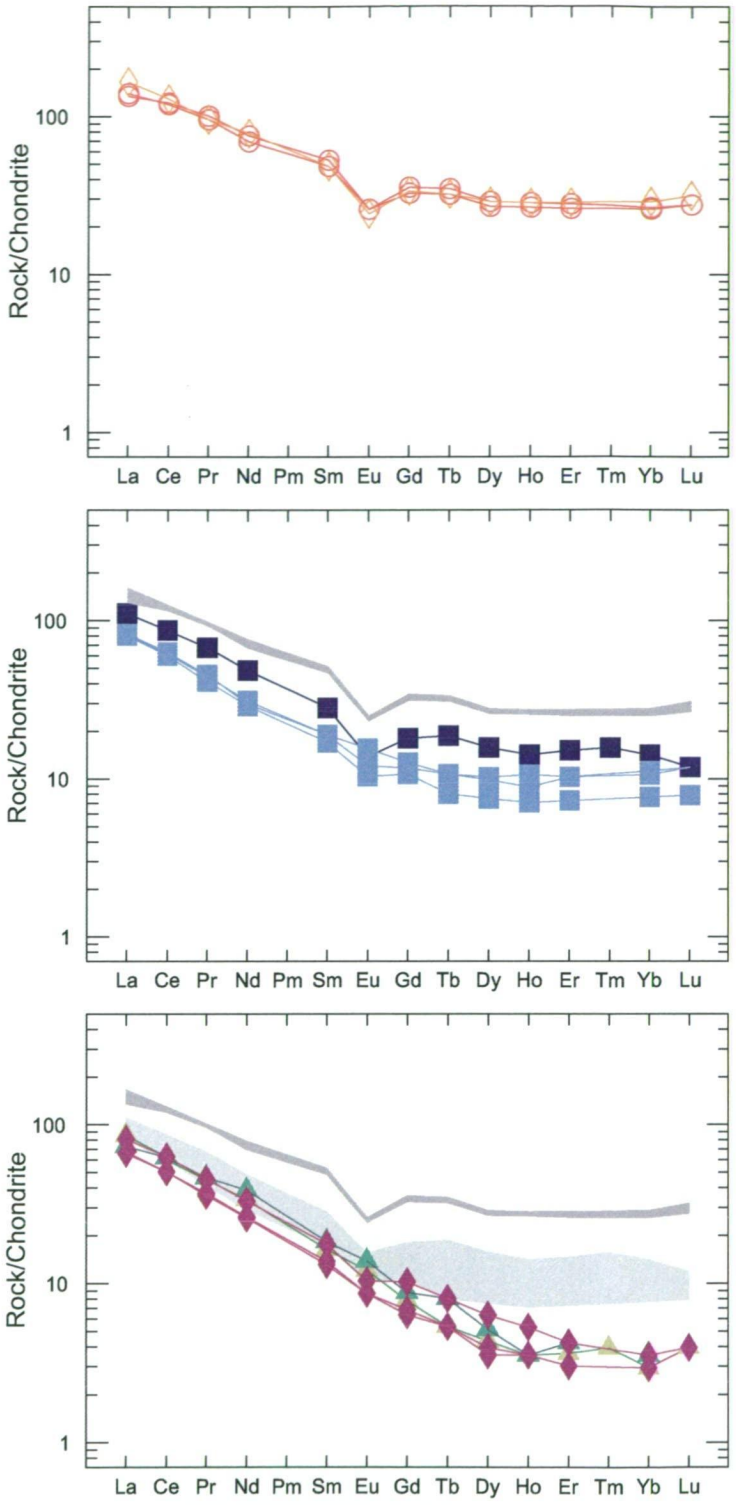

Figure 4.5. Chondrite-normalized REE profiles of selected Collahuasi igneous rocks. C1 normalizing values are those of Sun and McDonough (1989). **A)** Collahuasi Formation volcanic rocks. **B)** Mesozoic plutonic rocks. Dark grey field encompasses compositional range of Collahuasi Formation volcanic rocks. **C)** Rosario, Ujina and Inca porphyries. Light grey field encompasses compositional range of the Mesozoic intrusions.

Chondrite-normalised La/Yb values, plotted as functions of the age of the rock and SiO_2, are illustrated in Figures 4.6a and 4.6b, respectively. The highest La_{cn}/Yb_{cn} ratios belong to the youngest intrusions, and include the ore-related Rosario, Ujina and Inca porphyries (values of 20.1-27.5). The barren Profunda and Collahuasi plutons show La_{cn}/Yb_{cn} values of 7.5-10.3, whereas volcanic rocks from the Collahuasi Formation at Rosario display the lowest La_{cn}/Yb_{cn} values of 5.0-5.7. In general, chondrite normalised La/Yb values discriminate productive porphyries (values ≥ 20) from barren intrusions and volcanic country-rock (values ≤ 11; Table 4.1). Additionally, chondrite-normalised La/Y ratios can also be used to distinguish the productive and barren intrusions at Rosario and Ujina (Figs. 4.6c and 4.6d). In this case, Y is substituted for Yb as it has similar chemical and behavioural characteristics to HREE (similar ionic radius to Ho) and can be analysed quickly and cost-effectively by the XRF method.

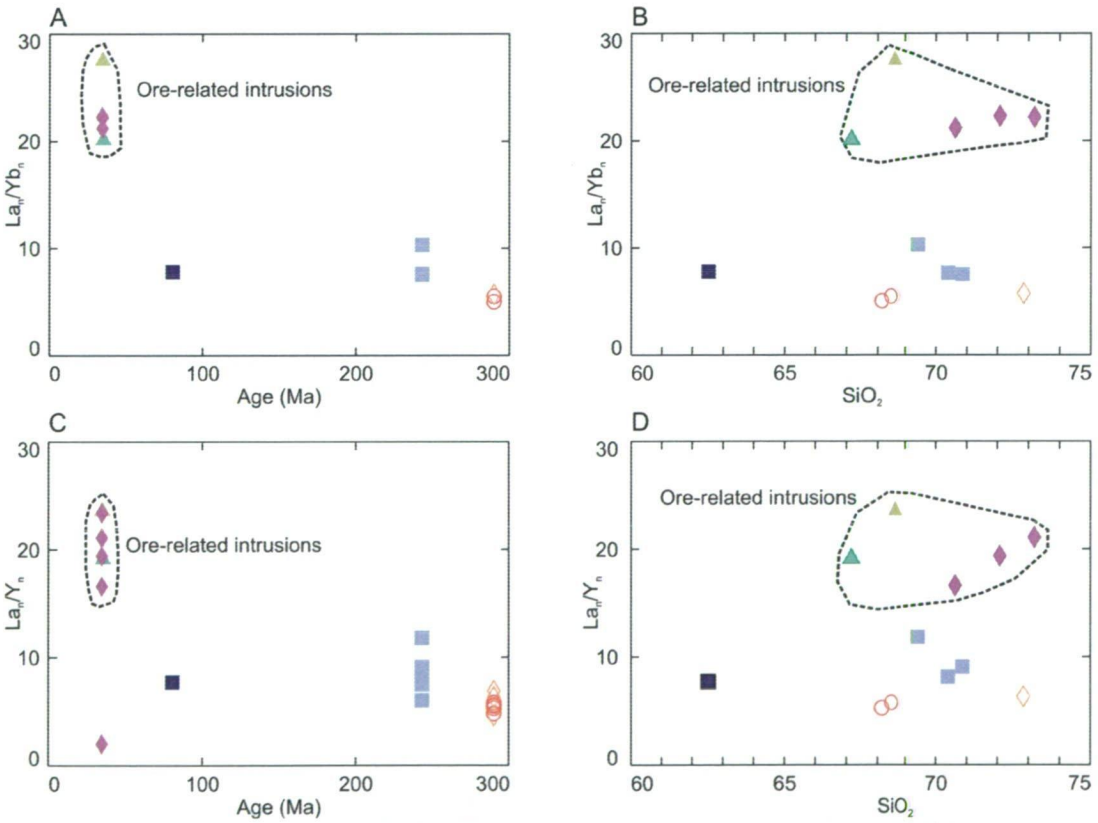

Figure 4.6. Chondrite-normalized REE bivariate diagrams plotted as function of age and SiO_2. Normalizing values are those of Sun and McDonough (1989). **A)** La_n/Yb_n-Age diagram. **B)** La_n/Yb_n-SiO_2 diagram. **C)** La_n/Y_n-Age diagram. **D)** La_n/Y_n-SiO_2.

Rb/Sr, Sm/Nd Isotopes

Rb/Sr and Sm/Nd whole-rock isotope compositions were analysed for the ore-related Rosario, Ujina and Inca porphyries, as well as five samples of Mesozoic and Paleozoic basement. Corrections have been made to account for subsequent *in situ* decay of Rb and Sm using the $^{40}Ar/^{39}Ar$ biotite ages of the Rosario, Ujina, Inca and La Profunda intrusions (Chapter 6) and the U/Pb ages of the Collahuasi Porphyry and rhyodacitic ignimbrite from the Collahuasi Formation (Chapter 3). Measured and initial isotope ratios are listed in Table 4.1. The initial $^{87}Sr/^{86}Sr$ and $^{143}Nd/^{144}Nd$ isotope correlation diagrams are illustrated in Figure 4.7, where the data are compared with oceanic mantle (DM, EMI and EMII), and crustal reservoirs (MORB and IAV). Terrane-specific fields are also shown, including the Jurassic-lower Cretaceous arc, the late Oligocene-late Miocene arc, the Northern Volcanic Zone (NVC), the Central Volcanic Zone (CVZ), and the Southern Volcanic Zone (SVZ).

Initial $^{87}Sr/^{86}Sr$ ratios cluster between 0.7050 and 0.7053 and initial $^{143}Nd/^{144}Nd$ values vary from 0.5124 to 0.5126 in the ore-related porphyries at Ujina (samples *R200031* and *R200032*) and Rosario (Fig. 4.7). All porphyries have negative εNd_T, varying between -0.29 and -3.21 (Table 4.1). Whole rock isotopic compositions of other ore-related porphyries in northern Chile, including El Salvador, El Abra and Chuquicamata (data from Maksaev, 1990), are also shown in Figure 4.7. Ore-related porphyries from other late Eocene-early Oligocene Cu deposits contain less radiogenic Sr (0.70380-0.70465) than the Rosario and Ujina Porphyries, and display positive εNd_T ranging from +1.33 to +4.48 ($^{143}Nd/^{144}Nd$ = 0.5127-0.5129). The data from the Rosario and Ujina deposits occupy a distinct field with little overlap of the data from El Salvador, El Abra and Chuquicamata.

$^{87}Sr/^{86}Sr$ isotopic compositions of Paleozoic and Mesozoic basement at Rosario range from 0.7024 to 0.7106, whereas εNd_T values cluster between 0.08 and 0.4 (Figure 4.7). Rhyodacite (*R990260*) from the Early Permian basement at Rosario, together with the Middle Triassic Collahuasi porphyry (*R200142*) contain less radiogenic Sr than that of the Late Cretaceous Profunda granodiorite pluton (*R200041*), although all samples have εNd_T values close to CHUR.

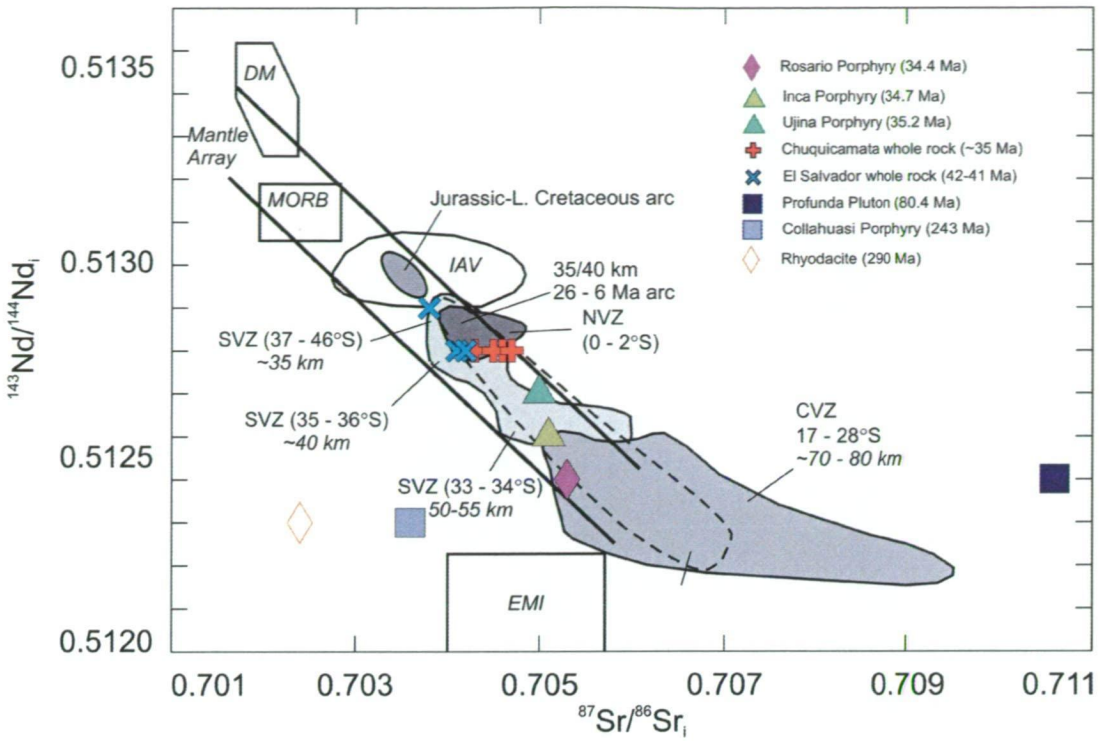

Figure 4.7. Initial Sr- and Nd-isotopic ratios of selected igneous rocks from the Collahuasi district. Shown for comparison are the oceanic and sub-continental mantle reservoirs (DM: depleted mantle; EMI: enriched mantle I; EMII: enriched mantle II; Zindler and Hart 1986), as well as the MORB and IAV crustal reservoirs (Taylor et al. 1984; Davidson et al., 1990). Central Andean terrane-specific fields include the Jurassic-lower Cretaceous volcanic arc (Rogers and Hawkesworth, 1989; Haschke et al., 2002); the late Oligocene-late Miocene arc (Kay et al., 1999), the Northern Volcanic Zone (NVC; Davidson et al., 1990), the Central Volcanic Zone (CVZ; Hawkesworth et al., 1982; James, 1982; Wörner et al., 1988; Rogers and Hawkesworth, 1989; Davidson et al., 1990; Kay et al., 1994), and the Southern Volcanic Zone (SVZ; Hickey et al., 1986; Kay et al., 1987; Hildreth and Moorbath, 1988; Kay et al., 1991).

The ore-related (e.g., Rosario, Ujina and Inca porphyries) and barren intrusions (e.g., Collahuasi and Profunda intrusions) are distinguished from the Permian basement rocks by their $^{143}Nd/^{144}Nd$ and initial $^{87}Sr/^{86}Sr$ isotope signatures (Fig. 4.7). The Rosario, Ujina and Inca Porphyries plot within the mantle array along with ore-related intrusions from El Salvador and Chuquicamata. The oldest ore-related intrusions (e.g., El Salvador, El Abra), have the most radiogenic Nd (εNd_T values of +1.34 to +4.48) and least radiogenic Sr. Conversely, the youngest ore-related intrusions have the least radiogenic Nd (initial $^{143}Nd/^{144}Nd$ of 0.5124 to 0.5126, Fig. 4.7; εNd_T values of -0.29 to -3.21, Table 4.1) and the most radiogenic Sr (initial $^{87}Sr/^{86}Sr$ of 0.7050 and 0.7053; Fig. 4.7). In contrast to the ore-related intrusions, barren stocks show no correlation with the mantle array.

Pb isotopes

The measured Pb isotopic compositions of all samples have been corrected for *in situ* decay of U, and are presented as initial ratios, together with their measured ratios in Table 4.1. In Figure 4.8a, the data are compared with isotopic compositions of the main crustal reservoirs, including MORB, and the upper and lower continental crust (Taylor et al., 1984; Rollinson, 1993), as well as the main oceanic mantle reservoirs of Zindler and Hart (1986). Pb isotope compositions are also compared in Figure 4.8b with those of terrane-specific data of the Andean margin in northern Chile.

Productive porphyries at Rosario and Ujina show a narrow range of initial Pb isotopic compositions ($^{206}Pb/^{204}Pb$ = 18.555-18.585; $^{207}Pb/^{204}Pb$ = 15.587-15.613 ; $^{208}Pb/^{204}Pb$ = 38.428-38.528: Figs. 4.8a and 4.8b). The data coincide with the isotopic composition of the lower continental crust, and lie between the fields of MORB and a mantle reservoir enriched in ^{207}Pb. In Figure 4.8b, the data correspond with $^{207}Pb/^{204}Pb$ and $^{206}Pb/^{204}Pb$ isotopic compositions of the SVZ, with minor overlap into the fields of enriched mantle and Nazca Plate metalliferous sediments. The Rosario and Ujina data are indistinguishable from the El Salvador, El Abra, Chuquicamata (Maksaev, 1990), and Escondida data (Puig, 1988).

Paleozoic volcanic basement (Collahuasi Formation) and Mesozoic intrusions (Collahuasi and Profunda intrusions) in the Collahuasi district are generally less radiogenic than those of the productive porphyries ($^{206}Pb/^{204}Pb$ = 16.996-18.557; $^{207}Pb/^{204}Pb$ = 15.483-15.616 ; $^{208}Pb/^{204}Pb$ = 36.307-38.363; Figs. 4.8a and 4.8b). Rocks from the Collahuasi Formation show a broad range of initial Pb compositions, trending from low $^{207}Pb/^{204}Pb$ and $^{206}Pb/^{204}Pb$ values to more radiogenic values (Fig. 4.8). Basement volcanic and intrusive rocks overlap with the Pb isotopic composition of the lower continental crust (Fig. 4.8a). The oldest basement rocks (Collahuasi Formation volcanic units) have the least radiogenic $^{207}Pb/^{204}Pb$ and $^{206}Pb/^{204}Pb$ ratios, whereas the barren intrusions have evolved to higher radiogenic Pb isotope compositions (Fig. 4.8b). The youngest of the barren intrusions, the Profunda Pluton, has the most radiogenic initial $^{207}Pb/^{204}Pb$ and $^{206}Pb/^{204}Pb$ ratios (18.5775 and 15.6156, respectively).

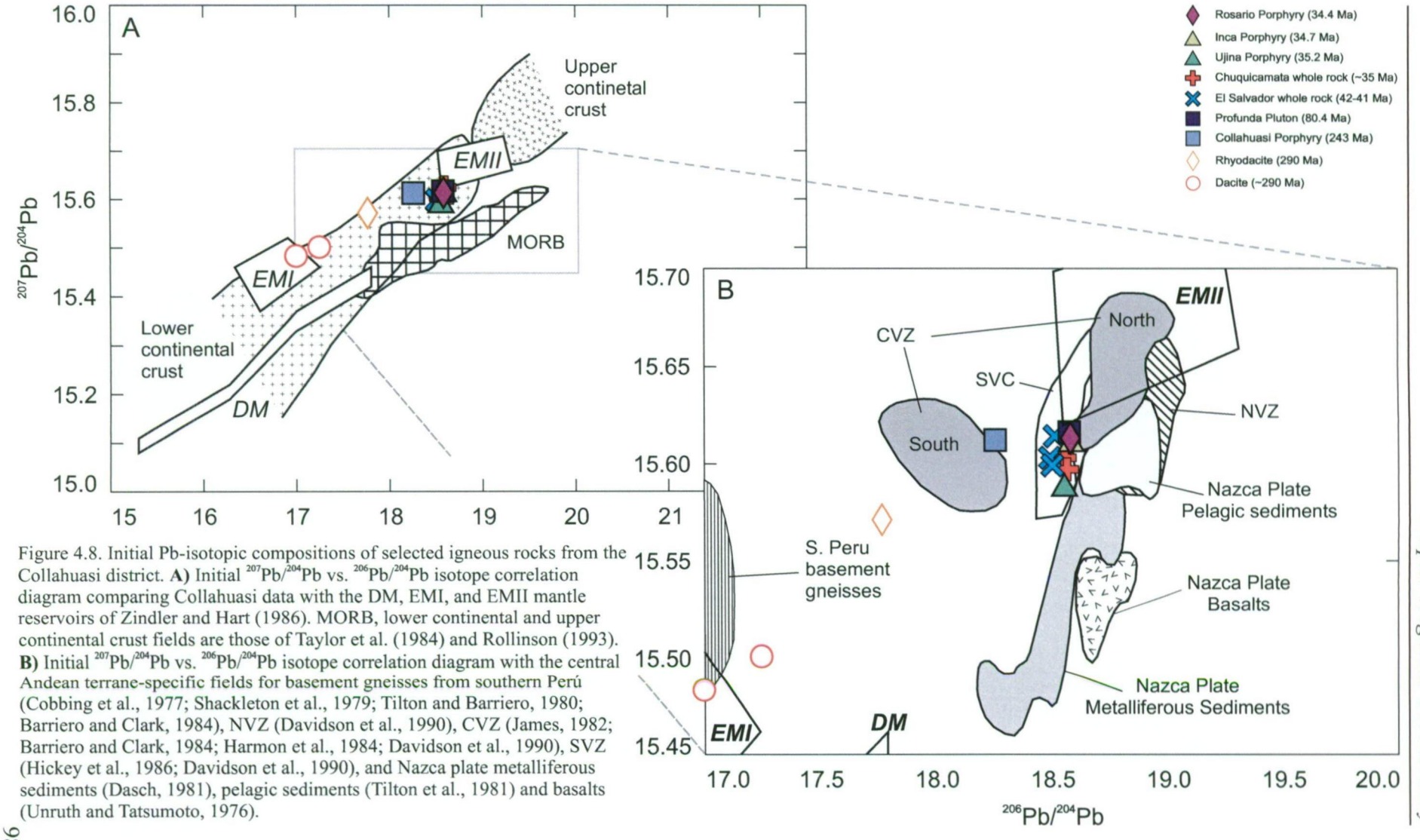

Figure 4.8. Initial Pb-isotopic compositions of selected igneous rocks from the Collahuasi district. **A)** Initial $^{207}Pb/^{204}Pb$ vs. $^{206}Pb/^{204}Pb$ isotope correlation diagram comparing Collahuasi data with the DM, EMI, and EMII mantle reservoirs of Zindler and Hart (1986). MORB, lower continental and upper continental crust fields are those of Taylor et al. (1984) and Rollinson (1993). **B)** Initial $^{207}Pb/^{204}Pb$ vs. $^{206}Pb/^{204}Pb$ isotope correlation diagram with the central Andean terrane-specific fields for basement gneisses from southern Perú (Cobbing et al., 1977; Shackleton et al., 1979; Tilton and Barriero, 1980; Barriero and Clark, 1984), NVZ (Davidson et al., 1990), CVZ (James, 1982; Barriero and Clark, 1984; Harmon et al., 1984; Davidson et al., 1990), SVZ (Hickey et al., 1986; Davidson et al., 1990), and Nazca plate metalliferous sediments (Dasch, 1981), pelagic sediments (Tilton et al., 1981) and basalts (Unruth and Tatsumoto, 1976).

Potential Sources of Igneous Rocks in the Collahuasi District

$^{87}Sr/^{86}Sr$ and $^{143}Nd/^{144}Nd$ reservoirs

Radiogenic isotope compositions of the Collahuasi ore-related intrusions can be used as indicators of magmas sources and of the crustal thickness through which they passed (e.g., Kay et al., 1999; Haschke et al., 2002). Initial $^{87}Sr/^{86}Sr$ and $^{143}Nd/^{144}Nd$ compositions of the Rosario and Ujina porphyries, and ore-related intrusions at El Salvador, El Abra and Chuquicamata, correspond with isotopic values of volcanic rocks in the SVZ (Fig. 4.7). These values are consistent with partial melting of a subduction modified enriched mantle source (e.g., the asthenospheric mantle wedge) contaminated by the lower crust and lithospheric mantle.

In the SVZ, Hildreth and Moorbath (1988) noted that initial Sr and Nd values, increased and decreased, respectively, northward along the arc. They interpreted this trend to reflect the depth of the zone of melting, assimilation, storage and homogenisation (MASH), which occurs at the crust-mantle interface. Thus SVZ rocks derived from the base of thick crust (50-60 km) have more radiogenic Sr and less radiogenic Nd than rocks derived from the base of thin crust (30-40 km). These isotopic signatures vary with crustal thickness because magmas produced in MASH zones under thick crust have been more contaminated by that crust than the rocks generated beneath thin crust (Hildreth and Moorbath, 1988).

The rise of $^{87}Sr/^{86}Sr$ and complimentary fall of $^{143}Nd/^{144}Nd$ values from the oldest to youngest late Eocene-early Oligocene ore-related intrusions in northern Chile is analogous to the trends observed in the SVZ. It is inferred that, at the time the oldest deposits formed (e.g., El Salvador and El Abra), ore-related magmas had interacted with the upper plate lithosphere at the base of thinner crust (35-40 km), relative to those associated with the youngest porphyry Cu deposits (e.g., Chuquicamata, Rosario and Ujina), which passed through 50-55 km thick crust.

Radiogenic isotopic signatures of the Permian volcanic rocks and Mesozoic intrusions differ significantly from those of the Rosario and Ujina ore-related intrusions (e.g., Figs. 4.7 and 4.8). The different isotopic signatures are interpreted as evidence that the porphyry magmas were not contaminated in the upper crust after their emplacement. The isotopic signatures of basement country-rock, which lie outside the mantle array, imply that they were sourced from crustally-derived magmas.

$^{207}Pb/^{204}Pb$ and $^{206}Pb/^{204}Pb$ reservoirs

Homogeneity of $^{207}Pb/^{204}Pb$ and $^{206}Pb/^{204}Pb$ isotope compositions for ore-related intrusions at Rosario and Ujina, together with those at El Salvador, El Abra, Escondida, and Chuquicamata, imply either a single Pb source, or an effective mechanism of homogenising Pb from multiple sources (Maksaev, 1990). All of the these intrusions have enriched $^{207}Pb/^{204}Pb$ isotopic signatures relative to MORB. These isotopically enriched magmatic rocks are either primitive mantle-derived melts contaminated by the crust, or partial melts of an enriched mantle source region (Kay et al., 1999). Several mechanisms have been proposed to explain LILE and $^{87}Sr/^{86}Sr$ mafic magma enrichment before they enter the crust. Suggested enrichment sources include: (1) old enriched lithospheric mantle (Rogers and Hawkesworth, 1989); (2) intra-plate (hot-spot) asthenospheric mantle (Kay et al., 1999); (3) subducted sediment and fluids from the slab (Stern, 1991); (4) recycled continental crust incorporated into the mantle from the fore-arc or the base of the crust (Stern, 1991; von Huene and Scholl, 1991; Kay and Abbruzzi, 1996).

Paleozoic volcanic and Mesozoic plutonic country-rocks in the Collahuasi district define a mixing line between an enriched mantle component (subcontinental lithosphere) and Precambrian gneissic crustal rocks from southern Peru. The more radiogenic Pb compositions of the intermediate Mesozoic intrusions (granodiorite) probably reflect derivation from an enriched mantle source and minor variable contamination by a crustal component. Conversely, the less radiogenic Pb isotope compositions of the felsic volcanic rocks from the Paleozoic Collahuasi Formation indicate that they are derivatives of anatectic crustal melts that reflect the composition of the Precambrian Gondwana basement (Macfarlane et al., 1990; Aitcheson et al., 1995; Tosdal, 1996). The homogeneous Pb isotope values of ore-related porphyry magmas appear not to have been influenced by Paleozoic and Mesozoic country rocks in the Collahuasi district, thereby precluding contamination of these magmas Pb by a shallow crustal source.

Evolution of the Andean Crust at 21°S

Although crustal shortening has been a major factor in the development of the Andes, balanced crustal reconstructions in northern Chile indicate that crustal shortening alone could not have produced the present-day crustal thickness of 70 km beneath the Western Cordillera (Schmitz, 1994). Thus an additional 20% of crustal

material is required from elsewhere. During the last 26 m.y., simple magmatic addition to the base of the crust by mantle-derived magmas can only account for ~20-40 km^3 km^{-1} $m.y.^{-1}$ (Reymer and Schubert, 1984; Francis and Hawkesworth, 1994) or about 5% of the large amount of crustal material required to balance this deficit (~500-800 km^3 km^{-1} $m.y.^{-1}$; Allmendinger et al., 1997). Therefore, the remaining crustal material must have come from magmatic episodes older than 26 Ma (Haschke et al., 2002).

Assuming that the crust was ~30-35 km thick in Jurassic times (Schmitz, 1994), then potentially most of the missing crustal volume was added by mafic magma underplating in the late Eocene-early Oligocene. Haschke et al. (2002) suggested that underplating has increased crustal thickness by ~5-10 km between the late Cretaceous and middle to late Eocene, and concluded that overall crustal thickness was increased ~45 km during the late Eocene Incaic shortening event. Crustal thickening, induced by a combination of shortening and magma underplating is consistent with the Rb/Sr and Sm/Nd isotopic signatures of the late Eocene-early Oligocene porphyry magmas, and their incompatible trace element compositions (e.g. REE patterns and high La/Yb values).

REE Behaviour: High-pressure partial melting or low-pressure fractional crystallisation?

Variations in REE patterns of intermediate to felsic rocks through time provide insights to changing pressure, temperature, and fluid conditions under which the magmas evolved (Kay et al., 1999). For example, feldspar, which is stable at low pressures, accommodates Eu. Amphibole, and to a lesser extent clinopyroxene, which are stable at medium pressures, accommodate the middle and heavy REE, whereas garnet has a strong affinity for the heaviest REE and Y, and is stable at high pressures. Increasing the pressure in the source region of magma generation results in steepening of the REE profiles in the differentiated magma (e.g., increasing La/Yb or La/Y ratios). A decrease in the size of the Eu anomaly, coupled with increasing Na_2O and Sr abundances, signifies plagioclase destabilisation in the residue as pressure increases. High pressure evolution in the continental crust can result in steep REE profiles. On the other hand, flat REE profiles with a negative Eu anomaly can signal evolutions of a magma source region below thin crust at low pressure.

Amphibole that is enriched in middle and heavy REE, can potentially steepen REE profiles of differentiated partial melts (Lang and Titley, 1998). However, without garnet, even extreme amphibole fractionation produces maximum La/Yb values of 14-15 (Haschke et al., 2002). The REE concentrations in the Rosario, Ujina and Inca porphyries are depressed through the middle REE (moderate upward concavity), suggesting the presence of amphibole either in the source residuum or as a fractionated phase in a shallow-level magma chamber.

Drummond and Defant (1990) and Haschke et al. (2002) simulated the effects of partially melting different mafic garnet- and amphibole-bearing source mineralogies on La/Yb ratios. They concluded that 10-20% partial melt from a garnet-amphibolite (10 wt. % garnet, 90 wt. % amphibole) source, with a MORB starting composition, was capable of producing La/Yb > 15, consistent with those of porphyry magmas in the Collahuasi district. These high values are interpreted to reflect the transition from a low-pressure plagioclase + clinopyroxene dominated residual assemblage towards an amphibole + garnet source composition, when the crust was migrating through the garnet stability field at ≥12 kbar or crust ≥ 40 km thick (Rapp and Watson, 1995; Petford and Atherton, 1996). Thus the high La/Yb values (>20) of the Rosario and Ujina Porphyries, indicate that garnet was present in the source region.

Petrogenesis

Adakites

Compositions of the Rosario and Ujina Porphyries are similar to those described for adakites. Adakites are characterised by $SiO_2 \geq 56$ wt.%, $Al_2O_3 \geq 15$ wt.%, MgO usually <3 wt.%, low Y (≤ 18 ppm), low HREE (e.g., Yb ≤ 1.9 ppm), high Sr (rarely < 400 ppm) and $^{87}Sr/^{86}Sr < 0.7040$ (Defant and Drummond, 1990). They are indistinguishable petrographically from typical calc-alkaline andesites and dacites with phenocrysts of plagioclase and amphibole common. Adakites have been described in many subduction settings, but predominantly occur in island arcs.

The origin of adakitic magmas has been attributed to the partial melting of subducted eclogite facies oceanic basalt (Defant and Drummond, 1990) at temperatures in excess of 700°C and at depths between 75 and 85 km (Sajona et al., 1993). High temperatures are attainable at these shallow depths of subduction if young (< 25 m.y.) and hot oceanic crust is subducted (Defant and Drummond, 1990; Sajona

et al., 1993). Other tectonic settings have been proposed also; namely the initiation or termination of subduction (Sajona et al., 2000); subduction associated with high shear stresses (> 100 MPa; Peacock et al., 1994); and subduction of oceanic crust at a low angle. (i.e., <30°; Gutscher et al., 2000). However, all these models emphasise the genesis of adakites in island arcs, not continental arcs, and thus do not take into account potential for the primary magma to be contaminated by crustal sources (Richards, 2002).

The evolved Sr isotopic composition of the ore-related porphyries in the Collahuasi district (0.7050-0.7053) exceeds the initial $^{87}Sr/^{86}Sr$ value (0.7040) that is generally accepted for adakites. These radiogenic Sr values suggest contamination of mantle-derived melts during passage through old and thickened crust, rather than derivation from partial melting of the subducted slab and direct passage to shallow crustal levels (cf. Oyarzun et al., 2001). Moreover, it appears that the low HREE and MREE abundances in the Rosario and Ujina Porphyries reflect interaction of mantle-derived mafic magmas with garnet-stable lower crustal rocks, followed by shallow-level amphibole fractionation.

MASH Processes

Potentially, direct partial melting of mantle wedge garnet-peridotite, and subsequent olivine ± clinopyroxene fractionation can produce similar trace element compositions to those in ore-related intrusions at Collahuasi. The high LILE and LREE abundances in the source region would thus require addition of these components to the melts, possibly from the subducted slab (e.g., slab-sediment dehydration or partial melting of eclogite). However, Hildreth and Moorbath (1988) argued that depressed HREE compositions were more likely caused by differentiation from a high-pressure garnet-bearing lower crust. They suggested that crustal contamination was an integral component of Andean magma genesis, as indicated by Sr and O isotope concentrations in northern SVZ volcanic rocks.

HREE fractionation and radiogenic isotope enrichment in melts potentially occurs by hybridisation of mantle-derived melts with deep crustal-derived melts in the MASH zone (Hildreth and Moorbath, 1988). In this model, basaltic melts ascending from the mantle wedge achieve neutral buoyancy at the lower crust density interface where they locally induce partial melting of the lower crust, Ultimately, the different melts in the MASH zone will mix. The hybrid magmas that result either crystallise

completely, or fractionate to the necessary degree to re-establish magma ascent of evolved intermediate to felsic melts. If the MASH zone was deepened as a result of crustal thickening, then the products of hybridisation of mantle-derived basaltic melts with those derived from a high-pressure, garnet-stable, crustal source, would have a depleted HREE signature.

MASH interaction of the sub-arc mantle and lower continental crust possibly explains the decrease of $^{207}Pb/^{204}Pb$ values in the ore-related porphyry intrusions. Some of the scatter in the data may be related to incorporation of radiogenic Pb, derived from continental sediments subducted into the mantle wedge. However, Pb isotope signatures of Nazca Plate basalts and sediments appear not to have significantly influenced the overall isotopic compositions of ore-related porphyries. The $^{207}Pb/^{204}Pb$ and $^{206}Pb/^{204}Pb$ isotope compositions of ore-related intrusions closely correspond to the Pb-isotopic signature of SVZ volcanic rocks, which along with Sr-Nd data, was interpreted by Hildreth and Moorbath (1988) to have resulted from MASH processes. The Pb (and Sr-Nd) isotope composition of the ore-related intrusions at Collahuasi are therefore inferred to have originated by blending of subcrustal and mantle-derived magmas in MASH zones.

Evolution of the ore-related plutons at Collahuasi

Late Eocene crustal thickening, advanced by mafic melt underplating and crustal shortening, is inferred to have deepened the MASH zone where the residual mineral composition evolved concomitantly from low-pressure, hydrous amphibolite to high-pressure dehydrated garnet amphibolite (e.g. Kay et al., 1991; Haschke et al., 1999). Flat subduction of the oceanic lithosphere between 35 and 25 Ma is reflected by a volcanic hiatus during this period. Flattening of the slab thinned the mantle wedge and forced the asthenosphere to retreat. The lack of hot asthenosphere beneath the arc diminished mantle-derived mafic recharge to the MASH zone, and probably shut down magmastism. The last fractionated melts that ascended into the crust were metal- and volatile-rich.

Magmas ascending from the MASH zone ranged in composition from andesite to dacite. These volatile and metal-enriched magmas ascended to epizonal levels and formed the parent plutons from which the Rosario and Ujina porphyry intrusions were sourced. Elevated crustal temperatures (due to mafic-magma underplating, Leitch and Weinberg, 2002), and exhumation of the overlying crustal block (Chapter 3), promoted

rapid ascent of the magmas.

Evolution of igneous rocks in the Collahuasi district appears to be similar to the magmatic cycle documented in the Maricunga, El Indio and El Teniente metallogenic belts by Kay et al. (1999). In their model, Kay et al. (1999) proposed that a garnet source residuum was present in the MASH zone and that increasing La/Yb ratios marked the transformation from amphibole- to garnet-stable conditions within the MASH zone, and surrounding ambient lower crust. They inferred that fluids were released in the transition from amphibole to garnet and may have become involved in the genesis of major Cu and Au porphyry- and epithermal-related deposits in central and northern Chile. However it is more likely that this process formed hydrous magmas, not a free fluid phase that existed in large volumes in the crust.

High La/Yb, similar to those outlined for the metallogenic belts of central Chile (Kay et al., 1999) have been identified in ore-related intrusions at Rosario and Ujina, as well as in other ore-related intrusions from the porphyry Cu province of northern Chile (e.g., El Salvador: La_{cn}/Yb_{cn} = 15-25, Cornejo et al., 1997; Escondida: La_{cn}/Yb_{cn} = 19-30, Richards et al., 2001; Chuquicamata: La_{cn}/Yb_{cn} = 15-25, Maksaev, 1990). The high La_{cn}/Yb_{cn} values at Rosario and Ujina are interpreted as evidence that the parent magmas were derived from partial melting of the asthenospheric mantle and interacted with the MASH zone at the base of thick continental crust.

In a study of the geochemical characteristics of igneous rocks at Escondida, Richards et al. (2001) interpreted the depressed MREE and zero to slightly positive Eu anomalies in the ore-related, felsic intrusions to indicate low-pressure hornblende fractionation. Moreover amphibole was replaced by biotite as the cotectic phase in the Escondida porphyries, which had fractionated from hornblende-bearing diorite intrusions. Although there is no evidence of co-magmatic hornblende-bearing intermediate intrusions at Rosario and Ujina, the presence of biotite, rather than amphibole in the mineralised porphyries is interpreted as evidence that amphibole may have fractionated from a shallow crustal magma chamber. The incompatible trace element compositions of the ore-related intrusions, including Eu/Eu* values between 0.91 and 0.98 and depleted MREE, are consistent with crystallisation from hydrous magmas. This is because the high fH_20 required to crystallise MREE-enriched amphibole possibly suppressed plagioclase fractionation (Naney, 1983; Rutherford and Hill, 1993; Candela, 1997; Richards et al., 2001), and produced porphyry intrusions

that lacked negative Eu anomalies. These rocks are distinguished from the feldspar-fractionated and anhydrous Paleozoic volcanic and Mesozoic plutonic rocks, which have distinct negative Eu anomalies (Eu/Eu* = 0.59-0.62).

Conclusions

Major element compositions do not reliably discriminate igneous rocks in the Rosario and Ujina porphyry deposits. Many of the rocks have been affected by incipient hydrothermal alteration, which may have mobilised the major elements and added silica as vein quartz. The immobile trace element classifications are more effective than the major elements in discriminating igneous rocks. On a plot of Zr/TiO_2 vs. Nb/Y, the Rosario, Ujina and Inca Porphyries are monzonites, whereas the Collahuasi Porphyry and Profunda Pluton are granodiorites. Bivariate major and trace element patterns define sub-linear to linear trends; however these rocks are not comagmatic. Instead, the rocks were deposited and emplaced at different periods between the Permian and early Oligocene.

Sr, Nd and Pb isotopes of ore-related porphyry magmas at Rosario and Ujina indicate that they were derived from MASH zones (similar to rocks of the SVZ), where mantle-derived and crust-derived magmas hybridised at or near the mantle-crust boundary. Higher initial $^{87}Sr/^{86}Sr$ and lower initial $^{143}Nd/^{144}Nd$ values in the Rosario and Ujina porphyries, relative to intrusions associated with earlier-formed porphyry Cu deposits in the late Eocene-early Oligocene porphyry province (e.g., El Salvador and El Abra) reflects higher degrees of crustal contamination in the younger magmas.

Steep REE patterns, and high La_{cn}/Yb_{cn} (>20) and Sr/Y (>20) values suggest that partial melts, from which the ore-related intrusions were sourced, were derived from a garnet-bearing source mineralogy. The heavy REE-depleted patterns imply that magmas associated with ore deposits were derived from mantle melts that interacted with the lower crust at pressures ≥12 kbar or ≥ 40 km. Magma mixing occurred in MASH zones that evolved from a hydrous (amphibole-bearing) to an anhydrous (garnet-bearing) residual source. Deepening of the MASH zone to a high pressure, garnet-stable environment occurred in response to tectonic thickening and mafic magma underplating during the Incaic crustal shortening episode in the late Eocene. Dehydration melting of garnet-amphibolite destabilised plagioclase in the source region and produced hydrous melts enriched in Sr and Eu, but depleted in HREE.

Chapter 5. Veins and Altered Rocks

Introduction

Many porphyry deposits are associated with zones of advanced argillic alteration. Some of these alteration zones host high-sulfidation epithermal deposits (e.g., Lepanto-Far Southeast in the Philippines, Arribas et al., 1995b; Hedenquist et al., 1998; La Mejicana-Nevados del Famatina, Argentina, Losada-Calderón, 1992; Losada-Calderón et al., 1994). The advanced argillic alteration assemblage typically forms at shallow crustal levels (200-1000 m below the paleowater table; Arribas, 1995; Cooke and Simmons, 2000) in contrast to the zone of potassic alteration (ca. 1-3 km; Sillitoe, 2000). In northern Chile, several of the major Eocene-Oligocene porphyry Cu-Mo deposits are characterised by zones of advanced argillic alteration superimposed directly onto K-silicate altered rocks. The best documented example occurs at Chuquicamata where structurally controlled phyllic and advanced argillic assemblages, associated with Butte-style Cu-Ag veins (Sillitoe, 2000; Ossandon et al., 2001), have cross-cut a broad zone of potassic alteration. Similar reverse-zoned alteration patterns, fringed by propylitic alteration of the country rock, have also been described at Rosario (Dick et al., 1994; Lee, 1994), Mansa Mina (Sillitoe et al., 1996), Escondida (Padilla Garza et al., 2001), and Quebrada Blanca (Hunt et al., 1983).

This chapter describes the porphyry-style hydrothermal mineral assemblages and cross-cutting enargite-tennantite-bearing massive sulfide veins at the Rosario deposit, and addresses potential genetic relationships. Previous descriptions of the Rosario deposit, summarised in Chapter 1 (e.g., Munchmeyer et al., 1984; Hunt, 1985; Dick et al., 1994; Lee, 1994), identified some advanced argillic minerals (e.g., pyrophyllite, andalusite) in the bleached "phyllic" envelope that surrounds the massive sulfide veins. Despite the recognition of these minerals, the extent and distribution of the advanced argillic assemblage has not been delineated previously. A major aim of this study has been to determine the mineralogy of advanced argillic alteration assemblages at Rosario, and their spatial distributions relative to the K-silicate and phyllic altered rocks documented in previous studies. A description of the La Grande enargite-pyrite-chalcocite-bornite veins, located 1.5 km southwest of Rosario, is included for comparison and for later discussion of the district-scale evolution of hydrothermal activity.

Determination of the temporal evolution of hydrothermal mineral assemblages has been based on cross-cutting vein relationships, and associated overprinting hydrothermal alteration textures. These results build on the work of previous studies that addressed the geology, geochronology, hydrothermal alteration and ore paragenesis at Rosario (Dick et al., 1994; Lee, 1994; Clark et al., 1998).

Alteration and Ore Mineral Mapping

Zones of ore and alteration mineral associations were mapped in detail across three northeast cross-sections at the Rosario deposit and a single east-west section through the La Grande Vein. Drill core logging was augmented by a short-wave infrared absorption (SWIR) spectroscopic study that identified fine-grained alteration minerals. In total, nineteen Rosario (7,470 m) and two La Grande (1,100 m) diamond drill holes were logged graphically. Rock-type, structure, vein types and paragenesis, relative ages of intrusions, ore and alteration mineral associations and their distribution, and approximate volume percent of the main mineral constituents were recorded. SWIR spectra, analysed by an Integrated Spectronics Pty. Ltd. portable infrared microanalyser (PIMA), were measured on 1,046 diamond drill core samples. Detailed examination of sulfide and alteration overprinting relationships was carried out on 120 polished thin sections using transmitted and reflected light microscopy.

SWIR Spectroscopy

Fine-grained alteration minerals associated with advanced argillic (pyrophyllite, muscovite, diaspore, alunite), phyllic (muscovite, illite) and argillic (illite, smectite, kaolinite) assemblages are difficult to identify in the field. Moreover, petrographic identification is complicated in rocks that contain both muscovite and illite, or both pyrophyllite and muscovite, as these minerals have very similar optical properties. The PIMA has enabled rapid identification of the fine-grained alteration minerals at Rosario and La Grande, without recourse to expensive, detailed XRD analyses. Zones of bleached alteration were analysed every 4 m to evaluate small scale mineralogic variations in drill core intersections through zones of clay and white mica alteration. Sample spacing was 8 to 16 m in zones of hydrothermal alteration that lacked white micas and clay (e.g., biotite or chlorite altered rocks). An example of a graphic log showing downhole geology and alteration mineralogy is shown with the corresponding downhole SWIR spectra in Figure 5.1

Figure 5.1. Summary log from a section of diamond core in drill hole C177 showing downhole geology, alteration mineralogy, main structures, SWIR spectra and copper grades. Alteration minerals were identified by comparing the measured spectra to the TSG^{TM} spectral database (Mason et al., 1999). Each spectrum has been with the mineral identified.

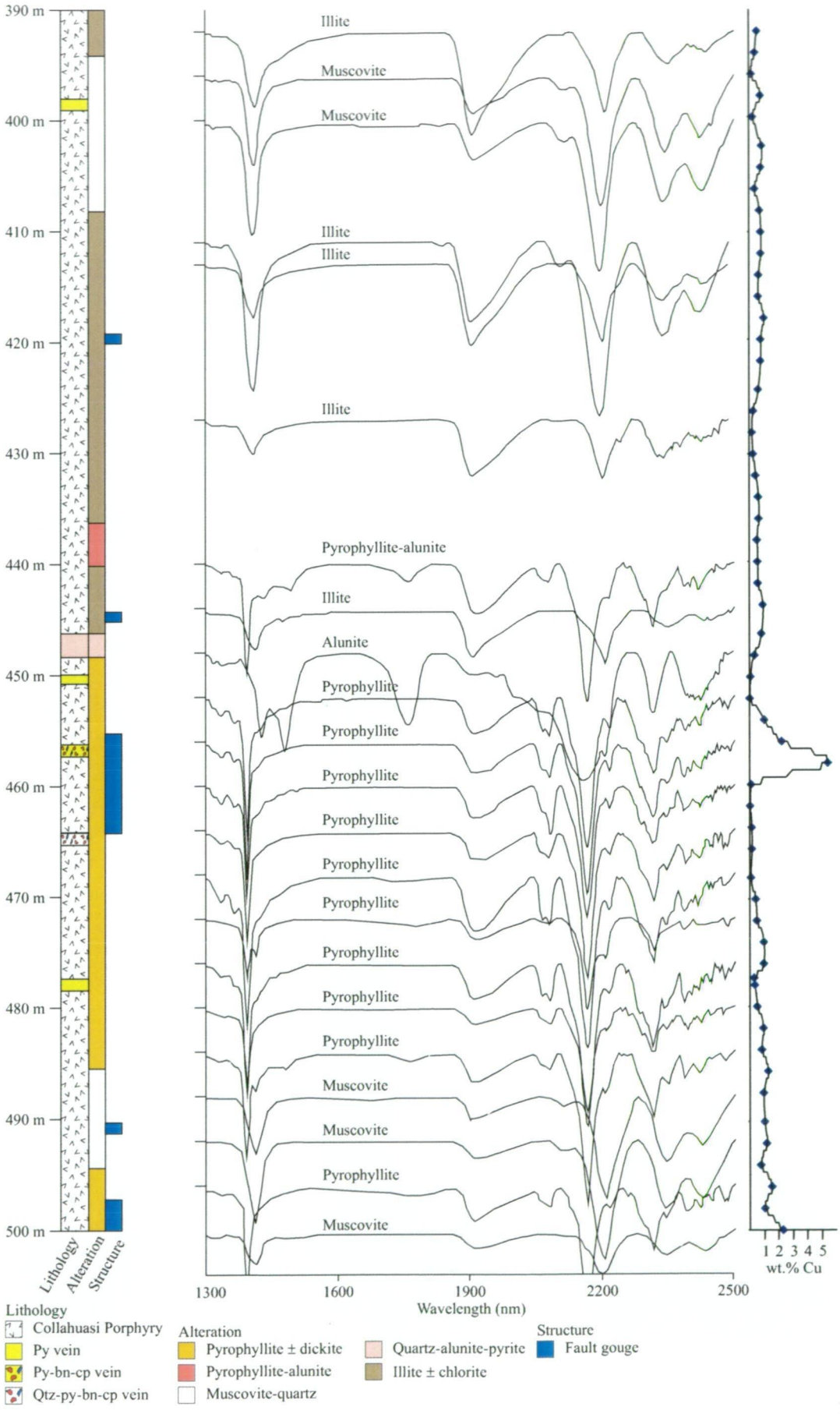
390 m
400 m
410 m
420 m
430 m
440 m
450 m
460 m
470 m
480 m
490 m
500 m
Lithology
Alteration
Structure
Illite
Muscovite
Muscovite
Illite
Illite
Illite
Pyrophyllite-alunite
Illite
Alunite
Pyrophyllite
Pyrophyllite
Pyrophyllite
Pyrophyllite
Pyrophyllite
Pyrophyllite
Pyrophyllite
Pyrophyllite
Pyrophyllite
Muscovite
Muscovite
Pyrophyllite
Muscovite
1300
1600
1900
2200
2500
Wavelength (nm)
1 2 3 4 5
wt.% Cu
Lithology
Collahuasi Porphyry
Py vein
Py-bn-cp vein
Qtz-py-bn-cp vein
Alteration
Pyrophyllite ± dickite
Pyrophyllite-alunite
Muscovite-quartz
Quartz-alunite-pyrite
Illite ± chlorite
Structure
Fault gouge

Multiple spots were analysed by the PIMA in each core sample following the procedure of Thompson et al. (1999). Mineral identification was made by comparing each measured spectra to a reference database using The Spectral Geologist processing software (AUSSPEC International Pty. Ltd; Mason et al., 1999). Spectral mineral identification was confirmed by detailed petrographic examination of the altered rocks, as well as electron microprobe analyses, which was used to determine fine-scale compositional variations in individual minerals.

Terminology

Mineral assemblages are defined in this study as groupings of minerals that occur in direct contact and that do not display evidence of reaction with one another (Barton et al., 1963). In the later discussion between various ore and alteration assemblages, the term *equilibrium assemblage* is used where the textural relationships are interpreted as evidence that the minerals formed contemporaneously, or that they equilibrated with each other. Groups of minerals that are characteristic of a given alteration domain, but which are not all in contact and were not necessarily deposited at the same time are referred to as *mineral associations. Alteration zones* are defined as domains of mineral associations, rather than of mineral assemblages.

Terms describing alteration texture and vein form, adopted from the classification scheme of Titley (1982), are listed in Table 5.1. The vein classification scheme (e.g., A, B and D veins) established by Gustafson and Hunt (1975), at the El Salvador porphyry ore deposit, has been used to classify the various Rosario vein-types. However, this vein nomenclature has been modified to accommodate some additional vein-types that occur at Rosario. These include C veins, first described by Dilles and Einaudi (1992) at the Ann Mason porphyry ore deposit at Yerington, Nevada. A new term, "E vein", is introduced in this study to describe the tennantite-enargite bearing massive sulfide veins in the Rosario deposit.

Table 5.1. Alteration and vein terminology (from Titley, 1982).

Term	Definition
Selectively pervasive alteration	Complete alteration of specific mineral in the rocks (e.g., feldspar and/or mafic phenocrysts), commonly enhances rock texture
Pervasive alteration	Texturally destructive alteration of the entire rock
Domainal alteration	Selective or pervasive alteration that occur in domains
Incipient alteration	Partial alteration of a specific mineral in the rock
Weak, moderate or intense alteration	Describe relative intensity of alteration based on subjective visual estimates
Vein	Fracture filled by hydrothermal minerals, minimum width 5 mm
Veinlet	Fracture filled by hydrothermal minerals, maximum width 5 mm
Vein selvage	Hydrothermal minerals that occur exclusively on veins walls
Envelope	Extent of an alteration assemblage surrounding and directly related to a vein

Vein and Alteration Mineral Assemblages

Nine major vein stages were recognised during drill core examination and follow-up petrographic work (Table 5.2). Seven of these vein stages (M, A-1, A-2, A-3, B, C, and D veins) are related to porphyry-style ore and alteration types, of which there are four distinct alteration assemblages. These are the magnetite, biotite-albite, K-feldspar, and illite-chlorite assemblages. About 50% of the copper at Rosario is associated with the A-stage veins, and most of the molybdenite occurs in the B veins. The spatial and temporal distribution of veins and associated alteration, based on vein cross-cutting relationships and mineral overprinting textures, is illustrated in Figure 5.2 and summarised in Table 5.2.

Figure 5.2. Schematic time-space diagram showing the vein and alteration paragenesis in the Rosario and La Grande deposits. The earliest events are at the bottom of the diagram The length of the bars show the lateral distribution of vein development or an alteration assemblage relative to the Rosario Porphyry. In the late-stage veins, sulfide paragenesis is shown as a series of vein infill stages. Vein and alteration paragenesis are based cross-cutting and overprinting relationships observed in drill core and detailed petrography.

Rock abbreviations: PCO = Collahuasi Porphyry, PRO = Rosario Porphyry

Mineral abbreviations : alb = albite, alun = alunite, and = andalusite, APS = aluminium-phosphorous-sulfate minerals, bar = barite, bio = biotite, bn = bornite, cal = calcite, cc = chalcocite, chl = chlorite, col = colusite, cp = chalcopyrite, dg = digenite, dias = diaspore, dick = dickite, dj = djurleite, en = enargite, ep = epidote, gar = garnet, ill = illite, ka = kaolinite, ksp = K feldspar, mt = magnetite, mo = molybdenite, mw = mawsonite, prl = pyrophyllite, py = pyrite, qtz = quartz, rut = rutile, sl = sphalerite, tn = tennantite, vin = vinciennite, zun = zunyite

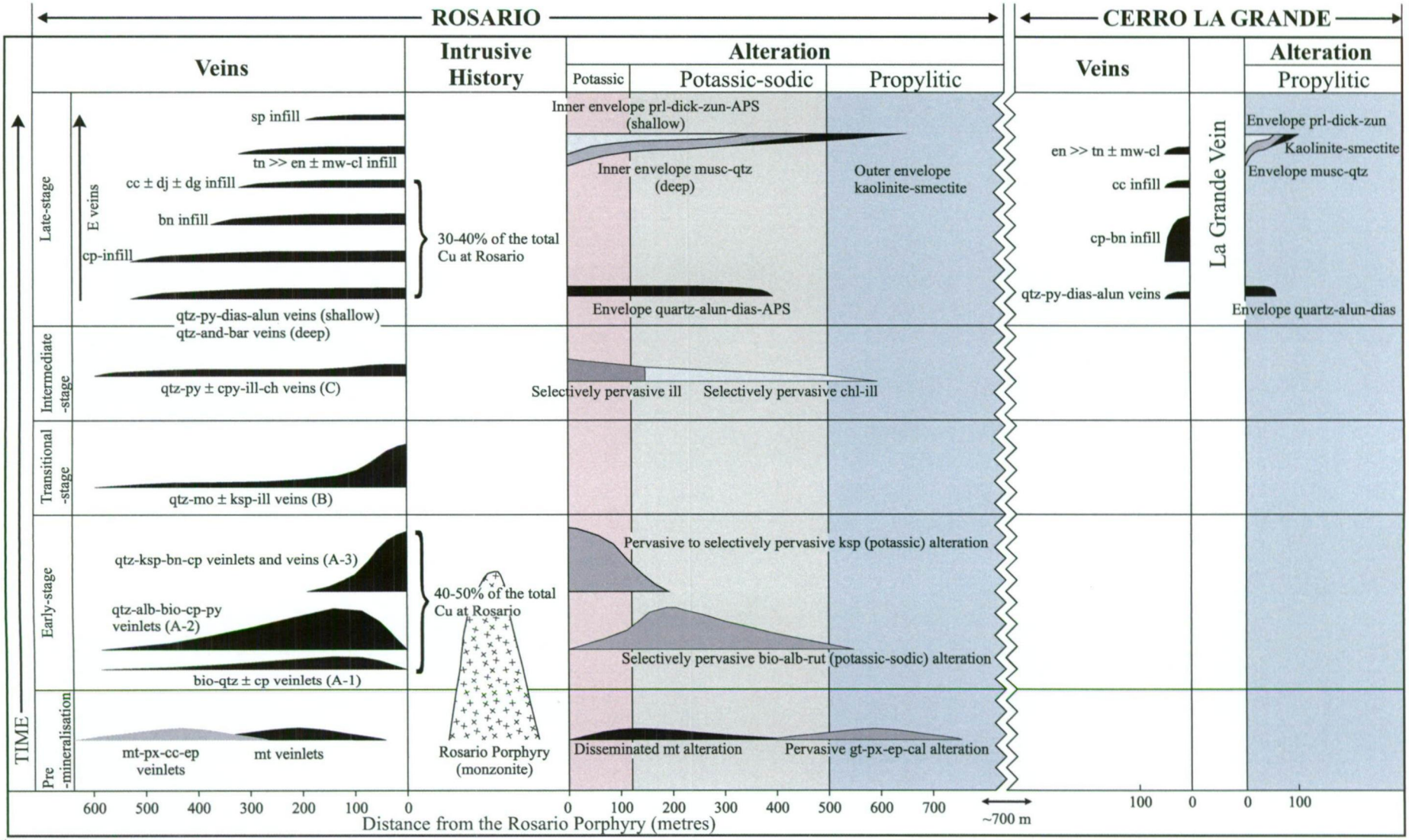
ROSARIO
CERRO LA GRANDE
Veins
Intrusive History
Alteration
Potassic
Potassic-sodic
Propylitic
Veins
Alteration
Propylitic
TIME
Late-stage
Intermediate -stage
Transitional -stage
Early-stage
Pre -mineralisation
E veins
sp infill
tn >> en ± mw-cl infill
cc ± dj ± dg infill
bn infill
cp-infill
qtz-py-dias-alun veins (shallow)
qtz-and-bar veins (deep)
qtz-py ± cpy-ill-ch veins (C)
qtz-mo ± ksp-ill veins (B)
qtz-ksp-bn-cp veinlets and veins (A-3)
qtz-alb-bio-cp-py veinlets (A-2)
bio-qtz ± cp veinlets (A-1)
mt-px-cc-ep veinlets
mt veinlets
30-40% of the total Cu at Rosario
40-50% of the total Cu at Rosario
Rosario Porphyry (monzonite)
Inner envelope prl-dick-zun-APS (shallow)
Inner envelope musc-qtz (deep)
Outer envelope kaolinite-smectite
Envelope quartz-alun-dias-APS
Selectively pervasive ill
Selectively pervasive chl-ill
Pervasive to selectively pervasive ksp (potassic) alteration
Selectively pervasive bio-alb-rut (potassic-sodic) alteration
Disseminated mt alteration
Pervasive gt-px-ep-cal alteration
en >> tn ± mw-cl
cc infill
cp-bn infill
qtz-py-dias-alun veins
La Grande Vein
Envelope prl-dick-zun
Kaolinite-smectite
Envelope musc-qtz
Envelope quartz-alun-dias
600 500 400 300 200 100 0
0 100 200 300 400 500 600 700
~700 m
100 0
0 100
Distance from the Rosario Porphyry (metres)

Table 5.2. Summary of vein types and associated mineral assemblages, listed in sequence from oldest (1) to youngest (9). Abbreviations listed in Figure 5.1.

Vein type	Distribution	Vein Textures	Vein Infill						Wall-rock alteration halo			Age relative to other veins	
			Major		Minor								
			Gangue	Opaque	Gangue	Opaque	Thickness	Structure	Major	Minor	Thickness	Postdate	Predate
M-veinlets													
1. mt	Moderately abundant in country rock, absent in PRO	Chains and/or beads	-	mt	-	-	< 0.3 mm	No wall definition	-	-	-	PCO	PRO, 2, 3, 4, 5, 6, 7
A-veins/veinlets													
2. bio-qtz	Abundant in country rock, rare in PRO	Wavy, discontinuous	bio	-	qtz	cp	< 0.3 mm	Irregular walls	-	-	-	PCO, 1, PRO, 3	3, 4, 5, 6, 7
3. qtz-alb-bio-cp-py	Moderately abundant in country rock proximal to PRO, rare in PRO + distal country rock	Anhedral, granular qtz	qtz-alb-bio	cp, py		rut	< 5.0 mm	Irregular, non-parallel walls, no internal symmetry	alb, bio	rut	< 2 mm	PCO, 1, PRO, 2	2, 4, 5, 6, 7
4. qtz-ksp-cp-bn	Abundant in PRO, moderately abundant in country rock proximal to PRO	Anhedral, granular (sugary) quartz	qtz, ksp	cp, bn	bio	rut	< 2.0 cm	Irregular to regular walls, lack of internal symmetry	ksp	bio, rut	< 2 mm	PCO, 1, PRO, 2, 3	5, 6, 7, 8, 9
B-veins													
5 qtz-mo	Abundant in and proximal to PRO	Subhedral to euhedral quartz, flaky molybdenite	qtz	mo	ksp, ill, chl	py, rut	generally 1 - 3 cm, up to 15 cm	Regular walls	-	ksp, ill, chl, qtz	< 1 cm	PCO, 1, PRO, 2, 3, 4	6, 7, 8, 9
C-veins													
6. qtz-cp-py-ill-chl	Moderately abundant throughout PRO and country-rock	Subhedral to euhedral quartz	qtz	cp, py	ill, chl	rut	< 3.0 mm	Regular walls	ill, chl, qtz	py, rut	< 2 cm	PCO, 1, PRO, 2, 3, 4, 5	7, 8, 9
D-veins													
7. py-cpy	Most abundant in structurally-controlled zone of muscovite alteration	semi-massive sulfide, euhedral quartz	-	py, cp	mu, qtz	rut	< 1.0 cm	Regular walls	mu, qtz	chl	< 10 cm	PCO, 1, PRO,2, 3, 4, 5, 6, 7, 8, 9	8, 9
Polymetallic veins													
8. E veins: py-bn-cpy-tn-cc infill	Major polymetallic veins occur in strands of the Rosario Fault System, subsidiary veins limited to quartz-alunite-pyrite alteration envelopes	Semi-massive to massive sulfide, minor euhedral quartz	-	py, bn, cp, cc	qtz, alun, dias, APS, zun	dj, dg	centimetres to metres	Regular walls	qtz, alun, dias	zun, APS minerals, rut	centimetres to metres	PCO, PRO, 4, 5, 6, 7	7
9. TES veins: tn-en infill	Generally occur as an overprint in E veins; associated with pyrophyllite-dickite alteration that has overprinted the quartz-alunite-diaspore assemblage	Semi-massive to massive sulfide, minor euhedral quartz	-	tn, en	prl, dick	mw, col, vin, sp	centimetres to metres	Regular, parallel walls	prl, dick, musc	zun, APS minerals	centimetres	PCO, 1, PRO, 2, 3, 4, 5, 6, 7	7

Fault-hosted polymetallic massive sulfide (E) veins are the last vein type to have formed at Rosario (Fig.5.2). E veins are characterised by two main infill stages. The first consists of pyrite, chalcopyrite, bornite and chalcocite massive sulfides, and is associated with the alteration assemblage quartz-alunite ± diaspore ± andalusite ± barite. The second is the tennantite-enargite stage (TES), which also contains minor mawsonite, colusite and vinciennite $\{Cu_{10}Fe_4Sn(As,Sb)S_{16}\}$. The TES is associated with pyrophyllite-dickite alteration proximal to veins, and phyllic (muscovite) grading out to argillic (illite-smectite) alteration assemblages distal from veins. The pyrophyllite-dickite alteration assemblage has overprinted the earlier-formed assemblage of quartz-alunite-pyrite. The muscovite-quartz and illite-smectite assemblages are interpreted to have formed contemporaneously with the pyrophyllite-dickite assemblage (Fig. 5.2). The late-stage veins account for about 30-40% of the total copper at Rosario.

Alteration Zones

Overprinting of early equilibrium alteration assemblages by late assemblages has resulted in composite alteration zones. For example, the K-feldspar equilibrium alteration assemblage has been overprinted by illite (± chlorite) in the core of the deposit. They are described here together as the K-feldspar-illite zone. Seven main alteration zones have been delineated in this way. The distribution of the various alteration zones is shown in a series of stacked northeast cross-sections in Figure 5.3.

The K-feldspar-illite zone is localised within and around the Rosario Porphyry. This is fringed by a zone of biotite-albite-magnetite-illite-chlorite altered andesitic and dacitic wall rocks. Stratabound garnet-epidote-pyroxene (calc-silicate) altered rocks occur on the northeastern side of the Rosario Porphyry. A zone of chlorite-epidote altered rocks surrounds the biotite-albite-magnetite-illite-chlorite and calc-silicate zones, but juxtaposes structurally controlled domains of pyrophyllite-dickite-alunite-quartz, muscovite-quartz and kaolinite-illite-smectite altered rocks southwest of the Rosario Porphyry (Fig. 5.3).

Figure 5.3. Stacked northeast-southwest alteration sections in the Rosario deposit (see Figs. 3.1 and 3.2 for section localities). All sections have the same coordinates on the northeast section lines. Contours of hypogene copper grades are shown at the 0.6, 1.0, and 1.5 wt. % Cu values. The Rosario Fault System controls pyrophyllite-rich alteration that grades out to muscovite fringed by zones of kaolinite-illite-smectite. K-feldspar alteration in the core of the deposit is enveloped by biotite-magnetite-albite alteration. Chlorite-epidote alteration surrounds all other alteration types on the margins of the deposit.

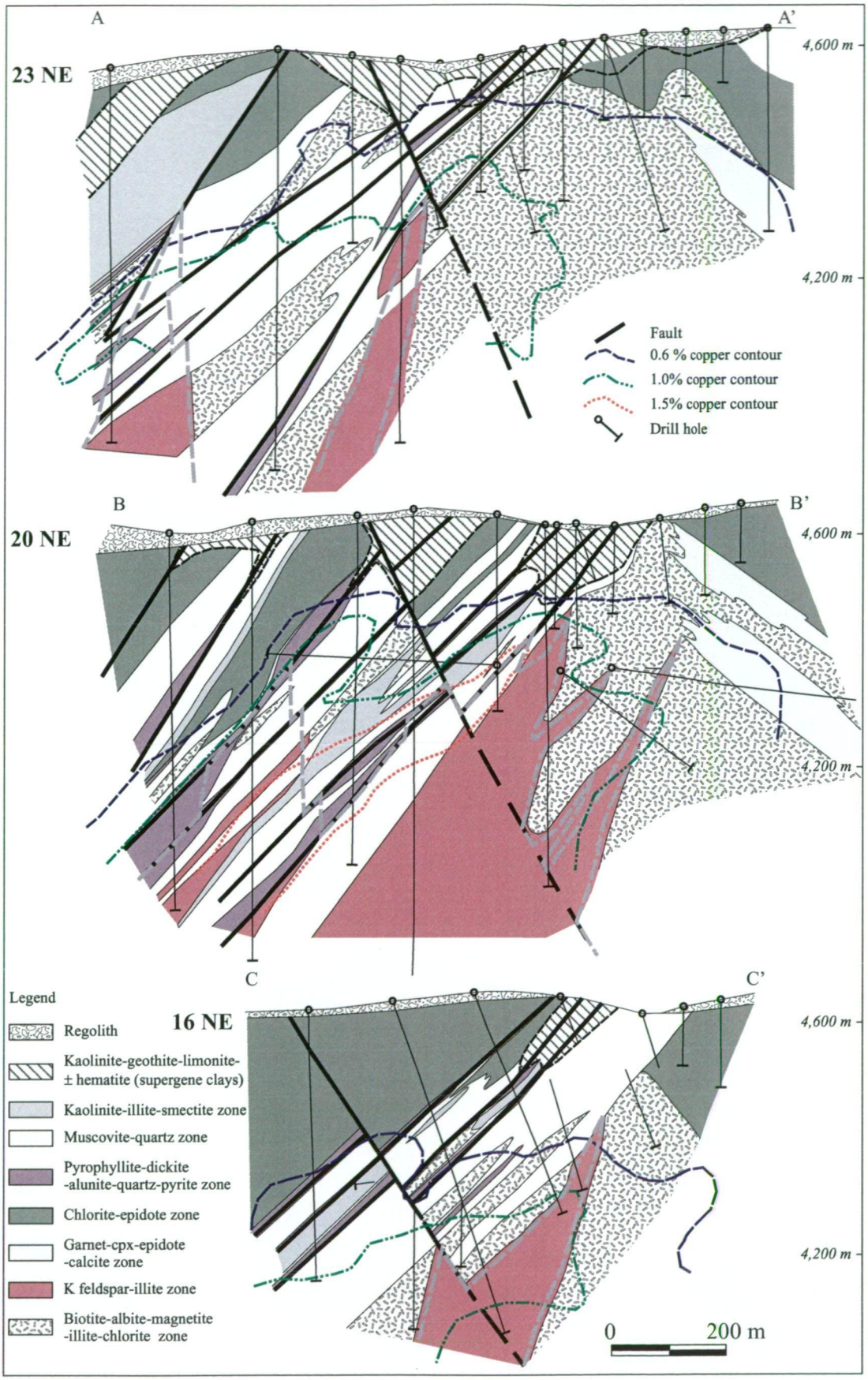
A
A'
23 NE
4,600 m
4,200 m
Fault
0.6 % copper contour
1.0% copper contour
1.5% copper contour
Drill hole
B
B'
20 NE
4,600 m
4,200 m
C
C'
16 NE
4,600 m
4,200 m
Legend
Regolith
Kaolinite-geothite-limonite- ± hematite (supergene clays)
Kaolinite-illite-smectite zone
Muscovite-quartz zone
Pyrophyllite-dickite -alunite-quartz-pyrite zone
Chlorite-epidote zone
Garnet-cpx-epidote -calcite zone
K feldspar-illite zone
Biotite-albite-magnetite -illite-chlorite zone
0
200 m

Porphyry-Type Veins

M veinlets

Irregular, discontinuous magnetite (M) veinlets occur only in the Permo-Triassic host rocks that surround the Rosario Porphyry. They are generally <0.3 mm wide and are the earliest vein type seen in the Rosario deposit (Fig. 5.4a). M veinlets comprise chains and beads of magnetite. The veinlets lack definitive walls and have no internal structure. Electron microprobe analyses of veinlet magnetite are listed in Appendix 2. They have low TiO_2 contents (<0.3 wt.%) and intermediate to high V_2O_3/Al_2O_3 values (0.2 to 6.5; Appendix 2). M veinlets are interpreted to have formed in part by replacement of wall rock, because there is no evidence of open-space filling.

A-1 and A-2 veinlets

Irregular and segmented A-1 veinlets contain biotite, minor quartz and chalcopyrite. Quartz-albite-biotite A-2 veinlets are discontinuous, range from <0.3 mm to 5 mm wide, have sharp irregular walls and contain minor chalcopyrite and pyrite, rutile and magnetite (Fig. 5.4b). Both of these vein types occur in the biotite-albite-magnetite-illite-chlorite altered zone (Fig. 5.3). The alteration halos that surround A1 veins are in places indistinguishable from the strongly developed shreddy biotite that occurs as a background alteration assemblage. By contrast, A-2 veins have well defined albite haloes, stained brown by the presence of fine-grained biotite (Fig. 5.4c). Secondary albite in these haloes has replaced primary plagioclase in contact with the veinlets (Fig. 5.4d). The composition of albite in A-2 vein haloes shows restricted ranges of $Ab_{96}Or_4$ to $Ab_{99}Or_1$ and $Ab_{96}An_3Or_1$ to $Ab_{92}An_3Ce_2$, (celsian indicates the presence of the Ba-rich molecule; see Appendix 2 from electron microprobe analyses). A-1 veinlets are locally cut by A-2 veinlets. Both vein types have cut M veinlets (Fig 5.4a).

Figure 5.4. Photographs and photomicrographs of M and A veins from zones of biotite-magnetite-albite and K-feldspar alteration.

A) *Sample R990213.* Plane-polarised light photomicrograph of a biotite-quartz-chalcopyrite (A-1) vein that cuts a magnetite vein in biotite-magnetite-albite altered porphyritic andesite. Scale bar = 1 mm.

B) *Sample R990026.* Cross-polarised light photomicrograph of porphyritic andesite, cut by an quartz-albite-chalcopyrite (A-2) with an envelope of shreddy biotite. Scale bar = 1 mm.

C) *Sample R200171.* Photograph of biotite-, magnetite-albite-chlorite-illite altered porphyritic dacite. Dark clots disseminated through the rock are biotite-magnetite-chlorite intergrowths. The cores of feldspar phenocrysts have been replaced by illite. The rock is cut by several generations of A-2 veins. The light-brown stain in the bleached vein envelopes indicates the presence of biotite inclusions in secondary albite. Scale bar = 10 mm.

D) *Sample R990007.* Cross-polarised light photomicrograph of an A-2 vein that cuts porphyritic dacite. Feldspar phenocrysts in contact with the vein have been altered to albite. Some vein albite appears to have nucleated at points where phenocrysts were cut by the vein. Scale bar = 100 μm.

E) *Sample R200108.* Photograph of irregular quartz-K-feldspar veins that have cut the Rosario Porphyry. The pink groundmass is secondary K-feldspar. Cores of feldspar phenocryst cores have been altered by illite. Scale bar = 10 mm.

F) *Sample R200135.* Cross-polarised light photomicrograph of a quartz-chalcopyrite-bornite-K-feldspar vein in the Rosario Porphyry. The alteration envelope consists of perthitic K-feldspar replacement of plagioclase phenocrysts beside the vein. Cross-hatched domains of platy illite commonly occur in plagioclase phenocrysts. Scale bar = 500 μm.

Abbreviations: alb = albite, bi = biotite, bn = bornite, cp = chalcopyrite, ill = illite, K-fsp = K-feldspar, mt = magnetite, qtz = quartz.

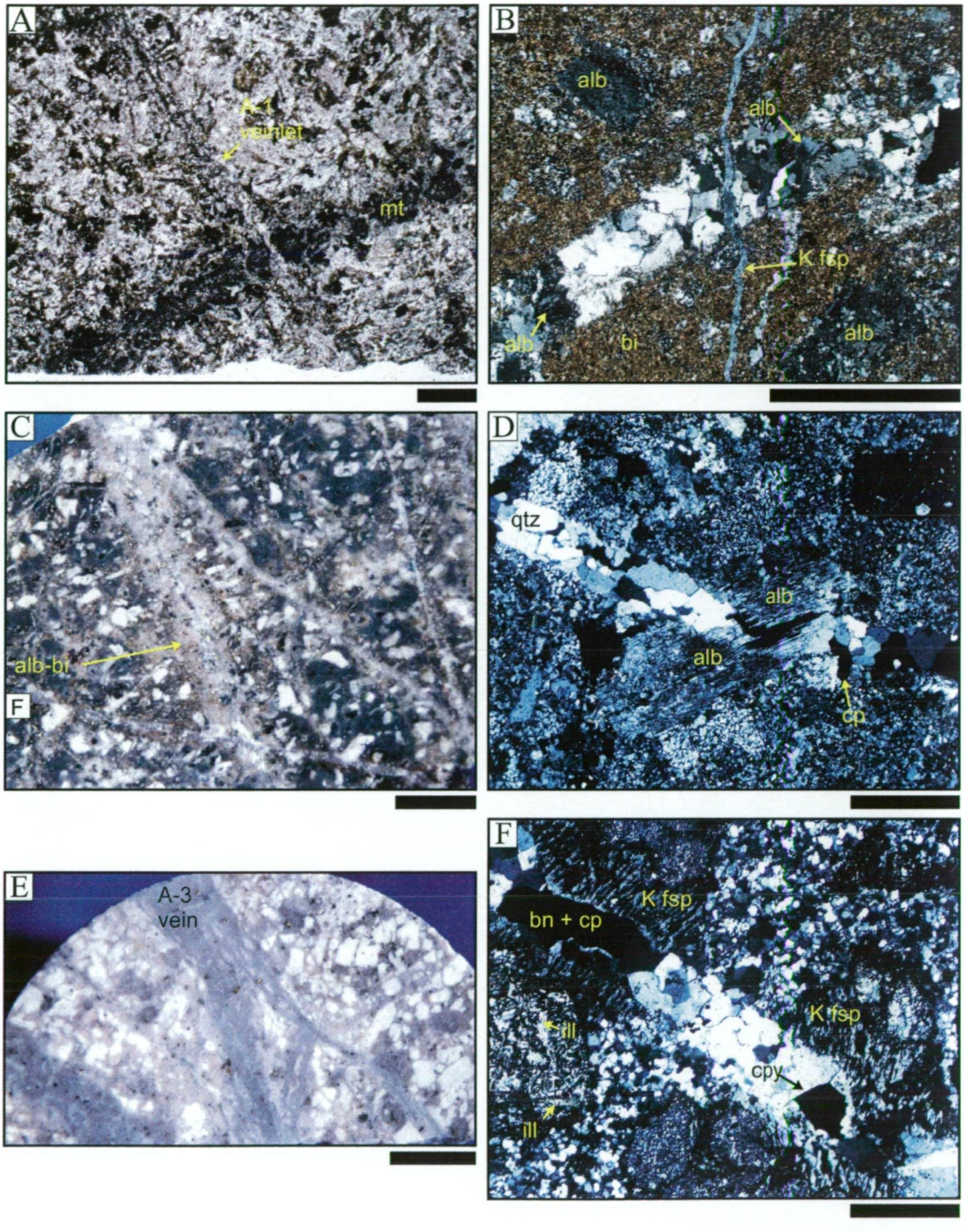
A
A-1 veinlet
mt
B
alb
alb
K fsp
alb
bi
alb
C
alb-bi
F
D
qtz
alb
alb
cp
E
A-3 vein
F
K fsp
bn + cp
ill
K fsp
cpy
ill

A-3 veinlets/veins

K-feldspar-bearing A-3 veins have cut M, A-1 and A-2 veinlets (Fig. 5.4b), and are most abundant in the Rosario Porphyry. The composition of vein and envelope K-feldspar is mostly $Or_{96}Ab_4$ with minor sanidine ($Or_{50}Ab_{50}$; Appendix 2) and celsian (up to 3 wt.%). Chalcopyrite and bornite are the main ore minerals in these veins. A-3 veins are 5 mm to 2 cm wide and exhibit either irregular, discontinuous and segmented walls, or regular, continuous and parallel walls (Figs. 5.4e). No cross-cutting relationships were observed between the regular and irregular A-3 veins in the Rosario Porphyry. Alteration envelopes associated with A-3 veins are easily recognised in rocks that lack pervasive secondary K-feldspar, as the pink K-feldspar haloes are clearly distinguishable. The envelopes are generally 2 mm to 5 cm wide, and comprise perthitic K-feldspar, and minor chalcopyrite and bornite (Fig. 5.4f). Pervasive K-feldspar altered rock is spatially associated with high densities of A-3 veins.

B veins

B veins at Rosario are continuous planar fractures, with parallel walls that have been infilled by anhedral to subhedral quartz and minor K-feldspar. Some B veins have parallel lateral bands of flaky molybdenite intergrown with granular quartz. Molybdenite more typically occurs in vein selvages together with anhedral quartz and K-feldspar (Fig. 5.5a). B veins do not have alteration envelopes.

Anhedral quartz has been overgrown by euhedral quartz and central voids have been filled by chalcopyrite and/or pyrite in some B veins (Fig. 5.5b). Both types of quartz contain fluid inclusions, and show undulose extinction, with minor sub-grain development on grain boundaries. Some chalcopyrite and pyrite grains in the veins contain inclusions of molybdenite, whereas others have truncated molybdenite grain boundaries. B veins that contain euhedral quartz and chalcopyrite-pyrite centre-lines typically have alteration haloes of texturally destructive, fine-grained muscovite.

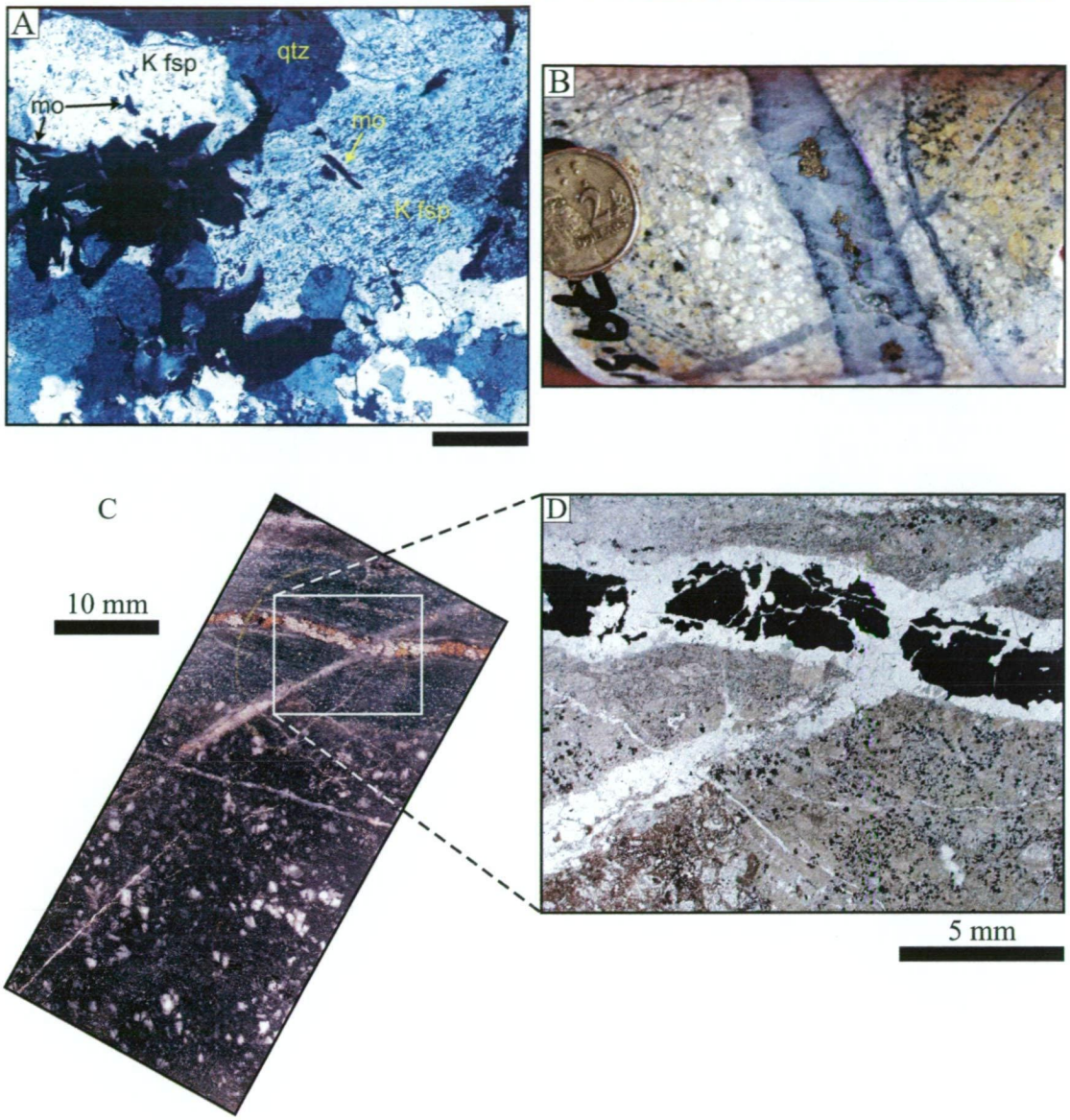

Figure 5.5. Examples of B and C veins.

A) *Sample R990134.* Cross-polarised light photomicrograph of flaky molybdenite inclusions in K-feldspar. Molybdenite and K-feldspar are associated with subhedral quartz and chalcopyrite in the vein selvage. Scale bar = 200 μm.

B) *Sample R990021.* Drill core photograph of the Rosario Porphyry, cut by quartz-chalcopyrite-molybdenite and quartz-K-feldspar-chalcopyrite veins. In this example, the quartz-chalcopyrite-molybdenite vein cuts the quartz-K-feldspar-chalcopyrite veins. Flaky molybdenite is associated with anhedral to subhedral quartz in the vein selvage, whereas chalcopyrite occupies central part of the vein. Phenocryst shapes in the bleached vein envelope, consist entirely of muscovite. Bleached phenocrysts outside the envelope are illite. Diameter of coin = 20 mm.

C) *Sample R990026.* Photograph of biotite-magnetite-albite altered andesite, cut by a pyrite-chalcopyrite-quartz (C) vein with a chlorite-illite alteration envelope.

D) *Sample R990026.* Inset from C. Plane-polarised light photomicrograph of the vein and alteration envelope. Note that the chlorite-illite envelope around the late vein overprints the shreddy biotite envelope around the early vein. Scale bar = 5 mm.

Abbreviations: K-fsp = K-feldspar, mo = molybdenite, qtz = quartz.

C veins

C veins have regular, continuous walls, some internal banding, and vary from <3 mm to 2 cm wide. C veins cut B veins, A veins and M veinlets. They occur throughout the K-feldspar-illite and biotite-albite-magnetite-illite-chlorite alteration zones. The veins are infilled by quartz and pyrite, together with minor chalcopyrite, illite and chlorite. Quartz is typically euhedral, perpendicular to the vein walls and distributed symmetrically on both sides of the vein. Quartz prisms, attached to vein walls, terminate in central domains now infilled by pyrite and chalcopyrite. C vein envelopes contain chlorite and minor illite, which are best developed in the biotite-albite-magnetite-illite-chlorite alteration zone (Figs. 5.5c and 5.5d). Wide C veins (>5 mm) have zoned halos that grade out from illite next to the vein through illite-chlorite to background chlorite over distances of 5 mm to 2 cm. In the K-feldspar-illite alteration zone, C veins have illite, rather than illite-chlorite alteration halos.

D veins

These are planar and continuous veins of pyrite, with subordinate quartz, muscovite and chalcopyrite. They typically occur parallel to the orientation of the Rosario Fault System (Fig. 5.3). D veins are less than 1 mm to more than 20 cm wide, and have cut M, A, B and C veins in all alteration zones. Pyrite is the principal infill mineral, with minor chalcopyrite. Euhedral quartz, present in some veins, shows undulose extinction and contains abundant fluid inclusions. D veins have muscovite alteration halos. In the biotite-albite-magnetite-illite-chlorite alteration zone, D vein alteration halos are zoned outward from feldspar-destructive muscovite through muscovite-chlorite to chlorite.

Porphyry-Type Alteration Assemblages

Magnetite alteration

Both magmatic and hydrothermal types of magnetite are recognised (Figs. 5.6a and 5.6b). Magmatic magnetite is disseminated in the volcanic country rock, and characterised by grains with irregular ilmenite exsolution lamellae, high TiO_2 contents (12.3 to 3 wt. %; Appendix 2) and low to intermediate V_2O_3/Al_2O_3 values (0.1 to 1.0; Fig. 5.6c; Appendix 2). Hydrothermal magnetite occurs as disseminations spatially associated with M veinlets. The hydrothermal magnetite has identical TiO_2 contents and V_2O_3/Al_2O_3 to the veinlet magnetite (Fig. 5.6c) and is characterised by

homogeneous grains without exsolution textures. There is no magnetite preserved in the Rosario Porphyry.

Biotite-albite assemblage

The biotite-albite assemblage occurs in coherent and clastic volcanic rocks on the northeast side of the Rosario Porphyry and grades outwards and upwards to the chlorite-epidote alteration assemblage (Fig. 5.3). Biotite-albite altered rocks on the southwest side of the Rosario Porphyry are cut by structurally controlled zones of white mica- and clay-altered rock. Shreddy biotite is spatially associated with secondary albite. Partial replacement of ferromagnesian phenocrysts is typical in volcanic rocks distal from the Rosario Porphyry (Fig. 5.6d). Clots of shreddy biotite, associated with magnetite, are common near the Rosario Porphyry (Fig. 5.6e). Hydrothermal biotite is distinguished compositionally from igneous biotite in the Rosario Porphyry by lower, but variable Ti contents and lower overall Mg numbers (Mg/[Mg + Fe]; Fig. 5.6f; Appendix 2). Both primary and secondary biotite are depleted in iron, with Mg numbers varying between 0.65 and 0.87. The K content of the interlayer site is similar in both hydrothermal and primary biotite, with fluorine in the hydroxyl site varying from 0.4 to 0.7, with the higher values occurring in primary biotite (Appendix 2).

Aggregates of secondary biotite have replaced both primary and secondary magnetite. The biotite is associated with rutile, which may occupy up to 30 vol % of an individual biotite aggregate. Generally, rutile grains occur near, or against grain boundaries of magmatic magnetite (Figs. 5.6a and 5.6b). The degree of rutile abundance appears to reflect the extent of magnetite (magmatic) dissolution by biotite. For example, biotite aggregates in which magmatic magnetite has been preserved have lower rutile contents (Figs. 5.7a and 5.7b), whereas the highest abundances (>20 vol. %) are concentrated in shreddy biotite clots that lack magnetite (Figs. 5.7c and 5.7d). The TiO_2 content of magmatic magnetite varies from 12.3 to 27.3 wt. %, whereas secondary biotite contains 2.7 to 3.4 wt. % TiO_2 (Appendix 2). Biotite replacement of the hydrothermal magnetite lacks rutile.

Figure 5.6.

A) *Sample R990002.* Reflected light photomicrograph of an igneous magnetite grain. Rutile and biotite are present around the grain margins of the magnetite. Note the irregular ilmenite exsolution, characteristic of the primary magnetite. Scale bar = 200 μm.

B) *Sample R990127.* Reflected light photomicrograph of hydrothermal magnetite surrounded by chalcopyrite. Hydrothermal magnetite typically lacks exsolution textures. Scale bar = 100 μm.

C) Magmatic and hydrothermal magnetite compositions from Rosario. The slopes for different V_2O_3/ Al_2O_3 values are also shown. High and low V_2O_3/Al_2O_3 values are inferred to indicate oxidised and reduced conditions, respectively. The diagram allows primary magnetite to be distinguished from hydrothermal magnetite formed at different redox conditions. The titanium content of magnetite is inferred to increase with temperature (Walshe et al., 2003).

D) *Sample R990213.* Plane-polarised light photomicrograph of biotite shreds that have partially replaced a hornblende phenocryst in fine grained andesite. Scale bar = 100 μm.

E) *Sample R990002.* Cross-polarised light photomicrograph of a clot of shreddy biotite interpreted to have completely replaced a primary ferromagnesian mineral. Scale bar = 50 μm.

F) Magnesium number vs. Ti (number of cations) for magmatic and hydrothermal biotite.

Abbreviations: bi = biotite, cp = chalcopyrite, hb = hornblende, mt = magnetite, qtz = quartz, rut = rutile

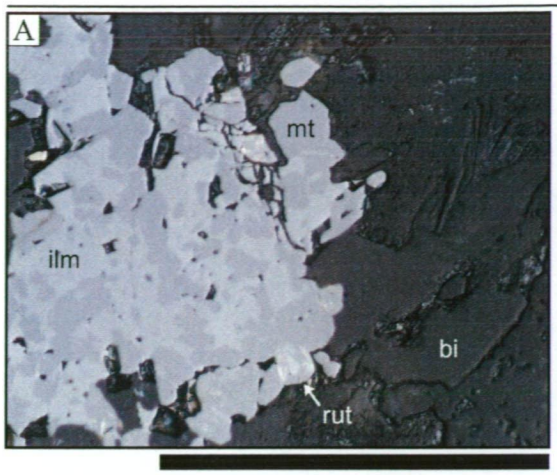

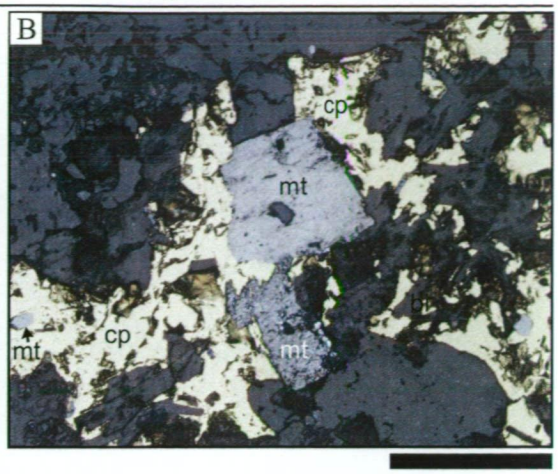

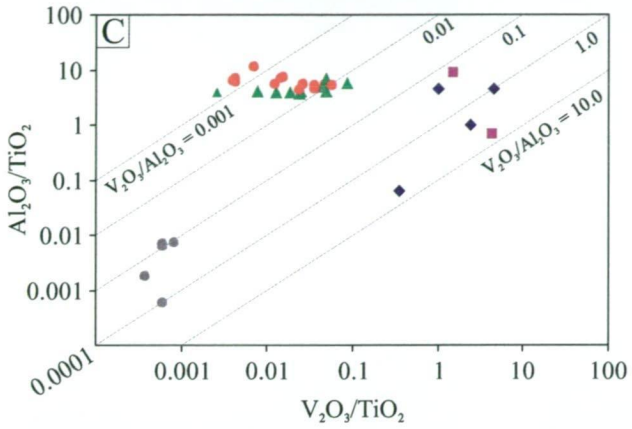

Hydrothermal magnetite
- Disseminated
- Vein

Primary magnetite

Primary biotite

Hydrothermal biotite

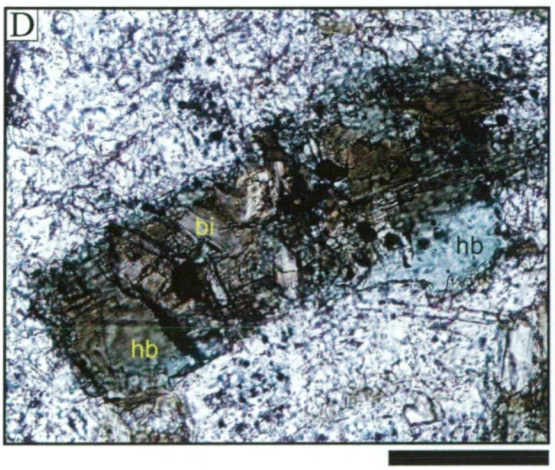

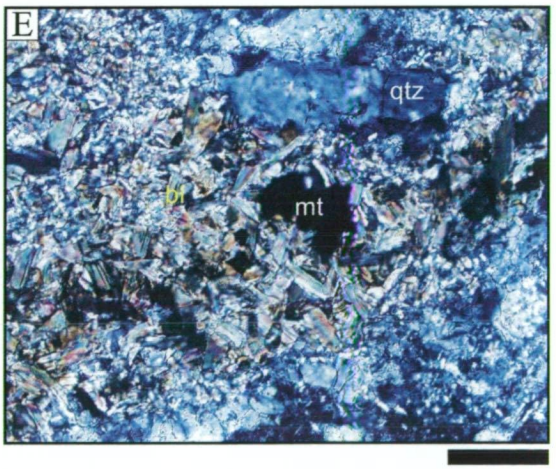

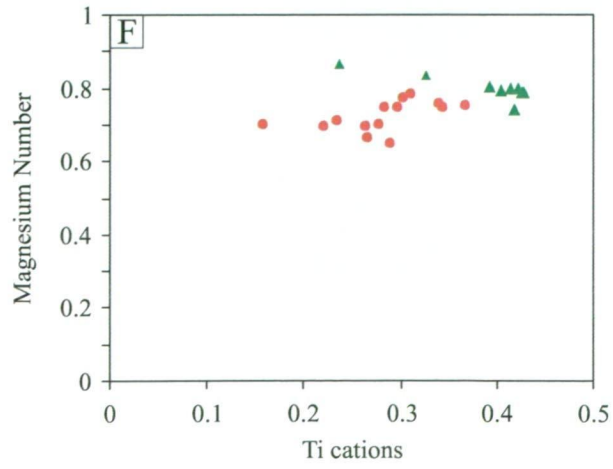

Igneous biotite

Hydrothermal biotite

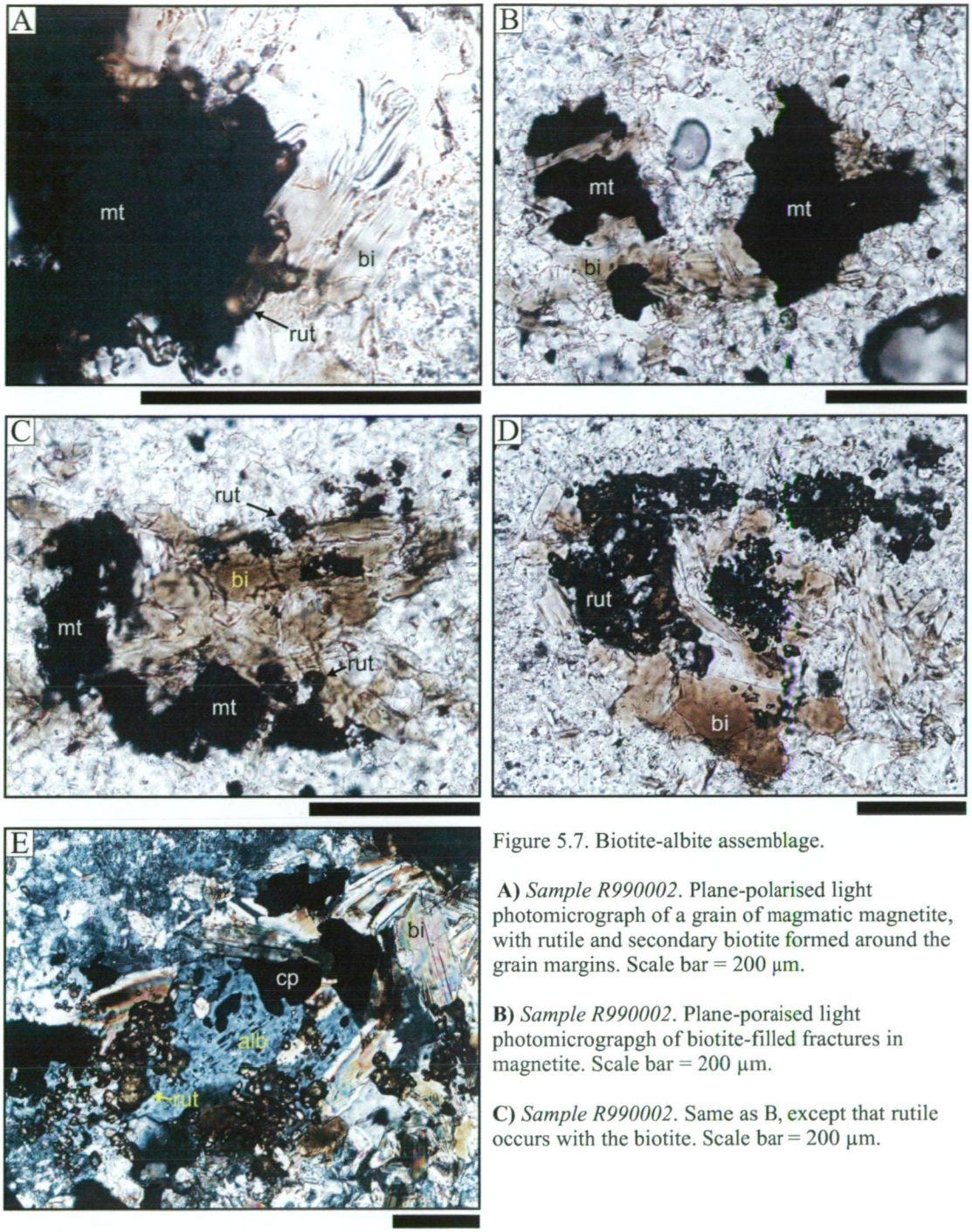

Figure 5.7. Biotite-albite assemblage.

A) *Sample R990002*. Plane-polarised light photomicrograph of a grain of magmatic magnetite, with rutile and secondary biotite formed around the grain margins. Scale bar = 200 μm.

B) *Sample R990002*. Plane-poraised light photomicrograpgh of biotite-filled fractures in magnetite. Scale bar = 200 μm.

C) *Sample R990002*. Same as B, except that rutile occurs with the biotite. Scale bar = 200 μm.

D) *Sample R990002*. Plane-polarised light photomicrograph. Complete replacement of primary magnetite has resulted in aggregates of shreddy biotite and blebby rutile. Scale bar = 200 μm.

E) *Sample R990002*. Cross-polarised light photomicrograpgh of biotite-magnetite-albite altered dacite. Shreddy biotite typically surrounds magnetite or fills embayments that cut into magnetite grains. Rutile is inferred to have been derived from the dissolution of magnetite. Plagioclase phenocrysts have been replaced by albite and/or contain albite inclusions connected to albitised grain margins by small fractures. Some phenocrysts are entirely turbid albite, with no residual calcic plagioclase. Scale bar = 200 μm.

Abbreviations: alb = albite, bi = biotite, cp = chalcopyrite, mt = magnetite, rut = rutile.

Chalcopyrite and pyrite associated with the biotite-albite assemblage occur as individual and composite disseminated grains (1 to 3 vol.%). Chalcopyrite and pyrite have locally replaced magnetite (Fig. 5.6b). Patches of shreddy biotite commonly contain grains of chalcopyrite, pyrite, and/or rutile. Rutile inclusions are also present in some aggregates of pyrite and, less commonly, chalcopyrite. Pyrite and chalcopyrite typically have mutual grain boundaries, which are interpreted to be the product of co-precipitation.

K-feldspar alteration

The K-feldspar alteration assemblage is characterised by K-feldspar with minor secondary albite and shreddy biotite. Subordinate bornite, chalcopyrite, pyrite and rutile are disseminated throughout this zone. Secondary K-feldspar has pervasively altered domains of the Rosario Porphyry intersected by deep drilling. The K-feldspar altered rocks have been cut by advanced argillic and phyllic alteration assemblages on the southwest side of the intrusion (Fig. 5.3). On the northeast side, there is a gradational transition to the zone of biotite-albite-magnetite-illite-chlorite alteration, marked by lower amounts of secondary K-feldspar with increased distance from the Rosario Porphyry.

At the current level of exposure, most of the K-feldspar alteration is selectively pervasive. In the Rosario Porphyry, rims of turbid K-feldspar surround phenocrysts of albite-oligoclase or biotite (Figs.5.8a and 5.8b, respectively), with some of the primary plagioclase completely replaced by K-feldspar. The groundmass comprises K-feldspar (Fig. 5.8c), minor quartz and trace quantities of plagioclase, and is analogous to the K-feldspar groundmass flooding reported from several porphyry copper deposits of the southwest United States (e.g., Titley, 1982). Pervasive K-feldspar alteration was observed in only a few deep exposures at Rosario (below 4,100 m elevation), and is associated with high abundances of A-3 veins. The porphyritic texture in the Rosario Porphyry has been destroyed in these zones. In hand specimen these rocks are pink and aplitic (Fig. 5.8d), whereas in thin section, turbid K-feldspar is fine grained and intergrown with minor quartz.

Figure 5.8. Photographs and photomicrographs of samples from the K-feldspar zone.

A) *Sample R200130.* Cross-polarised light photomicrograph of plagioclase phenocryst in the Rosario porphyry replaced by K-feldspar around the grain margins. Scale bar = 200 μm.

B) *Sample R200130.* Cross-polarised light photomicrograph of biotite phenocrysts in the Rosario Porphyry with perthitic K-feldspar rims. Scale bar = 200 μm.

C) *Sample R200114.* Photograph of an irregular quartz-K-feldspar-bornite-chalcopyrite vein that has cut the Rosario Porphyry. The vein contains anhedral to subhedral quartz and K-feldspar. The groundmass next to the vein has been completely altered to K-feldspar. The cores of feldspar phenocrysts have been replaced by illite. Scale bar = 10 mm.

D) *Sample R990108.* Example of pervasive K-feldspar alteration in the Rosario Porphyry. Note that porphyritic texture has been destroyed in the rock on the right hand side of the sample. This zone corresponds with a high density of A-3 veins. On the left hand side phenocrysts have been enhanced by illite replacement of the feldspar. Scale bar = 2 cm.

E) *Sample R200113.* Reflected light photomicrograph of bornite-chalcopyrite ore from potassic alteration in the Rosario Porphyry. The chalcopyrite occurs as inclusions in bornite. Scale bar = 200 μm.

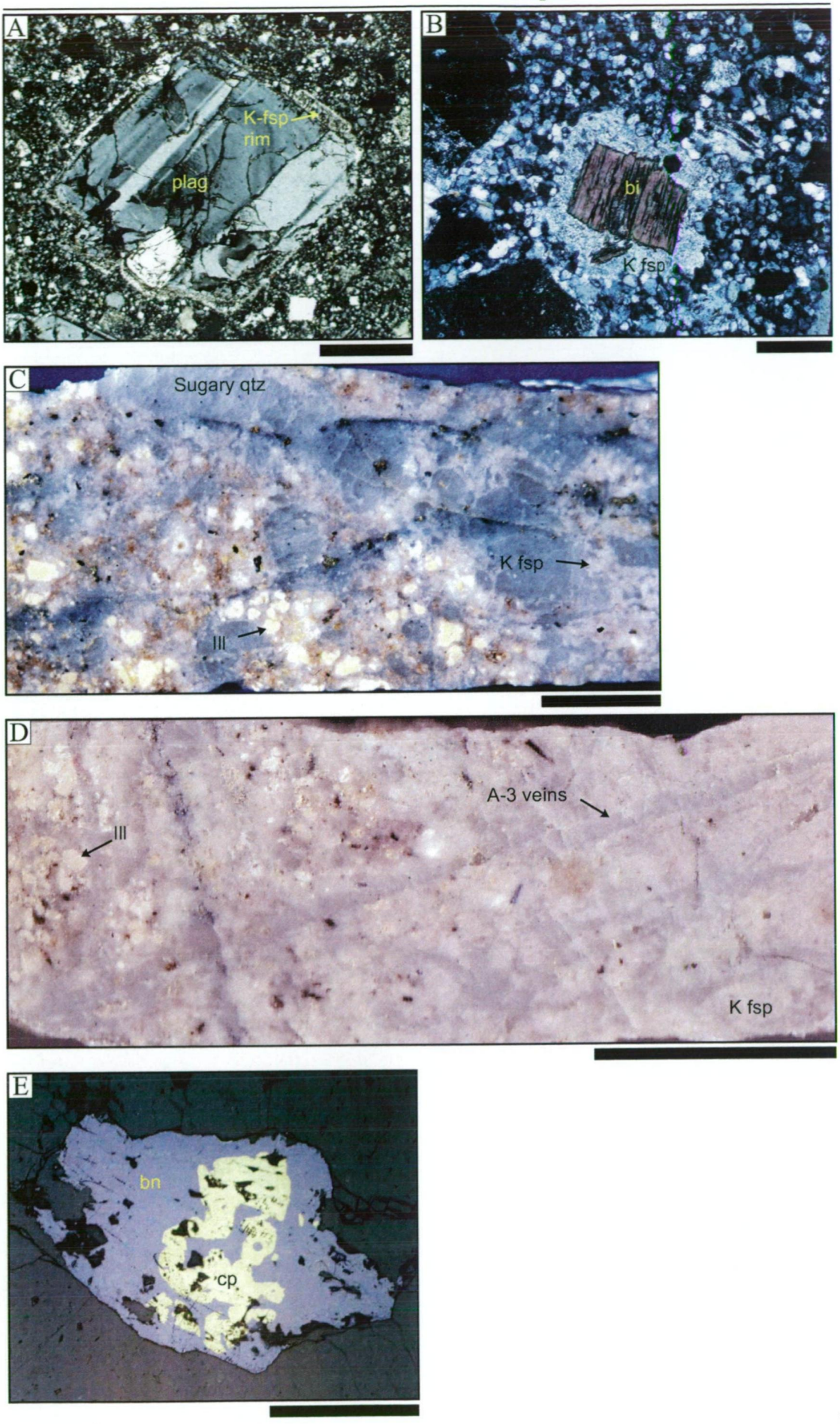
A
K-fsp
rim
plag
B
bi
K fsp
C
Sugary qtz
K fsp
III
D
A-3 veins
III
K fsp
E
bn
cp

Chalcopyrite, bornite and trace pyrite are the main sulfides disseminated within the K-feldspar altered rocks, and constitute 1 to 5 % of the total rock volume. Mutual chalcopyrite-bornite grain boundaries are typically irregular, with chalcopyrite occurring as inclusions in bornite (Fig. 5.8e). However, the reverse relationship is also observed, suggesting either co-precipitation or multiple cycles of bornite and chalcopyrite deposition.

Garnet, epidote, clinopyroxene assemblage

Garnet, epidote, and clinopyroxene, calcite, magnetite and chlorite are the diagnostic minerals in the stratabound zone of calc-silicate alteration northeast of the Rosario Porphyry (Figs. 3.3e and 5.3). Garnet, and subordinate epidote are abundant in zones that contain calcite (Fig. 5.9a). By contrast, thin quartz sandstone bands (1 to 5 cm thick) are interfingered with the domains of garnet and calcite, and contain minor epidote, garnet and clinopyroxene. Garnet grains are typically zoned from andradite in their cores to solid-solution andradite-grossular-almandine-spessartine on the edges. Chemical compositions range from $Alm_3Sp_3Gro_{17}And_{77}$ to $Sp_1Gro_{63}And_{36}$ (Appendix 2). The calc-silicate-altered rocks are cut by veins of quartz-calcite-epidote ± chalcopyrite ± pyrite ± molybdenite (Fig. 3.3e and 5.9b). Prismatic clinopyroxene occurs with or without chlorite in vein envelopes, and is also present in the veins as intergrowths with quartz, calcite and epidote (Figs. 5.8c). The calc-silicate assemblage is interpreted to be skarn based on the definition of Meinert (1992).

Illite-chlorite assemblage

In the Rosario Porphyry, texturally destructive illite alteration has occurred around C veins. It grades out to incipient and selectively pervasive illite altered rock. The illite occurs as fine-grained plates in the cores of primary plagioclase and has replaced biotite phenocrysts around grain margins and along cleavage (Fig. 5.9d). Selectively pervasive illite alteration has enhanced the porphyritic textures in the Rosario (Fig 5.8c) and Collahuasi Porphyries, by whitening the feldspar phenocrysts.

Figure 5.9. Photomicrographs of samples from the zones of garnet-epidote-clinopyroxene and illite-chlorite altered rocks.

A) *Sample R990062.* Plane-polarised light photomicrograph of a calcite-quartz-pyrite-chalcopyrite vein, with an epidote selvage, that has cut wall-rock garnet alteration. Scale bar = 500 μm.

B) *Sample R990046.* Cross-polarised light photomicrograph of flaky molybdenite inclusions in vein quartz, calcite and epidote. Scale bar = 200 μm.

C) *Sample R990046.* Cross-polarised light photomicrograph of a quartz-clinopyroxene-epidote-calcite vein. Scale bar = 200 μm.

D) *Sample R200124.* Cross-polarised light photomicrograph of a biotite phenocryst in the Rosario Porphyry, replaced around the margins and along cleavage by illite. The groundmass surrounding the biotite grain consists of fine-grained perthitic K-feldspar and quartz. Scale bar = 500 μm.

E) *Sample R200064.* Cross-polarised light photomicrograph of biotite, chlorite, illite and rutile in porphyritic dacite. Illite and chlorite have enclosed biotite grains and also occur along biotite cleavage surfaces. Chlorite typically displays shreddy textures, similar to that of secondary biotite, as seen in the bottom left of the diagram. These textural relationships are interpreted as evidence that chlorite replaced hydrothermal biotite Scale bar = 200 μm.

F) *Sample R990134.* Plane-polarised light photomicrograph of chlorite, rutile, and biotite in porphyritic dacite. Intimately intergrown chlorite-biotite shreds are associated with aggregates of fine-grained rutile. Scale = 200 μm.

Abbreviations: alb = albite, bi = biotite, cal = calcite, chl = chlorite, cp = chalcopyrite, cpx = clinopyroxene, ep = epidote, gar = garnet, ill = illite, mo = molybdenite , mt = magnetite, py = pyrite, rut = rutile.

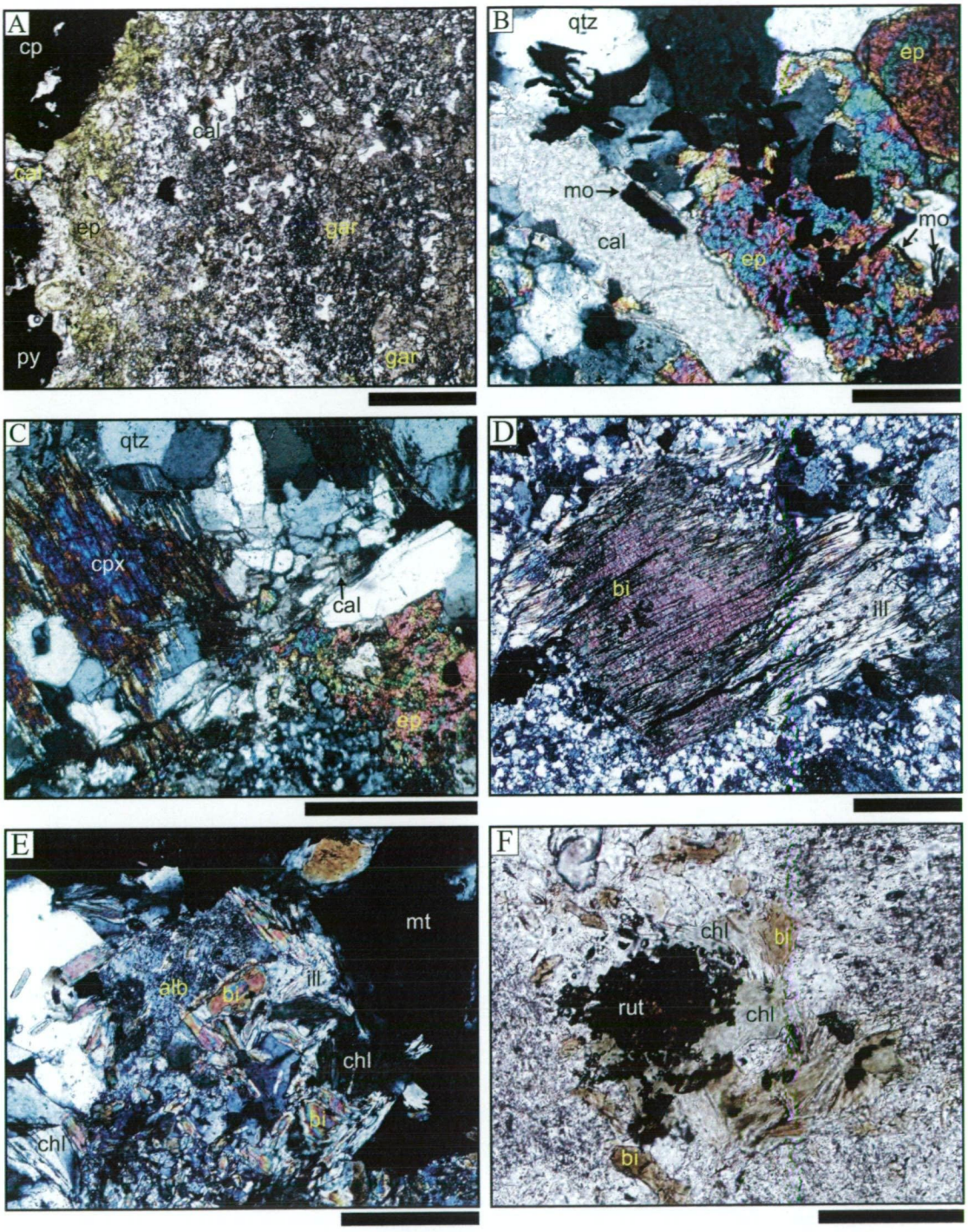
A
cp
cal
cal
ep
gar
py
gar
B
qtz
ep
mo
cal
mo
ep
C
qtz
cpx
cal
ep
D
bi
ill
E
mt
alb
bi
ill
chl
bi
chl
F
chl
bi
rut
chl
bi

C vein alteration envelopes grade out to incipient and selectively pervasive chlorite alteration in the Permo-Triassic host rocks. Chlorite commonly occurs around the edges, and in cleavage of secondary biotite (Figs. 5.9e and 5.9f), and is intimately intergrown with subordinate illite and rutile. Fine grained platy illite domains occur in feldspar phenocrysts that have not been affected by secondary albite or K-feldspar.

Chlorite-epidote assemblage

The assemblage chlorite-epidote dominates the peripheral alteration zone to the Rosario deposit (Fig. 5.3). Chlorite-epidote altered rocks contain minor magnetite, illite and smectite. They surround the zone of biotite-albite-magnetite-illite-chlorite altered rocks (Fig. 5.3), but only occur in direct contact with K-feldspar alteration where both zones are separated by faults (Fig. 5.3). Advanced argillic and phyllic alteration assemblages have cut the chlorite-epidote altered zone along southwest-dipping faults (Fig. 5.3).

Epidote occurs as euhedral prisms in the cores of plagioclase phenocrysts (Fig. 3.3a), and is intergrown with chlorite where it has pseudomorphed ferromagnesian phenocrysts (Fig. 5.10a). In amygdaloidal andesite, there are epidote-quartz-chlorite filled amygdales (Fig. 5.10b) that also contain minor illite and smectite. Where present, illite occurs in contact with chlorite, but mutual grain boundaries with epidote are uncommon (Figs. 5.10c and 5.10d). The rhyodacite that lies directly above and to the side of the Rosario Porphyry (Fig. 3.2) contains pumpellyite along with epidote and chlorite in pseudomorphs of ferromagnesian phenocrysts.

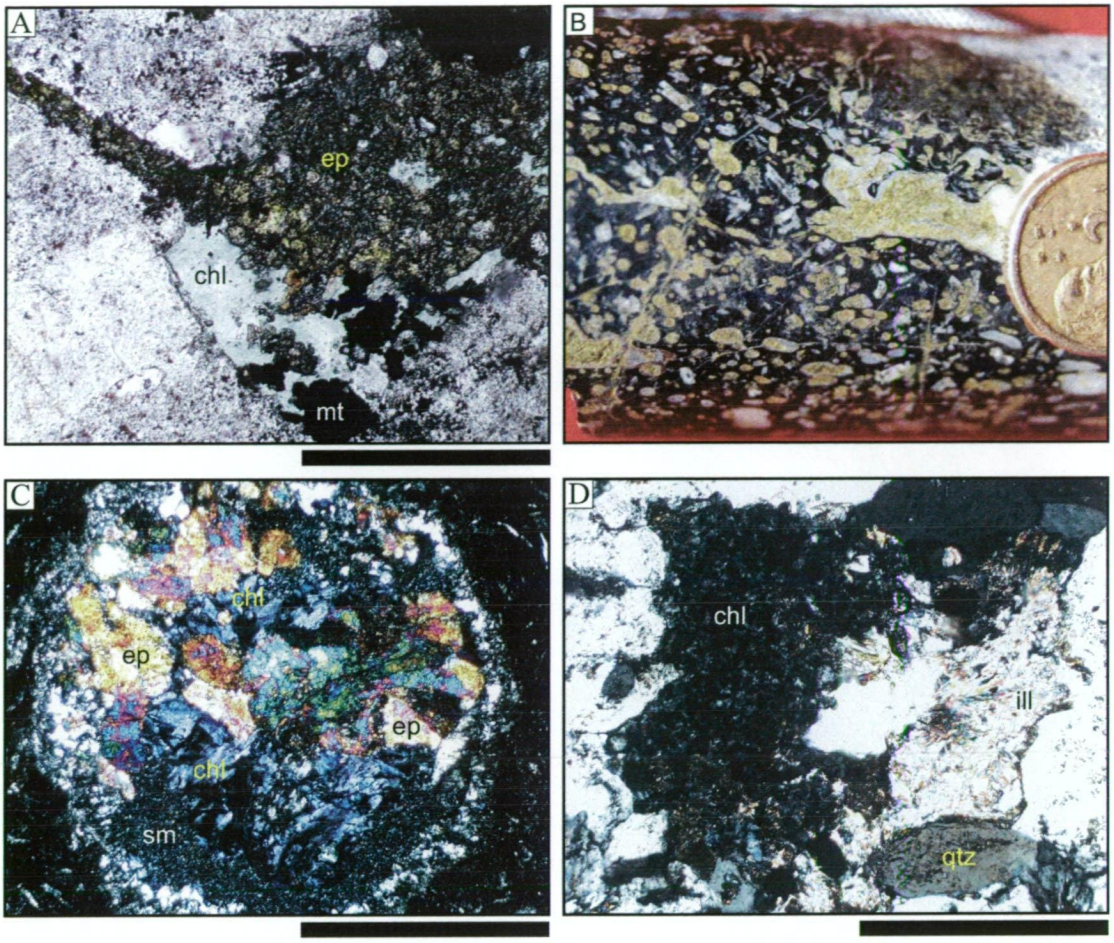

Figure 5.10. Photographs and photomicrographs of samples from the chlorite-epidote zone.

A) *Sample R990217.* Plane-polarised light photomicrograph of fine-grained chlorite and subhedral epidote contained within the shape of an amphibole phenocryst in rhyodacite. Chlorite-epidote replacement of the amphibole is associated with the small veinlet that cuts the phenocryst. Scale bar = 500 μm.

B) *Sample R990319.* Drill core photograph of weakly plagioclase-phyric, amygdaloidal andesite approximately 1 km south of the Rosario Porphyry. Amygdale infill comprises epidote and quartz (80-95 vol. %), subordinate chlorite (5-20 vol. %), and trace illite (<1 vol. %). Diameter of coin = 20 mm.

C) *Sample R990314.* Cross-polarised light photomicrograph of an epidote-quartz-chlorite-filled amygdale in weakly feldspar-phyric andesite. Scale bar = 500 μm.

D) *Sample R990314.* Cross-polarised light photomicrograph of tabular chlorite crystals intergrown with subhedral to euhedral quartz and platy illite aggregates in weakly plagioclase-phyric andesite.

Polymetallic Sulfide Veins

Polymetallic massive sulfide (E) veins have cut all other veins, except for some D veins at Rosario. The widest E veins (0.5 to 5 m) occur in strands of the Rosario Fault System (Fig. 5.3). Smaller veins (0.5 to 10 cm) are concentrated near the faults, but decrease in abundance away from these zones. The main sulfides in E veins are pyrite, chalcopyrite, bornite, chalcocite, tennantite and enargite (Fig. 5.11a). Gangue minerals, which constitute up to 20 vol. % of veins, include quartz, alunite, diaspore and zunyite $\{Al_{13}Si_5O_{20}(OH,F)_{18}Cl\}$ ± andalusite, barite and pyrophyllite. Vein alunite, which occurs as euhedral blades, contains anhedral inclusions of diaspore and APS minerals (Fig. 5.11b).

E veins: pyrite-chalcopyrite-bornite-chalcocite infill

Figure 5.2 summarises the temporal sequence of sulfide deposition in E veins. The various sulfide mineral assemblages are illustrated in Figures 5.11c to 5.11g. At Rosario, both clast and cement-supported vein breccia, characterised by angular, monomict pyrite clasts, have been cemented by chalcopyrite (Fig. 5.11c). These breccias are interpreted to have formed by tectonic fracturing, related to multiple reactivation of the Rosario Fault System. In some veins, specular hematite is associated with chalcopyrite (Fig. 5.11d).

Bornite has partly to entirely replaced chalcopyrite cement in E vein breccias (Fig. 3.11e), and embayed and infilled fractures in pyrite. Figure 5.11f shows a more advanced stage of chalcopyrite dissolution, where bornite in the breccia cement is interconnected and has enclosed residual pyrite grains, with or without rims of chalcopyrite. In places, the bornite has cut across the chalcopyrite rim and into the pyrite. This cross-cutting relationship suggests that bornite and pyrite are not an equilibrium assemblage (cf. Lee, 1994). Veinlets of chalcocite have cut chalcopyrite and bornite. Lamellar chalcocite replacement of bornite has resulted in ragged and irregular grain boundaries (Fig. 5.11g).

Figure 5.11. Photomicrographs of sulfide paragenesis and alteration mineral assemblages in E-veins (A, and C to G = reflected light; C and H = cross-polarised light).

A) *Sample R990230.* Pyrite, tennantite, bornite, and chalcopyrite in an E-vein from Rosario. Scale bar = 500 μm.

B) *Sample R990170.* APS mineral inclusion contained within tabular alunite. Composition of the APS mineral is svanbergite. Scale bar = 200 μm.

C) *Sample R200026 (Rosario).* Fragmented pyrite cemented by chalcopyrite. Scale bar = 500 μm.

D) *Sample R200008 (Rosario).* Specular hematite, chalcopyrite and sphalerite cement in disaggregated pyrite. Hematite and chalcopyrite have mutual contacts, and neither mineral contains inclusions of the other. By contrast, sphalerite contains inclusions of both hematite and chalcopyrite. Scale bar = 200 μm.

E) *Sample R200015 (Rosario).* Disaggregated pyrite clast with chalcopyrite infill, enveloped by bornite. Re-entrants in the chalcopyrite, above the pyrite clast, have been filled by bornite. These textures are interpreted as partial bornite replacement of chalcopyrite. Scale bar = 500 μm.

F) *Sample R200002 (Rosario).* Pyrite fragments surrounded by chalcopyrite in bornite cement. Scale bar = 200 μm.

G) *Sample R200023.* Lamellar chalcocite replacement of bornite. Scale bar = 100 μm.

H) *Sample R990211.* Tabular andalusite coexists with barite in the selvage of a chalcopyrite-bornite-pyrite E-vein. Platy muscovite is present in the alteration envelope. Scale bar = 200 μm.

Abbreviations: and = andalusite, alun = alunite, APS = aluminium-phosphate-sulfate minerals, bar = barite, bn = bornite, cc = chalcocite, cp = chalcopyrite, hm = specular hematite, mu = muscovite, prl = pyrophyllite, py = pyrite, qtz = quartz, sl = sphalerite.

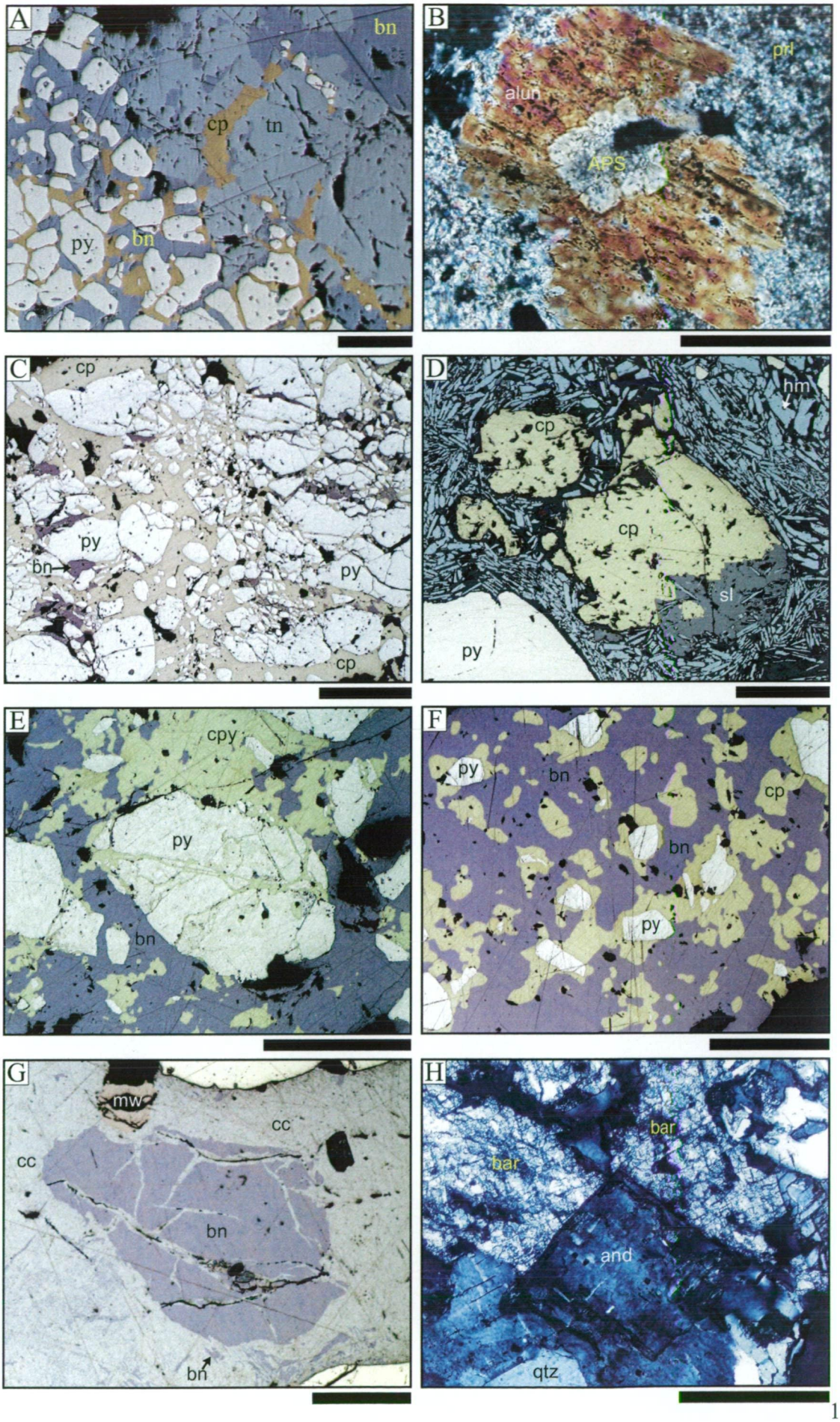
A
bn
cp
tn
py
bn
B
prl
alun
APS
C
cp
py
bn
py
cp
D
hm
cp
cp
sl
py
E
cpy
py
bn
F
py
bn
cp
bn
py
G
mw
cc
cc
bn
bn
H
bar
bar
and
qtz

The infill mineralogy of E veins varies with proximity to the main massive sulfide veins. Near the faults, thick (> 10cm) E veins comprise pyrite, bornite and chalcopyrite, with only minor quartz-alunite-diaspore gangue. Beyond the faults, in the deepest exposures of the deposit (below 4,000 m elevation), thin E veins (<2 cm) have sulfide compositions identical to the massive veins, but contain more euhedral quartz, as well as andalusite and barite (Fig. 5.11h). In shallow exposures (>4,300 m elevation), E veins contain major euhedral quartz, minor chalcopyrite and pyrite, but lack andalusite and barite.

E veins have cut or reopened most of the other vein stages at Rosario, although their relationship to D veins is ambiguous. Pyrite, recognised as the earliest sulfide mineral in E veins, is inferred to be the same generation as pyrite in D veins. However, E veins are locally cut by D veins, suggesting multiple cycles of E- and D vein formation.

Tennantite-enargite stage (TES)

Tennantite and enargite occur generally as replacement of pyrite, bornite, chalcopyrite, and chalcocite in E veins (Figs. 5.12a and 3.12b). Minor Sn-bearing sulfides, including mawsonite $\{Cu_6Fe_2SnS_8\}$, colusite $\{Cu_3(As,Sn,V,Fe)S_4\}$ and vinciennite $\{Cu_{10}Fe_4SnAsS_{16}\}$, have also cut bornite, chalcocite and chalcopyrite (Fig. 5.12c), and appear to have formed contemporaneously with tennantite and enargite. Micro-fractures (<50 μm wide) that have cut bornite-chalcopyrite cement in some E veins are lined with a selvage of djurleite $\{Cu_{1.9}S\}$ and digenite (Cu_9S_5; Fig. 5.12c). Djurleite-digenite micro-veins generally terminate against domains of tennantite, mawsonite and colusite (Fig. 5.12d).

Sphalerite cementation of angular sulfide fragments has occurred in clast-supported vein microbreccia (Fig. 5.12e). This is interpreted to be the last stage of sulfide precipitation at Rosario. Sulfide clasts in microbreccia range from 10 μm to less than 1 μm in diameter, and appear to have been milled. Sphalerite has filled fractures in mawsonite and tennantite (Fig. 5.12f), and occurs in the centre lines of re-opened djurleite-digenite veinlets (Fig. 5.12g). The sphalerite precipitated in open spaces that were created by either hydraulic and/or tectonic brecciation of the earlier vein sulfides, presumably during reactivation of the Rosario Fault System.

Figure 5.12. Reflected light photomicrographs of cross-cutting sulfide relationships in enargite-tennantite bearing E-veins at Rosario.

A) *Sample R990237.* Partial tennantite-mawsonite replacement of bornite and chalcopyrite. Scale = 100 μm.

B) *Sample R200023.* A large enargite crystal has cut grain boundaries in pyrite, chalcocite and bornite. Scale = 100 μm.

C) *Sample R990237.* Colusite inclusion in mawsonite within the bornite-chalcopyrite cement of an E-vein. Note that micro-fractures lack djurleite-digenite where they have penetrated the mawsonite and colusite. Scale = 100 μm.

D) *Sample R990237.* Djurleite-digenite-bearing micro-fractures have cut bornite and chalcopyrite, but terminate against tennantite. The fractures were re-opened after formation of djurleite-digenite, and then penetrated tennantite. Scale = 200 μm.

E) *Sample R990237.* Sphalerite-cemented micro breccia. The earlier formed sulfides occurs as breccia clasts. Scale = 100 μm.

F) *Sample R990237.* Sphalerite-filled micro-fractures in mawsonite. The sphalerite has also overgrown djurleite and digenite in microfractures outside of the mawsonite. The lack of djurleite-digenite in the mawsonite indicates that the djurleite-digenite formed before mawsonite. Sphalerite formation succeeded that of mawsonite and was deposited in the re-opened micro-fractures. Scale = 100 μm.

Abbreviations: bn = bornite, cc = chalcocite, col = colusite, cp = chalcopyrite, dg = digenite, dj = djurleite, en = enargite, mw = mawsonite, py = pyrite, sp = sphalerite, tn = tennantite.

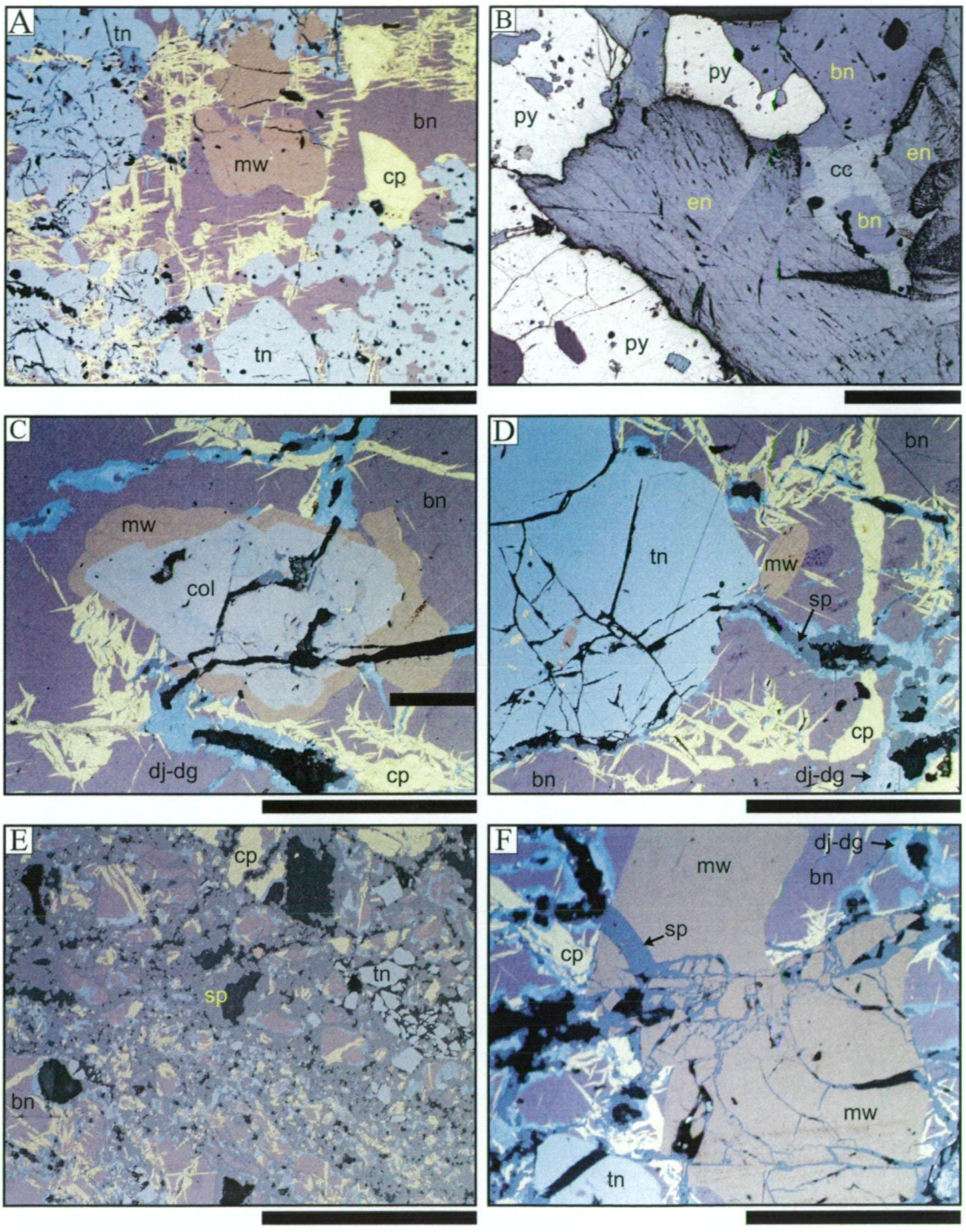
A
tn
bn
mw
cp
tn
B
py
bn
py
en
cc
en
bn
py
C
bn
mw
col
dj-dg
cp
D
bn
tn
mw
sp
cp
bn
dj-dg
E
cp
tn
sp
bn
F
dj-dg
mw
bn
sp
cp
mw
tn

Late-Stage Alteration Assemblages

Quartz-alunite-pyrite assemblage

Alteration of wall rocks next to E veins has produced mineral assemblages identical to the vein gangue mineralogy (Fig. 5.2). These altered zones comprise fine to medium grained-subhedral or microcrystalline quartz, intergrown with subhedral bladed alunite, diaspore, and zunyite ± pyrophyllite (Fig. 3.13a). The extent of this assemblage in the wall rock could not be fully delineated, as it has been extensively overprinted by pyrophyllite and muscovite associated with tennantite-enargite veins.

Small kernels of massive bladed alunite, minor pyrite and euhedral quartz occur within the quartz-alunite-diaspore altered rocks (Fig. 3.13b). Where observed in contact, the euhedral pyrite and alunite have mutual grain boundaries suggesting that they coprecipitated. The euhedral alunite has K_2O and Na_2O contents of 7.0 to 9.0 wt. % and 1.5 to 2.4 wt. %, respectively (Appendix 2). Pseudocubic aluminium-phosphate-sulfate (APS) minerals occur locally in the cores of euhedral alunite, commonly in perfect optical continuity (Fig.5.11b). Svanbergite $\{SrAl_3(PO_4)(SO_4)(OH)_6\}$ is the most common APS mineral based on microprobe results (Appendix 2). It also occurs in solid solution with woodhouseite $\{CaAl_3(PO_4)(SO_4)(OH)_6\}$.

Pyrophyllite-dickite alteration

Fault-controlled pyrophyllite-dickite constitutes the bulk of the advanced argillic alteration assemblage shown in Figure 5.3. This alteration assemblage is related spatially to the TES veins, and has overprinted the quartz-alunite-diaspore-zunyite alteration assemblage. Pyrophyllite-dickite alteration zones are typically 5 to 80m wide and have cut all other alteration assemblages, except the calc-silicate altered rocks. A muscovite-quartz alteration assemblage surrounds the pyrophyllite-dickite zone. The muscovite-quartz altered zone is typically wider than the pyrophyllite-dickite zone (but < 100 m) and passes out to a mixed kaolinite-illite-smectite alteration assemblage (Fig. 5.3). Transitions from one alteration assemblage to another are typically gradational over several metres.

Figure 5.13. Photomicrographs of early and late-stage advanced argillic alteration at Rosario (A to D and H = cross-polarised light; .E to F = reflected light; G = plane-polarised light).

A) *Sample R990170.* An example of the Collahuasi Porphyry overprinted by pervasive quartz-diaspore-alunite-± pyrophyllite-zunyite. The isotropic crystal with cubic habit is zunyite. Scale bar = 200 μm.

B) *Sample R990188.* Tabular alunite crystals intergrown with euhedral quartz and pyrite. Scale bar = 200 μm.

C) *Sample R990170.* Veinlet of pyrophyllite has cut tabular alunite. Scale = 200 μm.

D) *Sample R990170.* Extensive replacement of alunite by pyrophyllite. Scale = 200 μm.

E) *Sample R200024.* Zunyite-filled fracture in bornite-chalcopyrite cement of a pyrite vein breccia. Scale = 200 μm.

F) *Sample R200024.* Zunyite within the bornite-chalcopyrite cement has cut pyrite grain boundaries. The zunyite is interpreted to have replaced the bornite and chalcopyrite. Scale = 50 μm.

G) *Sample R200024.* Zunyite coexists with pyrophyllite and APS minerals in veinlets that have cut pyrite. Scale = 100 μm.

H) *Sample R200107.* Zoned APS mineral within massive pyrophyllite. The compositional zones correspond with different birefringence colours. End member compositions of each zone are either svanbergite and woodhouseite. Scale = 50 μm.

Abbreviations: alun = alunite, APS = aluminium-phosphate-sulfate minerals, bn = bornite, cp = chalcopyrite, dias = diaspore, prl = pyrophyllite, py = pyrite, qtz = quartz, sv = svanbergite, wh = woodhouseite, zun = zunyite.

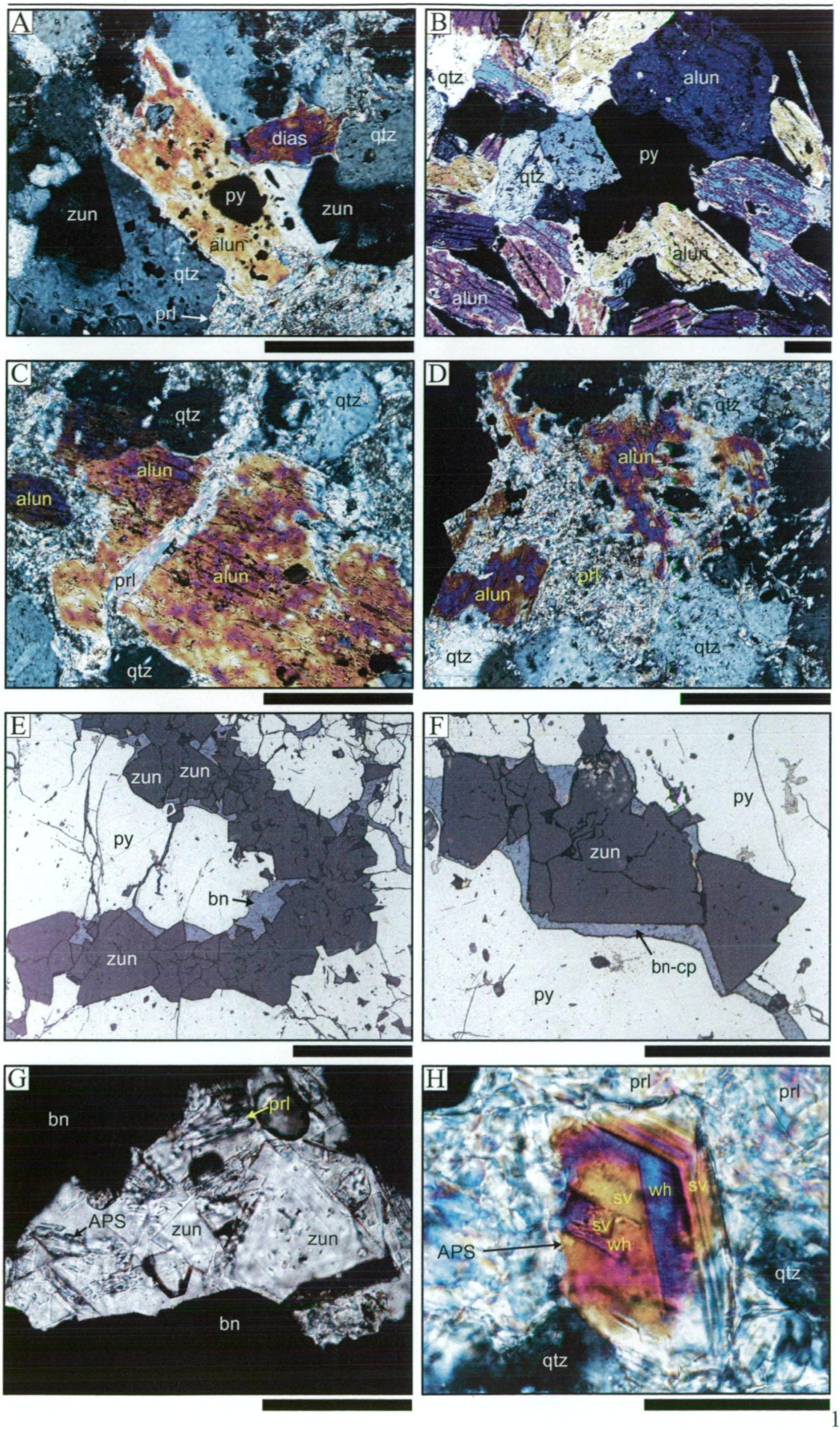
A
dias
qtz
py
zun
zun
alun
qtz
prl
B
qtz
alun
py
qtz
alun
alun
C
qtz
qtz
alun
alun
prl
alun
qtz
D
qtz
alun
prl
alun
qtz
qtz
E
zun
zun
py
bn
zun
F
py
zun
bn-cp
py
G
bn
prl
APS
zun
zun
bn
H
prl
prl
sv
wh
sv
sv
wh
APS
qtz
qtz

Pyrophyllite has pervasively altered rocks near the faults. It has a platy habit in veinlets, and occurs as masses that have overprinted the early quartz-alunite diaspore assemblage in the wall rocks. Figure 5.13c shows pyrophyllite plates in a veinlet that has cut tabular alunite, as well as subhedral grains of quartz. Partial replacement of tabular alunite by pyrophyllite is shown in Figure 5.13d, with quartz grains also cut by veinlets of pyrophyllite. These features indicate that pyrophyllite is paragenetically later than the quartz-alunite-diaspore-zunyite assemblage and associated E veins.

In some E veins, cubic zunyite, associated with pyrophyllite (Fig 5.13e and 5.13f), occurs as veinlets that have cut sulfide domains in E veins. Zunyite has overgrown bornite-chalcopyrite and cemented fractured pyrite clasts (Fig. 5.13f). Euhedral zunyite has also penetrated the pyrite grain boundaries, indicating that it is late relative to the quartz-alunite-pyrite-diaspore assemblage. Minor pyrophyllite and APS minerals are intergrown with the zunyite (Fig. 5.13g). In places, massive pyrophyllite, associated with pyrite disseminations and veinlets, contains small pseudocubic APS inclusions. Most of the APS inclusions are svanbergite, but some inclusions exhibit oscillatory zoning with compositions that vary between svanbergite and woodhousite (Fig. 5.13h).

Muscovite alteration

E veins that occur in rocks outside the pyrophyllite zone have been overprinted by muscovite-quartz alteration. Muscovite blades have partially replaced bornite, chalcopyrite and chalcocite, cutting into the sulfide grain boundaries (Fig. 5.14a). More extensive replacement has resulted in relict atolls of bornite-chalcopyrite, as well as isolated grains of residual pyrite, with or without bornite-chalcopyrite rims (Fig. 5.14b). In places, coarse muscovite blades occur within veinlets that have disrupted the sulfides (Figs. 5.14c and 5.14d) and that have also cut the diaspore and quartz gangue. Figure 5.14e shows a tabular diaspore grain, cut by a veinlet of muscovite, which terminates as radiating blades in bornite. The irregular and ragged contact of muscovite against bornite implies that muscovite corroded the embayment in bornite. A trail of rutile grains, present along the contact between the muscovite and diaspore, is interpreted to mark the position of the original bornite grain boundary, before dissolution by muscovite (Fig. 5.14e).

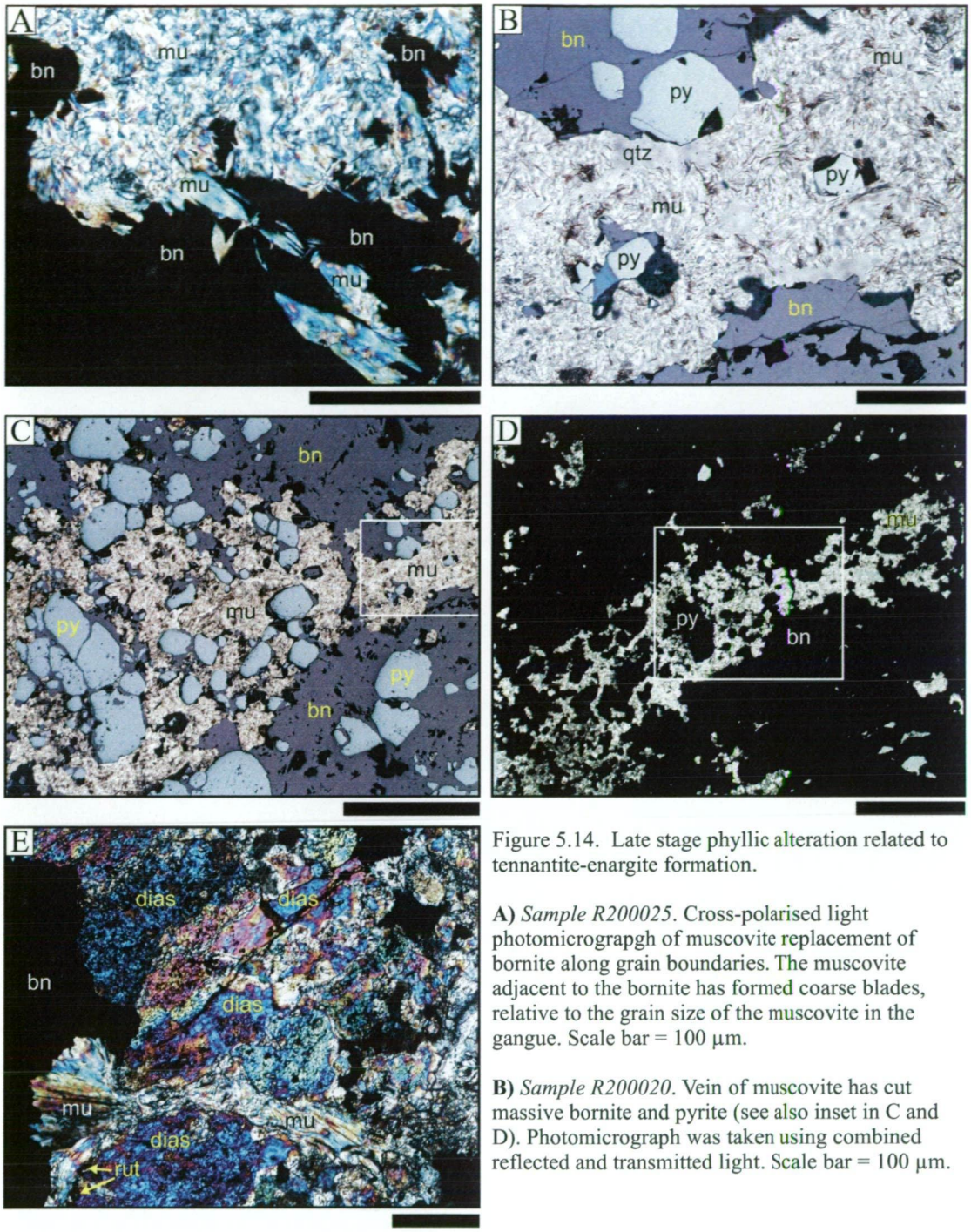

Figure 5.14. Late stage phyllic alteration related to tennantite-enargite formation.

A) *Sample R200025.* Cross-polarised light photomicrograpgh of muscovite replacement of bornite along grain boundaries. The muscovite adjacent to the bornite has formed coarse blades, relative to the grain size of the muscovite in the gangue. Scale bar = 100 μm.

B) *Sample R200020.* Vein of muscovite has cut massive bornite and pyrite (see also inset in C and D). Photomicrograph was taken using combined reflected and transmitted light. Scale bar = 100 μm.

C) *Sample R200020.* Less extensive replacement in the vein has resulted in relict atolls of bornite in the muscovite (see also inset in D). Photomicrograph was taken using combined reflected and transmitted light. Scale bar = 500 μm.

D) *Sample R200020.* Larger scale perspective of the muscovite veinlet in B and C that has cut massive bornite-pyrite-chalcopyrite. Photomicrograph taken under cross-polarised light. Scale bar = 1000 μm.

E) *Sample R200023.* Diaspore coexists with quartz next to veins of bornite (opaque). The diaspore in the bottom-centre of the photomicrograph has been cut by a veinlet of muscovite that terminates in the bornite. The muscovite has cut the bornite grain boundary, indicating that muscovite is younger than bornite and diaspore. Photomicrograph taken under cross-polarised light. Scale bar = 100 μm.

Abbreviations: bn = bornite, dias = diaspore, mu = muscovite, py = pyrite, qtz = quartz.

Some E veins have been cut by veins of euhedral quartz (Fig. 5.15). The edges of the veins consist of isolated, euhedral grains of quartz within a cement of bornite-chalcopyrite-chalcocite. The central part of the veins contain coarse grained euhedral quartz. The quartz is intergrown with coarse radiating blades of muscovite, and has enclosed pyrite, rare bornite and chalcopyrite. Veins of euhedral quartz are surrounded by envelopes of muscovite that have replaced bornite and chalcopyrite (Fig. 5.15a). Figures 5.15b and 15c show textural evidence for the replacement of bornite by muscovite. The spatial distribution of euhedral quartz and muscovite indicates that this assemblage formed late (synchronous with enargite and tennantite), and has overprinted the bornite-chalcocite cement in E veins. Muscovite alteration of the wall rock is characterised by partial to complete platy muscovite replacement of phenocryst and groundmass feldspar. This alteration has typically enhanced the porphyritic texture of the host intrusions by whitening the feldspar phenocrysts. Biotite phenocrysts are completely pseudomorphed by coarse-grained muscovite, accompanied by blebby aggregates of rutile.

Kaolinite, and illite-smectite alteration

A clay-bearing alteration assemblage comprising kaolinite and smectite surrounds the zone of muscovite-quartz alteration. Illite is typically dusted through feldspar as fine-grained platy inclusions. In zones of intense clay alteration, feldspars have been completely replaced by kaolinite, but the rock texture has been preserved. Some rocks contain primary and secondary biotite replaced by a brown pleochroic, amorphous mineral. PIMA spectra have confirmed the presence of mixed montmorillonite-illite compositions in these rocks, implying that this amorphous substance may be smectite.

Figure 5.15. *Sample R200025.* Vein of euhedral quartz that has cut massive bornite-pyrite-chalcopyrite.

A) The walls of the vein are annotated in yellow. Thin slivers of bornite that occur within the vein are inferred to have been torn from the selvage during crack-seal precipitation of quartz. An envelope of muscovite ± quartz alteration surrounds the vein, and has partially replaced the massive bornite-chalcopyrite. The fragmented pyrite appears to be unaffected by the muscovite and quartz alteration. The insets in B and C show the quartz infill and muscovite alteration either side of the vein wall. The photomicrograph was taken using combined reflected and transmitted light

B) This inset highlights the extensive fine grained muscovite on the left hand side of vein wall (position annotated in yellow). Bornite grain margins are highly irregular with sharp boundaries against blades of muscovite, which is dispersed throughout the bornite. Photomicrograph taken under cross-polarised light.

C) The muscovite against the boundaries of massive bornite is coarse grained relative to the surrounding muscovite. Euhedral quartz in the vein contains abundant inclusions of bornite. These features imply that that euhedral quartz and muscovite formed after the massive bornite-pyrite-chalcopyrite. Photomicrograph taken under cross-polarised light.

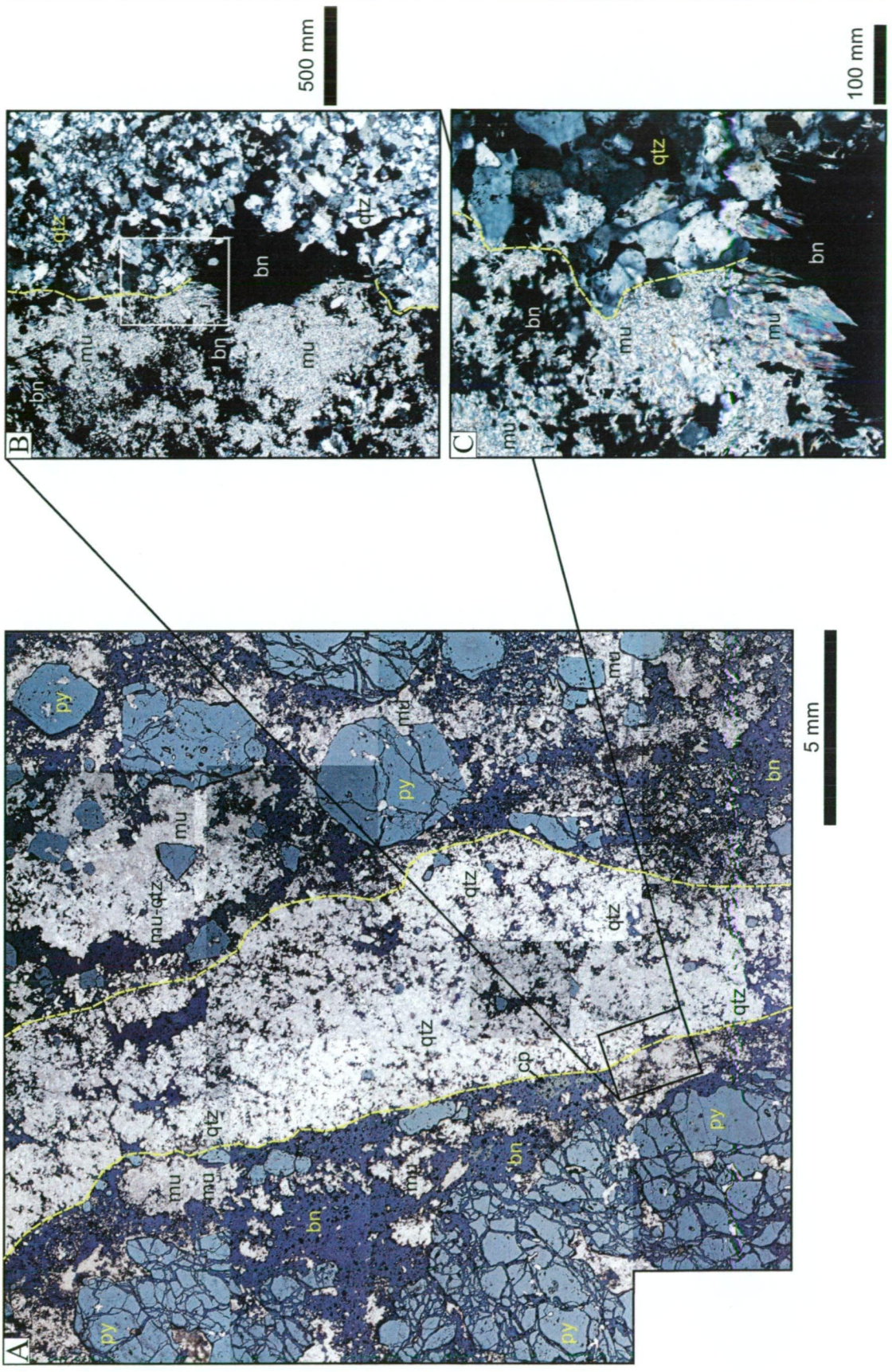
A
B
C
500 mm
100 mm
5 mm
py
mu
mu-qtz
qtz
cp
bn

The La Grande Veins

Subvertical massive sulfide veins have formed in tilted volcanic rocks of the Collahuasi Formation at La Grande (Fig. 5.16), 1.5 km southwest of Rosario. Amygdaloidal andesite interbedded with crystal-sandstone at the bottom of the sequence, is overlain by porphyritic andesite, megacrystic andesite and porphyritic dacite. Hydrothermal alteration of the wall rocks occurs as subvertical halos to the veins. Alteration is zoned outwards from inner pyrophyllite-dickite-quartz-diaspore-alunite (± APS minerals)-zunyite altered rocks out through muscovite and illite-smectite assemblages to outer propylitic alteration of the volcanic rocks. The maximum width of the alteration envelope is 50 m.

Vein Form and Sulfide Paragenesis

E veins at La Grande are 0.5 to 15 m wide, with smaller veins (1 to 20 cm wide) typically restricted to pyrophyllite envelopes (<20 m wide) around the major veins. Enargite, pyrite, chalcocite, and bornite are the main sulfides (Fig. 5.17a), with subordinate colusite and mawsonite. The main La Grande vein lacks gangue, but the small veins contain up to 50 vol. % quartz, dickite, zunyite, pyrophyllite, and minor APS minerals, with or without alunite.

The sequence of vein mineralisation at La Grande is essentially the same as that at Rosario (Fig. 5.2), in which brecciated pyrite is cemented by bornite, with lamellar chalcocite replacement of the bornite. Enargite constitutes the bulk of the sulfide assemblage and has overprinted all other copper-bearing sulfides (Fig. 5.17a). Colusite and mawsonite appear to have formed contemporaneously with enargite. Tennantite, djurleite-digenite and sphalerite have not been observed in the La Grande vein, in contrast to the Rosario veins (Fig. 5.2). Pyrite breccia veins, cemented by chalcocite, contain up to 50 vol. % euhedral quartz. Quartz crystals have been overgrown by pyrite and then replaced by chalcocite (Fig. 5.17b).

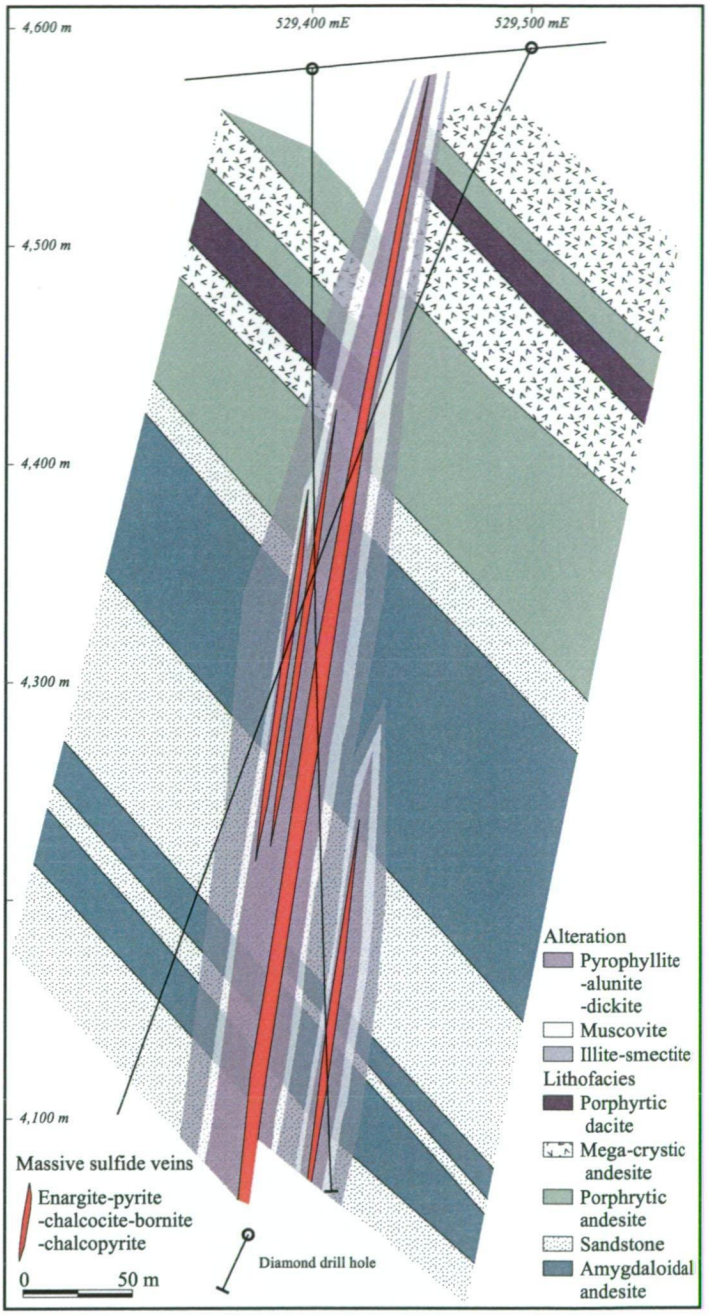

Figure 5.16. East-west cross-section through the La Grande veins. The subvertical veins cut coherent volcanic rocks, interbedded with thick (10-50 m) sedimentary units. The rocks dip 40° to the northeast. Amygdaloidal andesite interbedded with crystal-sandstone at the bottom of the sequence, are overlain by porphyritic and mega-crystic andesite, and porphyritic dacite. Hydrothermal alteration of the wall rocks is typically restricted to a zone, 25 m wide, either side of the veins, but reaches 50 m in the amygdaloidal andesite. Alteration zoning is characterised by pyrophyllite-alunite-dickite next to the vein, surrounded by muscovite that grades out to an illite-smectite fringe. The volcanic rocks are altered to epidote-chlorite beyond the zone of illite-smectite alteration. Vein minerals are pyrite, enargite, chalcocite, and bornite. The vein has a maximum thickness of 15 m, and averages 30 wt. % Cu, 70 g/t Ag and 0.8 g/t Au.

Quartz-diaspore-alunite assemblage

In deep exposures of the La Grande deposit, thin pyrite-chalcocite ± bornite breccia veins (1 – 30 cm wide) contain quartz-diaspore-alunite ± pyrophyllite gangue. Wall rock alteration next to these veins is dominated by medium to fine grained quartz and microcrystalline quartz. Subhedral alunite and diaspore are intimately intergrown in the altered wall rock (Fig. 5.17c). Fine grained pyrophyllite is abundant and occurs with quartz. Pyrophyllite is interpreted to have formed later than the quartz-diaspore assemblage, based on overprinting relationships (see below). The quartz-diaspore ± pyrophyllite altered wall rock (Fig. 5.17d) contains small disseminations of pyrite, cemented by chalcocite ± bornite. The euhedral quartz and diaspore do not contain sulfide inclusions, suggesting that they were precipitated prior to or contemporaneous with the sulfides.

Dickite-pyrophyllite assemblage

A dickite-pyrophyllite alteration assemblage occurs in zones, 2-10 m wide, that surround the massive sulfide veins (Fig. 5.16). Zunyite, APS minerals and alunite form a minor part of the assemblage. Transitions between the dickite-pyrophyllite and quartz-diaspore-alunite altered rock are typically sharp, but locally gradational. Small veins of dickite, pyrophyllite and zunyite have cut the early quartz-diaspore-alunite assemblage (Figs. 5.17e and 5.17f), and also cut large chalcocite-cemented pyrite breccia veins. In the pyrite-chalcocite veins, euhedral quartz gangue has been replaced around grain margins by dickite (Fig. 5.17b). These dickite replacement rims have truncated the chalcocite-filled fractures within the pyrite, indicating that dickite formed after the chalcocite and euhedral quartz.

In vein selvages, dickite has completely pseudomorphed vein quartz and has an abrupt contact with the zone of fine-grained pyrophyllite alteration (Fig. 5.17g). Beyond the veins, the transition from dickite pseudomorphs to quartz preservation occurs over a distance of 2 mm. In this zone, pyrophyllite is more abundant than dickite and coexists with euhedral quartz in the outer alteration envelope. APS inclusions occur in the dickite selvages of sulfide veins, as well as in the dickite pseudomorphs after quartz (Figs. 5.17h). The APS inclusions comprise woodhouseite and minor svanbergite, with solid solution minerals of both end member compositions common. Between 0.5 and 2.6 wt % Ba, and trace amounts (<1.0 wt. %) of K and Na are also present in the APS minerals (Appendix 2).

Figure 5.17. Advanced argillic assemblages associated with the La Grande massive sulfide vein.

A) *Sample R990293.* Reflected light photomicrograph of E-vein massive sulfides in the La Grande Vein. Enargite coexists with pyrite, chalcocite and bornite. Scale bar = 200 μm.

B) *Sample R990311.* Combined reflected and transmitted light photomicrograph of euhedral quartz and pyrite. The pyrite has been cut by chalcocite-filled veinlets. Chalcocite has also overgrown quartz. Platy dickite occurs around the margins of the euhedral quartz against the pyrite and truncates the veinlets of chalcocite. Scale bar = 200 μm.

C) *Sample R990312.* Cross-polarised light photomicrograph of quartz-alunite diaspore alteration. The irregular diaspore boundaries suggest partial dissolution after formation. Scale bar = 100 μm.

D) *Sample R990299.* Cross-polarised light photomicrograph of pervasive advanced argillic wall-rock alteration at La Grande. Quartz and diaspore coexist with pyrophyllite, but elsewhere the pyrophyllite has replaced quartz and diaspore. These features indicate that the pyrophyllite formed late and is not in equilibrium with the quartz and diaspore. Scale bar = 200 μm.

E) *Sample R990311.* Plane polarised light photomicrograph of a vein of dickite, zunyite and pyrophyllite veinlet that cuts pervasive fine grained quartz. Some pyrophyllite occurs with the quartz, which interpreted to reflect alteration associated with the cross-cutting vein. Not the abundance of cubic zunyite. Scale bar = 500 μm.

F) *Sample R990311.* Same as E, but photographed under cross-polarised light. Scale bar = 500 μm.

G) *Sample R900311.* Cross-polarised light photomicrograph. A sharp transition from dickite to pyrophyllite alteration, zoned outward from a sulfide vein. The dickite has pseudomorphed quartz in the selvage of the sulfide vein, as well euhedral quartz that was present in the wall rock. Small APS inclusions occur within the pseudomorphous dickite. The quartz is stable in the outer zone of pyrophyllite, which has enveloped the dickite. Scale bar = 1000 μm.

H) *Sample R990311.* Cross-polarised light photomicrograph of woodhouseite ± svanbergite (APS) inclusions in dickite, where it has pseudomorphed the euhedral quartz. Scale bar = 200 μm.

Abbreviations: alun = alunite, APS = aluminium-phosphate-sulfate minerals, bn = bornite, cc = chalcocite, dias = diaspore, dick = dickite, prl = pyrophyllite, py = pyrite, zun = zunyite.

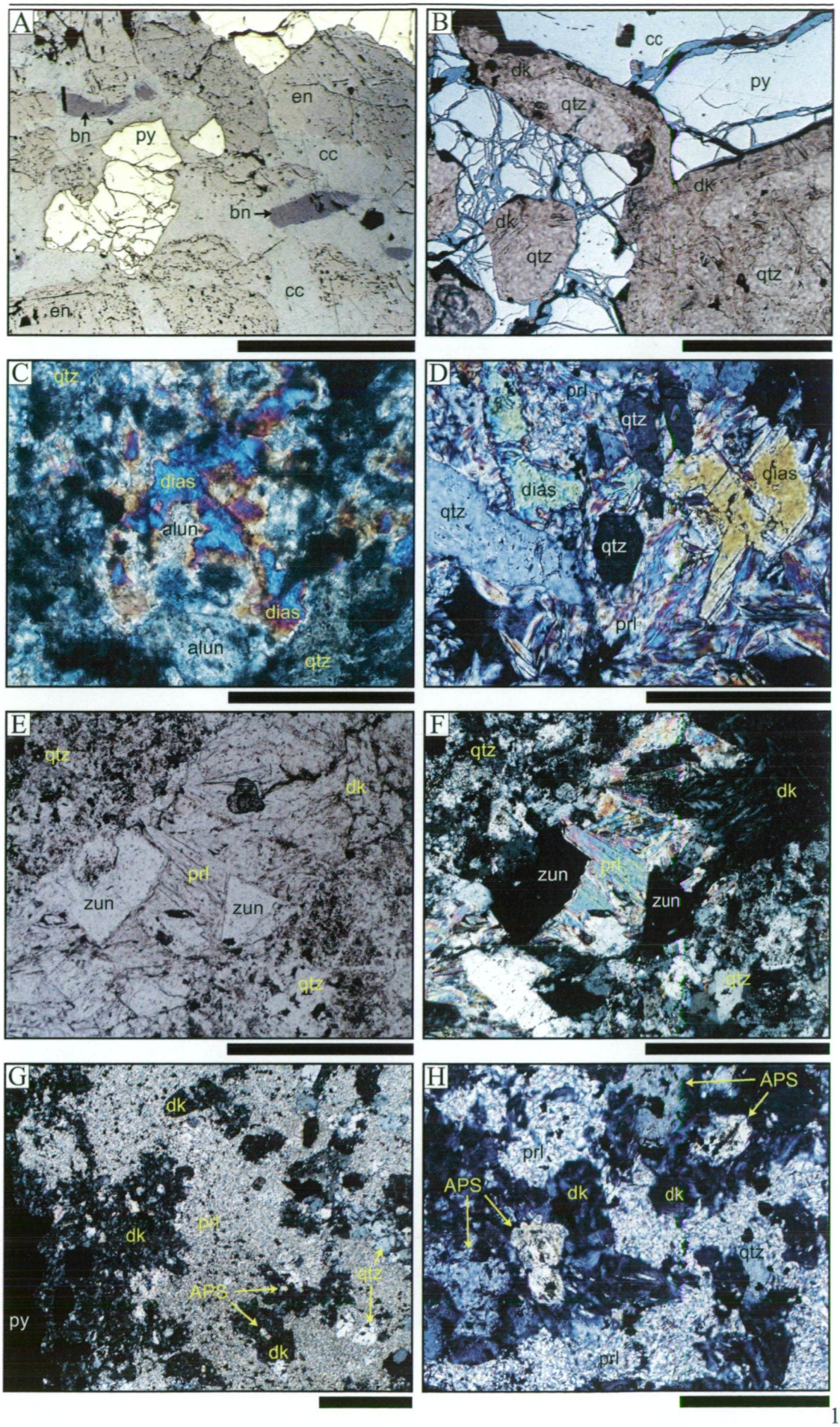
A
en
bn
py
cc
bn
cc
en
B
cc
dk
py
qtz
dk
dk
qtz
qtz
C
qtz
dias
alun
dias
alun
qtz
D
prl
qtz
dias
dias
qtz
qtz
prl
E
qtz
dk
prl
zun
zun
qtz
F
qtz
dk
zun
prl
zun
qtz
G
dk
dk
prl
qtz
APS
py
dk
H
APS
prl
APS
dk
dk
qtz
prl

Direct contact relationships between enargite-tennantite and pyrophyllite-dickite have not been observed at La Grande. Despite the lack of definitive textural evidence, it is inferred that both assemblages are temporally and spatially related. This is based on observations of similar Cu-As sulfide and alteration mineral occurrences at Rosario, where direct contact relationships between these assemblages have been interpreted as evidence that they formed contemporaneously.

Ore Mineral Distribution and Grade Correlation

Ore minerals at Rosario are zoned upward and outward from a bornite-dominant core, through chalcopyrite, to a pyrite-rich fringe (Fig. 5.18a). The distribution of copper grades highlights the structural controls on high-grade Cu (>1.5 wt. % Cu) in the core of the deposit (Fig. 5.18b). The transition between chalcopyrite- and pyrite-dominant zones, corresponds with the outer edge of the 0.6-1.0% Cu zone. The bornite core and chalcopyrite fringe are focused on the Rosario Porphyry, whereas the pyrite-rich zone flanks the margins of the intrusion (Fig. 5.18a).

Grades that exceed 1.0% Cu are spatially associated with the Rosario Porphyry (Fig. 5.18b). In three dimensions, the shape of the ore body defines an asymmetric, inverted trough, in which the axis has been tilted to the southwest. Molybdenum is closely associated with the distribution of B veins. The outer extent of the B veins surrounds the top and sides of the Rosario Porphyry, and corresponds with the 0.01 wt. % Mo and 0.6 wt. % Cu contours (Figs. 5.18a and 5.18b). The highest Mo values (>0.02 wt. % Mo) occur within the Rosario Porphyry (Fig. 5.18b), and overlap with the chalcopyrite ± bornite zone.

Although difficult to quantify, there appears to have been two main stages of copper formation at Rosario. The first stage corresponds with the development of the A veins, during which significant copper was introduced (Fig. 5.2). In particular, the deposition of bornite-rich A-3 veins deep within the deposit has resulted in high tenor copper ore zones. The second major stage of copper ore formation is related to the bornite- and chalcopyrite-rich E veins (Fig. 5.2). According to Dick et al. (1994), approximately 10 wt. % of the Rosario copper resource is contained within the thick, fault-controlled E veins. Their estimate does not include the small E veins that are concentrated near the faults, and that are also abundant distal from the major structures. The contribution to the copper budget by E veins is considered to more significant than that estimated by Dick et al. (1994), and may have been up to 30 to 40

wt. % of the total resource. Additional copper was contributed by late-stage tennantite and enargite-bearing veins, but this was minor, relative to the A and E stage veins.

Most of the ore at Rosario is hypogene, with only 5% of the mining reserve classified as supergene ore (Collahuasi Prefeasibility Study, 1993). A weakly mineralised copper-oxide blanket occurs across the Rosario fault system and in the footwall to depths of 100 m (Fig. 5.18b). Copper grades in the blanket are generally 1% or less, and the main ore minerals are chrysocolla and copper wad. Mixed oxide and secondary sulfide ore is localised to depths of 400 m in various segments of the Rosario fault system. Supergene grades in the faults average 1 to 2% Cu. The main secondary sulfide mineral is chalcocite, which occurs predominantly as a sooty coating of pyrite.

Massive sulfide veins

Rosario: Bornite-pyrite-chalcopyrite-tennantite-enargite (E) veins are most abundant between elevations of 4,350 m and 4,000 m. Below this interval, E veins lack tennantite and enargite. Between, 4,350 m and 4,300 m elevation, the veins contain abundant pyrite, with subordinate bornite and chalcopyrite. Secondary sulfide and oxide minerals, including chalcocite, covellite, pyrite, hematite, and chrysocolla are abundant above 4,300 m. In a detailed study of sulfide distribution in the Rosario massive sulfide veins, Lee (1994) documented an upward zoned pattern of deep-level bornite-pyrite, intermediate pyrite-chalcopyrite-bornite and shallow pyrite-chalcopyrite. This zonation is consistent with observations made in the present study, although the pyrite- and chalcopyrite-rich veins are not restricted to the shallow levels. They have been noted also in some deep exposures (below 4,200 m elevation) of the deposit (Figs. 5.18a and 5.18b).

La Grande: Sulfide minerals in the La Grande veins are zoned from deep pyrite-chalcocite ± bornite-chalcopyrite (4,100 m to 3,900 m elevation) to shallow pyrite-enargite-chalcocite-bornite (4,400 m to 4,200 m elevation). One diamond drill hole, GC198, intersected obliquely an interval of 144 m grading 10% Cu, including 43 m of massive sulfides in the main La Grande vein @ 30% Cu and 70 g/t Ag. True thickness of the mineralised intervals were 50 m and 15 m, respectively. Gold is abundant in the massive sulfide vein with 37 m @ 0.8 g/t Au. Arsenic concentrations, although not available, are inferred to be high, as the vein contains between 20% and 90% enargite.

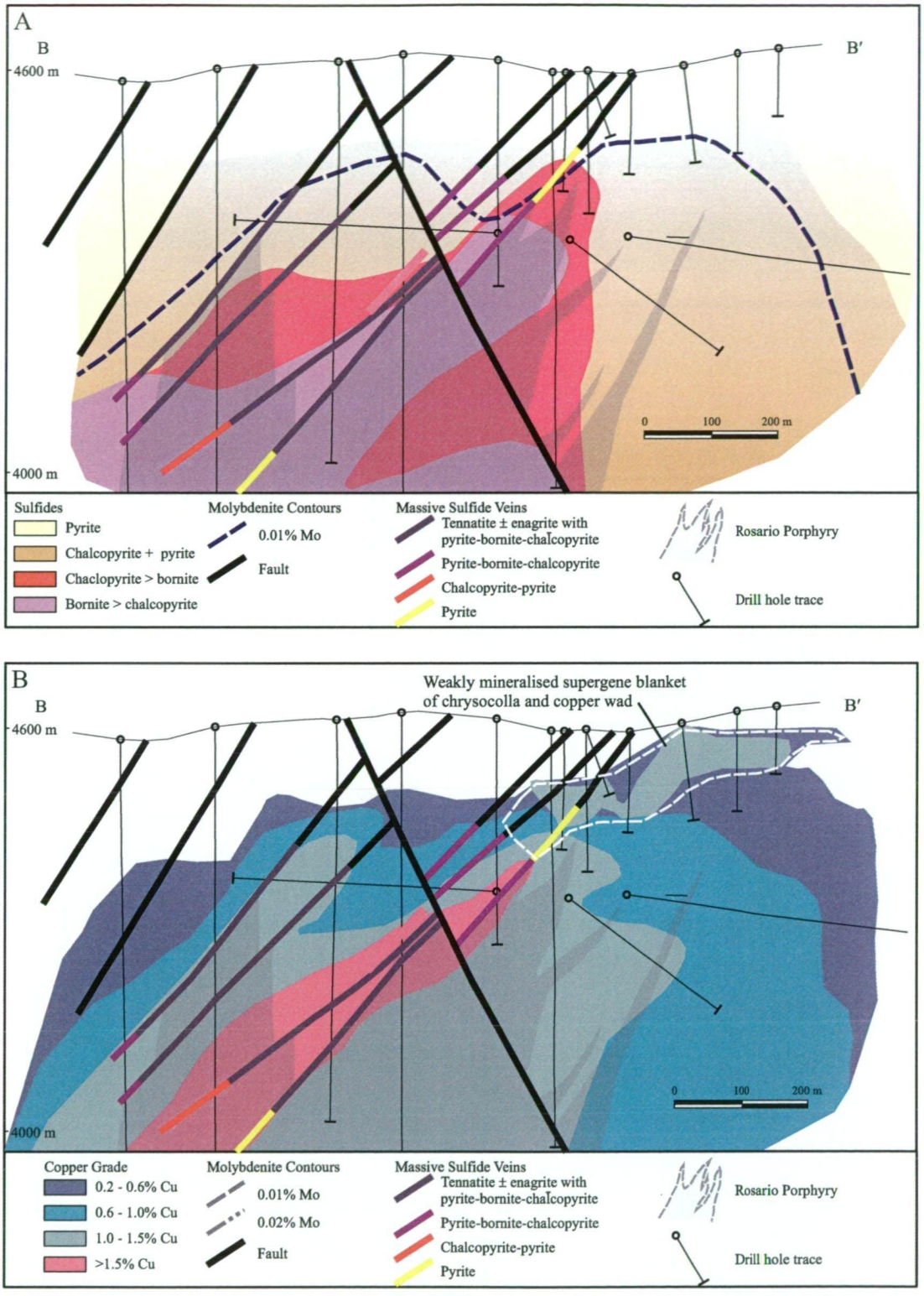

Figure 5.18. Sulfide and metal zoning on section 20 NE at Rosario (see Figs. 3.1 and 3.2 for section locality).

A) Distribution of the bornite-chalcopyrite, chalcopyrite-bornite, chalcopyrite-pyrite, and pyrite-chalcopyrite zones, relative to the Rosario Porphyry (heavy dashed grey line). The outer extent of molybdenum, defined as the 0.01 % Mo contour is shown together with the main massive sulfide veins.

B) Copper and molybdenite grades with respect to the Rosario Porphyry, and main massive sulfide veins. Supergene copper zone from Collahuasi Prefeasibility Study (1993).

District scale metal zonation

The precious and base metal sulfide mineral assemblages within E veins are zoned at the district scale between Rosario and Cerro La Grande (Fig. 5.19). Historically, major veins on Cerro La Grande, 2-3 km south of Rosario, were mined for Cu and Au. Samples of veins in the historical Don Eduardo, Forastera and Anita workings returned Ag:Au values of 25:1, 22:1 and 5:1, respectively (Platt, 1988). By comparison, the Poderosa veins located 500 m south east of Rosario, were mined predominantly for Cu and Ag, and have Ag:Au values of 65:1 (Munchmeyer et al., 1984). This contrasts with silver to gold ratios in the La Grande vein, 1 km southwest of Rosario (Fig. 5.19), which are an order of magnitude higher at 100:1.

Cu-As (TES) sulfides are zoned from enargite in the Cerro La Grande veins to tennantite ± enargite at Rosario (Fig. 5.19). Sphalerite is present in E veins at Rosario, but not in veins at Cerro La Grande. Overall, precious metals and Cu-As sulfides are zoned from Au-bearing enargite veins, lacking Zn at Cerro La Grande to Ag-rich tennantite veins with Zn at Rosario. However, the correlation of sulfosalts and precious metal zonation is not uniform. In the La Grande vein (between Rosario and Cerro La Grande), enargite-rich massive sulfides have grades of 1 g/t Au, and high Ag:Au values (100:1). It appears that whereas enargite is potentially an indicator for Au in the Collahuasi district, it does not always guarantee the presence of Au. It is also associated with abundant Ag locally.

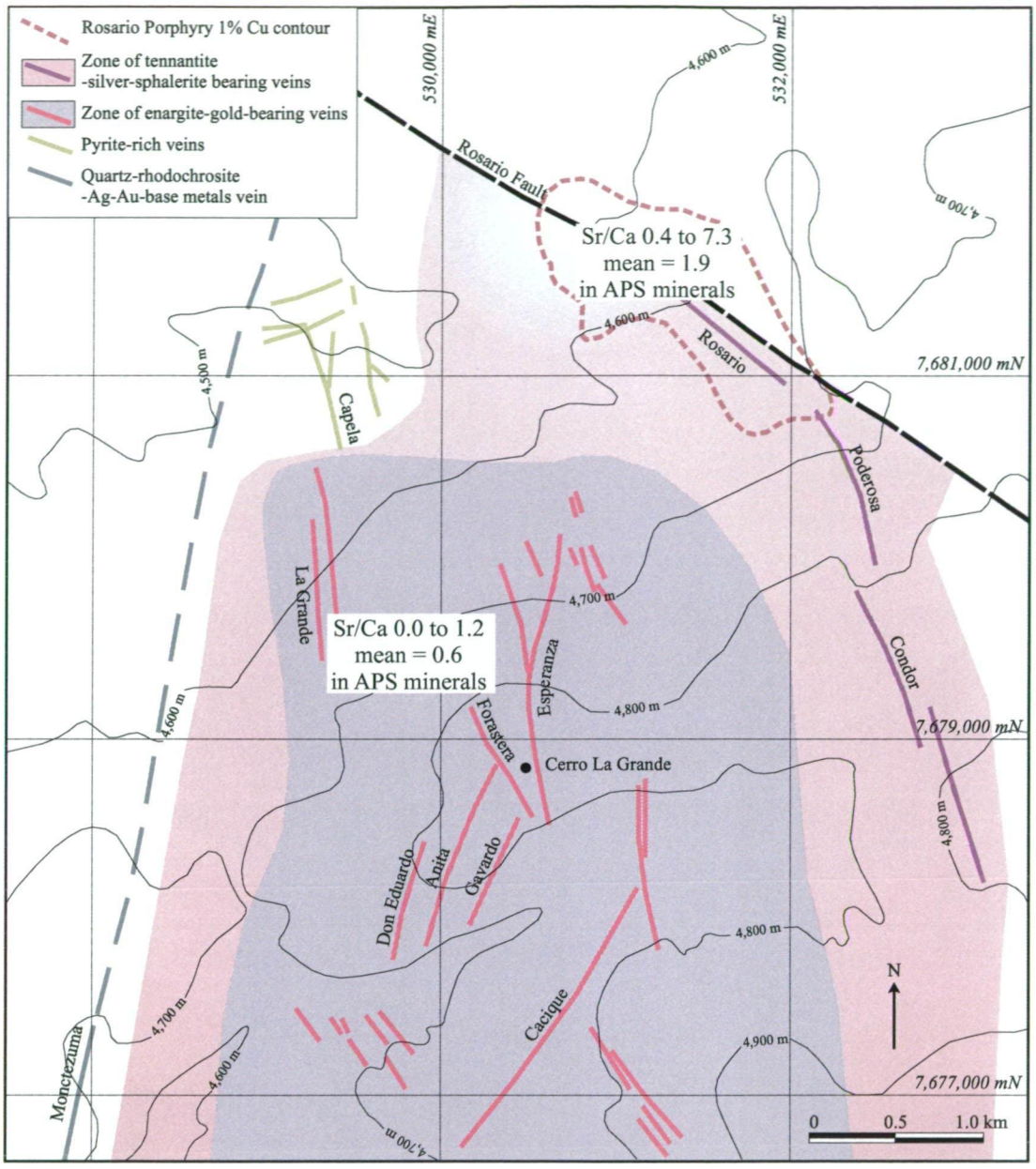

Figure 5.19. Plan view of the major veins in the Rosario - Cerro La Grande area. Coloured zones highlight the distribution of base and precious metals. Enargite-bearing veins with low Ag:Au occur at Cerro La Grande. Tennantite-veins, with high Ag:Au occur in the north and east at Rosario/Poderosa and Condor, respectively. Sr/Ca values of APS minerals (determined by electron microprobe analysis; data in Appendix 2) in the advanced argillic altered rocks at Rosario and La Grande are also shown. The La Grande and Rosario veins are both exposed between 4600 and 4100 m a.s.l., with some of the Rosario veins open down dip below 4,100 m. Veins on Cerro La Grande crop out at 4,800 m a.s.l. The deepest exposures occur in the Don Eduardo and Forastera veins, which have been worked from surface to elevations of 4,610 and 4,530 m, respectively (190-350 m below surface).

Discussion

Time-Space Evolution

The nine main equilibrium assemblages at Rosario are classified here as iron-oxide, sodic-potassic, potassic, calc-silicate, propylitic, intermediate argillic, advanced argillic, phyllic, and argillic alteration assemblages (Fig. 5.2). These assemblages and their overprinting relationships define the chemical evolution of the hydrothermal system in space and time.

Secondary magnetite is characteristic of the oldest equilibrium assemblage (iron-oxide), which formed before final solidification of the Rosario Porphyry (Fig. 5.2). The sodic-potassic and skarn equilibrium assemblages are spatially and temporally associated with emplacement and crystallisation of the porphyry intrusion (Fig. 5.2), but potassic alteration has cut the stock and overprinted the sodic-potassic assemblage. Intermediate argillic alteration, zoned from illite-rich in the core of the Rosario Porphyry to chlorite-illite in the surrounding country rock, has overprinted the potassic and sodic-potassic equilibrium assemblages. Advanced argillic alteration, restricted to low angle faults, formed contemporaneously with the phyllic and argillic equilibrium assemblages (Fig. 5.2). The advanced argillic, phyllic and argillic equilibrium alteration assemblages, recognised in the La Grande vein, are interpreted to have formed at the same time as those assemblages at Rosario.

Late stage alteration and vein paragenesis at Rosario; correlated with La Grande

There is a similar sulfide paragenesis in the E veins at Rosario and La Grande (Fig. 5.2) Early hydraulic pyrite vein breccia has been cemented by chalcopyrite. Bornite subsequently replaced chalcopyrite and pyrite, but was in turn cut by chalcocite. At Rosario, the chalcocite stage is correlated with djurleite-digenite micro-veinlets. Djurleite and digenite were not observed in the La Grande veins. Tennantite with minor enargite and tetrahedrite (TES), overprinted chalcocite and the other early sulfides at Rosario. At La Grande, enargite is the principal sulfosalt and it has cut early pyrite, chalcopyrite, bornite and chalcocite. Mawsonite and colusite co-precipitated with tennantite at Rosario and accompanied enargite deposition at La Grande. Sphalerite is the last sulfide precipitated at Rosario, but does not occur in the La Grande Vein.

The Sr/Ca values of APS minerals in the late advanced argillic assemblage at Rosario (0.38 to 7.32; mean = 1.86) are higher than in the La Grande vein (0.02 to1.23; mean = 0.55; Fig. 5.19). Zoned Sr/Ca values have also been described at La Mejicana and Nevados del Famatina in Argentina (Losada-Calderón, 1992), Summitville, Colorado (Stoffregen, 1987; Stoffregen and Alpers, 1987), and at La Escondida in Chile (Stoffregen and Alpers, 1987). In these deposits, the lowest Sr/Ca values were encountered in APS minerals proximal to intrusive bodies, whereas the ratio increased with elevation or distance from the intrusions. Zoning of Sr/Ca values at Rosario and La Grande is not systematic relative to the Rosario Porphyry, but is consistent with a buried intrusive body beneath the La Grande Veins (Fig. 5.19).

Alteration rank

Temperature stability ranges of hydrothermal minerals common in epithermal systems have been deduced from empirical studies of active geothermal systems (e.g., Reyes, 1990) and by experimental modelling (e.g., Hemley et al., 1980; Fig. 5.20). The temperature variation of the hydrothermal fluids can be estimated using zones of mineral assemblages and thus can provide a useful guide of the paleoisotherms in fossil epithermal systems.

Experimental studies indicate that alunite, diaspore and APS minerals coexist at temperatures between 250° and 320°C (Fig. 5.20). However if andalusite is present, the stability range of this assemblage is 260° to 400°C (Hemley et al., 1980; Watanabe and Hedenquist, 2001). Dickite and pyrophyllite occur over a wide temperature range, depending on the silica saturation (Hemley et al., 1980). At quartz solubility, the temperature of coexistence is about 280° to 300°C, whereas if cristabolite (or amorphous silica) controls the silica solubility, the temperature can be as low as 160° C. Zunyite is stable at temperatures between 250° and 300°C (Fig. 5.20), and is part of the equilibrium assemblage with pyrophyllite and dickite at Rosario and La Grande. So at quartz saturation, the formation temperature of this assemblage was probably between 250° and 300°C.

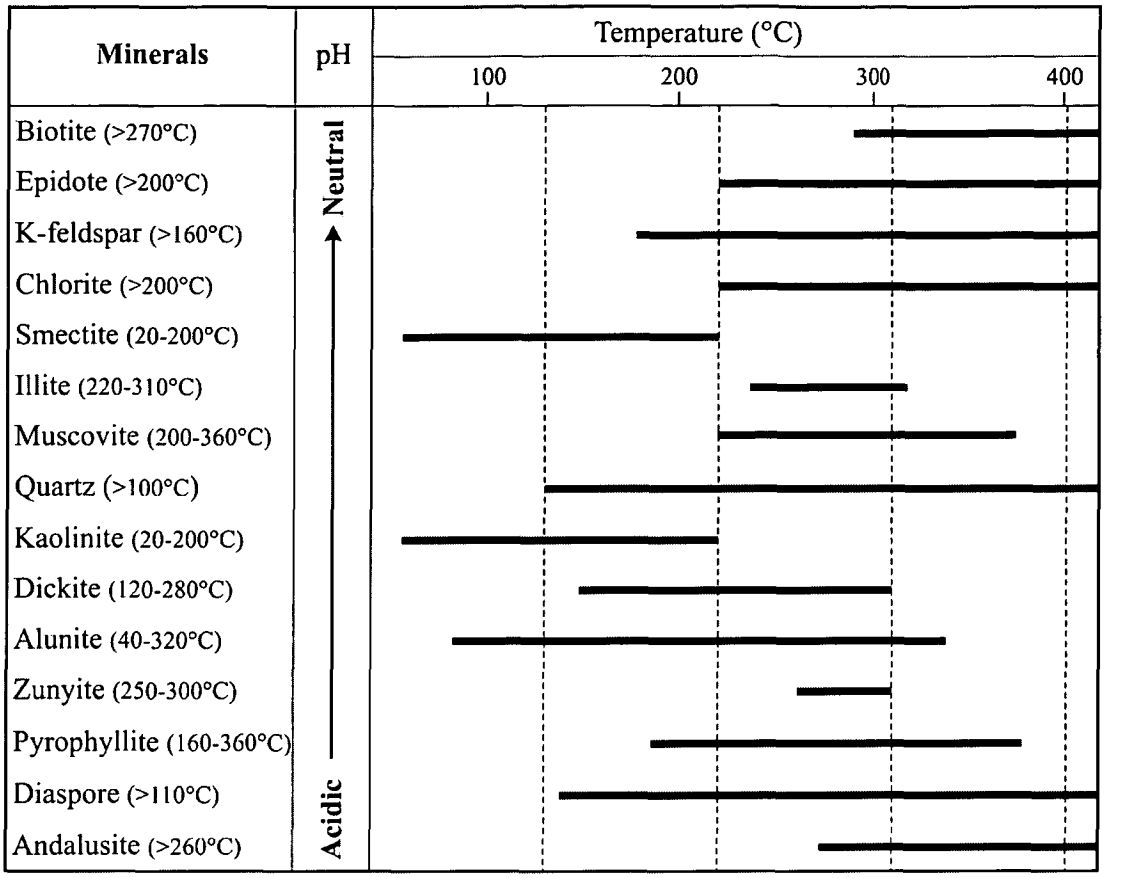

Figure 5.20. Temperature stability of hydrothermal minerals (deduced empirically from active geothermal systems and from experimental modelling; Hemley et al., 1980; Reyes, 1990) that occur at Rosario and La Grande, arranged by their stability with respect to pH.

The maximum temperature for the illite-smectite assemblage is ~200°C (Fig. 5.20). By contrast, the thermal stability range of epidote is broad (200° to >340°C; Reyes, 1990), but is inferred to be narrower for euhedral epidote that occurs in amygdales and that has replaced plagioclase (250° to >300°C). The propylitic assemblage of chlorite-epidote that fringes Rosario is thus inferred to have formed at temperatures exceeding 250°C.

Temperature gradients

Thermal and pH gradients can be inferred in the late-stage alteration at Rosario and La Grande. These gradients reflect evolution of the hydrothermal fluids in time and space (Figs. 5.20 and 5.21), as they cooled and were neutralised. Wall rock reactions that neutralised the fluids also changed its chemistry, thus the minerals that formed in response to these chemical changes also reflected temperature changes (Fig. 5.21).

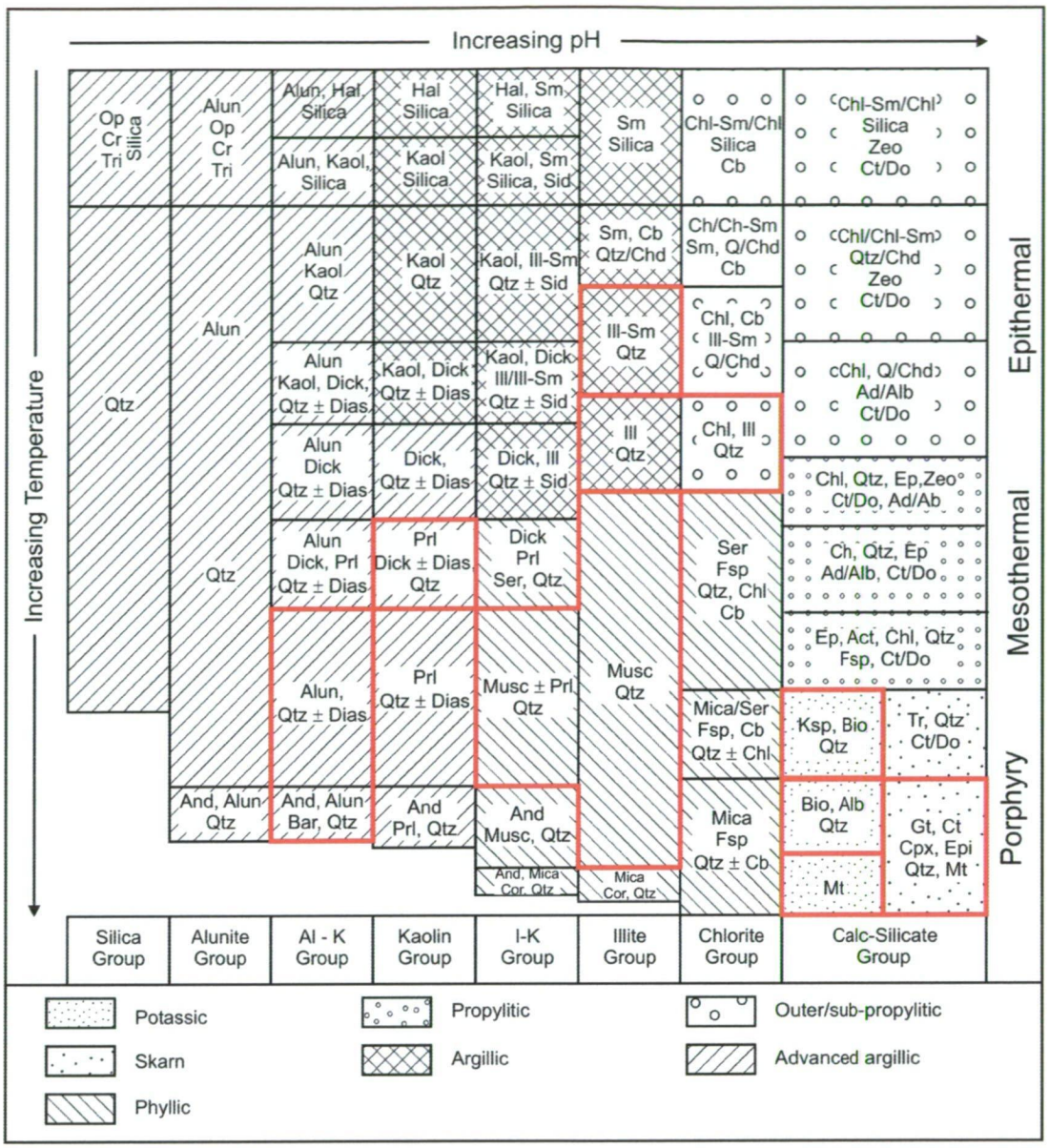

Figure 5.21. Temperature and pH stability ranges of common alteration assemblages in porphyry and epithermal deposits. The nine equilibrium assemblages at Rosario are highlighted in red. Modified from Corbett and Leach (1988).

Mineral abbreviations: Alb = albite, Act = actinolite, Ad = adularia, Alun = alunite, And = andalusite, Bio = biotite, Cb = carbonate (Ca, Mg, Mn, Fe), Chl = chlorite, Chd = chalcedony, Chl-Sm = chlorite-smectite, Cor = corundum, Cpx = clinopyroxene, Cr = cristobalite, Ct = calcite, Dias = diaspore, Dick = dickite, Do = dolomite, Ep = epidote, Fsp = feldspar, Gt = garnet, Hal = halloysite, Ill = Illite, Ill-Sm = illite-smectite, Kaol = kaolinite, Mt = magnetite, Op = opaline silica, Prl = pyrophyllite, Qtz, = quartz, Ser = Sericite, Sid = siderite, Sm = smectite, Tr = tremolite,, Tri = tridymite, Wo = wollastonite, Zeo = zeolite.

Advanced argillic alteration at Rosario and La Grande is characteristic of alteration proximal to gold and copper mineralisation in high-sulfidation epithermal deposits (Arribas, 1995). A notable exception, however, is that vuggy or residual quartz, typically the principal host to gold and copper in many high-sulfidation deposits, is not part of the advanced argillic alteration assemblage at Rosario and La

Grande. Instead, the advanced argillic alteration around E veins is characterised by early alteration assemblages that vary from deep quartz-andalusite-barite to shallow quartz diaspore-alunite. These alteration assemblages suggest that the fluid temperatures decreased from ≤400°C to between 250° and 320°C as they ascended along the faults (Fig. 5.20).

Vuggy quartz may not have formed because the temperatures were too high for its formation, or the physiochemical gradients did not favour quartz deposition. The high temperatures inferred at Rosario and La Grande may have limited the reactivity of the fluids (Giggenbach, 1997), and prevented strong and extensive leaching that can lead to vuggy quartz formation, characteristic of high-sulfidation epithermal deposits. A similar model was proposed for Peak Hill high-sulfidation Au-Cu deposit (NSW), where the pyrophyllite-diaspore assemblage (>280°C) in the core of the alteration zone reflected fluid temperatures that were too high to produce vuggy quartz (Masterman et al., 2002).

The pyrophyllite-dickite alteration assemblage is inferred to have formed synchronous with the muscovite-quartz and kaolinite-illite-smectite alteration assemblages. The temperature of formation of the pyrophyllite dickite assemblage was 250° to 300°C, whereas the distal kaolinite-illite-smectite assemblage formed at temperatures ≤200°C. Thus the muscovite-quartz alteration assemblage that separates the advanced argillic and argillic assemblages probably formed between 200° and 250°C, consistent with the temperature stability of muscovite shown in Figure 5.20. The chlorite-epidote assemblage that encloses the argillic zone on the southwest side of the Rosario Porphyry (Fig. 5.3) is inferred to have formed at higher temperatures (200° and 250°C) than the kaolinite-illite-smectite alteration assemblage. This implies that epidote-chlorite alteration of the rocks occurred before formation of the argillic assemblage.

pH gradients

The fluids responsible for the quartz-alunite-diaspore and pyrophyllite-dickite alteration assemblages were highly corrosive solutions (Fig. 5.21). Quartz-diaspore-alunite and pyrophyllite dickite alteration assemblages form under strong acid conditions, at a pH between 2 and 3 (Stoffregen, 1987). If the pH was lower, then aluminium would dissolve and so pyrophyllite, diaspore and andalusite could not form. (cf., the vuggy quartz zones typical in high-sulfidation deposits where everything

except silica is dissolved; Arribas, 1995).

The lateral zonation from pyrophyllite-dickite through muscovite-quartz to kaolinite-illite-smectite alteration assemblages is inferred to be the result of wall-rock reaction that neutralised acid fluids. Similar alteration zonation has been documented in the Peak Hill Au-Cu deposit (NSW; Masterman et al., 2002). At Peak Hill the hydrothermal alteration is zoned laterally from a pyrophyllite core through muscovite and kaolinite-illite-smectite to outer chlorite-epidote alteration assemblages. This alteration pattern was interpreted as neutralisation of the acid fluids as they were dispersed laterally from the axis of flow (Masterman et al., 2002).

Hydrology appears to have impacted the style of advanced argillic alteration at Rosario and La Grande. Vuggy and residual quartz form by replacement of the rocks when they react with strongly acid fluids in zones of high permeability (e.g. major fracture zones or porous volcanic rocks). These reactions enhance permeability and encourage the influx of more fluid (White, 1991). At Rosario and La Grande, the advanced argillic assemblages occur as tight alteration envelopes around faults that host massive sulfides (cf. with the mushroom-shaped cross-section of vuggy quartz at Lepanto; Hedenquist et al., 1998). This implies that, at the current level of exposure, the principal direction of paleofluid flow in the faults was upwards. The alteration beside the veins thus reflects lateral seepage of acid fluids from the faults, rather than flow into a permeable zone.

Formation of pyrophyllite and dickite may occur by two distinct processes: (1) condensation into groundwater of magmatic vapour forms very acidic solutions, producing silicic and quartz-alunite alteration (Hemley et al., 1969; Hedenquist et al., 1994a; 1994b); (2) and in a retrograde situation, cooling of a fluid in equilibrium with sericite (muscovite) at constant K/H mole ratio results in pyrophyllite formation (Hemley, 1959; Sverjensky et al., 1991; Hedenquist et al., 1998). The two ways of producing the advanced argillic assemblage are illustrated in Figure 5.22. At Rosario and La Grande, the zonation from muscovite altered rocks in deep levels to pyrophyllite-dickite altered rocks at shallow levels is inferred to have occurred by cooling of a fluid, at constant K/H values, as it ascended from the muscovite-quartz zone to the pyrophyllite-dickite zone.

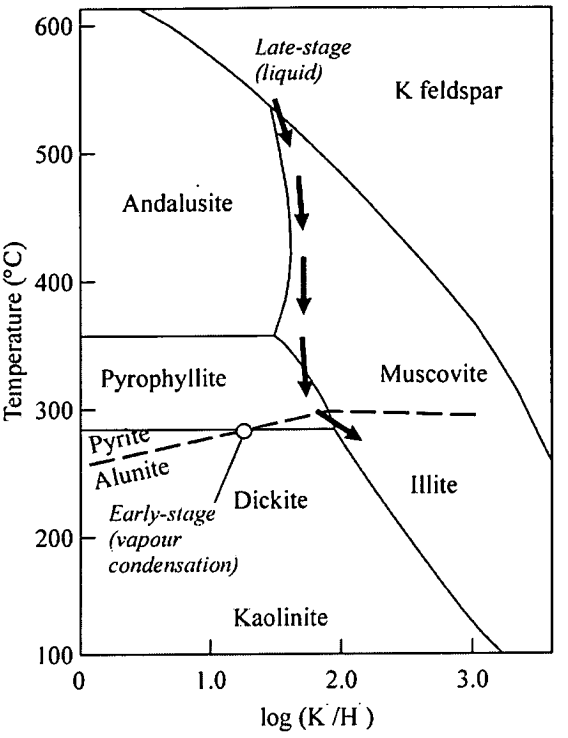

Figure 5.22. Temperature-log (K/H) diagram showing the stabilities of Al silicate minerals at quartz saturation (from Hemley, 1959; Sverjensky et al., 1991; adapted from Hedenquist et al., 1998; Watanabe and Hedenquist, 2001). The position of the pyrite-alunite coexistence line was approximated from thermodynamic data and relationships in active geothermal systems (Giggenbach, 1992; 1997). However, under the acidic conditions of this mineral pair, silica precipitates as either chalcedony or amorphous silica (Fournier, 1985), implying that pyrophyllite and kaolinite coexist at lower temperature (Hemley et al., 1980). At high water to rock ratios, the fluid cools from muscovite-stable to pyrophyllite-stable, which is the path taken by the late-stage fluids at Cerro La Grande and Rosario (solid arrows). As a result, muscovite occurs in the deep, high temperature parts of the system, whereas pyrophyllite is stable in the low temperature parts. Pyrophyllite can also occur with alunite and kaolinite, where magmatic vapours condense into ground water to produce an acidic solution at temperatures from 250° to 300°C. However, at Rosario and La Grande, pyrophyllite cuts and replaces the assemblage alunite-quartz, implying that it formed from a fluid that cooled between muscovite-stability and pyrophyllite stability as it ascended.

Unlike in the deep phyllic alteration zones, muscovite that surrounds the pyrophyllite-dickite altered rocks at shallow levels formed from fluids that evolved to higher K/H values and higher pH on the margins of the advanced argillic alteration zone (Fig. 5.22). This outward change was possibly caused by lower fluid to rock ratios, implying greater neutralising capacity as the fluids moved laterally into the wall rocks. Illite-smectite altered rocks in the outer envelope of late-stage alteration reflects slightly acid to near-neutral pH fluids (Fig. 5.21).

Chapter 6. $^{40}Ar/^{39}Ar$ and Re/Os Geochronology

Introduction

In a comparison of giant and small porphyry Cu deposits from Chile, Perú, Southwest USA, and British Columbia, Clark (1993) suggested that the scale of mineralisation in giant, high-grade systems reflects the involvement of both enormous volumes of "effective hydrothermal fluid" and anomalously high copper concentrations in those fluids. He addressed the possibility that the duration of hydrothermal activity may be one of the determining factors in whether or not a giant system is formed, although questioning the available database. This work led to the first detailed geochronologic study at Rosario (Clark et al., 1998), and to the evaluation of the hypothesis that the hydrothermal centre incorporated Paleocene and Eocene mineralisation events. However, results of that dating study were interpreted as indicating that the large scale of mineralisation was formed over a very brief time interval relative to that reported for other giant deposits. For example, the duration of hydrothermal activity at Chuquicamata encompasses a period of 2.3 ± 0.4 m.y (Zentilli et al., 1996, Reynolds et al., 1997). At La Escondida, hydrothermal activity associated with mineralisation is constrained by syn- and post-mineralisation intrusions that are 37.9 ± 1.1 Ma and 34.7 ± 1.7 Ma, respectively (Richards et al., 1999).

Prior to the present study, geochronologic data indicated that the age of porphyry magmatism in the Collahuasi district ranged from 59 Ma (Vergara, 1978) to 33 Ma (Clark et al., 1998). Munchmeyer et al. (1984) and Clark et al. (1998) determined that early biotite alteration and late-stage muscovite alteration formed between 34 and 33 Ma. On this basis, Clark et al. (1998) proposed that deposits at the latitude of the Collahuasi district, including the small molybdenum-rich Copaquire deposit (36.3 ± 0.6 Ma; Maksaev, 1990), become younger from west to east and that the magmatic front associated with porphyry copper emplacement migrated eastward in the early Oligocene.

The purpose of the current study was to re-evaluate these preliminary concepts through detailed determination of the age and duration of hydrothermal activity at Rosario and Ujina. In addition, geochronologic data is used to evaluate whether a genetic link is viable between the late-stage E veins and porphyry-style A, B, C and D veins at Rosario. This has involved laser probe $^{40}Ar/^{39}Ar$ analyses of igneous biotite in

mineralised intrusions at Rosario and Ujina, together with secondary illite (stage C veins) and hypogene alunite (stage E veins) at Rosario. The $^{40}Ar/^{39}Ar$ dating was carried out in the Geochronology Laboratory at Queens University, Kingston, Ontario. Molybdenite from a B vein has been dated at the University of Arizona using the Re-Os method.

In the final section of this chapter, the new radiogenic isotope ages have been used to constrain the initial $^{187}Os/^{188}Os$ composition of bornite from the Rosario deposit, allowing a brief discussion of metal sources. Rhenium and osmium concentrations in bornite were analysed at the University of Arizona.

Previous Geochronologic Work

Previous $^{40}Ar/^{39}Ar$ and K/Ar age data for hypogene alteration events in the Collahuasi district are summarised in Table 6.1. $^{40}Ar/^{39}Ar$ ages for the Quebrada Blanca deposit are also included. Clark et al. (1998) interpreted the results of their innovative $^{40}Ar/^{39}Ar$ spot fusion data for biotite (A veins) and muscovite (TES veins) as evidence that early and late-stage alteration-mineralisation events at Rosario were temporally discrete, but separated by a period $\leq$1.1 m.y. (at 2σ error). Critical to their interpretation was the observation that biotite alteration in the Collahuasi porphyry pre-dated the intrusion of the Rosario porphyry, thereby placing the timing of intrusion between the age of biotite (32.9 ± 0.5 Ma) and the age of muscovite alteration (32.9 ± 0.6 Ma). A K/Ar age of 34.2 ± 1.5 Ma (Munchmeyer et al., 1984) for hydrothermal biotite is in agreement with the biotite age reported by Clark et al. (1998).

Table 6.1. Summary of Existing Radiometric Ages for the Collahuasi Porphyry Deposits.

Sector	Lithology	Alteration	Material analysed	Age (2σ) Ma	Analytical method	References
Rosario	Collahuasi Porphyry	Potassic	Biotite (secondary)	32.9 ± 0.5	$^{40}Ar/^{39}Ar$	Clark et al. (1998)
Rosario	Collahuasi Porphyry	Phyllic	Muscovite	32.9 ± 0.6	$^{40}Ar/^{39}Ar$	Clark et al. (1998)
Rosario	Andesite	Biotitic	Biotite	34.2 ± 1.5	K/Ar	Munchmeyer et al. (1984)
Quebrada Blanca	Granodiorite porphyry	Potassic	Biotite (secondary)	34.9 ± 0.4	$^{40}Ar/^{39}Ar$	Maksaev (1990)
Rosario	Collahuasi Porphyry	Pre-mineral Collahuasi Porphyry	Whole rock	59.4 ± 1.2	K/Ar	Vergara (1978)

$^{40}Ar/^{39}Ar$ Analyses

Samples Dated

Descriptions of the three Rosario samples dated during the current study are given in Table 6.2. Euhedral primary biotite books (sample R200152), separated from the Rosario porphyry, varied from 0.2 to 3.0 mm in grain size and contain abundant rutile needles throughout biotite basal [001] sections. Minor grain boundary replacement by white mica was evident in some phenocrysts, but the biotite was not chloritised. Short wave infrared analysis of white mica in the Collahuasi Porphyry sample (R200153: porphyritic granodiorite) indicates that it is illite. Illite varies in size from 2 to 10 μm and has incipiently to pervasively replaced plagioclase phenocrysts. Stage E alunite was extracted from advanced argillically-altered Collahuasi porphyry (sample R200157). Pink alunite domains comprise euhedral blades 0.3 to 2.0 mm in length, intimately intergrown with pyrite and subordinate quartz and pyrophyllite.

Stage E alunite was also separated from advanced argillic-altered volcaniclastic sandstone that hosts the La Grande vein (sample R200158; Table 6.2). This alunite ranged in size from 70 μm to 2mm, and occurred as bladed crystals that had pseudomorphed plagioclase grains, and in the sediment matrix. Fine-grained pyrophyllite and quartz were intimately intergrown with alunite.

Igneous biotite from the Ujina deposit was liberated from the pre- to syn-mineralisation Ujina Porphyry and syn- to post-mineralisation Inca Porphyry (Table 6.2; Fig. 2.9a). The Ujina biotite (sample R200154) consisted of euhedral books 40 μm to 3.0 mm in size. Minor chlorite has replaced between 2 and 25 vol. percent of the biotite along grain margins and cleavage surfaces. Trace rutile was observed in biotite basal [001] sections. A second sample of coarse biotite (book size 0.2 to 3.0 mm) was removed from the Inca Porphyry (sample R200155). Primary biotite (100 to 400 μm long, sample R200156), liberated from the biotite granite at La Profunda (locality shown in Figure 1.3), was variably chloritised along cleavage surfaces and around grain margins (Table 6.2).

Table 6.2. Samples prepared for laser probe $^{40}Ar/^{39}Ar$ analysis from Rosario, La Grande, Ujina and La Profunda.

Deposit	Sample number, drill hole and depth	Lithology	Alteration	Mineral separate	Mineral chemistry[1]
Rosario	R200152, C316: 363.8 m	Rosario Porphyry	Illite overprint on K feldspar alteration, primary biotite books unaltered	25 clean biotite grains, 0.5-2.0 mm	K_2O: 9.65 to 10.25 wt. % H_2O: 2.70 to 3.08 wt. %
	R200153, C155: 32.9 m	Collahuasi Porphyry	Incipient illite of feldspar, overprints secondary biotite-orthoclase alteration	20 altered plagioclase grains hand-picked; SWIR analysis revealed they are illite	K_2O: 10.16 to 10.87 wt. %
	R200157, C177: 447.3 m	Collahuasi Porphyry	Pervasive alunite-pyrite-quartz	20 clean alunite grains, 0.2-2.0 mm	K_2O: 5.82 to 7.84 wt. %
La Grande	R200158 GC198: 335.5 m	Sandstone	Alunite, overprinted by pyrophyllite-dickite ± muscovite	15 alunite pieces, 0.5-1.0 mm	5.80 to 6.11 wt. % K_2O
Ujina	R200154, UC447: 510.3 m	Ujina Porphyry	Weak white mica overprint on K feldspar alteration, primary biotite books unaltered	20 fresh biotite grains, 1.0-2.0 mm	K_2O: 8.97 to 9.35 wt. % H_2O: 3.37 to 3.50 wt. %
	R200155, UC392: 485.8 m	Inca Porphyry	Trace amounts of white mica in plagioclase, minor chloritisation of biotite	20 fresh biotite grains, 1.0-3.0 mm	K_2O: 8.98 to 9.58 wt. % H_2O: 3.66 to 3.74 wt. %
La Profunda	R200156, UC612: 178.3 m	Biotite granite	Weak to strong chloritisation of biotite		K_2O: 3.82 to 6.93 wt. % H_2O: 3.83 to 4.08 wt. %

[1] determined by electron microprobe analysis (Appendix 2)

$^{40}Ar/^{39}Ar$ analytical method

Mineral separates were loaded into aluminium foil packets together with neutron flux monitors (24.36 Ma MAC-83 biotite of Sandeman et al., 1999) and stacked vertically into a 11.5 cm long and 2.0 cm diameter container. Samples were then irradiated with fast neutrons at the McMaster nuclear reactor (Hamilton, Ontario) in two 29-hour irradiations. Groups of flux monitors were located at 1 cm intervals along the irradiation container and J values for individual samples were determined by second-order polynomial interpolation. J values of the dated samples varied from 2.04 x 10^{-3} to 2.06 x 10^{-3}, and differed by <0.015 x 10^{-3} over the length of the sample chamber.

Samples and monitors were unwrapped and placed in individual pits of a stainless-steel chamber connected to an ultra-high vacuum purification system. Before analysis, samples and monitors were baked in the chamber overnight at 200°C. At least 14 flux monitors (MAC-83, six grains each) were individually degassed by total fusion using a focused 8W Lexel 3500 continuous argon ion laser. For step-heating, the laser

beam was defocused to cover the entire sample for periods of 3 minutes at instrumental power settings increasing from 0.25 to 8.0 W. After purification in an SAES C50 getter (5 minutes), the evolved gas was admitted to an online, Mass Analyser Products 216 mass spectrometer, with a Baur Signer source and an electron multiplier set to a gain of 10,000. System blanks were measured every 6 to 12 steps and subtracted from subsequent sample gas fractions. Extraction blank volumes during these analyses did not vary significantly during the course of individual experiments and averaged 160 x 10^{-13}, 11 x 10^{-13}, 1 x 10^{-13} and 0.7 x 10^{-13} cm^{-3} STP for masses 40, 39, 37 and 36, respectively.

Measured argon isotope peak heights were extrapolated to zero time, normalized to the $^{40}Ar/^{36}Ar$ atmospheric ratio (295.5) using measured values of atmospheric argon and corrected for neutron-induced ^{40}Ar from potassium, ^{39}Ar and ^{36}Ar from calcium (using the production ratios of Onstott and Peacock, 1987), and ^{36}Ar from chlorine (Roddick, 1983). Individual dates and errors were calculated using formulas given by Dalrymple et al. (1981) and the constants recommended by Steiger and Jäger (1977). Isotope correlation analysis was based on the formulas and error propagation of Hall (1981) and the regression and calculation of the mean square of weighted deviates (MSWD) goodness-of-fit statistic of York (1969).

$^{40}Ar/^{39}Ar$ age data

The results of the argon analyses are summarised in Table 6.3. Age plateaus (Fig. 6.1) were defined using the criteria of Lanphere and Dalrymple (1978), and McDougall and Harrison (1988 and 1999). The plateau includes three or more contiguous gas fractions that together represent more than 50% of the total ^{39}Ar released from the sample. Dates are concordant at the 95% level of confidence as defined by the critical value test (McIntyre, 1963). All errors shown on the age spectrum and isotope correlation diagrams represent analytical precision at 2σ and include the estimated error in the J value. Plateau ages were calculated by weighting individual plateau steps by the inverse of the variance and corrected for excess scatter about the mean when the F ratio statistic MSWD was greater than one. Corresponding isotope correlation diagrams for each sample are also presented in Figure 6.1.

Rosario $^{40}Ar/^{39}Ar$ ages: Laser heating of primary biotite from the Rosario Porphyry (R200152) produced a weighted mean plateau age of 34.4 ± 0.3 Ma between steps 7 and 18 (Fig. 6.1a), accounting for 77.2% of the ^{39}Ar released. This date is

indistinguishable from the isotope correlation age of 34.3 ± 0.2 Ma. The initial $^{40}Ar/^{36}Ar$ ratio is slightly higher than atmospheric (Fig. 6.1b) and may indicate that excess argon was released between steps 4 and 7. The age interpreted for Rosario biotite is the weighted mean plateau date of 34.4 ± 0.3 Ma.

The integrated age of illite associated with the intermediate-stage alteration event is 34.1 ± 0.6 Ma, with 77.6% of the ^{39}Ar released defining a plateau age of 34.5 ± 0.5 Ma (Fig 6.1c; steps 7-13). The ^{39}Ar release profile shows a slight disturbance in the low temperature steps, leading to younger apparent ages, but forms a plateau in the high temperature steps. High Ca/K values between steps 12 and 13 (Table 6.3) suggest that small amounts of relict primary plagioclase from the older Collahuasi Porphyry were present in the sample. The inverse isochron age is identical to the plateau age.

Alunite crystals from the late-stage, advanced argillic alteration event (sample R200157) were incrementally heated in twelve 3-minute steps. Total fusion was avoided to prevent SO_2 contamination of the mass spectrometer. A plateau is defined between steps 4 and 12 (1.0-3.5 W), passing the critical value test and defining a weighted mean date of 32.6 ± 0.3 Ma (Fig. 6.1e). The integrated and isotope correlation ages (32.9 ± 0.4 Ma and 32.5 ± 0.6 Ma respectively; Fig. 6.1f) are statistically indistinguishable from the preferred $^{40}Ar/^{39}Ar$ plateau age (Fig. 6.1e).

La Grande $^{40}Ar/^{39}Ar$ age: Incremental laser-heating of alunite from the advanced argillic alteration zone at La Grande (sample R200158) yielded an age plateau of 32.7 ± 1.6 Ma, defined between steps 2 and 7 (Fig. 6.1g). This is the preferred $^{40}Ar/^{39}Ar$ age for the La Grande alunite, but it is indistinguishable from the integrated age of 32.6 ± 1.7 Ma (Table 6.3). However, total argon release in this experiment was very low (2.28 x 10-10 cm3 NTP for ^{39}Ar), resulting in undesirably large errors for both the plateau and integrated ages.

Table 6.3. Incremental heating data for the Rosario, La Grande, Ujina and La Profunda samples.

Laser Power[1]	Isotope Ratios				Atmospheric					
(watts)	$^{40}Ar/^{39}Ar$	$^{38}Ar/^{39}Ar$	$^{37}Ar/^{39}Ar$	$^{36}Ar/^{39}Ar$	Ca/K[2]	Cl/K[3]	$\%^{40}Ar$ atm[4]	$\%^{39}Ar$[5]	$^{40}Ar^*/^{39}ArK$[6]	Age ± 2σ
R200152, biotite, J = 0.002042 ± 0.000012 (2σ); volume $^{39}Ar_K$ = 38.18 x $10^{-10}cm^3$, Integrated age = 34.41 ± 0.27 Ma (2σ)										
0.25	455.766	0.445	0.054	1.580	0.052	0.027	97.11	0.20	16.114	58.41 ± 42.55
0.75	79.878	0.123	0.026	0.273	0.034	0.011	93.69	0.72	5.329	19.53 ± 7.57
1.25>	14.736	0.086	0.006	0.022	0.008	0.015	37.49	3.19	9.309	33.97 ± 1.14
1.50>	11.574	0.088	0.003	0.009	0.004	0.016	18.37	5.69	9.513	34.71 ± 0.59
1.75>	10.517	0.087	0.003	0.005	0.002	0.016	9.41	6.05	9.587	34.98 ± 0.48
2.00>	10.070	0.087	0.002	0.004	0.002	0.016	6.30	7.00	9.491	34.63 ± 0.45
<2.25>	9.851	0.087	0.002	0.002	0.002	0.016	3.82	9.05	9.528	34.76 ± 0.41
<2.50>	9.708	0.087	0.002	0.002	0.002	0.016	2.84	7.96	9.484	34.61 ± 0.37
<2.75>	9.733	0.087	0.002	0.003	0.002	0.016	3.19	6.86	9.476	34.57 ± 0.45
<3.25>	9.781	0.085	0.003	0.003	0.003	0.016	4.21	4.69	9.446	34.47 ± 0.76
<4.00>	10.117	0.084	0.005	0.006	0.005	0.015	6.68	2.81	9.542	34.81 ± 1.33
<5.00>	9.833	0.084	0.005	0.005	0.005	0.015	4.63	2.87	9.475	34.57 ± 0.96
<6.00>	9.718	0.086	0.005	0.004	0.005	0.016	3.65	3.61	9.448	34.48 ± 0.83
<7.00>	9.639	0.088	0.004	0.003	0.005	0.016	3.38	6.17	9.379	34.23 ± 0.54
<8.00>	9.557	0.088	0.002	0.002	0.003	0.016	2.70	6.44	9.363	34.17 ± 0.53
<7.53>	9.567	0.090	0.004	0.004	0.003	0.017	2.38	2.96	9.428	34.40 ± 0.95
<8.86>	9.507	0.090	0.001	0.001	0.001	0.017	1.91	15.96	9.378	34.22 ± 0.34
<7.00>	9.482	0.089	0.001	0.002	0.001	0.017	1.93	7.79	9.361	34.16 ± 0.39
R200153, illite, J = 0.002045 ± 0.000012 (2σ); volume $^{39}Ar_K$ = 9.22 x $10^{-10}cm^3$, Integrated date = 34.12 ± 0.59 Ma (2σ)										
0.25>	290.240	0.890	0.152	1.071	0.272	0.197	98.72	0.26	5.291	19.42 ± 68.46
0.75>	64.240	0.236	0.087	0.214	0.192	0.041	90.89	2.81	6.066	22.24 ± 7.09
1.00>	24.123	0.088	0.058	0.066	0.116	0.012	64.79	2.74	8.766	32.06 ± 5.27
1.50>	18.430	0.051	0.042	0.037	0.091	0.006	49.42	6.91	9.444	34.51 ± 2.50
2.00>	13.338	0.039	0.026	0.016	0.056	0.004	28.42	13.27	9.615	35.13 ± 1.07
2.50>	11.112	0.025	0.017	0.008	0.037	0.002	14.53	14.77	9.547	34.88 ± 1.04
<3.00>	10.774	0.026	0.018	0.008	0.037	0.002	12.57	11.94	9.463	34.58 ± 1.07
<3.50>	10.789	0.030	0.018	0.008	0.038	0.003	13.08	11.48	9.418	34.42 ± 1.12
<4.00>	10.815	0.035	0.021	0.010	0.043	0.004	13.84	8.73	9.356	34.19 ± 1.49
<5.00>	11.615	0.053	0.029	0.012	0.063	0.008	20.90	10.50	9.233	33.75 ± 1.18
<6.00>	14.236	0.108	0.050	0.021	0.112	0.020	34.99	9.07	9.324	34.08 ± 1.43
<7.00>	22.272	0.286	0.120	0.055	0.278	0.060	58.83	3.32	9.394	34.33 ± 4.14
<7.00>	36.868	0.544	0.211	0.102	0.507	0.119	73.72	4.20	9.949	36.34 ± 3.99
R200157, hypogene alunite, J = 0.002060 ± 0.000012 (2σ); volume $^{39}Ar_K$ = 21.54 x $10^{-10}cm^3$, Integrated date = 32.89 ± 0.41 Ma (2σ)										
0.25>	2304.443	1.925	0.175	7.948	0.321	0.172	97.24	0.05	158.010	508.37 ± 377.82
0.50>	689.543	0.735	0.163	2.513	0.190	0.071	98.88	0.03	26.128	94.58 ± 273.95
0.75>	129.511	0.215	0.085	0.490	0.084	0.013	95.71	0.18	7.868	29.01 ± 40.46
<1.00>	14.142	0.021	0.012	0.022	0.021	-0.000	37.65	4.94	8.932	32.89 ± 1.51
<1.25>	10.466	0.015	0.005	0.007	0.010	-0.000	16.14	12.95	8.836	32.54 ± 0.58
<1.50>	10.277	0.015	0.007	0.006	0.014	-0.000	14.53	15.29	8.841	32.56 ± 0.48
<1.75>	10.386	0.015	0.006	0.006	0.012	-0.000	15.03	20.46	8.878	32.70 ± 0.60
<2.25>	9.416	0.014	0.005	0.004	0.008	-0.000	7.14	16.12	8.794	32.39 ± 0.64
<2.50>	9.354	0.015	0.006	0.003	0.010	-0.000	6.03	12.55	8.847	32.58 ± 0.52
<2.75>	9.962	0.017	0.009	0.007	0.016	-0.000	11.42	5.81	8.905	32.79 ± 1.12
<3.00>	9.932	0.017	0.011	0.007	0.019	-0.000	11.69	5.72	8.853	32.61 ± 1.07
<3.50>	10.196	0.017	0.012	0.008	0.022	-0.000	14.28	5.89	8.822	32.49 ± 1.09

Table 6.3. continued

Laser Power[1]	Isotope Ratios				Atmospheric					
(watts)	$^{40}Ar/^{39}Ar$	$^{38}Ar/^{39}Ar$	$^{37}Ar/^{39}Ar$	$^{36}Ar/^{39}Ar$	Ca/K[2]	Cl/K[3]	$\%^{40}Ar$ atm[4]	$\%^{39}Ar$[5]	$^{40}Ar^*/^{39}ArK$[6]	Age ± 2σ
R200158, hypogene alunite, J = 0.002063 ± 0.000012 (2σ); volume $^{39}Ar_K$ = 2.28 x $10^{-10}cm^3$, Integrated date = 32.58 ± 1.73 Ma (2σ)										
<0.75>	58.639	0.097	0.019	0.180	0.025	0.009	83.91	16.60	9.805	36.13 ± 5.48
<1.00>	18.921	0.033	0.019	0.041	0.034	0.001	53.80	27.92	8.890	32.79 ± 2.37
<1.25>	16.112	0.033	0.038	0.035	0.074	0.001	47.27	15.91	8.686	32.04 ± 3.52
<1.75>	15.002	0.035	0.039	0.035	0.070	0.000	45.86	12.83	8.313	30.68 ± 4.30
<2.25>	16.102	0.046	0.042	0.048	0.059	0.001	51.09	7.15	8.212	30.31 ± 6.99
<3.50>	15.707	0.032	0.031	0.032	0.059	0.001	45.52	19.49	8.711	32.13 ± 2.63
R200154, igneous biotite, J = 0.002049 ± 0.000012 (2σ); volume $^{39}Ar_K$ = 35.86 x $10^{-10}cm^3$, Integrated date = 35.02 ± 0.27 Ma (2σ)										
0.75	126.415	0.214	0.313	0.446	0.825	0.022	97.55	0.41	3.613	13.31 ± 14.79
1.50>	21.764	0.122	0.129	0.051	0.306	0.021	62.13	1.92	8.510	31.19 ± 2.27
2.00>	13.291	0.118	0.052	0.017	0.119	0.022	30.48	3.86	9.383	34.36 ± 1.03
2.50>	11.078	0.117	0.025	0.008	0.056	0.023	14.84	5.55	9.537	34.91 ± 0.66
<3.00>	10.291	0.116	0.011	0.004	0.024	0.023	7.29	7.53	9.626	35.24 ± 0.46
<3.50>	9.998	0.117	0.015	0.003	0.033	0.023	3.88	5.61	9.705	35.52 ± 0.61
<4.25>	10.053	0.117	0.027	0.003	0.063	0.023	4.24	8.26	9.707	35.53 ± 0.48
<5.00>	9.992	0.118	0.045	0.002	0.104	0.023	3.68	8.22	9.703	35.51 ± 0.47
<5.75>	9.799	0.120	0.044	0.002	0.103	0.024	3.06	8.34	9.581	35.07 ± 0.62
<6.50>	9.698	0.120	0.033	0.002	0.075	0.024	1.75	8.59	9.576	35.05 ± 0.66
<7.00>	9.764	0.119	0.044	0.002	0.101	0.024	2.27	9.84	9.598	35.14 ± 0.39
<8.00>	9.742	0.120	0.044	0.002	0.102	0.024	2.33	7.30	9.574	35.05 ± 0.49
<7.53>	9.880	0.123	0.039	0.006	0.083	0.024	2.60	1.96	9.716	35.56 ± 1.82
<8.02>	9.694	0.121	0.028	0.002	0.063	0.024	1.43	6.49	9.616	35.20 ± 0.52
<9.88>	9.690	0.122	0.030	0.001	0.071	0.025	1.34	16.11	9.611	35.18 ± 0.38
R200155, igneous biotite, J = 0.002052 ± 0.000012 (2σ); volume $^{39}Ar_K$ = 24.50 x $10^{-10}cm^3$ Integrated date = 34.75 ± 0.28 Ma (2σ)										
0.75	70.985	0.135	0.156	0.251	0.365	0.014	95.45	0.74	3.500	12.91 ± 9.70
1.50	15.678	0.091	0.018	0.026	0.036	0.016	41.54	4.15	9.284	34.05 ± 1.40
2.25>	10.937	0.086	0.010	0.007	0.021	0.016	13.61	8.44	9.513	34.88 ± 0.66
3.75>	10.116	0.087	0.014	0.003	0.030	0.016	5.21	11.56	9.636	35.33 ± 0.69
4.50>	9.925	0.087	0.021	0.002	0.047	0.016	2.43	9.08	9.742	35.71 ± 0.54
<5.25>	9.684	0.087	0.029	0.002	0.067	0.016	1.69	11.20	9.575	35.10 ± 0.47
<6.00>	9.536	0.087	0.035	0.001	0.082	0.016	0.95	16.23	9.497	34.82 ± 0.34
<6.75>	9.482	0.087	0.032	0.001	0.075	0.017	0.92	14.71	9.446	34.63 ± 0.37
<7.50>	9.508	0.088	0.032	0.002	0.072	0.016	1.06	7.16	9.464	34.70 ± 0.73
<8.25>	9.517	0.086	0.017	0.002	0.036	0.016	1.18	6.53	9.461	34.69 ± 0.72
<7.53>	9.497	0.092	0.026	0.010	0.042	0.016	1.56	1.42	9.441	34.62 ± 3.17
<9.88>	9.542	0.086	0.024	0.002	0.054	0.016	1.15	8.79	9.485	34.78 ± 0.57
R200156, primary biotite, J = 0.002056 ± 0.000012 (2σ); volume $^{39}Ar_K$ = 2.38 x $10^{-10}cm^3$, Integrated date = 71.13 ± 4.17 Ma (2σ)										
0.50	399.153	0.365	0.993	1.373	2.495	0.021	97.56	10.67	10.464	38.40 ± 34.74
1.00	66.291	0.105	2.052	0.196	5.037	0.011	81.78	22.11	12.524	45.87 ± 5.15
1.50	37.586	0.056	4.505	0.069	11.084	0.005	47.35	23.46	20.497	74.47 ± 2.91
2.00	38.708	0.067	9.547 8	0.072	24.335	0.006	42.38	11.56	23.792	86.16 ± 4.68
<2.75>	27.821	0.047	1.267	0.032	3.150	0.004	22.00	13.81	22.671	82.19 ± 3.90
<3.50>	24.485	0.052	0.448	0.030	1.124	0.003	13.57	7.14	22.726	82.39 ± 7.02
<4.50>	28.672	0.152	0.830	0.067	2.217	0.025	39.10	4.34	19.635	71.40 ± 11.48
6.50>	38.095	0.857	3.455	0.114	10.017	0.219	57.80	3.08	19.128	69.59 ± 16.34
7.00	63.446	1.882	5.643	0.106	16.051	0.497	32.87	3.82	50.400	177.88 ± 16.43

[1] "<" indicates step used in plateau age calculations, ">" indicates step used in inverse correlation calculations
[2] $Ca/K = 1.83 \times (^{37}Ar_{Ca}/^{39}Ar_K)$
[3] Cl/K ratios are calculated using data from Roddick (1983)
[4] % atmospheric ^{40}Ar in this step relative to % radiogenic ^{40}Ar
[5] % ^{39}Ar in this step relative to total ^{39}Ar in the sample
[6] $^{40}Ar^*$ = radiogenic ^{40}Ar
Isotope production ratios: $(^{40}Ar/^{39}Ar)_K = 0.0302$, $(^{37}Ar/^{39}Ar)_{Ca} = 1416.4306$, $(^{36}Ar/^{39}Ar)_{Ca} = 0.3952$, $Ca/K = 1.83 \times (^{37}Ar_{Ca}/^{39}Ar_K)$;
$^{40}Ar^*$ = radiogenic ^{40}Ar

Figure 6.1. Laser-heated $^{40}Ar/^{39}Ar$ age spectra and inverse isochron correlation diagrams $^{40}Ar/^{39}Ar$. A and B) Rosario Porphyry biotite. C and D) Rosario illite. E and F) Rosario alunite. G and H) La Grande alunite. I and J) Ujina Porphyry biotite. K and L) Inca Porphyry biotite. M and N) La Profunda biotite. Steps included in the weighted average plateau ages are indicated by the thin dotted lines. The steps included in the isochron calculations are the same as those in plateau ages. The dashed lines are the least squares regressions of the steps indicated in Table 5 (with elliptical error bars), calculated using the method of York (1969). The solid diagonal line is a reference line between the calculated $^{39}Ar/^{40}Ar$ intercept and the inverse atmospheric ratio $^{36}Ar/^{40}Ar$ (1/295.5). The plateau and correlation ages and initial $^{40}Ar/^{36}Ar$ ratio are given at 2σ. The mean square of weighted deviates (MSWD) is also given.

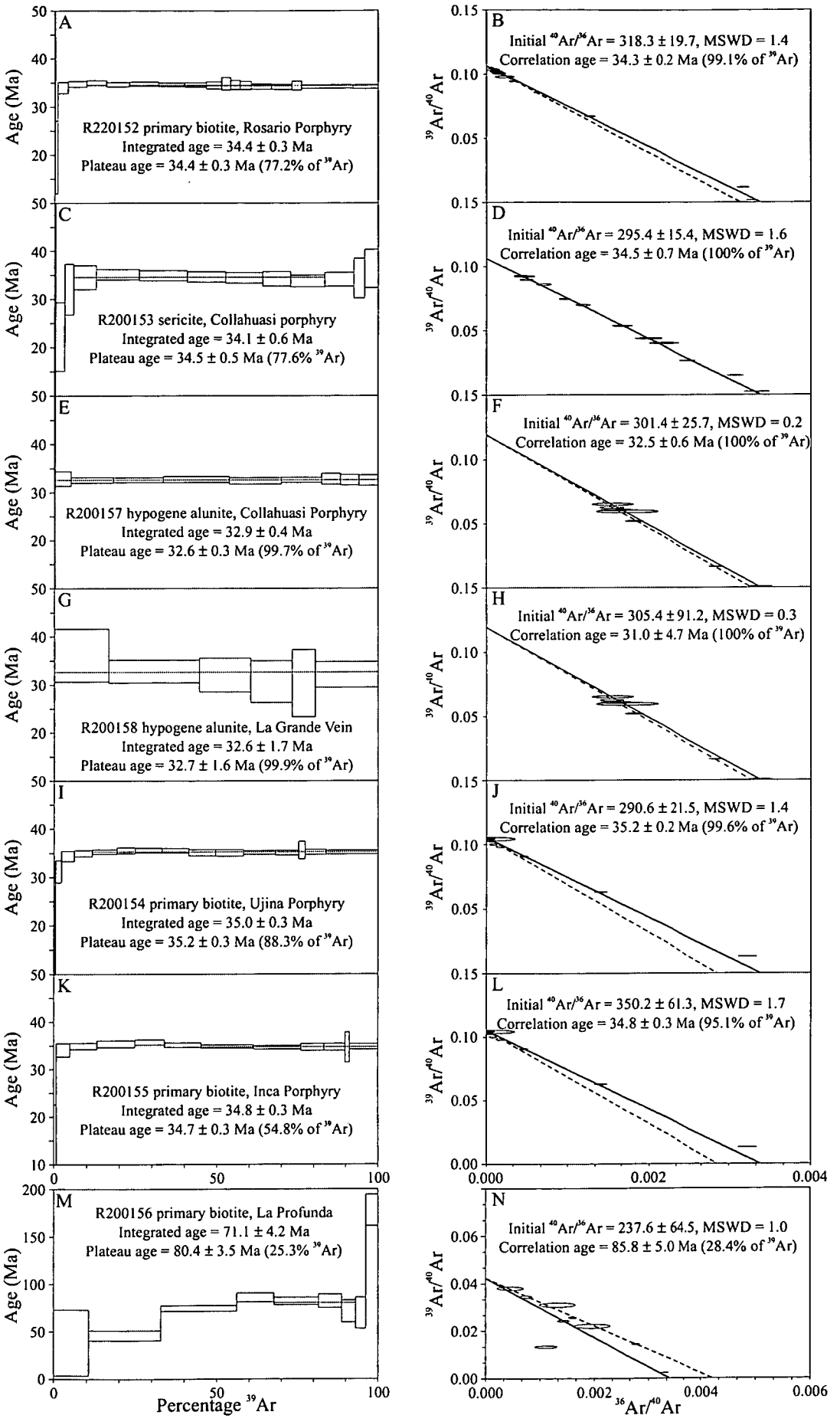
A
R220152 primary biotite, Rosario Porphyry
Integrated age = 34.4 ± 0.3 Ma
Plateau age = 34.4 ± 0.3 Ma (77.2% of 39Ar)
B
Initial 40Ar/36Ar = 318.3 ± 19.7, MSWD = 1.4
Correlation age = 34.3 ± 0.2 Ma (99.1% of 39Ar)
C
R200153 sericite, Collahuasi porphyry
Integrated age = 34.1 ± 0.6 Ma
Plateau age = 34.5 ± 0.5 Ma (77.6% 39Ar)
D
Initial 40Ar/36Ar = 295.4 ± 15.4, MSWD = 1.6
Correlation age = 34.5 ± 0.7 Ma (100% of 39Ar)
E
R200157 hypogene alunite, Collahuasi Porphyry
Integrated age = 32.9 ± 0.4 Ma
Plateau age = 32.6 ± 0.3 Ma (99.7% of 39Ar)
F
Initial 40Ar/36Ar = 301.4 ± 25.7, MSWD = 0.2
Correlation age = 32.5 ± 0.6 Ma (100% of 39Ar)
G
R200158 hypogene alunite, La Grande Vein
Integrated age = 32.6 ± 1.7 Ma
Plateau age = 32.7 ± 1.6 Ma (99.9% of 39Ar)
H
Initial 40Ar/36Ar = 305.4 ± 91.2, MSWD = 0.3
Correlation age = 31.0 ± 4.7 Ma (100% of 39Ar)
I
R200154 primary biotite, Ujina Porphyry
Integrated age = 35.0 ± 0.3 Ma
Plateau age = 35.2 ± 0.3 Ma (88.3% of 39Ar)
J
Initial 40Ar/36Ar = 290.6 ± 21.5, MSWD = 1.4
Correlation age = 35.2 ± 0.2 Ma (99.6% of 39Ar)
K
R200155 primary biotite, Inca Porphyry
Integrated age = 34.8 ± 0.3 Ma
Plateau age = 34.7 ± 0.3 Ma (54.8% of 39Ar)
L
Initial 40Ar/36Ar = 350.2 ± 61.3, MSWD = 1.7
Correlation age = 34.8 ± 0.3 Ma (95.1% of 39Ar)
M
R200156 primary biotite, La Profunda
Integrated age = 71.1 ± 4.2 Ma
Plateau age = 80.4 ± 3.5 Ma (25.3% 39Ar)
N
Initial 40Ar/36Ar = 237.6 ± 64.5, MSWD = 1.0
Correlation age = 85.8 ± 5.0 Ma (28.4% of 39Ar)
Age (Ma)
39Ar/40Ar
Percentage 39Ar
36Ar/40Ar

Ujina $^{40}Ar/^{39}Ar$ ages: The plateau age of 35.2 ± 0.3 Ma for primary biotite in the Ujina Porphyry (sample R200154) was calculated across steps 5-15, representing 88.3% of the total argon release (Fig 6.1i). The integrated date of 35.0 ± 0.3 Ma (Table 6.3) is slightly younger than the plateau age. The difference between these is attributed to partial ^{40}Ar loss, evident in the low temperature steps (0.75-2.50 W). The observed interlayer chloritisation of biotite indicates that ^{39}Ar recoil probably affected the age data. This is seen by the subtle crest through the mid-temperature increments (3.0-5.0 W; Fig. 6.1i). Initial $^{40}Ar/^{36}Ar$ ratios are very close to atmospheric, indicating that excess argon did not contribute to the slightly elevated ages through the mid-temperature steps (Table 6.3, Fig. 6.1j). The decreasing ages for the high-temperature steps (5.75-8.00 W) are interpreted to have been caused by argon outgassing from chlorite, which has higher argon retentivity than biotite.

Primary biotite (sample R200155) from the younger Inca Porphyry appears to contain excess ^{40}Ar through the mid-temperature steps (4-6; Fig. 6.1k), but these higher values may also be the result of argon recoil effects. This is consistent with chlorite replacement around biotite grain margins and along cleavage surfaces. Partial overprinting by a late thermal event is again seen in the low temperature steps (0.75-1.50 W). A plateau age of 34.7 ± 0.3 Ma is defined for 54.8% of the ^{39}Ar total release (Fig. 6.1k).

La Profunda $^{40}Ar/^{39}Ar$ age: Igneous biotite from the La Profunda intrusion yielded a poorly defined quasi-plateau age of 80.4 ± 3.5 Ma (25.3% of the total ^{39}Ar yield; Fig. 6.1m). This corresponds with the correlation age of 85.8 ± 5.0 Ma, again using only 28% of the ^{39}Ar released (Fig. 6.1n). The low-temperature steps 1-3 (0.5-1.5 W) indicate disturbance by a thermal event with a maximum age of 38 ± 34 Ma. This partial resetting coincides temporally with the emplacement of the Ujina intrusive complex at 35 Ma. The young integrated age (71.1 ± 4.2 Ma) and low initial $^{40}Ar/^{36}Ar$ ratio (237.6 ± 64.5) are also consistent with ^{40}Ar degassing associated with a thermal resetting event.

Re/Os age of molybdenite from Rosario

Re/Os dating of molybdenite

Molybdenite is the most robust mineral for Re/Os geochronometry because Re concentrations in molybdenite are generally >50 ppm (Stein et al., 1998a). Molybdenite contains negligible initial ^{187}Os, and therefore molybdenite ages can be determined by a single analysis, assuming no initial Os (Luck and Allegre, 1982), or by isotope correlation of Re and Os concentrations from multiple analyses (Stein et al., 1998b). The capacity of the Re/Os system to remain isotopically closed following molybdenite crystallization is a focus of ongoing debate (McCandless and Ruiz, 1993; Stein et al., 1998b; Selby and Creaser, 2001), particularly regarding the effects of post-ore saline fluids on molybdenite crystals (Suzuki et al., 2000). A detailed discussion of this problem is presented in Barra et al. (2003).

Sample dated, Re/Os analytical method and results

A drill core intersection of vein molybdenite was sampled from the Rosario deposit (Table 6.4). Flaky molybdenite aggregates (sample R990137), varying in size from 10 to 200 μm diameter, were extracted from a B vein that also contains anhedral quartz overgrown by euhedral quartz and chalcopyrite in the centrally filled void. The vein has a texturally destructive muscovite-quartz alteration envelope. The euhedral quartz and chalcopyrite are inferred to be associated with the muscovite-quartz assemblage, superimposed on the vein after molybdenite deposition. Individual molybdenite grains are intergrown with up to 5% chalcopyrite, and small amounts of white mica.

The sample was crushed and handpicked, and approximately 0.1 gram separated for analysis. Re and Os concentrations were determined by isotope dilution, and measured on the Negative Thermal Ionization Mass Spectrometer at the University of Arizona. The Carius tubes method was used to digest samples (Shirey and Walker, 1995), and Re and Os were separated using a distillation technique described in Mathur (2000). A total error of 0.5% has been assumed for the analysis, based on the pervious Re/Os experiments at the University of Arizona (Mathur, 2000; Barra et al., 2003), which represents the greatest possible deviation caused by a combination of spike calibration errors, under/over spiking, instrumental counting statistics, and the uncertainty in the decay constant of Re.

The molybdenite age was calculated using a ^{187}Re decay constant of 1.666×10^{-11} y^{-1} (Smoliar et al, 1996). Analysed Re and Os concentrations in the sample were 367 ppm and 129 ppb, respectively (Table 6.4). A Re/Os date of 33.3 ± 0.2 Ma was calculated for the Rosario molybdenite, assuming no initial ^{187}Os.

Initial $^{187}Os/^{188}Os$ compositions of bornite and pyrite

Initial $^{187}Os/^{188}Os$ compositions were calculated from Re/Os analytical data obtained from bornite and pyrite (Table 6.4). The bornite was sampled in this study from an E vein at Rosario and analysed at the University of Arizona. Mineral separation and the analytical procedure is the same as that described for the Re/Os dating of molybdenite. The initial $^{187}Os/^{188}Os$ value of a pyrite sample from Mathur et al. (2000) was recalculated using the new $^{40}Ar/^{39}Ar$ age data in this chapter. According to Mathur et al. (2000), the pyrite was collected from veins associated with orthoclase-biotite alteration at Rosario, which corresponds with the A-2 vein stage in this study. However, the relationship was neither spatially nor temporally confirmed by this study, as geological control for the sample could not be retrieved. Consequently, a range of initial Os values are reported to encompass the maximum and minimum ages of pyrite formation at Rosario.

Analytical results, including initial $^{187}Os/^{188}Os$ compositions, are presented in Table 6.4. The Os concentrations of bornite and pyrite range from between 5 to 12 parts per trillion, whereas Re concentrations range from 155 to 808 parts per billion. The age used to determine the initial Os ratio of the bornite was 32.6 Ma, and provided an initial $^{187}Os/^{188}Os$ value of 0.39. By contrast, the age range used for the pyrite was 34.4 to 32.6 Ma, giving an initial $^{187}Os/^{188}Os$ values of 0.62 to 0.73.

Table 6.4. Re-Os data.

Sample	Mineral	Vein type	Os	Re[2]	Age (Ma)	$^{187}Os/^{188}Os$	$^{187}Re/^{188}Os$	Initial Os ratio	Source
R990137	Molybdenite	B	129.4 ppb[1]	367.6 ppm	33.3 ± 0.2	-	-	-	This study
R200002	bornite	E	5 ppt	1,551 ppt	32.6	1.36	1778	0.39	this study
Coya-6	pyrite	A (?)	12 ppt	8,078 ppt	34.4 to 32.6	2.61	3465	0.62 to 0.73	Mathur et al. (2000)

[1] All measured Os is radiogenic ^{187}Os (assuming no initial Os)
[2] ^{187}Re = 62.602 % of total Re concentration
^{187}Re decay constant = $1.666 \times 10\text{-}11$ y^{-1}

Discussion

The new age data from $^{40}Ar/^{39}Ar$ geochronologic experiments at Rosario, La Grande and Ujina, as well as the Rosario molybdenite Re/Os analysis, are summarised in Table 6.5. Although the geochronologic model presented here for the Collahuasi district is still based on a limited dataset, it does provide an understanding of the timing of hydrothermal activity in this richly endowed porphyry copper district. At Rosario, the $^{40}Ar/^{39}Ar$ age of primary biotite (34.4 ± 0.3 Ma) in the Rosario Porphyry is the time at which biotite cooled through its closure temperature (300° to 350°C; McDougall and Harrison, 1999). This is slightly younger than the biotite cooling age of 35.2 ± 0.3 Ma in the Ujina Porphyry. The biotite granite from the La Profunda prospect has a disturbed isotopic system that yielded a plateau age of 80.4 ± 3.5 Ma. Thus the La Profunda Pluton appears to be unrelated to Tertiary magmatism in the Collahuasi district.

The minimum age of the early porphyry-style mineralisation at Rosario is constrained by the $^{40}Ar/^{39}Ar$ ages of 34.5 ± 0.5 Ma (C stage illite) and 34.4 ± 0.3 Ma (primary biotite), and by the Re/Os age of 33.3 ± 0.2 Ma (B stage molybdenite). The similar illite and biotite ages reflect resetting of the biotite, which probably occurred during the hydrothermal event that formed illite. Thus the primary biotite age is not the age of magmatism, rather it is the age of hydrothermal activity that produced either biotite-albite-K feldspar or illite-chlorite alteration of the rocks. The age of latest alteration and mineralisation at Rosario corresponds with the $^{40}Ar/^{39}Ar$ date of 32.6 ± 0.3 Ma for hypogene E stage alunite. An age of 32.7 ± 1.6 Ma for hypogene alunite in advanced argillic alteration assemblages at La Grande is identical to that from Rosario, evidence that the high grade Cu-Ag-(Au) veins formed during the same hydrothermal event.

At Ujina, the $^{40}Ar/^{39}Ar$ biotite age of the Inca Porphyry (34.7 ± 0.3 Ma) may only be slightly younger than its emplacement age, as it has not been affected by biotite-K feldspar and white mica alteration. By contrast, the $^{40}Ar/^{39}Ar$ age of primary biotite in the Ujina Porphyry is interpreted to record the age of the last hydrothermal event that exceeded temperatures of 300°C. The $^{40}Ar/^{39}Ar$ age of the Inca Porphyry serves as a minimum age for both magmatism and hydrothermal alteration at Ujina.

Table 6.5. Summary of Preferred Geochronologic Ages at Rosario, La Grande, Ujina and La Profunda.

Deposit or prospect	Mineral	Relationship between intrusive activity and mineralization-alteration	Age ± 2s (Ma)	Analytical technique
Rosario	Biotite	Cooling age of biotite reflecting the age of the early hydrothermal event	34.4 ± 0.3	$^{40}Ar/^{39}Ar$
	Molybdenite	Age reset between the early and late hydrothermal events	33.3 ± 0.2	Re/Os
	Illite	Minimum age of the early alteration event	34.5 ± 0.5	$^{40}Ar/^{39}Ar$
	Alunite	Age of the late hydrothermal event	32.6 ± 0.3	$^{40}Ar/^{39}Ar$
La Grande	Alunite	Age of the late hydrothermal event that affected Rosario	32.7 ± 1.6	$^{40}Ar/^{39}Ar$
Ujina	Biotite	Cooling age of biotite possibly reflecting the age of hydrothermal alteration of the Ujina Porphyry	35.2 ± 0.3	$^{40}Ar/^{39}Ar$
	Biotite	Cooling age of biotite reflecting minimum age of magmatism at Ujina	34.7 ± 0.3	$^{40}Ar/^{39}Ar$
La Profunda	Biotite	Disturbed biotite age possibly reflecting emplacement of the Ujina Porphyry near the La Profunda pluton	80.4 ± 3.5	$^{40}Ar/^{39}Ar$

Age of hydrothermal events at Rosario

Hydrothermal biotite typically forms in porphyry deposits at temperatures >400°C (Titley and Beane, 1981; Titley, 1993). The $^{40}Ar/^{39}Ar$ dates therefore do not give the age of formation of either primary or secondary biotite, Instead, they indicate the age of the last hydrothermal event above 300°C. The period that separates the cooling age of biotite from that of the hypogene alunite (~280°C; Love et al., 1998) corresponds to a hiatus between two discrete and short-lived episodes of hydrothermal activity. The minimum age of the first episode corresponds with the $^{40}Ar/^{39}Ar$ ages of C stage illite and primary biotite (34.5 ± 0.5 to 34.4 ± 0.3 Ma). The second was marked by the formation of E stage alunite, which has an $^{40}Ar/^{39}Ar$ age of 32.6 ± 0.3 Ma. By incorporating the 2σ error envelopes, this implies that the minimum hiatus between porphyry-type mineralisation-alteration and the massive sulfide (E) veins was 1.8 ± 0.4 Ma.

The Re/Os age of molybdenite (33.3 ± 0.2 Ma) is between the $^{40}Ar/^{39}Ar$ ages of the two main hydrothermal events at Rosario. The paragenesis indicates that molybdenite veins are associated with the early hydrothermal event. However, euhedral quartz and chalcopyrite-pyrite ± muscovite has overgrown anhedral quartz and molybdenite in the central part of the sampled vein. The overgrowth assemblage is interpreted to have been superimposed on earlier-formed molybdenite. McCandless et

al. (1993) have assessed the effects of K- and Al-silicate alteration superimposed on molybdenite in veins from several porphyry deposits in the southwestern USA (e.g., Bagdad, Morenci, Silver Bell and Questa). These authors concluded that white mica and clay intergrowths may be enriched in Re, which possibly caused erroneous younger ages in the molybdenite. Disturbed Re/Os ages in molybdenite have also been reported from the Bingham deposit (Utah), in which the dates obtained were interpreted to be younger than the formation age of molybdenite (Chelsey and Ruiz, 1997). Late hydrothermal alteration at Rosario may have disturbed the Re/Os isotopic system in molybdenite. Alternatively, there was another episode of molybdenite mineralisation that was not observed in this study. Additional Re/Os dating is required to check whether this age is reproducible in this and other molybdenite veins. At present, the Re/Os age of 33.3 ± 0.2 Ma provides no additional constraints on the duration of the early hydrothermal activity at Rosario. However, it is possible that the Re/Os age has recorded a minor hydrothermal event that did not reset the 40Ar/39Ar systematic of the A- and C-stage samples.

The discrete time gap between the main alteration events at Rosario contradicts the model advanced by Clark et al. (1998) based on $^{40}Ar/^{39}Ar$ ages of early-stage hydrothermal biotite (32.9 ± 0.5 Ma) and late-stage muscovite (32.9 ± 0.6 Ma). In their model, early- and late-stage alteration events were temporally indistinguishable and it was concluded that the late-stage muscovite alteration recorded by Lee (1994), which correlates with the pyrophyllite-dickite (TES) altered rocks, occurred shortly after formation of the early porphyry stockwork. It should be emphasised that the $^{40}Ar/^{39}Ar$ study of Clark et al. (1998) employed a new experimental technique based on *in situ* fusion of minerals in rock wafers, an approach to improve paragenetic control, but which has not been evaluated elsewhere. Therefore the dates may be inherently different from ages determined for high-quality mineral concentrates.

The closure temperature of muscovite (~350°C, McDougall and Harrison, 1999) is slightly higher than that of biotite (300°-330°C). The identical ages determined by Clark et al. (1998) may also indicate that the $^{40}Ar/^{39}Ar$ biotite age was reset by hydrothermal fluids that produced the younger muscovite-quartz assemblage. The age of the muscovite dated by Clark et al. (1998) is in good agreement with our alunite age of 32.6 ± 0.3 Ma, suggesting that muscovite formation was synchronous with the alunite. Based on the alteration paragenesis and $^{40}Ar/^{39}Ar$ data it is concluded that the

pyrophyllite-dickite assemblage formed coeval with the muscovite and after the quartz-alunite-pyrite alteration event.

Temporal relationships between high-sulfidation and porphyry mineralisation

Geochronologic investigations into the longevity of magmatic-hydrothermal systems related to porphyry copper deposits indicate durations of 1 m.y. to <300,000 years between K silicate alteration (biotite + K feldspar) and the formation of high sulfidation mineralisation and alteration (e.g., Dilles and Wright, 1988; Arribas, et al., 1995b; Marsh et al., 1997; Parry et al. 1998; Watanabe et al., 1999; Gustafson et al., 2001; Muntean and Einaudi, 2001). Based on $^{40}Ar/^{39}Ar$ ages of porphyry and epithermal mineralisation in the Maricunga Belt, northern Chile, Muntean and Einaudi (2001) proposed that a time gap of less than 1 m.y. is indicative of a genetic link between porphyry and epithermal environments. Time gaps exceeding 1 m.y., but less than 2 m.y., suggested no genetic connection. At Rosario, the minimum apparent time interval separating the early- and late-stage alteration events is 1.4 m.y. This is greater than the maximum hiatus of 1 m.y. proposed by Muntean and Einaudi (2001). The new age constraints on early- and late-stage hydrothermal activity at Rosario reflect punctuated magmatic-hydrothermal events within the overall evolution of the Collahuasi district.

Potential Metal Sources

Possible sources of Os, and by inference Cu, in porphyry Cu deposits emplaced in continental arcs can include the mantle wedge, the subducting slab and associated sediments, and diverse reservoirs in the upper and lower crust (Esser and Turekian, 1993; Brandon et al., 1996; Chelsey and Ruiz, 1998; Saal et al., 1998). The initial Os compositions of bornite and pyrite at Rosario are more radiogenic than the composition of the mantle beneath the continental crust (0.13 to 0.15; Brandon et al., 1996), and indicates a crustal contribution of Os to the porphyry deposit. The initial $^{187}Os/^{188}Os$ composition of bornite is less radiogenic than the range of values determined for pyrite, implying that the pyrite contains more crustally-derived Os than the bornite.

At Chuquicamata, the source of Os changed through the evolution of the ore-forming system, in which the primitive compositions corresponded with the early-stages of ore formation (Mathur et al., 2000). In the later stages of sulfide formation, initial Os values (~1) are more radiogenic than those in the early stages (0.15) and

reflect the dominance of magmatic waters in the early stages of ore formation. As the system evolved, the Os isotope values became more radiogenic (Mathur et al., 2000). Arguably, the radiogenic bornite and pyrite from Rosario may indicate the involvement of non-magmatic fluids. Alternatively, the radiogenic Os may have been sourced from modified lower continental crust, assimilated in the magmas that formed the mineralised porphyry stocks. A potential lower crustal source of Os is consistent with the Sr, Nd and Pb isotope data from the Rosario Porphyry, which suggest that the melts were generated in the MASH zone at the base of the crust (Chapter 3).

Overall, the initial Os compositions from Rosario overlap those of the other giant porphyry ore deposits in Chile, including Chuquicamata and El Salvador (Fig. 6.2). That El Teniente has a similar initial Os ratio to the giant late Eocene-early Oligocene deposits is surprising, as the deposits in northern Chile generally have much lower initial $^{187}Os/^{188}Os$ than those of Paleocene (e.g., Cerro Colorado) and Miocene (Agua Rica) age. Mathur et al. (2000) proposed that the low initial Os compositions may occur in deposits that are associated with deep structures, which permitted mantle-derived magmas to ascend with limited crustal interaction. Moreover, Mathur et al. (2000) noted that the older and smaller deposits (e.g., Quebrada Blanca) within the porphyry province in northern Chile had higher Os ratios than the younger, giant deposits (e.g., Chuquicamata, El Salvador). This relationship implies that the larger deposits acquired a greater proportion of Os from the mantle.

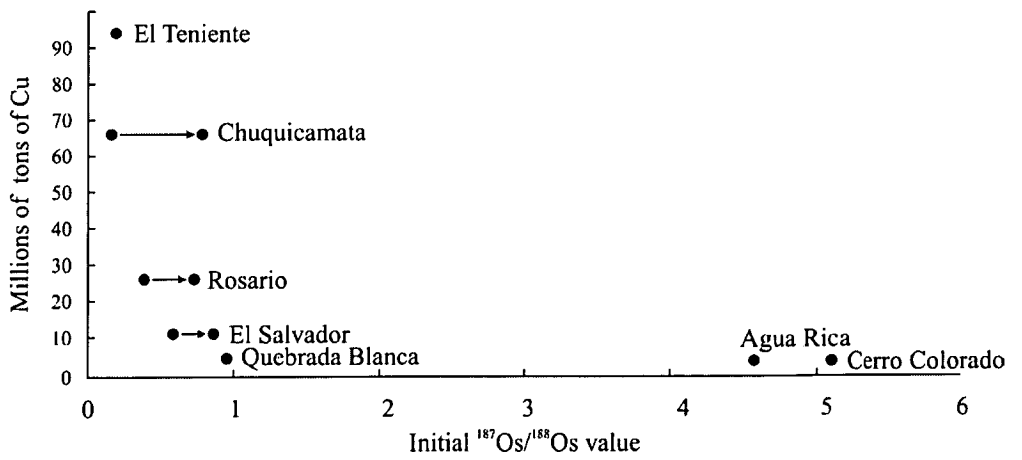

Figure 6.2. Initial $^{187}Os/^{188}Os$ values plotted against contained copper metal for the Rosario deposit. The initial $^{187}Os/^{188}Os$ values for El Teniente, Chuquicamata, El Salvador, Quebrada Blanca, Agua Rica, and Cerro Colorado are from Mathur et al. (2000). Copper tonnages are from Camus (2002).

Conclusions

Primary biotite from the mineralised and altered Rosario Porphyry cooled through its blocking temperature at 34.4 ± 0.3 Ma. Based on the vein paragenesis and alteration overprinting relationships, this age is interpreted as a minimum for porphyry ore formation at Rosario. Hypogene alunite (32.6 ± 0.3 Ma) associated with the type E massive sulfide veins at Rosario formed at the same time as alunite in type E veins at Cerro La Grande (32.7 ± 1.6 Ma). The alunite ages indicate that both systems are related to the same hydrothermal event. The Rosario $^{40}Ar/^{39}Ar$ ages record two discrete and short-lived episodes of hydrothermal activity, separated by a minimum period of 1.8 ± 0.4 m.y. Type B vein molybdenite has a Re/Os age of 33.2 ± 0.3 Ma that may have been reset by the hydrothermal fluids associated with the late hydrothermal event. Alternatively there is a second molybdenite event that possibly occurs between the early and late hydrothermal stage at Rosario. Additional dating of molybdenite and other hydrothermal minerals is required to resolve this problem.

At Ujina, the minimum age hydrothermal activity is constrained by $^{40}Ar/^{39}Ar$ age of the Inca Porphyry (34.7 ± 0.3 Ma). This age is also the minimum age of magmatism at Ujina, because there is no evidence of high-temperature alteration minerals that would have disturbed the $^{40}Ar/^{39}Ar$ systematics. The $^{40}Ar/^{39}Ar$ age of primary biotite in the Ujina Porphyry (35.2 ± 0.3 Ma) is interpreted to be the age of cooling through 350° to 300°C, and is possibly related to the formation of secondary K-feldspar-biotite or white mica alteration. Primary biotite from the La Profunda Pluton yielded an $^{40}Ar/^{39}Ar$ plateau age of 80.4 ± 3.5 Ma. This age indicates that the La Profunda Pluton is unrelated to late Eocene-early Oligocene magmatism in the Collahuasi district.

Radiogenic $^{187}Os/^{188}Os$ values in bornite and pyrite suggest a crustal contribution of rhenium to the Rosario deposit. This is consistent with the Sr, Nd and Pb isotope data (Chapter 4), implying that sub-arc magmas interacted with continental crust as they ascended to shallow crustal levels. The initial $^{187}Os/^{188}Os$ compositions of ore minerals at Rosario are similar to those reported for other giant Chilean porphyry deposits (e.g., Chuquicamata, El Teniente; Mathur et al., 2000). In general the larger deposits have less radiogenic initial $^{187}Os/^{188}Os$ compositions than smaller deposits. This implies that the giant deposits acquired more Os from the mantle than smaller deposits, which appear to contain more crustally-derived Os (e.g., Mathur et al., 2000).

Chapter 7. Fluid Chemistry

Introduction

In Chapter 6 it was concluded that a 1.8 m.y. hiatus separated the formation of porphyry-style A to C veins (± D veins) at Rosario from formation of the structurally controlled E and TES (massive sulfide) veins. In this chapter, the character and origins of the ore-forming fluids in the A, B, C, E and TES veins are assessed by fluid inclusion petrography and microthermometry, and by stable isotope geochemistry. The aim is to determine potential sources of sulphur and metals, as well as the origins of the hydrothermal fluids. These results are also used to discuss briefly whether there could be potential for gold mineralisation in the district.

Fluid Inclusion Petrography

A reconnaissance study of fluid inclusions was carried out to assess the spatial and temporal evolution of hydrothermal fluids at Rosario and La Grande. Homogenisation and final ice melting temperatures provide constraints on temperature and salinity of the hydrothermal fluids, and can be used to estimate trapping pressures. Heating and freezing measurements were made on aqueous fluid inclusions in quartz associated with each of the main vein stages at Rosario. Microthermometric data was also collected from the La Grande vein to compare the spatial variability of fluid temperature and salinity, and the depth of formation of both deposits.

Experimental Methods

Quartz containing workable fluid inclusions was sampled from diamond drill core. A total of 21 doubly polished wafers (150 μm thick) were examined petrographically, including samples from each vein stage. Ten wafers were selected for heating and freezing measurements (Appendix 3). Microthermometry, undertaken on a Linkam MDS600 heating/freezing stage, involved measurements of the temperature of liquid-vapour homogenisation, dissolution of salt daughter crystals and the final melting of ice. The Linkam stage has a maximum temperature limit of 600°C, and was calibrated using synthetic fluid inclusions supplied by Synflinc Inc., with precisions of ± 1.0°C for heating and 0.3°C for freezing. Heating and freezing measurements were made on 470 individual fluid inclusions.

Salinities of halite-undersaturated fluid inclusions, determined as NaCl equivalent weight percent (eq. wt. % NaCl), were calculated from freezing point depression temperatures (final ice melting) using the method of Potter et al. (1978). Equivalent weight percent NaCl was calculated for halite-saturated fluid inclusions by the algorithm of Sterner et al. (1988). The computer program SALTY (Bodnar et al., 1989) was used to calculate the concentrations of NaCl and KCl in fluid inclusions that contained both halite and sylvite daughter crystals.

Classification and description of fluid inclusions

Three major types of fluid inclusions, and 10 subtypes have been identified at Rosario and La Grande. These inclusions are summarised in Table 7.1. They have been classified by the number of phases present at room temperature, using the scheme of Nash (1976). Silicate melt inclusions have also been recognised.

Type Ia fluid inclusions are liquid-rich and halite-undersaturated, and homogenise by disappearance of the vapour phase (Fig. 7.1a). Type Ib fluid inclusions are also liquid-rich, but contain a small translucent daughter crystal and in places a triangular or cubic opaque phase (Fig. 7.1b).

Type II fluid inclusions are vapour-rich and homogenise by expansion of the vapour phase. They have been subdivided into type IIa and IIb fluid inclusions. Type IIa fluid inclusions contain only vapour and liquid phases at room temperature (Fig. 7.1c), whereas type IIb fluid inclusions also contain triangular or opaque minerals with or without a translucent daughter crystal (Fig. 7.1d). Type II fluid inclusions range in size from <3 to 30 μm. Those fluid inclusions <6 μm are filled almost entirely with vapour, whereas larger type II fluid inclusions usually contain a small amount of liquid.

Table 7.1. Summary of inclusion types (fluid and melt), including their morphology, phases present at 25°C, and homogenisation behaviour.

	Fluid Inclusions				Phases at 25°C			Homogenisation behaviour
	Type	Subtype	Inclusion shape	Size (μm)	Number	Dominant	Types	
Fluid inclusions	I	a	elongate, negative crystals or rounded, less commonly irregular	<5 to 50	2	liquid	liquid + vapour	vapour disappearance
		b	elongate, negative crystals or rounded, less commonly irregular	<5 to 30	3-5	liquid	liquid + vapour ± opaque ± hematite ± insoluble unknown	vapour disappearance
	II	a	stubby negative crystals, less commonly rounded	5 to 30	2	vapour	vapour + liquid	liquid disappearance
		b	stubby negative crystals, less commonly rounded	5 to 30	3-5	vapour	vapour + liquid + opaque ± hematite ± insoluble unknowns	liquid disappearance
	III	a_l	negative crystals, rounded or irregular	5 to 30	3	liquid	liquid + vapour + halite	vapour disappearance
		a_h	negative crystals, rounded or irregular	5 to 30	3	liquid	liquid + vapour + halite	salt dissolution
		b_l	negative crystals, rounded or irregular	<5 to 40	4-6	liquid	liquid + vapour + halite ± hematite ± insoluble unknown ± opaque	vapour disappearance
		b_h	negative crystals, rounded or irregular	<5 to 40	4-6	liquid	liquid + vapour + halite ± hematite ± insoluble unknown ± opaque	salt dissolution
		c_l	negative crystals, rounded or irregular	10 to 40	4-7	liquid	liquid + vapour + halite + sylvite ± hematite ± insoluble unknown ± opaque	vapour disappearance
		c_h	negative crystals, rounded or irregular	10 to 40	4-7	liquid	liquid + vapour + halite + sylvite ± hematite ± insoluble unknown ± opaque	salt dissolution
Melt inclusions			rounded or irregular	20 to 40	3-11	daughter minerals	silicate daughter minerals + shrinkage bubble ± cubic mineral (halite?) ± opaque ± liquid	did not homogenise below 600°C

Figure 7.1. Photomicrographs of fluid and melt inclusions in vein quartz from Rosario. All photos were taken under plane-polarised light. All scale bars are 20 μm.

A) *Sample R200021.* Liquid-rich Ia inclusions in quartz from an E vein.

B) *Sample R990106.* Liquid-rich Ib inclusion that contains a solid opaque mineral trapped next to type IIIb inclusions in an A-3 vein. The brine inclusion contains halite and an opaque mineral

C) *Sample R990106.* Type IIa vapour-rich inclusion from an A-3 vein showing characteristic negative crystal shape.

D) *Sample R990106.* Vapour-rich inclusion from an A-3 vein, typical of the IIb type with negative crystal shape and multiple daughter minerals. The solid orange-coloured phases hematite, the prismatic crystal is birefringent and may be anhydrite. The aqueous component of this inclusion homogenised by expansion of the bubble, even though it contains approximately 50 vol. % liquid. The presence of daughter minerals and substantial liquid suggests liquid and gas may have been heterogeneously trapped in this inclusion.

E) *Sample R200021.* Type IIIa brine inclusion from an E vein containing a single cubic salt phase identified as halite.

F) *Sample R990106.* Brine inclusion from an A-3 vein characteristic of type IIIc. It contains multiple daughter crystals identified as halite, sylvite and an opaque phase.

G) *Sample R990106.* Example of a melt inclusion in vein quartz from an A-3 vein, containing multiple anisotropic silicate phases, hematite, chalcopyrite and a shrinkage bubble. All phases quenched to homogeneous silicate glass after the inclusion was heated overnight at 800°C. The appearance of two shrinkage bubbles, when quenched, confirms that this was a silicate melt inclusion (V. Kamanetsky, pers. comm., 2003).

H) *Sample R990106.* Another example of a melt inclusion contained in vein quartz from an A-3 vein. This inclusion comprises multiple anisotropic silicate phases, and also contains an aqueous solution and vapour bubble. It is interpreted that the liquid and vapour was exsolved in situ, but may it have been trapped heterogeneously (V. Kamanetsky, pers. comm., 2003).

Abbreviations. A = anisotropic daughter mineral, Cpy = chalcopyrite, H = halite, Hm = hematite, L = liquid, O = opaque, S = sylvite, SB = shrinkage bubble, V = vapour.

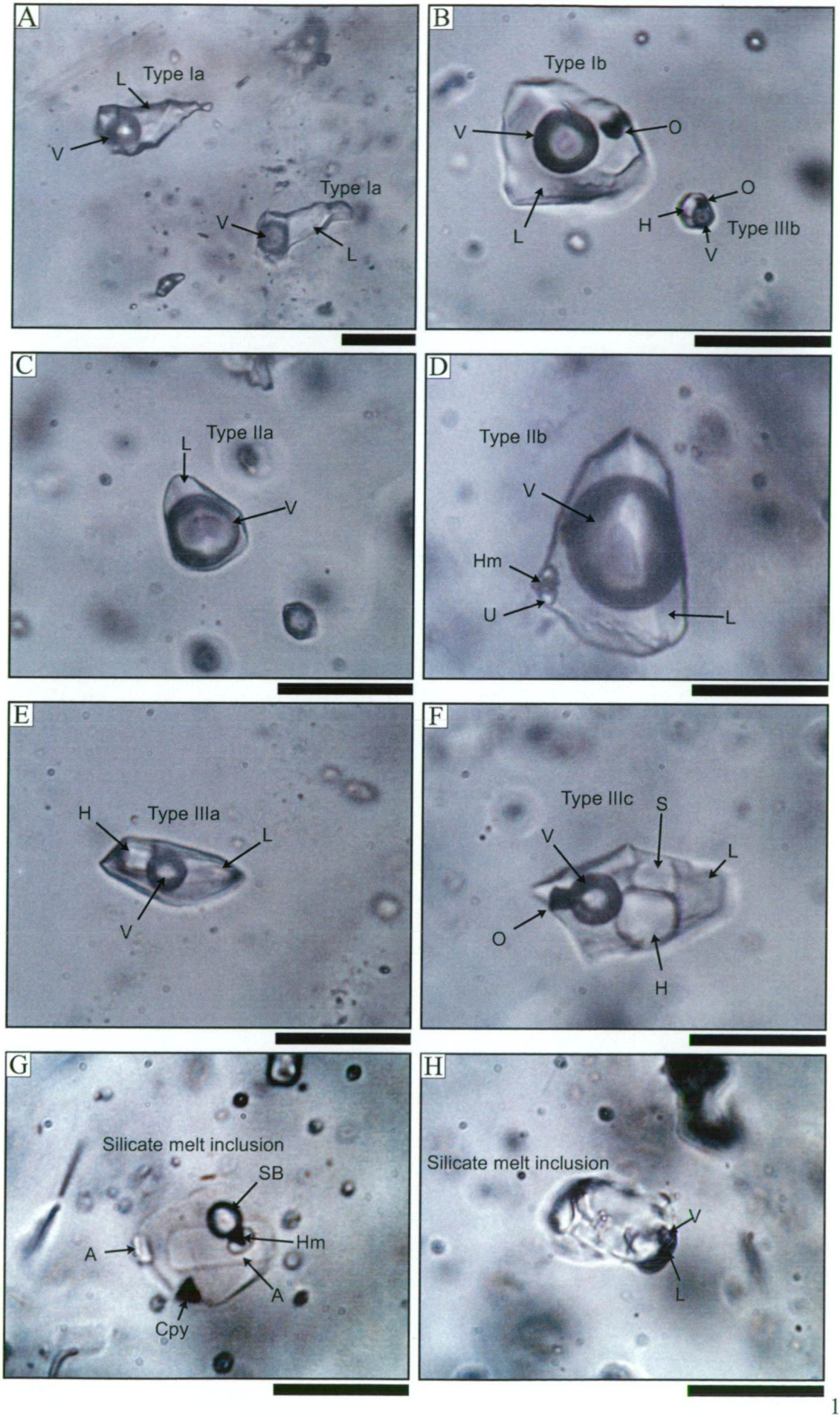
A
L
Type Ia
V
Type Ia
V
L
B
Type Ib
V
O
O
H
Type IIIb
L
V
C
L
Type IIa
V
D
Type IIb
V
Hm
U
L
E
H
Type IIIa
L
V
F
Type IIIc
S
V
L
O
H
G
Silicate melt inclusion
SB
Hm
A
A
Cpy
H
Silicate melt inclusion
V
L

Type III fluid inclusions are halite-saturated and homogenise either by disappearance of the vapour phase (Tv→l) or dissolution of the halite daughter crystal (Ts halite). These fluid inclusions are subdivided into types IIIa, IIIb and IIIc, based on the quantity and type of daughter minerals present. Type IIIa fluid inclusions contain only a single soluble daughter mineral (halite; Fig. 7.1e), whereas those that contain halite plus one or more insoluble daughter minerals are defined as type IIIb. Type IIIc contain halite and sylvite, as well as multiple insoluble daughter minerals (Fig. 7.1f). In all type IIIc inclusions, rounded sylvite crystals are smaller and dissolve at lower temperatures than halite. Insoluble daughter phases contained in type IIIb and IIIc fluid inclusions are triangular (chalcopyrite?) and cubic (pyrite?) opaque minerals with or without hexagonal platelets of hematite opaque minerals. In addition, translucent prisms, with high relief and moderate birefringence, thought to be anhydrite, also occur in type IIIb and IIIc fluid inclusions.

Silicate melt inclusions have been recognised in quartz from some A-3 veins within the Rosario Porphyry (V. Kamanetsky, pers. comm., 2003; Figs. 7.1g and 7.1h). These melt inclusions are typically rounded or irregular, but may have negative crystal shapes. They all contain a single shrinkage bubble and multiple silicate daughter crystals. Accessory phase assemblages include isotropic cubic minerals that may be halite, as well as translucent birefringent prisms (anhydrite?), pleochroic brown plates (biotite?) and hematite. Some melt inclusions contain a small amount of aqueous fluid and a vapour bubble (Fig. 7.1h).

Distribution of fluid inclusions

The major veins in the Rosario deposit are interpreted to have formed by episodic re-opening and filling during the evolution of the ore-forming system. All of the quartz veins have experienced repeated fracturing in the presence of an aqueous fluid, as indicated by crack-seal textures and the abundant planes of secondary fluid inclusions observed at low magnification. This has resulted in complex overlapping of various fluid inclusion populations, so it is almost impossible to establish convincing age relationships amongst the different fluid inclusions within any single vein of quartz. For this reason, fluid inclusions have not been classified as primary, secondary or pseudo-secondary. Instead, a method of relating groups of fluid inclusions to the various stages of vein development, based on the detailed paragenesis in Chapter 5 and similar to those outlined by Bodnar and Beane (1980) and Bloom (1981), has been

adopted to deduce the sequence of fluids which deposited quartz and associated ore minerals.

Type I fluid inclusions are observed in every vein stage at Rosario, and are also present in the E/TES (massive sulfide) veins at La Grande. Low density type II fluid inclusions are most abundant in A-2 and A-3 veins, but small quantities also occur in B and E veins. Type III saline and hypersaline brine fluid inclusions occur mainly in the A-2 and A-3 vein stages where they coexist with the type I and II fluid inclusions. The abundance of type II fluid inclusions in A-2 and A-3 veins exceeds, by an order of magnitude, that of type III fluid inclusions which homogenise by vapour disappearance. By contrast, 75% of all type III fluid inclusions in A-2 and A-3 veins homogenised by halite dissolution. Type III fluid inclusions also occur in milky quartz within E veins.

Fluid inclusion populations

Veins stages are summarised in Figure 5.2 and Table 5.2. Each vein stage contains a discrete population of fluid inclusions, summarised in Table 7.2. Population A-2, comprising type IIa + IIb +IIIa + IIIb + Ia + Ib inclusions, occurs in the A-2 veins. The two samples (*R990007 and R990124*) containing inclusions of the A-2 population are from the biotite-magnetite-albite zone on the northeast side of the Rosario Porphyry (Fig. 7.2). Population A-3 consists of inclusion types IIa + IIb + IIIa + IIIb + IIIc + Ia + Ib, and is restricted to A-3 veins. Three samples containing the A-3 population were collected from different depths in the zone of K feldspar alteration. Two samples (*R990106* and *R990108*), are from deep levels in the K feldspar-altered Rosario Porphyry. The other sample (*R990085*) is from the Collahuasi Porphyry, in which K feldspar has replaced biotite-magnetite-albite alteration (Fig. 7.2).

Table 7.2. Summary of fluid inclusion populations in porphyry-type veins, listed with the corresponding vein stage and alteration assemblage in the Rosario deposits.

Vein stage	Vein mineralogy	Alteration assemblage	Population	Inclusion types	T_h[1] min to max (°C)	Model T_h[2] (°C)	Ts sylvite[3] min to max (°C)	Model Ts sylvite[2,3] (°C)	Ts halite min to max (°C)	Model Ts halite[2,3] (°C)	Salinity min to max (eq. wt. % NaCl)	Salinity mean (eq. wt. % NaCl)
Porphyry-type veins												
A-2	qtz-alb-bi-cp-py	Bi-alb	A-2	IIa + IIb	385 to > 600	493 to >600	-	-	-	-	1.8 to 18.9	10.8
				$IIIa_h$ + $IIIb_h$	158 to 298	241 to 298	-	-	246 to 497	359 to 497	34.4 to 59.3	44.1
				Ia + Ib	320 to 524	426 to 524	-	-	-	-	13.0 to 25.2	17.7
				$IIIa_l$ + $IIIb_l$	260 to 433	333 to 433	-	-	149 to 401	285 to 401	29.7 to 47.6	37.9
A-3	qtz-K-fsp-bn-cp	K-fsp	A-3	IIa + IIb	369 to > 600	500 to >600	-	-	-	-	3.3 to 21.4	12.3
				$IIIa_h$ +$IIIb_h$ + $IIIc_h$	124 to 449	256 to 449	52 to 374	103 to 374	215 to 593	354 to 593	33.0 to 73.0	45.3
				$IIIa_l$ + $IIIb_l$	223 to 539	326 to 539	56 to 136	96 to 136	171 to 460	263 to 460	31.0 to 55.0	37.3
				Ia + Ib	203 to 451	317 to 451	-	-	-	-	1.2 to 25.6	14.5
				IV	336 to 490	425 to 490	-	-	-	-	-	-
B	qtz-K-fsp-ill-mo	(K-fsp-ill)	B	Ia + Ib	261 to 408	349 to 408	-	-	-	-	1.3 to 23	8.5
				IIa	342 to 457	407 to 457	-	-	-	-	2.7 to 7.7	5.2
C	qtz-cp-py-illite-chlorite	Ill-chl	C	Ia + Ib	153 to 408	245 to 408	-	-	-	-	3.1 to 23	15.8
Polymetallic veins												
E	py-bn-cp-cc-qtz	qtz-alun-dias	E	Ia + Ib	153 to 453	353 to 453	-	-	-	-	1.7 to 23.0	12.8
				IIa	404 to 484	436 to 484	-	-	-	-	4.5 to 12.5	8.6
				$IIIa_h$ + $IIIb_h$	189 to 246	213 to 246	-	-	242 to 310	278 to 310	34.2 to 38.9	36.7
				$IIIa_l$ + $IIIb_l$	250 to 347	293 to 347			149 to 221	175 to 221	29.6 to 33.0	30.8
TES			TES									
Rosario	tn-en-qtz	prl-dick		Ia + Ib	195 to 364	269 to 364	-	-	-	-	0.7 to 22.2	6.1
La Grande	en-qtz	prl-dick		Ia + Ib	236 to 342	297 to 342	-	-	-	-	0.7 to 6.8	3.5

[1] T_h = temperature of vapour bubble disappearance in type I and type III fluid inclusions, or temperature of complete vapour bubble expansion in type II fluid inclusions
[2] Model temperature is taken as the range from the mean to maximum homogenisation temperature for a fluid inclusion type in a given sample
[3] Ts = temperature of salt dissolution

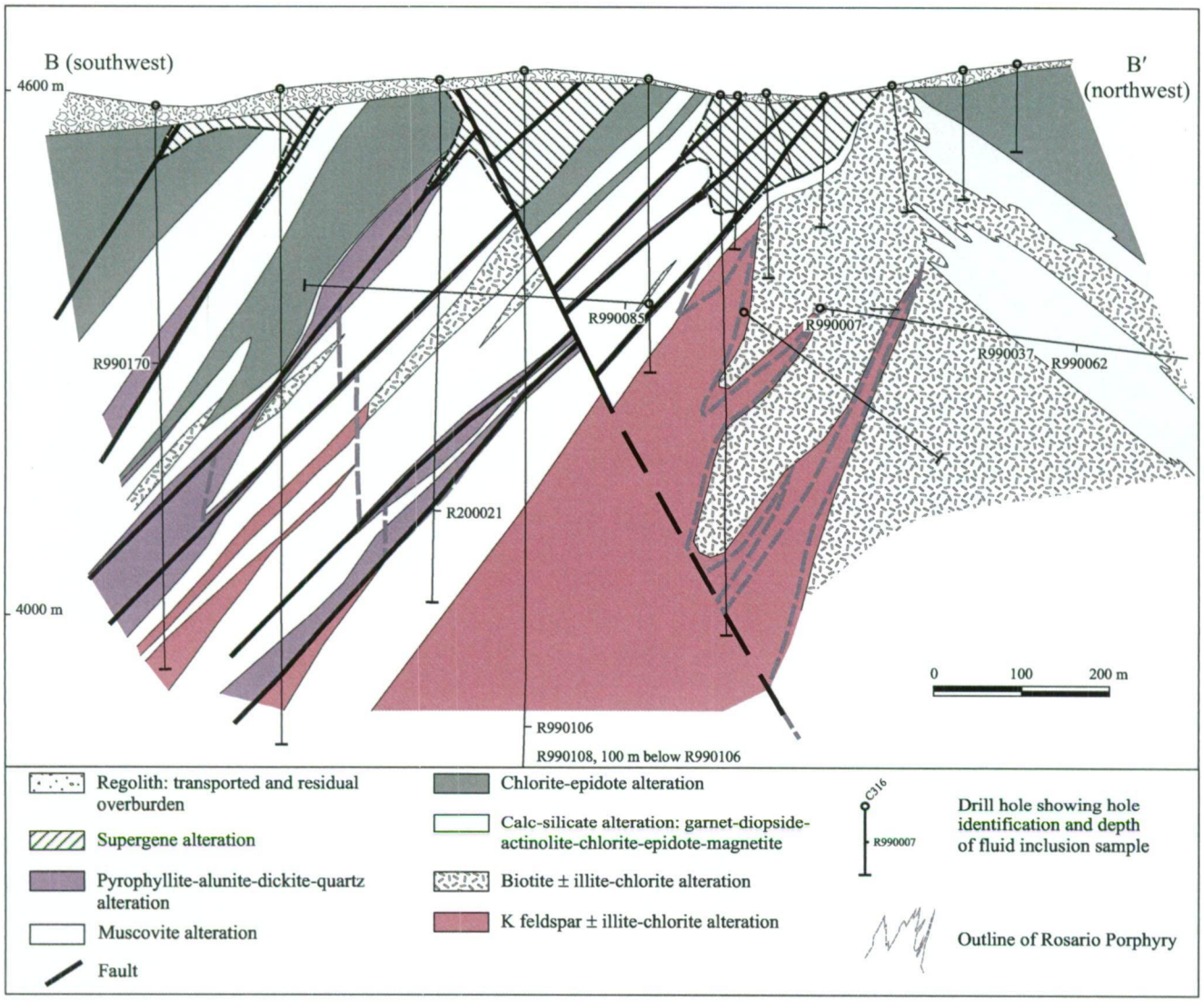

Figure 7.2. Northeast alteration section through the Rosario deposit showing the localities of the fluid inclusion samples. Refer to Figure 3.1 for section locality.

Population B contains type Ia + Ib + IIa inclusions present in molybdenite-bearing B veins (sample *R990108*, Fig. 7.2). Population C inclusions, comprising type Ia + Ib inclusions (sample *R990085*), occur in C veins associated with the illite-chlorite assemblage. Quartz gangue associated with the pyrite-bornite-chalcopyrite-chalcocite (E) veins contain type Ia + Ib + IIIa + IIIb + IIa fluid inclusions. These fluid inclusions constitute the E population in samples *R990170* and *R200021* (Fig. 7.2). Sample *R990037* also contains E population fluid inclusions in an E vein that has cut biotite-magnetite-albite altered andesite. Tennantite-enargite stage (TES) population contain type Ia and Ib fluid inclusions in quartz gangue associated with the tennantite-enargite veins at Rosario (sample *R200021*). This population also occurs in enargite veins at La Grande (*samples R990299* and *R990324* from 4,280 m and 3,880 m elevation, respectively).

Microthermometry

A veins

Thermometric data for the A veins is presented in Figures 7.3a to 7.3c and is listed in Appendix 3. Data for the A-2 population have been merged with that from the A-3 veins in Figure 7.3, as both generations are broadly contemporaneous and encompass similar trapping conditions and fluid compositions. Fluid inclusions in the A-2 veins homogenise between 246°C and >600°C, with 65% of all fluid inclusions homogenising at temperatures >400°C (Table 7.2). Type IIa and IIb fluid inclusions have the highest apparent homogenisation temperatures (385° to >600°C), although these may be 150° to 300°C below their real homogenisation temperature owing to difficulty associated with observing the final disappearance of the liquid (Bodnar et al., 1985). This problem arises because a film of liquid may still be present on the wall of the fluid inclusion when it appears to have homogenised (Bodnar et al., 1985; Sterner, 1992). The salinities of vapour-rich fluid inclusions ranged from 1.8 to 18.9 eq. wt. % NaCl (Fig. 7.3c).

Most hypersaline brine fluid inclusions homogenised by halite dissolution, although 40% of type III fluid inclusions homogenised by vapour disappearance. Final homogenisation temperatures, either by vapour disappearance or halite dissolution, ranged from 255° to 497°C, and averaged 350°C (Fig. 7.3b and Table 7.2). Salt dissolution temperatures for type III fluid inclusions ranged between 246° to 497°C, corresponding to calculated salinities of 34.4 to 59.3 eq. wt. % NaCl (average of 41.7

eq. wt. % NaCl; Fig. 7.3c). Liquid-rich type I fluid inclusions have a salinity range of 13 to 25.2 eq. wt. % NaCl, and homogenise from 320° to 524°C (426°C average temperature).

A-3 veins contain abundant vapour rich fluid inclusions that homogenise between 369° to >600°C (Table 7.2), although the actual temperatures of homogenisation could be up to several hundred degrees higher, as discussed above. Salinities of the type II fluid inclusions vary from 3.3 to 21.4 eq. wt. % NaCl (Fig. 7.3c). These temperatures correspond with a small number of type III inclusions that homogenise by vapour disappearance between 447° and 539°C (Fig. 7.3a). Most of the type III fluid inclusions (79%) in A-3 veins homogenise by halite dissolution, with a bimodal temperature distribution; 215° to 300°C and 340° to 480°C. These dissolution temperatures indicate salinities of 33 to 73 eq. wt. % NaCl (mean = 45.3 eq. wt. % NaCl; Fig. 7.3c). Some type IIIc inclusions are present, with KCl concentrations that range from 12.7 to 19 wt.% KCl and Na/(Na + K) atomic values of 0.68 to 0.75. The total salinities of type IIIc fluid inclusions range from 43.4 to 72.8 eq. wt. % NaCl + KCl. Liquid-rich type Ia and Ib fluid inclusions occur in the same quartz grains as vapour-rich (type II) and hypersaline brine (type III) inclusions, and show variable homogenisation temperatures and salinities that range from 203° to 451°C and 1.2 to 25.6 eq. wt. % NaCl, respectively (Table 7.2, Figs. 7.3b and 7.3c).

B veins

Population B fluid inclusions, characterised by inclusion types I and II, homogenise between 261° and 457°C (Table 7.2, Figs. 7.3d and 7.3e; Appendix 3), with 60% of fluid inclusions homogenising at temperatures >350°C. The highest temperature liquid-rich fluid inclusions (>340°C) overlap the homogenisation temperatures of coexisting vapour-rich fluid inclusions, which vary from 342° to 457°C. Salinities of the type I and II fluid inclusions range from 1.3 to 23 and 2.7 to 7.7 eq. wt. % NaCl, respectively (Fig.7.3f).

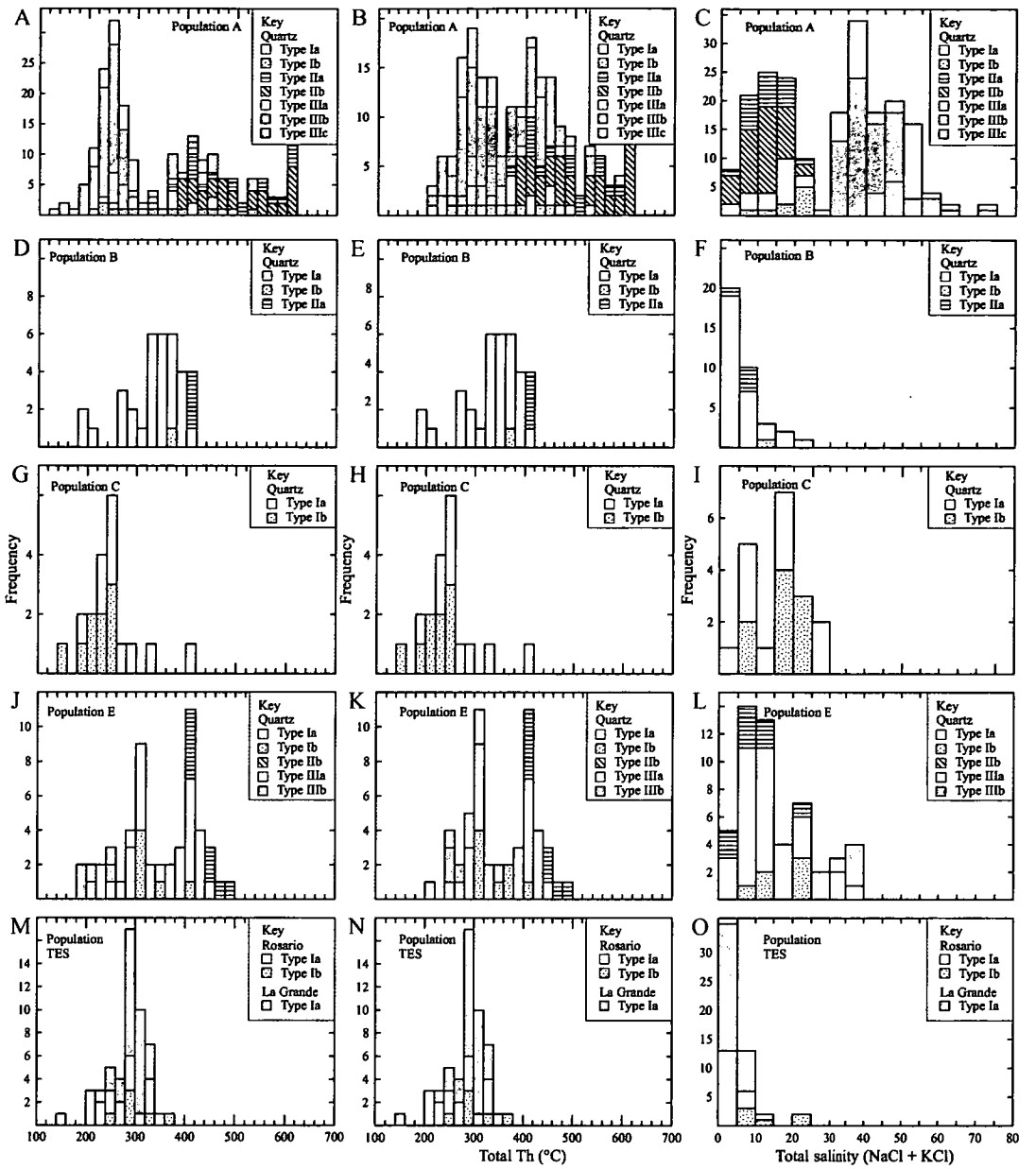

Figure 7.3. Summary of microthermometric data for the various fluid inclusions populations. They are grouped across the page by population-type and ordered down the page from the earliest formed fluid inclusions (A veins) to those that formed last (TES veins). Histograms down the left hand column summarise vapour to liquid homogenisation temperatures for type I and type III inclusions. Homogenisation temperatures of type II inclusions are the temperatures of homogenisation to the vapour phase. The centre column shows total homogenisation temperature by either vapour to liquid, liquid to vapour, or by halite dissolution, whichever occurred last. The right hand column depicts the salinities of all fluid inclusions, calculated either by final ice melting temperature (e.g., for the liquid and vapour-rich inclusions) or by halite dissolution temperature (e.g., for the brine inclusions). **A to C)** Populations A-2 and A-3. **D to F)** Population B. **G to I)** Population C. **J to L)** Population E. **M to O)** Population TES

C veins

Type I fluid inclusions in C veins homogenise between 153° and 400°C, although 90% of the data are between 200° and 300°C (Table 7.2, Figs. 7.3g to 7.3h; Appendix 3). Calculated salinities range from 3.1 to 23 eq. wt. % NaCl, and average 15.8 eq. wt. % NaCl (Fig. 7.3i), with 63% of analyses falling between the mean and maximum values (15.8 to 23 eq. wt. % NaCl).

E veins

Population E fluid inclusions in quartz gangue associated with pyrite-bornite-chalcopyrite massive sulfide veins homogenise between 153° and 453°C, with two discrete populations occurring between 200° to 320°C (mode 300°C) and 360° to 440°C (mode 400°C; Figs. 7.3j and 7.3k; Appendix 3). Calculated salinity values for type I and II fluid inclusions vary from 1.7 to 23.0 eq. wt. % NaCl, and have a mean of 12.8 eq. wt. % NaCl (Fig. 7.3l). The small number of type III fluid inclusions homogenise predominantly by halite dissolution between 149° and 314°C, indicating salinities of 29.6 to 39.3 eq. wt. % NaCl. The high temperature (360° to 440°C) distribution of type I fluid inclusions overlaps homogenisation temperatures of the type II fluid inclusions (400° to 500°C), whereas the lower temperature population (200° to 340°C) corresponds with those of liquid-rich fluid inclusions in the TES veins.

TES veins

TES population fluid inclusions occur in quartz associated with tennantite-enargite mineralisation at Rosario, and homogenise between 155° and 364°C. About 85% of these fluid inclusions homogenise between 220° and 320°C (270°C mean homogenisation temperature; Figs. 7.3m and 7.3n; data in Appendix 3). Calculated salinities are between 0.7 and 22.2 eq. wt. % NaCl, with an average of 6.1 eq. wt. % NaCl (Fig. 7.3o). At La Grande, TES inclusions that occur in samples at 3,880 m elevation, homogenise on average at 320°C (± 20°C). By contrast, quartz-hosted fluid inclusions from 4,280 m elevation have a mean homogenisation temperature of 280°C (± 30°C). Calculated salinities range from 0.7 to 6.8 eq. wt. NaCl in both samples.

Discussion of Fluid Inclusions Results

Temperature variation with time

Fluid inclusion populations in all vein stages at Rosario show a wide range of homogenisation temperatures, but the spread is more restricted in the TES veins than in the earlier veins. Previous studies of fluid inclusions in porphyry ore deposits have encountered similar spreads in homogenisation temperatures within individual populations. For example, Losada-Calderón (1992) noted temperature variations of up to 75°C in single samples in early-stage veins from the Nevados del Famatina porphyry Cu-Au deposit in northwest Argentina. By contrast, the temperature range was restricted to 25°C in the late stage veins. Wide ranges of homogenisation temperatures have also been noted at Red Mountain, Arizona (Bodnar and Beane, 1980), Questa, New Mexico (Bloom, 1981; Cline and Vanko, 1995), Santa Rita, New Mexico (Ahmad and Rose, 1980; Reynolds and Beane, 1985), Dinkidi, Philippines (Wolfe, 2001), as well as in the barren porphyry-style K silicate altered intrusive centre at Palinpinon in the Philippines (Rae, 2002).

At Rosario, the fluid inclusions analysed showed no evidence of natural leakage, so necking is not considered to have caused the wide range in homogenisation temperatures (e.g., Ahmad and Rose, 1980). Fluid inclusion populations in the A-2 and A-3 veins, which show the greatest temperature variability, include a small number of liquid-rich fluid inclusions that occur with the type II and type III inclusions (Figs. 7.4a). In both populations, these type I inclusions have salinities and temperatures similar to those in subsequently formed populations, implying that all liquid-rich fluid inclusions may be related to fluids that formed the later veins (e.g. Reynolds and Beane, 1985).

Although the measured temperature ranges are large, average homogenisation temperatures decrease from the A-2 and A-3 to the B and C populations (Figs. 7.3 and 7.4). The low temperature distribution of type I, II and III fluid inclusions is common in both the A-2 and A-3 populations (Fig. 7.4a), and may be related to cooling of the hydrothermal fluids. Alternatively, these fluid inclusions may have formed from fluids that generated the E and TES populations, as the distribution of homogenisation temperatures is similar. High homogenisation temperatures (>400°C) and the presence of multiple salt, silicate and sulfide daughter minerals in type III inclusions in A veins is interpreted as evidence that the fluids were magmatic-hydrothermal in origin.

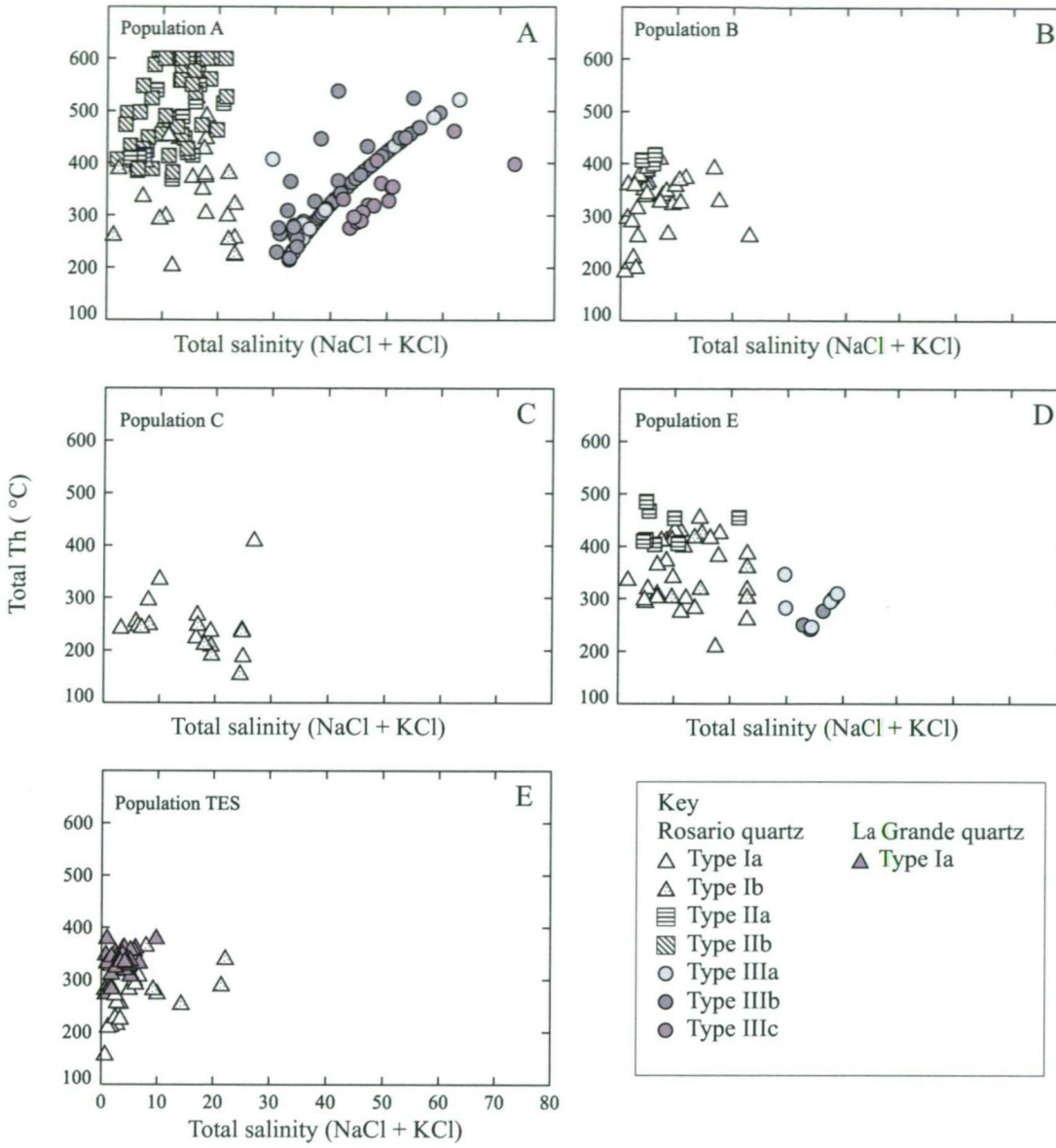

Figure 7.4. Comparative plots of total homogenisation temperature vs. salinity for inclusions in each of the populations. **A)** Populations A-2 and A-3. **B)** Population B. **C)** Population C. **D)** Population E. **E)** Population TES.

The model temperature range of the B population occurs between 350° and 410°C (Fig. 7.4b), and is on average cooler than those of the A-2 and A-3 populations, in which the entire populations range between 430° and >600°C, and 380° and >600°C, respectively. Type I fluid inclusions in C veins homogenise between 200° and 300°C (Fig. 7.4c), temperatures cooler than those associated with A and B veins.

Fluid inclusion homogenisation temperatures in E veins exhibit a bimodal distribution (Figs. 7.3j and 7.3k). The high temperature type II inclusions occur in quartz associated with alunite, pyrite and diaspore. Type I and type III inclusions define the low temperature distribution. The type III inclusions occur in quartz gangue associated with the type E massive sulfides. However, they have not been observed in the TES veins. The low temperature type I inclusions correspond with homogenisation temperatures in the TES population. Thus, it is inferred that the low temperature type I inclusions are related to formation of the TES veins, and have overprinted type II and type III inclusions in E veins. The same E vein populations can be discriminated in the temperature-salinity diagram in Figure 7.4d.

Temperature variation in space

The spatial variation of fluid temperatures was evaluated for the early-stage A veins and late-stage E veins (Fig. 7.5). Average homogenisation temperatures for A-3 population fluid inclusions are higher in veins sampled deep in the Rosario Porphyry, relative to those in quartz sampled higher in the intrusion and surrounding country rock. In the core of the Rosario Porphyry (3,750 m elevation), the temperature overlap between type II and III fluid inclusions in A veins is 390° to 450°C. Samples collected from an elevation of 3,850 m have a temperature overlap between 430° and 540°C (Fig. 7.5). At higher elevation (4,360 m), the temperature overlap in A veins is 370° to 450°C.

In the E veins, homogenisation temperatures of type I fluid inclusions vary with elevation relative to the main trend of the Rosario Fault System. For example, liquid-rich fluid inclusions in quartz from E veins in the Rosario fault system vary from 390° to 450°C at 4,100 m elevation (Fig. 7.5). The temperatures range from 320° to 420°C temperatures up dip in another fault strand. In the footwall, temperatures decrease away from the Rosario Fault System. For example, 200 m northeast of the fault at 4,100 m elevation, the temperature varies between 360° and 430°C. Two hundred metres further northeast, the temperatures are marginally lower (between 340° and

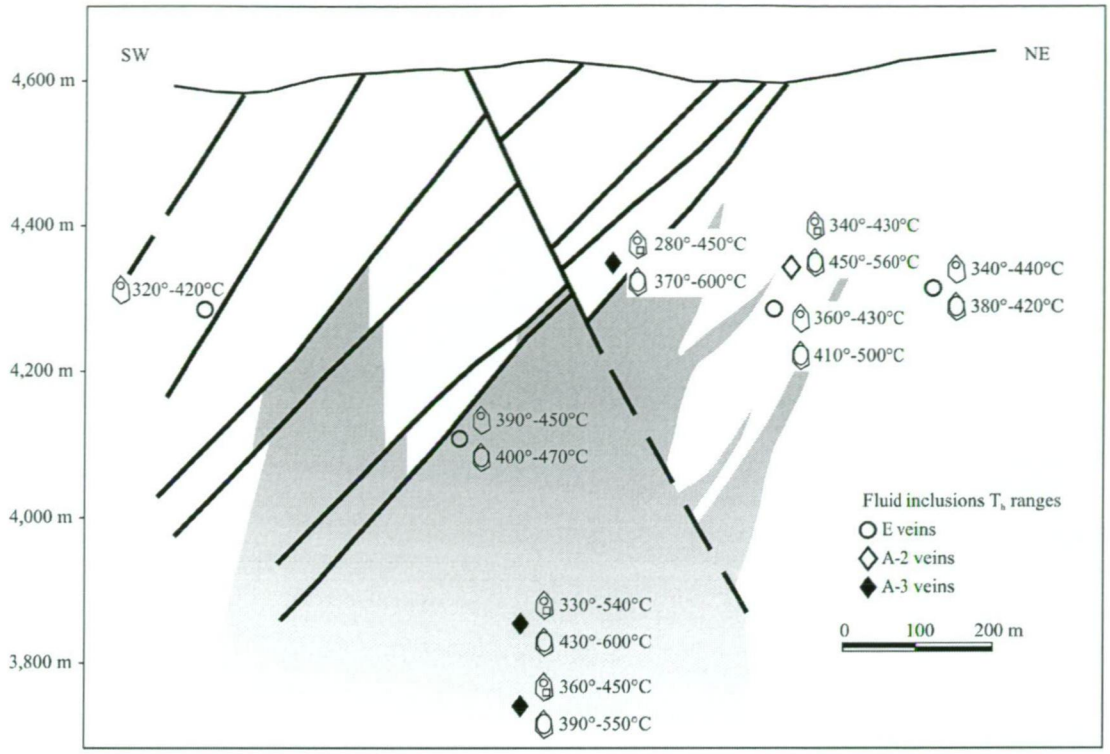

Figure 7.5. Northeast-southwest alteration section through the Rosario deposit (see Fig. 3.1 for section locality) showing spatial distribution of fluid inclusions from the boiling population in four samples of A veins, and homogenisation temperatures of inclusions in four E vein samples.

440°C). Type II inclusions in E veins overlap the highest temperature type I inclusions, suggesting that the fluids may have coexisted at these temperatures.

Evidence of phase separation

Microthermometric measurements have revealed that hypersaline brine (25 to 78 eq. wt. % NaCl) and low salinity vapour (0 to 23 eq. wt. % NaCl) were present in A and E veins at the time of trapping (Figs. 7.3c and 7.3l). In A-2 and A-3 veins, a small number of type III inclusions homogenise by disappearance of the vapour bubble at the same homogenisation temperatures measured for coexisting low-density vapour-rich (type II) fluid inclusions (Fig. 7.4a). That type II and III fluid inclusions (Figs 7.6a and 7.6b) coexist over the same range of temperatures implies that brines and gases were present as separate phases when A vein quartz precipitated.

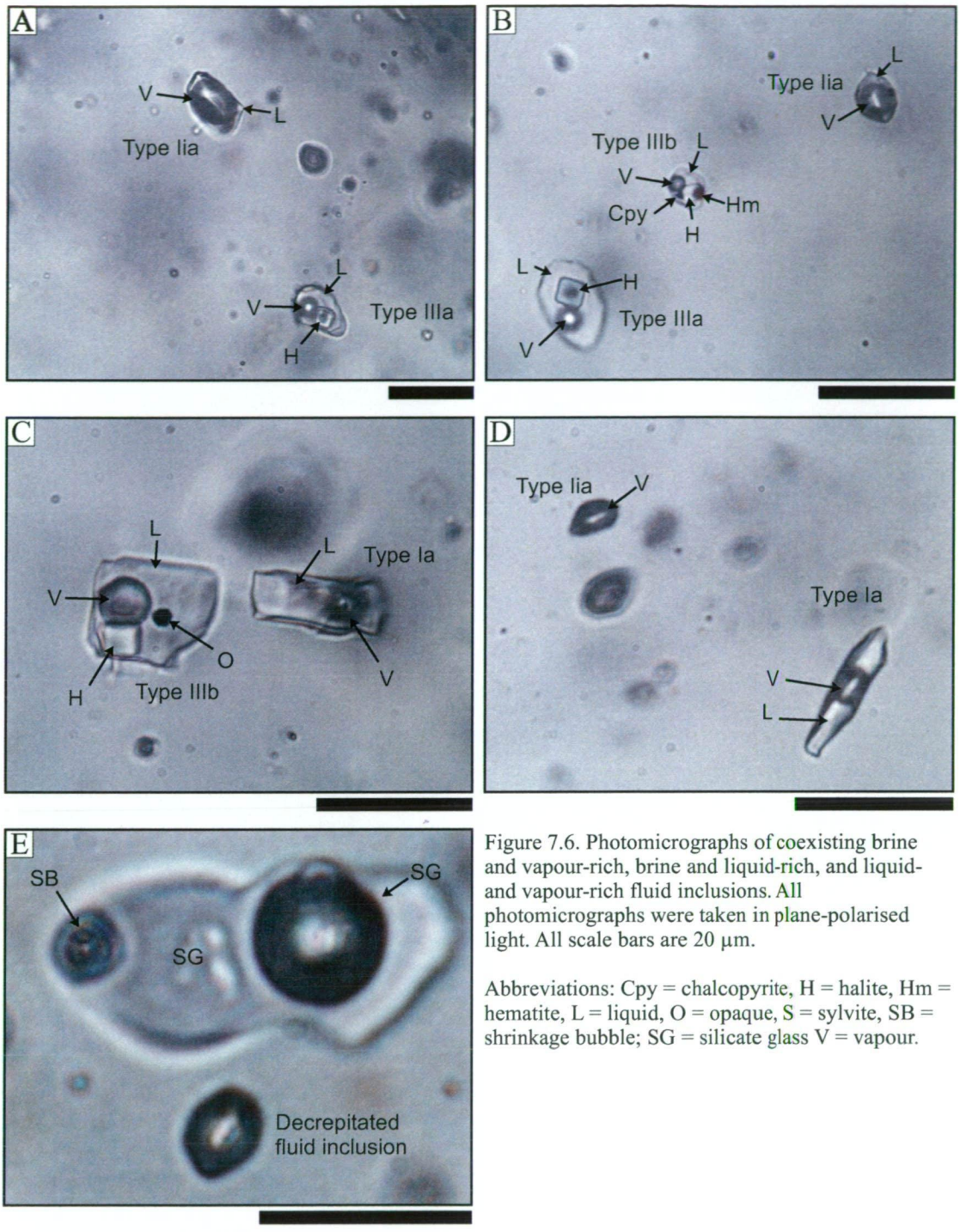

Figure 7.6. Photomicrographs of coexisting brine and vapour-rich, brine and liquid-rich, and liquid- and vapour-rich fluid inclusions. All photomicrographs were taken in plane-polarised light. All scale bars are 20 μm.

Abbreviations: Cpy = chalcopyrite, H = halite, Hm = hematite, L = liquid, O = opaque, S = sylvite, SB = shrinkage bubble; SG = silicate glass V = vapour.

A) Sample R990106. Type IIa and IIIb quartz-hosted fluid inclusions in an A-3 vein. **B)** Sample R990106. Type IIa, IIIa and IIIb fluid inclusions in an A-3 vein. **C)** Sample R990106. Coexisting type IIIb and Ia inclusions in quartz from an A-3 vein. **D)** Sample R200021. Type Ia and IIa inclusions in quartz from an E vein. **E)** Two phase melt inclusion of silicate glass and two shrinkage bubbles. The melt inclusion was photographed after a 12 hour heating experiment at 800°C. The two shrinkage bubbles are typical of silicate melt inclusions that have been quenched after melting. Note the decrepitated fluid inclusion beneath the melt inclusion.

Coexisting vapour-rich and brine fluid inclusions have been reported in other porphyry ore deposits such as Panguna (Eastoe, 1978), Santa Rita (Reynolds and Beane, 1985), Acupan South (Cooke and Bloom, 1990), Far Southeast (Hedenquist et al., 1998), Pancho (Muntean and Einaudi, 2000) and Bajo de la Alumbrera (Ulrich et al., 2001). Such fluid inclusions have been interpreted to be the product of physical separation of magmatic-derived fluid into a low density vapour and a high density brine (Roedder, 1984; Bodnar et al., 1985; Bodnar, 1995), volumetrically dominated by the low density phase (Candela, 1991). This is consistent with the paucity of type III fluid inclusions that homogenise by vapour disappearance in A-2 and A-3 veins, compared with the abundant coexisting vapour-rich fluid inclusions. Liquid-rich type I fluid inclusions in A-2 and A-3 fluid inclusion populations may have formed by condensation of the low density phase into the brine, following initial phase separation of the magmatic fluid, as predicted by Roedder (1984). Alternatively, they may also be the result of a secondary generation of dilute groundwaters that have overprinted the brine and gas population.

Salinity variations

Salinities of type II fluid inclusions vary markedly in the early-stage A-2 and A-3 veins (Figs. 7.3c and 7.4a), which is consistent with the results of experimental studies on synthetic vapour rich fluid inclusions conducted by Bodnar et al. (1985). They asserted that the vapour-rich fluid inclusions heterogeneously trapped a small amount of high salinity liquid which resulted in the range of salinities calculated from freezing point depression measurements. Vapour-rich fluid inclusions with the lowest salinities are inferred to be inclusions that trap the least amount of liquid. Bodnar et al. (1985) concluded that the lowest salinity measured in vapour-rich fluid inclusions should closely approximate the concentration of salts in the low density phase. Phase ratios in type II fluid inclusions are not constant at room temperature (degree of liquid fill varies from 0.4 to 0.7), which suggests, but does not prove, that some (or all) of the vapour-rich fluid inclusions in these veins trapped a small amount of liquid together with the vapour.

Halite homogenising fluid inclusions

Fluid inclusions that homogenise by halite dissolution exhibit a wide range of homogenisation temperatures and salinities, and constitute ~75% of type III fluid inclusions in A-2 and A-3 veins. Brine fluid inclusions that homogenise by dissolution

of halite cannot be trapped in equilibrium with a vapour phase in the H_2O-NaCl system (Roedder and Bodnar, 1980; Bodnar, 1994). Instead, phase equilibria constraints require that halite-homogenising fluid inclusions be trapped in the liquid-stable, vapour-absent field (Fig. 7.7). Therefore, if these dense brines formed by aqueous fluid immiscibility, the brine must have been physically separated from the vapour phase, as they cannot have coexisted at the time of trapping (Cline and Vanko, 1995; Muntean, 1998). Alternatively, these brines were exsolved directly from the crystallising intrusion under high pressure (e.g., Wilson et al., in press).

Fluid inclusions that homogenise by halite dissolution have been documented in many porphyry deposits (e.g., Panguna, Eastoe, 1978; Red Mountain, Bodnar and Beane, 1980; Hudson Bay Mountain and Endako, Bloom, 1981; Santa Rita, Reynolds and Beane, 1985; Acupan South, Cooke and Bloom, 1990;Yerington, Dilles and Einaudi, 1992; Questa, Cline and Vanko, 1995; Casale Hill and Cavancha, Muntean and Einaudi, 2000; Bajo de la Alumbrera, Ulrich et al., 2001; Ridgeway, NSW, Wilson et al., in press). Several mechanisms have been advanced to explain the formation of halite-homogenising fluid inclusions. For example, Eastoe (1982), and Richards and Kerrich (1993) proposed that halite crystals were trapped as accidental solid inclusions with fluids in the liquid-vapour stable field. By contrast, Eastoe (1978) and Audetát and Günther (1999) concluded that post-entrapment modification of fluid inclusions (e.g., water loss) was responsible for the presence of a salt crystal above the liquid-vapour homogenisation of many brine fluid inclusions.

Post-entrapment modification of fluid inclusions in quartz veins at Rosario is one possible way of generating halite-homogenising fluid inclusions, particularly as some of these occurred within the same plane as the fluid inclusion that constitute the "boiling population" (e.g., the vapour-rich fluid inclusions that coexist with brines that homogenise by vapour disappearance). Some hypersaline brine fluid inclusions that coexist with vapour-rich fluid inclusions in quartz from the Mole Granite, Australia, were found to homogenise by halite dissolution, whereas others homogenised by vapour disappearance. The halite homogenising fluid inclusions were interpreted to have either lost H_2O or were deformed after entrapment. Hypersaline brine inclusions that homogenised via dissolution of halite in the Mole Granite quartz exhibited sweat halos and appeared to have migrated away from the trails (Audetát and Günther, 1999).

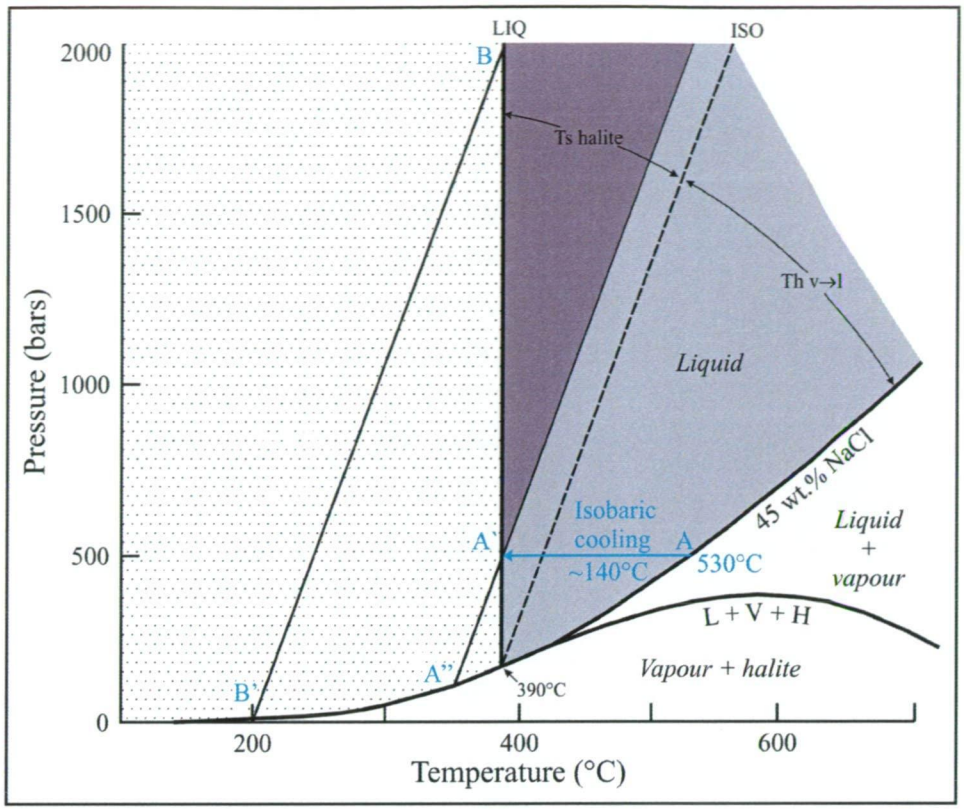

Figure 7.7. Pressure-temperature diagram illustrating trapping conditions in the NaCl-H_2O system, from 100° to 700°C for a 45 wt.% fluid, based on data of Bodnar (1994), Cline and Bodnar (1994), and Cline and Vanko (1995). The liquid to vapour curve (L-V) separates the stability field for liquid + vapour and liquid; liquid-vapour-halite curve (L-V-H) separates stability fields for liquid + vapour and vapour + halite; liquidus (LIQ) separates stability fields for liquid + halite and liquid. An isochore (ISO) divides the liquid stable field into two regions; inclusions trapped on the high temperature side of the isochore (Th v→l) will exhibit final homogenisation to the liquid; inclusions trapped on the low temperature side of the isochore (Ts halite) will exhibit final homogenisation via halite dissolution. Fluids that undergo final homogenisation by halite dissolution are interpreted to have formed by isobaric cooling. The example illustrated here is a 45 wt. % NaCl fluid that evolved by phase separation on the liquid-vapour curve (L-V) at ca. 530°C (path A to A'). Inclusions trapped in the purple shaded region homogenised to the liquid between 200° and 350°C (between paths A' to A'' and B to B'), and exhibited final homogenisation at ca. 390°C (between A' and B). Those inclusions that homogenised to liquid at temperatures down to 200°C were trapped at pressures as high as 2 kbars, implying that the cooling fluids were overpressured. The interpretation that fluid pressures fluctuated during vein formation at Rosario is based on the multiple cross-cutting relationships, and crack-seal textures in the A-3 veins (e.g., Figs. 5.4e and 5.8d).

At Rosario, the lack of solid halite inclusions or their relict shapes in A vein quartz indicate that accidental trapping of halite crystals was unlikely. Furthermore, fluid inclusion trails show no evidence of textural disturbance, such as shape deformation, displacement or sweat halos. That the halite-homogenising fluid inclusions were only observed in the A and E veins implies that post-entrapment modification is not responsible for the formation of these type III inclusions. If the fluid inclusions had been significantly disturbed after formation, then it is expected that halite homogenising fluid inclusions would be present in all vein stages, as volume reduction by water loss should have saturated halite in some of the higher salinity

liquid-rich fluid inclusions (which occur in all vein stages), assuming salt species were not diffused along with the water. Halite homogenising inclusions have not been observed in the B, C and TES populations.

In the A-2 and A-3 populations, halite homogenising fluid inclusions are present across a wide range of temperatures. Figure 7.7 illustrates a possible mechanism for their formation. Isobaric cooling of hypersaline brines can cause them to evolve from the field of liquid-vapour saturation into the liquid + halite field (Fig. 7.7). The highest temperature halite homogenising fluid inclusions from Rosario (530°C and 45 eq. wt. % NaCl) potentially evolved from immiscible brine and vapour that separated at 600°C (path A to A'). The main group of halite-homogenising fluid inclusions occur between the trajectories A' to A'' and B to B'. The intermediate to low (<400°C) temperature brines were cooled in the absence of a vapour-rich phase, as there are no type II inclusions that homogenise below temperatures of 400°C. Isobaric cooling implies that the veins sealed due to quartz precipitation, so that phase separation must have ceased. Otherwise, if a hydrostatic pressure regime prevailed, the fluids would have cooled along trajectory A to A'', as has happened in a small number of type III inclusions that homogenise by disappearance of the vapour bubble. The population of halite-homogenising fluid inclusions would have formed when Ts halite exceeded Th v→l by 50° to 100°C, and rarely up to 200°C (Fig. 7.7). About 140°C of isobaric cooling is required to produce the intermediate to low temperature range of fluid inclusions that homogenise by halite dissolution (Fig. 7.7). This can explain homogenisation of the hypersaline brine fluid inclusions from Rosario that homogenise to liquid between 200° and 350°C, and by halite dissolution at ~390°C.

Juxtaposition of the "boiling" population fluid inclusions with those that homogenise via halite dissolution may be achieved by multiple cycles of fracturing, dilation, dissolution, precipitation, and recrystallisation of the host quartz grains which occurs at the scale of the fluid inclusions themselves. In a study of quartz from the pre-main stage porphyry-stye veins at Butte, Montana, Rusk and Reed (2002) identified complex quartz growth textures using scanning electron microscope-cathodeluminescence (SEM-CL). These textures, which include fracturing, deposition (sealing), annealing and recrystallisation, were not visible using the optical microscope. At Rosario, it is probable that quartz in all the veins was subjected to complex growth histories, such as those demonstrated to have occurred at Butte.

Moreover, it is possible that fluid inclusions, related to any given stage of growth, would have formed next to fluid inclusion populations related to pre-existing stages of quartz formation. These individual populations may be separated from each other by distances of only 10 to 50 μm, which is consistent with the observations of boiling populations that apparently coexist next to the halite homogenising fluid inclusions. Future work on the Rosario fluid inclusions should incorporate an SEM-CL study.

A small number of halite-saturated fluid inclusions in vein quartz associated with E veins, homogenised between 240° and 350°C. These homogenisation temperatures are lower than the coexisting type I and type II inclusions, implying discrete fluids formed the type I, type II and type III fluid inclusions. It was suggested above that the type I fluid inclusions are related to acidic fluids that caused the advanced argillic alteration. Most of the brines homogenise via halite dissolution, implying that the fluids were overpressured. This is a process consistent with the presence of sulfide breccias in the E veins, which are interpreted to have formed by hydraulic and tectonic rupturing. The brines in type E veins are therefore inferred to be related to formation of the massive sulfides.

Melt Inclusions

Melt inclusions from an A-3 quartz vein were heated at 800°C for a period of 12 hours to assess their behaviour after melt homogenisation and subsequent quenching. After the sample was quenched, some of the inclusions contained homogenous silicate glass with concomitant double shrinkage bubbles (Fig. 7.6e), whereas all other inclusions had decrepitated. The formation of homogenous silicate glass and double shrinkage bubbles is typical of silicate melt inclusions that have been melted and quenched (V. Kamenetsky, pers. comm., 2003). Coexisting type I, II and IIII fluid inclusions decrepitated during the experiment. It is concluded that silicate melt coexisted with hydrothermal fluids in these A veins at Rosario, providing evidence for a magmatic-hydrothermal origin of the vein stage.

Further heating experiments are required to fully assess the melting behaviour of melt inclusions in A-3 quartz veins at Rosario. However several inferences can be made based on the nature of the solid and aqueous phases observed in some of the melt inclusions. The presence of various salt crystals in A-3 vein melt inclusions, and the coexistence of hypersaline type III fluid inclusions, suggests that silicate melt and hypersaline brine were present together at the time of trapping. Moreover, some of

these multiphase melt inclusions contain small amounts of aqueous fluid and a vapour bubble (e.g., Fig. 7.1h), which were possibly exsolved *in situ*, or trapped heterogeneously with the melt. The presence of triangular opaque daughter minerals, interpreted to be chalcopyrite, in some melt inclusions (Fig. 7.1g) supports the view that late magmatic phases at Rosario were effective in sequestering ore-forming components (e.g., Candela, 1989; Cline and Bodnar, 1991; Candela and Piccoli, 1995). Microanalytical techniques, such as proton-induced x-ray emission (PIXE) and LA-ICPMS have detected high concentrations of ore-forming components (e.g., copper, gold, etc.) in multiphase melt and hypersaline brine fluid inclusions in several magmatic-hydrothermal systems (e.g., Heinrich et al., 1992; Wilkinson et al., 1994; Audetát et al., 1998; Heinrich et al., 1999). Similar work is required at Rosario to compare the metal contents of melt inclusions, brines and vapours in the A-3 veins.

At the Dinkidi porphyry copper-gold deposit (Philippines), coexisting silicate melt and multiphase salt-rich aqueous inclusions in clinopyroxene from the mineralised Balut dike were interpreted to have formed as immiscible phases at magmatic temperatures (Kamenetsky et al., 1999). The A-3 veins at Rosario that contain silicate melt inclusions and multiphase hypersaline type III and vapour-rich type II fluid inclusions are also interpreted as having formed as immiscible phases at magmatic temperatures. Furthermore, it is inferred that A-3 veins mark the transition from magmatic to hydrothermal conditions after emplacement of the Rosario Porphyry. This transition is consistent with the orthomagmatic model of ore formation in porphyry copper deposits (e.g., Burnham, 1997).

Pressure and depth estimates

Pressure of formation can be approximated modelling populations of immiscible vapour-rich and brine fluid inclusions using the NaCl-H_2O system (Bodnar et al., 1985; Fournier, 1999). Alternatively, the method of Bodnar (1994) and Cline and Bodnar (1994) estimates trapping pressures for fluid inclusions that homogenise via halite dissolution. The minimum pressure of formation is estimated to be 500 bars for the highest temperature fluid inclusions in the A-3 population (Fig. 7.8a). At this pressure and 450° to 540°C the rock is quasi-ductile and behaves in a plastic manner, preventing formation of open fractures, except for episodic breaches of the impermeable rock by short periods of shear failure (Fournier, 1991, 1999). Thus, pressures were lithostatic and required an overburden of at least 2 km. At pressures of

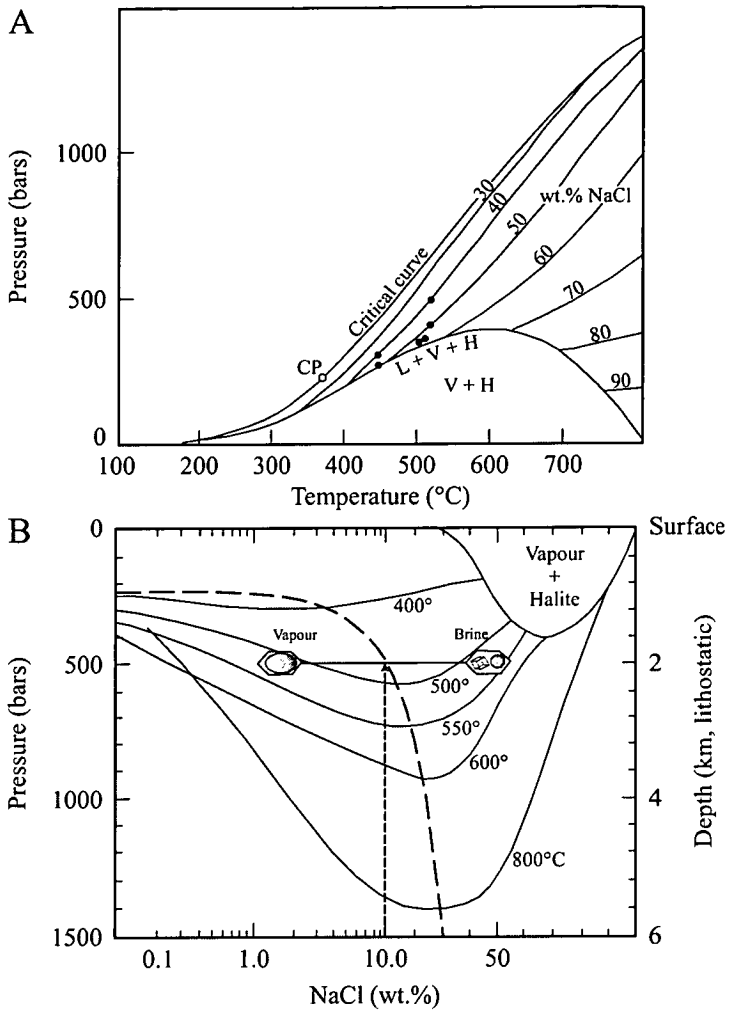

Figure 7.8. **A)** Pressure-temperature diagram illustrating formation conditions of brine inclusions in A-2 and A-3 veins that exhibit final homogenisation by disappearance of the vapour bubble. Assuming the NaCl-saturated brines were trapped in the presence of a vapour, then the homogenisation temperature is the true temperature of entrapment, and the entrapment pressure is constrained by the position on the liquid-vapour curve at that temperature. Data for a selection of individual halite-saturated inclusions are plotted on the corresponding liquid-vapour curves. The pressure of formation of the highest temperature inclusions in the A veins is ca. 500 bars. Figure modified from Bodnar et al. (1985a) and Hedenquist et al. (1998). **B)** Isothermal projections of coexisting phases in the NaCl-H_2O system from Sourirajan and Kennedy (1962), Bodnar et al. (1985a), and Pitzer and Pabalan (1986). Note the change from logarithmic to linear scale at 10 wt.% NaCl. Immiscible vapour (2-3 wt.% NaCl) and brine (ca. 45 wt.% NaCl) will separate at 530°C and at 500 bars from a fluid with bulk composition of 10 wt.% NaCl that ascended from the magma chamber (short dashed arrow). These conditions correspond with the average homogenisation temperature and compositions of inclusions in the boiling population from the early veins at Rosario. The curved dashed line is the critical curve.

500 bars, a one-phase magmatic fluid of 10 wt.% NaCl intersects its solvus at 500°C (Fig. 7.8b), and separates into vapour (2 to 3 wt.% NaCl) and brine (45 wt.% NaCl). These temperatures and salinities are consistent with the thermometric data obtained from the boiling population in the A-2 and A-3 veins.

The three modes of homogenisation reflect different P-T conditions of entrapment of the halite-bearing fluid inclusions (Fig. 7.9). They are consistent with fluctuations in fluid pressure combined with cooling of the fluids, as modelled for the 45 wt.% NaCl fluid in Figure 7.7. Fluid inclusions that homogenise by vapour-phase disappearance, simultaneous halite dissolution and vapour-phase disappearance, and by halite dissolution are depicted by the fields 1, 2 and 3, respectively, in Figure 7.9a and 7.9b. Cooling of a 45 wt.% NaCl brine, physically separated from the vapour phase, would lead to trapping, at a minimum pressure of 500 bars, of fluid inclusions in fields 2 and 3 in Figures 7.9a and 7.9b, and along the path A' to A'' in Figure 7.7. The minimum temperature of 200°C for fluid inclusions that homogenise by halite dissolution at 390°C corresponds with pressures as high as 2 kbars, however it is inferred that these elevated pressures record fluid overpressuring, caused by the tensile strength of the overlying rock, rather than deep formation of the veins (e.g., Kontak and Clark, 2002). The data suggest that cooling and overpressuring existed down to 250°C and salinities of ~35 wt.% NaCl.

Coexisting high temperature vapour and liquid-rich fluid inclusions in the B population is evidence that the fluids that formed B veins were potentially boiling. At a salinity of 10 eq. wt. % NaCl, boiling of a 350°C fluid corresponds to a minimum pressure of 200 bars. At this temperature, the rock behaves in a brittle fashion, indicating that the pressure regime was hydrostatic. Under hydrostatic pressure, the type B veins formed at a similar depth to that estimated for the A veins (~2 km; Haas, 1971). Temperatures of 250° to 350°C and depths of approximately 1.8 km are indicated for the formation of C veins if the fluid was boiling.

Type I and II fluid inclusions in quartz from E veins homogenise at about 330° to 450°C. In Figure 7.10, the range of temperatures is plotted in histograms as a function of depth below the paleosurface compared to the hydrostatic and lithostatic boiling curves. The T_h values range between hydrostatic and lithostatic and possibly reflects either discrete fluids, differences in elevation of the paleowater table, or changes from lithostatic to hydrostatic pressures during formation of E veins. The presence of halite

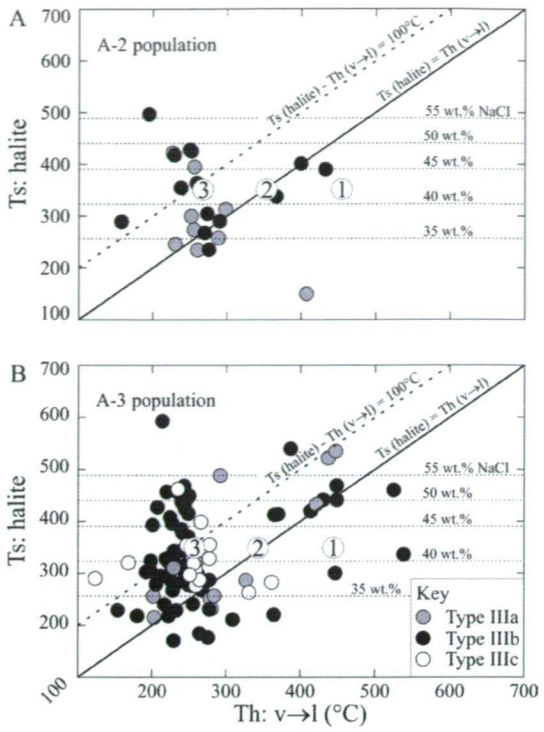

Figure 7.9. Binary plot of homogenisation temperature for halite-saturated brine inclusions. **A)** A-2 veins. **B)** A-3 veins. The circled numbers delineate the three different homogenisation modes for type III inclusions, the significance of which is discussed in the text. The horizontal dashed lines are the NaCl concentrations derived from halite dissolution temperatures (Bodnar and Vityk, 1994). The diagonal dashed line is a reference line for inclusions exhibiting halite homogenisation at ≤100°C above the temperature of bubble disappearance. Inclusions trapped above and within the region encompassed by the two diagonal lines suggest they were trapped under conditions of fluid overpressuring.

homogenising brine inclusions in the same vein quartz are consistent with high confining pressures. E veins may therefore have formed as the pressure fluctuated between lithostatic and hydrostatic conditions, possibly as a result of fluid overpressures as the veins sealed by quartz deposition. Boiling of a 10 wt.% NaCl fluid at these temperatures, corresponds with a minimum pressure of about 200 bars. Thus, under lithostatic conditions, the formation depth was at least 0.8 km. However, if the boiling fluids contained CO_2 and other volatiles, then the depth would have been greater (Hedenquist and Henley, 1985).

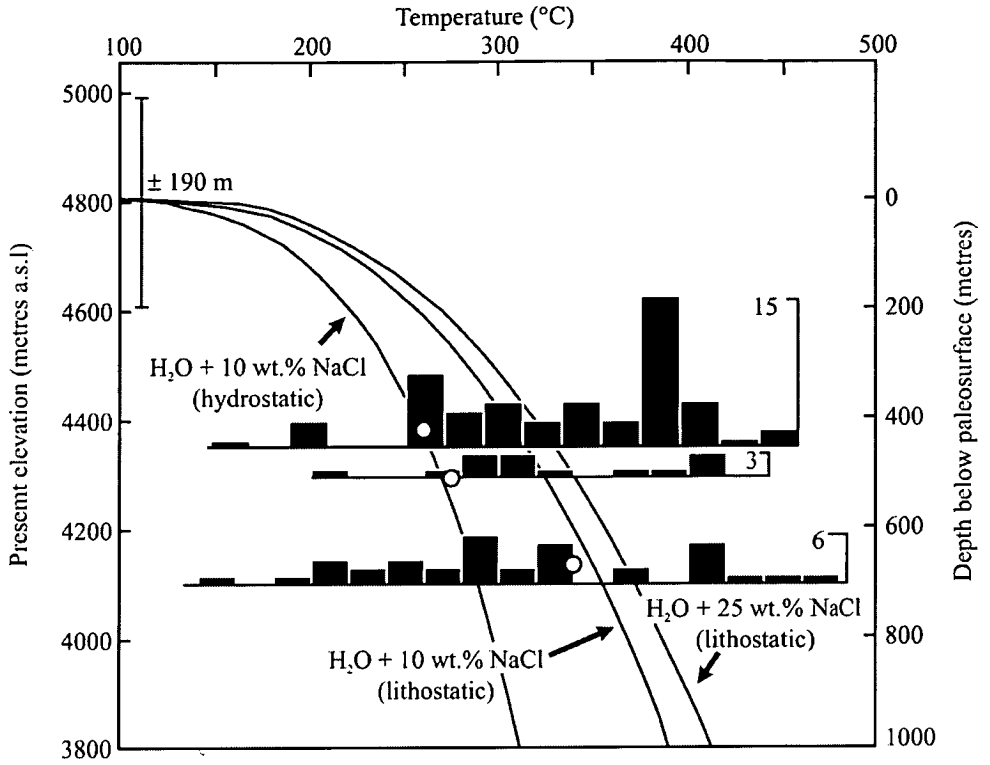

Figure 7.10. Fluid inclusion temperatures from three E veins samples plotted in histograms as a function of depth compared to hydrostatic (10 wt.% NaCl) and lithostatic (10 and 25 wt.% NaCl) vapour-saturated curves. Also shown are the temperatures calculated, based on $\Delta^{34}S_{SO4\text{-}FeS2}$, for three coexisting alunite-pyrite samples (large black circles). The hydrostatic boiling curve was calculated using the data of Haas (1971), and fitted by eye to the low temperature alunite-pyrite equilibrium pairs. The corresponding lithostatic boiling curves were plotted relative to the hydrostatic curve using the data of Fournier (1987). Inclusions that homogenise to the right of the lithostatic boiling curves were possibly trapped when fluids were overpressured. Alternatively, these inclusions may have been trapped in veins that formed deep in the system, then re-opened at shallow depth in the presence of a different hydrothermal fluid. An uncertainty of ±190 m, based on the estimated uncertainty of alunite-pyrite temperatures, is shown for the hydrostatic boiling curve at a temperature of 275°C.

The formation pressure of TES fluids at Rosario is constrained from the hydrostatic boiling point with depth curve by a temperature of 270°C (average homogenisation) for a salinity of 6 eq. wt. % NaCl. Under hydrostatic pressure, the minimum formation depth is 600 m beneath the water table (Haas, 1971). These veins are likely to have formed at greater depths as there is no fluid inclusion evidence for boiling in the TES veins. In the La Grande vein, the TES veins formed from non-boiling fluids at a minimum depth of 720 to 1,160 m beneath the water table (280° to 310°C and ~3 eq. wt. % NaCl).

Rate of exhumation

Based on fluid inclusion pressure-depth estimates, the paleosurface at Rosario was 1200 to 1300 m above the present surface during formation of the A and B veins (Fig. 7.11a). It was eroded to approximately 1000 m above the present surface by the time the C veins had formed (Fig. 7.11b), and was only 400 m above the present surface during formation of the E veins (Fig.7.11c). Assuming the paleowater table was near surface when the TES veins formed, then the paleosurface was 200 m above the present surface at Rosario (Fig. 7.11d) and 200 to 300 m above that at Cerro La Grande.

The cooling age of alunite (32.6 ± 0.3 Ma), associated with the formation of the E veins, is circa 1.8 m.y. younger than that of primary biotite and illite (34.4 ± 0.3 Ma and 34.1 ± 0.6 Ma, respectively), which reflect the ages of the A and B veins at Rosario. However, the age of alunite is indistinguishable from that of muscovite (32.9 ± 0.6 Ma; Clark et al., 1998), implying that formation of E veins and the TES, was broadly contemporaneous, or that muscovite formation reset the alunite age. Based on the temporally constrained pressure-depth estimates, a minimum of 1 km of overburden is estimated to have been eroded at Rosario over a 1.8 m.y. period, which equates to an exhumation rate of 0.6 km/million years. This rate is almost twice the rate of exhumation estimated by Maksaev and Zentilli (2000) based on fission track data from the Domeyko Cordillera. Rapid exhumation at Rosario between 34.3 and

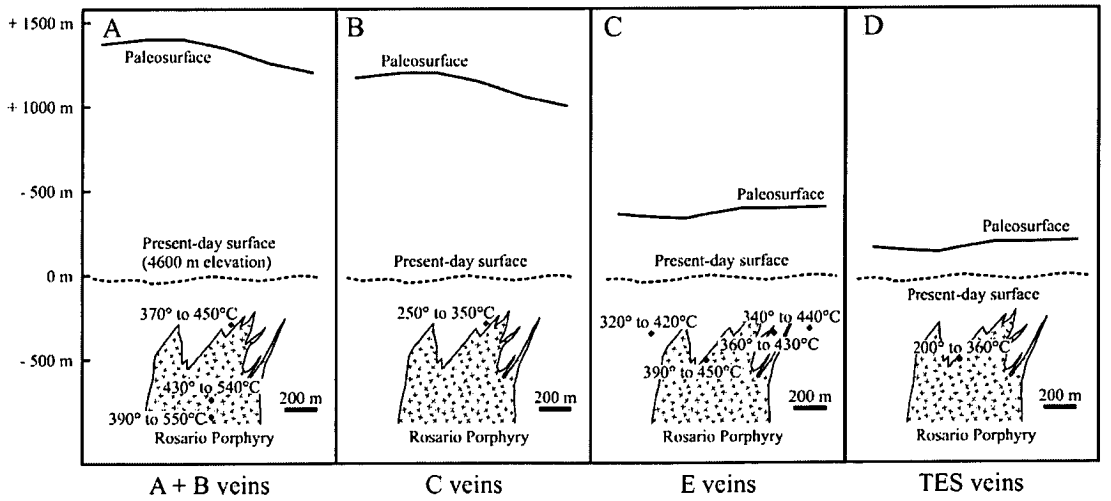

Figure 7.11. Schematic depth vs. temperature diagram for the evolution of the Rosario deposit. The panels show homogenisation temperatures of fluid inclusions in the various vein stages used to calculate depths of formation. The present-day surface occurs at an elevation of 4600 m, but is shown at zero metres relative elevation on this figure. **A)** Estimated paleosurface at the time of A and B vein formation based on fluid data. **B)** Estimated paleosurface at the time of C vein formation. **C)** Estimated paleosurface at the time of E vein formation. **D)** Position of the estimated paleosurface at the time of TES vein formation.

32.6 Ma is consistent with a model of shallow crustal normal faults that formed in response to gravitational collapse following the Incaic orogeny (Chapter 2). The exhumation rate at Rosario has been ~10 m/million years since the formation of the E and TES veins. This is less than the average rate (50 m/million years) estimated for the corresponding period across the Domeyko Cordillera by Maksaev and Zentilli (2000).

Stable Isotope Geochemistry

Sulfides and sulfates were sampled at the Rosario and La Grande deposits, and their sulfur isotope compositions measured. Pyrite, chalcopyrite, bornite and alunite were the principal minerals analysed, as they are abundant and potentially provide insights into the physiochemical conditions and mechanisms of sulfide deposition. Several pyrite-alunite pairs were analysed from E veins where the textural evidence indicated that they coexist as an equilibrium assemblage. Alunite was also analysed for its oxygen and deuterium isotope composition, whereas hydrothermal biotite and pyrophyllite were analysed for oxygen only. The O and H isotope results permit determination of the isotopic composition of the hydrothermal fluids in equilibrium with these hydroxyl-bearing minerals, if paleotemperature indicators, such as fluid inclusion data (see above), S isotope fractionation and hydrothermal mineral stabilities, are available.

Analytical methods

Sulfur isotope compositions were analysed conventionally and by laser ablation. Conventional analyses were carried out on mineral separates drilled from samples of coarse grained sulfides, using the method of Robinson and Kusakabe (1975). The procedure of Huston et al. (1995) was adopted for the laser ablation analyses, which was done on fine grain sulfides that could not be drilled and extracted as pure mono-mineralic separates. Sulfur isotope values of SO_4 in alunite were determined by conventional procedures on $BaSO_4$ precipitated by the NaOH technique and direct thermal decomposition (Holt and Engelkemeir, 1970). All sulfur isotope ratios were measured on a VG Micromass 602D mass spectrometer, at the Central Science Laboratory, University of Tasmania. Internal standards were run with an SO_2 reference gas, and calibrated against international sphalerite standards IAEA NZ1 and NBS 123. The results are expressed in standard $\delta^{34}S$ per mil (‰) notation, relative to the Canyon Diablo Troilite (CDT). Analytical uncertainty is ±0.2 per mil, and fractionation factors in the laser analyses of pyrite, chalcopyrite and bornite are

estimated to be 5.75‰, 3.82‰ and 4.44‰ (Huston et al., 1995). A small number of samples were analysed both conventionally and by laser ablation using identical sample material to check for internal consistency between the two analytical methods. The maximum difference between the results of conventional and averaged laser ablation analyses was about 1 per mil, which exceeds the analytical errors of the mass spectrometers. These differences are attributed to variablity of $\delta^{34}S$ values at the microscopic scale, which can vary by up to 2 per mil (e.g., Huston et al., 1995).

Considerable effort was expended to obtain pure (>90%) alunite, pyrophyllite and biotite separates for oxygen and deuterium isotope analyses. Alunite sample preparation followed a technique modified from Wasserman et al. (1992) and Arehart et al. (1992). The pyrophyllite was sampled from massive monomineralic occurrences of the mineral, and biotite was hand picked from monomineralic veins where it was present as coarse crystals. Alunite oxygen was extracted online by continuous flow technology and analysed in a Finnigan MAT 252 mass spectrometer at the Stable Isotope and ICP/MS Laboratory, Queens University, Kingston, Canada. Deuterium from alunite was extracted offline following the methodology outlined by Wasserman et al. (1992), and Stoffregen and Alpers (1992), and also analysed in the Finnigan MAT 252 mass spectrometer. Oxygen compositions of pyrophyllite and biotite were analysed using conventional preparation techniques (Bigeleisen et al., 1952; Clayton and Mayeda, 1963) on a Micromass 602D, at the CSIRO Division of Exploration and mining, North Ryde, Australia. Deuterium isotope compositions of pyrophyllite and biotite were not analysed due to a line failure at North Ryde laboratory. All $\delta^{18}O$ and δD values were corrected to the international standard NBS-127, and the results are reported using standard notation δ per mil (‰) relative to Standard Mean Ocean Water (SMOW). Errors are typically ± 0.1 per mil for $\delta^{18}O$ and ± 2 per mil for δD.

Sulfur isotope compositions

Sulfur isotope compositions were measured from 100 sulfide samples at Rosario and La Grande. These results are shown together with five analyses of alunite in Figure 7.12 (data in Appendix 4). Of these analyses, 21 were carried out on bornite and chalcopyrite in A veins, four on molybdenite in B veins, and 39 on pyrite, chalcopyrite, bornite and enargite in E veins. The $\delta^{34}S$ values of A vein bornite and chalcopyrite range from -3.9 to 0.6 and -2.7 to 1.2 per mil, respectively (Fig. 7.12a). Molybdenite data form a tight group of values from 1.4 and 2 per mil. The

molybdenites are enriched in $\delta^{34}S$ compared to A vein Cu-Fe sulfides (Fig. 7.12a).

E vein pyrite, intimately associated with alunite, have $\delta^{34}S$ values of -3 to 2.5 per mil. The pyrite data have a mode between 1 and 2 per mil, with most of the data skewed to more positive $\delta^{34}S$ values (Fig. 7.12c). Pyrite in E veins has been replaced by chalcopyrite that has $\delta^{34}S$ values between -5.5 and 2.1 per mil (Fig. 7.12e). The $\delta^{34}S$ values of bornite, which has replaced both chalcopyrite and pyrite, are all negative and range from -5.4 to -0.5 per mil (Fig. 7.12e).

The sulfur isotope compositions of alunite range from 19 to 23.4 per mil $\delta^{34}S$ (Figure 7.12c). This tight cluster of values indicates that alunite formed at high temperature (>200°C), and was not significantly modified by post-formation processes such as supergene alteration. The lightest values either indicate higher temperatures of formation, assuming they precipitated in equilibrium with pyrite, or minor supergene weathering around the margins of some alunite grains.

Source of sulfur

The range of sulfur isotope compositions for all the sulfide minerals analysed is -5.5. to 2.5 per mil, with a mean of -0.4 per mil. Models of sulfur isotope fractionation in pyrite, chalcopyrite, bornite, $SO_{2(g)}$, and $SO_{4(aq)}$, were generated using different values of $\Sigma^{34}S$ (bulk sulfur composition of the hydrothermal fluid) and H_2S/SO_4 (measure of fO_2). Results of the modelling are illustrated in Figure 7.12. A series of sulfur fractionation curves were calculated to fit the ranges of $\delta^{34}S$ values obtained from sulfides (and sulfate) within the range of temperatures indicated by the fluid inclusion and sulfide-sulfate equilibrium pairs. In all cases, a $\Sigma^{34}S$ of 3 per mil was used as it was the optimum value for calculating the models to fit the range of $\delta^{34}S$ values in each stage of the sulfide paragenesis. Furthermore, this value falls within the average range reported for most porphyry copper deposits worldwide (Ohmoto and Rye, 1979; Sasaki et al., 1984; Taylor, 1987). These values are compatible with derivation from an igneous source, either as magmatic-hydrothermal fluids or by dissolution of igneous sulfides (Ohmoto and Rye, 1979). The presumption that the $\delta^{34}S$ value of the hydrothermal fluids remained constant throughout formation of different sulfide generations implies that there was no contamination by exotic sulfur, from isotopically heavy evaporite sulfate, or isotopically light sedimentary sulfide. These external sulphur reservoirs occur in the Jurassic and Early Cretaceous sedimentary basins west of Collahuasi, but do not appear to have influenced mineralisation at Rosario.

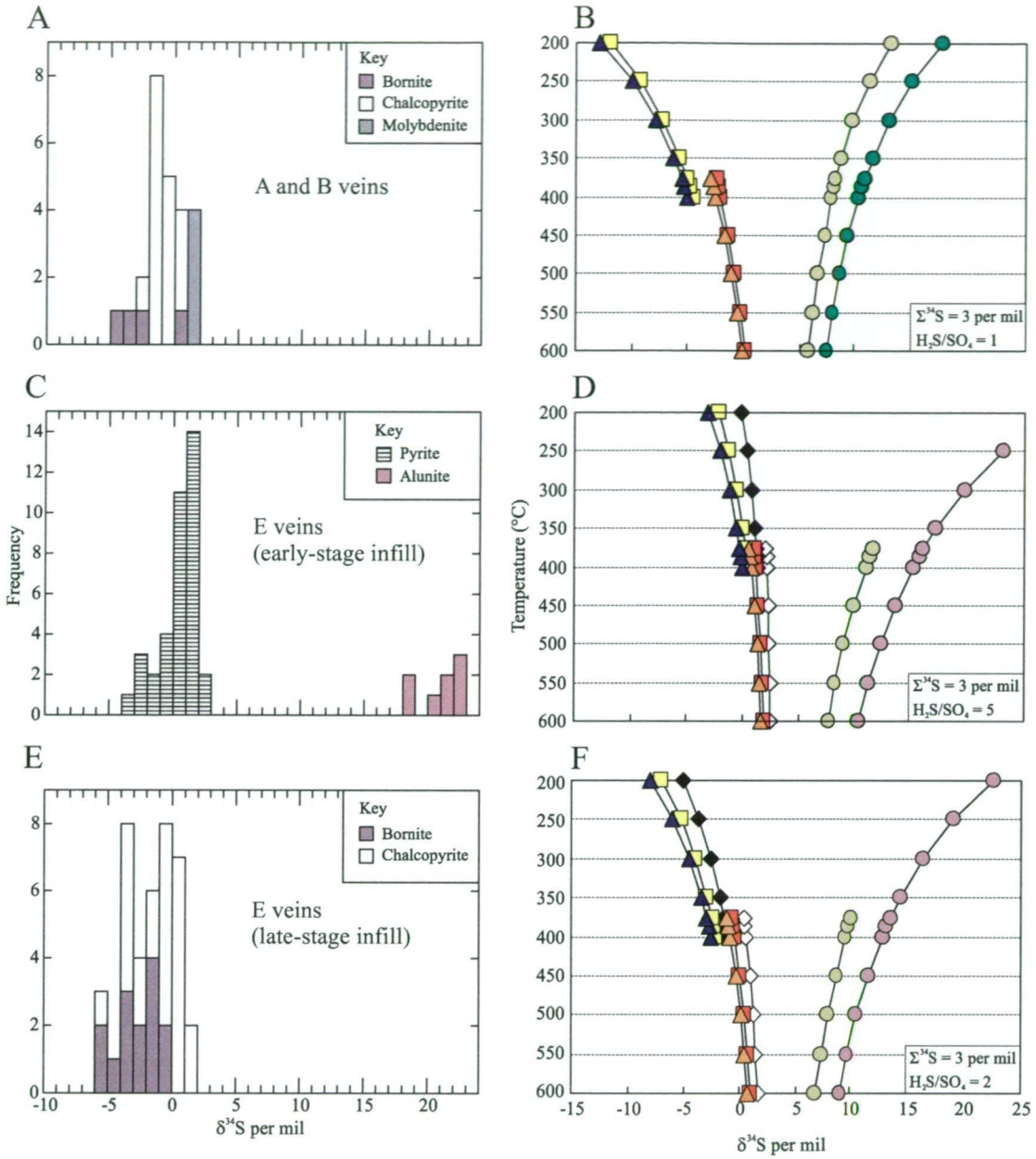

Figure 7.12. Sulfur isotope ranges and sulfide-sulfate fractionation models from the veins stages at Rosario. Sulfide-sulfate fractionation curves were calculated using the relations of Ohmoto and Rye (1979). Different values of $\delta^{34}S$ and H_2S/SO_4 were used to calculate curves that encompassed the range of $\delta^{34}S$ compositions of sulfides (and alunite), constrained by the temperatures indicated by the fluid inclusion data. Calculations were made using an unpublished spreadsheet (G. Davidson, unpublished data). **A)** $\delta^{34}S$ values from A and B veins. **B)** Modelling results from sulfides in A veins. **C)** $\delta^{34}S$ values from early-stage pyrite and alunite in E veins. **D)** Modelling results from E vein alunite and pyrite. **E)** $\delta^{34}S$ values for late-stage chalcopyrite and bornite in E veins. **F)** Modelling results from E vein chalcopyrite and pyrite.

Formation of light $\delta^{34}S$ values

Chalcopyrite and bornite in A veins have light $\delta^{34}S$ compositions (Fig, 7.12a). Sulfur isotope compositions of chalcopyrite and bornite in the E veins are isotopically lighter than the pyrite associated with alunite (Figs. 7.12c and 7.12e). Negative sulphur isotope compositions have been reported for other porphyry ore deposits, including Butte (Lang and Cheney, 1971), El Salvador (Field and Gustafson, 1976), Valley Copper (Osatenko and Jones, 1976), Endeavour 26 North (Heithersay and Walshe, 1995), and Dinkidi (Wolfe, 2001). The range of sulfide $\delta^{34}S$ values form Collahuasi and these other deposits suggest that the sulfides precipitated from fluids with compositions close to the H_2S/SO_4 buffer (Heithersay and Walshe, 1995). In order to explain the data, coprecipitation of Cu-Fe sulfides with anhydrite (even though it is not preserved at Rosario) and equilibrium SO_2 was modelled for A vein chalcopyrite and bornite compositions (Fig. 7.12b). Similar models were constructed for E vein alunite-pyrite (Fig. 7.12d), and for E vein alunite-chalcopyrite-bornite (Fig. 7.12f).

The fractionation model for A vein sulfides was fitted to sulfur isotope values for conditions near the H_2S/SO_4 buffer, using a $\Sigma^{34}S$ value of 3 per mil. The range of measured $\delta^{34}S$ values (-4 to 1 ‰) is consistent with those predicted by the model when a fluid is cooled from 600° to 400°C (temperatures determined in the fluid inclusion study). Heithersay and Walshe (1995) modelled sulfur isotope compositions of bornite and chalcopyrite in the Endeavour 26 North deposit, in NSW, Australia, and encountered a similar range of $\delta^{34}S$ values from temperatures of 700° to 250°C, which they attributed to cooling of an oxidised, sulfate-predominant fluid.

The $\delta^{34}S$ compositions measured from chalcopyrite and bornite varied by a similar amount in E veins (-5.4 to 1.8 ‰) to A veins (-4 to 1 ‰). These data can be explained by the same bulk sulphur value (e.g., $\Sigma^{34}S \approx 3$ ‰), but different H_2S/SO_4 (A veins = 1; E veins = 2; Fig. 7.12f). The $\delta^{34}S$ values for E vein sulfides extend to more negative values than in the A veins, possibly due to a change in oxidised sulfur speciation, because SO_2 disproportionates to SO_4 (in equilibrium with H_2S) at ~400°C; (Ohmoto and Rye, 1979; Rye et al., 1992).

Formation of heavy $\delta^{34}S$ values

$\delta^{34}S$ values of -3.0 to 2.5, (mean value is 0.7 ‰) for pyrite in E veins are consistent with the inferred bulk composition of sulphur in the hydrothermal fluid (3 ‰), whereas those of alunite are much heavier (21.0 to 23.4; Fig. 7.12c). Despite the abundance of alunite, modelling results indicate that fluids were H_2S-rich with average H_2S/SO_4 values of about 5:1 (Fig. 7.12d). These systematics, which are typical of magmatic-hydrothermal acid-sulfate alteration, indicate that the fluids which formed the pyrite-alunite assemblage were more reducing than the primary magmatic fluids (Rye et al., 1992). The data are consistent with the inference that sulfuric acid was derived from the disproportionation of SO_2 during the condensation of magmatic vapour at temperatures below 400°C.

The heavy $\delta^{34}S$ values of sulfides and sulfates at Rosario are interpreted as evidence that the fluids most likely followed a reducing path after exsolution from the magma (Rye, 1993). Pyrite-alunite fractionation at Summitville (Stoffregen, 1987; Rye et al., 1990), and in the Julcani district (Deen, 1990; Rye et al., 1992; Rye, 1993), Perú, exhibit similar reducing paths to that at Rosario. As at Summitville and Julcani, the redox potential of the Rosario fluids appears to have been governed by exchange with rocks deep in the system. At Rosario, it is speculated that this probably involved pre-existing sulfide mineralisation (vein stages A to D) within the Rosario Porphyry.

Pyrite-alunite equilibrium temperatures for E veins

Three alunite-pyrite pairs were analysed from E veins sampled at different levels in the Rosario deposit. The $\delta^{34}S$ value of the deepest alunite (*sample R990188;* 4140 m elevation) is 21 per mil, and that of coexisting pyrite is 2.5 per mil. The calculated isotopic equilibrium temperature is 340°C using the equation of Ohmoto and Rye 1979; Fig.7.13). At higher elevation (4290 m), the alunite composition is 23.1 per mil, and coexisting pyrite is 1.5 per mil, corresponding to a calculated equilibrium temperature of 275°C. The sulfur isotope compositions of alunite and pyrite pairs, at 4,380 m is 23.3 and 1 per mil, respectively, corresponding to a temperature of 260°C (Fig. 7.13). The uncertainty in the calculated temperatures is ±10°C because of the uncertainty in the isotope thermometer equations of Ohmoto and Rye (1979). An additional uncertainty of ±5°C applies to the calculated temperatures if analytical uncertainty is assumed to be 0.2 per mil.

The alunite-pyrite equilibrium temperatures are consistent with the fluid inclusion temperature ranges measured from quartz infill in associated veins. Equilibrium temperatures decrease from 340° to 260°C over a vertical interval of 240 m (Fig. 7.13) and reflect a temperature gradient in the system. However, this gradient is inconsistent with the decrease in temperature expected from a boiling, 10 wt. % NaCl fluid over the same interval. For example, assuming that the lowest temperature, 260°C, represents the fluid boiling under hydrostatic pressure at 500 m below the paleosurface, then at 750 m that fluid would be boiling at 285°C (Fig. 7.13).

The deepest E vein alunite-pyrite equilibrium temperature suggests that fluid temperature at this paleoelevation was 340°C. In Figure 7.10, this sample plots near, and is within error of (±10° to 15°C) the lithostatic boiling curve for a 10 wt. % NaCl fluid. By contrast, calculated temperatures of the two other equilibrium pairs plot near, or lie on the hydrostatic boiling curve for a fluid with the same salinity (Fig. 7.10). The calculated equilibrium temperatures are within the range of temperatures measured in E vein fluid inclusions from similar elevations, and consistent with formation under conditions that fluctuated between lithostatic and hydrostatic.

It is possible that the transition from lithostatic to hydrostatic conditions, at the time of E vein formation, was between the elevations of the deep and shallow alunite-pyrite pairs, approximately 850 m below the paleosurface. At the Summitville Au-Ag-Cu deposit (Colorado, USA), equilibrium temperatures of deep alunite-pyrite occurrences were shown to plot near the lithostatic boiling curve, whereas those at higher elevations (900 m above) plotted near the hydrostatic boiling curve (Stoffregen, 1987; Rye et al., 1990). The deepest alunite was interpreted to have formed at the base of the vapour plume, which corresponded with the transition from lithostatic to hydrostatic pressure.

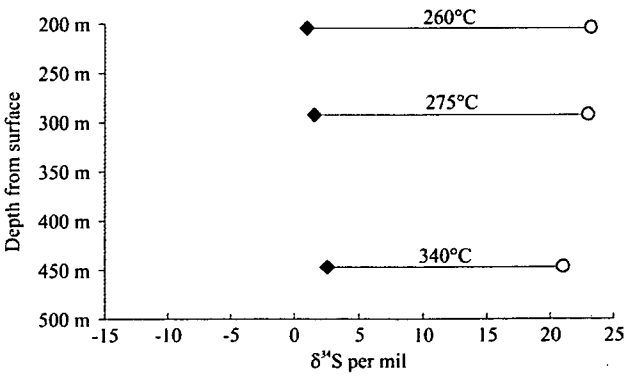

Figure 7.13. Alunite-pyrite sulfur isotope equilibrium temperatures calculated using the equation of Ohmoto and Rye (1979), and plotted as function of sample depth relative to the present-day surface. Black diamonds are pyrite, pink circles are alunite.

Oxygen and deuterium isotope compositions of hydrothermal minerals

The $\delta^{18}O$ and δD results are give in Appendix 4, and plotted in Figure 7.14. $\delta^{18}O$ compositions of A-2 vein biotite cluster between 5.6 to 5.9 per mil. The $\delta^{18}O$ values of the two E vein alunite samples are 11.7 and 13.1 per mil, and their corresponding δD values are -39 and -40, respectively. The $\delta^{18}O$ composition of TES vein pyrophyllite ranges from 8.3 to 9.8 per mil.

Oxygen and deuterium compositions of the fluids

Magmatic and meteoric waters: Exsolution of magmatic fluid (degassing) from a typical felsic magma at 3 to 5 wt.% water results in δD enrichment of about 15 to 20 per mil, but may be as high as 40 per mil (Taylor, 1992). Magmatic water that discharges to the surface via volcanic fumaroles has heavy δD values, about -20 ± 10 per mil (Giggenbach, 1992), consistent with an initial melt composition of -20 to -45 per mil δD and a fractionation factor of approximately 20 per mil (Hedenquist et al., 1998). The water that remains behind in the crystallising intrusion is isotopically light. Hedenquist et al. (1998) suggested that this water should be re-defined as "residual magmatic water", rather than as "primary magmatic water," (e.g., Sheppard et al., 1969; 1971). Further isotopic fractionation occurs upon phase separation in which the vapour is enriched relative to the brine by 10 to 20 per mil δD and about 1 per mil $\delta^{18}O$ (Horita et al., 1995). Therefore the net enrichment of the brine, depending on the amount of exsolution and salinities of immiscible brine and vapour, will vary by ± 10 per mil δD, but only about 1 per mil $\delta^{18}O$, relative to the starting composition of the melt.

The composition of meteoric water at Rosario was not measured, but it is assumed to be similar to that of modern-day meteoric water from the El Tatio geothermal field (Fig. 7.14a; Giggenbach, 1978), located at similar elevations, 100 km south-southeast of the Collahuasi district. El Tatio water values (-8.5 per mil $\delta^{18}O$ and -52 per mil δD) overlap the composition of groundwater which formed the supergene kaolinite at El Salvador (Watanabe and Hedenquist, 2001). Supergene oxidation operated at various times in Northern Chile between 34 and 14 m.y., although these processes predominantly affected the late Eocene-early Oligocene porphyry belt in the early and middle Miocene (Sillitoe and McKee, 1996). At El Salvador, Watanabe and Hedenquist (2001) assumed that calculated water values from the supergene kaolinite was close to that of paleometeoric water at the time of hydrothermal activity (ca. 41

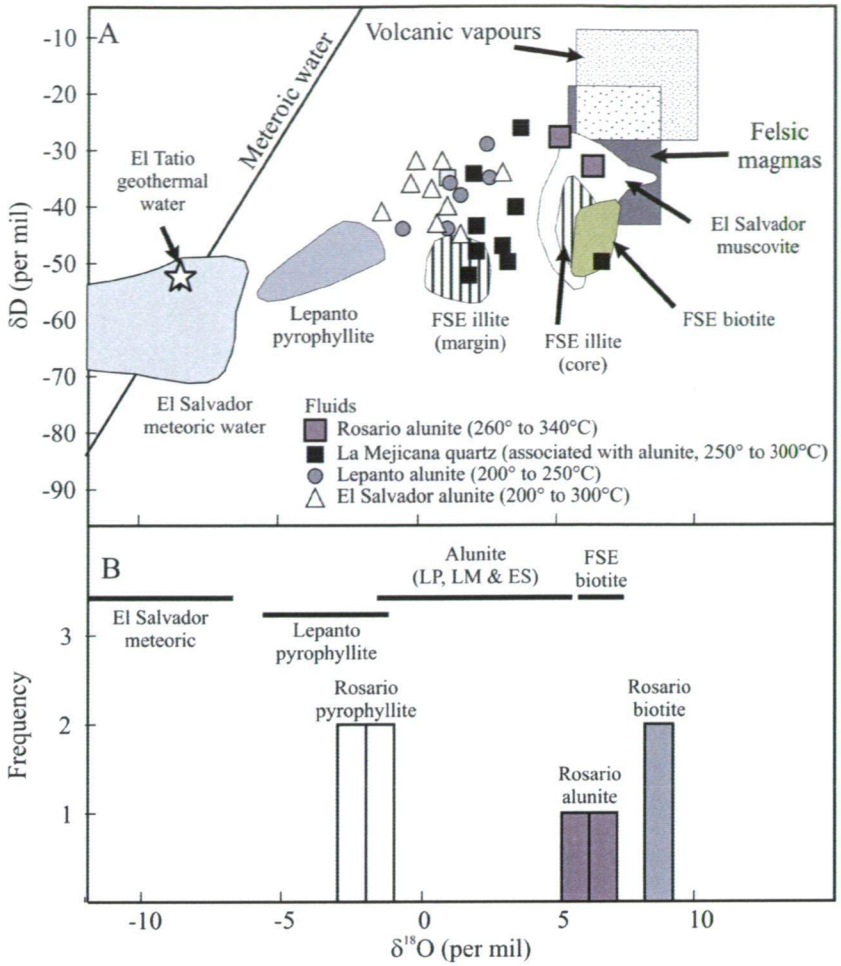

Figure 7.14. **A)** Oxygen and hydrogen isotope compositions of water, calculated from alunite analyses at temperatures determined from sulfur isotope geothermometry. Fractionation factors used are from Hedenquist et al. (1998). Fractionation factors for muscovite were used to calculate the composition of water in equilibrium with pyrophyllite. The compositions of water dissolved in felsic melts are from Taylor (1992), and water associated with high-temperature fumaroles are from Giggenbach (1992). Also shown for reference are fluid compositions, equilibrated with alunite, from La Mejicana (Losada-Calerón, 1992), Lepanto (Hedenquist et al., 1998) and El Salvador (Watanabe and Hedenquist, 2001), along with fields of Lepanto pyrophyllite, and Far Southeast (FSE) illite and hydrothermal biotite (Hedenquist et al., 1998). The composition of the fluid in equilibrium with the deep alunite at Rosario is of magmatic derivation, although there may have been a small amount of meteoric water mixing with magmatic fluid to generate the shallow alunite. **B)** The $\delta^{18}O$ compositions of waters in equilibrium with hydrothermal biotite, alunite and pyrophyllite from Rosario (see text for discussion).

Ma). The El Salvador kaolinite provides only an estimate of the potential paleoground water compositions at the time of ore formation. Figure 7.14a shows the field of potential $\delta^{18}O$ and δD compositions for meteoric water, at the time of hydrothermal activity in the Collahuasi district (ca. 34-32 Ma).

Potassic assemblage: The $\delta^{18}O$ composition of the fluid that formed biotite in A-2 veins was 8 to 8.3 per mil (calculated assuming an average temperature of 500°C based on the fluid inclusion data). The calculated $\delta^{18}O$ values are consistent with a magmatic origin, similar to magmatic water responsible for K-silicate alteration in

most other porphyry ore deposits (e.g., Bingham and Santa Rita, Sheppard et al., 1971; El Salvador, Sheppard and Gustafson, 1976; Rio Blanco and El Teniente, Kusakabe et al., 1990; Nevada del Famatina, Losada-Calderón, 1992; Far Southeast, Hedenquist et al., 1998; Bajo del Alumbrera, Ulrich et al., 2001).

Quartz-alunite-pyrite assemblage: Alunite in deep E veins formed from 340°C fluids that had calculated $\delta^{18}O$ and δD values of 6.4 and -33 per mil, respectively. Fluids that deposited alunite in shallow E veins were 260°C and have calculated $\delta^{18}O$ and δD values of 5.2 and -28 per mil, respectively. Fluids in equilibrium with alunite had $\delta^{18}O$ and δD values comparable with several other high sulfidation and porphyry ore deposits (Fig.7.14a). The fluid compositions calculated from alunite are consistent with a magmatic origin, possibly with minor mixing with meteoric water.

Similar alunite-forming fluid compositions have been calculated at Julcani (Rye, 1993; Deen et al., 1994). The calculated $\delta^{18}O$ and δD values of the fluids that deposited the Julcani alunite were interpreted as evidence that the fluids were magmatic-hydrothermal, but had evolved through exchange with deep crystalline rocks in a low water to rock environment. At Rosario, the redox state of the fluids is inferred to have been governed by interaction with A to D vein stage disseminated sulfides formed before E vein alunite and pyrite.

Pyrophyllite-dickite assemblage: The $\delta^{18}O$ composition of the fluid that precipitated TES vein pyrophyllite was calculated using the average homogenisation temperature of quartz-hosted type I fluid inclusions. The calculated $\delta^{18}O$ fluid compositions ranges from -3 to -1.6 per mil, at 270°C (Fig. 7.14b). This compositional range is between the compositions of magmatic vapours and meteoric water, implying that TES vein pyrophyllite formed by local groundwater absorption of volcanic vapour. Hydrogen isotope compositions are needed in order to determine the relative proportions of magmatic water and meteoric water.

Potential for Gold Mineralisation

Because the alteration mineral assemblages associated with E and TES veins at Rosario and La Grande are analogous to those assemblages in high-sulfidation gold deposits (e.g., Hedenquist, 1987; White and Hedenquist, 1990; White and Hedenquist, 1995), it is possible that gold may have been transported by the Rosario and Cerro La Grande mineralising fluids. Both of these vein systems are known to contain significant amounts of copper and silver, but their potential for gold mineralisation has never been fully assessed. This section evaluates whether the late-stage hydrothermal brines, associated with chalcopyrite-bornite-chalcocite deposition, had the potential to transport gold.

The transport and deposition of gold depends on several physical and chemical factors. In the epithermal environment, these include speciation (e.g., aqueous gold halide or hydrosulfide complexes), temperature, salinity, pH and oxidation state of the fluids. At Cerro La Grande and Rosario, the temperature (290° to 350°C; Table 7.2) and salinity (30 wt. % NaCl; Table 7.2) of the fluids related to E vein formation has been constrained by fluid inclusion microthermometry. The fluids were most likely reducing (H_2S:$SO_4 \approx 2$) based on the results of sulfur isotope modelling (Fig. 7.12f). Figure 7.15a shows Fe-O-S and K-alumnosilicate mineral stability fields and the predominance fields for oxidised and reduced sulphur species. The mineral assemblages in E veins (e.g., pyrite, alunite, pyrophyllite, muscovite, enargite, tennantite) broadly constrain the oxidation state, consistent with the sulphur isotope modelling, and indicate that the fluids were acidic, with a pH of around 3 (Fig. 7.15a).

The speciation of gold in hydrothermal fluids was reviewed in detail in Seward (1991). Gold occurs in the +1 valance state (Au^+) in aqueous species in hydrothermal solutions (Seward, 1991). It can be highly soluble when it is complexed with various ligands to form hydrosulfide (e.g., $Au(HS)_2^-$; Seward, 1973; Shenberger and Barnes, 1989; Gammons and Williams-Jones, 1995; Benning and Seward, 1996; $HAu(HS)_{2(aq)}$, Hiyashi and Ohmoto, 1991; $AuHS_{(aq)}$, Benning and Seward, 1996) and/or halide complexes (e.g., AuI_2^-, $AuBr_2^-$, $AuCl_2^-$, AuF_2^-; Seward, 1991). Under strongly acidic conditions (pH <3) and at temperatures >280°C, $AuCl_2^-$ is the predominant gold-bearing species at high salinities (e.g., 25 wt.% NaCl; Figs. 7.15b and 7.16). At lower temperatures (160° to 280°C), AuHS is the predominant gold-bearing species in reduced acid brines (Fig. 7.16; Cooke and Simmons, 2000). Based on the estimated

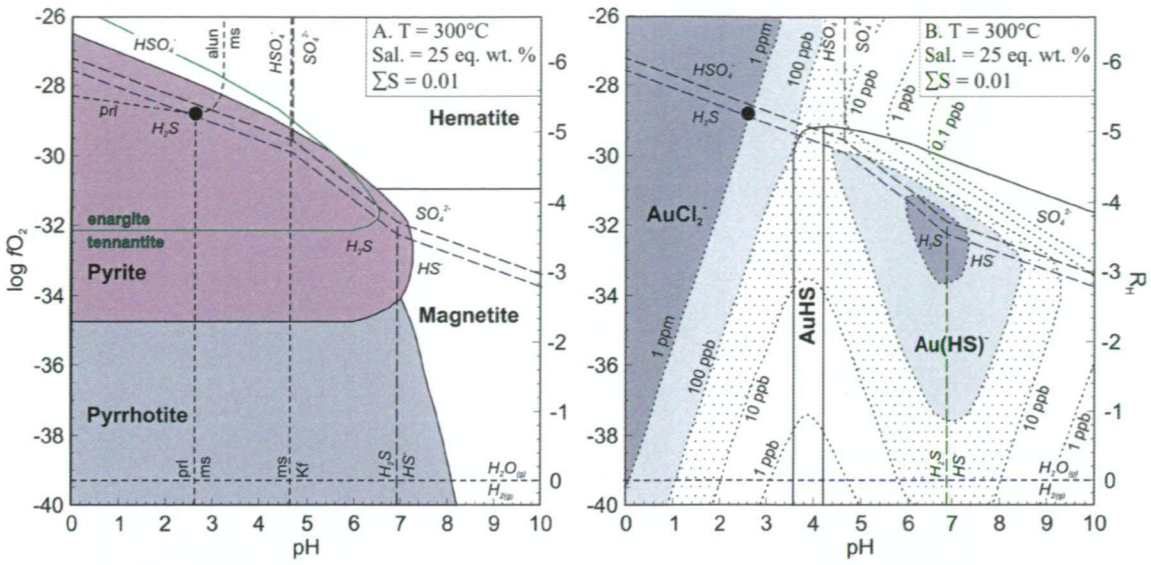

Figure 7.15. Log *f*O2 – pH diagrams at 300°C and 25 wt. % NaCl. **A)** The stability fields of Fe oxides and sulfides, Cu-As sulfides, K-feldspar (Kf), muscovite (ms), alunite (alun), pyrophyllite (prl), and the predominance fields of aqueous sulfur bearing species. **B)** Gold solubility contours and the predominance fields of $Au(HS)_2^-$, AuHS, $AuCl_2^-$ and aqueous sulfur-bearing species. Shaded areas in B mark conditions of high gold solubility. R_H values are shown on the right vertical axis for comparative purposes. The black circles in A and B represent the estimated composition for stage E mineralising fluids at Rosario and La Grande. The blue dashed line corresponds to $a_{H2S}/a_{SO4}^{2-} = 5$. $\Sigma S = 0.01$ *m*; salinity = 25 wt. %; $\Sigma C = 0.26$ *m*; $a_{K^+} = 0.805$; $a_{Ca^{2+}} = 0.541$. Modified from Cooke and Simmons (2000).

pH, fO_2, ΣS, temperature and salinity, more than 100 ppb gold could have been transported in the late-stage mineralising solutions at Cerro La Grande and Rosario as $AuCl_2^-$ (Fig. 7.15b). This is consistent with the predictions of high gold solubilities in high-temperature acidic brines made by Cooke and Simmons (2000; Fig. 5.16).

Gold and copper are probably transported together as chloride complexes (e.g., $AuCl_2^-$, $CuCl_2^-$) in strongly acidic magmatic-hydrothermal brines (e.g., White and Hedenquist, 1990). High-salinity fluid inclusion data has been reported from some high-sulfidation deposits, permissive of gold transport as chloride complexes (e.g., Nevados del Famatina and La Mejicana veins, Argentina, Losada-Calderon, 1992; Losada-Calderón and McPhail, 1996; Rodalquilar, Spain, Arribas et al., 1995a; Kyushu, Nansatsu district, Japan, Hedenquist et al., 1994b). In these systems, gold transport as a chloride complex may have occurred under oxidised or reduced conditions, if the mineralising brines were sufficiently acidic and hot (Cooke and Simmons, 2000).

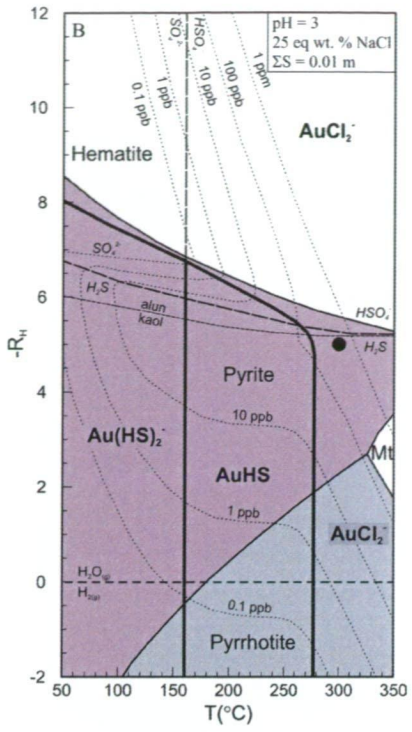

Figure 7.16. $-R_H$ - T diagram showing the stability fields of Fe oxides, Fe sulfides, kaolinite (kaol), alunite (alun), gold solubility contours and predominance fields for aqueous sulfur-bearing and gold-bearing species. $-R_H$ is defined as $-\log (fH_2/fH_2O)$, and is a measure of oxidation potential, with high values of $-R_H$ corresponding to more oxidised conditions. The black circle represents the estimated composition for the E stage mineralising fluids at Rosario and La Grande. $\Sigma S = 0.01$ *m*, pH = 3, salinity = 25 wt. %, $\Sigma C = 0.26$ *m*, $a_{K^+} = 0.805$; $a_{Ca^{2+}} = 0.541$. Mt = magnetite. From Cooke and Simmons (2000).

The thermodynamic models in Figures 7.15 and 7.16 indicate that the mineralising fluids associated with E veins in the Collahuasi district potentially transported significant amounts of gold. However, there is no guarantee that gold was deposited. Precipitation from solutions in which gold has formed $AuCl_2^-$ complexes may occur in response to cooling, pH increase, reduction and/or dilution (e.g., salinity decrease; Cooke and Simmons, 2000). Fluid mixing (e.g., interaction of the brine with groundwater) may also have favoured gold deposition. However, mixing and dilution can also lower gold concentrations and therefore may have prevented saturation (Cooke and Simmons, 2000). Furthermore, the conditions that promoted E veins Cu-Fe sulfide copper deposition may not have favoured gold precipitation. If this were the case, then gold may have stayed in solution and ultimately been dispersed during fluid outflow.

It is concluded that E stage fluids had high gold transporting potential, although it is uncertain how much of the gold was precipitated together with copper and silver. Historical mining records and the limited gold assay data from Rosario and La Grande (Chapter 5) indicate that gold does occur in E veins, consistent with the hypothesis

presented here. It is therefore recommended that gold be included in the element suite when drill core and rock chip samples are assayed. Dick et al. (1994) estimated that massive sulfides in E veins comprised 10 wt. % (100 Mt) of the Rosario mining reserve. There is potentially a significant undefined gold resource associated with E veins at Rosario.

Conclusions

Fluid inclusion microthermometry indicates the fluids that formed the A-2 and A-3 veins at Rosario consisted of hypersaline brine (~40 to 45 wt.% NaCl) and low density vapour. These brine and vapour inclusions homogenised between 400° to 600°C. Sulfides deposited in the early formed A veins, were enriched in $\delta^{32}S$, relative to $\delta^{34}S$, indicating that the bulk $\delta^{34}S$ composition of the fluid was about 3 per mil and was close to the H_2S/SO_4 buffer.

Molybdenite was precipitated in B veins from brines (10 to 15 wt.% NaCl) that homogenised at moderate temperatures (350° to 400°C). The absence of alteration envelopes in B veins implies that the fluids were in equilibrium with the K feldspar-altered Rosario Porphyry.

Fluids responsible for the C veins and associated illite-chlorite alteration assemblage were cooler (homogenisation between 250° and 410°C) and less saline (16 to 23 wt. % NaCl) than those that formed the A and B veins. That the fluids were cooler implies that the porphyry-related hydrothermal system waned from stage A to C.

Structurally-controlled E veins formed from fluids in which vapour is interpreted to have condensed at temperatures between 300° and 400°C. Condensation produced a moderately saline (10 to 15 wt.% NaCl), highly corrosive solution that altered the rocks and formed an alunite-quartz assemblage. This fluid had a bulk sulphur isotopic composition of 3 per mil, and H_2S/SO_4 of 5:1 (i.e., a reducing composition). Copper precipitated from low temperature (250° to 350°C) hypersaline brines (30 wt.% NaCl) that were probably injected along the Rosario fault system during shifts from lithostatic to hydrostatic pressure conditions. TES veins and pyrophyllite-dickite altered rocks were deposited by 250° to 320°C and 5 to 10 wt. % NaCl fluids.

The pressure regime cycled between lithostatic and hydrostatic during evolution of the Rosario ore forming system. The A-2 and A-3 veins formed at depths of 2 km

below the paleosurface under lithostatic pressure. Higher pressures (~900 bars) are indicated by the high temperature halite homogenising hypersaline brine fluid inclusions. The paleosurface remained at 1.8 to 2 km above the site of formation for B and C veins, but was eroded significantly by the time that the E veins and TES veins formed. Fluid inclusion evidence suggests that the TES veins formed between 600 to 850 m below the paleowater table under hydrostatic pressure, but this is considered to be a minimum depth, as the fluid inclusions show no evidence of boiling. At least 1 km of rock was exhumed at the Rosario deposit between formation of the potassic and advanced argillic assemblages.

Oxygen and hydrogen isotope evidence indicate that the fluids present in each mineralisation stage were sourced predominantly from magmatic solutions. Only the very late stage fluids, associated with advanced argillic alteration (pyrophyllite-dickite), show some evidence of absorption of magmatic fluid into meteoric water. Although the latest fluids mixed with meteoric water, they contained a significant magmatic component, implying that the late-stage high-sulfidation fluids were dominantly derived from a blind intrusion potentially centred beneath La Grande.

The mineralising fluids associated with deposition of stage E massive sulfides at Rosario were hot acidic brines capable of transporting significant amounts of gold. However it is uncertain how much gold was precipitated along with copper and silver in these veins. Based on the thermodynamic modelling, it is recommended that gold is also analysed when drill core is assayed, as there is potentially a significant undefined gold resource associated with E veins Rosario.

Chapter 8. Conclusions and Genetic Model

This chapter is divided into three parts. First, the main conclusions of this research project are outlined. Based on these conclusions, a genetic model of the evolution of the Rosario magmatic-hydrothermal centre is then presented. Implications for exploration and recommendations for further work are discussed at the end of the chapter.

Main Conclusions

Tectonic Setting

The late Eocene-early Oligocene Rosario porphyry Cu deposit is hosted by the Rosario Porphyry, a monzonite intrusion ($^{40}Ar/^{39}Ar$ minimum age of 34.4 ± 0.3 Ma) emplaced into Permian volcanic (U/Pb age = 293 ± 14 Ma) and sedimentary rocks of the Collahuasi Formation, and Triassic plutons (ca. 240-211 Ma). Deposition of the host sequence is interpreted to have occurred in a shallow subaqueous to subaerial volcanic arc setting. The Collahuasi Porphyry is a granodiorite intrusion discordant to stratigraphy with a U/Pb age of 245 ± 12 Ma. It is unrelated to Tertiary magmatism and ore formation at Rosario.

Radiogenic isotope compositions and REE chemistry suggests that the parent magma to the Rosario Porphyry was derived from sub-arc mantle melts that interacted with a garnet-bearing source mineralogy at the base of old and thickened crust (Table 4.1). Similar geochemical characteristics have been recognised in pre- and post-mineralisation intrusions at the Ujina deposit (Table 4.1). Depleted MREE and Eu/Eu* values between 0.91 and 0.98 suggests that the Rosario and Ujina porphyry intrusions evolved from shallow-crustal, hornblende-fractionated hydrous bodies.

Structural Localisation of the Mineralised Veins

Structural orientations of vein types A to D at Rosario indicate that they formed under extension (i.e., the principal maximum compressive stress direction was subvertical). The high-grade type E Rosario veins are hosted by the southwest dipping Rosario fault system, which has cut the Rosario Porphyry and the earlier-formed A to D veins. Type E veins appear to have formed during normal movement on this low-angle fault system. North-northeast-trending, steeply dipping sinistral faults at Cerro La Grande host high-grade veins that are similar to the type E veins at Rosario. Normal

movement on the Rosario faults and sinistral movement on the La Grande faults are interpreted to have been contemporaneous. Local maximum and minimum compressive stress directions at the time of E vein formation at Rosario and La Grande were oriented northeast and southwest, respectively. The main northwest-trending faults at Rosario were reactivated as dextral faults after the mineralising event. Dextral movement on these structures is inferred to have occurred when the principal maximum compressive stress was south-southeast-directed.

The regional maximum compressive paleostress in the late Eocene was directed to the north-northeast (based on the reconstructions of Pardo-Casas and Molnar, 1987). Thus the local paleostress regime at Rosario was inconsistent with the regional paleostress field expected for the late Eocene-early Oligocene period. The late Eocene-early Oligocene structural evolution of other porphyry copper deposits in northern Chile (e.g., Chuquicamata, Lindsay et al., 1995; Reutter et al., 1996; Escondida, Richards et al., 2001) also formed under paleostress fields that were inconsistent with the orientation of regional stress. One mechanism advanced to explain this phenomenon was that movement on the Domeyko fault system changed from dextral to sinistral at about the time of late Eocene-early Oligocene porphyry ore formation (Lindsay et al., 1995; Reutter et al., 1996; Richards et al., 2001). Stress axis rotation (from northeast- to southeast-directed compression) was possibly the result of subduction of a southward propagating flat slab segment (James and Sacks, 1999), or of temporary trench blockages caused by subduction of seamounts or ocean ridges (Richards, 2000).

Contradicting regional and local stress fields possibly reflected a state in which upper crustal stress was decoupled from stress in the lower crust (which would possibly reflect the regional stress field). Propagation of normal faults in the upper crust may have been topographically driven. Alternatively, they may have resulted from partial gravitational collapse and isostatic rebound in the Domeyko Cordillera after the Incaic orogeny. Under gravitational collapse, southwest escape on the northwest-trending Rosario Fault and concomitant sinistral movement on the north-northeast-trending La Grande faults would have been constrained by the southeast directed maximum compressive stress. The local stress regime modelled for Rosario is consistent with paleostress fields observed at Chuquicamata (Lindsay et al., 1995; Reutter et al., 1996) and Escondida (Richards et al., 2001) at and after the time of porphyry ore formation.

The Rosario fault did not directly control emplacement of the Rosario Porphyry, rather the ore-related magmas ascended during exhumation of the Permian basement. Propagation of normal faults was contemporaneous with this period of exhumation. Furthermore, although porphyry copper deposits in the Collahuasi district are spatially associated with the Domeyko fault system, their emplacement, at least at the current erosion level, does not appear to have been directly controlled by this structure. Instead, subsidiary structures (e.g., the Rosario fault system) linking major regional faults (e.g., the Domeyko and Loa fault systems) are likely to have been important in localising emplacement of porphyry copper deposits in the Collahuasi district.

Vein and alteration paragenesis

Nine main vein stages have been recognised at Rosario:

- M veinlets: apparently barren beads and chains of magnetite occur in varying proportions throughout all rock-types except the Rosario Porphyry.
- A-1 and A-2 veinlets: biotite-quartz-chalcopyrite and quartz-albite-biotite-chalcopyrite-pyrite veinlets associated with the potassic-sodic alteration assemblage of biotite and albite. The greatest proportions of secondary biotite and albite occur in the country-rocks surrounding the Rosario Porphyry, with only small amounts occurring in the intrusion itself.
- A-3 veinlets/veins: quartz-K-feldspar-bornite-chalcopyrite surrounded by K-feldspar ± biotite-albite (potassic) alteration envelopes. The potassic assemblage is most abundant in the Rosario Porphyry and passes out to biotite-albite altered rocks in the Collahuasi Formation.
- B veins: molybdenite intergrown with quartz, minor K-feldspar and illite. These veins constitute the main molybdenite mineralising event at Rosario. B veins generally lack alteration envelopes.
- C veins: quartz-pyrite ± illite ± chlorite ± chalcopyrite. In the Rosario Porphyry, C veins are associated with illite alteration envelopes, but in the Collahuasi Formation, these veins are surrounded by alteration halos predominantly composed of chlorite.
- D veins: pyrite ± chalcopyrite ± quartz infill with quartz-muscovite alteration envelopes.

- E veins: sulfide minerals include pyrite, bornite, chalcopyrite, chalcocite, covellite, mawsonite and colusite. Quartz-alunite-pyrite altered rocks occur proximal to the veins.
- TES veins: tennantite-enargite infill have been superimposed on pyrite-chalcopyrite-bornite in E veins. Pyrophyllite-dickite alteration proximal to TES veins has overprinted the quartz-alunite-pyrite alteration envelopes associated with E veins. The pyrophyllite-dickite assemblage passes out through muscovite-quartz-pyrite to illite-smectite altered rocks distal from the veins. The muscovite-quartz-pyrite assemblage is interpreted to have formed contemporaneously with the pyrophyllite-dickite assemblage.

$^{40}Ar/^{39}Ar$ Geochronology

Results of $^{40}Ar/^{39}Ar$ geochronology indicate that two discrete and short-lived episodes of hydrothermal activity produced the observed ore and alteration mineral assemblages. The first episode is bracketed by the ages of primary biotite and C vein illite, which cooled through their blocking temperatures at 34.3 ± 0.3 and 34.5 ± 0.5 Ma, respectively. The second episode is constrained by the formation of E vein alunite (32.6 ± 0.3 Ma) and TES vein muscovite (32.9 ± 0.6 Ma; Clark et al., 1998), indicating that a period of 1.8 ± 0.4 m.y. separated the two hydrothermal events. An alunite age of 32.7 ± 1.6 Ma for E veins at La Grande indicates that the Rosario and La Grande massive sulfide veins formed during the same hydrothermal event. A Re/Os age of 33.3 ± 0.2 Ma was determined for molybdenite in a B vein from Rosario. Muscovite-quartz alteration superimposed on the vein may have disturbed the Re/Os isotopic system, or the molybdenite separate possibly contained K- and Al-silicate inclusions that were undetected. The Re/Os age may therefore have been reset by the hydrothermal fluids that formed muscovite, and is so, provides no additional constraints on the timing and duration of hydrothermal activity at Rosario.

At the Ujina deposit, primary biotite in the pre-mineralisation Ujina Porphyry yielded an $^{40}Ar/^{39}Ar$ age of 35.2 ± 0.3 Ma. This is the age at which biotite cooled through its closure temperature, and may be the minimum age of either the K-feldspar-biotite, or white mica-quartz alteration assemblage. The $^{40}Ar/^{39}Ar$ age of 34.7 ± 0.3 Ma for primary biotite in the post-mineralisation Inca Porphyry constrains the minimum age of magmatism and alteration at the Ujina deposit. Biotite in the Inca Porphyry may be only slightly younger than the magmatic age, because there are no high-temperature

alteration minerals in this intrusion to indicate that the biotite $^{40}Ar/^{39}Ar$ systematics were reset. The disturbed $^{40}Ar/^{39}Ar$ isotopic age of biotite in the La Profunda Pluton (80.4 ± 0.3 Ma) indicates that this intrusion is unrelated to late Eocene-early Oligocene magmatism in the Collahuasi district.

Fluid chemistry

The hydrothermal fluid responsible for the biotite-albite (A-1 and A-2 veins) and K-feldspar (A-3 veins) alteration assemblages were high temperature (400° to >600°C) hypersaline brines (40 to 45 eq. wt. % NaCl) and coexisting vapour. These fluids were oxidised ($H_2S/SO_4 \approx 1$) and had a bulk sulfur composition ($\Sigma^{34}S$) of about 3 per mil. The $\delta^{18}O$ composition of the fluids in equilibrium with biotite was 8.0 to 8.3 per mil, typical of hypersaline liquid exsolved from felsic magma (Fig. 7.14). Sulfide deposition occurred in the presence of H_2S, and in combination with water-rock interaction, when the fluids cooled below 400°C. Approximately half of the copper at Rosario is contained in the A veins.

Fluids that deposited quartz, and by association molybdenite, in B veins were high temperature (350° to 400°C) , moderate salinity brines (10 to 15 eq. wt. % NaCl). The weakly mineralised C veins and associated illite-chlorite alteration assemblage formed from cooler fluids (250° to 350°C) that had similar salinities (10 to 15 wt.% NaCl) to B veins. The quartz-alunite-pyrite-bearing E veins formed from 300° to 400°C and 10 wt.% NaCl fluids, whereas E vein chalcopyrite and bornite appear to have precipitated from 30 eq. wt. % NaCl brines at temperatures of 250° to 300°C. TES veins and associated pyrophyllite-dickite alteration assemblage formed between 250° and 320°C from dilute (5 eq. wt. % NaCl) fluids.

The acidic water that deposited alunite is inferred to have formed from magmatic vapour that condensed into liquid (e.g., Arribas, 1995), together with minor mixing with meteoric water. The bulk sulphur composition of the fluid was around 3 per mil. Despite the abundance of alunite, the fluids that formed this assemblage were reducing ($H_2S/SO_4 \approx 5$), consistent with magmatic-hydrothermal alunite from Julcani in Perú and Summitville, Colorado (Rye, 1993). The late Rosario veins appear to have been associated with 30 to 40% of the total copper deposition at Rosario. Textures indicative of hydraulic brecciation in the veins implies fluid overpressuring. The fluids that deposited E vein chalcopyrite-bornite-chalcocite were more oxidised ($H_2S/SO_4 \approx 2$) than the fluids that caused the earlier pyrite-alunite precipitation, but less oxidised

than the fluids that deposited A veins chalcopyrite-bornite ($H_2S/SO_4 \approx 1$). Deposition of E vein chalcopyrite-bornite-chalcocite potentially responded to flashing of slightly reduced brine, induced by hydraulic rupturing in the veins. TES veins formed from mixed magmatic-meteoric water (-3 to –1.6 ‰ $\delta^{18}O$) isotopically stable with pyrophyllite.

Depth of Formation

Pressure estimates from fluid inclusion data indicate that pressure conditions cycled between lithostatic and hydrostatic during both major episodes of hydrothermal activity at Rosario. The early A veins formed predominantly under lithostatic pressure at ~2 km depth. The pressure regime switched to hydrostatic by the time B and C veins had formed, but formation depth remained approximately constant between 1.8 and 2.0 km. The second major hydrothermal period saw the formation of E and TES veins. It occurred predominantly under hydrostatic conditions at depths of 600 to 800 m.

Depth estimates for the two main hydrothermal events at Rosario indicate that at least 1 km of rock was eroded between 34.4 and 32.6 Ma. Normal faulting at Rosario, possibly induced by gravitational collapse, accelerated exhumation of the Permian basement block and helped to promote telescoping of the high-sulfidation environment onto the Rosario Porphyry. No direct field evidence has been documented for these mass flow deposits, but careful analysis of clast types in the Tertiary gravels of the Sichal Formation may reveal evidence for exhumation of this and other hydrothermal centres in the Domeyko Cordillera.

Evolution of the Rosario Hydrothermal System

Figure 8.1 summarises the temporal evolution of the Rosario porphyry copper deposit. Formation of the Rosario porphyry Cu-Mo and related tennantite-enargite-bearing massive sulfide veins formed in two discrete hydrothermal events, separated by a 1.8 m.y. hiatus. The Rosario Porphyry was emplaced some time before 34.4 Ma, and the hydrothermal system that resulted in high temperature (>400°C) porphyry-style ore and alteration assemblages established itself as the intrusion crystallised. Hydrothermal activity related to the Rosario Porphyry continued to about 34.0 Ma when the system cooled to temperatures at which the assemblage illite-chlorite was stable (~250°C). Development at 32.6 Ma of the high temperature (300° to 400°C) quartz-alunite-pyrite and subsequent lower temperature (270°C) pyrophyllite-dickite alteration accompanied formation of tennantite-enargite-bearing massive sulfide veins.

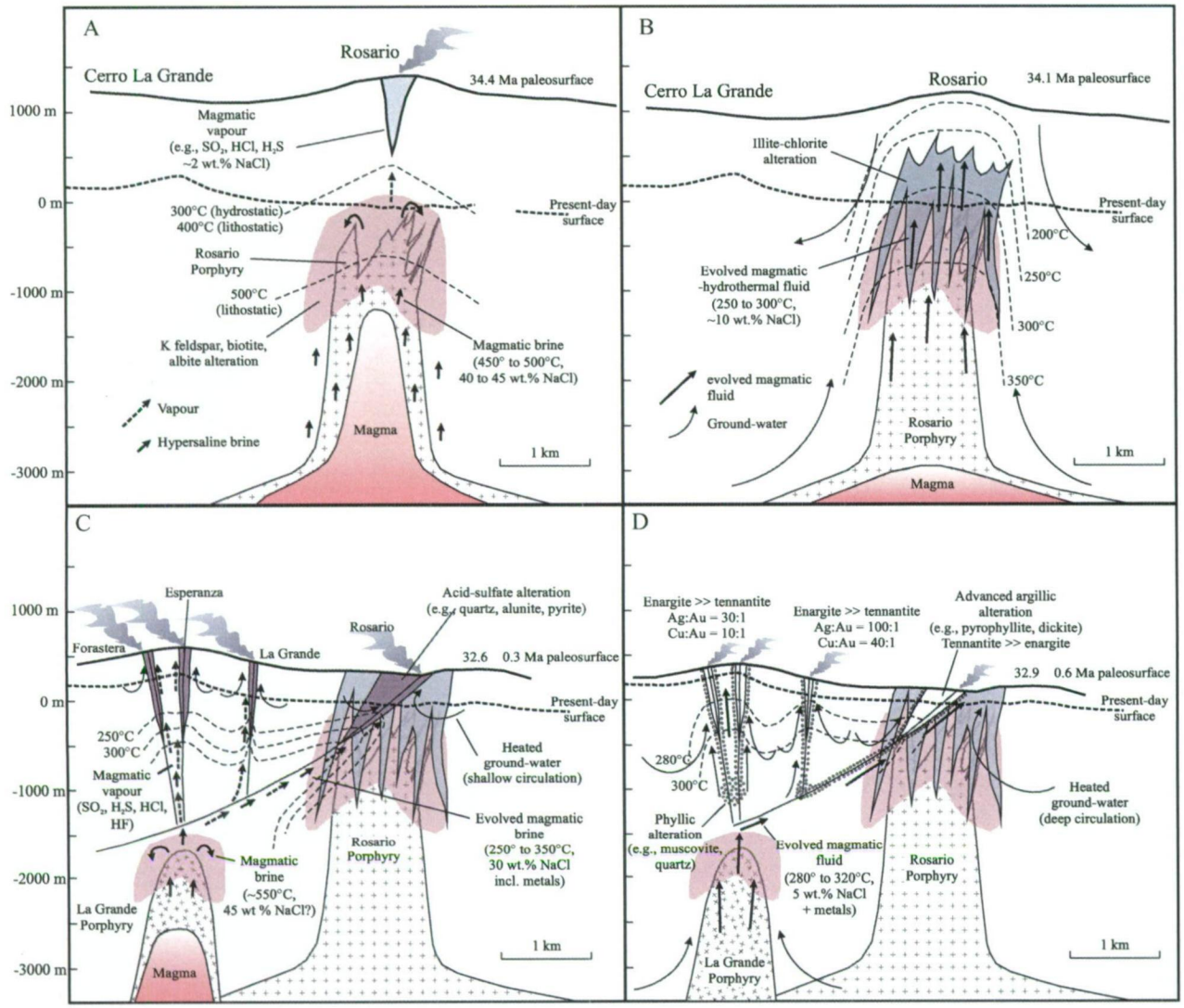

Figure 8.1. Schematic cross-sections through the Rosario and La Grande deposits, showing evolution of the Rosario magmatic-hydrothermal system. The present-day surface elevation at Rosario (4600 m a.s.l.) is shown as zero metres relative depth.

A) Position of the paleosurface at ca. 34.4 Ma, relative to the present-day surface, at the time of A vein formation and related biotite-albite and K feldspar alteration. Location of the isotherms is based on fluid inclusion homogenisation temperatures.

B) By about 34.0 Ma (minimum $^{40}Ar/^{39}Ar$ age of illite), the system was dominated by moderate salinity evolved magmatic-hydrothermal waters that produced B and C veins.

C) At 32.6 Ma, normal movement on the Rosario Fault (shallow apparent dip) coincided with emplacement of a second intrusion beneath Cerro La Grande. Magmatic vapour ascended along the faults and condensed to form the quartz-alunite-pyrite-diaspore assemblage associated with E veins. Fault-valve activity in the veins promoted discharge of overpressured brines and subsequent self-sealing by sulfide deposition, consistent with sulfide breccia and cementation textures in the veins.

D) Late stage TES veins and related pyrophyllite-dickite and muscovite-quartz alteration formed by 32.3 Ma (minimum $^{39}Ar/^{40}Ar$ age of muscovite). The hydrothermal system was probably dominated by cool, low salinity magmatic water, mixed with a small amount of meteoric water. Tennantite, enargite and precious metals were deposited during formation of pyrophyllite (and muscovite), presumably in response to mixing of the magmatic fluid with ground water.

A. Stock emplacement and early K-silicate alteration

Primary biotite in the Rosario Porphyry cooled through its closure temperature at 34.4 Ma. Emplacement of the stock into the deformed Permian volcanic terrane occurred some time before this. After emplacement, magmatic fluids were exsolved from the uppermost part of the crystallising stock at temperatures exceeding 500°C. The presence of melt inclusions coexisting with immiscible low density vapour and high density brine in A-3 veins within the Rosario Porphyry is evidence that exsolution of hydrothermal fluids was contemporaneous with magma crystallisation. Based on the cross-cutting relationships between M, A-1, A-2, and A-3 veins, it is possible that the magnetite alteration assemblage and some of the biotite-albite alteration assemblage formed from fluids that exsolved from a deeper-seated magma chamber and migrated to the site of ore formation prior to emplacement of the Rosario Porphyry.

At the site of A vein formation, magmatic-hydrothermal fluids had temperatures of 500°C and consisted of hypersaline brine (~ 45 wt.% NaCl) and low density vapour (2 wt.% NaCl). At temperatures above 400°C and low strain rates ($<10^{-14}$/s) the porphyry and country rock would have behaved quasi-plastically. This would have limited fracture propagation, except in periods of high strain in which the rocks respond to dike emplacement or tectonic activity (Fournier, 1987, 1999). Thus the pressure regime at Rosario was lithostatic, and any fractures that formed by fluid overpressures would have sealed quickly by quartz precipitation (Fournier, 1999). Cycling between fluid overpressuring and decompression possibly explains the presence of halite-homogenising brine inclusions in quartz samples from A-2 and A-3 veins. These veins also contain hypersaline fluid inclusions that homogenise by disappearance of the vapour bubble, which probably formed by phase separation of magmatic-hydrothermal fluid when the rock fractured.

In the model presented here, a supercritical fluid containing about 10 wt.% NaCl at temperatures >600°C was generated in a shallow crystallising magma body at depths of 5 to 6 km. The fluid ascended in the single phase field below its condensation point curve and intersected its solvus at about 2.4 km (path 1, Fig. 8.2). In the two-phase region, the fluid separated into high density brine and low density vapour. Biotite-albite and K-feldspar alteration assemblages, associated with A veins, were superimposed on the host rocks when the magmatic-hydrothermal brines reacted with the wall rocks (Fig. 8.1a). That the biotite-albite and K-feldspar alteration assemblages

formed from magmatic-hydrothermal fluids is evident from the fluid inclusions in A veins and in the oxygen isotope composition of the fluids that formed hydrothermal biotite in the Rosario Porphyry. It is possible that vapour separated from the brine and ascended buoyantly to the crustal level where it condensed into liquid and caused high level advanced argillic alteration near the outflow zone (Fig. 8.1a). No evidence of this potentially early-formed advanced argillic alteration is preserved in the rock record, as over 1 km of rock has been eroded since formation of the A veins and related potassic alteration.

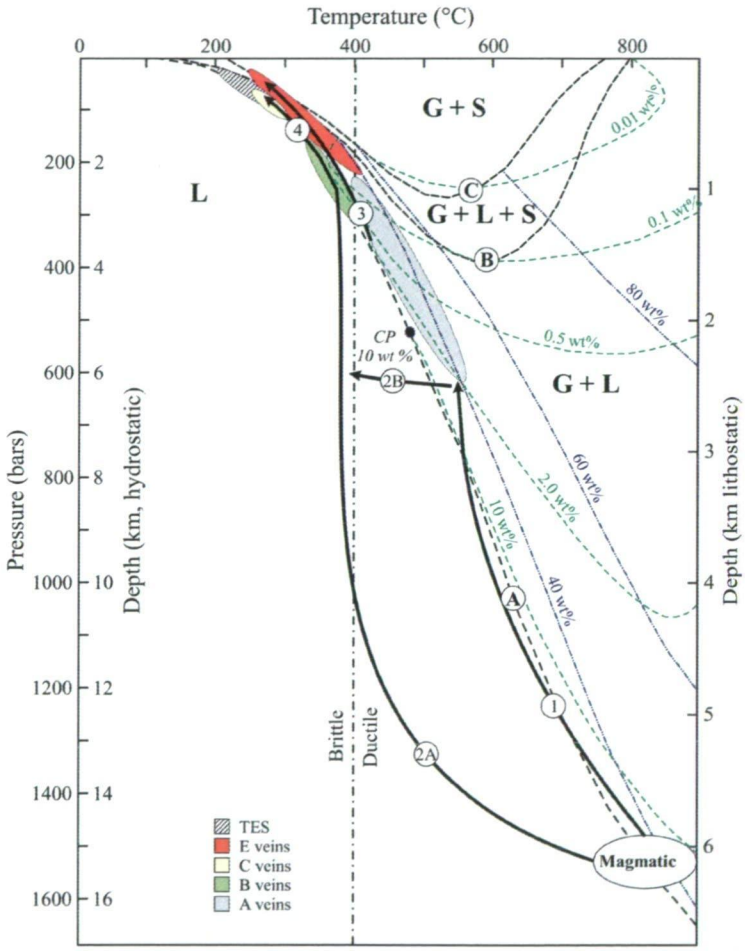

Figure 8.2. Pressure-temperature diagram showing phase relations in the NaCl-H_2O system at lithostatic and hydrostatic pressures. Based on data of Bodnar et al. (1985a), and Pitzer and Pabalan (1986), adapted from Fournier (1987; 1999), and Muntean and Einaudi (2001). G = gas, L = liquid, S = solid salt. Double dot-dashed lines are contours of constant wt.% NaCl dissolved in brine; short dashed lines show the condensation point curves for steam containing the indicated values of wt. percent NaCl. Curve A shows the boiling point curve for a 10 wt.% NaCl solution at pressures and temperatures below its critical point (CP), and the condensation point curve for steam containing 10 wt.% NaCl at temperatures and pressures above the critical point. Curve B shows the three phase boundary, G + L +S, for the system NaCl-H_2O; curve C shows the three phase boundary, G + L + S, for the system NaCl-KCl-H_2O, with Na/K in solution fixed by equilibration with albite and K feldspar at the indicated temperatures. The vertical dashed-dot line shows the approximate temperature of the brittle-ductile boundary when the strain rate is 10^{-14} s^{-1}. Ascent paths for the various exsolved magmatic fluids are shown with the corresponding fields of fluid inclusion populations.

B. Collapse of the Rosario magmatic-hydrothermal system

As cooling of a stock progresses, convection in the magma stops and the fluid and heat flux from the conductively cooling parent magma chamber decreases abruptly (Hedenquist et al., 1998). Conductive cooling and downward retraction of the magma crystallisation front results in collapse of the isotherms in the upper part of the system, with temperature gradients attenuated down through the crystallised part of the stock. Deepening of the K-silicate assemblage will occur if fluids continue to be exsolved during retreat of the crystallisation front.

Deposition of molybdenite-bearing B veins at Rosario post-dated the M and A veins, but pre-dated C veins and related illite-chlorite alteration. The highest concentrations of molybdenite occur within the Rosario Porphyry in quartz veins that lack alteration envelopes, implying that the fluids were in equilibrium with the pre-existing K-feldspar-biotite-albite alteration. Fluid inclusion evidence indicates that molybdenite was deposited with quartz at temperatures between 350° and 400°C, so these fluids were cooler than those that caused the K-feldspar-biotite-albite alteration (500°C). It is inferred that the molybdenite-bearing veins formed when the isotherms collapsed as the stock cooled and crystallised.

Magmatic-derived hydrothermal fluids that ascended to high levels in the crystallising intrusion would have passed through a column of feldspar-rich alteration, which potentially buffered any acid present. The illite-chlorite alteration assemblage at Rosario represents domains of early acid neutralisation by feldspar-altered wall rocks. (Fig. 8.1b). Fluid inclusion evidence indicates that the type C veins associated with illite-chlorite alteration formed at about 250°C, consistent with mineral stability temperatures defined empirically for this assemblage by Reyes (1990). There are two possible pressure-temperature pathways for the type C hydrothermal fluids, assuming they were of magmatic derivation. Either the fluid exsolved from the magma never intersected its solvus during ascent (path 2A, Fig. 8.2) and its salinity (15 wt.% NaCl) reflects the bulk salinity of the magmatic fluid (Hedenquist et al., 1998), or the fluid was a low density, moderate salinity vapour that cooled isobarically and condensed into itself (path 2B, Fig. 8.2; Heinrich, in press). Both paths can potentially lead to sericite alteration by cooling, if the fluid was stable with K-feldspar and K/H mole ratios remain constant (Hemley, 1959; Sverjensky et al., 1991; Hedenquist et al., 1998). The salinity of the type C fluid was probably too high to have been transported

as vapour. Thus the preferred explanation is that of Hedenquist et al. (1998), in which the fluids failed to intersect their solvus and resulted in intermediate argillic alteration through K-Mg metasomatism as the fluids cooled. The small amounts of chalcopyrite in C veins may have been derived by local dissolution and reprecipitation as the wall rock neutralised the acid fluids, but there is no clear textural evidence of this. Alternatively, the copper precipitated in C veins represented new additions to the ore deposit.

The age of illite-chlorite alteration (34.5 ± 0.5 Ma) is indistinguishable from that of the cooling age of primary biotite in the Rosario Porphyry. It is interpreted to be the time when the fluids cooled sufficiently to stabilise the assemblage illite-chlorite. The duration of hydrothermal activity at Rosario is consistent with the expected longevity of a hydrothermal system related to a single, unreplenished intrusion that typically crystallises and cools in <100,000 years (Cathles, 1977; Norton, 1982; Hedenquist and Richards, 1998). Fluid inclusion data indicate that the fluids that formed the B veins had a temperature between 350° and 400°C with an average salinity of 9 wt.% NaCl, whereas those that deposited the illite-chlorite assemblage reached a maximum temperature of 350°C with an average salinity of 15 wt.% NaCl. At hydrostatic pressure, these temperatures are consistent with paleowater table depths of about 1.6 km to 1.8 km, similar to the lithostatic depth inferred for the K-silicate alteration. Thus there was little erosion between formation of K-silicate and intermediate argillic alteration assemblages. The major transition was structural, with the development of faults that connected the porphyry environment to the surface, consistent with the temperature decrease below that where the rocks deform in a quasi-plastic style.

At Far Southeast, Shinohara and Hedenquist (1997) modelled a 2 km thick convecting magma chamber, emplaced at 6 km depth and at 800°C. They concluded that thermal collapse of the magmatic-hydrothermal system occurred within 3000 years of emplacement, long before the ca. 5000 to 10,000 years required to fully establish meteoric convection (Cathles, 1977). Lower temperature magmatic fluids can thus ascend, under hydrostatic pressure, without mixing with meteoric water, which may explain the potential magmatic origin of the C type fluid that caused illite-chlorite alteration at Rosario. Fluid to rock ratios are inferred to have been higher in the core than on the margins, given the zonation from an inner core of illite to chlorite-illite alteration.

C. Quartz-alunite-pyrite alteration and formation of the E veins

The stable isotope data indicate that E veins and quartz-alunite-pyrite altered rocks formed from magmatic dominated fluids. At Rosario this assemblage is controlled by the moderately southwest-dipping Rosario Fault, whereas at Cerro La Grande it is controlled by steep faults (Fig. 8.1c). These structures are inferred to intersect ~1.6 km below the present surface at Cerro La Grande (Fig. 8.1c), implying that the acid fluids that caused the quartz-alunite-pyrite-diaspore alteration originated in the region beneath Cerro La Grande.

Fluid inclusion and sulfur isotope data indicate that temperatures at the base of the quartz-alunite-pyrite zone were between 350° and 400°C (4,140 m elevation), whereas, temperatures decreased to 260°C by the time the fluids ascended to 4,290 m elevation. The sharp temperature gradient implies that the hydrothermal system operated in the transition from lithostatic to hydrostatic pressures at about 800 m paleodepth. The E type fluid that formed quartz-alunite-pyrite-diaspore alteration is inferred to have followed path 3 in Figure 8.2. A low density vapour separated from the magmatic-hydrothermal fluid when it entered the two phase (liquid + gas) region, and ascended buoyantly ahead of the dense brine.

The acid nature of the fluid resulted from disproportionation of SO_2 at <400°C to form H_2SO_4 and H_2S (Holland, 1965; Rye et al., 1992). However, the high temperatures estimated for the quartz-alunite-pyrite assemblage may have limited reactivity of the fluids (Giggenbach, 1997) and resulted in the formation of quartz-alunite-pyrite-diaspore, rather than strong leaching and residual quartz development (Masterman et al., 2002). Although sufficiently oxidised to precipitate abundant alunite, the fluids were clearly H_2S-predominant with average H_2S/SO_4 values of 5:1. The oxidation state of the fluid appears to have been controlled by interaction with earlier-formed sulfides deeper along the flow path.

The hydrothermal system associated with the Rosario Porphyry had waned before the formation of the E veins at Rosario. That fluid temperatures increased again (Figs. 7.3 and 7.4) implies the presence of a blind intrusion at depth. It is inferred that the intrusion was emplaced beneath or at the intersection of structures that controlled hydrothermal fluid flow between La Grande and Rosario (Fig. 8.1c).

In the Rosario E veins, pyrite was the earliest-formed sulfide, and is correlated with alunite (Fig. 5.2). The pyrite occurs as clasts that are partly disaggregated and cemented by chalcopyrite, bornite and chalcocite. This relationship is interpreted as evidence that Cu-Fe sulfide deposition in E veins followed formation of the quartz-alunite-pyrite assemblage. Fluid inclusion data from quartz gangue indicates the fluids that deposited Cu-Fe sulfides were moderate temperature (mean 290°C) and saline (30 eq. wt. % NaCl) brines. Some brine inclusions homogenised via halite dissolution, indicating that they possibly formed when the fluids were overpressured.

High-angle normal faults (≥60°) are well oriented for reactivation, but do not sustain significant fluid overpressures. Low-angle normal faults (≤40°) tend not to be seismically active and are potentially locked up (Jackson and White, 1989). In contrast to high-angle normal faults, low-angle normal faults are capable of sustaining high levels of fluid overpressure (Sibson, 2001). Valving action is inferred to have discharged overpressured fluids along the Rosario fault system. Reversion towards hydrostatic fluid pressures after the veins ruptured, promoted self-sealing by sulfide deposition (e.g., Sibson, 2001). Eventually fluid overpressures were re-established at depth and the cycle of fault rupturing and fluid discharge was repeated. Breccia textures in the sulfide-rich parts of E veins are consistent with the possibility of cyclic fluid overpressuring and decompression during formation of the E veins. Similar processes occurred during sinistral strike-slip movement on the La Grande fault system.

With the exception of the lack of a silicified core zone, the styles of alteration and the spatial zonation of the altered zones associated with the Collahuasi district massive sulfide veins are characteristic of high sulfidation deposits worldwide (Arribas, 1995). White (1991) proposed a two-stage genetic model for high sulfidation deposits, in which the first stage is characterised by magmatic gases which cause intense acid leaching and development of advanced argillic alteration assemblages. Mineral deposition occurs in stage two when dense liquids exploit the permeable acid-leached zone and precipitate metals. Arribas (1995) advanced this model by invoking two possible origins for the mineralising stage two fluids. Magmatic gases condensed or dissolved into a heated groundwater convection cell, can produce an acidic, low-salinity mineralising water. Alternatively, mineralising magmatic brines ascend to the region of advanced argillic alteration, where they mix with ground waters and precipitate high-sulfidation ore.

The possibility of a late-stage magmatic brine precipitating ore minerals is consistent with the observed paragenetic relationships and measured salinities at Rosario. The mineralising fluid most likely transported copper as a chloride complex (e.g., $CuCl_{(aq)}$ or $CuCl_2^-{}_{(aq)}$). This brine lagged behind the less dense, faster moving front of magmatic vapour. Copper-silver ore precipitated from the brine in veins surrounded by envelopes of advanced argillic alteration that formed due to action of the vapour phase (e.g., White, 1991). Gold solubility in these brines is predicted to have been high (Figs. 7.15 and 7.16). However it not certain how much gold was precipitated with the copper and silver, due to a lack of assay data. Liquid-rich inclusions with variable salinities coexist with the brine inclusions and homogenise at similar temperatures. Some of these inclusions may have been trapped contemporaneously with brine inclusions, and may provide evidence that the brine mixed with a low salinity fluid, although the oxygen and deuterium isotopes provide little, if any, evidence for meteoric input. Mixing possibly caused metals to deposit in response to dilution (lowering $[Cl^-]$ and pH), and cooling.

D. TES veins and pyrophyllite-dickite alteration

Chalcopyrite, bornite and chalcocite in the E veins, and alunite and quartz in the associated alteration envelopes have been replaced by pyrophyllite and dickite. This is inferred to have occurred synchronous with tennantite and enargite deposition at Rosario and La Grande. Spatial zonation of the sulfosalts is characterised by the predominance of tennantite at Rosario, and enargite at Cerro La Grande (Fig. 8.1d). Historical mining records indicate that massive sulfide veins on Cerro La Grande were exploited for Cu and Au, whereas those at Rosario and Poderosa were mined for Cu and Ag. Based on the spatial distribution of sulfosalts and precious metals, and geometry of the fault system, it is inferred that the Ag-rich tennantite (TES) veins at Rosario formed on the margins of the 32.9 Ma hydrothermal system. By contrast, proximal Au-rich enargite veins at Cerro La Grande are inferred to occur directly above a blind intrusion emplaced at this time.

Alteration at the highest levels of exposure at Rosario and La Grande are characterised by pyrophyllite and dickite passing downward and outward to muscovite alteration (Fig. 8.1d). Pyrophyllite and dickite do not occur in equilibrium with the alunite-bearing assemblage. The age of muscovite (32.9 ± 0.6 Ma; Clark et al., 1998), and by association pyrophyllite, is indistinguishable from the age of alunite. This

suggests that the pyrophyllite-dickite assemblage formed after quartz-alunite-pyrite-alteration of the rocks. Pyrophyllite-rich alteration is interpreted to have resulted from upward cooling of a fluid initially in equilibrium with sericite. Muscovite occurs beneath the pyrophyllite zone in the La Grande vein, and occurs at deep levels at Rosario (Fig. 8.1d). That muscovite occurs as a halo to the pyrophyllite-dickite alteration assemblage in higher levels at Rosario and La Grande reflects increasing K/H values in the fluids as they were neutralised by reaction with the wall rock. The oxygen and deuterium isotopic composition of the fluids that formed pyrophyllite differ significantly from those that deposited alunite The alunite-forming fluids were dominantly magmatic, whereas those that precipitated pyrophyllite exhibit mixed magmatic-meteoric compositions. The fluid that caused pyrophyllite alteration also appears to be responsible for the enargite and tennantite mineralisation. Thus the process of absorption of magmatic fluid by meteoric water, which formed the pyrophyllite alteration, may have also caused sulfosalts to precipitate. Similar mixing processes were argued by Hedenquist et al. (1998) to explain contemporaneous enargite-pyrophyllite formation in the Lepanto ore body in the Philippines.

Fluid inclusion data indicate that quartz gangue in the TES veins was deposited at a minimum paleodepth of 600 m. The Rosario porphyry system was therefore partially exhumed at the time the Rosario veins formed. Exhumation resulted in telescoping of the epithermal environment onto the core of the Rosario Porphyry, and superimposed two distinct mineralisation styles within the same ore deposit.

Implications for Exploration

Cooling and collapse of the Rosario hydrothermal system implies emplacement of a second blind intrusion, somewhere beneath the Rosario and Cerro La Grande high-sulfidation vein systems. Precious metal zoning at the district scale, together with the overall fault geometries (Fig. 8.2d), suggest that rejuvenated magmatic-hydrothermal activity was focused between Cerro La Grande. Exploration for additional copper resources in the Rosario area should thus be guided by the distribution of the phyllic assemblage beneath Cerro La Grande, as this alteration represents the root zone of the epithermal system, and potentially occurs at the top of an as yet undrilled porphyry-style ore deposit.

The potential for Au mineralisation in the Rosario and La Grande vein systems has been highlighted in the thermodynamic modelling (Chapter 7). The results of this

modelling show the fluids that deposited sulfides in the late Rosario and La Grande veins, also had the capacity to transport gold. Moreover, significant quantities of gold were mined in the historical workings on Cerro La Grande. It is therefore recommended that gold and silver are included in the element suite when drill core and rock chip samples are assayed. Potentially there is a significant gold resource at Rosario in addition to the enormous copper reserves. Given the discovery of copper-molybdenite skarn mineralisation on the northeast side of the Rosario Porphyry, there may also be potential for distal base metal (Zn, Pb) and/or precious metal (Au, Ag) carbonate-hosted deposits.

Reconnaissance short wave infrared (SWIR) spectroscopy has identified variable white mica compositions in the hydrothermally altered rocks at Rosario and La Grande. The presence of muscovite may indicate lateral proximity to advanced argillic alteration, potentially associated with massive sulfide veins. Alternatively, muscovite may occur in the vertical transition between the epithermal and porphyry environments (e.g., Lepanto-FSE; Hedenquist et al., 1998). Illite occurs with or without chlorite in the weakly mineralised assemblage that is the latest stage of porphyry-style alteration and mineralisation at Rosario. However, illite is also present in an assemblage with smectite, distal from advanced argillic altered rocks that surround massive-sulfide veins. The presence of illite ± chlorite may therefore indicate proximity to porphyry style mineralisation in the Collahuasi district, whereas the assemblage illite-smectite may be the outer zone of alteration related to high level epithermal veins. An SWIR spectrometer (e.g., a PIMA) should be a standard exploration tool at Collahuasi, as it can discriminate the compositions of white micas (and other fine grained hydrothermal minerals) in the field, and can help evaluate the distribution of alteration assemblages. Ultimately, when integrated with other exploration data, the alteration mineral assemblages can be used to guide exploration in the Collahuasi district.

Future Work

Some recommendations for future research are:

- The $^{40}Ar/^{39}Ar$ geochronology only determined the cooling ages of primary biotite in the ore-related intrusions at Rosario and Ujina. Additional U/Pb geochronology of these intrusions is needed to establish their emplacement ages and to fully evaluate their cooling histories.

- U/Th/He thermochronology of rocks in the host sequence and mineralised intrusions would augment and/or refine the exhumation model which is currently based on pressure-depth estimates derived from fluid inclusion data and temporally constrained by $^{40}Ar/^{39}Ar$ geochronology.
- Further $\delta^{18}O$ and δD analyses on the various alteration minerals (e.g., biotite, illite, muscovite, pyrophyllite, dickite, alunite, etc.) would improve constraints on the various types of hydrothermal fluids involved in alteration of the rocks and ore formation, and on the amount of mixing that occurred between the different fluids.
- Pb isotope work on the various sulfide and sulfate stages would further evaluate all possible reservoirs of the ore-forming fluids.
- Structural mapping in the new open pit at Rosario may help to refine the structural model for the district.

References

Ahmad, S. N., and Rose, A. W., 1980, Fluid inclusions in porphyry and skarn ore at Santa Rita, New Mexico: Economic Geology, v. 75, p. 229-250.

Aitcheson, S. J., Harmon, R. S., Moorbath, S., Schnieder, A., Soria, E. E., Steele, G., Swainbank, I., and Wörner, G., 1995, Pb isotopes define basement domains of the Altiplano, central Andes: Geology, v. 23, p. 555-558.

Allmendinger, R. W., Jordon, T. E., Kay, S. M., and Isacks, B. L., 1997, The evolution of the Altiplano-Puna plateau of the central Andes: Annual Reviews of Earth and Planetary Sciences, v. 25, p. 139-174.

Alpers, S. N., and Brimhall, G. H., 1989, Paleohydrologic evolution and geochemical dynamics of cumulative supergene metal enrichment at La Escondida, Atacama Desert, northern Chile: Economic Geology, v. 84, p. 229-255.

Anon, 1993, Collahuasi Prefeasibility Study: Internal Company Report, Compañia Minera Doña Inés de Collahuasi, Santiago, 53 p.

Arehart, G. B., Kesler, S. J., O'Neill, J. R., and Foland, K. A., 1992, Evidence for the supergene origin of alunite in sediment-hosted micron gold deposits, Nevada: Economic Geology, v. 87, p. 263-270.

Arribas, A., Jr., 1995, Characteristics of high-sulfidation epithermal deposits, and their relation to magmatic fluid, *in* Thompson, J. F. H., ed., Magmas, Fluids, and Ore Deposits: Mineralogical Association of Canada Short Course Series, v. 23, p. 419-454.

Arribas, A., Jr., Cunningham, C. G., Rytuba, J. J., Rye, R. O., Kelly, W. C., Podwysocki, M. H., McKee, E. H., and Tosdal, R. M., 1995a, Geology, geochronology, fluid inclusions and isotope geochemistry of the Rodalquilar gold alunite deposit, Spain: Economic Geology, v. 90, p. 795-822.

Arribas, A. Jr., Hedenquist, J. W., Itaya, T., Okada, T., Concepcion, R. A., and Garcia, J. S. J., 1995b, Contemporaneous formation of adjacent porphyry and epithermal Cu-Au deposits over 3000 Ka in northern Luzon, Philippines: Geology, v. 23, p. 337-340.

Atkinson, W. W., Jr., Souviron, A., Vehrs, T. I., and Faunes, A., 1996, Geology and mineral zoning of the Los Pelambres porphyry copper deposit, Chile, *in* Camus, F., Sillitoe, R. M., and Petersen, R., eds., Andean copper deposits: New discoveries, mineralization, styles and metallogeny: Society of Economic Geologists Special Publication, n. 6, p. 131-156.

Audetát, A., and Günther, D., 1999, Mobility and H_2O loss from inclusions in natural quartz crystals: Contributions to Mineralogy, v. 137, p. 1-14.

Audetát, A., Günther, D., and Heinrich, C., 1998, Formation of a magmatic-hydrothermal ore deposit: Insights with LA-ICPMS analysis of fluid inclusions: Science, v. 279, p. 2091-2094.

Bahlburg, H., and Breitkreuz, C., 1991, Paleozoic evolution of active margin basins in the southern Central Andes (northwestern Argentina and northern Chile): Journal of South American Earth Sciences, v. 4, p. 171-188.

Barra, F., Ruiz, J., Mathur, R., and Titley, S., 2003, A Re-Os study of sulfide minerals from the Bagdad porphyry Cu-Mo deposit, northern Arizona, USA: Mineralium Deposita, http://link.springer-ny.com/link/service/journals/00126/contents/02/00341/paper/s00126-002-0341-0ch000.html.

Barriero, B. A., and Clark, A. H., 1984, Lead isotopic evidence for evolutionary changes in magma-crust interaction, Central Andes, southern Perú: Earth and Planetary Science Letters, v. 69, p. 30-42.

Barton, P. B., Bethke, P. M., and Toulmin, P., 1963, Equilibrium in ore deposits: Symposium on the mineralogy of sulfides: International Mineralogical Association, 3rd General Meeting, Washington, DC, 1963, p. 171-185.

Barton, P. B., Jr., and Skinner, B. J., 1967, Sulfide mineral stabilities, *in* Barnes, H. L., ed., Geochemistry of hydrothermal ore deposits: New York, Holt, Rinehart and Winston, p. 236-333.

Baumer, R. E., and Fraser, R. B., 1975, Panguna porphyry copper deposit, Bougainville, *in* Knight, C. L., ed., Economic Geology of Australia and Papua New Guinea: Australian Institute of Mining and Metallurgy Monograph 5, p. 235-263.

Belousova, E. A., Griffin, W. L., Shee, S. R., Jackson, S. E., and O'Reilly, S. Y., 2001, Two age populations of zircons from the Timber Creek kimberlites, Northern Territory, as determined by laser-ablation ICP-MS analysis: Australian Journal of Earth Sciences, v. 48, p. 757-765.

Benning, L. G., and Seward, T. M., 1996, Hydrosulfide complexing of Au (I) in hydrothermal solutions from 150° to 400°C and 500 to 1500 bars: Geochimica et Cosmochimica Acta, v. 60, p. 1849-1871.

Berry, R. F., 1989, The history of movement on the Henty Fault Zone, western Tasmania: An analysis of fault striations: Australian Journal of Earth Sciences, v. 36, p. 189-206.

Berry, R. F., Jenner, G. A., Meffre, S., and Tubrett, M. N., 2001, A North American provenance for Neoproterozoic to Cambrian sandstones in Tasmania?: Earth and Planetary Science Letters, v. 192, p. 207-222.

Bigeleisen, J., Periman, M. L., and Posser, H. C., 1952, Conversion of hydrogenic materials to hydrogen for isotopic analysis: Analytical Chemistry, v. 27, p. 1356-1357.

Bisso, C. B., Duran, M., and Gonzales, A. A., 1998, Geology of the Ujina and Rosario copper porphyry deposits, Collahuasi district, Chile, *in* Porter, M.T, ed., Porphyry and hydrothermal copper and gold deposits: A global perspective, Conference proceedings, Perth, Australia, p. 217-232.

Black, L. P., and Gulson, B. L., 1978, The age of the Mud Tank Carbonatite, Strangeways Range, Northern Territory: Bureau of Mineral Resources Journal of Australian Geology and Geophysics, v. 3, p. 227-232.

Black, L. P., Kamo, S. L., Williams, I. S., Foudoulis, C., Claoué-Long, J. C., Korsch, R. J., and Davis, D. W., 2000, The quest for a high-quality zircon standard for microbeam Pb-U-Th geochronology: 15th Australian Geological Convention, Geological Society of Australia Abstracts, n. 59, p. 43.

Bloom, M. S., 1981, Chemistry of inclusion fluids: Stockwork molybdenum deposits from Questa, New Mexico, and Hudson Bay Mountain and Endako, British Columbia: Economic Geology, v. 76, p. 1906-1920.

Bodnar, R. J., 1994, Synthetic fluid inclusions XII. Experimental determinations of the liquidus and isochores for a 40 wt. % H_2O-NaCl solution: Geochimica et Cosmochimica Acta, v. 55, p. 1053-1063.

Bodnar, R. J., 1995, Fluid inclusion evidence for a magmatic source for metals in porphyry copper deposits, *in* Thompson, J. F. H., ed., Magmas, Fluids, and Ore Deposits: Mineralogical Society of Canada Short Course Series, v. 23, p. 139-152.

Bodnar, R. J., and Beane, R. E., 1980, Temporal and spatial variations in hydrothermal fluid characteristics during vein filling in pre-ore cover overlying deeply buried porphyry copper-type mineralisation at Red Mountain, Arizona: Economic Geology, v. 75, p. 876-893.

Bodnar, R. J., Burnham, C. W., and Sterner, S. M., 1985, Synthetic fluid inclusions in natural quartz. III. Determination of phase equilibrium properties in the system H_20-NaCl to 1000°C and 1500 bars: Geochimica Cosmochimica Acta, v. 49, p. 1861-1873.

Bodnar, R. J., Sterner, S. M., and Hall, D. L., 1989, SALTY: A FORTRAN program to calculate compositions of fluid inclusions in the system NaCl-KCl-H_2O: Computers and Geosciences, v. 15, p. 19-41.

Bodnar, R. J., and Vityk, M. O., 1994, Interpretation of microthermometric data for H_2O-NaCl fluid inclusions, *in* De Vivo, B., and Frezzotti, M. L., eds., Fluid inclusions in minerals: Methods and applications, Short Course of the Working Group (IMA) Inclusions in Minerals, p. 117-130.

Brandon, A. D., Creaser, R. A., Shirey, S. B., and Carlson, R. W., 1996, Osmium recycling in subduction zones: Science, v. 272.

Burnham, W. C., 1997, Magmas and hydrothermal fluids, *in* Barnes, H. L., ed., Geochemistry of hydrothermal ore deposits: New York, Wiley, p. 63-123.

Camus, F., 1975, Geology of the El Teniente orebody with emphasis on wall-rock alteration: Economic Geology, v. 70, p. 1341-1372.

Camus, F., 2002, The Andean porphyry systems, *in* Cooke, D.R. and Pongratz, J., eds., Giant ore deposits: Characteristics, genesis and exploration: CODES Special Publication 4, University of Tasmania, Hobart, Australia, p. 5-21.

Candela, P. A., 1989, Magmatic ore-forming fluids: Thermodynamics and mass transfer calculation of metal concentrations, *in* Whitney, J. A., and Naldrett, A. J., eds., Ore deposition associated with magmas: Reviews in Economic Geology, v. 4, p. 203-221.

Candela, P. A., 1991, Physics of aqueous phase evolution in plutonic arc environments: American Mineralogist, v. 76, p. 1081-1091.

Candela, P. A., 1997, A review of shallow, ore-related granites: Textures, volatiles, and ore metals: Journal of Petrology, v. 38, p. 1619-1633.

Candela, P. A., and Piccoli, P. M., 1995, Model ore-metal partitioning from melts into vapour and vapour/brine mixtures, *in* Thompson, J. F. H., ed., Magmas, fluids and ore deposits: Mineralogical Association of Canada Short Course Series, v. 23, p. 101-127.

Cathles, L. M., II, 1977, An analysis of the cooling of intrusives by groundwater convection that includes boiling: Economic Geology, v. 72, p. 804-826.

Chesley, J. T., and Ruiz, J., 1997, Preliminary Re-Os dating on molybdenite mineralization from the Bingham Canyon porphyry copper deposit, Utah, *in* John, D. A., and Ballantyne, G. H., eds., Geology and ore deposits of the Oquirrh and Wasatch Mountains, Utah, 29. Society of Economic Geologists Guidebook, p. 237-244.

Chelsey, J. T., and Ruiz, J., 1998, Implications from the Re-Os systematics of the Columbia River flood basalts: Earth and Planetary Science Letters, v. 154, p. 1-11.

Clark, A., H., 1993, Are outsize porphyry copper deposits either anatomically or environmentally distinctive?, *in* Whiting, B. H., Hodgson, C. J., and Mason, R., eds., Giant ore deposits: Society of Economic Geologists Special Publication, n. 2, p. 213-283.

Clark, A. H., Archibald, D. A., Lee, A. W., Farra, E., and Hodgson, C. J., 1998, Laser probe $^{40}Ar/^{39}Ar$ ages of early- and late-stage alteration assemblages, Rosario porphyry copper-molybdenum deposit, Collahuasi District, I Region, Chile: Economic Geology, v. 93, p. 326-337.

Clark, A. H., Farra, E., Kontak, D. J., Langridge, R. J., Arenas F., M. J., France, L. J., McBride, S. L., Woodman, P. L., Wasteneys, H. A., Sandeman, H. A., and Archibald, D. A., 1990, Geologic and geochronologic constraints on the metallogenic evolution of the Andes of southeastern Perú: Economic Geology, v. 85, p. 1520-1583.

Clark, A. H., Farrar, E., Camus, F., and Quirt, G. S., 1983, K-Ar data for the El Teniente porphyry copper deposit, central Chile: Economic Geology,, v. 78, p. 1003-1006.

Clayton, R. N., and Mayeda, T. K., 1963, The use of bromine pentafluoride in the extraction of oxygen from oxides and silicates for isotopic analysis: Geochimica et Cosmochimica Acta, v. 27, p. 43-52.

Cline, J. S., and Bodnar, R. J., 1991, Can economic porphyry copper mineralisation be generated by a typical calc-alkaline melt: Journal of Geophysical Research, v. 96, p. 8113-8126.

Cline, J. S., and Bodnar, R. J., 1994, Direct evolution of brine from a crystallising silicic melt at Questa, New Mexico, molybdenum deposit: Economic Geology, v. 89, p. 1780-1802.

Cline, J. S., and Vanko, D. A., 1995, Magmatically generated saline brines related to molybdenum at Questa, New Mexico, USA, *in* Thompson, J. F. H., ed., Magmas, fluids and ore deposits: Mineralogical Association of Canada Short Course Series, v. 23, p. 153-174.

Cobbing, E. J., Ozard, J. M., and Snelling, N. J., 1977, Reconnaissance geology of the crystalline basement rocks of the Coastal Cordillera of southern Perú: Geological Society of America Bulletin, v. 88, p. 241-246.

Coira, B., Davidson, J., Mpodozis, C., and Ramos, V., 1982, Tectonic and magmatic evolution of the Andes of Northern Argentina and Chile: Earth-Science Reviews, v. 18, p. 303-332.

Cooke, D. R., and Bloom, M. S., 1990, Epithermal and subjacent porphyry mineralisation, Acupan, Baguio district, Philippines: A fluid inclusion and paragenetic study: Journal of Geochemical Exploration, v. 35, p. 297-340.

Cooke, D. R., Hollings, P., Gow, P., and Walshe, J. L., 2002, Geodynamic evolution, crustal architecture and mineral resources of the northern Chile porphyry Cu-Mo province, AMIRA Project P511: Hydrothermal systems, giant ore deposits and a new paradigm for predictive mineral exploration, Chilean Atlas, Volume 1, Final Report, p. 6.1-6.57.

Cooke, D. R., and Simmons, S. F., 2000, Characteristics and genesis of epithermal gold deposits, Gold in 2000: Reviews in Economic Geology v. 13, p. 221-244.

Corbett, G. J., and Leach , T. M., 1998, Southwest Pacific Rim gold-copper systems: Structure, alteration and mineralization: Society of Economic Geologists Special Publication, n. 6, 236 p.

Cornejo, P., Tosdal, R. M., Mpodozis, C., Tomlinson, A. J., Rivera, O., and Fanning, C. M., 1997, El Salvador, Chile porphyry copper deposit revisited: Geologic, and geochronologic framework: International Geology Reviews, v. 39, p. 22-54.

Cuadra, P., and Camus, F., 1998, The Radomiro Tomic porphyry copper deposit, northern Chile, *in* Porter, M.T, ed., Porphyry and hydrothermal copper and gold deposits: A global perspective, Conference Proceedings, Perth, Australia, p. 99-109.

Cumming, G. L., and Richards, J. R., 1975, Ore lead isotope ratios in a continuously changing Earth: Earth and Planetary Science Letters, v. 28, p. 155-171.

Dalrymple, G. B., Alexander Jr., E. C., Lanphere, M. A., and Kraker, G. P., 1981, Irradiation of samples for $^{40}Ar/^{39}Ar$ dating using the Geological Survey TRIGA Reactor: US Geological Survey Professional Paper, v. 1176, p. 55.

Dalziel, I. W. D., 1986, Collision and cordilleran orogenesis: An Andean perspective: Geological Society of London Publication 19, p. 389-404.

Dasch, E. J., 1981, Lead isotopic compositions of metalliferous sediments from the Nazca Plate: Geological Society of America Memoirs, v. 154, p. 199-209.

Davidson, J. P., McMillan, N. J., Moorbath, S., Wörner, G., Harmon, R. S., and Lopez-Escobar, L., 1990, The Nevados de Payachata volcanic region (18°S/69°W, N. Chile). II. Evidence for widespread crustal involvement in Andean magmatism: Contributions to Mineralogy and Petrology, v. 105, p. 412-432.

DeBeer, L. J., and Dick, L. A., 1994, Development of the Collahuasi copper deposits, a world class copper project in the Andes of Northern Chile: Conference proceedings volume, Mining Latin America, Santiago, Chile, 1994, p. 181-195.

Deen, J. A., 1990, Hydrothermal ore deposition related to high-level igneous activity: A stable isotope study of the Julcani mining district, Perú: Unpub. PhD thesis, University of Colorado, Denver, USA, 246 p.

Deen, J. A., Rye, R. O., Munoz, J. L., and Drexler, J. W., 1994, The magmatic-hydrothermal system at Julcani, Perú: Evidence from fluid inclusions and hydrogen and oxygen isotopes: Economic Geology, v. 89, p. 1924-1938.

Defant, M. J., and Drummond, M. S., 1990, Derivation of some modern arc magmas by melting of young subducted lithosphere: Nature, v. 347, p. 662-665.

Dick, L. A., Chavez, W. X., Gonzales, A., and Bisso, C., 1994, Geologic setting and mineralogy of the Cu-Ag-(As) Rosario vein system, Collahuasi District, Chile: Society of Economic Geologists Newsletter, n. 19, p. 1, 6-11.

Dilles, J., H., and Einaudi, M., T., 1992, Wall-rock alteration and hydrothermal flow paths about the Ann-Mason porphyry copper deposit, Nevada - a 6km vertical reconstruction: Economic Geology, v. 87, p. 1963-2001.

Dilles, J. H., Tomlinson, A. J., Martin, M. W., and Blanco, N., 1997, El Abra and Fortuna complexes: A porphyry copper batholith sinistrally displaced by the Falla Oeste [extended abs.]: Congreso Geológico Chileno, VIII, Antofagasta, Chile, p. 1883-1887.

Dilles, J. H., and Wright, J. E., 1988, The chronology of early Mesozoic arc magmatism in the Yerington district of western Nevada and it regional implications: Geological Society of America Bulletin, v. 100, p. 644-652.

Doblas, M., 1998, Slickenside kinematic indicators: Tectonophysics, v. 295, p. 187-197.

Drummond, M. S., and Defant, M. J., 1990, A model for trondhjemite-tonalite-dacite genesis and crustal growth via slab melting: Archean to modern comparisons: Journal of Geophysical Research, v. 95, p. 21,503-21,521.

Dunn, P. G., 1982, Geology of the Copper Flat porphyry copper deposit, *in* Titley, S. R., ed., Advances in geology of the porphyry copper deposits, southwestern North America: Tucson, University of Arizona Press, p. 313-325.

Eastoe, C. J., 1978, A fluid inclusion study of the Panguna porphyry copper deposit, Bougainville, Papua New Guinea: Economic Geology, v. 73, p. 721-748.

Eastoe, C. J., 1982, Physics and chemistry of the hydrothermal system at the Panguna porphyry copper deposit, Bougainville, Papua New Guinea: Economic Geology, v. 77, p. 127-153.

Elburg, M., and Foden, J., 1998, Sources for magmatism in central Sulawesi: Geochemical and Sr-Nd-Pb constraints: Chemical Geology, v. 156, p. 67-93.

Esser, B. K., and Turekian, K. K., 1993, The osmium isotopic composition of the continental crust: Geochimica et Cosmochimica Acta, v. 57, p. 3093-3104.

Etchecopar, A., Vasseur, G., and Gaignieres, M., 1981, An inverse problem in microtectonics for the determination of stress tensors from fault striation analysis: Journal of Structural Geology, v. 3, p. 51-65.

Field, C. W., and Gustafson, L. B., 1976, Sulfur isotopes in the porphyry copper deposit at El Salvador: Economic Geology, v. 71, p. 1533-1552.

Foden, J., Mawby, J., Kelley, S., Turner, S., and Bruce, D., 1995, Metamorphic events in the eastern Arunta inlier. Part 2. Nd-Sr-Ar isotopic constraints: Precambrian Research, v. 71, p. 207-227.

Fournier, R. O., 1985, The behaviour of silica in hydrothermal solutions, *in* Berger, B. R., and Bethke, P. M., eds., Geology and geochemistry of epithermal systems: Reviews in Economic Geology, v. 2, p. 45-61.

Fournier, R. O., 1987, Conceptual models of brine evolution in magmatic-hydrothermal systems: U.S. Geological Survey Professional Paper 1350, p. 1487-1506.

Fournier, R. O., 1991, Transition from hydrostatic to greater than hydrostatic fluid pressure in presently active hydrothermal systems in crystalline rocks: Geophysical Research Letters, v. 18, p. 955-958.

Fournier, R. O., 1999, Hydrothermal processes related to movement of fluid from plastic rock into brittle rock in the magmatic-epithermal environment: Economic Geology, v. 94, p. 1193-1211.

Francis, P. W., and Hawkesworth, C. J., 1994, Late Cenozoic rates of magmatic activity in the central Andes and their relationships to continental crust formation and thickening: Journal of the Geological Society of London, v. 151, p. 845-854.

Gammons, C. H., and Williams-Jones, A. E., 1995, The solubility of Au:Ag alloy + AgCl in HCl/NaCl solutions at 300°C: New data on the stability of Au (I) chloride complexes in hydrothermal fluids: Geochimica et Cosmochimica Acta, v. 59, p. 3453-3468.

Gardeweg, M., C., 1993, Eventual erupción al este de Collahuasi: Un programma de trabajo para minimiza sus efectos: Internal company report, Compañia Minera Doña Inés de Collahuasi, Santiago, Chile, 24 p.

Giggenbach, W., 1978, The isotopic composition of waters from the El Tatio geothermal field, Northern Chile: Geochimica et Cosmochimica Acta, v. 42, p. 979-988.

Giggenbach, W. F., 1992, Magma degassing and mineral deposition in hydrothermal systems along convergent plate boundaries: Economic Geology, v. 87, p. 1927-1944.

Giggenbach, W. F., 1997, The origin and evolution of fluids in magmatic-hydrothermal systems, *in* Barnes, H. L., ed., Geochemistry of hydrothermal ore deposits, New York, Wiley Interscience, p. 737-796.

Günther, A., Haschke, M., Reutter, K.-J., and Scheuber, E., 1997, Repeated reactivation of an ancient fault zone under changing kinematic conditions: The Sierra de Moreno fault system (SMFS) (N-Chilean Precordillera) [extended abs.]: Congreso Geológico Chileno, VIII, Antofagasta, Chile, 1997, p. 85-89.

Gustafson, L., B., and Hunt, J., P., 1975, The Porphyry Copper Deposit at El Salvador, Chile: Economic Geology, v. 70, p. 857-912.

Gustafson, L. B., Orquera, W., McWilliams, M., Castro, M., Olivarez, O., Rojas, G., Maluenda, J., and Mendez, M., 2001, Multiple centers of mineralization in the Indio Muerto district, El Salvador, Chile: Economic Geology, v. 96, p. 325-350.

Gutscher, M. A., 2002, Andean subduction style and their effect on thermal structure and interplate coupling: Journal of South American Earth Sciences, v. 15, p. 3-10.

Gutscher, M. A., Maury, R., Eissen, J. P., and Bourdon, E., 2000, Can slab melting be caused by flat subduction: Geology, v. 28, p. 535-538.

Haas, J. L. Jr, 1971, The effect of salinity on the maxim thermal gradient of a hydrothermal system at hydrostatic pressure: Economic Geology, v. 66, p. 940-946.

Hall, C. M., 1981, The application of K/Ar and $^{40}Ar/^{39}Ar$ methods to the dating of recent volcanics and the Laschamp event: Unpub. PhD thesis, University of Toronto, Toronto, Canada, 186 p.

Harmon, R., Barriero, B. A., Moorbath, S., Hoefs, J., Francis, P. W., Thorpe, R. S., Deruelle, B., McHugh, J., and Viglinio, J. A., 1984, Regional O-, Sr- and Pb-isotope relationships in late Cenozoic calc-alkaline lavas of the Andean Cordillera: Journal of the Geological Society of London, v. 141, p. 803-822.

Haschke, M., Günther, A., Siebel, W., Scheuber, E., and Reutter, K.-J., 1999, Magma source variations of late Cretaceous - late Eocene magmatic rocks of the Chilean Precordillera (21.5°- 26°S): Due to variable water fugacity or crustal thickening, Institut fur Geologie, Geophysik, und Geoinformatik, Freie Universitat Berlin http://sfb267.geoinf.fu-berlin.de/web/de/poster/posterb.asp.

Haschke, M., Siebel, W., Günther, A., and Scheuber, E., 2002, Repeated crustal thickening and recycling during the Andean orogeny in north Chile (21°-26°S): Journal of Geophysical Research, v. 107, p. 6.1-6.17.

Hawkesworth, C. J., Hammill, M., Gledhill, A. R., Erlank, A. J., and Norry, M. J., 1982, Isotope and trace element evidence for late-stage intra-crustal melting in the high Andes: Earth and Planetary Science Letters, v. 58, p. 240-254.

Hedenquist, J. W., 1987, Volcanic-related hydrothermal systems in the Circum-Pacific basin and their potential for mineralisation: Mining Geology, v. 37, p. 347-364.

Hedenquist, J. W., Aoki, M., and Shinohara, H., 1994a, Flux of volatiles and ore-forming metals from the magmatic-hydrothermal system of Satsuma Iwojima volcano: Geology, v. 22, p. 585-588.

Hedenquist, J. W., Arribas, A., Jr., and Reynolds, T. J., 1998, Evolution of an intrusion-centred hydrothermal system: Far Southeast-Lepanto Porphyry and Epithermal Cu-Au deposits, Philippines: Economic Geology, v. 93, p. 373-404.

Hedenquist, J. W., and Henley, R. W., 1985, The importance of CO_2 on freezing point measurements of fluid inclusions: Evidence from active geothermal systems and implications for epithermal ore deposition: Economic Geology, v. 80, p. 1379-1406.

Hedenquist, J. W., Matsuhisa, Y., Izawa, E., White, N. C., Giggenbach, W. F., and Aoki, M., 1994b, Geology and geochemistry of high-sulfidation mineralization in the Nansatsu district, Japan: Economic Geology, v. 89, p. 1-30.

Hedenquist, J. W., and Richards, J. P., 1998, The influence of geochemical techniques on the development of genetic models for porphyry copper deposits: Reviews in Economic Geology, v. 10, p. 235-256.

Heidrick, T. L., and Titley, S. R., 1982, Fracture and dike patterns in Laramide plutons and their structural and tectonic implications, *in* Titley, S. R., ed., Advances in geology of the porphyry copper deposits of southwestern North America, Tucson, Arizona, University of Arizona Press, p. 73-91.

Heinrich, C., Ryan, C. G., Mernagh, T. P., and Eadington, P. J., 1992, Segregation of ore metals between magmatic brine and vapour: A fluid inclusion study using PIXE microanalysis: Economic Geology, v. 87, p. 1566-1583.

Heinrich, C. A., in press, Magmatic vapour condensation and the relation between porphyries and epithermal Au-(Cu-As) mineralisation: thermodynamic constraints. Seventh Biennial SGA Meeting, 2003: Mineral exploration and sustainable development, Athens, Greece.

Heinrich, C. A., Günther, D., Audetát, A., and Ulrich, T., 1999, Metal fractionation between magmatic brine and vapour, determined by microanalysis of fluid inclusions: Geology, v. 27, p. 755-758.

Heithersay, P. S., and Walshe, J. L., 1995, Endeavour 26 North: A porphyry copper-gold deposit in the late Ordovician, shoshonitic Goonumbla Volcanic Complex, New South Wales, Australia: Economic Geology, v. 90, p. 1506-1532.

Hemley, J. J., 1959, Some mineralogical equilibria in the system K_2O-Al_2O_3-SiO_2-H_2O: American Journal of Science, v. 257, p. 241-270.

Hemley, J. J., Hostetler, P. B., Gude, A. J., and Mountjoy, W. T., 1969, Some stability relations of alunite: Economic Geology, v. 64, p. 599-612.

Hemley, J. J., Montoya, J. W., Marinenko, J. W., and Luce, R. W., 1980, Equilibria in the system Al_2O_3-SiO_2-H_2O and some general implications for alteration/mineralization: Economic Geology, v. 73, p. 210-228.

Hickey, R. L., Frey, F. A., and Gerlach, D. C., 1986, Multiple sources for basaltic arc rocks from the southern volcanic zone of the Andes (34° to 41°S): Trace element and isotopic evidence for contributions from subducted oceanic crust, mantle, and continental crust: Journal of Geophysical Research, v. 91, p. 5963-5983.

Hildreth, W., and Moorbath, S., 1988, Crustal contributions to arc magmatism in the Andes of central Chile: Contributions to Mineralogy and Petrology, v. 98, p. 455-489.

Hiyashi, K., and Ohmoto, H., 1991, Solubility of gold in NaCl- and H_2S-bearing aqueous solutions at 250-350°C: Geochimica et Cosmochimica Acta, v. 55, p. 2111-2126.

Hoaglin, D. C., Mosteller, F., and Tukey, J. W., 1983, Understanding robust and exploratory data analysis: New York, John Wiley and Sons, 427 p.

Holland, H. D., 1965, Some applications of thermochemical data to problems of ore deposits, II. Mineral assemblages and the composition of ore-forming fluids: Economic Geology, v. 60, p. 1101-1166.

Holt, B. D., and Engelkemeir, A. G., 1970, The thermal decomposition of barium sulfate to sulfur dioxide for mass spectrometer analysis: Analytical Chemistry, v. 42., p. 1451-1453

Horita, J., Cole, D. R., and Weslowski, D. J., 1995, The activity composition relationship of oxygen and hydrogen isotopes in aqueous salt solutions. III. Vapour-liquid equilibration of NaCl solutions to 350°C: Geochimica et Cosmochimica Acta, v. 59, p. 1139-1151.

Hunt, J., P., 1985, Applied geology at Quebrada Blanca and Collahuasi, Chile, and the future of U.S metal mining: Economic Geology, v. 80, p. 794-800.

Hunt, J. P., Bratt, J. A., and Marquardt, L., 1983, Quebrada Blanca, Chile: An enriched porphyry copper deposit: Mining Engineering, v. 35, p. 636-644.

Huston, D. L., Power, M., Gemmell, J. B., and Large, R. R., 1995, Design, calibration and geological application of the first operational laser ablation sulfur isotope microprobe: Australian Journal of Earth Sciences, v. 42, p. 549-555.

Jackson, J. A., and White, N. J., 1989, Normal faulting in the upper continental crust: Observations from regions of active extension: Journal of Structural Geology, v. 11, p. 15-36.

James, D. E., 1982, A combined O, Sr, Nd and Pb isotopic and trace element study of crustal contamination in central Andean lavas: Earth and Planetary Science Letters, v. 57, p. 47-62.

James, D. E., and Sacks, I. W., 1999, Cenozoic formation of the central Andes: A geophysical perspective, *in* Skinner, B. J., ed., Geology and ore deposits of the central Andes: Society of Economic Geologists Special Publication, n. 7, p. 1-25.

Jordan, T. E., and Gardeweg, M., 1989, Tectonic evolution of the late Cenozoic central Andes (20° - 33°S): Oxford Monographs on Geology and Geophysics 8, p. 193-207.

Kamenetsky, V. S., Wolfe, R. C., Eggins, S. M., Mernagh, T. P., and Bastrakov, E., 1999, Volatile exsolution at the Dinkindi Cu-Au porphyry deposit, Philippines: A melt inclusions record of the initial ore-forming process: Geology, v. 27, p. 691-694.

Kay, S., Mpodozis, C., and Coira, B., 1999, Neogene magmatism, tectonism, and mineral deposits of the central Andes (22° to 33°S latitude), *in* Skinner, B. J., ed., Geology and ore deposits of the Central Andes: Society of Economic Geologists Special Publication, n. 7, p. 27-59.

Kay, S., Mpodozis, C., Ramos, V. A., and Munizaga, F., 1991, Magma source variations for mid-late Tertiary magmatic rocks associated with a shallow subduction zone and a thickening crust in the central Andes (28° to 33°S): Geological Society of America Special Paper, v. 265, p. 113-137.

Kay, S. M., and Abbruzzi, J. M., 1996, Magmatic evidence for Neogene lithospheric evolution on the central Andean "flat slab" between 30° and 32°S: Tectonophysics, v. 259, p. 15-28.

Kay, S. M., Maksaev, V., Moscoso, R., Mpodozis, C., and Nasi, C., 1987, Probing the evolving Andean lithosphere: Mid-Tertiary magmatism in Chile (29° - 30°S) over the modern zone of subhorizontal subduction: Journal of Geophysical Research, v. 92, p. 6173-6189.

Kay, S. M., Mpodozis, C., Tittler, A., and Cornejo, P., 1994, Tertiary magmatic evolution of the Maricunga Belt in Chile: International Geology Reviews, v. 36, p. 1079-1112.

Kitto, P. A., 1994, Structural and geochemical controls on mineralisation at Renison, Tasmania: Unpub. PhD thesis, University of Tasmania, Hobart, Australia, 484 p.

Kontak, D. J., and Clark, A. H., 2002, Genesis of the giant, bonanza San Rafael lode tin deposit, Perú: Origin and significance of pervasive alteration: Economic Geology, v. 97, p. 1741-1777.

Kuhn, D., and Reuther, C. D., 1999, Strike-slip faulting and nested block rotations: structural evidence from the Cordillera de Domeyko, northern Chile: Tectonophysics, v. 313, p. 383-398.

Kusakabe, M., Hori, M., and Matsuhisa, Y., 1990, Primary mineralisation of the El Teniente and Rio Blanco porphyry copper deposits, Chile: Stable isotopes, fluid inclusions and $Mg^{2+}/Fe^{2+}/Fe^{3+}$ ratios of hydrothermal biotite: University of Western Australia Geology Department Publication 30, p. 244-259.

Lang, I. M., and Cheney, E. S., 1971, Sulfur isotope reconnaissance of Butte, Montana: Economic Geology, v. 66, p. 63-74.

Lang, J. R., and Titley, S. R., 1998, Isotopic and geochemical characteristics of Laramide magmatic systems in Arizona and implications for the genesis of porphyry copper deposits: Economic Geology, v. 93, p. 138-170.

Langerfield, H., 1964, The pebble dikes at El Salvador, Unpublished company report to Anaconda, 64 p.

Lanphere, M. A., and Dalrymple, G. B., 1978, The use of $^{40}Ar/^{39}Ar$ data in evaluation of disturbed K-Ar systems, U.S. Geological Survey, p. 241-243.

Le Maitre, R. W., Bateman, P., Dudek, A., Keller, J., Lameyre Le Bas, M. J., Sabine, P. A., Schmid, R., Sorensen, H., Streckeisen, A., Woolley, A. R., and Zanettin, B., 1989, A classification of igneous rocks and glossary of terms: Oxford, UK, Blackwell.

Lee, A. W., 1994, Evolution of the Rosario copper-molybdenum porphyry deposit and associated copper-silver vein system, Collahuasi District, I Region, Northern Chile: Unpub. masters thesis, Queens University, Kingston, Ontario, Canada, 75 p.

Leitch, A. M., and Weinberg, R. F., 2002, Modelling granite migration by mesoscale pervasive flow: Earth and Planetary Science Letters, v. 200, p. 131-146.

Lindsay, D. D., Zentilli, M., and Rojas De La Rivera, J., 1995, Evolution of an active ductile to brittle shear system controlling mineralisation at the Chuquicamata porphyry copper deposit, northern Chile: International Geology Reviews, v. 37, p. 945-958.

Losada-Calderón, A. J., 1992, Geology and geochemistry of Nevados del Famatina and La Mejicana deposits, La Rioja Province, Argentina: Unpub. PhD thesis, Monash University, Melbourne, Australia, 320 p.

Losada-Calderón, A. J., McBride, S. L., and McPhail, D. C., 1994, The geology and $^{40}Ar/^{39}Ar$ geochronology of magmatic activity and related mineralization in the Nevados Famatina mining district, La Rioja province, Argentina: Journal of South American Earth Sciences, v. 7, p. 9-24.

Losada-Calderón, A. J., and McPhail, D. C., 1996, Porphyry and high-sulfidation epithermal mineralisation in the Nevados del Famatina mining district of Argentina, *in* Camus, F., Sillitoe, R. H., and Petersen, R., eds., Society of Economic Geologists Special Publication, n. 5, p. 91-117.

Love, D. A., Clark, A. H., Hodgson, C. J., Mortensen, J. K., Archibald, D. A., and Farrar, E., 1998, The timing of adularia-sericite-type mineralization and alunite-kaolinite-type alteration, Mount Skukum epithermal gold deposit, Yukon Territory, Canada: ^{40}Ar-^{39}Ar and U-Pb geochronology: Economic Geology, v. 93, p. 437-462.

Lowell, J. D., and Guilbert, J. M., 1970, Lateral and vertical alteration-mineralization zoning in porphyry ore deposits: Economic Geology, v. 65, p. 373-408.

Luck, J. M., and Allegre, C. J., 1982, The study of molybdenites through the ^{187}Re-^{187}Os chronometer: Earth and Planetary Science Letters, v. 61, p. 291-296.

Ludwig, K. R., 2001, Isoplot/Ex rev. 2.49: Berkeley Geochronology Centre, Special Publication No. 1a: Berkley, California.

Macfarlane, A. W., Marcet, P., LeHuray, A. P., and Petersen, U., 1990, Lead isotope provinces of the central Andes inferred from ores and crustal rocks: Economic Geology, v. 85, p. 1857-1880.

Machado, N., and Gauthier, G., 1996, Determination of $^{207}Pb/^{206}Pb$ ages on zircon and monazite by laser-ablation ICPMS and application to a study of sedimentary provenance and metamorphism in southeastern Brazil: Geochimica et Cosmochimica Acta, v. 60, p. 5063-5073.

Machado, N., Schrank, A., Noce, C. M., and Gauthier, G., 1996, Ages of detrital zircon from Archean-Paleoproterozoic sequences; implications for greenstone belt setting and evolution of a Transamazonian foreland basin in Quadrilatero Ferrifero, Southeast Brazil: Earth and Planetary Science Letters, v. 141, p. 259-276.

Maksaev, V., 1990, Metallogeny, geological evolution, and thermochronology of the Chilean Andes between latitudes 21° and 26° South, and the origin of major porphyry copper deposits: Unpub. PhD thesis, Dalhousie University, Halifax, Canada, 554 p.

Maksaev, V., and Zentilli, M., 1988, Marco metalogénico regional de los megadepósitos de tipo pórfido cuprífero del norte grande de Chile [extended abs.]: Congreso Geológico Chileno, V, Santiago, p. B181-B212.

Maksaev, V., and Zentilli, M., 2000, Fission track thermochronology of the Domeyko Cordillera, northern Chile: Implications for Andean Tectonics and porphyry copper metallogenesis: Exploration and Mining Geology, v. 8, p. 65-89.

Maksaev, V., Zentilli, M., and Reynolds, P. M., 1988, Geocronología $^{40}Ar/^{39}Ar$ de depósitos tipo pórfido cuprífero del Norte Grande de Chile [extended abs.]: Congreso Geológico Chileno, V, Santiago, p. B109-133.

Marinović, N., and Lahsen, A., 1984, Hoja Calama. Carta Geológica de Chile, Escala 1:250,000: Servicio Nacional de Geología y Minería, p. 58.

Marsh, T. M., Einaudi, M. T., and McWilliams, M., 1997, $^{40}Ar/^{39}Ar$ geochronology of Cu-Au and Au-Ag mineralization in the Potrerillos district, Chile: Economic Geology, v. 92, p. 784-806.

Mason, P., Berman, M., Bischof, L., and Huntington, 1999, The Spectral Geologist, Version 2: AusSpec International Pty. Ltd., Melbourne, Commonwealth Scientific and Industrial Research Organisation.

Masterman, G. J., White, N. C., Wilson, C. J. L., and Pape, D., 2002, High-sulfidation gold deposits in ancient volcanic terranes: Insights from the Mid-Paleozoic Peak Hill deposit, NSW: Society of Economic Geologists Newsletter, n. 51, p. 1, 10-16.

Mathur, R., 2000, Re-Os isotopes of base metal porphyry deposits: Unpub. PhD thesis, University of Arizona, Tucson, USA 154 p.

Mathur, R., Ruiz, J., and Munizaga, F., 2000, Relationship between copper tonnage of Chilean base-metal porphyry deposits and Os isotope ratios: Geology, v. 28, p. 555-558.

McCandless, T. E., and Ruiz, J., 1993, Rhenium-osmium evidence for regional mineralization in southwestern North America: Science, v. 261, p. 1262-1266.

McClay, K., Skarmeta, J., and Bertens, A., 2002, Structural controls on porphyry copper deposits in northern Chile: New models and implications for Cu-Mo mineralization in subduction orogens [abs.]: Applied structural geology for mineral exploration and mining, Kalgoorlie, Western Australia, 2002, p. 127.

McDougall, I., and Harrison, M. T., 1988, Geochronology and thermochronology by the $^{40}Ar/^{39}Ar$ Method: New York, NY, Oxford University Press, 212 p.

McDougall, I., and Harrison, M. T., 1999, Geochronology and thermochronology by the $^{40}Ar/^{39}Ar$ Method: New York, NY, Oxford University Press, 269 p.

McInnes, B., I., A., Farley, K., A., Sillitoe, R., H., and Kohn, B., P., 1999, Application of apatite (U-Th)/He thermochronometry to the determination of the sense and amount of vertical fault displacement at the Chuquicamata porphyry copper deposit, Chile: Economic Geology, v. 94, p. 937-948.

McIntyre, G. A., 1963, Precision and resolution in geochronometry, *in* Albritton, C. C., ed., The fabric of geology: Reading, Massachusetts, Addison Wesley Publishing Company, p. 112-134.

McPhie, J., Doyle, M., and Allen, R., 1993, Volcanic Textures: A guide to the interpretation of textures in volcanic rocks, Centre for Ore Deposit Research, University of Tasmania, 198 p.

Meinert, L. D., 1992, Skarns and skarn deposits: Geological Association of Canada Special Paper, v. 40, p. 569-583.

Moore, R. L., and Masterman, G. J., 2002, The geology and corporate discovery history of the Collahuasi district porphyry copper deposits, Chile, *in* Cooke, D.R. and Pongratz, J., Giant ore deposits: characteristics, genesis and exploration: CODES Special Publication 4, University of Tasmania, Hobart, Australia, p. 23-50.

Mpodozis, C., and Cornejo, P., 1997, El rift Triasico-Sinemuriano de Sierra Exploradora, Cordillera de Domeyko (25° - 26°S): Asociaciones de facies y reconstruccion tectonica [extended abs.]: Congreso Geológico Chileno, VIII, Proceedings, 1997, p. 550-554.

Mpodozis, C., and Ramos, V., 1989, The Andes of Argentina, *in* Ericksen, G. E., Canas-Pinochet, M. T., and Reinmund, J. A., eds., Geology of the Andes and its relation to hydrocarbon and mineral resources, n. 11: Houston, Texas, Circum-Pacific Council for Energy and Mineral Resources, p. 59-90.

Mpodozis, C., Tomlinson, A. J., and Cornejo, P., 1994, Acerca del control estructural de intrusivos Eocenos y pórfidos cupríferos en la región de Potrerillos - El Salvador [extended abs.]: Congreso Geológico Chileno, VII, Concepcion, Chile, p. 1596-1600.

Munchmeyer, C., 1996, Exotic deposits: products of lateral migration of supergene solutions from porphyry copper deposits, *in* Camus, F., Sillitoe, R. H., and Petersen, R., eds., Andean copper deposits: New discoveries, mineralization, styles and metallogeny. Society of Economic Geologists Special Publication n. 5, p. 42-58.

Munchmeyer, C., Hunt, J. P., and Ware, H., 1984, Geología del distrito de Collahuasi y del pórfido cuprífero Rosario: Internal company report, Compañia Doña Inés de Collahuasi, Santiago, Chile, 84 p.

Muntean, J. L., 1998, Magmatic-hydrothermal gold deposits of the Maricunga Belt, northern Chile: Unpub. PhD thesis, Stanford University, California, USA, 400 p.

Muntean, J. L., and Einaudi, M. T., 2000, Porphyry gold deposits of the Refugio district, Maricunga Belt, northern Chile: Economic Geology, v. 95, p. 1445-1472.

Muntean, J. L., and Einaudi, M. T., 2001, Porphyry-epithermal transition: Maricunga Belt, Northern Chile: Economic Geology, v. 96, p. 743-772.

Naney, M. T., 1983, Phase equilibria of rock-forming ferromagnesian silicates in granitic systems: American Journal of Science, v. 283, p. 993-1033.

Nash, J. T., 1976, Fluid inclusion petrography-data from porphyry copper deposits and application to exploration: U.S. Geological Survey Professional Paper 907D, 16 p.

Norton, D. L., 1982, Fluid and heat transport phenomena typical of copper-bearing pluton environments, *in* Titley, S. R., ed., Advances in geology of porphyry copper deposits of southwestern North America: Tucson, University of Arizona Press, p. 59-72.

Ohmoto, H., and Rye, R. O., 1979, Isotopes of sulfur and carbon, *in* Barnes, H. L., ed., Geochemistry of hydrothermal ore deposits: New York, Wiley Interscience, p. 509-567.

Onstott, T. C., and Peacock, M. W., 1987, Argon retentivity of hornblendes: A field experiment in a slowly cooled metamorphic terrane: Geochimica et Cosmochimica Acta, v. 51, p. 2891-2904.

Osatenko, M. J., and Jones, M. B., 1976, Valley Copper: Canadian Institute of Mining Special Volume 15, p. 130-143.

Ossandon C., G., Freraut C., R., Gustafson, L. B., Lindsay, D. D., and Zentilli, M., 2001, Geology of the Chuquicamata mine: a progress report: Economic Geology, v. 96, p. 249-270.

Oyarzun, R., Márquez, A., Lillo, J., López, I., and Rivera, S., 2001, Giant versus small porphyry copper deposits of Cenozoic age in northern Chile: Adakitic versus normal calc-alkaline magmatism: Mineralium Deposita, v. 36, p. 794-798.

Padilla Garza, R. A., Titley, S. R., and Pimentel B., F., 2001, Geology of the Escondida porphyry copper deposit, Antofagasta Region, Chile: Economic Geology, v. 96, p. 307-324.

Padilla, H., 1988, Eventos intrusivos y deformaciones en la Cordillera de Domeyko a latitud del salar Punta Negra: Antecedentes geochronologicos K-Ar [extended abs.]: Congreso Geológico Chileno, V, Santiago, Chile, 1988, p. I229-I243.

Pardo-Casas, F., and Molnar, P., 1987, Relative motion of the Nazca (Farallón) and South American plates since Late Cretaceous time: Tectonics, v. 6, p. 233-248.

Parry, W. T., Wilson, P. N., Jasumback, M., and Heizler, M. T., 1998, Clay mineralogy and $^{40}Ar/^{39}Ar$ dating of phyllic and argillic alteration at Bingham, Utah, *in* John, D. A., and Ballantyne, G. H., eds., Geology and ore deposits of the Oquirrh and Wasatch Mountains, Utah: Society of Economic Geologists, Guidebook Series, v. 29, p. 171-188.

Peacock, S. M., Rushmer, T., and Thompson, A. B., 1994, Partial melting of subducting oceanic crust: Earth and Planetary Science Letters, v. 121, p. 227-244.

Pericillo, R., and Taylor, S. R., 1976, Geochemistry of Eocene calc-alkaline volcanic rocks from the Kastamonu area, northern Turkey: Contributions to Mineralogy and Petrology, v. 58, p. 63-81.

Petford, N., and Atherton, A., 1996, Na-rich partial melts from newly underplated basaltic crust: The Cordillera Blanca Batholith, Perú: Journal of Petrology, v. 37, p. 1491-1521.

Petit, J. P., 1987, Criteria for sense of movement on fault surfaces in brittle rocks: Journal of Structural Geology, v. 9, p. 597-608.

Pitzer, K. S., and Pabalan, R. T., 1986, Thermodynamics of NaCl in steam: Geochimica et Cosmochimica, v. 50, p. 1445-1454.

Platt, J., 1988, La Grande vein project exploration proposal: Internal company report, Compañia Minera Doña Inés de Collahuasi, Santiago, Chile, 13 p.

Potter, R. W., Clynne, M. A., and Brown, D. L., 1978, Freezing point depressions of aqueous sodium chloride solutions: Economic Geology, v. 73, p. 284-285.

Prinz, P., Wilke, H., G., and von Hillerbrandt, A., 1994, Sediment accumulation and subsidence history in the Mesozoic marginal basin of northern Chile, *in* Reutter, K.-J., Scheuber, E., and Wigger, P. J., eds., Tectonics of the southern central Andes: Structure and evolution of an active continental margin, Springer-Verlag, p. 219-232.

Puig, A., 1988, Geologic and metallogenic significance of lead in galenas of the Chilean Andes: Economic Geology, v. 83, p. 843-858.

Rae, A. J., 2002, Alteration systematics and mineralising potential of the Palinpinon geothermal filed, Negros Island, Philippines: Unpub. PhD thesis, University of Tasmania, Hobart, Australia, 243 p.

Ramos, V., 1994, Terranes of southern Gondwanaland and their control in the Andean structure (30° - 33°S latitude), *in* Reutter, K.-J., Scheuber, E., and Wigger, P. J., eds., Tectonics of the southern central Andes: Structure and evolution of an active continental margin, Springer-Verlag, p. 249-261.

Ramos, V. A., Jordan, T. E., Allmendinger, R. W., Mpodozis, C., Kay, S. M., Cortes, J. M., and Palma, M., 1986, Paleozoic terranes of the central Argentine-Chilean Andes: Tectonics, v. 5, p. 855-880.

Rapp, R., and Watson, E., 1995, Dehydration melting of metabasalt at 8-32 kbar: Implications for continental growth and crust-mantle recycling: Journal of Petrology, v. 36, p. 891-931.

Reutter, K. J., Scheuber, E., and Chong, G., 1996, The Precordilleran fault system of Chuquicamata, Northern Chile: Evidence for reversals along arc-parallel strike-slip faults: Tectonophysics, v. 259, p. 213-228.

Rey, P., Vanderhaeghe, O., and Teyssier, C., 2001, Gravitational collapse on the continental crust and flow of orogens: Tectonophysics, v. 342, p. 435-449.

Reyes, A. G., 1990, Petrology of Philippine geothermal systems and the application of alteration mineralogy to their assessment: Journal of Volcanology and Geothermal Research, v. 43, p. 279-309.

Reymer, A., and Schubert, G., 1984, Phanerozoic addition rates to the continental crust and crustal growth: Tectonics, v. 3, p. 63-77.

Reynolds, P., Ravenhurst, C., Zentilli, M., and Lindsay, D., 1997, High precision $^{40}Ar/^{39}Ar$ dating of two consecutive hydrothermal events in the Chuquicamata porphyry copper system, Chile [abs.]: Geological Association of Canada-Mineralogical Association of Canada, Program with Abstracts, v. 22, p. A-125.

Reynolds, T. J., and Beane, R. E., 1985, Evolution of hydrothermal fluid characteristics at the Santa Rita, New Mexico, porphyry copper deposit: Economic Geology, v. 80, p. 1328-1347.

Richards, J. P., 2000, Lineaments revisited: Society of Economic Geologists Newsletter, n. 42, p. 1, 14-20.

Richards, J. P., 2002, Discussion on " Giant versus small porphyry copper deposits of Cenozoic age in northern Chile: Adakitic versus normal calc-alkaline magmatism" by Oyarzun et al. (Mineralium Deposita 36: 794-798, 2001): Mineralium Deposita, v. 37, p. 788-790.

Richards, J. P., Boyce, A. J., and Pringle, M. S., 2001, Geologic evolution of the Escondida area, northern Chile: A model for spatial and temporal localization of porphyry copper mineralization: Economic Geology, v. 96, p. 271-305.

Richards, J. P., and Kerrich, R., 1993, The Porgera gold mine, Papua New Guinea: Magmatic-hydrothermal to epithermal evolution of an alkalic precious metal deposit: Economic Geology, v. 88, p. 1017-1052.

Richards, J. P., Noble, S. R., and Pringle, M. S., 1999, A revised late Eocene age for porphyry copper magmatism in the Escondida area, northern Chile: Economic Geology, v. 94, p. 1231-1248.

Rickwood, P. C., 1989, Boundary lines within petrologic diagrams which use oxides of major and minor elements: Lithos, v. 22, p. 247-263.

Robinson, B. W., and Kusakabe, M., 1975, Quantitative preparation of sulfur dioxide for $^{34}S/^{32}S$ analyses, from sulfides by combustion with cuprous oxide: Analytical Chemistry, v. 47, p. 1179-1181.

Robinson, P., Townsend, A. T., Yu, Z., and Munker, C., 1999, Determination of scandium, yttrium and rare earth elements in rocks by high resolution inductively coupled plasma-mass spectrometry: Geostandards Newsletter: The Journal of Geostandards and Geoanalysis, v. 23, p. 31-46.

Roddick, J. C., 1983, High precision intercalibration of $^{40}Ar/^{39}Ar$ standards: Geochimica et Cosmochimica Acta, v. 47, p. 887-898.

Roedder, E., 1984, Fluid Inclusions, *in* Ribbe, P. H., ed., Reviews in Mineralogy, 16, Mineralogical Society of America, 644 p.

Roedder, E., and Bodnar, R. J., 1980, Geologic pressure determinations from fluid inclusion studies: Annual Reviews in Earth and Planetary Sciences, v. 8, p. 263-301.

Rogers, G. R., and Hawkesworth, C. J., 1989, A geochemical traverse across the north Chilean Andes: Evidence for crust generation from the mantle wedge: Earth and Planetary Science Letters, v. 91, p. 271-285.

Rollinson, H. R., 1993, Using geochemical data: Evaluation, presentation, interpretation: Harlow, UK, Longman, 352 p.

Rowland, M. G., 1998, The role of magmatic processes in the development of hypogene mineralisation at Quebrada Blanca, northern Chile: Unpub. PhD thesis, University of London, United Kingdom, 240 p.

Rowland, M. G., and Wilkinson, J. J., 1998, A hybrid origin for porphyritic magmas sourcing mineralising fluids, *in* Hudson, A., ed., Water-Rock Interaction: Rotterdam, Balkema, p. 569-573.

Rowland, M. G., and Wilkinson, J. J., 1999, Significance of intermediate stage veins at Quebrada Blanca, Chile, *in* Stanley et al., eds., Mineral Deposits: Processes to processing: Rotterdam, Balkema, p. 99-102.

Rusk, B., and Reed, M., 2002, Scanning electron microscope-cathodeluminescence analysis of quartz reveals complex growth histories in veins from the Butte porphyry copper deposit, Montana: Geology, v. 30, p. 727-730.

Rutherford, M. J., and Hill, P. M., 1993, Magma ascent rates from amphibole breakdown: An experimental study applied to the 1980-1986 Mount St. Helens eruptions: Journal of Geophysical Research, v. 98, p. 19667-19685.

Rye, R., 1993, The evolution of magmatic fluids in the epithermal environment: The stable isotope perspective: Economic Geology, v. 88, p. 733-753.

Rye, R. O., Bethke, P. M., and Wasserman, M. D., 1992, The stable isotope geochemistry of acid sulfate alteration: Economic Geology, v. 87, p. 225-262.

Rye, R. O., Stoffregen, R. E., and Bethke, P. M., 1990, Stable isotope systematics and magmatic-hydrothermal processes in the Summitville, Colorado gold deposit: U.S.G.S. Open File Report 90-626, p. 31.

Saal, A. E., Rudnick, R. L., Ravizza, G. E., and Hart, S. R., 1998, Re-Os isotope evidence for the composition, formation and age of the lower continental crust: Nature, v. 393, p. 58-61.

Sajona, F. G., Maury, R. C., Bellon, H., Cotten, J., Defant, M. J., and Pubellier, M., 1993, Initiation of subduction and the generation of slab melts in western and eastern Mindanao, Philippines: Geology, v. 21, p. 1007-1010.

Sajona, F. G., Maury, R. C., Pubellier, M., Leterrier, J., Bellon, H., and Cotten, J., 2000, Magmatic source enrichment by slab-derived melts in young post-collisional setting, central Mindanao Philippines: Lithos, v. 54, p. 173-206.

Salfity, J. A., 1985, Lineamientos traversales al rumbo andino en el noroeste Argentino [extended abs.]: Congreso Geológico Chileno, IV, Antofagasta, Chile, 1985a, p. 119-137.

Sandeman, H. A., Clark, A. H., and Farrar, E., 1995, An integrated tectono-magmatic model for the evolution of the southern Peruvian Andes (13° - 20°S) since 55 Ma: International Geology Reviews, v. 37, p. 1039-1073.

Sandeman, H. J., Archibald, D. A., Grant, J., Villenueve, M. E., and Ford, F., 1999, Characterization of the chemical composition and ^{40}Ar-^{39}Ar systematics of intralaboratory standard MAC-83 biotite: Radiogenic age and isotopic studies, Report 12, Geological Survey of Canada, p. 13.-26.

Sasaki, A., Ulriksen, C. E., Sato, K., and Ishihara, S., 1984, Sulfur isotope reconnaissance of porphyry copper and manto-type deposits in Chile and the Philippines: Bulletin of the Geological Survey of Japan, v. 35.

Scheuber, E., and Andrissen, P. A. M., 1990, The kinematic and geodynamic significance of the Atacama fault zone, northern Chile: Journal of Structural Geology, v. 12, p. 243-257.

Scheuber, E., Bogdanic, T. V., Jensen, A., and Reutter, K.-J., 1994, Tectonic development of the north Chilean Andes in relation to plate convergence and magmatism since the Jurassic, *in* Reutter, K.-J., Scheuber, E., and Wigger, P. J., eds., Tectonics of the Southern Central Andes: Structure and evolution of an active continental margin, Springer-Verlag, p. 121-139.

Scheuber, E., and Reutter, K., J., 1992, Magmatic arc tectonics in the central Andes between 21° and 25°S: Tectonophysics, v. 205, p. 127-140.

Schmitz, M., 1994, A balanced model of the southern Central Andes: Tectonics, v. 13, p. 484-492.

Sebrier, M., and Soler, P., 1991, Tectonics and magmatism in the Peruvian Andes from late Oligocene time to Present: Geological Society of America Special Paper 265, p. 259-278.

Selby, D., and Creaser, R. A., 2001, Re-Os geochronology and systematics in molybdenite from the Endako porphyry molybdenum deposit, British Columbia, Canada: Economic Geology, v. 96, p. 197-204.

Serrano, L., Vargas, R., Stambuk, V., Aguilar, C., Galeb, M., Holmgren, C., Contreras, A., Godoy, S., Vela, I., Skewes, M. A., and Stern, C. R., 1996, The late Miocene to early Pliocene Río Blanco-Los Bronces copper deposit, central Chilean Andes, *in* Camus, F., Sillitoe, R. M., and Petersen, R., eds., Andean copper deposits: New discoveries, mineralization, styles and metallogeny. Society of Economic Geologists Special Publication, n. 5, p. 119-130.

Seward, T. M., 1973, Thio complexes of gold and the transport of gold in hydrothermal ore solutions: Geochimica et Cosmochimica Acta, v. 37, p. 379-399.

Seward, T. M., 1991, The hydrothermal chemistry of gold, *in* Forster, R. P., ed., Gold metallogeny and exploration: London, Blackie and Son, p. 37-62.

Shackleton, R. M., Ries, A. C., Coward, M. P., and Coobold, P. R., 1979, Structure, metamorphism and geochronology of the Arequipa massif of coastal Perú: Journal of the Geological Society of London, v. 136, p. 195-214.

Shatwell, D., 1995, Accreted terranes and porphyry copper deposits in the Central Andes: Pacific Rim Congress 1995, Sydney, Australian Institute of Mining and Metallurgy, p. 515-520.

Shenberger, D. M., and Barnes, H. L., 1989, Solubility of gold in aqueous sulfide solutions from 150° to 350°C: Geochimica et Cosmochimica Acta, v. 53, p. 269-278.

Sheppard, S. M. F., and Gustafson, L. B., 1976, Oxygen and hydrogen isotopes in the porphyry copper deposit at El Salvador: Economic Geology, v. 71.

Sheppard, S. M. F., Nielsen, R. L., Taylor, H. P., and , J., 1969, Oxygen and hydrogen isotope ratios of clay minerals from porphyry copper deposits: Economic Geology, v. 64, p. 755-777.

Sheppard, S. M. F., Nielsen, R. L., and Taylor, H. P., Jr., 1971, Hydrogen and oxygen isotope ratios in minerals from porphyry copper deposits: Economic Geology, v. 66, p. 515-542.

Shinohara, H., and Hedenquist, J. W., 1997, Constraints on magma degassing beneath the Far Southeast porphyry Cu-Au deposit, Philippines: Journal of Petrology, v. 38, p. 1741-1752.

Shirey, S., and Walker, R., 1995, Carius tube digestion for low-blank rhenium-osmium analysis: Analytical Chemistry, v. 67, p. 2136-2141.

Sibson, R. H., 2001, Seismogenic framework for hydrothermal transport and ore deposition, *in* Richards, J. P., and Tosdal, R. M., eds., Structural controls on ore genesis: Reviews in Economic Geology, v. 14, p. 25-50.

Sillitoe, R., H., 1988, Epochs of intrusion-related copper mineralization in the Andes: Journal of South American Earth Sciences, v. 1, p. 89-108.

Sillitoe, R., H., 1992, Gold and copper metallogeny of the Central Andes: Past, present, and future exploration objectives: Economic Geology, v. 87, p. 2205-2216.

Sillitoe, R. H., 2000, Styles of high-sulfidation gold, silver and copper mineralisation in porphyry and epithermal environments [extended abs], Pacific Rim Congress 1999: Bali, Indonesia, The Australian Institute of Mining and Metallurgy, p. 19-34.

Sillitoe, R. H., Marquardt, J. C., Ramirez, F., Becerra, H., and Gomez, M., 1996, Geology of the concealed MM porphyry copper deposit, Chuquicamata district, northern Chile, *in* Camus, F., Sillitoe, R. H., and Petersen, R., eds., Andean copper deposits: New discoveries, mineralization, styles and metallogeny: Society of Economic Geologists Special Publication, n. 5, p. 59-70.

Sillitoe, R. H., and McKee, E. H., 1996, Age of supergene oxidation and enrichment in the Chilean porphyry copper province: Economic Geology, v. 91, p. 164-179.

Skewes, M., Alexandra, and Stern, C., R., 1995, Genesis of the Giant Upper Miocene-to-Pliocene Cu deposits of central Chile in the context of Andean magmatic and tectonic evolution [extended. abs.], *in* Clark, A. H., ed., Giant Ore Deposits Workshop, 2nd Proceedings: Controls on the scale of orogenic magmatic-hydrothermal mineralisation, Queens University, Kingston, Canada, 38-56 p.

Smoliar M.I., Walker R.J., Morgan J.W., 1996, Re-Os ages of group IIA, IIIA, IVA and IVB iron meteorites: Science, v. 271, 1099-1102.

Sourirajan, S., and Kennedy, G. C., 1962, The system of H_2O-NaCl at elevated temperatures and pressures: American Journal of Science, v. 260, p. 115-141.

Steiger, R. H., and Jäger, E., 1977, Subcommission on geochronology: Convention on the use of decay constants in geo- and cosmo-chronology: Earth and Planetary Science Letters, v. 36, p. 359-362.

Stein, H.J., Morgan, J.W., Markey, R.J., Hanna, J.L., 1998a, An introduction to Re-Os: What's in it for the mineral industry? Society of Economic Geologists Newsletter, n. 32, p. 1, 8-15.

Stein, H. J., Sundblad, K., Markey, R., Morgan, J. W., and Motuza, G., 1998b, Re-Os ages for Archean molybdenite and pyrite, Kuittila-Kiviso, Finland and Proterozoic molybdenite, Kabeliai, Lithuania: Testing the chronometer in a metamorphic and metasomatic setting: Mineralium Deposita, v. 33, p. 329-345.

Stern, C. R., 1991, Role of subduction erosion in the generation of Andean magmas: Geology, v. 19, p. 79-81.

Sterner, S. M., 1992, Homogenisation of fluid inclusions to the vapour phase: The apparent homogenisation phenomenon: Economic Geology, v. 87, p. 1616-1623.

Sterner, S. M., Hall, D. L., and Bodnar, R. J., 1988, Synthetic fluid inclusions. V. Solubility relations in the system NaCl-KCl-H_2O under vapour-saturated conditions: Geochimica et Cosmochimica Acta, v. 52, p. 989-1005.

Stoffregen, R., 1987, Genesis of acid-sulfate alteration and Au-Cu-Ag mineralization at Summitville, Colorado: Economic Geology, v. 82, p. 1575-1591.

Stoffregen, R. E., and Alpers, C. N., 1987, Woodhouseite and svanbergite in hydrothermal ore deposits: Products of apatite destruction during advanced argillic alteration: Canadian Mineralogist, v. 25, p. 201-211.

Stoffregen, R. E., and Alpers, C. N., 1992, Observations on the unit-cell dimensions, H_2O contents, and δD values of natural and synthetic alunite: American Mineralogist, v. 77, p. 1092-1098.

Streickeisen, A. L., 1979, Classification and nomenclature of volcanic rocks, lamprophyres, carbonatites, and melitic rocks: Recommendation and suggestions of the I.U.G.S. subcommission on the systematics of igneous rocks: Geology, v. 7, p. 331-335.

Sun, S. S., and McDonough, W. F., 1989, Chemical and isotopic systematics of oceanic basalts: Implications for mantle composition and processes, *in* Saunders, A. D., and Norry, M. J., eds., Magmatism in the ocean basins, Geological Society of America Special Publication, n. 42, p. 313-345.

Suzuki, K., Kagi, H., Takano, B., and Nozaki, Y., 2000, Experimental alteration of molybdenite: evaluation of the Re-Os system, infrared spectroscopic profile and polytype: Geochimica et Cosmochimica Acta, v. 64, p. 223-232.

Sverjensky, D. A., Hemley, J. J., and D'Angelo, W. M., 1991, Thermodynamic assessment of hydrothermal alkali feldspar-mica-alumnosilicate equilibria: Geochimica et Cosmochimica Acta, v. 55, p. 989-1004.

Taylor, B. E., 1992, Degassing of H_2O from rhyolite magma during eruption and shallow intrusion, and the isotopic composition of magmatic water in hydrothermal systems: Japan Geological Survey Report 279, p. 190-194.

Taylor, H. P., 1987, Isotopes of ore forming fluids, *in* Kyser, T. K., ed., Short course in stable isotope geochemistry of low temperature fluids: Mineralogical Association of Canada Short Course, v 13.

Taylor, P. N., Jones, N. W., and Moorbath, S., 1984, Isotopic assessment of relative contributions from crust and mantle sources to magma genesis of Precambrian granitoid rocks: Phil. Trans. R. Soc. Lond., v. A310, p. 605-625.

Thompson, A. J. B., Hauff, P. L., and Robitalle, A. J., 1999, Alteration mapping in exploration: Application of short-wave infrared (SWIR) spectroscopy: Society of Economic Geologists Newsletter, n. 39, p. 1, 16-17.

Tilton, G. R., and Barriero, B. A., 1980, Origin of lead in Andean calc-alkaline lavas, southern Perú: Science, v. 210, p. 1245-1247.

Tilton, G. R., Pollak, R. J., Clark, A. H., and Robertson, R. C. R., 1981, Isotopic composition of lead in central Andean ore deposits: Geological Society of America Memoirs, v. 254, p. 791-816.

Titley, S. R., 1982, The style and progress of mineralization and alteration in porphyry copper systems, *in* Titley, S. R., ed., Advances in geology of the porphyry copper deposits, southwestern North America: Tucson, Arizona, University of Arizona Press, p. 93-116.

Titley, S. R., 1993, Characteristics of porphyry copper occurrence in the American Southwest, *in* Kirkham, R. V., Sinclair, W. D., Thorpe, R. I., and Duke, J. M., eds., Mineral deposit modelling: Geological Society of Canada Special Paper 40, p. 433-464.

Titley, S. R., and Beane, R. E., 1981, Porphyry copper deposits. Part I. Geologic settings, petrology, and tectonogenesis: Economic Geology 75th Anniversary Volume, p. 214-235.

Todt, W., Cliff, R. A., Hanser, A., and Hofmann, A. W., 1993, Re-calibration of NBS standards using a $^{207}Pb/^{206}Pb$ double spike: Terra Abstracts, v. 5, p. 396.

Tomlinson, A. J., and Blanco, N., 1997a, Structural evolution and displacement history of the West Fault system, Precordillera, Chile: Part 1, synmineral history [extended abs.]: Congreso Geológico Chileno, VIII, Antofagasta, Chile, 1997a, p. 1873-1877.

Tomlinson, A. J., and Blanco, N., 1997b, Structural evolution and displacement history of the West fault system, Precordillera, Chile: Part 2, postmineral history [extended abs]: Congreso Geológico Chileno, VIII, Antofagasta, Chile, 1997b, p. 1878-1882.

Tosdal, R. M., 1996, The Amazon-Luarentian connection as viewed from the Middle Proterozoic rocks in the central Andes, western Bolivia and northern Chile: Tectonics, v. 15, p. 827-842.

Tosdal, R. M., and Richards, J. P., 2001, Magmatic and structural controls on the development of porphyry Cu-Mo-Au deposits: Reviews in Economic Geology, v. 14, p. 157-181.

Ulrich, T., Günther, D., and Heinrich, C. A., 2001, The evolution of a porphyry Cu-Au deposit, based on LA-ICP-MS analysis of fluid inclusions: Bajo de la Alumbrera, Argentina: Economic Geology, v. 96, p. 1743-1774.

Unruth, D. M., and Tatsumoto, M., 1976, Lead isotopic composition and uranium, thorium and lead concentrations in sediments and basalts from the Nazca plate: Deep Sea Drilling Project Initial Reports, v. 34.

van Achterbergh, E., Ryan, C. G., Jackson, S. E., and Griffin, W. L., 2001, Data reduction software for LA-ICP-MS: Mineralogical Association of Canada Short Course Handbook, v. 29, p. 239-243.

Vanderhaeghe, O., and Teyssier, C., 2001, Crustal-scale rheological transitions during late orogenic collapse: Tectonophysics, v. 335, p. 211-228.

Vargas, R., Gustafson, L. B., Vukasovic, M., Tidy, E., and Skewes, M. A., 1999, Ore breccias in the Rio Blanco-Los Bronces porphyry copper deposit, Chile, *in* Skinner, B. J., Geology and ore deposits of the Central Andes: Society of Economic Geologists Special Publication, n. 7, p. 281-297.

Vergara, H., 1978, Cuardrangulo Ujina, Región de Tarapacá, Carta Geológica de Chile, Escala 1:50,000: Santiago, Instituto de Investigaciones Geológicas, 63 p.

Vergara, H. L., and Thomas, A. N., 1984, Hoja Collacagua, Región de Tarapacá, Carta Geológica de Chile, Escala 1:250,000: Santiago, Servicio Nacional de Geología y Minería, 79 p.

von Huene, R., and Scholl, D. W., 1991, Observations at convergent margins concerning sediment subduction, subduction erosion, and the growth of continental crust: Reviews of Geophysics, v. 29, p. 279-316.

Walshe, J. L., Cooke, D. R., Cannell, J., Frikken, P., Hollings, P., Masterman, G. J., Skarmeta, J., Camus, F., Gow, P., and Midgley, G., in press, Physiochemical gradients and architectural constraints on fluid-mixing models of porphyry copper formation: Seventh Biennial SGA Meeting, 2003: Mineral exploration and sustainable development, Athens, Greece.

Warnaars, F. W., Holmgren, D. C, and Barassi, S. F, 1985, Porphyry copper and tourmaline breccias at Los Bronces-Rio Blanco, Chile: Economic Geology, v. 80, p. 1544-1565.

Wasserman, M. D., Rye, R. O., Bethke, P. M., and Arribas, A. Jr., 1992, Methods for separation and total stable isotope analysis of alunite, U.S.G.S. Open File Report 92-9, p. 1-20.

Watanabe, W., and Hedenquist, J. W., 2001, Mineralogic and stable isotope zonation at the surface over the El Salvador porphyry copper deposit, Chile: Economic Geology, v. 96, p. 1775-1797.

Watanabe, Y., Stein, H. J., Morgan, J. W., and Markey, R. J., 1999, Re-Os geochronology brackets the timing and duration of mineralization for the El Salvador porphyry Cu-Mo deposit, Chile: Geological Society of America Abstracts with Program v. 30, 1999, p. A-30.

White, N. C., 1991, High-sulfidation epithermal gold deposits: Characteristics and a model for their origin: Geological Survey of Japan Report, v. 277, p. 9-20.

White, N. C., and Hedenquist, J. W., 1990, Epithermal environments and styles of mineralization: variations and their causes, and guidelines for exploration, *in* Hedenquist, J. W., White, N. C., and Siddeley, G., eds., Epithermal gold mineralization of the Circum-Pacific: Geology, geochemistry, origin and exploration. II: Journal of

Geochemical Exploration, vol. 36, p. 445-474.

White, N. C., and Hedenquist, J. W., 1995, Epithermal gold deposits: Styles, characteristics and exploration, Society of Economic Geologists Newsletter, n. 23, p. 1, 9-13.

Wilkinson, J. J., Rankin, A. H., Mulshaw, S. C., Nolan, J., and Ramsey, M. H., 1994, Laser ablation ICP-AES for the determination of metals in fluid inclusions: An application to the study of magmatic ore fluids: Geochimica et Cosmochimica Acta, v. 58, p. 1133-1146.

Williams, I. S., and Hergt, J. M., 2000, U-Pb dating of Tasmanian dolerites: a cautionary tale of SHRIMP analysis of high-U zircon [abs], Beyond 2000: New frontiers in isotope geoscience, University of Melbourne, Lorne, Australia, 2000, p. 185-186.

Wilson, A. J., Cooke, D. R., and Harper, B. L., in press., The Ridgeway gold-copper deposit: A high grade alkalic porphyry system in the Lachlan Fold Belt, NSW, Australia: Economic Geology.

Winchester, J. A., and Floyd, P. A., 1976, Geochemical magma type discrimination: Application to altered and metamorphosed basic igneous rocks: Earth and Planetary Science Letters, v. 28, p. 459-469.

Winchester, J. A., and Floyd, P. A., 1977, Geochemical discrimination of different magma series and their differentiation products using immobile elements: Chemical Geology, v. 20, p. 325-343.

Wolfe, R. C., 2001, Geology of the Didipio region and paragenesis of the Dinkidi Cu-Au porphyry deposit: Unpub. PhD thesis, University of Tasmania, Hobart, Australia, 200 p.

Wörner, G., Harmon, R. S., Davidson, J. P., Moorbath, S., Turner, D. L., McMillan, N. J., Nye, C., Lopez-Escobar, L., and Moreno, H., 1988, The Nevados de Payachata Volcanic region (18°S/69°W, N. Chile), I: Geological, geochemical and isotopic observations: Bulletin of Volcanology, v. 50, p. 278-303.

York, D., 1969, Least squares fitting of a straight line with correlated errors: Earth and Planetary Science Letters, v. 5, p. 320-324.

Yu, Z., Robinson, P., and McGoldrick, P., 2001, An evaluation of methods for the chemical decomposition of geological materials for trace element determination using ICP-MS: Geostandards Newsletter: The Journal of Geostandards and Geoanalysis, v. 25, p. 199-217.

Yu, Z., Robinson, P., Townsend, A. T., Munker, C., and Crawford, A. J., 2000, Determination of high field strength elements, Rb, Sr, Mo, Sb, Cs, Tl, and Bi at ng g^{-1} levels in geological reference materials by magnetic sector ICP-MS after $HF/HClO_4$ high pressure digestions: Geostandards Newsletter: The Journal of Geostandards and Geoanalysis, v. 24, p. 39-50.

Zentilli, M. Graves, M., Lindsay, D., Ossandón, G., and Camus, F., 1996, Recurrent mineralization in the Chuquicamata porphyry copper system: Restriction on genesis from mineralogical, geochronological and isotopic studies [extended abs.], *in* Clark, A. H., ed., Giant Ore Deposits Workshop, 2nd Proceedings, Controls on the scale of orogenic magmatic-hydrothermal mineralisation, Queens University, Kingston, Ontario, p. 90-113.

Zentilli, M., and Maksaev, V., 1996, Metallogenetic model for the late Eocene-early Oligocene supergiant porphyry event, northern Chile [extended. abs.], *in* Clark, A. H., ed., Giant Ore Deposits Workshop, 2nd Proceedings: Controls on the scale of orogenic magmatic-hydrothermal mineralisation, Queens University, Kingston, Canada, p. 152-156.

Zindler, A., and Hart, S. R., 1986, Chemical geodynamics: Annual Reviews Earth and Planetary Sciences, v. 14, p. 493-571.

APPENDIX 1

List of Diamond Drill Holes Graphically Logged

Detailed graphic logs (1:200 scale) can be obtained by request from the author

Rosario drill holes

Section 16 northeast:	C170; 28 to 465 m
	C189; 15 to 548 m
	C190; 17 to 600.0 m
Section 20 northeast:	C049; 12 to 400 m, 600 to 903 m
	C084; 6 to 338 m
	C092; 290 to 510 m
	C124; 6 to 280 m
	C153; 0 to 422 m
	C155; 0 to 400 m
	C158; 0 to 300 m
	C177; 28 to 650 m
	C194; 19 to 608 m
	C248; 32 to 150 m
	C288; 136 to 400 m
	C316: 280 to 700 m
Section 23 northeast:	C168; 32.0 to 640.0 m
	C228; 0 to 200 m
	C291; 200 to 720 m
	C293; 200 to 560 m

La Grande drill holes

Section 80150 north:	GC198; 52 to 520 m
	GC201; 31 to 761 m

APPENDIX 2

ELECTRON MICROPROBE DATA

All minerals were analysed using a Cameca SX-50 electron microprobe at the Central Science Laboratory, University of Tasmania

Appendix 2-1. *Electron Microprobe Data*

Primary feldspar

	SiO_2	TiO_2	Al_2O_3	Fe_2O_3	MnO	MgO	CaO	SrO	BaO	Na_2O	K_2O	P_2O_5	Sum Ox%	Ab	An	Or	Celsian
r200124_P24_ksp1-6-1	67.74	0.00	21.04	0.11	0.00	0.01	1.16	0.00	0.00	10.71	0.30	0.04	101.11	92.75	5.56	1.69	0.01
r200124_P24_ksp2-10-1	67.30	0.01	21.09	0.03	0.01	0.00	1.35	0.00	0.02	10.52	0.15	0.01	100.51	92.56	6.55	0.86	0.03
r200124_P24_ksp3-12-1	68.04	0.02	20.48	0.08	0.00	0.02	0.78	0.00	0.06	10.79	0.36	0.01	100.62	94.08	3.75	2.07	0.10
r200124_P24_plag1-3-1	68.96	0.00	20.06	0.03	0.06	0.00	0.17	0.00	0.02	11.23	0.20	0.00	100.71	98.03	0.80	1.14	0.03
r200124_P24_plag2-7-1	69.03	0.00	20.11	0.01	0.00	0.01	0.16	0.00	0.00	11.28	0.10	0.03	100.74	98.63	0.78	0.59	0.00
r200124_P24_plag3-11-1	66.78	0.02	21.50	0.07	0.00	0.00	1.70	0.00	0.00	10.33	0.34	0.01	100.75	89.89	8.18	1.92	0.01
r200124_P25_plag1-15-1	66.93	0.01	21.04	0.14	0.00	0.00	1.37	0.00	0.00	10.41	0.60	0.00	100.50	90.05	6.53	3.42	0.00
r200124_P25_plag2-16-1	68.49	0.00	20.31	0.03	0.01	0.00	0.34	0.00	0.00	11.07	0.21	0.02	100.48	97.15	1.66	1.19	0.00
r200124_P26_ksp1-25-1	67.49	0.02	21.23	0.07	0.02	0.00	1.32	0.00	0.02	10.60	0.26	0.00	101.03	92.16	6.33	1.49	0.03
r200124_P26_ksp2-26-1	67.39	0.02	21.01	0.12	0.00	0.00	1.29	0.00	0.00	10.52	0.40	0.00	100.75	91.49	6.22	2.29	0.00
r200124_P26_ksp3-27-1	67.74	0.01	20.96	0.05	0.00	0.01	0.98	0.00	0.06	10.60	0.38	0.03	100.83	92.93	4.77	2.20	0.11
r200124_P26_plag1-20-1	68.83	0.00	20.10	0.00	0.00	0.00	0.14	0.00	0.00	11.29	0.20	0.00	100.57	98.19	0.66	1.15	0.00
r200124_P26_plag2-24-1	68.87	0.00	20.41	0.03	0.03	0.00	0.25	0.00	0.16	11.13	0.20	0.02	101.10	97.34	1.22	1.16	0.28
r200124b_fsp_pheno_10-10-1	66.45	0.02	21.32	0.10	0.03	0.02	2.03	0.04	0.02	10.06	0.40	0.00	100.47	87.81	9.78	2.27	0.03
r200124b_fsp_pheno_1-1-1	67.26	0.02	21.26	0.20	0.00	0.00	1.68	0.07	0.06	10.21	0.34	0.00	101.10	89.58	8.15	1.98	0.10
r200124b_fsp_pheno_2-2-1	67.57	0.00	21.06	0.11	0.00	0.00	1.32	0.09	0.01	10.45	0.40	0.06	101.07	91.10	6.36	2.28	0.02
r200124b_fsp_pheno_3-3-1	66.24	0.00	21.72	0.04	0.00	0.01	2.17	0.07	0.01	9.99	0.33	0.05	100.64	87.41	10.50	1.89	0.02
r200124b_fsp_pheno_4-4-1	61.87	0.04	24.40	0.17	0.05	0.00	5.79	0.15	0.00	7.83	0.64	0.00	100.95	68.14	27.83	3.64	0.00
r200124b_fsp_pheno_5-5-1	62.06	0.00	24.42	0.25	0.00	0.00	5.76	0.15	0.06	8.01	0.67	0.03	101.40	68.53	27.22	3.75	0.11
r200124b_fsp_pheno_6-6-1	66.34	0.02	21.36	0.12	0.00	0.00	2.08	0.11	0.02	9.95	0.51	0.02	100.55	86.74	10.02	2.92	0.03
r200124b_fsp_pheno_7-7-1	60.93	0.03	25.08	0.16	0.07	0.00	6.66	0.17	0.06	7.70	0.48	0.00	101.34	65.51	31.30	2.66	0.10
r200124b_fsp_pheno_8-8-1	62.54	0.00	23.87	0.20	0.00	0.01	5.40	0.17	0.05	8.13	0.67	0.01	101.04	69.99	25.71	3.78	0.08
r200124b_fsp_pheno_9-9-1	62.34	0.05	23.99	0.15	0.00	0.01	5.41	0.26	0.00	8.22	0.56	0.03	101.01	70.51	25.67	3.14	0.00
r200130_P3_ksp1-8-1	68.64	0.00	20.45	0.00	0.00	0.00	0.45	0.00	0.00	10.96	0.16	0.00	100.67	96.84	2.22	0.94	0.00
r200130_P3_ksp2-10-1	68.72	0.02	20.42	0.03	0.05	0.00	0.40	0.00	0.01	11.08	0.24	0.02	101.01	96.67	1.93	1.38	0.02
r200130_P3_plag1-9-1	62.37	0.00	23.97	0.19	0.00	0.00	4.91	0.00	0.05	8.47	0.53	0.00	100.50	73.41	23.50	3.00	0.10
r200130b_fsp_pheno_10-10-1	61.52	0.02	24.68	0.15	0.00	0.00	6.19	0.26	0.04	7.94	0.40	0.06	101.27	67.78	29.23	2.25	0.08
r200130b_fsp_pheno_1-1-1	63.30	0.02	23.80	0.12	0.03	0.00	4.71	0.13	0.01	8.64	0.58	0.00	101.35	74.06	22.33	3.26	0.01
r200130b_fsp_pheno_11-11-1	61.92	0.00	24.63	0.13	0.02	0.01	5.87	0.09	0.00	8.01	0.48	0.02	101.18	69.08	27.96	2.72	0.00
r200130b_fsp_pheno_12-12-1	62.09	0.00	24.45	0.18	0.01	0.00	5.65	0.18	0.06	8.09	0.54	0.02	101.26	69.54	26.85	3.06	0.10
r200130b_fsp_pheno_13-13-1	62.77	0.00	24.02	0.15	0.01	0.00	5.25	0.13	0.00	8.48	0.34	0.00	101.15	72.81	24.91	1.94	0.00
r200130b_fsp_pheno_2-2-1	65.03	0.02	22.70	0.05	0.02	0.00	3.48	0.09	0.00	9.34	0.36	0.00	101.08	81.06	16.67	2.05	0.00
r200130b_fsp_pheno_3-3-1	62.30	0.01	24.21	0.16	0.01	0.00	5.45	0.17	0.02	8.19	0.63	0.03	101.17	70.16	25.83	3.54	0.03
r200130b_fsp_pheno_4-4-1	62.09	0.01	24.58	0.09	0.00	0.00	5.76	0.18	0.02	8.05	0.53	0.08	101.39	69.16	27.37	2.98	0.04
r200130b_fsp_pheno_5-5-1	63.53	0.01	23.23	0.15	0.02	0.01	4.48	0.17	0.00	8.69	0.65	0.02	100.98	74.61	21.25	3.70	0.01
r200130b_fsp_pheno_6-6-1	63.86	0.02	23.50	0.13	0.00	0.00	4.49	0.15	0.03	8.73	0.54	0.04	101.49	75.12	21.37	3.08	0.06
r200130b_fsp_pheno_7-7-1	63.75	0.01	23.75	0.09	0.00	0.01	4.62	0.15	0.00	8.69	0.46	0.00	101.53	74.96	22.02	2.62	0.00
r200130b_fsp_pheno_8-8-1	62.29	0.05	24.36	0.13	0.00	0.01	5.52	0.16	0.06	8.35	0.50	0.00	101.43	70.83	25.87	2.80	0.10
r200130b_fsp_pheno_9-9-1	66.98	0.00	20.94	0.13	0.00	0.00	1.47	0.08	0.05	10.30	0.39	0.01	100.36	90.34	7.13	2.24	0.09
r200143b_fsp_pheno_10-10-1	68.29	0.02	20.46	0.03	0.00	0.01	0.58	0.08	0.05	11.04	0.10	0.03	100.69	96.35	2.78	0.57	0.09
r200143b_fsp_pheno_1-1-1	65.39	0.01	19.70	0.00	0.00	0.01	0.51	0.11	0.05	4.76	9.16	0.02	99.70	42.83	2.53	54.25	0.09
r200143b_fsp_pheno_11-11-1	68.32	0.02	20.39	0.03	0.03	0.00	0.51	0.06	0.01	11.01	0.15	0.04	100.58	96.49	2.47	0.86	0.02
r200143b_fsp_pheno_12-12-1	67.89	0.00	20.41	0.13	0.00	0.00	0.53	0.07	0.04	10.49	0.66	0.00	100.22	93.29	2.60	3.85	0.07
r200143b_fsp_pheno_2-2-1	64.49	0.01	19.22	0.06	0.00	0.00	0.07	0.03	0.42	1.36	14.59	0.02	100.27	12.28	0.34	86.54	0.76
r200143b_fsp_pheno_3-3-1	66.07	0.01	20.02	0.03	0.00	0.00	0.53	0.05	0.07	7.03	5.95	0.02	99.78	62.40	2.59	34.76	0.12
r200143b_fsp_pheno_4-4-1	67.35	0.00	20.14	0.03	0.00	0.02	0.39	0.04	0.04	9.16	3.11	0.00	100.27	80.07	1.87	17.88	0.07
r200143b_fsp_pheno_5-5-1	63.64	0.02	22.78	1.33	0.00	0.21	0.97	0.12	0.05	8.73	2.69	0.00	100.55	78.74	4.85	15.98	0.10
r200143b_fsp_pheno_6-6-1	64.27	0.00	19.10	0.04	0.06	0.01	0.00	0.06	0.47	0.84	15.48	0.05	100.37	7.54	0.00	91.45	0.86
r200143b_fsp_pheno_7-7-1	67.68	0.01	20.70	0.04	0.01	0.00	0.43	0.07	0.11	10.78	0.35	0.03	100.23	95.44	2.12	2.06	0.19
r200143b_fsp_pheno_8-8-1	67.57	0.00	19.85	0.10	0.02	0.00	0.38	0.06	0.00	9.29	2.78	0.03	100.08	81.86	1.83	16.14	0.00
r200143b_fsp_pheno_9-9-1	67.30	0.02	20.87	0.11	0.01	0.00	1.07	0.07	0.02	10.13	0.86	0.00	100.47	89.51	5.24	5.03	0.05

Secondary feldspar

	SiO_2	TiO_2	Al_2O_3	Fe_2O_3	MnO	MgO	CaO	SrO	BaO	Na_2O	K_2O	P_2O_5	Sum Ox%	Ab	An	Or	Celsian
r200130_P1_ksp1-1-1	68.84	0.00	20.39	0.03	0.00	0.01	0.35	0.00	0.00	11.14	0.19	0.02	100.96	97.24	1.67	1.09	0.00
r200130_P1_plag1-2-1	68.94	0.01	20.30	0.01	0.01	0.00	0.14	0.00	0.05	11.38	0.18	0.00	101.02	98.24	0.68	1.01	0.08
r200130_P1_plag2-3-1	68.75	0.00	20.24	0.10	0.00	0.00	0.15	0.00	0.02	11.26	0.14	0.04	100.72	98.40	0.73	0.83	0.04
r200130_P1_plag2-5-1	68.98	0.00	20.07	0.00	0.00	0.00	0.08	0.00	0.00	11.33	0.19	0.06	100.71	98.55	0.37	1.08	0.00
r200130_P1_plag3-4-1	69.28	0.00	20.31	0.00	0.07	0.00	0.16	0.00	0.00	11.44	0.13	0.06	101.46	98.51	0.78	0.71	0.00
r200130_P4_ksp1-11-1	68.06	0.00	20.65	0.06	0.02	0.00	0.66	0.00	0.00	10.96	0.17	0.04	100.62	95.86	3.19	0.96	0.00
r200130_P4_ksp2-12-1	68.31	0.02	19.95	0.13	0.00	0.01	0.14	0.00	0.00	9.99	2.26	0.04	100.86	86.44	0.68	12.89	0.00
r200130_P4_ksp3-13-1	68.91	0.04	19.93	0.04	0.00	0.01	0.14	0.00	0.03	11.03	0.33	0.05	100.50	97.34	0.68	1.93	0.06
r200130_P4_ksp4-18-1	69.35	0.00	20.01	0.00	0.02	0.00	0.12	0.00	0.00	10.98	0.09	0.00	100.58	98.85	0.60	0.55	0.00
r200130_P4_plag1-14-1	68.49	0.04	20.34	0.05	0.04	0.00	0.37	0.00	0.00	11.23	0.12	0.00	100.68	97.55	1.75	0.69	0.00
r200130_P4_plag2-15-1	68.74	0.02	20.10	0.00	0.00	0.00	0.14	0.00	0.02	11.26	0.15	0.06	100.49	98.43	0.67	0.87	0.03
r200130_P4_plag3-16-1	69.32	0.01	19.55	0.00	0.00	0.02	0.15	0.00	0.00	11.05	0.20	0.00	100.30	98.09	0.74	1.17	0.00
r200130_P4_plag4-17-1	68.85	0.03	20.16	0.06	0.01	0.01	0.12	0.00	0.00	11.21	0.14	0.01	100.60	98.63	0.56	0.81	0.00
r200130_P6_ksp1-22-1	98.11	0.00	1.59	0.00	0.00	0.00	0.03	0.00	0.06	0.56	0.03	0.03	100.42	91.68	2.92	3.31	2.10
r200130_P6_ksp2-23-1	94.76	0.02	3.86	0.01	0.01	0.01	0.09	0.00	0.00	1.89	0.04	0.00	100.69	96.14	2.61	1.26	0.00
r200130_P6_ksp3-24-1	68.85	0.00	20.16	0.00	0.01	0.01	0.16	0.00	0.00	11.24	0.26	0.00	100.69	97.76	0.76	1.48	0.00
r200135_P19_ksp10-10-1	62.69	0.01	6.81	0.16	0.00	0.26	0.32	0.00	0.00	0.01	0.07	0.04	70.36	4.97	75.80	19.22	0.02
r200135_P19_ksp1-1-1	65.11	0.02	18.97	0.06	0.04	0.00	0.02	0.00	0.03	0.89	16.06	0.00	101.19	7.76	0.09	92.10	0.05
r200135_P19_ksp11-11-1	58.71	0.02	12.26	0.11	0.00	0.28	0.22	0.00	0.01	0.02	0.42	0.01	72.05	4.60	29.04	65.87	0.48
r200135_P19_ksp12-12-1	99.45	0.02	0.53	0.00	0.00	0.00	0.00	0.00	0.04	0.01	0.46	0.05	100.57	3.11	0.03	94.09	2.77
r200135_P19_ksp2-2-1	55.04	0.03	8.63	0.08	0.02	0.22	0.15	0.00	0.07	0.01	0.06	0.04	64.32	7.56	56.46	25.82	10.16
r200135_P19_ksp3-3-1	64.62	0.00	18.81	0.06	0.00	0.00	0.00	0.00	0.09	0.51	16.83	0.00	100.92	4.41	0.01	95.42	0.15
r200135_P19_ksp4-4-1	66.68	0.00	19.64	0.00	0.03	0.00	0.10	0.00	0.00	5.83	8.74	0.02	101.02	50.11	0.46	49.43	0.00
r200135_P19_ksp5-5-1	63.07	0.04	14.15	0.24	0.05	0.33	0.21	0.00	0.00	0.00	0.05	0.00	78.15	3.09	74.79	22.10	0.02
r200135_P19_ksp6-6-1	57.57	0.00	20.92	0.15	0.08	1.46	0.28	0.00	0.00	0.04	0.08	0.02	80.60	15.31	63.61	21.07	0.01
r200135_P19_ksp7-7-1	64.32	0.02	18.75	0.04	0.00	0.00	0.10	0.00	0.14	0.40	16.66	0.04	100.48	3.48	0.47	95.80	0.25
r200135_P19_ksp8-8-1	58.66	0.00	18.90	0.27	0.00	0.27	0.18	0.00	0.01	0.03	1.62	0.05	80.00	2.75	8.43	88.59	0.24
r200135_P19_ksp9-9-1	64.80	0.05	18.43	0.12	0.00	0.00	0.00	0.00	0.00	0.50	16.02	0.08	100.00	4.53	0.01	95.45	0.00
r990007_P1_ab1-1-1	68.41	0.00	20.12	0.06	0.03	0.00	0.13	0.00	0.04	11.13	0.43	0.06	100.41	96.84	0.61	2.47	0.08
r990007_P1_ksp1-2-1	68.26	0.00	20.14	0.02	0.01	0.02	0.25	0.00	0.04	11.02	0.34	0.07	100.17	96.75	1.23	1.96	0.07
r990007_P2_ab1-6-1	68.89	0.00	19.85	0.08	0.04	0.00	0.08	0.00	0.00	11.20	0.29	0.02	100.46	97.95	0.39	1.66	0.01
r990007_P2_ab2-7-1	67.61	0.00	19.82	0.03	0.00	0.00	0.00	0.00	0.13	7.83	5.29	0.00	100.72	69.10	0.00	30.67	0.23
r990007_P2_ksp1-4-1	68.77	0.00	19.80	0.03	0.00	0.01	0.06	0.00	0.09	11.28	0.30	0.02	100.37	97.86	0.29	1.69	0.16
r990007_P3_ab1-10-1	64.20	0.00	18.85	0.16	0.02	0.01	0.00	0.00	0.13	0.35	14.46	0.17	98.36	3.54	0.00	96.19	0.26
r990007_P3_ksp1-12-1	68.72	0.00	19.98	0.07	0.01	0.00	0.16	0.00	0.00	11.20	0.22	0.00	100.38	97.93	0.79	1.28	0.00
r990007_P4_ab1-14-1	68.76	0.00	20.14	0.08	0.02	0.02	0.16	0.00	0.05	11.28	0.22	0.06	100.79	97.88	0.77	1.26	0.09
r990007_P4_ksp1-17-1	68.54	0.01	20.22	0.00	0.08	0.00	0.36	0.00	0.02	10.96	0.35	0.05	100.59	96.18	1.75	2.04	0.03
r990007_P6_ab1-18-1	69.26	0.00	20.23	0.22	0.00	0.02	0.01	0.00	0.00	11.50	0.11	0.02	101.36	99.31	0.06	0.63	0.00
R99008484a_ksp3	64.36	0.01	18.63	0.05	0.00	0.00	0.00	0.00	0.23	0.56	16.20	0.07	100.12	4.94	0.00	94.64	0.42
R99008484a_ksp4	65.78	0.00	19.12	0.19	0.03	0.01	0.04	0.00	0.17	3.83	11.10	0.00	100.27	34.20	0.18	65.31	0.32
R990084a_ksp1	64.91	0.01	18.79	0.23	0.00	0.00	0.00	0.00	0.16	0.53	16.15	0.01	100.80	4.75	0.00	94.97	0.29
R990084a_ksp2	64.10	0.00	19.08	0.11	0.03	0.00	0.00	0.00	0.28	0.90	15.74	0.06	100.30	8.00	0.00	91.51	0.49
r990085_P11_plag1-10-1	69.07	0.04	19.98	0.03	0.00	0.01	0.02	0.00	0.01	11.24	0.26	0.08	100.74	98.39	0.11	1.49	0.01
r990085_P13_ab1-13-1	69.36	0.00	20.09	0.03	0.02	0.00	0.07	0.00	0.00	11.34	0.23	0.07	101.21	98.34	0.35	1.31	0.00
r990085_P13_ksp1-12-1	64.62	0.00	18.89	0.01	0.00	0.00	0.00	0.00	0.32	0.34	17.00	0.05	101.23	2.97	0.00	96.47	0.56
r990085_P7_ksp1-1-1	64.18	0.02	18.83	0.06	0.01	0.01	0.00	0.00	0.52	0.50	16.56	0.00	100.69	4.36	0.02	94.70	0.91
r990085_P9_ksp1-7-1	64.34	0.00	18.79	0.01	0.00	0.00	0.00	0.00	0.39	0.32	16.76	0.03	100.64	2.81	0.00	96.49	0.70

Magnetite

	SiO_2	TiO_2	Al_2O_3	Cr_2O_3	Fe_2O_3(c)	FeO	V_2O_3	CaO	MnO	MgO	ZnO	NiO	Sum Ox%	XCr	XFe^{2+}	YFe^{3+}
r200143_P16_mt1-8-1	0.21	0.02	0.09	0.01	67.54	30.89	0.09	0.00	0.00	0.05	0.06	0.02	98.98	5.55	99.71	99.79
r200143_P16_mt2-9-1	0.02	0.31	0.02	0.01	68.46	31.36	0.11	0.08	0.01	0.00	0.00	0.00	100.38	22.05	100.00	99.94
r200143_P17_mt1-10-1	0.78	0.03	0.02	0.04	66.80	32.03	0.13	0.00	0.02	0.00	0.01	0.00	99.86	51.33	100.00	99.88
r200143_P17_mt2-13-1	1.74	0.04	0.35	0.03	64.76	33.61	0.06	0.00	0.00	0.01	0.04	0.00	100.67	6.05	99.94	99.11
r990002_mt_2-2-1	0.86	0.09	0.40	0.00	64.52	30.80	0.09	0.00	0.06	0.36	0.01	0.06	97.25	0.02	97.97	99.04
r990002_mt_3-3-1	0.06	0.07	0.07	0.01	66.42	30.16	0.17	0.00	0.03	0.01	0.09	0.02	97.11	10.85	99.95	99.83
r990002_mt_4-6-1	0.02	16.66	0.11	0.04	28.93	43.05	0.00	0.00	0.00	0.04	0.00	0.00	88.85	17.38	99.84	99.26
r990002_mt_5-7-1	0.01	16.77	0.12	0.07	29.54	43.43	0.00	0.01	0.07	0.01	0.00	0.07	90.11	27.63	99.95	99.10
r990002_mt_6-9-1	0.00	12.26	0.09	0.00	39.11	39.59	0.00	0.03	0.02	0.03	0.00	0.00	91.13	0.11	99.85	99.66
r990002_mt_7-10-1	0.03	27.29	0.05	0.00	7.50	52.44	0.00	0.00	0.04	0.03	0.03	0.02	87.44	0.19	99.91	98.96
r990002_mt_8-11-1	0.06	16.72	0.00	0.00	29.39	43.38	0.00	0.03	0.00	0.00	0.00	0.01	89.60	21.79	100.00	100.00

Primary biotite

	SiO_2	TiO_2	Al_2O_3	Cr_2O_3	FeO	V_2O_3	ZnO	MnO	MgO	CaO	Na_2O	K_2O	BaO	SrO	NiO	CuO	F	Cl	H_2O(c)	O=F	O=Cl	Sum Ox%	XMg	Oct	Int
r200030bi1-1-1	37.21	4.07	15.08	0.00	18.00	0.01	0.01	0.09	12.14	0.00	0.19	9.13	0.24	0.00	0.04	-	0.57	0.09	3.70	0.24	0.02	100.32	0.55	5.70	1.82
r200030bi2-3-1	37.39	4.00	15.58	0.00	16.82	0.03	0.00	0.11	12.41	0.00	0.19	9.58	0.06	0.00	0.05	-	0.60	0.09	3.71	0.25	0.02	100.35	0.57	5.65	1.88
r200030bi3-4-1	37.10	3.99	15.00	0.00	17.59	0.00	0.06	0.10	12.94	0.01	0.18	9.20	0.21	0.00	0.02	-	0.66	0.09	3.67	0.28	0.02	100.53	0.57	5.76	1.82
r200030bi4-5-1	37.16	3.77	14.41	0.00	17.58	0.00	0.15	0.19	13.05	0.00	0.20	9.30	0.10	0.00	0.00	-	0.63	0.11	3.66	0.26	0.02	100.02	0.57	5.77	1.85
r200030bi5-6-1	37.56	3.87	16.28	0.02	17.13	0.04	0.00	0.09	11.46	0.00	0.17	9.44	0.17	0.00	0.03	-	0.64	0.10	3.69	0.27	0.02	100.41	0.54	5.60	1.86
r200030bi6-7-1	37.26	3.86	16.07	0.00	17.39	0.00	0.03	0.10	11.65	0.00	0.18	8.98	0.20	0.00	0.06	-	0.50	0.10	3.74	0.21	0.02	99.88	0.54	5.67	1.78
r200035bi1-1-1	37.31	3.87	14.89	0.06	14.91	0.02	0.00	0.15	14.42	0.05	0.23	8.97	0.07	0.00	0.01	-	1.01	0.15	3.49	0.43	0.03	99.15	0.63	5.76	1.79
r200035bi2-2-1	37.37	3.84	15.11	0.00	14.64	0.00	0.02	0.22	14.54	0.01	0.20	9.11	0.12	0.00	0.00	-	1.05	0.17	3.48	0.44	0.04	99.41	0.64	5.76	1.80
r200035bi3-3-1	37.46	3.96	14.96	0.03	14.19	0.03	0.07	0.20	14.72	0.03	0.27	9.11	0.27	0.00	0.00	-	1.04	0.18	3.49	0.44	0.04	99.55	0.65	5.73	1.83
r200035bi4-4-1	38.05	4.08	15.36	0.00	12.93	0.00	0.00	0.11	15.82	0.00	0.26	9.33	0.19	0.00	0.02	-	1.15	0.18	3.50	0.49	0.04	100.46	0.69	5.73	1.83
r200035bi5-5-1	37.92	3.67	15.48	0.02	11.96	0.06	0.00	0.07	16.41	0.00	0.27	9.35	0.15	0.00	0.03	-	1.42	0.16	3.37	0.60	0.04	99.72	0.71	5.74	1.84
r200035bi6-6-1	37.39	3.88	15.07	0.00	14.97	0.00	0.18	0.07	14.52	0.00	0.26	9.22	0.21	0.00	0.05	-	1.08	0.21	3.46	0.45	0.05	100.08	0.63	5.76	1.84
r200040-5-1	35.88	0.27	23.01	0.02	16.48	0.09	0.04	0.11	9.73	0.09	0.03	4.09	0.01	0.00	0.00	-	0.15	0.02	3.85	0.06	0.00	93.79	0.51	5.99	0.82
r200040bi1-1-1	34.46	2.20	21.82	0.00	16.41	0.10	0.03	0.25	10.80	0.07	0.04	3.82	0.01	0.00	0.08	-	0.16	0.02	3.83	0.07	0.01	94.04	0.54	6.09	0.77
r200040bi2-3-1	38.75	0.18	25.93	0.01	14.15	0.14	0.22	0.05	8.31	0.07	0.04	5.45	0.00	0.00	0.03	-	0.13	0.00	4.08	0.05	0.00	97.48	0.51	5.61	1.03
r200040bi4-6-1	40.28	0.31	26.75	0.05	11.83	0.14	0.04	0.10	6.58	0.05	0.04	6.93	0.05	0.00	0.00	-	0.20	0.01	4.07	0.09	0.00	97.35	0.50	5.22	1.29
r200124_P24_bi1-1-1	38.31	3.92	14.98	0.00	9.06	0.00	0.00	0.03	18.65	0.00	0.31	10.08	0.33	0.00	0.00	-	2.28	0.12	3.01	0.96	0.03	100.11	0.79	5.72	1.98
r200124_P24_bi2-8-1	39.07	3.64	17.86	0.03	7.54	0.16	0.00	0.01	17.08	0.03	0.19	9.50	0.33	0.00	0.03	-	2.29	0.10	3.08	0.96	0.02	99.96	0.80	5.56	1.81
r200124_P24_bi3-9-1	38.69	3.80	15.01	0.00	8.60	0.07	0.06	0.05	18.96	0.00	0.28	10.08	0.36	0.00	0.05	-	2.47	0.12	2.94	1.04	0.03	100.47	0.80	5.71	1.96
r200124_P24_bi4-13-1	38.51	4.18	15.29	0.00	8.21	0.10	0.05	0.01	19.00	0.00	0.23	10.25	0.29	0.00	0.05	-	2.33	0.10	3.03	0.98	0.02	100.61	0.81	5.69	1.97
r200124_P25_bi1-14-1	39.52	3.02	17.42	0.00	6.44	0.26	0.00	0.03	17.95	0.00	0.16	9.71	0.05	0.00	0.04	-	2.46	0.10	2.99	1.03	0.02	99.08	0.83	5.57	1.83
r200124_P25_bi2-18-1	41.95	2.23	15.65	0.00	5.54	0.11	0.06	0.06	20.25	0.01	0.12	9.65	0.00	0.00	0.00	-	3.25	0.07	2.70	1.37	0.02	100.26	0.87	5.66	1.77
r200124_P26_bi1-19-1	38.78	3.72	15.09	0.03	8.75	0.09	0.04	0.04	18.89	0.00	0.29	10.00	0.25	0.00	0.03	-	2.43	0.11	2.97	1.02	0.03	100.46	0.79	5.72	1.94
r200124_P26_bi2-23-1	38.24	3.88	14.81	0.00	9.15	0.05	0.09	0.00	18.72	0.00	0.28	9.97	0.25	0.00	0.00	-	2.25	0.09	3.03	0.95	0.02	99.85	0.79	5.74	1.95
r200130_P3_bi1-6-1	38.62	3.84	15.48	0.00	10.80	0.03	0.03	0.10	17.15	0.00	0.32	10.07	0.00	0.00	0.00	-	2.20	0.13	3.07	0.92	0.03	100.89	0.74	5.68	1.95
r200130_P3_bi2-7-1	38.36	3.87	15.56	0.00	8.47	0.19	0.02	0.02	18.53	0.00	0.26	10.02	0.07	0.00	0.05	-	2.46	0.13	2.94	1.04	0.03	99.88	0.80	5.69	1.93
r200130_P5_bi1-19-1	48.52	0.28	33.14	0.00	0.65	0.04	0.00	0.03	1.81	0.00	0.40	10.84	0.38	0.00	0.02	-	0.43	0.00	4.35	0.18	0.00	100.71	0.83	4.01	1.95

Secondary biotite

	SiO_2	TiO_2	Al_2O_3	Cr_2O_3	FeO	V_2O_3	ZnO	MnO	MgO	CaO	Na_2O	K_2O	BaO	SrO	NiO	CuO	F	Cl	H_2O(c)	O=F	O=Cl	Sum Ox%	XMg	Oct	Int
r200143_P15_bi1-2-1	38.87	1.98	14.43	0.00	13.13	0.03	0.04	0.04	16.57	0.02	0.19	10.03	0.00	0.00	0.00	-	2.26	0.18	2.93	0.95	0.04	99.72	0.69	5.78	1.95
r200143_P15_bi2-4-1	38.92	1.43	16.30	0.00	12.78	0.00	0.05	0.04	16.69	0.00	0.20	9.06	0.00	0.00	0.06	-	1.91	0.17	3.15	0.80	0.04	99.94	0.70	5.87	1.75
r990002_bi_1-4-1	37.08	2.34	15.99	0.04	13.17	0.00	0.09	0.29	14.56	0.00	0.16	9.64	0.18	0.01	0.01	1.65	0.15	3.14	0.70	0.03		97.78	5.61	1.92	
r990002_bi_2-5-1	36.42	2.52	15.58	0.03	13.89	0.00	0.00	0.27	14.38	0.00	0.13	9.89	0.04	0.00	0.00	1.55	0.16	3.15	0.65	0.04		97.32	5.57	1.97	
r990002_bi_3-8-1	38.42	2.34	13.75	0.05	12.98	0.00	0.09	0.09	16.66	0.00	0.16	9.61	0.05	0.02	0.05	2.11	0.15	2.96	0.89	0.03		98.56	5.75	1.88	
r990002_bi_4-12-1	38.45	2.46	13.73	0.04	12.72	0.03	0.04	0.08	16.62	0.00	0.14	9.58	0.00	0.02	0.06	2.27	0.14	2.89	0.96	0.03		98.27	5.76	1.87	
r990002_bi_5-13-1	38.54	2.08	14.50	0.00	12.03	0.03	0.00	0.14	16.64	0.00	0.09	9.69	0.06	0.02	0.00	2.30	0.13	2.89	0.97	0.03		98.14	5.76	1.88	
r990007_P2_bi1-8-1	39.38	2.77	14.41	0.04	9.79	0.10	0.00	0.08	18.76	0.01	0.21	9.91	0.00	0.00	0.00	-	2.11	0.10	3.10	0.89	0.02	99.86	0.77	5.77	1.90
r990007_P3_bi1-11-1	39.08	2.69	14.46	0.02	10.85	0.07	0.00	0.12	17.98	0.02	0.17	9.66	0.00	0.00	0.00	-	2.38	0.08	2.94	1.00	0.02	99.51	0.75	5.79	1.86
r990007_P4_bi1-13-1	39.15	3.13	14.23	0.00	10.97	0.11	0.06	0.10	17.89	0.00	0.18	9.98	0.00	0.00	0.09	-	2.25	0.11	3.02	0.95	0.03	100.30	0.74	5.75	1.91
r990007_P4_bi2-15-1	39.84	2.58	14.20	0.04	10.89	0.12	0.01	0.10	17.85	0.03	0.18	9.92	0.00	0.00	0.02	-	2.54	0.08	2.90	1.07	0.02	100.21	0.75	5.73	1.90
r990084a_bi1	38.89	3.38	14.56	0.06	10.85	0.08	0.06	0.02	18.29	0.01	0.17	9.96	0.00	0.00	0.00	-	2.67	0.13	2.83	1.13	0.03	100.80	0.75	5.78	1.89
r990084a_bi2	39.17	2.85	14.94	0.03	9.19	0.16	0.00	0.01	18.67	0.01	0.12	10.28	0.00	0.00	0.00	-	2.88	0.14	2.73	1.21	0.03	99.95	0.78	5.72	1.94
r990084a_bi3	38.53	3.08	14.61	0.03	10.34	0.14	0.19	0.04	18.09	0.00	0.15	10.08	0.00	0.00	0.00	-	2.50	0.13	2.87	1.05	0.03	99.70	0.76	5.76	1.93

Sericite

	SiO_2	TiO_2	Al_2O_3	Cr_2O_3	FeO	V_2O_3	ZnO	MnO	MgO	CaO	Na_2O	K_2O	BaO	SrO	NiO	F	Cl	H_2O(c)	O=F	O=Cl	Sum Ox%	XMg	Oct	Int
r200124_P24_ser1-2-1	49.64	0.13	33.87	0.00	0.63	0.10	0.09	0.00	1.61	0.06	0.04	5.63	0.02	0.00	0.01	0.60	0.01	4.24	0.25	0.00	96.43	0.82	4.27	0.97
r200124_P25_ser1-17-1	49.37	0.10	35.30	0.00	0.46	0.04	0.00	0.00	1.40	0.09	0.03	2.42	0.00	0.00	0.00	0.56	0.01	4.24	0.24	0.00	93.78	0.85	4.43	0.43
r200130_P5_ser1-20-1	48.89	0.23	33.27	0.01	0.77	0.00	0.01	0.07	1.84	0.00	0.33	10.38	0.38	0.00	0.00	0.35	0.01	4.40	0.15	0.00	100.79	0.81	4.05	1.84
r200130_P5_ser2-21-1	48.91	0.02	33.47	0.00	0.84	0.00	0.03	0.00	1.70	0.01	0.29	10.67	0.30	0.00	0.00	0.44	0.00	4.36	0.19	0.00	100.86	0.78	4.04	1.88
r200143_P18_ser1-14-1	45.60	0.19	34.08	0.00	3.18	0.01	0.01	0.03	1.59	0.00	0.51	10.82	0.04	0.00	0.00	0.17	0.02	4.39	0.07	0.00	100.58	0.47	4.19	1.99
r200143_P18_ser2-17-1	45.64	0.20	33.92	0.03	3.35	0.00	0.00	0.02	1.48	0.00	0.55	10.83	0.05	0.00	0.01	0.23	0.02	4.36	0.10	0.01	100.58	0.44	4.18	2.00
r990084a_ser1	47.23	0.11	35.86	0.00	1.23	0.04	0.07	0.06	0.91	0.05	0.35	10.19	0.15	0.00	0.04	0.23	0.00	4.46	0.10	0.00	100.88	0.57	4.09	1.81
r990084a_ser2	49.16	2.54	32.08	0.02	0.46	0.04	0.00	0.00	1.51	0.01	0.19	10.16	0.00	0.01	0.00	0.33	0.00	4.43	0.14	0.00	100.80	0.85	3.97	1.74
r990084a_ser3	48.29	0.25	33.82	0.00	0.73	0.03	0.05	0.01	1.52	0.04	0.32	10.62	0.08	0.00	0.00	0.36	0.00	4.38	0.15	0.00	100.33	0.79	4.03	1.88
r990084a_ser4	45.92	0.10	35.30	0.02	2.04	0.00	0.06	0.01	1.26	0.01	0.51	10.73	0.10	0.00	0.00	0.26	0.00	4.39	0.11	0.00	100.60	0.52	4.13	1.96
r990084a_ser5	48.52	0.45	34.07	0.05	0.65	0.03	0.13	0.00	1.41	0.00	0.23	10.38	0.06	0.00	0.00	0.31	0.01	4.42	0.13	0.00	100.59	0.79	4.05	1.80
r990084a_ser6	47.75	0.26	32.27	0.00	1.74	0.02	0.00	0.05	2.53	0.00	0.27	10.87	0.00	0.00	0.00	0.51	0.00	4.27	0.22	0.00	100.33	0.72	4.13	1.91
r990084a_ser7	38.27	0.13	36.16	0.00	1.61	0.07	0.00	0.07	8.62	0.01	2.37	0.02	0.00	0.00	0.03	0.19	0.00	4.20	0.08	0.00	91.68	0.91	5.32	0.65
r990084a_ser8	48.43	0.26	33.21	0.02	0.71	0.04	0.01	0.00	2.24	0.00	0.24	10.83	0.05	0.00	0.00	0.50	0.00	4.32	0.21	0.00	100.64	0.85	4.07	1.88

Garnet

	SiO_2	TiO_2	Al_2O_3	Cr_2O_3	$Fe_2O_3(c)$	FeO	MnO	MgO	CaO	ZrO_2	Y_2O_3	V_2O_3	Sum Ox%	Pyrope	Almandine	Spessartine	Andradite	Uvarovite	Grossular	XMg
r990062_P14_gt1-7-1	35.29	0.00	0.19	0.06	31.51	0.00	0.83	0.00	32.76	0.03	0.01	0.05	100.73	0.00	0.00	1.96	98.04	0.20	0.00	1.00
r990062_P14_gt2-8-1	36.08	0.06	4.84	0.02	25.24	0.00	1.17	0.01	33.28	0.04	0.00	0.00	100.72	0.04	0.00	2.69	77.99	0.07	19.21	1.00
r990062_P14_gt3-9-1	35.33	0.01	0.32	0.00	31.73	0.00	0.84	0.02	32.75	0.08	0.01	0.00	101.08	0.08	0.00	1.98	97.94	0.00	0.00	1.00
r990062_P14_gt4-10-1	35.24	0.01	0.32	0.01	30.81	0.00	0.79	0.00	33.03	0.05	0.00	0.00	100.25	0.00	0.00	1.86	98.14	0.04	0.00	1.00
r990062_P14_gt5-11-1	35.76	0.86	4.67	0.01	24.87	1.41	1.04	0.06	32.03	0.11	0.00	0.02	100.83	0.23	3.23	2.41	77.12	0.04	16.97	0.07
r990062_P14_gt6-12-1	36.12	0.03	5.38	0.00	24.72	0.00	0.99	0.01	33.54	0.08	0.00	0.00	100.89	0.06	0.00	2.28	75.99	0.00	21.68	1.00
r990062_P18_gt1-16-1	36.88	0.03	6.58	0.01	22.69	0.00	1.11	0.03	33.82	0.05	0.01	0.01	101.22	0.10	0.00	2.53	69.15	0.05	28.17	1.00
r990062_P18_gt2-17-1	37.03	0.70	7.51	0.03	20.72	0.18	0.45	0.04	34.55	0.11	0.00	0.08	101.41	0.17	0.40	1.02	63.03	0.11	35.28	0.29
r990062_P18_gt4-19-1	36.29	0.06	5.85	0.00	24.49	0.00	1.18	0.04	33.07	0.08	0.00	0.00	101.05	0.15	0.00	2.74	74.04	0.00	23.07	1.00
r990062_P18_gt5-20-1	36.84	0.43	8.04	0.09	20.63	0.00	0.79	0.02	34.72	0.05	0.00	0.00	101.62	0.09	0.00	1.78	62.64	0.27	35.21	1.00
r990062_P18_gt6-21-1	36.04	0.11	4.48	0.04	26.50	0.74	1.07	0.02	32.28	0.02	0.00	0.05	101.35	0.08	1.72	2.50	80.25	0.12	15.33	0.04
r990062_P18_gt7-22-1	36.62	0.30	6.84	0.00	21.87	0.00	0.65	0.02	34.62	0.05	0.00	0.04	101.01	0.08	0.00	1.46	67.57	0.00	30.89	1.00
r990062_P19_gt1-23-1	36.56	0.14	6.77	0.00	22.73	0.22	1.05	0.02	33.21	0.04	0.00	0.03	100.77	0.10	0.50	2.43	68.80	0.00	28.17	0.16
r990062_P19_gt2-24-1	37.01	0.62	9.45	0.00	18.02	0.00	0.58	0.07	34.93	0.03	0.02	0.07	100.81	0.29	0.00	1.30	54.86	0.00	43.55	1.00
r990062_P19_gt3-25-1	36.20	0.11	5.01	0.00	25.06	0.33	1.31	0.03	32.58	0.11	0.00	0.04	100.79	0.11	0.75	3.06	76.70	0.00	19.38	0.13
r990062_P19_gt4-26-1	36.28	0.24	8.29	0.00	20.59	0.00	0.68	0.03	34.42	0.02	0.00	0.05	100.60	0.11	0.00	1.54	62.80	0.00	35.56	1.00
r990062_P19_gt5-27-1	36.31	0.06	6.05	0.04	24.04	0.00	0.88	0.02	33.39	0.06	0.04	0.00	100.89	0.09	0.00	2.03	72.79	0.12	24.96	1.00
r990062_P19_gt6-28-1	36.18	0.05	14.76	0.00	11.70	0.00	0.42	0.00	36.68	0.07	0.00	0.15	100.00	0.00	0.00	0.90	35.71	0.00	63.38	1.00
r990062_P19_gt7-29-1	36.34	0.03	5.34	0.00	25.16	1.05	1.15	0.03	32.21	0.06	0.00	0.04	101.40	0.10	2.42	2.67	76.10	0.00	18.71	0.04
r990062_P19_gt8-30-1	36.87	0.48	8.99	0.01	18.75	0.00	0.87	0.06	34.52	0.11	0.00	0.11	100.77	0.24	0.00	1.94	57.14	0.05	40.63	1.00

Alunite

	W%(O)	W%(Na)	W%(Al)	W%(Si)	W%(P)	W%(S)	W%(K)	W%(Ca)	W%(Mn)	W%(Fe)	W%(Sr)	W%(Ba)
r990188_alun1-1-1	40.97	1.25	18.87	0.00	0.03	14.85	7.01	0.04	0.01	0.00	0.09	0.22
r990188_alun2-2-1	42.70	1.41	18.94	0.00	0.08	15.89	6.70	0.00	0.01	0.05	0.27	0.30
r990188_alun3-3-1	42.05	1.37	18.82	0.00	0.07	15.55	6.85	0.00	0.00	0.00	0.23	0.15
r990188_alun4-4-1	41.54	1.39	19.05	0.00	0.03	15.11	6.78	0.03	0.02	0.00	0.16	0.14
r990188_alun5-5-1	41.83	1.26	18.94	0.00	0.08	15.33	7.03	0.00	0.07	0.00	0.07	0.25
r990188_alun7-7-1	41.48	1.72	18.82	0.03	0.07	15.16	6.11	0.02	0.00	0.05	0.01	0.42
r990188_alun8-8-1	41.54	1.68	18.82	0.00	0.13	15.14	6.11	0.03	0.00	0.00	0.23	0.67
r990188_alun9-9-1	41.64	1.75	19.06	0.00	0.14	15.06	5.82	0.04	0.01	0.06	0.23	0.61
r990188_alun10-10-1	40.39	1.65	18.81	0.00	0.06	14.48	6.08	0.09	0.00	0.00	0.09	0.28
r990188_alun11-11-1	41.54	1.55	18.74	0.00	0.05	15.30	6.43	0.03	0.00	0.01	0.05	0.17
r990188_alun12-12-1	42.21	1.14	19.07	0.00	0.06	15.54	7.15	0.01	0.00	0.00	0.07	0.22
r990188_alun13-13-1	41.84	1.27	19.79	0.00	0.04	14.87	7.13	0.03	0.00	0.00	0.09	0.05
r990188_alun14-14-1	41.64	1.43	18.87	0.00	0.05	15.26	6.85	0.00	0.06	0.06	0.00	0.12
r990188_alun15-15-1	41.78	1.19	18.94	0.00	0.00	15.33	7.24	0.02	0.03	0.04	0.13	0.26
r990188_alun16-16-1	41.46	1.19	18.69	0.00	0.03	15.25	7.29	0.02	0.00	0.00	0.17	0.23
r990188_alun18-18-1	41.71	1.38	18.97	0.00	0.05	15.29	6.62	0.03	0.00	0.00	0.12	0.16
r990188_alun19-19-1	41.97	1.33	19.03	0.00	0.09	15.36	6.66	0.01	0.12	0.02	0.22	0.18
r990188_alun21-21-1	42.50	1.29	18.99	0.00	0.00	15.84	6.79	0.00	0.06	0.04	0.07	0.19
r990188_alun22-22-1	41.11	1.36	18.78	0.00	0.07	14.95	6.86	0.00	0.00	0.05	0.10	0.20
r990188_alun23-23-1	41.60	1.50	18.68	0.00	0.00	15.34	6.98	0.04	0.00	0.00	0.20	0.04
r990188_alun24-24-1	42.50	1.24	18.66	0.01	0.05	15.92	7.44	0.02	0.03	0.00	0.07	0.19
r990188_alun25-25-1	41.27	1.38	19.08	0.00	0.03	14.89	6.51	0.00	0.05	0.00	0.48	0.49
r990188_alun26-26-1	42.04	1.39	18.98	0.00	0.05	15.46	6.95	0.01	0.04	0.02	0.04	0.04

APS Minerals

	W%(O)	W%(Na)	W%(Al)	W%(Si)	W%(P)	W%(S')	W%(K)	W%(Ca)	W%(Mn)	W%(Fe)	W%(Sr)	W%(Ba)	Mineral
r990188_alun6-6-1	36.03	0.18	16.22	0.05	8.02	5.68	0.10	3.83	0.05	0.08	5.20	0.87	Svanbergite-Woodehousite
r990188_alun17-17-1	34.87	0.21	15.84	0.22	7.69	5.49	0.19	3.32	0.00	0.00	4.63	0.95	Svanbergite-Woodehousite
r990188_alun20-20-1	34.81	0.08	15.67	0.33	8.37	4.89	0.10	3.73	0.00	0.00	3.98	1.00	Svanbergite-Woodehousite
r990188_alun27-27-1	36.16	0.18	16.06	0.36	7.98	5.66	0.14	3.78	0.05	0.03	5.35	0.80	Svanbergite-Woodehousite
r200107_alun1-1-1	38.80	0.17	17.27	0.00	7.31	7.11	0.32	4.38	0.00	0.00	7.19	1.46	Svanbergite-Woodehousite
r200107_alun2-2-1	39.44	0.20	17.71	0.00	7.09	7.54	0.19	5.91	0.00	0.07	3.28	1.45	Woodhouseite-Svanbergite
r200107_alun3-3-1	40.17	0.03	17.74	0.00	7.51	7.46	0.04	7.12	0.00	0.00	3.20	0.72	Woodhouseite-Svanbergite
r200107_alun4-4-1	38.52	0.17	17.50	0.00	6.68	7.40	0.29	5.36	0.02	0.03	4.61	1.11	Woodhouseite-Svanbergite
r200107_alun5-5-1	38.12	0.13	17.32	0.00	6.98	7.00	0.17	4.71	0.00	0.06	6.32	0.92	Svanbergite-Woodhousite
r200107_alun6-6-1	37.78	0.10	16.87	0.00	7.14	7.11	0.31	4.38	0.00	0.27	3.94	2.32	Woodhouseite-Svanbergite
r200107_alun7-7-1	37.52	0.21	17.06	0.07	6.44	7.45	0.84	2.87	0.03	0.09	6.25	2.06	Svanbergite-Woodehousite
r200107_alun8-8-1	36.58	0.00	16.87	0.00	10.11	3.40	0.03	1.67	0.00	0.05	14.49	0.74	Svanbergite
r200107_alun9-9-1	38.95	0.20	17.62	0.00	6.41	7.87	0.40	4.45	0.03	0.02	6.06	1.51	Svanbergite-Woodehousite
r200107_alun10-10-1	35.78	0.19	16.31	0.33	5.92	7.28	0.58	2.95	0.09	0.02	3.69	2.58	Svanbergite-Woodehousite
r200107_alun11-11-1	38.72	0.11	17.31	0.00	7.29	7.17	0.19	4.91	0.06	0.03	5.10	1.56	Svanbergite-Woodehousite
r200107_alun12-12-1	36.99	0.48	16.77	0.32	4.95	8.56	1.04	2.45	0.00	0.05	4.67	2.37	Svanbergite-Woodehousite
r200107_alun14-14-1	36.69	0.03	16.50	0.51	8.10	5.15	0.23	1.82	0.08	0.14	12.84	0.56	Svanbergite
r200107_alun15-15-1	39.80	0.72	17.83	0.00	5.18	9.42	1.30	3.38	0.00	0.00	5.78	1.88	Svanbergite-Woodehousite
r200107_alun16-16-1	38.64	0.29	17.02	0.18	5.92	8.38	1.01	4.36	0.00	0.00	4.36	2.21	Svanbergite-Woodehousite
r200107_alun17-17-1	38.47	0.39	17.01	0.09	5.86	8.65	1.04	2.77	0.08	0.04	5.47	2.05	Svanbergite-Woodehousite
r200107_alun18-18-1	36.09	0.22	16.37	0.05	6.01	7.64	0.50	3.19	0.06	0.12	2.81	2.20	Woodhouseite-Svanbergite
r200107_alun19-19-1	38.11	0.01	16.93	0.00	9.97	4.38	0.00	2.89	0.01	0.06	13.04	0.52	Svanbergite
r200107_alun20-20-1	37.52	0.10	16.85	0.00	8.93	5.08	0.49	2.05	0.12	0.00	12.56	0.97	Svanbergite
r990311_alun1-1-1	39.78	0.19	17.74	0.25	6.75	7.93	0.79	5.21	0.03	0.09	3.60	1.18	Svanbergite
r990311_alun2-3-1	38.56	0.12	17.35	0.00	7.02	7.16	0.25	4.73	0.00	0.01	6.88	0.95	Svanbergite-Woodehousite
r990311_alun3-4-1	39.35	0.14	17.99	0.01	6.91	7.33	0.06	7.97	0.00	0.03	0.21	1.18	Woodhouseite
r990311_alun4-8-1	38.69	0.06	17.40	0.00	7.29	7.01	0.04	7.38	0.09	0.00	0.58	1.60	Woodhouseite
r990311_alun5-11-1	39.49	0.21	17.84	0.00	6.93	7.50	0.23	5.91	0.00	0.04	4.51	1.15	Woodhouseite-Svanbergite
r990311_alun6-16-1	39.78	0.10	17.56	0.15	7.26	7.50	0.17	6.91	0.04	0.05	2.41	0.80	Woodhouseite-Svanbergite
r990311_aps3-15-1	39.11	0.15	17.22	0.19	7.14	7.37	0.41	6.07	0.05	0.01	3.42	1.01	Woodhouseite-Svanbergite
r990311_aps5-19-1	38.84	0.05	17.74	0.24	7.12	6.90	0.11	7.34	0.00	0.00	0.78	1.18	Woodhouseite
r990311_aps6-20-1	39.72	0.03	17.68	0.08	7.26	7.49	0.09	7.61	0.03	0.00	0.47	1.37	Woodhouseite
r990311_aps7-21-1	39.40	0.10	17.10	0.81	6.92	7.44	0.36	4.92	0.06	0.00	5.55	0.77	Svanbergite-Woodehousite
r990311_aps8-22-1	38.83	0.20	17.43	0.00	6.61	7.66	0.34	4.86	0.00	0.01	6.17	1.00	Svanbergite-Woodehousite
r990311_aps9-23-1	38.28	0.13	17.23	0.99	6.62	6.95	0.26	4.04	0.00	0.04	5.83	0.85	Svanbergite-Woodehousite
r990311_aps10-24-1	39.75	0.10	17.42	0.46	7.41	7.27	0.25	6.24	0.02	0.00	3.22	0.96	Woodhouseite-Svanbergite

Sulfides

	W%(S)	W%(V)	W%(Mn)	W%(Fe)	W%(Co)	W%(Ni)	W%(Cu)	W%(Zn)	W%(Ge)	W%(As)	W%(Se)	W%(Mo)	W%(Ag)	W%(Cd)	W%(Sn)	W%(Sb)	W%(Te)	W%(Ba)	W%(Au)	W%(Hg)	W%(Pb)	W%(Bi)	Mineral
r200021_P7_st1-1-1	32.633		0.051	0.346	0.018	0.015	47.129	0.000	0.042	8.878	0.000	0.600	0.008	0.000	6.532	0.029	0.000	0.126	0.085	0.065	0.000	0.096	Colusite
r200021_P7_st2-2-1	31.641		0.010	0.755	0.032	0.010	47.140	0.000	0.052	8.182	0.060	0.821	0.000	0.021	6.735	1.044	0.000	0.171	0.170	0.172	0.067	0.000	Colusite
r200021_P8_st2-5-1	32.223		0.000	0.689	0.001	0.023	47.163	0.000	0.134	8.941	0.085	0.569	0.174	0.019	6.266	0.110	0.000	0.184	0.152	0.093	0.005	0.000	Colusite
r200021_P8_mw1-6-1	30.423		0.000	12.475	0.000	0.005	42.874	0.035	0.086	0.027	0.061	0.549	0.120	0.026	14.536	0.000	0.000	0.125	0.000	0.000	0.000	0.000	Mawsonite
r200021_P8_st3-7-1	31.649		0.002	1.151	0.000	0.000	47.409	0.000	0.057	7.154	0.013	0.588	0.088	0.000	7.358	1.608	0.000	0.083	0.000	0.036	0.129	0.000	Colusite
r200021_P8_cc1-8-1	28.174		0.030	3.333	0.025	0.000	46.080	0.617	0.036	16.951	0.036	0.465	0.332	0.019	0.000	3.128	0.000	0.152	0.151	0.000	0.178	0.109	Tennantite
r200021_P8_cc2-9-1	28.273		0.010	3.260	0.019	0.000	46.828	0.626	0.015	18.779	0.015	0.518	0.349	0.025	0.007	1.288	0.000	0.208	0.000	0.000	0.147	0.043	Tennantite
r200021_P9_mw1-12-1	30.217		0.032	12.705	0.000	0.000	41.987	0.000	0.000	0.000	0.084	0.425	0.089	0.000	14.053	0.000	0.000	0.114	0.027	0.000	0.000	0.000	Mawsonite
r200021_P9_mw2-13-1	30.118		0.000	12.672	0.000	0.001	41.064	0.265	0.117	0.056	0.042	0.404	0.016	0.000	14.141	0.000	0.000	0.122	0.000	0.000	0.060	0.000	Mawsonite
r200021_P9_bn1-14-1	26.850		0.008	11.104	0.000	0.029	60.017	0.000	0.000	0.025	0.000	0.481	0.209	0.035	0.017	0.000	0.022	0.206	0.132	0.000	0.000	0.000	Bornite
r200021_P9_cc1-15-1	28.265		0.000	2.661	0.000	0.016	46.747	0.472	0.011	18.665	0.014	0.450	0.213	0.000	0.000	0.631	0.000	0.281	0.080	0.076	0.033	0.067	Tennantite
r200021_P9_cpy1-16-1	35.529		0.005	29.527	0.000	0.013	33.263	0.042	0.016	0.048	0.018	0.668	0.000	0.000	0.000	0.000	0.000	0.163	0.231	0.005	0.000	0.000	Chalcopyrite
r200021_P10_mw1-17-1	30.196		0.000	12.422	0.000	0.000	40.920	0.002	0.088	0.108	0.055	0.475	0.023	0.000	14.555	0.000	0.000	0.131	0.000	0.021	0.000	0.000	Mawsonite
r200021_P10_mw2-18-1	30.224		0.000	12.216	0.000	0.000	40.644	0.000	0.075	0.070	0.064	0.582	0.031	0.000	14.302	0.000	0.000	0.127	0.178	0.005	0.000	0.000	Mawsonite
r200021_P10_mw3-19-1	32.171		0.000	12.932	0.000	0.000	40.608	0.002	0.073	4.459	0.032	0.506	0.070	0.082	7.605	0.000	0.000	0.119	0.000	0.050	0.000	0.031	Vinciennite
r200021_P10_st1-20-1	32.323		0.000	0.155	0.008	0.000	46.128	0.001	0.067	8.952	0.069	0.629	0.150	0.000	6.226	0.137	0.000	0.152	0.000	0.095	0.042	0.000	Colusite
r200021_P10_mw4-21-1	30.250		0.000	12.524	0.000	0.000	40.895	0.000	0.119	0.059	0.056	0.372	0.054	0.024	14.615	0.000	0.000	0.099	0.174	0.019	0.000	0.009	Mawsonite
r200021_P10_mw5-22-1	30.093		0.000	12.557	0.000	0.000	41.169	0.000	0.084	0.025	0.052	0.552	0.037	0.008	14.478	0.000	0.000	0.122	0.018	0.077	0.000	0.000	Mawsonite
r200021_P10_mw6-23-1	30.545		0.000	12.101	0.000	0.043	40.714	0.042	0.036	0.032	0.074	0.554	0.045	0.000	14.490	0.000	0.000	0.048	0.013	0.000	0.000	0.000	Mawsonite
r200021_P10_cp1-24-1	35.865		0.000	28.555	0.000	0.032	32.708	0.000	0.058	0.073	0.004	0.510	0.035	0.000	0.058	0.029	0.069	0.131	0.167	0.000	0.000	0.004	Chalcopyrite
r200021_P10_bn-25-1	26.584		0.000	10.096	0.000	0.018	59.833	0.000	0.111	0.093	0.000	0.493	0.222	0.000	0.000	0.000	0.011	0.240	0.200	0.175	0.000	0.000	Bornite
r200021_P10_cc1-26-1	28.484		0.000	2.677	0.008	0.017	45.813	0.465	0.015	18.933	0.016	0.440	0.205	0.006	0.046	0.689	0.000	0.201	0.316	0.000	0.000	0.053	Tennantite
r990293_P11_mw1-1-1	32.079		0.005	2.402	0.000	0.019	46.835	0.049	0.069	8.612	0.096	0.661	0.000	0.015	7.224	0.000	0.000	0.135	0.063	0.000	0.000	0.000	Colusite
r990293_P11_mw2-2-1	31.811		0.000	0.841	0.000	0.031	49.004	0.025	0.190	8.980	0.104	0.530	0.131	0.035	5.414	0.377	0.000	0.188	0.027	0.007	0.000	0.000	Colusite
r990293_P11_mw3-3-1	32.099		0.028	0.728	0.000	0.011	48.656	0.000	0.071	7.973	0.042	0.570	0.000	0.000	7.365	0.186	0.000	0.149	0.027	0.014	0.000	0.000	Colusite
r990293_P11_cv1-4-1	34.296		0.000	2.026	0.000	0.019	63.465	0.000	0.000	0.093	0.017	0.628	0.204	0.079	0.000	0.013	0.000	0.270	0.000	0.116	0.000	0.000	Covellite
r990293_P11_en1-5-1	33.758		0.000	0.014	0.017	0.033	47.977	0.000	0.105	18.259	0.047	0.601	0.006	0.091	0.000	0.213	0.000	0.229	0.000	0.000	0.000	0.000	Enargite
r990293_P11_cc1-6-1	21.541		0.001	0.002	0.001	0.000	77.037	0.064	0.021	0.085	0.014	0.390	0.051	0.000	0.000	0.000	0.000	0.342	0.104	0.075	0.000	0.000	Chalcocite
r990293_P12_en1-7-1	33.670		0.030	0.015	0.032	0.005	47.657	0.004	0.054	18.130	0.019	0.445	0.012	0.000	0.056	0.506	0.007	0.292	0.112	0.000	0.000	0.000	Enargite
r990293_P12_cc1-8-1	21.177		0.021	0.000	0.000	0.000	77.449	0.000	0.062	0.043	0.048	0.274	0.000	0.000	0.023	0.007	0.000	0.354	0.041	0.000	0.000	0.000	Chalcocite
r990293_P12_cv1-9-1	34.587		0.000	1.311	0.016	0.000	63.811	0.000	0.099	0.003	0.000	0.658	0.010	0.008	0.000	0.000	0.000	0.287	0.051	0.000	0.052	0.041	Covellite
r990293_P12_en2-10-1	33.707		0.000	0.079	0.014	0.000	47.646	0.000	0.000	18.349	0.068	0.453	0.035	0.036	0.000	0.326	0.000	0.228	0.000	0.000	0.000	0.000	Enargite
r990293_P13_bn1-11-1	26.259		0.000	11.261	0.000	0.004	61.092	0.007	0.024	0.000	0.030	0.401	0.000	0.055	0.016	0.000	0.000	0.263	0.041	0.000	0.000	0.014	Bornite
r990293_P13_bn2-12-1	26.709		0.000	11.121	0.000	0.001	60.806	0.000	0.023	0.061	0.056	0.385	0.000	0.065	0.000	0.000	0.000	0.268	0.296	0.078	0.058	0.000	Bornite
r990293_P13_bn3-13-1	26.633		0.000	11.134	0.000	0.032	61.321	0.001	0.158	0.018	0.000	0.337	0.057	0.000	0.000	0.000	0.000	0.298	0.000	0.082	0.000	0.180	Bornite
r990293_P13_cc1-14-1	21.142		0.034	0.584	0.000	0.000	76.349	0.000	0.039	0.071	0.011	0.389	0.014	0.026	0.049	0.049	0.000	0.352	0.388	0.000	0.000	0.162	Chalcocite
r990293_P13_cc2-15-1	21.449		0.009	0.023	0.009	0.000	77.507	0.055	0.093	0.006	0.000	0.431	0.035	0.066	0.007	0.005	0.033	0.409	0.154	0.000	0.000	0.000	Chalcocite
r990293_P13_cc3-16-1	21.118		0.000	0.038	0.000	0.000	77.737	0.000	0.000	0.066	0.039	0.360	0.021	0.000	0.019	0.000	0.000	0.349	0.068	0.000	0.000	0.086	Chalcocite
r990293_P13_en1-17-1	33.577		0.005	0.014	0.000	0.030	47.712	0.021	0.000	18.021	0.096	0.636	0.052	0.025	0.000	0.305	0.079	0.178	0.000	0.000	0.000	0.000	Enargite
r990293_P13_en2-18-1	33.609		0.032	0.019	0.026	0.024	47.238	0.000	0.000	18.527	0.019	0.603	0.085	0.000	0.068	0.325	0.051	0.203	0.022	0.000	0.000	0.085	Enargite
r990293_P13_en3-19-1	33.712		0.000	0.031	0.022	0.000	47.415	0.014	0.046	18.133	0.071	0.489	0.103	0.049	0.020	0.429	0.000	0.196	0.054	0.000	0.000	0.071	Enargite
r990293_P13_en4-20-1	33.303		0.041	0.003	0.008	0.023	47.102	0.000	0.092	18.109	0.017	0.493	0.000	0.000	0.033	0.622	0.025	0.198	0.000	0.068	0.000	0.000	Enargite
r990084a_cpy1-16-1	34.793	0.000	0.000	30.361			34.208	0.000	0.088	0.066	0.000		0.000	0.091	0.020	0.000	0.057		0.000		0.000	0.000	Chalcopyrite
r990084a_cpy2-17-1	35.264	0.000	0.000	30.382			34.381	0.000	0.177	0.052	0.015		0.000	0.021	0.071	0.000	0.047		0.267		0.000	0.000	Chalcopyrite
r990084a_cpy3-18-1	34.853	0.000	0.000	30.810			33.894	0.000	0.000	0.025	0.019		0.002	0.002	0.042	0.000	0.000		0.080		0.000	0.000	Chalcopyrite
r990084a_cpy4-19-1	34.873	0.000	0.005	30.615			32.970	0.020	0.096	0.071	0.000		0.000	0.000	0.009	0.000	0.027		0.000		0.015	0.022	Chalcopyrite
r990084a_cpy5-20-1	35.073	0.005	0.000	30.503			33.309	0.021	0.031	0.024	0.013		0.000	0.057	0.000	0.000	0.020		0.000		0.055	0.070	Chalcopyrite
r990084a_cpy6-21-1	35.313	0.000	0.042	30.443			34.370	0.066	0.000	0.060	0.003		0.035	0.000	0.058	0.002	0.025		0.000		0.000	0.000	Chalcopyrite
r990237_py1-1-1	53.457	0.000	0.000	47.354			0.060	0.001	0.000	0.053	0.000		0.044	0.000	0.011	0.049	0.039		0.000		0.142	0.008	Pyrite
r990237_py2-2-1	54.094	0.000	0.025	47.979			0.009	0.022	0.002	0.046	0.011		0.000	0.006	0.026	0.000	0.000		0.230		0.000	0.000	Pyrite
r990237_py3-3-1	54.224	0.004	0.003	47.274			0.024	0.021	0.000	0.083	0.000		0.048	0.000	0.008	0.000	0.001		0.082		0.000	0.000	Pyrite
r990237_py4-4-1	53.882	0.000	0.001	46.865			0.000	0.019	0.000	0.060	0.000		0.000	0.000	0.032	0.000	0.062		0.048		0.000	0.118	Pyrite

Appendix 2-8. *Electron Microprobe Data*

Sulfides

	W%(S)	W%(V)	W%(Mn)	W%(Fe)	W%(Co)	W%(Ni)	W%(Cu)	W%(Zn)	W%(Ge)	W%(As)	W%(Se)	W%(Mo)	W%(Ag)	W%(Cd)	W%(Sn)	W%(Sb)	W%(Te)	W%(Ba)	W%(Au)	W%(Hg)	W%(Pb)	W%(Bi)	Mineral
r990237_cpy1-5-1	35.152	0.000	0.018	30.348			33.897	0.121	0.068	0.083	0.000		0.081	0.000	0.043	0.000	0.000		0.000		0.000	0.092	Chalcopyrite
r990237_cpy2-6-1	35.281	0.000	0.004	30.505			33.812	0.010	0.000	0.105	0.000		0.103	0.017	0.000	0.000	0.000		0.000		0.000	0.000	Chalcopyrite
r990237_cpy3-7-1	34.971	0.021	0.019	30.330			33.900	0.000	0.000	0.022	0.000		0.069	0.019	0.021	0.000	0.000		0.122		0.000	0.000	Chalcopyrite
r990237_cpy4-8-1	34.934	0.035	0.000	30.266			33.937	0.006	0.000	0.041	0.000		0.093	0.019	0.000	0.026	0.000		0.061		0.000	0.000	Chalcopyrite
r990237_cpy5-9-1	35.366	0.000	0.000	30.368			34.363	0.076	0.053	0.039	0.000		0.045	0.000	0.000	0.033	0.000		0.000		0.020	0.000	Chalcopyrite
r990237_mw1-10-1	31.597	0.013	0.019	13.913			43.258	0.015	0.047	4.283	0.049		0.099	0.000	7.653	0.000	0.000		0.196		0.158	0.000	Vinciennite
r990237_mw2-11-1	27.339	0.000	0.000	11.797			39.009	0.000	0.077	0.045	0.063		0.045	0.000	13.317	0.000	0.000		0.000		0.000	0.000	Mawsonite
r990237_ct1-12-1	30.494	2.798	0.003	1.320			49.362	0.006	0.156	5.992	0.045		0.137	0.044	5.860	4.329	0.000		0.000		0.000	0.000	Colusite
r990237_ct2-13-1	31.017	2.814	0.015	0.650			48.610	0.000	0.280	6.680	0.053		0.010	0.000	5.503	4.529	0.000		0.000		0.057	0.000	Colusite
r990237_mw3-14-1	31.665	0.016	0.022	13.702			43.011	0.049	0.078	4.342	0.005		0.110	0.000	7.457	0.000	0.000		0.000		0.000	0.000	Mawsonite
r990237_mw4-15-1	29.872	0.000	0.000	13.100			43.905	0.000	0.042	0.063	0.001		0.040	0.016	14.538	0.000	0.000		0.000		0.000	0.000	Mawsonite
r990237_ct3-16-1	30.706	3.119	0.000	1.550			47.005	0.044	0.152	6.740	0.078		0.143	0.007	6.012	4.019	0.000		0.000		0.000	0.000	Colusite
r990237_tn1-18-1	21.701	0.003	0.000	0.674			77.305	0.032	0.000	0.072	0.052		0.399	0.082	0.000	0.000	0.047		0.060		0.000	0.061	Chalcocite
r990237_cov1-20-1	26.245	0.000	0.000	10.896			61.779	0.987	0.079	0.068	0.000		0.231	0.000	0.044	0.011	0.023		0.042		0.047	0.055	Bornite
r990237_dj1-21-1	32.895	0.000	0.008	0.583			2.681	65.221	0.000	0.000	0.000		0.085	0.000	0.072	0.000	0.006		0.433		0.000	0.000	Sphalerite
r990237_dj2-23-1	33.046	0.000	0.010	0.562			2.614	64.694	0.000	0.019	0.000		0.000	0.045	0.001	0.042	0.049		0.000		0.000	0.071	Sphalerite
r990237_dj3-24-1	24.903	0.000	0.001	0.615			55.645	17.145	0.081	0.000	0.000		0.223	0.000	0.000	0.000	0.003		0.032		0.032	0.061	?
r990237_bn1-25-1	26.200	0.000	0.010	11.176			61.089	0.000	0.021	0.045	0.015		0.260	0.000	0.000	0.006	0.035		0.000		0.005	0.055	Bornite
r990237_bn2-26-1	25.922	0.048	0.035	11.357			61.805	0.000	0.000	0.094	0.000		0.211	0.020	0.029	0.000	0.000		0.000		0.000	0.000	Bornite
r990237_bn3-27-1	25.890	0.012	0.000	11.364			61.177	0.040	0.000	0.085	0.004		0.288	0.007	0.006	0.032	0.000		0.000		0.000	0.000	Bornite
r990237_mw5-28-1	29.664	0.000	0.006	12.842			43.844	0.000	0.130	0.051	0.062		0.043	0.000	14.631	0.000	0.000		0.086		0.020	0.000	Mawsonite
r990237_mw6-29-1	29.634	0.000	0.010	13.109			44.174	0.019	0.042	0.052	0.090		0.066	0.000	14.401	0.000	0.000		0.000		0.000	0.000	Mawsonite
r990237_tn2-30-1	28.010	0.000	0.011	3.110			47.676	0.957	0.024	19.288	0.106		0.176	0.000	0.000	0.825	0.000		0.018		0.000	0.124	Tennantite
r990237_tn3-31-1	28.152	0.028	0.002	2.950			48.115	0.907	0.000	18.519	0.107		0.118	0.000	0.000	1.694	0.000		0.000		0.000	0.224	Tennantite
r990237_dj4-33-1	32.310	0.000	0.021	0.493			3.431	63.371	0.058	0.013	0.000		0.140	0.035	0.000	0.000	0.000		0.000		0.000	0.000	Sphalerite
r200135_cpy1-1-1	35.129	0.000	0.000	30.560			33.802	0.032	0.008	0.071	0.000		0.020	0.000	0.016	0.035	0.029		0.000		0.000	0.119	Chalcopyrite
r200135_bn1-2-1	26.885	0.000	0.015	11.347			61.275	0.000	0.087	0.067	0.000		0.083	0.004	0.009	0.000	0.069		0.000		0.000	0.115	Bornite
r200135_bn2-3-1	26.280	0.002	0.018	11.622			61.203	0.000	0.025	0.079	0.000		0.196	0.000	0.000	0.000	0.000		0.231		0.068	0.005	Bornite
r200135_bn3-4-1	26.060	0.000	0.000	11.478			62.485	0.000	0.008	0.043	0.010		0.158	0.000	0.014	0.000	0.001		0.304		0.000	0.032	Bornite
r200135_bn4-5-1	26.189	0.002	0.012	11.224			61.554	0.000	0.085	0.114	0.022		0.129	0.000	0.000	0.000	0.002		0.032		0.011	0.051	Bornite
r200135_bn5-6-1	26.080	0.035	0.021	11.100			62.390	0.022	0.000	0.073	0.000		0.092	0.000	0.055	0.000	0.000		0.134		0.000	0.000	Bornite
r200135_cpy2-7-1	35.127	0.035	0.000	30.418			33.481	0.000	0.119	0.014	0.000		0.038	0.009	0.054	0.000	0.024		0.187		0.000	0.000	Chalcopyrite
r200135_cpy6-8-1	35.206	0.000	0.000	30.192			34.040	0.000	0.002	0.061	0.000		0.065	0.074	0.000	0.000	0.000		0.211		0.025	0.000	Chalcopyrite
r200135_cpy3-9-1	35.069	0.000	0.003	30.570			33.736	0.000	0.010	0.027	0.000		0.000	0.019	0.048	0.000	0.021		0.127		0.000	0.000	Chalcopyrite
r200135_bn7-10-1	27.193	0.000	0.000	12.026			60.693	0.000	0.075	0.013	0.000		0.102	0.000	0.032	0.025	0.007		0.000		0.000	0.032	Bornite
r200135_cpy4-11-1	35.131	0.007	0.000	30.814			34.036	0.070	0.000	0.043	0.000		0.000	0.000	0.012	0.000	0.000		0.000		0.000	0.000	Chalcopyrite
r200135_bn8-12-1	26.357	0.000	0.000	11.581			61.812	0.000	0.056	0.031	0.013		0.173	0.004	0.000	0.000	0.000		0.157		0.184	0.000	Bornite

APPENDIX 3

FLUID INCLUSION DATA

Vein types are those defined in Table 5.2.

See Rock Catalogue (Appendix 5) for sample information.

IncNumber:	analysis number
IncType:	V + L = vapour + liquid
	V + L + S = vapour + liquid + solid
Type (Nash, 1976):	as defined in Table 7.1
Size in micrometres	
Fill:	degree of fill = volume of liquid/total volume
Te:	First ice melting temperature (eutectic temperature; °C)
Tm_ice:	Temperature of last ice melting (°C)
Ts_hal:	Temperature of halite dissolution (°C)
Ts_S2:	Temperature of sylvite dissolution (°C)
Th_aq:	Temperature of vapour bubble disappearance (°C)
Td:	Decrepitation temperature (°C)
Phase:	Final homogenisation phase
	Liquid = homogenisation via bubble disappearance
	Vapour = homogenisation via bubble expansion
	Halite = homogenisation via halite dissolution
Eq.wt.% NaCl:	Equivalent weight percent NaCl
T_total:	Total homogenisation temperature (°C)

Vein type	Sample	IncNum	Type (Nash 1976)	Shape	Size	Fill	Te	Tm_ice	Ts_hal	Ts_S2	Th_aq	Td	Phase	EqWt%NaCl	T_total
A-2	R990007	3f_A	Ia	Faceted	14.9	0.9	-36.8	-13.4			348.8		Liquid	17.2	348.8
A-2	R990007	3f_C	Ia	Rounded	7.8	0.8	-23.9	-11.4			371.1		Liquid	15.4	371.1
A-2	R990007	3i_A	Ia	Faceted	16.2	0.8	-25.9	-14.2			488.9		Liquid	17.9	488.9
A-2	R990007	3i_B	Ia	Faceted	11.7	0.8	-24.5	-16.0			461.9		Liquid	19.4	461.9
A-2	R990007	3j_C	Ia	Rounded	13.8	0.8	-25.6	-14.0			445.8		Liquid	17.8	445.8
A-2	R990007	3j_D	Ib	Rounded	15.0	0.8	-25.5	-13.7			425.9		Liquid	17.5	425.9
A-2	R990007	5b_D	Ib	Irregular	12.0	0.7	-35.2	-12.0			524.0		Liquid	16.0	524.0
A-2	R990124_A2	2a	Ib	Faceted	11.4	0.9	-34.8	-24.5			320.3		Liquid	25.2	320.3
A-2	R990124_A2	2b	Ib	Faceted	15.3	0.7	-39.0	-9.1			445.8		Liquid	13.0	445.8
A-2	R990007	1a	IIa	Faceted	9.6	0.8		-6.0			600.0		Vapour	9.2	600.0
A-2	R990007	1b_A	IIa	Faceted	12.5	0.8		-11.0			570.0	570.0	Vapour		570.0
A-2	R990007	1b_B	IIa	Rounded	7.8	0.5		-6.5			600.0		Vapour	9.8	600.0
A-2	R990007	1b_C	IIa	Rounded	8.0	0.8		-10.0			447.6		Liquid	13.9	447.6
A-2	R990007	1b_D	IIa	Rounded	6.2	0.6		-9.9			600.0		Vapour	13.8	600.0
A-2	R990007	4a	IIa	Irregular	16.0	0.7		-11.4			414.5		Vapour	15.4	414.5
A-2	R990007	5b_A	IIa	Irregular	10.4	0.6		-12.3			600.0		Vapour	16.2	600.0
A-2	R990007	5b_B	IIa	Rounded	12.1	0.6		-12.4			580.8		Vapour	16.3	580.8
A-2	R990007	5b_E	IIa	Faceted	10.1	0.5		-8.0			484.8		Vapour	11.7	484.8
A-2	R990124_A2	2c_A	IIa	Rounded	12.9	0.6		-2.9			404.9		Vapour	4.7	404.9
A-2	R990124_A2	2c_B	IIa	Rounded	11.0	0.6		-4.5			424.5		Vapour	7.1	424.5
A-2	R990007	1b_E	IIb	Rounded	5.8	0.7		-10.4			600.0		Vapour	14.4	600.0
A-2	R990007	2c	IIb	Faceted	12.9	0.5		-1.1			406.5		Vapour	1.8	406.5
A-2	R990007	2d	IIb	Faceted	10.4	0.6		-9.5			580.1		Vapour	13.4	580.1
A-2	R990007	3g_C	IIb	Faceted	16.5	0.8		-9.2			558.4		Vapour	13.1	558.4
A-2	R990007	3j_E	IIb	Faceted	8.0	0.8		-13.3			600.0		Vapour	17.2	600.0
A-2	R990007	4e_A	IIb	Faceted	11.6	0.4		-14.8			560.4		Vapour	18.5	560.4
A-2	R990007	4e_B	IIb	Faceted	15.5	0.6		-15.3			600.0		Vapour	18.9	600.0
A-2	R990007	5a_A	IIb	Faceted	25.5	0.5		-2.6			432.6		Vapour	4.2	432.6
A-2	R990007	5a_B	IIb	Faceted	11.4	0.4		-3.3			395.4		Vapour	5.3	395.4
A-2	R990007	5a_C	IIb	Faceted	8.7	0.4		-3.4			384.8		Vapour	5.5	384.8
A-2	R990007	5a_D	IIb	Rounded	9.6	0.5		-5.2			388.3		Vapour	8.1	388.3
A-2	R990007	5a_E	IIb	Faceted	9.8	0.5		-4.7			448.4		Vapour	7.4	448.4
A-2	R990007	5b_C	IIb	Faceted	12.6	0.5		-2.2			495.2		Vapour	3.6	495.2
A-2	R990124_A2	2b_D	IIb	Rounded	9.7	0.5		-10.5			419.5		Vapour	14.5	419.5
A-2	R990124_A2	2e	IIb	Irregular	12.2	0.5		-4.1			426.7		Vapour	6.5	426.7
A-2	R990007	2b_A	IIIa	Irregular	12.4	0.9			313.3		298.3		Liquid	39.2	313.3
A-2	R990007	2b_B	IIIa	Irregular	11.0	1.0			422.3		227.0		Liquid	49.9	422.3
A-2	R990007	3f_B	IIIa	Rounded	9.5	0.9			149.8		407.4		Liquid	29.7	407.4
A-2	R990007	4b_A	IIIa	Faceted	14.9	0.9			234.8		260.4		Liquid	33.8	260.4
A-2	R990007	4c_A	IIIa	Irregular	10.7	0.9			300.1		252.0		Liquid	38.2	300.1
A-2	R990007	4c_B	IIIa	Irregular	15.2	0.9			273.9		255.8		Liquid	36.3	273.9
A-2	R990007	4d_A	IIIa	Irregular	16.3	0.9			257.9		288.7		Liquid	35.2	288.7
A-2	R990007	4d_B	IIIa	Irregular	16.3	0.9			395.1		256.2		Liquid	46.9	395.1
A-2	R990124_A2	2d_D	IIIa	Irregular	9.3	0.9			245.9		230.5		Liquid	34.4	245.9
A-2	R990007	2a_A	IIIb	Irregular	19.8	0.9			289.5		157.9		Liquid	37.4	289.5
A-2	R990007	3a_A	IIIb	Faceted	11.3	1.0			304.9		273.6		Liquid	38.5	304.9
A-2	R990007	3a_B	IIIb	Irregular	18.3	0.9			417.9		229.1		Liquid	49.4	417.9
A-2	R990007	3a_D	IIIb	Faceted	7.8	0.9			354.9		238.0		Liquid	42.9	354.9
A-2	R990007	3a_E	IIIb	Faceted	8.7	0.9			425.5		252.3		Liquid	50.3	425.5
A-2	R990007	3b_A	IIIb	Irregular	11.4	0.9			337.9		366.8		Liquid	41.3	366.8
A-2	R990007	3c_A	IIIb	Irregular	16.7	0.9			363.9		259.5		Liquid	43.7	363.9
A-2	R990007	3d_A	IIIb	Rounded	8.7	0.9			428.2		250.1		Liquid	50.6	428.2
A-2	R990007	3e_A	IIIb	Rounded	10.6	0.9			389.9		432.6		Liquid	46.4	432.6
A-2	R990007	4b_B	IIIb	Faceted	14.1	0.8			401.1		399.8		Liquid	47.6	401.1
A-2	R990007	4d_C	IIIb	Faceted	6.8	0.8			290.4		290.4		Liquid	37.4	290.4
A-2	R990007	4f	IIIb	Irregular	9.8	0.9			267.9		270.2		Liquid	35.8	270.2
A-2	R990124_A2	2d_C	IIIb	Rounded	10.5	0.9			235.4		275.9		Liquid	33.8	275.9
A-2	R990124_A2	2f	IIIb	Faceted	8.8	0.9			496.8		194.7	496.8	Liquid	59.3	496.8
A-3	R990085_A3	1a_E	Ia	Irregular	13.9	0.8	-49.2	-25.3			255.8		Liquid	25.6	255.8
A-3	R990085_A3	1b_A	Ia	Irregular	12.3	0.9	-43.9	-14.0			303.1		Liquid	17.8	303.1
A-3	R990085_A3	1h_E	Ia	Faceted	7.2	0.7		-7.5			451.4		Liquid	11.1	451.4
A-3	R990106	2d_A	Ia	Irregular	11.1	0.9	-46.9	-19.1			298.2		Liquid	21.7	298.2
A-3	R990106	2e_B	Ia	Irregular	8.6	0.9		-8.1			202.5		Liquid	11.8	202.5
A-3	R990106	2e_D	Ia	Irregular	8.2	0.9		-7.1			297.2		Liquid	10.6	297.2
A-3	R990106	2f_E	Ia	Faceted	18.3	0.7		-13.9			372.9		Liquid	17.7	372.9
A-3	R990106	2f_F	Ia	Irregular	17.2	0.7		-13.9			377.1		Liquid	17.7	377.1
A-3	R990106	4a_C	Ia	Irregular	45.6	0.6		-4.1			400.8		Liquid	6.5	400.8
A-3	R990108_A3	1a_B	Ia	Faceted	11.7	0.6		-4.4			400.5		Liquid	7.0	400.5
A-3	R990108_A3	1c	Ia	Irregular	19.3	0.9		-4.1			334.5		Liquid	6.5	334.5
A-3	R990085_A3	1d_A	Ib	Faceted	14.4	0.8	-39.0	-19.3			379.1		Liquid	21.9	379.1
A-3	R990085_A3	1d_B	Ib	Faceted	8.0	0.9		-23.8			222.9		Liquid	24.8	222.9
A-3	R990085_A3	1d_E	Ib	Faceted	4.8	0.8		-24.6			224.3		Liquid	25.2	224.3
A-3	R990106	2d_B	Ib	Faceted	14.1	0.9		-0.7			260.2		Liquid	1.2	260.2
A-3	R990106	2e_A	Ib	Faceted	16.5	0.9	-31.3	-19.4			252.7		Liquid	21.9	252.7
A-3	R990106	2e_C	Ib	Faceted	8.3	0.9		-6.2			291.9		Liquid	9.5	291.9
A-3	R990106	4a_B	Ib	Irregular	33.5	0.6		-1.3			387.2		Liquid	2.1	387.2
A-3	R990085_A3	1h_A	IIa	Faceted	11.7	0.4		-18.0			514.0		Vapour	20.9	514.0
A-3	R990085_A3	1h_C	IIa	Rounded	8.9	0.5		-11.9			517.4		Vapour	15.9	517.4
A-3	R990085_A3	1l_A	IIa	Faceted	10.7	0.4		-8.0			368.7		Vapour	11.7	368.7
A-3	R990106	1e_A	IIa	Irregular	20.6	0.6		-7.6			600.0		Vapour	11.2	600.0
A-3	R990106	2f_B	IIa	Faceted	11.6	0.6		-9.6			488.8		Vapour	13.5	488.8
A-3	R990106	7c_G	IIa	Faceted	9.8	0.6		-12.6			Tyoe I		Vapour	16.5	549.9
A-3	R990108_A3	1b_A	IIa	Irregular	18.6	0.7		-4.2			415.1		Vapour	6.7	415.1
A-3	R990108_A3	1b_B	IIa	Irregular	17.1	0.6		-3.6			410.5		Vapour	5.8	410.5
A-3	R990108_A3	2c_A	IIa	Irregular	19.5	0.7		-5.7			540.0	545.0	Vapour	8.8	540.0
A-3	R990085_A3	1c_B	IIb	Faceted	14.9	0.4		-8.1			381.9		Vapour	11.8	381.9
A-3	R990085_A3	1g_B	IIb	Faceted	7.3	0.6		-18.4			600.0		Vapour	21.2	600.0
A-3	R990085_A3	1h_B	IIb	Irregular	10.8	0.5		-16.5			463.0		Vapour	19.8	463.0
A-3	R990085_A3	1h_F	IIb	Faceted	9.3	0.5		-7.5			413.7		Vapour	11.1	413.7
A-3	R990085_A3	1l_B	IIb	Irregular	9.1	0.7		-3.7			496.8		Vapour	5.9	496.8
A-3	R990106	1c_A	IIb	Irregular	13.8	0.6	-43.4	-5.5			587.8		Vapour	8.5	587.8
A-3	R990106	1c_B	IIb	Faceted	9.4	0.6		-9.3			600.0		Vapour	13.2	600.0
A-3	R990106	1f_B	IIb	Faceted	17.1	0.6		-6.9			600.0		Vapour	10.4	600.0
A-3	R990106	1f_C	IIb	Faceted	15.7	0.6		-6.8			461.7		Vapour	10.2	461.7
A-3	R990106	1f_D	IIb	Faceted	10.9	0.5		-2.0			472.9		Vapour	3.3	472.9
A-3	R990106	2f_A	IIb	Faceted	15.0	0.6		-10.4			427.4		Liquid	14.4	427.4
A-3	R990106	2f_C	IIb	Faceted	12.8	0.6		-9.5			453.9		Liquid	13.4	453.9
A-3	R990106	2j_A	IIb	Faceted	26.3	0.6		-8.8			469.0		Vapour	12.6	469.0
A-3	R990106	3b	IIb	Irregular	24.9	0.6		-13.1			472.3	472.3	Vapour	17.0	472.3
A-3	R990106	4a_A	IIb	Faceted	24.1	0.6		-11.8			534.6		Vapour	15.8	534.6
A-3	R990106	7c_A	IIb	Faceted	25.9	0.5	-38.3	-11.6			576.2		Vapour	15.6	576.2
A-3	R990106	7c_B	IIb	Faceted	15.3	0.6	-40.0	-9.5			600.0		Vapour	13.4	600.0
A-3	R990106	7c_E	IIb	Faceted	9.7	0.5		-9.4			558.7		Vapour	13.3	558.7
A-3	R990106	7c_F	IIb	Faceted	12.2	0.6		-5.1			524.0		Vapour	8.0	524.0
A-3	R990106	7c_H	IIb	Faceted	7.8	0.6		-11.2			550.8		Vapour	15.2	550.8

Vein type	Sample	IncNum	Type (Nash 1976)	Shape	Size	Fill	Te	Tm_ice	Ts_hal	Ts_S2	Th_aq	Td	Phase	EqWt%NaCl	T_total
A-3	R990106	7d_A	IIb	Faceted	12.3	0.6		-14.2			600.0		Vapour	17.9	600.0
A-3	R990106	7d_E	IIb	Faceted	11.4	0.7		-18.6			526.9		Vapour	21.4	526.9
A-3	R990108_A3	1b_C	IIb	Rounded	13.5	0.6		-2.6			409.8		Vapour	4.2	409.8
A-3	R990108_A3	2a_A	IIb	Irregular	30.1	0.5		-6.5			454.5		Vapour	9.8	454.5
A-3	R990108_A3	2a_B	IIb	Irregular	31.1	0.4		-3.5			388.1		Vapour	5.6	388.1
A-3	R990108_A3	2b	IIb	Rounded	13.1	0.6		-7.0			489.5		Vapour	10.5	489.5
A-3	R990108_A3	2d	IIb	Irregular	13.3	0.6		-4.1			547.6		Vapour	6.5	547.6
A-3	R990085_A3	1a_D	IIIa	Faceted	10.7	0.9			310.7		229.7		Halite	39.0	310.7
A-3	R990085_A3	1a_F	IIIa	Faceted	6.9	0.9			522.0		437.5		Halite	62.8	522.0
A-3	R990085_A3	1b_B	IIIa	Irregular	5.9	0.9			256.0		201.9		Halite	35.1	256.0
A-3	R990085_A3	1b_C	IIIa	Faceted	9.5	0.9			295.0		211.4		Halite	37.8	295.0
A-3	R990085_A3	1f_E	IIIa	Faceted	7.4	0.9			433.1		421.8		Halite	51.2	433.1
A-3	R990085_A3	1l_E	IIIa	Rounded	6.8	0.8			251.2		279.3		Liquid	34.8	279.3
A-3	R990106	10a_D	IIIa	Irregular	19.5	0.8			231.8		281.0		Liquid	33.6	281.0
A-3	R990106	2c_A	IIIa	Faceted	11.4	0.8			488.3		292.1		Halite	58.2	488.3
A-3	R990106	3a_B	IIIa	Irregular	19.5	0.9			331.5		255.2		Halite	40.7	331.5
A-3	R990106	4d_A	IIIa	Irregular	24.2	0.9			286.9		327.2	450.0	Liquid	37.2	327.2
A-3	R990106	5a_C	IIIa	Rounded	22.3	0.8			322.6		260.0		Halite	40.0	322.6
A-3	R990106	7a_A	IIIa	Faceted	19.9	0.8			256.9		284.7		Liquid	35.1	284.7
A-3	R990106	8a_F	IIIa	Faceted	6.8	0.8			215.0		203.1		Halite	32.7	215.0
A-3	R990108_A3	1a_A	IIIa	Irregular	28.6	0.9			274.5		261.7		Halite	36.3	274.5
A-3	R990085_A3	1a_A	IIIb	Irregular	12.7	0.8			456.1		235.2		Halite	54.0	456.1
A-3	R990085_A3	1a_C	IIIb	Faceted	7.6	0.9			267.5		228.3		Halite	35.8	267.5
A-3	R990085_A3	1b_D	IIIb	Faceted	11.7	0.9			280.1		232.4		Halite	36.7	280.1
A-3	R990085_A3	1b_E	IIIb	Faceted	8.2	0.9			303.9		198.6		Halite	38.5	303.9
A-3	R990085_A3	1b_F	IIIb	Faceted	12.8	0.9			393.2		200.8		Halite	46.7	393.2
A-3	R990085_A3	1d_C	IIIb	Faceted	8.6	0.9			228.9		233.1		Liquid	33.4	233.1
A-3	R990085_A3	1d_F	IIIb	Faceted	6.9	0.9			441.4		448.9		Liquid	52.2	448.9
A-3	R990085_A3	1e_A	IIIb	Faceted	10.1	0.8			276.4		254.0		Halite	36.4	276.4
A-3	R990085_A3	1e_B	IIIb	Rounded	7.5	0.9			468.1		243.4		Halite	55.5	468.1
A-3	R990085_A3	1e_C	IIIb	Faceted	4.8	0.8			385.0		239.9		Halite	45.8	385.0
A-3	R990085_A3	1e_D	IIIb	Faceted	6.5	0.8			287.7		224.9		Halite	37.2	287.7
A-3	R990085_A3	1e_E	IIIb	Irregular	5.9	0.9			593.0		213.7		Halite	73.0	593.0
A-3	R990085_A3	1f_A	IIIb	Faceted	4.8	0.8			441.8		431.0		Halite	52.3	441.8
A-3	R990085_A3	1f_B	IIIb	Irregular	8.3	0.9			414.1		370.4		Halite	49.0	414.1
A-3	R990085_A3	1g_A	IIIb	Faceted	5.4	0.8			469.0		448.7		Halite	55.7	469.0
A-3	R990085_A3	1i_C	IIIb	Irregular	13.2	0.9			170.6		229.7		Liquid	30.5	229.7
A-3	R990085_A3	1i_D	IIIb	Irregular	8.5	0.9			217.9		222.6		Liquid	32.8	222.6
A-3	R990085_A3	1k_A	IIIb	Irregular	12.5	0.8			443.2		247.3		Halite	52.4	443.2
A-3	R990085_A3	1k_B	IIIb	Faceted	11.0	0.9			437.4		240.5		Halite	51.7	437.4
A-3	R990085_A3	1l_A	IIIb	Faceted	11.9	0.8			457.0		219.9		Halite	54.1	457.0
A-3	R990085_A3	1l_B	IIIb	Faceted	13.5	0.8			311.9		232.2		Halite	39.1	311.9
A-3	R990085_A3	1l_C	IIIb	Faceted	16.4	0.8			415.1		249.2		Halite	49.1	415.1
A-3	R990085_A3	1l_D	IIIb	Rounded	8.7	0.8			299.3		261.9		Halite	38.1	299.3
A-3	R990085_A3	1l_F	IIIb	Rounded	5.7	0.8			449.4		250.5		Halite	53.2	449.4
A-3	R990085_A3	1l_F	IIIb	Faceted	6.5	0.8			424.9		244.6		Halite	50.2	424.9
A-3	R990106	10a_A	IIIb	Faceted	11.5	0.8			211.1		309.4		Liquid	32.4	309.4
A-3	R990106	10a_C	IIIb	Faceted	12.4	0.8			322.4		254.8		Halite	40.0	322.4
A-3	R990106	10a_E	IIIb	Irregular	37.5	0.8			300.5		447.0		Liquid	38.2	447.0
A-3	R990106	10b_A	IIIb	Faceted	10.8	0.9			321.4		230.3		Halite	39.9	321.4
A-3	R990106	10b_B	IIIb	Faceted	6.1	0.8			288.7		258.4		Halite	37.3	288.7
A-3	R990106	1g_A	IIIb	Rounded	17.4	1.0			241.1		255.6		Liquid	34.1	255.6
A-3	R990106	1g_B	IIIb	Faceted	27.1	0.9			184.1		264.6		Liquid	31.1	264.6
A-3	R990106	1h_A	IIIb	Faceted	17.4	0.9			342.4		235.3		Halite	41.7	342.4
A-3	R990106	1h_B	IIIb	Faceted	6.4	0.9			313.4		240.2		Halite	39.2	313.4
A-3	R990106	2a	IIIb	Irregular	25.2	0.9			267.1		268.7		Liquid	35.8	268.7
A-3	R990106	2b	IIIb	Faceted	7.8	0.9			322.9		221.7		Halite	40.0	322.9
A-3	R990106	2c_B	IIIb	Faceted	11.0	0.9			287.4		277.9		Halite	37.2	287.4
A-3	R990106	2c_C	IIIb	Faceted	8.3	0.9			220.5		365.1		Liquid	32.9	365.1
A-3	R990106	3a_A	IIIb	Faceted	24.2	0.9			326.4		250.6		Halite	40.3	326.4
A-3	R990106	3f	IIIb	Irregular	28.5	0.7			460.4		525.1	525.1	Liquid	54.6	525.1
A-3	R990106	5a_B	IIIb	Irregular	17.7	0.7			300.0		252.8		Halite	38.2	300.0
A-3	R990106	6c	IIIb	Irregular	38.7	0.9			297.8		245.4		Halite	38.0	297.8
A-3	R990106	7a_E	IIIb	Faceted	14.0	0.9			230.8		277.7		Liquid	33.5	277.7
A-3	R990106	7a_F	IIIb	Faceted	13.6	0.8			176.6		276.2		Liquid	30.8	276.2
A-3	R990106	7e_A	IIIb	Irregular	26.2	0.9			277.7		250.1		Halite	36.5	277.7
A-3	R990106	7e_C	IIIb	Faceted	15.4	0.9			371.1		248.6		Halite	44.4	371.1
A-3	R990106	7e_D	IIIb	Faceted	8.7	0.9			343.1		230.2		Halite	41.8	343.1
A-3	R990106	8a_A	IIIb	Faceted	7.0	0.8			324.0		198.4		Halite	40.1	324.0
A-3	R990106	8a_B	IIIb	Faceted	5.1	0.8			229.1		153.9		Halite	33.4	229.1
A-3	R990106	8a_C	IIIb	Faceted	14.3	0.8			336.6		538.7		Liquid	41.2	538.7
A-3	R990106	8a_D	IIIb	Faceted	7.5	0.8			218.2		180.2		Halite	32.8	218.2
A-3	R990106	8a_E	IIIb	Faceted	5.6	0.8			240.0		217.0		Halite	34.1	240.0
A-3	R990106	8b_A	IIIb	Faceted	9.0	0.8			278.9		205.6		Halite	36.6	278.9
A-3	R990106	9a_A	IIIb	Rounded	11.2	0.8			328.4		219.0		Halite	40.5	328.4
A-3	R990106	9a_B	IIIb	Faceted	6.9	0.9			302.8		191.9		Halite	38.4	302.8
A-3	R990106	9b	IIIb	Faceted	7.1	0.8			287.3		244.1		Halite	37.2	287.3
A-3	R990106	9c_A	IIIb	Faceted	7.3	0.9			407.7		224.5		Halite	48.3	407.7
A-3	R990106	9c_B	IIIb	Faceted	14.5	0.9			396.5		227.3		Halite	47.1	396.5
A-3	R990106	9c_C	IIIb	Faceted	8.9	0.8			413.1		365.6		Halite	48.9	413.1
A-3	R990106	9c_D	IIIb	Faceted	7.2	0.9			427.2		207.4		Halite	50.5	427.2
A-3	R990106	9c_E	IIIb	Faceted	7.2	0.9			378.3		241.5		Halite	45.2	378.3
A-3	R990106	9d	IIIb	Faceted	7.4	0.9			307.1		227.1		Halite	38.7	307.1
A-3	R990108_A3	2c_C	IIIb	Faceted	15.2	0.5			420.0		414.0	420.0	Halite	49.7	420.0
A-3	R990085_A3	1J	IIIc	Faceted	11.9	0.9			398.7	374.4	266.2		Halite	47.3	398.7
A-3	R990106	10a_B	IIIc	Faceted	11.0	0.9			320.2	64.1	168.3		Halite	39.8	320.2
A-3	R990106	2h	IIIc	Irregular	27.1	1.0			328.5	111.8	277.8	484.5	Halite	40.5	328.5
A-3	R990106	2i	IIIc	Faceted	26.2	0.9			355.1	89.0	278.1		Halite	42.9	355.1
A-3	R990106	3a_C	IIIc	Irregular	31.9	0.9			287.5	69.0	264.6		Halite	37.2	287.5
A-3	R990106	3a_D	IIIc	Irregular	13.9	0.9			276.4	61.4	259.8		Halite	36.4	276.4
A-3	R990106	3a_E	IIIc	Irregular	21.1	0.9			263.3	56.4	331.5		Liquid	35.5	331.5
A-3	R990106	5a_A	IIIc	Irregular	38.2	0.9			319.0	79.3	256.5		Halite	39.7	319.0
A-3	R990106	5a_D	IIIc	Rounded	17.7	0.9			290.0	75.3	123.5		Halite	37.4	290.0
A-3	R990106	7a_D	IIIc	Faceted	18.3	0.8			297.2	52.2	251.5		Halite	37.9	297.2
A-3	R990106	7d_B	IIIc	Faceted	15.0	0.9			306.5	64.4	259.0		Halite	38.7	306.5
A-3	R990106	7d_C	IIIc	Faceted	9.4	0.9			354.2	86.9	247.1		Halite	42.8	354.2
A-3	R990106	7e_B	IIIc	Faceted	11.2	0.9			462.0	107.1	235.1		Halite	54.8	462.0
A-3	R990108_A3	1e_A	IIIc	Irregular	21.1	0.9			282.8	136.3	362.1		Halite	36.9	362.1
A-3	R990106	3c	IV	Rounded	26.5	0.8			405.6		405.6		Liquid	48.1	405.6
B	R990106	1a	Ia	Irregular	35.8	0.9	-28.7	-4.8			338.6		Liquid	7.5	338.6
B	R990106	1d	Ia	Irregular	26.0	0.9		-2.8			360.3		Liquid	4.5	360.3
B	R990106	1f_A	Ia	Irregular	23.9	0.9		-6.1			321.2		Liquid	9.3	321.2
B	R990106	1f_B	Ia	Faceted	17.5	0.8	-35.6	-7.2			324.5		Liquid	10.7	324.5
B	R990106	2a_A	Ia	Irregular	30.0	0.8		-5.3			346.8		Liquid	8.2	346.8
B	R990106	2a_B	Ia	Irregular	19.9	0.9		-20.9			260.8		Liquid	23.0	260.8

Vein type	Sample	IncNum	Type (Nash 1976)	Shape	Size	Fill	Te	Tm_ice	Ts_hal	Ts_S2	Th_aq	Td Phase	EqWt%NaCl	T_total
B	R990106	2b_B	Ia	Irregular	10.6	0.9		-6.5			356.3	Liquid	9.8	356.3
B	R990106	2c	Ia	Rounded	15.9	0.7		-12.8			390.1	Liquid	16.7	390.1
B	R990106	3a_A	Ia	Irregular	16.7	0.9		-7.9			371.6	Liquid	11.6	371.6
B	R990106	3a_B	Ia	Irregular	18.6	0.9		-5.5			264.7	Liquid	8.5	264.7
B	R990106	3c_A	Ia	Irregular	32.4	0.8		-2.6			350.0	Liquid	4.2	350.0
B	R990106	3c_B	Ia	Irregular	16.7	0.9		-4.5			326.1	Liquid	7.1	326.1
B	R990106	3c_D	Ia	Rounded	7.1	0.6		-2.9			391.2	Liquid	4.7	391.2
B	R990106	3c_F	Ia	Rounded	12.7	0.6		-2.9			384.9	Liquid	4.7	384.9
B	R990106	3d_A	Ia	Rounded	25.9	0.6		-4.4			408.2	Vapour	7.0	408.2
B	R990106	3d_B	Ia	Faceted	10.9	0.9		-13.8			327.1	Liquid	17.6	327.1
B	R990106	4a_A	Ia	Irregular	36.4	0.8		-2.9			342.2	Liquid	4.7	342.2
B	R990106	4a_B	Ia	Rounded	15.3	0.8		-2.7			337.1	Liquid	4.4	337.1
B	R990106	4c_A	Ia	Rounded	17.8	0.7		-2.0			374.2	Liquid	3.3	374.2
B	R990106	4d	Ia	Irregular	13.7	0.7		-0.8			359.8	Liquid	1.3	359.8
B	R990106	4a_E	Ib	Rounded	12.3	0.8		-7.0			367.7	Liquid	10.5	367.7
B	R990106	3b	IIa	Irregular	13.9	0.7		-4.9			456.6	Vapour	7.7	456.6
B	R990106	3c_C	IIa	Irregular	23.2	0.6		-3.6			400.1	Vapour	5.8	400.1
B	R990106	4b	IIa	Irregular	27.8	0.5		-2.3			407.0	Vapour	3.8	407.0
B	R990106	4c_B	IIa	Rounded	16.6	0.5		-3.8			417.2	Vapour	6.1	417.2
B	R990106	4a_C	IIIb	Faceted	8.8	0.9			197.0		248.5	Liquid	31.7	248.5
B	R990106	1e	IIIc	Irregular	44.1	0.9			600.0	279.1	600.0	Liquid	74.0	600.0
C	R990085_C	1a	Ia	Faceted	5.3	0.9		-12.7			222.8	Liquid	16.6	222.8
C	R990085_C	1b	Ia	Irregular	8.7	0.8		-27.5			407.6	Liquid	26.9	407.6
C	R990085_C	2a_B	Ia	Faceted	4.6	0.7		-3.6			253.3	Liquid	5.8	253.3
C	R990085_C	2a_C	Ia	Faceted	3.1	0.8		-12.9			266.4	Liquid	16.8	266.4
C	R990085_C	2c_A	Ia	Faceted	3.5	0.8		-24.2			186.7	Liquid	25.0	186.7
C	R990085_C	2c_B	Ia	Irregular	4.6	0.8		-3.9			245.4	Liquid	6.2	245.4
C	R990085_C	2d_A	Ia	Irregular	8.3	0.8		-15.7			235.4	Liquid	19.2	235.4
C	R990085_C	3a_A	Ia	Irregular	4.4	0.8		-5.1			294.5	Liquid	8.0	294.5
C	R990085_C	3a_B	Ia	Faceted	3.7	0.8		-1.9			240.5	Liquid	3.1	240.5
C	R990085_C	3b_B	Ia	Faceted	4.3	0.8		-6.6			334.1	Liquid	10.0	334.1
C	R990085_C	2a_A	Ib	Faceted	11.2	0.9		-23.3			153.0	Liquid	24.5	153.0
C	R990085_C	2d_B	Ib	Faceted	4.3	0.9		-13.0			246.6	Liquid	16.9	246.6
C	R990085_C	2d_C	Ib	Faceted	4.7	0.9		-15.8			207.1	Liquid	19.3	207.1
C	R990085_C	2d_D	Ib	Irregular	4.7	0.8		-16.0			189.8	Liquid	19.4	189.8
C	R990085_C	2d_E	Ib	Faceted	3.6	0.8		-5.3			247.5	Liquid	8.2	247.5
C	R990085_C	3b_A	Ib	Irregular	5.2	0.8		-4.3			241.6	Liquid	6.8	241.6
C	R990085_C	3c_A	Ib	Faceted	6.8	0.9		-23.9			237.7	Liquid	24.8	237.7
C	R990085_C	3c_B	Ib	Faceted	4.5	0.8		-14.4			210.0	Liquid	18.1	210.0
C	R990085_C	3d_B	Ib	Faceted	6.8	0.8		-23.8			234.5	Liquid	24.8	234.5
C	R990085_C	2b_B	IIIa	Faceted	3.5	0.9			402.8		196.1	Halite	47.7	402.8
C	R990085_C	1c_C	IIIb	Faceted	7.5	0.9			419.3		289.1	Liquid	49.6	419.3
C	R990085_C	1d	IIIb	Faceted	5.7	0.9			282.2		228.9	Liquid	36.8	282.2
C	R990085_C	2b_A	IIIb	Faceted	6.8	0.9			314.1		202.0	Liquid	39.3	314.1
C	R990085_C	2b_C	IIIb	Faceted	4.0	0.9			433.1		199.9	Liquid	51.2	433.1
C	R990085_C	3b_C	IIIb	Faceted	6.4	0.9			294.5		196.0	Liquid	37.7	294.5
C	R990085_C	3e_A	IIIb	Faceted	8.8	0.9			443.2		218.2	Liquid	52.4	443.2
C	R990085_C	3e_E	IIIb	Faceted	7.9	0.9			302.5		205.7	Liquid	38.4	302.5
C	R990085_C	3e_F	IIIb	Faceted	10.0	0.9			500.0		232.2	Liquid	59.8	500.0
E	R200021	1a_A	Ia	Faceted	15.8	0.8	-34.9	-5.6			409.5	Liquid	8.6	409.5
E	R200021	1a_B	Ia	Faceted	8.4	0.8	-29.7	-4.4			307.9	Liquid	7.0	307.9
E	R200021	1b_D	Ia	Irregular	11.8	0.8	-28.1	-6.5			339.7	Liquid	9.8	339.7
E	R200021	1b_E	Ia	Irregular	10.3	0.9		-5.6			371.7	Liquid	8.6	371.7
E	R200021	1c_A	Ia	Faceted	11.3	0.5		-10.5			453.2	Liquid	14.5	453.2
E	R200021	1d_C	Ia	Rounded	12.0	0.7		-6.1			412.7	Liquid	9.3	412.7
E	R200021	1d_D	Ia	Irregular	9.7	0.9		-7.3			402.4	Liquid	10.9	402.4
E	R200021	1d_F	Ia	Faceted	14.3	0.7		-7.5			428.5	Liquid	11.1	428.5
E	R990170	1a_B	Ia	Irregular	7.3	0.9		-8.3			300.1	Liquid	12.1	300.1
E	R990170	1a_C	Ia	Irregular	11.5	0.8		-9.8			280.9	Liquid	13.7	280.9
E	R990170	1b_A	Ia	Irregular	8.5	0.9		-7.6			273.7	Liquid	11.2	273.7
E	R990170	1b_B	Ia	Irregular	13.5	0.9		-12.5			414.6	Liquid	16.4	414.6
E	R990170	1c_A	Ia	Irregular	13.8	0.8		-4.4			301.2	Liquid	7.0	301.2
E	R990170	2a_A	Ia	Irregular	8.2	0.8		-3.0			292.6	Liquid	4.9	292.6
E	R990170	2a_B	Ia	Irregular	16.2	0.7		-1.0			334.4	Liquid	1.7	334.4
E	R990170	2b	Ia	Faceted	11.4	0.7		-23.6			385.2	Liquid	24.6	385.2
E	R990170	3a_A	Ia	Faceted	6.2	0.7		-4.4			363.7	Liquid	7.0	363.7
E	R990170	3a_B	Ia	Faceted	7.3	0.8		-2.9			297.0	Liquid	4.7	297.0
E	R990170	3b_B	Ia	Irregular	8.0	0.9		-13.6			207.5	Liquid	17.4	207.5
E	R990170	3b_C	Ia	Irregular	10.7	0.7		-4.9			410.0	Liquid	7.7	410.0
E	R990170	1a_A	Ib	Irregular	9.5	0.7		-9.7			415.5	Liquid	13.6	415.5
E	R990170	3b_A	Ib	Irregular	9.2	0.8		-6.3			301.5	Liquid	9.6	301.5
E	R990037	1a_A	Ia	Rounded	9.9	0.7		-4.4			389.8	Liquid	7.0	389.8
E	R990037	1a_B	Ia	Faceted	7.0	0.8		-4.1			335.4	Liquid	6.5	335.4
E	R990037	1a_C	Ia	Faceted	5.0	0.8		-4.9			391.0	Liquid	7.7	391.0
E	R990037	1a_D	Ia	Irregular	11.7	0.8		-7.6			329.2	Liquid	11.2	329.2
E	R990037	1a_E	Ia	Faceted	7.4	0.8		-9.1			358.8	Liquid	13.0	358.8
E	R990037	1a_F	Ia	Irregular	19.4	0.8		-8.9			388.5	Liquid	12.7	388.5
E	R990037	2a	Ia	Irregular	11.2	0.9		-1.5			170.1	Liquid	2.5	170.1
E	R990037	3a_B	Ia	Faceted	22.3	0.8	-35.5	-5.6			401.1	Liquid	8.6	401.1
E	R990037	3a_C	Ia	Faceted	15.9	0.8	-45.4	-19.8			369.6	Liquid	22.2	369.6
E	R990037	3a_D	Ia	Faceted	14.5	0.6		-6.6			384.0	Liquid	10.0	384.0
E	R990037	3a_G	Ia	Faceted	18.8	0.8		-4.2			402.6	Liquid	6.7	402.6
E	R990037	3b_A	Ia	Irregular	20.4	0.9		-3.8			294.4	Liquid	6.1	294.4
E	R990037	3b_B	Ia	Faceted	12.2	0.7		-3.1			359.7	Liquid	5.0	359.7
E	R990037	3b_C	Ia	Faceted	9.4	0.7		-6.5			387.8	Liquid	9.8	387.8
E	R990037	3b_D	Ia	Faceted	14.5	0.8	-34.8	-5.0			386.7	Liquid	7.8	386.7
E	R990037	4a_A	Ia	Irregular	13.9	0.9	-46.2	-2.5			200.1	Liquid	4.1	200.1
E	R990037	4a_B	Ia	Irregular	11.1	0.8	-45.7	-22.0			350.1	Liquid	23.7	350.1
E	R990037	4b_A	Ia	Faceted	10.4	0.8		-1.0			273.4	Liquid	1.7	273.4
E	R990037	4b_B	Ia	Faceted	8.5	0.7		-21.7			392.9	Liquid	23.5	392.9
E	R990037	4c_B	Ia	Faceted	6.0	0.7		-1.9			394.1	Liquid	3.1	394.1
E	R990037	4c_C	Ia	Faceted	8.2	0.8		-4.7			392.8	Liquid	7.4	392.8
E	R990037	4d_A	Ia	Faceted	9.6	0.7		-3.4			399.2	Liquid	5.5	399.2
E	R990037	4d_B	Ia	Faceted	11.5	0.8	-45.4	-19.0			297.0	Liquid	21.7	297.0
E	R990037	5a_A	Ia	Faceted	14.4	0.8	-48.1	-18.9			314.6	Liquid	21.6	314.6
E	R990037	5a_B	Ia	Faceted	21.6	0.8		-20.2			346.1	Liquid	22.5	346.1
E	R990037	5a_C	Ia	Faceted	8.5	0.8		-20.8			331.8	Liquid	22.9	331.8
E	R990037	5a_D	Ia	Faceted	8.5	0.7		-5.2			390.3	Liquid	8.1	390.3
E	R990037	5a_E	Ia	Faceted	12.2	0.8		-10.2			275.7	Liquid	14.2	275.7
E	R990037	5b_A	Ia	Irregular	17.6	0.8		-1.7			273.3	Liquid	2.8	273.3
E	R990037	5b_B	Ia	Irregular	46.3	0.8		-0.9			302.3	Liquid	1.5	302.3
E	R990037	5b_C	Ia	Irregular	18.1	0.9		-12.5			300.7	Liquid	16.4	300.7
E	R990037	5c_A	Ia	Irregular	12.0	0.7		-0.4			359.8	Liquid	0.7	359.8
E	R990037	5c_B	Ia	Faceted	12.6	0.9		-1.0			266.7	Liquid	1.7	266.7
E	R990037	5c_C	Ia	Faceted	9.1	0.8		-3.2			213.5	Liquid	5.2	213.5

Vein type	Sample	IncNum	Type (Nash 1976)	Shape	Size	Fill	Te	Tm_ice	Ts_hal	Ts_S2	Th_aq	Td Phase	EqWt%NaCl	T_total
E	R990037	5c_D	Ia	Irregular	19.8	0.9		-3.0			218.9	Liquid	4.9	218.9
E	R990037	6a_A	Ia	Faceted	10.6	0.8		-21.9			411.5	Liquid	23.6	411.5
E	R990037	6a_B	Ia	Rounded	10.4	0.8		-16.7			377.1	Liquid	20.0	377.1
E	R990037	6a_C	Ia	Irregular	25.3	0.7		-8.0			386.0	Liquid	11.7	386.0
E	R990037	6a_F	Ia	Faceted	10.1	0.7		-13.3			441.7	Liquid	17.2	441.7
E	R990037	6a_G	Ia	Faceted	8.2	0.8		-23.4			383.2	Liquid	24.5	383.2
E	R990037	6b_B	Ia	Faceted	6.8	0.8		-2.9			313.2	Liquid	4.7	313.2
E	R990037	6b_C	Ia	Faceted	6.2	0.7		-3.5			428.7	Liquid	5.6	428.7
E	R990037	6b_D	Ia	Faceted	7.8	0.8		-0.1			281.8	Liquid	0.2	281.8
E	R990037	6b_E	Ia	Faceted	10.8	0.8		-0.2			278.5	Liquid	0.3	278.5
E	R990037	6b_F	Ia	Faceted	9.4	0.8		-1.9			314.5	Liquid	3.1	314.5
E	R990037	7a_A	Ia	Faceted	14.8	0.8		-1.9			272.3	Liquid	3.1	272.3
E	R990037	7a_B	Ia	Faceted	17.8	0.6		-9.5			444.7	Liquid	13.4	444.7
E	R990037	7a_E	Ia	Irregular	10.2	0.9		-1.2			275.5	Liquid	2.0	275.5
E	R990037	7a_F	Ia	Rounded	9.4	0.8		-1.4			296.8	Liquid	2.3	296.8
E	R990124_E	1a_B	Ia	Irregular	19.6	0.7	-35.5	-6.7			429.4	Liquid	10.1	429.4
E	R990124_E	1d_A	Ia	Rounded	19.1	0.9	-31.6				259.8	Liquid	25.0	259.8
E	R990124_E	1d_B	Ia	Faceted	16.5	0.7		-14.4			423.9	Liquid	18.1	423.9
E	R990124_E	1e_A	Ia	Faceted	18.9	0.7	-48.0	-14.1			380.8	Liquid	17.9	380.8
E	R990124_E	1f_E	Ia	Irregular	26.8	0.9		-3.3			318.6	Liquid	5.3	318.6
E	R990124_E	1h_A	Ia	Faceted	21.7	0.9	-40.2	-10.9			423.4	Liquid	14.9	423.4
E	R990124_E	1h_B	Ia	Irregular	16.3	0.9	-50.1	-8.0			398.6	Liquid	11.7	398.6
E	R990124_E	1i_A	Ia	Irregular	17.0	0.8	-41.8				316.5	Liquid	24.8	316.5
E	R990124_E	1j_B	Ia	Irregular	9.1	0.7		-6.3			411.3	Liquid	9.6	411.3
E	R990124_E	1a_A	Ib	Rounded	23.1	0.8	-40.2	-10.7			317.1	Liquid	14.7	317.1
E	R990124_E	1c_B	Ib	Rounded	13.2	0.9	-37.1				359.1	Liquid	24.9	359.1
E	R990124_E	1c_C	Ib	Rounded	10.2	0.9	-37.4				301.6	Liquid	24.9	301.6
E	R990124_E	1e_B	Ib	Irregular	25.7	0.9	-31.8				300.8	Liquid	25.2	300.8
E	R990037	3a_A	Ib	Irregular	28.5	0.8	-43.6	-16.5			377.6	Liquid	19.8	377.6
E	R990037	3a_E	Ib	Rounded	12.8	0.8		-16.0			273.9	Liquid	19.4	273.9
E	R990037	3a_F	Ib	Faceted	9.3	0.7		-4.7			397.4	Liquid	7.4	397.4
E	R990037	4c_A	Ib	Irregular	13.0	0.7		-3.6			395.3	Liquid	5.8	395.3
TES	R200021	2a_A	Ia	Irregular	10.8	0.9		-3.5			195.1	Liquid	5.6	195.1
TES	R200021	2b_A	Ia	Irregular	11.3	0.9		-1.7			213.4	Liquid	2.8	213.4
TES	R200021	2c_A	Ia	Irregular	10.0	0.9		-1.0			209.7	Liquid	1.7	209.7
TES	R200021	2c_B	Ia	Irregular	9.3	0.9		-0.7			208.0	Liquid	1.2	208.0
TES	R200021	2d_A	Ia	Irregular	16.0	0.9		-0.4			155.1	Liquid	0.7	155.1
TES	R200021	2e_A	Ia	Irregular	27.4	0.9		-2.1			253.7	Liquid	3.4	253.7
TES	R200021	2e_B	Ia	Irregular	13.8	0.9		-1.5			225.7	Liquid	2.5	225.7
TES	R200021	2f_A	Ia	Irregular	16.3	0.9		-1.7			254.9	Liquid	2.8	254.9
TES	R200021	2f_B	Ia	Irregular	6.2	0.9		-2.1			223.5	Liquid	3.4	223.5
TES	R200021	2f_C	Ia	Faceted	14.1	0.9		-3.1			280.3	Liquid	5.0	280.3
TES	R200021	3a_A	Ia	Faceted	10.7	0.9		-1.7			330.1	Liquid	2.8	330.1
TES	R200021	3a_B	Ia	Irregular	8.3	0.9		-1.0			286.6	Liquid	1.7	286.6
TES	R200021	3a_C	Ia	Irregular	9.3	0.8		-1.0			326.2	Liquid	1.7	326.2
TES	R200021	3a_D	Ia	Irregular	6.4	0.9		-1.5			269.9	Liquid	2.5	269.9
TES	R200021	3b_D	Ia	Faceted	7.8	0.9		-4.2			306.0	Liquid	6.7	306.0
TES	R200021	3c_A	Ia	Rounded	9.8	0.9		-3.7			297.6	Liquid	5.9	297.6
TES	R200021	3c_D	Ia	Faceted	6.4	0.9		-6.6			272.2	Liquid	10.0	272.2
TES	R200021	4b_B	Ia	Rounded	6.9	0.8		-2.3			328.7	Liquid	3.8	328.7
TES	R200021	3b_A	Ib	Faceted	16.6	0.9		-6.1			280.1	Liquid	9.3	280.1
TES	R200021	3b_B	Ib	Faceted	7.3	0.9		-10.3			252.1	Liquid	14.3	252.1
TES	R200021	3b_E	Ib	Faceted	12.2	0.9		-19.8			338.4	Liquid	22.2	338.4
TES	R200021	3b_F	Ib	Faceted	7.7	1.0		-18.7			287.7	Liquid	21.5	287.7
TES	R200021	3c_B	Ib	Faceted	10.2	0.9		-3.8			290.5	Liquid	6.1	290.5
TES	R200021	3c_F	Ib	Rounded	5.6	0.6		-5.1			363.5	Liquid	8.0	363.5
TES	R200021	3b_C	IIa	Rounded	17.5	0.6		-4.1			403.5	Vapour	6.5	403.5
TES	R200021	2a_B	IIIa	Irregular	14.2	0.9			300.5		222.0	Halite	38.2	300.5
TES	R200021	3c_C	IIIb	Faceted	9.9	0.9			241.9		192.3	Halite	34.2	241.9
TES	R200021	4a_A	IIIb	Faceted	12.0	0.9			276.6		189.4	Halite	36.4	276.6
TES	R990299	1a_A	Ia	Irregular	11.9	0.9		-1.1			245.3	Liquid	1.8	245.3
TES	R990299	1a_B	Ia	Faceted	12.5	0.8		-1.6			287.0	Liquid	2.6	287.0
TES	R990299	1a_C	Ia	Faceted	9	0.8		-0.5			310.4	Liquid	0.8	310.4
TES	R990299	1a_D	Ia	Faceted	8.2	0.8		-1.7			308.4	Liquid	2.8	308.4
TES	R990299	1a_E	Ia	Irregular	10.1	0.8		-0.6			294.9	Liquid	1.0	294.9
TES	R990299	1a_H	Ia	Irregular	24.1	0.9		-0.4			244.3	Liquid	0.7	244.3
TES	R990299	1a_I	Ia	Irregular	10	0.8		-2.1			297.9	Liquid	3.4	297.9
TES	R990299	1a_J	Ia	Irregular	10	0.9		-0.5			236.0	Liquid	0.8	236.0
TES	R990299	1a_K	Ia	Faceted	12.3	0.7		-1.1			273.3	Liquid	1.8	273.3
TES	R990299	1b_A	Ia	Rounded	8.5	0.8		-2.1			280.4	Liquid	3.4	280.4
TES	R990299	1b_B	Ia	Faceted	8.6	0.9		-1.1			306.9	Liquid	1.8	306.9
TES	R990324	1a_A	Ia	Irregular	14.2	0.8		-3.7			317.8	Liquid	5.9	317.8
TES	R990324	1a_B	Ia	Irregular	14.1	0.9		-3.2			270.1	Liquid	5.2	270.1
TES	R990324	1b_A	Ia	Faceted	11.4	0.9		-2.3			311.2	Liquid	3.8	311.2
TES	R990324	1b_B	Ia	Faceted	10.1	0.9		-0.6			342.0	Liquid	1.0	342.0
TES	R990324	1c	Ia	Rounded	14.0	0.9		-3.2			299.5	Liquid	5.2	299.5
TES	R990324	1d_A	Ia	Irregular	16.1	0.7	21.7	-3.2			319.5	Liquid	5.2	319.5
TES	R990324	1d_B	Ia	Irregular	13.3	0.8	-19.5	-2.4			323.3	Liquid	3.9	323.3
TES	R990324	2a_B	Ia	Irregular	7.2	0.9		-2.6			282.1	Liquid	4.2	282.1
TES	R990324	2b	Ia	Rounded	10.7	0.9		-2.0			309.1	Liquid	3.3	309.1
TES	R990324	2c	Ia	Irregular	10.2	0.9		-2.9			302.7	Liquid	4.7	302.7
TES	R990324	3a_A	Ia	Faceted	10.8	0.9		-2.7			299.1	Liquid	4.4	299.1
TES	R990324	3a_B	Ia	Irregular	11.5	0.9		-1.5			315.3	Liquid	2.5	315.3
TES	R990324	3a_C	Ia	Faceted	8.9	0.9		-3.1			290.7	Liquid	5.0	290.7
TES	R990324	3a_D	Ia	Rounded	6.1	0.8		-2.6			297.0	Liquid	4.2	297.0
TES	R990324	3a_E	Ia	Faceted	8.9	0.9		-4.3			295.0	Liquid	6.8	295.0
TES	R990324	3b_A	Ia	Faceted	13.9	0.9		-2.5			323.9	Liquid	4.1	323.9
TES	R990324	3b_B	Ia	Irregular	13.3	0.9		-3.8			323.9	Liquid	6.1	323.9
TES	R990324	3b_C	Ia	Faceted	18.5	0.8		-2.7			294.1	Liquid	4.4	294.1

APPENDIX 4

STABLE ISOTOPE DATA

See Rock Catalogue (Appendix 5) for sample information.

Vein types are those defined in Table 5.2.

Sample Number	Vein Type	Mineral	$\delta^{34}S$ (‰)	$\delta^{18}O$ (‰)	δD(‰)	H_2O (wt%)	T(°C)	$\delta^{18}O$ (‰)	δD (‰)
R990002	E	Pyrite	1.98						
R990003a	E	Pyrite	1.95						
R990021	E	Chalcopyrite	0.83						
R990023	E	Chalcopyrite	0.84						
R990037	E	Chalcopyrite	0.6						
R990059	D	Pyrite	1.24						
R990076	D	Pyrite	1.51						
R990084a	A-3	Chalcopyrite	-0.17						
R990084b	A-3	Chalcopyrite	-0.5						
R990084c	E	Pyrite	-0.08						
R990084d	A-3	Chalcopyrite	-0.18						
R990084e	E	Pyrite	-0.36						
R990089a	B	Molybdenite	1.38						
R990103a	A-2	Biotite		5.85			500	8.3	
R990103b	A-2	Biotite		5.6			500	8.0	
R990106a	A-3	Bornite	-3.18						
R990106b	A-3	Bornite	-2.1						
R990106c	A-3	Chalcopyrite	-0.83						
R990110	B	Molybdenite	2.03						
R990111	E	Chalcopyrite	1.01						
R990133a	A-2	Chalcopyrite	0.37						
R990133b	A-2	Chalcopyrite	-0.97						
R990133c	E	Pyrite	1.50						
R990133d	E	Pyrite	1.35						
R990137	B	Molybdenite	1.71						
R990155	E	Chalcopyrite	1.21						
R990188a	E	Alunite	21	11.7	-39	12	340	6.4	-33
R990188b	E	Pyrite	2.52						
R990188c	E	Alunite	21						
R990190a	TES	Pyrophyllite		9.68			270	-1.7	
R990190b	TES	Pyrophyllite		8.44			270	-2.9	
R990190c	TES	Pyrophyllite		9.76			270	-1.6	
R990190d	TES	Pyrophyllite		8.34			270	-3.0	
R990237a	E	Chalcopyrite	-3.25						
R990237b	E	Bornite	-1.21						
R990243	E	Chalcopyrite	-0.36						
R990247	E	Chalcopyrite	0.26						
R990293	E	Pyrite	1.45						
R990293a	E	Pyrite	0.53						
R990293b	E	Pyrite	-1.09						
R990297a	E	Pyrite	1.61						
R990297b	TES	Enargite	-0.68						
R990298	E	Pyrite	0.86						
R990298a	E	Bornite	-1.42						
R990298b	E	Bornite	-0.11						
R990299	E	Pyrite	1.18						
R990311	E	Pyrite	1.12						
R990324	E	Pyrite	1.60						
R990327	E	Alunite	23.2	13.1	-40	12	260	5.2	-28
R990327a	E	Alunite	23.2						
R990327b	E	Pyrite	0.97						
R990327c	E	Alunite	23.4						
R990463	E	Alunite	22.8						
R990463	E	Pyrite	2.44						
R200173	E	Alunite	23.1						

Sample Number	Vein Type	Mineral	$\delta^{34}S$ (‰)	$\delta^{18}O$ (‰)	δD(‰)	H_2O (wt%)	T(°C)	$\delta^{18}O$ (‰)	δD (‰)
R200002a	E	Chalcopyrite	-3.6						
R200002b	E	Chalcopyrite	-5.48						
R200002c	E	Bornite	-5.43						
R200002d	E	Bornite	-4.97						
R200002e	E	Pyrite	-2.07						
R200002f	E	Pyrite	-2.46						
R200002a	E	Chalcopyrite	2.06						
R200002c	E	Bornite	-1.92						
R200008	E	Pyrite	0.85						
R200009	E	Pyrite	1.34						
R200013	E	Chalcopyrite	1.76						
R200015	E	Chalcopyrite	-0.33						
R200015a	E	Chalcopyrite	-2.47						
R200015b	E	Chalcopyrite	-3.39						
R200015c	E	Bornite	-3.73						
R200015d	E	Bornite	-3.09						
R200015e	E	Pyrite	-3.02						
R200015f	E	Pyrite	-2.37						
R200016	E	Bornite	-0.04						
R200017	E	Pyrite	1.12						
R200020a	E	Bornite	-4.09						
R200020b	E	Chalcopyrite	-2.12						
R200020c	E	Pyrite	-0.65						
R200021	E	Chalcopyrite	-0.46						
R200021a	E	Chalcopyrite	-1.42						
R200021b	E	Chalcopyrite	-3.03						
R200023a	E	Pyrite	1.82						
R200024	E	Pyrite	2.02						
R200025a	E	Chalcopyrite	-2.81						
R200025b	E	Bornite	-0.95						
R200026a	E	Pyrite	1.17						
R200026b	E	Chalcopyrite	0.82						
R200027	E	Pyrite	0.72						
R200052a	E	Chalcopyrite	0.94						
R200052b	E	Bornite	-1.58						
R200052c	E	Pyrite	0.60						
R200068a	A-3	Chalcopyrite	-1.49						
R200068b	A-3	Chalcopyrite	-0.87						
R200089a	E	Chalcopyrite	-0.21						
R200089b	E	Chalcopyrite	-1.76						
R200089c	E	Bornite	-1.92						
R200089d	E	Bornite	-3.3						
R200089e	E	Pyrite	-0.76						
R200089f	E	Pyrite	-0.27						
R200089g	E	Pyrite	2.02						
R200101a	A-3	Bornite	-3.91						
R200101b	A-3	Bornite	0.54						
R200101c	A-3	Chalcopyrite	0.32						
R200101d	A-3	Chalcopyrite	1.17						
R200101e	A-3	Chalcopyrite	-1.66						
R200102	B	Molybdenite	1.78						
R200113a	A-3	Chalcopyrite	-0.83						
R200113b	A-3	Chalcopyrite	-2.74						
R200114	A-3	Chalcopyrite	-1.56						
R200120	A-3	Chalcopyrite	-1.33						
R200122a	A-3	Chalcopyrite	0.2						
R200122b	A-3	Chalcopyrite	-0.29						

Sample Number	Vein Type	Mineral	$\delta^{34}S$ (‰)	$\delta^{18}O$ (‰)	δD(‰)	H_2O (wt%)	T(°C)	$\delta^{18}O$ (‰)	δD (‰)
R200159	E	Alunite	22.4						
R200173	E	Pyrite	1.52						
R200173	E	Pyrite	1.52						

APPENDIX 5

Rock Sample Catalogue

UTas Catalogue#: University of Tasmania catalogue number.

Field#: Unique sample identifier give to drill core and surface outcrop samples.

Work completed: Type of work completed and sample types stored at the University of Tasmania rock store.

- HS: Hand specimen sample.
- PTS: Polished thin section.
- PB: Polished block.
- TS: Thin section.
- EMP: Electron microprobe analysis using PTS.
- XRF: Rock powder, fusion discs and pressed powder pills.
- ICPMS: Rock powder.
- S: Drilled powder or polished wafer for sulphur isotope analysis.
- O: Coarse crush residue of sample used in oxygen isotope analysis.
- D: Coarse crush residue of sample used in deuterium isotope analysis.
- U/Pb: Residual zircon separate used in U/Pb LA-ICMS analysis.
- $^{40}Ar/^{39}Ar$: Hand specimen and thin section of sample dated by the $^{40}Ar/^{39}Ar$ method.

UTas Catalogue#	Field sample#	Rock Name	Map grid	UTM North	UTM East	Drill Hole	Depth (m)	Country	State	Geographical Area	Mine/Prospect	Preparation
151447	R990002	Dacite	UTM Southern Hemisphere Zone 19	7681244.68	531341.89	C153	6.7	Chile	I Region	Collahuasi District	Rosario	PTS, S, EMP
151448	R990003	Dacite	UTM Southern Hemisphere Zone 19	7681244.68	531341.89	C153	7.5	Chile	I Region	Collahuasi District	Rosario	S
151449	R990004	Dacite	UTM Southern Hemisphere Zone 19	7681244.68	531341.89	C153	10.4	Chile	I Region	Collahuasi District	Rosario	XRF, ICPMS, RI
151450	R990007	Dacite	UTM Southern Hemisphere Zone 19	7681244.68	531341.89	C153	3.6	Chile	I Region	Collahuasi District	Rosario	PTS, FI, EMP
151451	R990008	Dacite	UTM Southern Hemisphere Zone 19	7681244.68	531341.89	C153	16.7	Chile	I Region	Collahuasi District	Rosario	XRF
151452	R990021	Rosario Porphyry	UTM Southern Hemisphere Zone 19	7681244.68	531341.89	C153	79.5	Chile	I Region	Collahuasi District	Rosario	PTS, S
151453	R990023	Andesite	UTM Southern Hemisphere Zone 19	7681244.68	531341.89	C153	110.35	Chile	I Region	Collahuasi District	Rosario	S
151454	R990037	Andesitic Sandstone	UTM Southern Hemisphere Zone 19	7681244.68	531341.89	C153	228.8	Chile	I Region	Collahuasi District	Rosario	PTS, FI, S
151455	R990046	Limestone	UTM Southern Hemisphere Zone 19	7681244.68	531341.89	C153	255.7	Chile	I Region	Collahuasi District	Rosario	TS
151456	R990059	Volcaniclastic Breccia	UTM Southern Hemisphere Zone 19	7681244.68	531341.89	C153	314	Chile	I Region	Collahuasi District	Rosario	S
151457	R990062	Limestone-Siltstone	UTM Southern Hemisphere Zone 19	7681244.68	531341.89	C153	318.2	Chile	I Region	Collahuasi District	Rosario	PTS, EMP
151458	R990063	Limestone-Siltstone	UTM Southern Hemisphere Zone 19	7681244.68	531341.89	C153	320	Chile	I Region	Collahuasi District	Rosario	TS
151459	R990076	Andesite	UTM Southern Hemisphere Zone 19	7681244.68	531341.89	C153	379.2	Chile	I Region	Collahuasi District	Rosario	TS, S
151460	R990084	Rosario Porphyry	UTM Southern Hemisphere Zone 19	7681235.59	531252.63	C155	33.4	Chile	I Region	Collahuasi District	Rosario	PTS, S, EMP
151461	R990085	Rosario Porphyry	UTM Southern Hemisphere Zone 19	7681235.59	531252.63	C155	37	Chile	I Region	Collahuasi District	Rosario	PTS, FI, EMP
151462	R990089	Dacite	UTM Southern Hemisphere Zone 19	7681235.59	531252.63	C155	123.4	Chile	I Region	Collahuasi District	Rosario	S
151463	R990092	Andesite	UTM Southern Hemisphere Zone 19	7681235.59	531252.63	C155	131	Chile	I Region	Collahuasi District	Rosario	PTS
151464	R990103	Rosario Porphyry	UTM Southern Hemisphere Zone 19	7681190.51	531102.56	C049	639.6	Chile	I Region	Collahuasi District	Rosario	O
151465	R990106	Rosario Porphyry	UTM Southern Hemisphere Zone 19	7681190.51	531102.56	C049	767.7	Chile	I Region	Collahuasi District	Rosario	PTS, FI, S
151466	R990108	Rosario Porphyry	UTM Southern Hemisphere Zone 19	7681190.51	531102.56	C049	871.6	Chile	I Region	Collahuasi District	Rosario	PTS, FI
151467	R990110	Dacite	UTM Southern Hemisphere Zone 19	7681328.30	531311.10	C158	4.8	Chile	I Region	Collahuasi District	Rosario	S
151468	R990111	Dacite	UTM Southern Hemisphere Zone 19	7681328.30	531311.10	C158	6.6	Chile	I Region	Collahuasi District	Rosario	S
151469	R990124	Dacite	UTM Southern Hemisphere Zone 19	7681328.30	531311.10	C158	102.8	Chile	I Region	Collahuasi District	Rosario	PTS, FI
151470	R990133	Dacite	UTM Southern Hemisphere Zone 19	7681328.30	531311.10	C158	232	Chile	I Region	Collahuasi District	Rosario	TS, S
151471	R990137	Dacite	UTM Southern Hemisphere Zone 19	7681328.30	531311.10	C158	293.9	Chile	I Region	Collahuasi District	Rosario	S, Re/Os
151472	R990143	Rosario Porphyry	UTM Southern Hemisphere Zone 19	7681190.51	531102.56	C049	681	Chile	I Region	Collahuasi District	Rosario	XRF, ICPMS
151473	R990145	Rosario Porphyry	UTM Southern Hemisphere Zone 19	7681190.51	531102.56	C049	895.9	Chile	I Region	Collahuasi District	Rosario	XRF, ICPMS, RI
151474	R990155	Rosario Porphyry	UTM Southern Hemisphere Zone 19	7681088.26	531098.69	C194	490.3	Chile	I Region	Collahuasi District	Rosario	S
151475	R990170	Collahuasi Porphyry	UTM Southern Hemisphere Zone 19	7680892.51	530801.71	C177	286.6	Chile	I Region	Collahuasi District	Rosario	PTS, FI
151476	R990173	Collahuasi Porphyry	UTM Southern Hemisphere Zone 19	7680892.51	530801.71	C177	380.52	Chile	I Region	Collahuasi District	Rosario	XRF
151477	R990188	Collahuasi Porphyry	UTM Southern Hemisphere Zone 19	7680892.51	530801.71	C177	447.3	Chile	I Region	Collahuasi District	Rosario	PTS, S, O, D, EMP
151478	R990190	Collahuasi Porphyry	UTM Southern Hemisphere Zone 19	7680892.51	530801.71	C177	449.7	Chile	I Region	Collahuasi District	Rosario	O
151479	R990206	Rosario Porphyry	UTM Southern Hemisphere Zone 19	7680892.51	530801.71	C177	616.4	Chile	I Region	Collahuasi District	Rosario	XRF
151480	R990214	Rhyodacite	UTM Southern Hemisphere Zone 19	7680989.50	531300.52	C190	66	Chile	I Region	Collahuasi District	Rosario	XRF
151481	R990237	Rosario Massive Sulphide Vein	UTM Southern Hemisphere Zone 19	7680989.50	531300.52	C190	367.1	Chile	I Region	Collahuasi District	Rosario	PTS, S, EMP
151482	R990243	Rosario Porphyry	UTM Southern Hemisphere Zone 19	7680989.50	531300.52	C190	401.3	Chile	I Region	Collahuasi District	Rosario	S
151483	R990247	Rosario Porphyry	UTM Southern Hemisphere Zone 19	7680989.50	531300.52	C190	503.8	Chile	I Region	Collahuasi District	Rosario	S
151484	R990252	Rhyodacite	UTM Southern Hemisphere Zone 19	7681088.42	531397.76	C189	46	Chile	I Region	Collahuasi District	Rosario	XRF
151485	R990254	Rhyodacite	UTM Southern Hemisphere Zone 19	7681088.42	531397.76	C189	66.1	Chile	I Region	Collahuasi District	Rosario	TS
151486	R990259	Rhyodacite	UTM Southern Hemisphere Zone 19	7681088.42	531397.76	C189	111.9	Chile	I Region	Collahuasi District	Rosario	TS, U/Pb
151487	R990260	Rhyodacite	UTM Southern Hemisphere Zone 19	7681088.42	531397.76	C189	114.9	Chile	I Region	Collahuasi District	Rosario	XRF, ICPMS, RI
151488	R990277	Ocoita Andesite	UTM Southern Hemisphere Zone 19	7680141.00	529399.00	GC198	142.4	Chile	I Region	Collahuasi District	Rosario	HS
151489	R990293	La Grande Massive Sulphide Vein	UTM Southern Hemisphere Zone 19	7680141.00	529399.00	GC198	292.6	Chile	I Region	Collahuasi District	Rosario	PTS, PB, S, EMP
151490	R990297	La Grande Massive Sulphide Vein	UTM Southern Hemisphere Zone 19	7680141.00	529399.00	GC198	303.45	Chile	I Region	Collahuasi District	Rosario	PTS, S
151491	R990298	La Grande Massive Sulphide Vein	UTM Southern Hemisphere Zone 19	7680141.00	529399.00	GC198	316.1	Chile	I Region	Collahuasi District	Rosario	PTS, S
151492	R990299	La Grande Massive Sulphide Vein	UTM Southern Hemisphere Zone 19	7680141.00	529399.00	GC198	322.2	Chile	I Region	Collahuasi District	Rosario	PTS, S

Appendix 5-2. *Rock Catalogue*

UTas Catalogue#	Field sample#	Rock Name	Map grid	UTM North	UTM East	Drill Hole	Depth (m)	Country	State	Geographical Area	Mine/Prospect	Preparation
151493	R990311	Andesite	UTM Southern Hemisphere Zone 19	7680141.00	529399.00	GC198	474.8	Chile	I Region	Collahuasi District	Rosario	PTS, S, EMP
151494	R990314	Amygdaloidal Andesite	UTM Southern Hemisphere Zone 19	7680141.00	529501.00	GC201	329.7	Chile	I Region	Collahuasi District	Rosario	TS
151495	R990324	La Grande Massive Sulphide Vein	UTM Southern Hemisphere Zone 19	7680141.00	529501.00	GC201	717.25	Chile	I Region	Collahuasi District	Rosario	PTS, FI, S
151496	R990327	Dacite	UTM Southern Hemisphere Zone 19	7681235.59	531252.63	C155	10	Chile	I Region	Collahuasi District	Rosario	S, O, D
151497	R990463	Collahuasi Porphyry	UTM Southern Hemisphere Zone 19	7680892.51	530801.71	C177	484	Chile	I Region	Collahuasi District	Rosario	S
151498	R200002	Rosario Massive Sulphide Vein	UTM Southern Hemisphere Zone 19	7681323.58	531311.59	C140	61	Chile	I Region	Collahuasi District	Rosario	PTS, S, Re/Os
151499	R200008	Rosario Massive Sulphide Vein	UTM Southern Hemisphere Zone 19	7681793.47	530701.17	C164	434.6	Chile	I Region	Collahuasi District	Rosario	PTS, S
151500	R200009	Rosario Massive Sulphide Vein	UTM Southern Hemisphere Zone 19	7681793.47	530701.17	C164	532.5	Chile	I Region	Collahuasi District	Rosario	PTS, S
151501	R200013	Rosario Massive Sulphide Vein	UTM Southern Hemisphere Zone 19	7680890.11	531390.49	C175	318	Chile	I Region	Collahuasi District	Rosario	PTS, S
151502	R200015	Rosario Massive Sulphide Vein	UTM Southern Hemisphere Zone 19	7681293.10	531102.20	C178	258.5	Chile	I Region	Collahuasi District	Rosario	PTS, S
151503	R200016	Rosario Massive Sulphide Vein	UTM Southern Hemisphere Zone 19	7681293.10	531102.20	C178	260	Chile	I Region	Collahuasi District	Rosario	PTS, S
151504	R200017	Rosario Massive Sulphide Vein	UTM Southern Hemisphere Zone 19	7681643.12	530751.94	C183	123.1	Chile	I Region	Collahuasi District	Rosario	PTS, S
151505	R200020	Rosario Massive Sulphide Vein	UTM Southern Hemisphere Zone 19	7680901.93	531501.33	C283	374.4	Chile	I Region	Collahuasi District	Rosario	PTS, S
151506	R200021	Rosario Massive Sulphide Vein	UTM Southern Hemisphere Zone 19	7680901.93	531501.33	C283	544	Chile	I Region	Collahuasi District	Rosario	PTS, FI, S, EMP
151507	R200023	Rosario Massive Sulphide Vein	UTM Southern Hemisphere Zone 19	7681000.26	531099.80	C284	503.6	Chile	I Region	Collahuasi District	Rosario	PTS, S
151508	R200024	Rosario Massive Sulphide Vein	UTM Southern Hemisphere Zone 19	7681099.88	530900.05	C285	560.5	Chile	I Region	Collahuasi District	Rosario	PTS, S
151509	R200025	Rosario Massive Sulphide Vein	UTM Southern Hemisphere Zone 19	7681724.29	530587.74	C289	368.8	Chile	I Region	Collahuasi District	Rosario	PTS, S
151510	R200026	Rosario Massive Sulphide Vein	UTM Southern Hemisphere Zone 19	7681349.85	530950.60	C293	288	Chile	I Region	Collahuasi District	Rosario	PTS, S
151511	R200027	Rosario Massive Sulphide Vein	UTM Southern Hemisphere Zone 19	7681503.54	530485.44	C296	583.8	Chile	I Region	Collahuasi District	Rosario	PTS, S
151512	R200030	Inca Porphyry	UTM Southern Hemisphere Zone 19	7678993.00	538006.00	UC 392	481.25	Chile	I Region	Collahuasi District	Ujina	PTS, EMP
151513	R200031	Ujina Porphyry	UTM Southern Hemisphere Zone 19	7678792.00	537907.00	UC 467	423.5	Chile	I Region	Collahuasi District	Ujina	XRF, ICPMS, RI
151514	R200032	Ujina Porphyry	UTM Southern Hemisphere Zone 19	767994.00	537208.00	UC426	636.8	Chile	I Region	Collahuasi District	Ujina	XRF, ICPMS, RI
151515	R200035	Ujina Porphyry	UTM Southern Hemisphere Zone 19	7678940.00	537658.00	UC447	514	Chile	I Region	Collahuasi District	Ujina	PTS, EMP
151516	R200040	La Profunda Porphyry	UTM Southern Hemisphere Zone 19	7676800.00	539453.00	UC612	178.5	Chile	I Region	Collahuasi District	Ujina	PTS, EMP
151517	R200041	La Profunda Porphyry	UTM Southern Hemisphere Zone 19	7676800.00	539453.00	UC612	189	Chile	I Region	Collahuasi District	Ujina	XRF, ICPMS, RI
151518	R200052	Massive Sulphide Vein	UTM Southern Hemisphere Zone 19	7681292.27	531202.07	C084	272	Chile	I Region	Collahuasi District	Rosario	PTS, S
151519	R200064	Dacite	UTM Southern Hemisphere Zone 19	7681398.52	531342.08	C124	261.2	Chile	I Region	Collahuasi District	Rosario	PTS, xrf, ICPMS, ri
151520	R200065	Collahuasi Porphyry	UTM Southern Hemisphere Zone 19	7680993.17	530597.82	C168	43	Chile	I Region	Collahuasi District	Rosario	XRF
151521	R200068	Collahuasi Porphyry	UTM Southern Hemisphere Zone 19	7680993.17	530597.82	C168	433.9	Chile	I Region	Collahuasi District	Rosario	PTS, S
151522	R200079	Rosario Porphyry	UTM Southern Hemisphere Zone 19	7681235.59	531252.63	C155	35.5	Chile	I Region	Collahuasi District	Rosario	XRF, ICPMS
151523	R200085	Collahuasi Porphyry	UTM Southern Hemisphere Zone 19	7680691.87	531503.79	C281	221.2	Chile	I Region	Collahuasi District	Rosario	XRF, ICPMS, U/Pb
151524	R200089	Rosario Porphyry	UTM Southern Hemisphere Zone 19	7681363.12	531247.64	C288	267.3	Chile	I Region	Collahuasi District	Rosario	PTS, S
151525	R200092	Rosario Porphyry	UTM Southern Hemisphere Zone 19	7681363.12	531247.64	C288	279.9	Chile	I Region	Collahuasi District	Rosario	XRF, ICPMS
151526	R200101	Sandstone	UTM Southern Hemisphere Zone 19	7681363.12	531247.64	C288	365.9	Chile	I Region	Collahuasi District	Rosario	PTS, S
151527	R200102	Rosario Porphyry	UTM Southern Hemisphere Zone 19	7681363.12	531247.64	C288	369.8	Chile	I Region	Collahuasi District	Rosario	S
151528	R200107	Collahuasi Porphyry	UTM Southern Hemisphere Zone 19	7681199.25	530800.68	C291	287.1	Chile	I Region	Collahuasi District	Rosario	PTS, EMP
151529	R200113	Collahuasi Porphyry	UTM Southern Hemisphere Zone 19	7681199.25	530800.68	C291	499.5	Chile	I Region	Collahuasi District	Rosario	PTS, XRF, S
151530	R200114	Collahuasi Porphyry	UTM Southern Hemisphere Zone 19	7681199.25	530800.68	C291	548.9	Chile	I Region	Collahuasi District	Rosario	PTS, S
151531	R200116	Rosario Porphyry	UTM Southern Hemisphere Zone 19	7681199.25	530800.68	C291	705	Chile	I Region	Collahuasi District	Rosario	XRF
151532	R200117	Collahuasi Porphyry	UTM Southern Hemisphere Zone 19	7681349.85	530950.60	C293	250.4	Chile	I Region	Collahuasi District	Rosario	HS
151533	R200120	Collahuasi Porphyry	UTM Southern Hemisphere Zone 19	7681349.85	530950.60	C293	369.2	Chile	I Region	Collahuasi District	Rosario	S
151534	R200122	Rosario Porphyry	UTM Southern Hemisphere Zone 19	7681349.85	530950.60	C293	480	Chile	I Region	Collahuasi District	Rosario	S
151535	R200124	Rosario Porphyry	UTM Southern Hemisphere Zone 19	7681001.93	530895.34	C316	360.4	Chile	I Region	Collahuasi District	Rosario	PTS, EMP
151536	R200129	Rosario Porphyry	UTM Southern Hemisphere Zone 19	7681001.93	530895.34	C316	470.1	Chile	I Region	Collahuasi District	Rosario	XRF
151537	R200130	Rosario Porphyry	UTM Southern Hemisphere Zone 19	7681001.93	530895.34	C316	470.5	Chile	I Region	Collahuasi District	Rosario	PTS, EMP
151538	R200135	Rosario Porphyry	UTM Southern Hemisphere Zone 19	7681001.93	530895.34	C316	554.6	Chile	I Region	Collahuasi District	Rosario	PTS, EMP

Appendix 5-3. *Rock Catalogue*

UTas Catalogue#	Field sample#	Rock Name	Map grid	UTM North	UTM East	Drill Hole	Depth (m)	Country	State	Geographical Area	Mine/Prospect	Preparation
151539	R200142	Collahuasi Porphyry	UTM Southern Hemisphere Zone 19	7681001.93	530895.34	C316	308.2	Chile	I Region	Collahuasi District	Rosario	XRF, ICPMS, RI
151540	R200143	Collahuasi Porphyry	UTM Southern Hemisphere Zone 19	7681001.93	530895.34	C316	314.7	Chile	I Region	Collahuasi District	Rosario	PTS, EMP
151541	R200145	Dacite	UTM Southern Hemisphere Zone 19	7681542.06	531152.38	C228	179.5	Chile	I Region	Collahuasi District	Rosario	XRF
151542	R200146	Dacite	UTM Southern Hemisphere Zone 19	7681235.59	531252.63	C155	177	Chile	I Region	Collahuasi District	Rosario	XRF
151543	R200152	Rosario Porphyry	UTM Southern Hemisphere Zone 19	7681001.93	530895.34	C316	363.8	Chile	I Region	Collahuasi District	Rosario	PTS, $^{40}Ar/^{39}Ar$
151544	R200153	Rosario Porphyry	UTM Southern Hemisphere Zone 19	7681235.59	531252.63	C155	32.9	Chile	I Region	Collahuasi District	Rosario	PTS, $^{40}Ar/^{39}Ar$
151545	R200154	Ujina Porphyry	UTM Southern Hemisphere Zone 19	7678940.00	537658.00	UC447	510.3	Chile	I Region	Collahuasi District	Ujina	PTS, $^{40}Ar/^{39}Ar$
151546	R200155	Inca Porphyry	UTM Southern Hemisphere Zone 19	7678993.00	538006.00	UC392	485.8	Chile	I Region	Collahuasi District	Ujina	PTS, $^{40}Ar/^{39}Ar$
151547	R200156	La Profunda Porphyry	UTM Southern Hemisphere Zone 19	7676800.00	539453.00	UC612	178.3	Chile	I Region	Collahuasi District	Ujina	PTS, $^{40}Ar/^{39}Ar$
151548	R200157	Collahuasi Porphyry	UTM Southern Hemisphere Zone 19	7680892.51	530801.71	C177	447.3	Chile	I Region	Collahuasi District	Rosario	PTS, $^{40}Ar/^{39}Ar$
151549	R200158	Sandstone	UTM Southern Hemisphere Zone 19	7680141.00	529399.00	GC198	335.5	Chile	I Region	Collahuasi District	Rosario	PTS, $^{40}Ar/^{39}Ar$
151550	R200159	Sandstone	UTM Southern Hemisphere Zone 19	7680141.00	529399.00	GC198	335.5	Chile	I Region	Collahuasi District	Rosario	PTS, $^{40}Ar/^{39}Ar$
151551	R200171	Dacite	UTM Southern Hemisphere Zone 19	7681235.59	531252.63	C155	10	Chile	I Region	Collahuasi District	Rosario	XRF
151552	R200173	Collahuasi Porphyry	UTM Southern Hemisphere Zone 19	7680892.51	530801.71	C177	293	Chile	I Region	Collahuasi District	Rosario	S
151553	ROS038	Rhyodacite	UTM Southern Hemisphere Zone 19	7681606.00	530781.00			Chile	I Region	Collahuasi District	Rosario	TS

Appendix 5-4. *Rock Catalogue*